
Electronic Thesis and Dissertation Repository

2-2-2024 11:00 AM

Modeling thermosyphon and heat pipe performance for mold cooling applications

Dwaipayan Sarkar,

Supervisor: DeGroot, Christopher, *The University of Western Ontario*

Co-Supervisor: Savory, Eric, *The University of Western Ontario*

A thesis submitted in partial fulfillment of the requirements for the Doctor of Philosophy degree in Mechanical and Materials Engineering

© Dwaipayan Sarkar 2024

Follow this and additional works at: <https://ir.lib.uwo.ca/etd>



Part of the [Energy Systems Commons](#), [Fluid Dynamics Commons](#), [Heat Transfer, Combustion Commons](#), and the [Other Mechanical Engineering Commons](#)

Recommended Citation

Sarkar, Dwaipayan, "Modeling thermosyphon and heat pipe performance for mold cooling applications" (2024). *Electronic Thesis and Dissertation Repository*. 9942.
<https://ir.lib.uwo.ca/etd/9942>

This Dissertation/Thesis is brought to you for free and open access by Scholarship@Western. It has been accepted for inclusion in Electronic Thesis and Dissertation Repository by an authorized administrator of Scholarship@Western. For more information, please contact wlsadmin@uwo.ca.

Abstract

Thermosyphons are enhanced heat transfer devices that can continuously transfer very large amounts of heat rapidly over long distances with small temperature difference. The high heat transfer rate is achieved through simultaneous boiling and condensation of the working fluid and the continuous heat transfer is achieved through recirculation of the working fluid in its liquid and vapor phase. A potentially important application of the thermosyphons have been towards reducing the cycle times of the mold cooling processes which would provide economic incentives to the automotive industry.

Different operational and geometrical parameters such as the input heating power, fill ratio (FR), aspect ratio (AR) and orientation influence the thermodynamic state of the working fluid and the boiling and condensation thermal resistances. The goal of the present work is to develop a more rigorous understanding of the thermal performance of thermosyphons as a function of their design parameters and operating conditions.

A thermodynamic model is developed to predict the thermodynamic state of the working fluid its related properties inside a thermosyphon and heat pipe at each stage of the thermodynamic cycle. The model can be used to predict the operating temperature of a thermosyphon and a heat pipe under a given geometrical and operating condition.

The existing predictive heat transfer correlations for estimating the boiling and condensation thermal resistances for thermosyphons are inadequate and lack consistency. Using non-dimensional analysis based on the Buckingham-pi theorem, a series of new analytical thermal resistance equations capable of predicting the boiling and condensation thermal resistance under different operational parameters are developed.

The thermal performance of ten distilled-water copper thermosyphons are experimentally investigated by varying the input heating power between 6.68 [W] and 32.98 [W], fill ratio between 0.35 - 0.75 and aspect ratio between 5.33 and 12.43 to understand the relationship between these operating parameters and the boiling and condensation thermal resistances.

The present experimental data when compared to the new thermal resistance expressions showed excellent agreement ($\pm 15\%$). The previous experimental data, however, showed a slightly worse agreement ($\pm 30\%$), which could be attributed to the overall energy balance and the uncertainties in the reported fill ratio. The results from this work can be useful for selecting thermosyphons for specific applications and optimize the existing designs of thermosyphons.

Keywords

Thermosyphons, heat pipes, heat transfer, mold cooling, thermodynamics, boiling, condensation, input heating power, aspect-ratio, fill-ratio, Buckingham pi-theorem, prediction, thermal resistance, copper thermosyphon.

Summary for Lay Audience

Thermosyphons (heat pipes), resemble copper pipes, have the ability to transport heat very rapidly (250 times that of regular copper pipes) from one location to another within a short period. This feature is used to cool mobile phones and laptops and provide heat inside buildings. Thermosyphons are used extensively in automotive mold manufacturing, heating ventilation and air-conditioning, and in spacecraft applications.

The device combines the effects of both conduction and phase-change heat transfer to achieve very high heat transfer rates. The present work aims to investigate the thermal performance of thermosyphons under different operating conditions encountered in various thermal system engineering applications. These conditions include variable dimensions (length and diameter of the thermosyphons), different working fluids and different orientations required in various engineering scenarios.

The study focuses on predicting an optimal combination of various operating to achieve the desired heat transfer rate. Both analytical methods and experiments are used to investigate the current problem.

The optimised thermosyphon thermal performance could serve as an effective solution to many thermal management problems, reducing the financial costs for heating ventilation and air-conditioning (HVAC) and mold technology companies in Canada.

Co-Authorship Statement

This thesis has been prepared in accordance with the regulations for a Monograph format thesis, as stipulated by the School of Graduate and Postdoctoral studies at The University of Western Ontario. This thesis includes co-authored articles and the following passages explicitly state the contributors, and the nature and extent of their contribution.

Chapter 2: Investigation of the influence of the operating parameters on the thermal performance of thermosyphons from previous studies

The synthesis and analysis of the previous experimental data was carried out by D. Sarkar, under the guidance of E. Savory and C. DeGroot. The text was primarily written by D. Sarkar, whilst E. Savory and C. DeGroot reviewed the results and final version of the chapter.

Results from Chapter 2 along with excerpts from Chapter 1 will be submitted for publication as a research article under the co-authorship of Sarkar, D and Savory, E and DeGroot, C.

Chapter 3: Thermodynamic modelling of thermosyphons and heat pipes

D. Sarkar developed the thermodynamic model under the guidance of E. Savory and C. DeGroot. The first draft of the chapter was written by D. Sarkar, whilst E. Savory and C. DeGroot contributed by reviewing the results and by providing important comments and providing recommendations for editing the manuscript.

Results from Chapter 3 along with excerpts from Chapter 1 is published as Thermodynamic modelling of thermosyphons and heat pipes in Physics of Fluids under the co-authorship of Sarkar, D and Savory, E and DeGroot, C.

Chapter 4: Predicting the boiling and condensation thermal resistance of the thermosyphons and heat pipes

D. Sarkar derived the boiling and condensation thermal resistance equations under the guidance of E. Savory and C. DeGroot. Z. Fan assisted in procuring the data from the previous literature. Excerpts from this Chapter and the results from Chapter 7 will be published as an article under the co-authorship of Sarkar, D and Savory, E and DeGroot C.

Chapter 6: Experimental results and Discussion

D. Sarkar designed and conducted the experiments with assistance from Sebastian Sanchez under the guidance of E. Savory and C. DeGroot. S. Sanchez and Z. Fan helped in troubleshooting experimental issues. D. Sarkar performed all the analysis of the experimental results under the guidance of E. Savory and C. DeGroot. Sebastian Sanchez plotted some preliminary results from the experiments under the guidance of D. Sarkar. The results from this Chapter along with experimental methodology from Chapter 5 will be published under the co-authorship of Sarkar, D, Sanchez, S, Savory, E and DeGroot, C.

To all the young minds out there.....

“The task is not to see what has never been seen before, but to think what has never been thought before”

-Arthur Schopenhauer

“Some scientists are born gifted; others build their successes on extreme perseverance and excessive effort”

-Unknown

Acknowledgments

No words can adequately express the gratitude that I owe to my supervisors, Dr. Eric Savory and Dr. Christopher DeGroot, for their unwavering support and patience over the past five years. Their mentorship has been instrumental in shaping me into an independent researcher. I would also like to thank my advisory committee members, Dr. Anthony Straatman and Dr. Kelly Ogden, for their patience and constructive suggestions during this journey.

I would like to express my sincere gratitude to John Hodgins, CEO of Acrolab Ltd., and Franklin Paul, lead engineer of Acrolab Ltd., for their continuous belief in me over the past five years. Acrolab Ltd. also partly sponsored this project.

Special appreciation goes to Eugene Porter, Ron Struke, Trent Steensma, and Robert Barbeito from the university electronics shop for their help in guiding me in setting up the necessary electronics for the experimental phase of this research.

I am also grateful to Cody Ruthman and colleagues from the University Machine Services (UMS) for their assistance in machining parts required to set up the experiment.

Thanks to Paul Sheller and Stephen Mallinson for their help in procuring the required items for the experiments.

I am grateful to Sebastian Sanchez and Zichen Fan for imparting fresh impetus to the experimental part of the project. Countless discussions with them have significantly contributed to the success of the experiments.

I acknowledge the support from my colleagues in the Advanced Fluid Mechanics Group, (Haoran Du, Niall Banning, Kyle Graat, Dr. Mark Parker, Shivani Jariwala). They have been very supportive throughout my research progression and always been available for a discussion.

Thanks to my former colleagues Dr. Shoyon Panday, Glen Dsouza and Raj Kumar Maloth for engaging discussions on various research topics.

I express gratitude for the financial support received from the MITACS Accelerate Program and the Department of Mechanical and Materials Engineering at Western University, and the Natural Sciences and Engineering Research Council (NSERC) of Canada.

Lastly, I am deeply thankful to my parents, Luna Sarkar and Dulal Chandra Sarkar, for their support at all times. I would like to express my gratitude to my friends in London, ON for adding joy to my life.

Table of Contents

Abstract.....	ii
Summary for Lay Audience.....	iv
Co-Authorship Statement.....	v
Acknowledgments.....	viii
Table of Contents.....	x
List of Tables.....	xvi
List of Figures.....	xxiii
List of Appendices.....	xxxvi
List of Abbreviations.....	xxxvii
List of Symbols.....	xxxviii
Subscripts.....	xlviii
Chapter 1.....	1
1 Introduction and background.....	1
1.1 HP and TS definitions and working principles.....	1
1.2 Theoretical background.....	6
1.2.1 The fluid mechanics of HP and TS.....	6
1.2.2 The thermodynamics of TS and HP.....	14
1.2.3 The Heat transfer theory of TS and HP.....	15
1.3 Review of previous work on TS and HP.....	19
1.4 Motivation and objectives of the present research.....	23
1.5 Scope of the present work.....	24
1.6 Thesis Organization.....	24
1.7 Summary.....	26

Chapter 2.....	27
2 Synthesis and analysis of the previous thermosyphon data	27
2.1 Effects of Q_{in} on the thermal performance of TS.....	28
2.1.1 Evaluation of the temperature distribution	28
2.1.2 Evaluation of the boiling thermal resistance, R_{boil}	31
2.1.3 Evaluation of the condensation thermal resistance, R_{cond}	39
2.1.4 Condensate flow states.....	43
2.1.5 Interim summary.....	47
2.2 Effects of the FR on the thermal performance of TS.....	48
2.2.1 Effects of FR on the temperature distribution.....	48
2.2.2 Evaluation of the pool boiling thermal resistance ($R_{B,P}$)	50
2.2.3 Evaluation of the film boiling resistance ($R_{B,F}$).....	53
2.2.4 Evaluation of the condensation thermal resistance, $R_{C,F}$	54
2.2.5 Interim summary.....	58
2.3 Summary and recommendations.....	58
Chapter 3.....	59
3 Thermodynamic modelling of a thermosyphon and a heat pipe	59
3.1 Previous thermodynamic studies and their deficiencies	60
3.2 Evaluation of the entropy changes of the thermodynamic processes inside a TS and a HP	66
3.2.1 Entropy change during process CF inside a TS	69
3.2.2 Entropy change during process CF inside a HP.....	73
3.2.3 Entropy change during process DE in a TS	77
3.2.4 Entropy change during process DE in a HP.....	81
3.2.5 Entropy change during process HA	85
3.2.6 Summary of the equations	92

3.3	Methods to validate the abovementioned analytical expressions	93
3.3.1	Experimental method	93
3.3.2	Numerical method (using computation fluid dynamics (CFD))	94
3.4	Other sources of entropy generation and its minimization	94
3.4.1	Entropy generation at the evaporator and the condenser wall	95
3.4.2	Entropy generation along the vapour flow	97
3.4.3	Entropy generation during boiling and the condensation process	98
3.4.4	Entropy generation due to the condensate flow in the condenser	98
3.5	Conclusions	99
Chapter 4		100
4	Predicting the boiling and condensation thermal resistance of a thermosyphon and a heat pipe	100
4.1	Evaluation of the previous expressions of boiling (R_{boil}) and the condensation (R_{cond}) thermal resistances	101
4.2	Identification of different boiling regimes	103
4.2.1	Pool boiling regime	103
4.2.2	Film boiling regime	105
4.3	Development of new correlations for R_{boil}	107
4.3.1	Expression for R_{boil} for natural convection in the liquid pool	109
4.3.2	Expression of R_{boil} for nucleate boiling in the liquid pool	113
4.3.3	Expression of R_{boil} for film evaporation	115
4.3.4	Expression of R_{boil} for the film nucleate boiling	118
4.4	Effects of θ on the liquid pool length, L_p	121
4.4.1	Critical angles of inclination (θ_{crit})	122
4.4.2	Estimates of (θ_{crit}) and modified liquid pool length (L_p')	122
4.5	Development of new correlations for R_{cond}	126

4.5.1	Prediction equations for $R_{C,F}$	127
4.6	Effects of θ on $R_{C,F}$	132
4.6.1	Effects of circumferential condensate film flow	133
4.6.2	Effects of the bottom condensate flow	136
4.6.3	Summary of the effects of θ	141
4.7	Evaluation of the prediction capabilities of R_{boil} and R_{cond}	142
4.8	Summary	143
Chapter 5	144
5	Experimental Methodology	144
5.1	Test-rig	144
5.2	Test- rig Instrumentation details	147
5.2.1	Water-recirculating chiller	148
5.2.2	Magnetic drive gear pump	148
5.2.3	Ultrasonic flow sensor	148
5.2.4	Data acquisition system	148
5.2.5	Thermocouples	149
5.2.6	Rope heaters	149
5.2.7	Variac	149
5.2.8	Power meter	149
5.2.9	Laser levels	150
5.3	Details of the TS	150
5.4	Experimental procedure	152
5.5	Data reduction techniques	152
5.6	Uncertainty in the measurements and repeatability of the experimental data	153
5.7	Parameters of investigation	153

5.8 Summary	154
Chapter 6	155
6 Experimental results and discussion	155
6.1 Effects of Q_{in} on the thermal performance of TS.....	155
6.1.1 Evaluation of the pool boiling resistance ($R_{B,P}$)	155
6.1.2 Evaluation of the film boiling resistance ($R_{B,F}$)	160
6.1.3 Evaluation of the condensation thermal resistance ($R_{C,F}$).....	164
6.2 Effects of the FR on the thermal performance of TS.....	176
6.2.1 Temperature distribution.....	176
6.2.2 Evaluation of pool boiling resistance ($R_{B,P}$)	178
6.2.3 Evaluation of the film boiling resistance ($R_{B,F}$).....	181
6.2.4 Evaluation of the condensation film resistance ($R_{C,F}$)	184
6.3 Summary	190
Chapter 7	192
7 Validation of the pool boiling and film boiling thermal resistance model	192
7.1 Criteria for inclusion and exclusion of the previous studies.....	192
7.2 Regression method.....	194
7.3 Pool boiling model validation.....	195
7.3.1 Present study	195
7.3.2 Previous studies	198
7.4 Film boiling model validation.....	201
7.4.1 Present study	201
7.4.2 Previous studies	203
7.5 Summary and recommendations.....	205
Chapter 8.....	207

8	Conclusions and recommendations for future work	207
8.1	Conclusions.....	207
8.1.1	Conclusions derived from the theoretical analyses.....	207
8.1.2	Conclusions derived from the experimental testing of TS.....	209
8.2	Novel contributions.....	211
8.3	Future work.....	212
8.3.1	Analytical/theoretical modelling.....	212
8.3.2	Experimental characterization	213
8.3.3	Computational fluid dynamics modelling (CFD) modelling	213
	References.....	214
	Appendices.....	233
	Curriculum Vitae	321

List of Tables

Table 1.1 The primary and secondary variables influencing the heat transfer rate in a TS and a HP.....	3
Table 1.2 Thermal resistance equations for different components of a TS.	17
Table 1.3 Thermal resistance equations for different components of a HP.....	19
Table 2.1 Comparison of n_2 , n_3 obtained from equations (2.4) and (2.7) and figures 2.4 and 2.5.....	36
Table 2.2 Comparisons of ΔT_P and $\Delta T_{P'}$ when $FR < 0.5$	37
Table 2.3 Comparison of n_5 , n_6 with that obtained from figures 2.7c, 2.7d and 2.7e, 2.7f. ...	42
Table 2.4 Estimates of Re_F and P for the different studies analyzed in the present work. The liquid properties are evaluated at the film temperature (T_f), whereas h'_{fg} is evaluated at T_{sat}	43
Table 2.5 Expressions of $Nu = f(Re_F)$ representing different condensate flow states.	44
Table 2.6 Re_v values estimated for the different studies based on Re_F	46
Table 2.7 Comparison of the condensate film thickness and the density ratio between Baojin et al. (2009) and Jafari et al. (2017b).	47
Table 2.8 Estimates of n_8 from figure 2.18.....	55
Table 3.1 Order of magnitude of $dh_{sat,l}$ and $dh_{sat,v}$ at different ΔT ranges. O represents the order of magnitude computed as $N = a \times 10^b$ where $1 \leq a \leq 10$	66
Table 3.2 Descriptions of the thermodynamic processes inside a TS and a HP.....	68
Table 3.3 Expressions of the first law of thermodynamics, the entropy changes and s_{gen} for the BC, CD, and GH processes inside a TS and a HP.....	69

Table 3.4 Illustration of different scenarios for $P_{F',HP}$ when $P_{F',HP} > P_c$	75
Table 3.5 Illustration of different scenarios when $P_{E',HP} > P_c$	84
Table 3.6 Expressions of the first law of thermodynamics, the entropy changes and s_{gen} for AB, CF, DE, FG, EG, HA, HH', H'A processes inside a TS and a HP.....	92
Table 3.7 Other sources of entropy generation inside a TS and a HP	95
Table 4.1 Thermal resistance expressions for different components of a TS and a HP adapted from Reay and Kew (2006).	101
Table 4.2 Definition of the various π terms influencing R_{boil}	108
Table 4.3 Estimation of L_p (m) at the critical Grashof number for two different superheat values.	113
Table 4.4 Critical angles of inclination for various FR.	124
Table 4.5 The modified liquid pool length, L'_p for different FR at various inclination angles. The angles have been represented in order of their magnitudes from higher to lower.	125
Table 4.6 Definition of the various π terms influencing $R_{C,F}$	129
Table 4.7 Table illustrating the solution of the partial differential equation at X_f for $0^\circ \leq \Phi \leq \Phi_f^\circ$ and at Φ_f° for $0 \leq X \leq X_f$	135
Table 4.8 Definition of the geometrical parameters associated with the bottom condensate flow	137
Table 4.9 Prediction equations for $R_{C,F}$ based on different operating conditions of θ and Φ	142
Table 5.1 Lists of all the instruments and its function.....	147

Table 5.2 Details of the TS for cases where FR is varied at a fixed AR. The TS are named in the same convention as it was tested during the experiments.....	150
Table 5.3 Details of the TS for cases where FR is varied at a fixed AR. The TS are named in the same convention as it was tested during the experiments.....	150
Table 5.4 Summary of the parameters of investigation	154
Table 6.1 Estimates of the slope obtained by fitting a power law function of the form given by equations (6.1), (6.5) and (6.7).....	159
Table 6.2 Film boiling behaviour for $FR > 0.3$ at different $\dot{Q}'_{in,f,F}$. NA denotes not available.	162
Table 6.3 Representative condensation equations derived from equation (6.12).	164
Table 6.4 The rate of change of $R_{C,F}$ with \dot{Q}_{in}	167
Table 6.5 Estimates of n_3 in Figure 6.15a.	179
Table 6.6 Estimates of the slopes in Figure 6.15b and 6.15c.....	181
Table 6.7 Estimates of n_4 and (n_3n_4) in Figure 6.17.....	183
Table 6.8 Estimates of n_5 from Figure 6.18a.	185
Table 6.9 Estimates of n_5 from Figure 6.19b.....	186
Table 6.10 Estimates of n_5 from Figure 6.21.....	188
Table 7.1 Details of the experimental conditions for the copper-water data sets used in the present analysis	193
Table 7.2 List of studies excluded from the present analysis.	193
Table 7.3 Estimated coefficients and exponents from the non-linear regression fitting	197
Table 7.4 Estimated coefficients and exponents from the non-linear regression fitting	199

Table 7.5 Estimated coefficients and exponents from the non-linear regression fitting	202
Table A.1 Expressions of ε_w , $D_{h,w}$ and $(f_{lam}Re_{liq,w})$ for various wick structures.	233
Table A.2 β for various flow conditions (adapted from Chi, 1976).	235
Table A.3 Expressions for f_v for different flow conditions (adapted from Chi, 1976).....	235
Table A.4 Expressions of r_c for various wick structures described in Table 1.2 (adapted from Chi, 1976).....	235
Table A.5 Expressions of the effective thermal conductivity, $k_{eff,wick}$ for various liquid saturated wick structures (adapted from Chi, 1976).	236
Table B.1 Compiled data from the previous studies showing geometrical parameters, the fill ratio (FR) and the aspect ratio (AR).....	237
Table B.2 Compiled heat transfer data from the previous studies.....	238
Table D.1 Previous nucleate-boiling heat transfer correlations. Stephan and Abdelsalam's (1980) correlation is not shown in the table since it was developed for natural convection. NB denotes nucleate boiling.	245
Table D.6 Modifications to h_{fg} considering the effects of sensible heat transfer and the temperature distribution across the condensate film. $c_2 = 1$ represent a linear temperature distribution, whilst $c_2 > 1$ represent a non-linear temperature distribution.	253
Table D.7 Magnitudes of $0.38c_{p,l}/h_{fg}$ and $0.68c_{p,l}/h_{fg}$ at different T_{sat} values.	254
Table D.8 Results of the numerical solution of equation (D.19).....	257
Table E.1 Comparison of the volume flow rates obtained from the bucket test and the flow sensor. F_{corr} is used to adjust the flow rate reading from the flow sensor.	259
Table E.2 Measured variables from the bucket test. V_E denotes the volume examined.	263

Table E.3 Precision and bias uncertainty in the measured values of M_B , ρ_w , t and $\dot{V}_{B,avg}$. The estimates are for 95% confidence levels. The units of ω_P change in each row and it is the units of the corresponding variable. 265

Table E.4 K-type thermocouple accuracy specifications, including CJC measurement error (adapted from OMB-DAQ-2416 manual). $\omega_{DAQ,max}$ and $\omega_{DAQ,typ}$ are the maximum and the typical values of ω_{DAQ} 267

Table E.5 Uncertainty estimates for the waterline and the surface thermocouples. ω_T is the estimated uncertainty in the average value. 268

Table E.6 Uncertainty estimates in the voltage measurements for the experiments where the fill ratio (FR) is varied from 0.35 to 0.75. The estimates are for 95% confidence levels. $\omega_{v,max}$ denote the maximum uncertainty levels. 269

Table E.7 Uncertainty estimates in the different current measurements for the experiments where the fill ratio (FR) is varied from 0.35 to 0.75. The estimates are for 95% confidence levels. $\omega_{I,max}$ denotes the maximum uncertainty levels. 269

Table E.8 Uncertainty estimates in \dot{Q}_{in} at different heat input rate measurements for the experiments where FR is varied from 0.35 to 0.75. The estimates are for 95% confidence levels. $\omega_{\dot{Q}_{in},max}$ denotes the maximum uncertainty levels. 269

Table E.9 Precision and bias uncertainty estimates in ρ_w , $\dot{V}_{B,avg}$, C_p , $T_{w,out}$, $T_{w,in}$ and $T_{w,in}$. The estimates are for 95% confidence levels. The precision uncertainty for $T_{w,out}$ corresponds to the eight different Q_{out} measurements. 271

Table E.10 Precision, bias and overall uncertainty estimates in the computed values of \dot{Q}_{out} when AR is varied from 5.3 to 12.43. $\omega_{B,\Delta T}$ denotes the bias uncertainties in ΔT_w . The estimates are for 95% confidence levels. 271

Table E.11 Bias uncertainty estimates in the computed values of R_2 , R_6 and R_8 for $L_e = 0.127m$ and $D_o = 0.016m$ and $D_i = 0.014m$. Similar estimations can be done for other values of L_e and D_i . The estimates are for 95% confidence levels. 273

Table E.12 Bias uncertainty estimates in the measured values of \dot{Q}_{avg} . The estimates are for 95% confidence levels. $S_{\dot{Q}_{avg}}$ denotes the precision index in the \dot{Q}_{avg} measurements...	275
Table E.13 Uncertainty estimates in FR for $L_e = 0.127m$. The estimates are for 95% confidence levels.....	275
Table E.14 Precision, bias and overall uncertainty estimates in the computed values of $R_{e,a,P}$ for FR = 0.35 and 0.75. The estimates are for 95% confidence levels.	276
Table E.15 Precision, bias and overall uncertainty estimates in the computed values of $R_{e,a,F}$ for FR = 0.35 and 0.75. The estimates are for 95% confidence levels.	277
Table E.16 Precision, bias and overall uncertainty estimates in the computed values of $R_{a,c}$ for FR = 0.35 and 0.75. The estimates are for 95% confidence levels.	278
Table E.17 Precision, bias and overall uncertainty estimates in the computed values of $R_{e,c}$ for FR = 0.35 and 0.75. The estimates are for 95% confidence levels.	278
Table F.1 TC locations on the standard TS.....	280
Table F.2 Variation within the temperatures obtained from the repeatability tests. Wrt denotes with respect to.....	282
Table F.3 Variation within ΔT_{ea} from the repeatability tests.....	283
Table F.4 Variation within ΔT_{ac} from the repeatability tests.....	284
Table F.5 Variations within $\left(\frac{1}{R_{B A_{e,i}}}\right)$ obtained from the repeatability tests.	285
Table F.6 Variations within $\left(\frac{1}{R_{C,F A_{c,i}}}\right)$ obtained from the repeatability tests.....	285
Table G.1 Heat transfer correlations to estimate the critical heat flux for dryout, burnout and entrainment limits.....	288

Table G.2 The heat flux limits for dryout, burnout and entrainment phenomena for the TS where FR is varied.	288
Table G.3 The heat flux limits for dryout, burnout and entrainment phenomena for the TS where AR is varied.....	288
Table G.4 Correlations to determine the minimum fill ratio requirement. Note that Bartsch and Unk's (1987) formulation require $(T_e - T_{sat})$ and $(T_e - T_P)$ <i>a priori</i> and, hence not used to determine L_p	289
Table G.5 Comparison between the minimum fill ratio estimated from the correlations and that within TS 1-5.....	289
Table G.6 Comparison between the minimum fill ratio estimated from the correlations and that within TS 6-10.....	289
Table H.1 Analysis of the dry patch stability for the present experimental data. $X_{dry-patch}$ and $F_{vapour-thrust}$ are estimated at $\theta_c = 45^\circ$	294
Table H.2 Condensation mode criteria adapted from Adamson (1990).	295
Table H.3 Nu versus Re_F correlations.....	296

List of Figures

Figure 1.1 a) Prototype of a cylindrical HP. b) Copper mesh wick extracted from a cylindrical HP.	2
Figure 1.2 Schematic diagram of the working principle of a HP, showing the wick and the WF circulation inside it.....	2
Figure 1.3 Schematic of a HP in operation.	3
Figure 1.4 a) Schematic showing the variation in fill ratio (FR) for a fixed aspect ratio (AR) (i.e. at fixed L_e and D_i). b) Schematic showing the variation in AR at fixed FR (i.e. fixed L_p).	4
Figure 1.5 a) Miniature flat HP inside a Laptop b) Miniature cylindrical HP inside a CPU core. Adapted from www.commons.wikimedia.org/	5
Figure 1.6 HP inside a mold cavity system. Adapted from www.norentthermal.com	5
Figure 1.7 Schematic of the falling liquid film showing all the relevant parameters. L_{ent} , L_{lam} and $L_{wavy,lam}$ are not drawn to scale.....	9
Figure 1.8 Development of the capillary pressure at the curve liquid-vapour interface.....	13
Figure 1.9 Thermal resistance network of a typical TS oriented in the horizontal direction. \dot{Q}_{in} and \dot{Q}_{out} are the input heating power and the output cooling power. The horizontal orientation is only for illustration of the different thermal resistance components.	16
Figure 1.10 Thermal resistance network of a typical HP oriented in the horizontal direction.	18
Figure 2.1 Temperature distributions along the length of a TS for varying \dot{Q}_{in} at fixed AR, FR and θ adapted from a) Alizadehdakhel, (2010) (AR = 22.86, FR = 0.5, $\theta = 90^\circ$) b) Amatachaya and Srimuang, (2010) (AR = 9.81, FR = 0.6, $\theta = 90^\circ$) c) Amatachaya and	

Srimuang, (2010) (AR = 11.78, FR = 0.6, $\theta = 90^\circ$) d) Baojin et al., (2009) (AR = 15.56, FR = 0.36, $\theta = 90^\circ$) e) Fadhl, (2016) (AR = 9.90, FR = 0.5, $\theta = 90^\circ$) f) Jafari et al., (2017b) (AR = 4.54, FR = 0.35, $\theta = 90^\circ$) g) Jafari et al., (2017b) (AR = 4.54, FR = 1.0, $\theta = 90^\circ$) h) Jouhara and Robinson, (2010) (AR = 6.67, FR = 1.59, $\theta = 90^\circ$) i) Noie et al., (2009) (AR = 9.81, FR = NA, $\theta = 90^\circ$)..... 31

Figure 2.2 Typical boiling curve for water at saturation pressure $P_{\text{sat}} = 101.325$ kPa from a plane horizontal heated surface (adapted and modified from (Cengel and Ghajar, 2020). Original plot was by Nukiyama (1966). 32

Figure 2.3 Characteristic boiling curve of the published data. 33

Figure 2.4 Variation of $1/(R_{B,P}A_{e,i}FR)$ with ΔT_P 34

Figure 2.5 Variation of $(1/R_{B,P}A_{e,i}PFR)$ with $\dot{Q}'_{in,f}$ 36

Figure 2.6 Typical condensation curve for steam at 1 atm pressure for a vertical circular copper plate (adapted and modified from Roshensow et al., 1998). The term V_g in the figure represents the steam velocity at which dropwise condensation occurs. Original plot was by Takeyama and Shimizu (1974). 39

Figure 2.7 Characteristic condensation curve. The green coloured dashed lines represent the slope of the data when $n_4 < 1$, whereas the red coloured dashed lines represent the slope of the data when $n_4 > 1$ 40

Figure 2.8 Variation of $1/(R_{C,F}A_{c,i})$ with $\Delta T_{C,F}$. The green coloured dashed lines represent the slope of the data when $R_{C,F}$ increases with $\Delta T_{C,F}$, whereas the red coloured dashed lines represent the slope when $R_{C,F}$ increases with $\Delta T_{C,F}$ 41

Figure 2.9 Variation of $1/(R_{C,F}A_{c,i})$ with $\dot{Q}'_{out,f}$. The green coloured dashed lines represent the slope of the data when $R_{C,F}$ increases with $\dot{Q}'_{out,f}$, whilst the red coloured dashed lines represent the slope when $R_{C,F}$ decreases with $\dot{Q}'_{out,f}$ 42

Figure 2.10 Plot of Nu versus Re_F . The solid and dashed coloured lines represent various values of the liquid Prandtl number. $Pr_l = 1$ (red), $Pr_l = 2$ (blue), $Pr_l = 3$ (cyan), $Pr_l = 4$ (magenta), $Pr_l = 5$ (yellow). The green coloured dotted lines represent the slope of the data.....	44
Figure 2.11 a) Plot of Nusselt number versus Re_F adapted from Gross et al. (1992) with permission. b) Plot of $h_{c,avg}$ versus $\Delta T_{C,F}$ adapted from Ueda et al. (1989). The author is awaiting permission.	45
Figure 2.12 Temperature distribution along the length of the TS for at three different FRs at fixed \dot{Q}_{in} , AR and θ adapted from a) Alizadehdakhel et al. (2010) ($\dot{Q}_{in} = 700[W]$, AR = 22.86, $\theta = 90^\circ$) b) Amatachaya and Srimuang (2010) ($\dot{Q}_{in} = 554.4[W]$, AR = 11.78, $\theta = 90^\circ$) c) Jafari et al. (2017a) ($\dot{Q}_{in} = 100[W]$, AR = 2.27, $\theta = 90^\circ$) d) Jafari et al. (2017b) ($\dot{Q}_{in} = 30[W]$, AR = 4.54, $\theta = 90^\circ$) e) Jafari et al. (2017b) ($\dot{Q}_{in} = 100[W]$, AR = 4.54, $\theta = 90^\circ$) f) Jafari et al. (2017b) ($\dot{Q}_{in} = 200[W]$, AR = 4.54, $\theta = 90^\circ$) g) Noie (2005) ($\dot{Q}_{in} = 215[W]$, AR = 9.52, $\theta = 90^\circ$) h) Noie (2005) ($\dot{Q}_{in} = 830[W]$, AR = 9.52, $\theta = 90^\circ$) i) Noie (2005) ($\dot{Q}_{in} = 670[W]$, AR = 15.08, $\theta = 90^\circ$) j) Noie (2005) ($\dot{Q}_{in} = 830[W]$, AR = 15.08, $\theta = 90^\circ$).	50
Figure 2.13 Variation in ΔT_P with FR.	51
Figure 2.14 Variation in $R_{B,P}$ vs ΔT_P	51
Figure 2.15 Variation in $R_{B,P}$ with FR.....	52
Figure 2.16 Variation in $R_{B,F}$ with ΔT_P	53
Figure 2.17 Variation in $R_{B,F}$ with $(1 - FR)$	54
Figure 2.18 Variation in $\Delta T_{C,F}$ with FR.....	55
Figure 2.19 Variation in $R_{C,F}$ with FR.	55

Figure 2.20 a) Variation in Re_F with FR b) Variation in $\left(\frac{\rho_l}{\rho_v}\right)$ with FR c) Variation in u_v with FR..... 57

Figure 3.1 T-s diagram of a HP proposed by Richter and Gottschlich (1990) (adapted directly from the original reference with permission). 60

Figure 3.2 Actual thermodynamic cycle on a T-s diagram of a HP proposed by Richter and Gottschlich (1990) (adapted directly from the original reference with permission)..... 61

Figure 3.3 T-s diagram proposed by Zuo and Faghri (1998). T_{HP} is the HP operating temperature calculated as the average of T_B and T_C (adapted from the original reference with permission)..... 62

Figure 3.4 a) T-s diagram showing the process line DA. The x-axis represents the specific entropy [kJ/kgK] and the y-axis represents the temperature [°C]. The yellow box represents the region that has been magnified in b) for better illustration. b) The process lines DA for three different scenarios are indicated by the roman numbers. 63

Figure 3.5 T-s diagram proposed by Khalkhali et al. (1999) (adapted from the original reference with permission)..... 64

Figure 3.6 T-s diagram showing the known state points B, C, D, G and H (green coloured circles) and the process lines BC, CD and GH (dashed gray lines) inside a TS and a HP. The solid red and black curves represent the constant enthalpy and the pressure lines, respectively. The state points E, F and A are not known a priori and are represented by purple coloured circles..... 68

Figure 3.7 a) T-s diagram showing the relevant superheated regime where process CF occurs within a TS. The yellow box represents the region of interest that that has been magnified in b) for better illustration. b) The magnified superheated regime showing different possible locations of the state point F along the constant enthalpy line, h_c . F_1 represents the state point F, when $P_{F,TS} > P_{int}$; $S_{F_1,TS} < S_{G,sat}$. F_2 is when $P_{F,TS} = P_{int}$; $S_{F_2,TS} = S_{G,sat}$. F_3 is when $P_c < P_{F,TS} < P_{int}$; $S_{F_3,TS} > S_{G,sat}$. F_4 is when $P_{F,TS} = P_c$; $S_{F_4,TS} = S_{F,TS,max} >$

$s_{G,sat}$. $T_{F_3,TS}$ is the temperature corresponding to the state point $F_{3,TS}$. The process line FG can be obtained by connecting the state points F and G. 73

Figure 3.8 a) T-s diagram showing the relevant superheated regime where process CF occurs within a HP. The yellow box represents the region of interest that that has been magnified in b) for better illustration. b) The magnified area of the superheated regime shows seven possible scenarios when $P_{F',HP} > P_c$ illustrated in Table 4.3. The process line FG can be obtained by joining the state points F and G. 76

Figure 3.9 a) T-s diagram showing the relevant superheated regime where process DE occurs within the HP. The yellow box represents the regime that that has been magnified in b) for better illustration. b) Possible locations of the state point E shown along the constant enthalpy line, h_D . E_1 represents the state point E, when $P_{E,TS} > P_{int,sh}$; $s_{E_1,TS} < s_{G,sat}$. E_2 is when $P_{E,TS} = P_{int,sh}$; $s_{E_2,TS} = s_{G,sat}$. E_3 is when $P_c < P_{E,TS} < P_{int,sh}$; $s_{E_3,TS} > s_{G,sat}$. E_4 is when $P_{E,TS} = P_c$; $s_{E_4,TS} = s_{E,TS,max} > s_{G,sat}$. $T_{E_1,TS}$ is the temperature corresponding to the state point $E_{1,TS}$. The state points F_1 , F_2 , F_3 and F_4 are shown by purple colour. The process line EG can be obtained by connecting the state points E and G. 80

Figure 3.10 a) T-s diagram showing the relevant superheated regime where process DE occurs within a HP. The yellow box has been magnified for better illustration. b) The magnified area of the superheated regime shows seven possible scenarios when $P_{E',HP} > P_c$ as illustrated in Table 2.3. The process line EG can be obtained by joining the state points E and G. 84

Figure 3.11 a) T-s diagram showing the relevant subcooled regime where process HA occurs within a TS. The yellow box represents the region of interest that that has been magnified for better illustration. b) The magnified subcooled regime showing possible locations of the state point A along the constant enthalpy line, h_H . A_1 represents the state point A, when the effects of both $\Delta P_{1,hydro}$ and ΔP_1 are present. $P_{A_1} < P_b$; $s_{A_1} < s_{H,sat}$. A_2 is when $\Delta P_{1,f}$ is negligible. $P_{A_2} < P_b$; $s_{A_2} < s_{H,sat}$. A_3 is the limiting case, when $P_{A_3} = P_b$; $s_{A_3} > s_{H,sat}$. T_{A_2} is the temperature corresponding to the state point A_2 . The process line AB can be obtained by connecting the state points A and B. 87

Figure 3.12 A magnified schematic of the subcooled regime showing the location of the state points H' and A along the constant pressure line, P_c and constant enthalpy line h_H . A_1 represents a possible location of the state point A when $|\Delta P_{\text{hydro},1}| < |\Delta P_1|$. A_2 represents the location of the state point A when $|\Delta P_{\text{hydro},1}| > |\Delta P_1|$. A_3 represents the state point A for the limiting case when s_A is maximum i.e. $s_{A,\text{max}}$. $T_{H,\text{sat}}$, T_A and $T_{H'}$ are the temperature corresponding to state points H, A and H', respectively. $P_{H'} = P_c$. $T_{H'} < T_{H,\text{sat}}$; $s_{H'} < s_{H,\text{sat}}$. $P_A < P_{H'}$; $s_A > s_{H'}$. The gray colored circles represent the state points of the WF when $T_{H'} = T_I$. Note that the approximation $T_{H'} \approx T_A$ is not shown here as the schematic depicts a general representation of the process H'A. 89

Figure 4.1 A schematic of a TS (HP) showing different pool boiling regimes adapted from El-Genk and Saber (1998a). a) Natural convection boiling (shown by black curve arrows) b) Mixed convection boiling c) Nucleate boiling. 104

Figure 4.2 A schematic of a TS (HP) showing different film boiling regimes. a) Film evaporation b) Mixed convection boiling c) Nucleate boiling. 105

Figure 4.3 A schematic showing the condensate film flow at the evaporator. $x = 0$ and $x = L_p$ denote the location of the film at the evaporator entrance and the liquid pool. 106

Figure 4.4 A schematic of the thin falling film boiling a) No nucleation at the falling film b) Maximum diameter of the nucleated bubble at the film. 120

Figure 4.5 Schematic of the TS (or HP) showing a) $\theta_{1,\text{crit}}$ and b) $\theta_{2,\text{crit}}$ for $0 < \text{FR} < 0.5$ c) $\theta_{1,\text{crit}}$ and d) $\theta_{2,\text{crit}}$ for $0.5 < \text{FR} < 1$ e) $\theta_{1,\text{crit}} = \theta_{2,\text{crit}}$ for $\text{FR} = 0.5$ f) $\theta_{2,\text{crit}} = 90^\circ$, $\theta_{1,\text{crit}} < \theta_{2,\text{crit}}$ for $\text{FR} = 1$. For all the cases the rotation of the TS (HP) is in clockwise direction. 124

Figure 4.6 Magnified schematic image of the liquid pool within the evaporator for $\theta = 45^\circ$ showing x' . x' will be equal to x_{L1} , x_{L2} , x_{L3} , x_{L4} and x_{L5} at different θ 126

Figure 4.7 a) Filmwise condensation b) Dropwise condensation. The black arrow shows the direction of the heat transfer from the vapour molecules. The green arrow shows the direction of the flow of the film and the drop under the action of gravity. 127

Figure 4.8 Schematic showing reduction of the average condensate film thickness due to the reduction of $\delta_{C,F}$ between the wave-crests. $\delta_{C,F,Red}$ is the reduced value of $\delta_{C,F}$	128
Figure 4.9 a) Schematic of the axial condensate film flow along the side walls. The decrement of the film thickness towards the evaporator section is typical. It may occur when the evaporator liquid pool is not sufficient, and the liquid film condensate starts to dry out. b) Schematic of the condensate film flow in the circumferential direction. x represents the direction along the tube in the downward direction, and the y direction is perpendicular to the fluid.	133
Figure 4.10 Geometry of the bottom condensate flow with all the geometrical variables annotated. The black and the red double arrow curve shows the wetted perimeter of the bottom condensate (P_l) and the vapour (P_v), respectively. The yellow (A_l) and the grey coloured (A_v) area shows the wetted cross-sectional area of the bottom condensate and the vapour, respectively. x denotes the centroid of the circular segment formed by the bottom condensate flow.	136
Figure 4.11 Plot of a typical Φ vs θ curve utilizing the method describe above (adapted from Chato, 1960).	140
Figure 5.1 Schematic of the test-rig.	145
Figure 5.2 Experimental test-rig	145
Figure 5.3 CAD model (created by Zichen Fan) showing the heating and the cooling arrangement of the TS inside the test-rig. The red arrows show the direction of the cooling water flowing through the condenser. The silver color coil represents the rope heater. The waterline TC are shown by vertical probes (represented by vertical lines) going into the water line.	146
Figure 5.4 Extractable end (evaporator end) and the capillary end cap (condenser end) of the TS.	151

Figure 6.1 a) Boiling characteristic curve. b) Variation of $1/(R_{B,P}A_{c,i}FR)$ with ΔT_P . c) Variation of $(1/R_{B,P}A_{c,i}FR)$ with $\dot{Q}'_{in,f}$. d) Magnified figure of c).	158
Figure 6.2 a) Variation of $R_{B,P}$ with \dot{Q}'_{in}	160
Figure 6.3 A schematic of the sectional front-view of a TS showing the formation of rivulets from the condensate film and nucleation within the rivulets (adapted from El-Genk and Saber, 1998b).....	161
Figure 6.4 Variation of $R_{B,F}$ with $\dot{Q}'_{in,f,F}$	163
Figure 6.5 a) Condensation characteristic curve. b) Variation of $1/(R_{C,F}A_{c,i})$ with $\Delta T_{C,F}$. c) Variation of $(1/R_{C,F}A_{c,i})$ with $\dot{Q}'_{out,f}$	166
Figure 6.6 Variation in $R_{C,F}$ with \dot{Q}'_{in}	167
Figure 6.7 Variation in $h_{C,F}$ with $\dot{Q}'_{out,f}$ adapted from Citakoglu and Rose (1968) with permission. Note that $\alpha \equiv h_{C,F}$ and $\dot{Q}'' \equiv \dot{Q}'_{out,f}$, respectively. The +, x and o symbols represent the data from Citakoglu and Rose (1968), whereas Δ and \blacktriangledown represent the data from Fevre and Rose (1965) and Tanner et al., (1965), respectively. The line (—) represent equation (30) in Fevre and Rose (1966).....	168
Figure 6.8 Variation in $h_{C,F}$ with $\dot{Q}'_{out,f}$ adapted from Graham and Griffith (1973) with permission. Note that $H \equiv h_c$ and $\frac{Q}{A} \equiv \dot{Q}'_{out,f}$, respectively. The “present work” highlighted in the plot with yellow outline refers to Graham’s (1969) own data.	168
Figure 6.9 a) Variation in Re_F with \dot{Q}'_{in} . b) Variation in T_f with \dot{Q}'_{in}	170
Figure 6.10 Variation in Nu with \dot{Q}'_{in} . The blue, red and green solid lines represent the equation from Nusselt’s theory (1916) (NT), Wilke’s theory (W) (1962) and McAdams (1954) (McA). The $Nu-Re_F$ equations from NT, W and McA are shown in Table H.3 in Appendix H.....	171

Figure 6.11 Variation in Nu with Re_F for ethanol WF at a) Small and intermediate FR and b) Intermediate and large FR. The figures are adapted from Andros (1980).	173
Figure 6.12 a) Variation in τ_i^* with \dot{Q}_{in} . b) Variation in Nu with τ_i^*	174
Figure 6.13 a) Variation in $\left(\frac{\rho_l}{\rho_v}\right)$ with \dot{Q}_{in} . b) Variation in T_a with \dot{Q}_{in} . c) Variation in Nu with $\left(\frac{\rho_l}{\rho_v}\right)$	176
Figure 6.14 Temperature distribution along the length of the TS with varying FR for different \dot{Q}_{in}	178
Figure 6.15 Variation in ΔT_P with FR. The data corresponding to FR = 0.65, have been highlighted in yellow for better visualizing the trend.	179
Figure 6.16 a) Variation in $R_{B,P}$ with ΔT_P c) Variation in $R_{B,P}$ with FR . The data corresponding to FR = 0.65, have been highlighted in yellow for better visualizing the trend without the data set.	181
Figure 6.17 a) Variation in $R_{B,F}$ with ΔT_P c) Variation in $R_{B,F}$ with FR. The data corresponding to FR = 0.65, have been highlighted in yellow for better visualizing the trend without that data set.	183
Figure 6.18 a) Variation in $\Delta T_{C,F}$ with FR. b) Condensation characteristic curve. The data corresponding to FR = 0.65, have been highlighted in yellow for better visualizing the trend without that data set.	184
Figure 6.19 a) Variation in $R_{C,F}$ with $\Delta T_{C,F}$ b) Variation in $R_{C,F}$ with FR. The data corresponding to FR = 0.65, have been highlighted in yellow for better visualizing the trend without that data set.	186
Figure 6.20 a) Variation in Re_F with FR b) Variation in T_F with FR. The data corresponding to FR = 0.65, have been highlighted in yellow for better visualizing the trend without that data set.	187

Figure 6.21 Variation in Nu with FR. The data corresponding to FR = 0.55, have been highlighted in yellow for better undersanding	188
Figure 6.22 Variation in τ_i^* with FR. The data corresponding to FR = 0.55, have been highlighted in yellow for better undersanding	189
Figure 6.23 a) Variation in T_a with FR b) Variation in $\left(\frac{\rho_l}{\rho_v}\right)$ with FR.	190
Figure 6.24 a) Variation in Nu with $\left(\frac{\rho_l}{\rho_v}\right)$	190
Figure 7.1 Plot of the predicted Y values versus the actual Y values.....	197
Figure 7.2 Plot showing 95% confidence intervals of the predicted data as error bars and the locations of the actual data on the error bars.	198
Figure 7.3 Comparison between the actual Y values and the predicted Y	199
Figure 7.4 Plot showing 95% confidence intervals of the predicted data as error bars and the locations of the actual data on the error bars.	201
Figure 7.5 Plot of the predicted Y values versus the actual Y values.....	202
Figure 7.6 Plot showing 95% confidence intervals of the predicted data as error bars and the locations of the actual data on the error bars.	203
Figure 7.7 Plot of the predicted Y values versus the actual Y values.....	204
Figure 7.8 Plot showing 95% confidence intervals of the predicted data as error bars and the locations of the actual data on the error bars.	205
Figure A.1 Geometries of the different heat pipe (HP) wick structures. a) Top view of the circular artery HP. b) Cross-section of the circular artery. c) Cross-section of the rectangular channel d) Top view of the axial rectangular groove HP e) Cross-section of the rectangular grooves f) Top view of the circular annular wick HP g) Cross-section of the circular annular wick h) Top view of the wrapped screen HP i) Cross-section of the	

square wire mesh screen j) Top view of the sintered metal HP k) Cross-section of the packed spherical particles. 234

Figure C.1 h-s diagram showing the known state points B, C, D, G and H (green colored circles) and the process lines BC, CD and GH inside a TS and a HP. The solid red and black curves represent the constant enthalpy and the pressure lines, respectively. The unknown state points E, F and A are represented by the purple colored circles. 240

Figure C.2 A magnified schematic of the superheated regime showing possible locations of the state point F along the constant enthalpy line, h_C . F_1 represents the state point F, when $P_{F,TS} > P_{int}$; $s_{F_1,TS} < s_{G,sat}$. F_2 is when $P_{F,TS} = P_{int}$; $s_{F_2,TS} = s_{G,sat}$. F_3 is when $P_c < P_{F,TS} < P_{int}$; $s_{F_3,TS} > s_{G,sat}$. F_4 is when $P_{F,TS} = P_c$; $s_{F_4,TS} = s_{F,TS,max} > s_{G,sat}$. $T_{F_3,TS}$ is the temperature corresponding to the state point $F_{3,TS}$. The process line FG can be obtained by connecting the state points F and G..... 241

Figure C.3 A magnified schematic of the superheated regime illustrating of seven possible scenarios on a h-s diagram when $P_{F',HP} > P_c$ shown in Table 3.4. The process line FG can be obtained by joining the state points F and G. 242

Figure C.4 A magnified schematic of the superheated regime showing possible locations of the state point E shown along the constant enthalpy line, h_D . E_1 represents the state point E, when $P_{E,TS} > P_{int,sh}$; $s_{E_1,TS} < s_{G,sat}$. E_2 is when $P_{E,TS} = P_{int,sh}$; $s_{E_2,TS} = s_{G,sat}$. E_3 is when $P_c < P_{E,TS} < P_{int,sh}$; $s_{E_3,TS} > s_{G,sat}$. E_4 is when $P_{E,TS} = P_c$; $s_{E_4,TS} = s_{E,TS,max} > s_{G,sat}$. $T_{E_1,TS}$ is the temperature corresponding to the state point $E_{1,TS}$. The state points F_1 , F_2 , F_3 and F_4 are shown by purple color. The process line EG can be obtained by connecting the state points E and G. 242

Figure C.5 A magnified schematic of the superheated regime illustrating seven possible scenarios on a h-s diagram when $P_{E',HP} > P_c$ as shown in Table 3.5. The process line EG can be obtained by joining state points E and G. 243

Figure C.6 A magnified schematic of the subcooled regime showing possible locations of the state point A along the constant enthalpy line, h_H . A_1 represents the state point A, when $|\Delta P_{\text{hydro},l}| > |\Delta P_1|$. $P_{A_1} < P_b$; $s_{A_1} < s_{H,\text{sat}}$. A_2 is when ΔP_1 is negligible. $P_{A_2} < P_b$; $s_{A_2} < s_{H,\text{sat}}$. A_3 is the limiting case, when $P_{A_3} = P_b$; $s_{A_3} > s_{H,\text{sat}}$. T_{A_2} is the temperature corresponding to the state point A_2 . The process line AB can be obtained by connecting the state points A and B. 244

Figure C.7 A magnified schematic of the subcooled regime showing the location of the state points H' and A along the constant pressure line, P_c and constant enthalpy line h_H . A_1 represents a possible location of the state point A when $|\Delta P_{\text{hydro},l}| < |\Delta P_1|$. A_2 represents the location of the state point A when $|\Delta P_{\text{hydro},l}| > |\Delta P_1|$. A_3 represents the state point A for the limiting case when s_A is maximum i.e. $s_{A,\text{max}}$. $T_{H,\text{sat}}$, $T_{A,\text{HP}}$ and $T_{H',\text{HP}}$ are the temperature corresponding to state points H, A and H', respectively. $P_{H'} = P_c$. $T_{H'} < T_{H,\text{sat}}$; $s_{H'} < s_{H,\text{sat}}$. $P_{A,\text{HP}} < P_{H',\text{HP}}$; $s_{A,\text{HP}} > s_{H',\text{HP}}$ 244

Figure D.1 Thermal resistance network model for dropwise condensation. 248

Figure E.1 Plot of \dot{V}_s versus $\dot{V}_{B,\text{avg}}$. The data close to 45° line indicate the closeness of \dot{V}_s to $\dot{V}_{B,\text{avg}}$ 259

Figure E.2 Plot of F_{corr} versus \dot{V}_s . A polynomial equation of order 2 represents the best fit curve to the data. 260

Figure E.3 Plot of ω_v as a function of \dot{V}_B along with the linear best fit to the data. 266

Figure E.4 Plot of $\omega_{\text{DAQ,max}}$ and $\omega_{\text{DAQ,typ}}$ as a function of sensor temperature. 267

Figure F.1 Temperature distribution along the axial length of the TS plotted for three repeated trials for different \dot{Q}_{in} . The \dot{Q}_{in} range is shown in Table F.2. 282

Figure F.2 Plot of the a) boiling curve and b) condensation curve for three repeated trials. 283

Figure F.3 a) Variation of $(1/R_{e,a}A_{e,i})$ with $\dot{Q}'_{\text{in},f}$ b) Variation of $(1/R_{a,c}A_{c,i})$ with $\dot{Q}'_{\text{out},f}$ 284

Figure H.1 Schematic showing dry patch formation and film breakdown. The purple colour point shows the stagnation point. σ is the surface tension and θ_c is the contact angle of the film at surface.....	291
Figure H.2 Evidence of local dry patch formation	292
Figure H.3 a) Variation in Pr_l with \dot{Q}_{in} . b) Variation in Nu with Pr_l	297
Figure H.4 a) Variation in Fr_v with \dot{Q}_{in} . b) Variation in Nu with Fr_v	299

List of Appendices

Appendix A: Appendix related to Chapter 1	233
Appendix B: Appendix related to Chapter 2.....	237
Appendix C: Appendix related to Chapter 3.....	240
Appendix D: Appendix related to Chapter 4	245
Appendix E: Appendix related to Chapter 5.....	258
Appendix F: Appendix related to Chapter 5.....	280
Appendix G: Appendix related to Chapter 5	286
Appendix H: Appendix related to Chapter 6	291
Appendix I: Copyright permissions	300

List of Abbreviations

CoV	Coefficient of variation
HP	Heat pipe
HVAC	Heating ventilation and air-conditioning
O	Order of magnitude
LHS	Left hand side
RHS	Right hand side
RMS	Root mean square
RMSE	Root mean square error
TS	Thermosyphon
WF	Working fluid

List of Symbols

Symbols	Definition
$\frac{8A_1 S_c}{D_1^3}$	Function appearing in equation (4.67) (dimensionless)
a - z, a ₁ - p ₁ , a ₂ - i ₂	Non-dimensional exponents from the thermal resistance equations (4.5 - 4.63)
A _{c,i}	Internal condenser area (m ²)
A _{eff}	Effective heat transfer area (m ²)
A _{e,i}	Internal evaporator area (m ²)
A _{e,o}	Evaporator outer surface area (m ²)
A _l	Wetted cross-sectional area of the bottom condensate (m ²)
Ar	Archimedes number
A _v	Vapour cross-sectional area (m ²) Wetted cross-sectional area of the vapour (m ²)
A _{wall}	Wall cross-sectional area of the thermosyphon/heat pipe (m ²)
AR	Aspect ratio
Bo	Bond number

c^*	Non-dimensional constant (Equation 1.18)
c_p	Specific heat (kJ/kgK)
C^*	Dimensional constant (Equation 1.24)
C, C', C''	Non-dimensional coefficients from the thermal resistance equations (equations 4.5 - 4.63)
C_1	Dimensional proportional constant related to the equation representing the boiling curve (equation 2.1)
C_2	Dimensional proportional constant related to the equation representing the condensation curve (equation 2.6)
C_3	Dimensional proportional constant related to the relationship between the wall superheat and the fill ratio (equation 2.13)
C_4	Dimensional proportional constant related to the relationship between the wall subcooling and the fill ratio (equation 2.18)
Co	Confinement number
d	Exact differential
d_{BC}	Depth of the bottom condensate (m)
dh	Differential changes in specific enthalpy per unit mass (kJ/kg)
$d(ke)$	Differential changes in kinetic energy per unit mass (kJ/kg)
$d(pe)$	Differential changes in potential energy per unit mass (kJ/kg)
D_h	Hydraulic diameter of the duct (m)

D_i	Internal diameter of the thermosyphon/heat pipe (m)
D_o	Outer diameter of the thermosyphon/heat pipe (m)
D_b	Departing bubble diameter (m)
D_v	Vapour core diameter (m)
f	Fanning friction factor
F	Frictional coefficient (Chapter 1)
Fr	Froude number
FR	Fill ratio
g	Acceleration due to gravity (m/s^2)
Gr	Grashof number
h	Specific enthalpy (kJ/kg)
h_{boil}, h_e	Boiling heat transfer coefficient (W/m^2K)
$h_{cond}, h_{C,F}, H$	Condensation heat transfer coefficient (W/m^2K)
h'_{fg}	Modified latent heat of vapourization (kJ/kg)
h_{fg}	Latent heat of vapourization (kJ/kg)
$h-s$	Specific enthalpy-specific entropy
Ja	Jakob number

k	Thermal conductivity (W/mK)
K	Wick permeability
L	Length along the thermosyphon (m)
L_a	Adiabatic length (m)
L_c	Condenser length (m)
L_e	Evaporator length (m)
L_{eff}	Effective length (m)
L_{ent}	Entrance length (m)
L_{ent}^+	Dimensionless entrance length
L_f	Length of the liquid film flow (m)
L'_p	Effective liquid pool length for an inclined thermosyphon/heat pipe (m)
L_p	Length of the liquid pool (m)
L_t	Total length of the thermosyphon/heat pipe (m)
\dot{m}_c	Condensate mass flow rate (kg/s)
\dot{m}_f	Film mass flow rate (kg/s)
n	Exponent of Re_F (Equation 1.18)

n_1, n_2, n_3	Exponents related to the equation representing the boiling curve (equation 2.1)
n_4, n_5, n_6	Dimensionless exponents related to the equation representing the condensation curve (equation 2.6)
n_7	Exponent related to the equation representing the relationship between the wall superheat and the fill ratio (equation 2.13)
n_8	Dimensional exponent related to equation (2.18)
$N_{\mu F}$	Viscosity number
Nu	Nusselt number
P	Non-dimensional parameter related to the film flow at the condenser
P_l	Wetted perimeter of the bottom condensate (m)
P_{sat}	Saturation pressure (Pa)
P_v	Wetted perimeter of the vapour/side wall condensate (m)
P_D	Pressure dependency term (dimensionless)
ΔP	Pressure drop (Pa)
ΔP_{cap}	Capillary pressure (Pa)
ΔP_{drive}	Pressure differential driving the fluid flow (Pa)
$\Delta P_{hydro,l}$	Hydrostatic pressure drop of the liquid (Pa)

$\Delta P_{\text{hydro,v}}$	Hydrostatic pressure drop of the vapour (Pa)
ΔP_1	Pressure drop due to friction during the liquid flow (Pa)
ΔP_{others}	Pressure drop from the other components (Pa)
ΔP_{therm}	Thermodynamic pressure differential (Pa)
ΔP_v	Pressure drop due to friction during the vapour flow (Pa)
Pr	Prandtl number
Q_{in}	Input heat (J)
\dot{Q}_{in}	Input heating rate (J/s)
$\dot{Q}_{\text{in,F}}$	Input heating rate to the liquid film (J/s)
$\dot{Q}_{\text{in,P}}$	Input heating rate to the liquid pool (J/s)
\dot{Q}'_{in}	Heat flux to the evaporator surface (W/m^2)
$\dot{Q}'_{\text{in,f}}$	Heat flux into the fluid (W/m^2)
$\dot{Q}'_{\text{in,f,v}}$	Heat flux based on the vapour cross sectional area (W/m^2)
\dot{Q}_{out}	Output cooling rate (W)
\dot{Q}'_{out}	Output heat flux from the condenser surface (W/m^2)
$\dot{Q}'_{\text{out,f}}$	Output heat flux from the fluid (W/m^2)

R_1, R_7	Thermal contact resistance (K/W)
R_2, R_6	Wall radial resistance (K/W)
$R_{2,w}, R_{6,w}$	Wick radial resistance (K/W)
R_3, R_{boil}	Boiling resistance (K/W)
R_4	Vapour channel axial resistance (K/W)
R_5, R_{cond}	Condensation resistance (K/W)
R_8	Wall axial resistance (K/W)
R_B	Boiling thermal resistance (K/W)
$R_{B,F}$	Film boiling thermal resistance (K/W)
$R_{B,P}$	Pool boiling thermal resistance (K/W)
$R_{O,HP}$	Overall thermal resistance of the heat pipe (K/W)
$R_{O,TS}$	Overall thermal resistance of the thermosyphon (K/W)
Ra	Rayleigh number
Re_b	Bubble Reynolds number
Re_F	Film flow Reynolds number
Re_v	Vapour Reynolds number
\bar{R}	Specific gas constant (J/kgK)

s	Specific entropy (J/kgK)
T	Temperature (K)
T_a	Average adiabatic surface temperature (K)
T_c	Average condenser surface temperature (K)
T_e	Average evaporator surface temperature (K)
T - s	Temperature-specific entropy
T_{sat}	Saturation temperature (K)
T_{source}	Temperature of the heating source (K)
T_{sink}	Temperature of the heat sink (K)
ΔT	Temperature differential (K)
$\Delta T_1, \Delta T_7$	Temperature drop across the thermal contacts in the evaporator, condenser (K)
$\Delta T_2, \Delta T_6$	Temperature drop across the copper wall in the radial direction (K)
ΔT_3	Temperature drop across the boiling interface (K)
ΔT_4	Temperature drop across the vapour channel (K)
ΔT_5	Temperature drop across the condensation interface (K)
ΔT_8	Temperature drop across the copper wall in the axial direction (K)

$\Delta T_1, \Delta T_7$	Temperature drop across the thermal contacts in the evaporator, condenser (K)
$\Delta T_{e,a} = T_e - T_a$	Temperature differential between the evaporator and the adiabatic section (K)
$\Delta T_{a,c} = T_a - T_c$	Temperature differential between the adiabatic and the condenser section (K)
$\Delta T_{e,c} = T_e - T_c$	Temperature differential between the evaporator and the condenser section (K)
$\Delta T_{C,F}$	Condenser wall subcooling (K)
ΔT_P	Wall-superheat at the pool (K)
u	Specific internal energy (J/kgK)
u_l	Mean velocity of the film flow (m/s)
u_v	Counter-current vapour velocity (m/s)
v	Specific volume (m ³ /kg)
w_{BC}	Width of the bottom condensate (m)
We	Weber number
x^+	Dimensionless distance in the x-direction (Chapter 4)
X_P	Non-dimensional parameter used to identify different pool boiling regimes (equation 4.1)
X	Dimensionless condenser length (Equation 4.64)

Y Non-dimensional form of the boiling thermal resistance
(Chapter 7)

Δz Elevation change of the working fluid during the flow (m)

Greek symbols

Definition

β Coefficient representing the vapour flow through different cross-sections

β_v Volumetric thermal expansion coefficient

δ Inexact differential

δ^* Non-dimensional modified film thickness

δq Differential amount of heat transfer into the system per unit mass
(J/m)

δs_{gen} Differential amount of specific entropy generated during the process (kJ/kgK)

δ_v Characteristic scale of the condensate film thickness (m)

δw Differential amount of work done by the system (i.e. the WF) on the surroundings per unit mass (J/m)

$\delta_{E,F}$ Characteristic thickness of the falling film at the evaporator (m)

$\delta_{C,F}$ Condensate film thickness (m)

ε_w Wick porosity

η Non-dimensional film parameter used to identify different film boiling regimes (equation 4.3)

μ Dynamic viscosity (kg/ms)

ν Kinematic viscosity (m²/s)

Ω_l Axial change in the liquid volumetric flow rate (m³/s-m)

Φ Peripheral angle of the condensate layer

Φ_C Central half angle subtended by the bottom condensate

$\Phi_{C,M}$	Mean of the various central half angle along the condenser length
Φ_M	Mean peripheral angle of the condensate
φ	Mixing coefficient
ψ	Non-dimensional local film thickness (Equation 4.64)
ρ_l	Density of the liquid phase (kg/m ³)
ρ_v	Density of the vapour phase (kg/m ³)
$\left(\frac{\rho_l}{\rho_v}\right)$	Density ratio
σ	Surface tension (N/m)
τ_i	Interfacial shear stress at the liquid-vapour interface (N/m ²)
τ_i^*	Non-dimensional interfacial shear stress
$\left(\frac{\Gamma_d}{L_F}\right)$	Droplet entrainment rate per unit length of the film heating length
$\left(\frac{\Gamma}{L_F}\right)$	Film flow rate per unit length of the heating length
θ	Inclination angle from the horizontal
θ_{crit}	Critical angle of inclination

Subscripts

a	Adiabatic
avg	Average
c	Condenser
cap	Capillary
d	Dynamic
e	Evaporator
eff	Effective
ent	Entrance

g, v	Vapour
gen	Generation
h	Hydraulic
hydro	Hydrostatic
i	Interfacial, internal
in	Inlet
int	Intermediate
l, f	Liquid
lam	Laminar
lat	Latent
liq	Liquid
max	Maximum
op	Operating
o	Outlet
O	Overall
sat	Saturation
therm	Thermodynamic
w	Wick

Chapter 1

1 Introduction and background

This chapter provides the reader with an introductory background knowledge on thermosyphons (TS) and heat pipes (HP) and is categorized into seven sections. The first section describes the working principle of a TS and a HP and the specific industrial application of the present research. The second section illustrates the relevant fluid mechanics, thermodynamics and heat transfer theory associated with a TS and HP. The third section briefly reviews the parametric studies on the heat transfer performance of TS and HP and identifies the primary knowledge gaps. The fourth section describes the motivation and defines the objectives of the present work. The fifth section describes the scope of the present work. The sixth section outlines the organization of the thesis and mentions the main topics discussed in each chapter. Finally, the present chapter is summarized in section seven.

1.1 HP and TS definitions and working principles

HP are two-phase, heat transfer devices (typically cylindrical or rectangular in cross-section) that can achieve very high heat transfer rates (250 times that of a copper pipe of an equivalent size; Grover et al., 1963) over long distances (3m ~ 100m) with minimal temperature difference (Takaoka et al., 1985, Storch et al., 2012). Figure 1.1a shows a prototype of a cylindrical HP. Their effectiveness lies in the fact that no external power source or active mechanical parts are required to drive the heat transfer process. HP have also been reported to last for more than 10000 hours without any performance degradation (Deverell, 1969, Gorbis and Savchenkov, 1976).

Typically, a HP contains a small amount of working fluid (WF) under sub-ambient pressure and a porous wick sealed inside it. Figure 1.1b shows a copper mesh wick extracted from a cylindrical HP. A HP without a mesh wick is known as a TS. The high heat transfer rate is achieved through phase change of the WF and the natural convection processes. Continuous heat transfer is achieved by recirculation of the WF from end-to-end in the HP or TS. Figure 1.2 shows a schematic of the flow recirculation inside a HP

along with the location of the wick inside it. A conventional HP (or a TS) is a closed cylindrical tube with an evaporator section and a condenser section at opposing ends and an adiabatic section between them (this section can be excluded from the design depending on the spatial limitations of the intended application).

Figure 1.3 shows a schematic of a HP in operation with all the key variables annotated. The primary and secondary variables affecting its heat transfer capability, identified from previous theories and experiments, are defined in Table 1.1. Among the primary variables listed, \dot{Q}_{in} and ΔT are the thermal operating parameters. The fill ratio (FR) is selected based on the amount of \dot{Q}_{in} desired to be transported and, hence, is also a thermal operating parameter. The aspect ratio (AR) and inclination angle (θ) are the geometrical operating parameters.



Figure 1.1 a) Prototype of a cylindrical HP. b) Copper mesh wick extracted from a cylindrical HP.

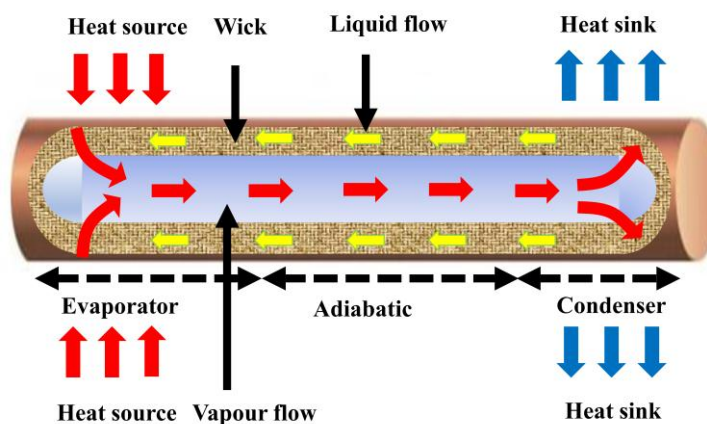


Figure 1.2 Schematic diagram of the working principle of a HP, showing the wick and the WF circulation inside it.

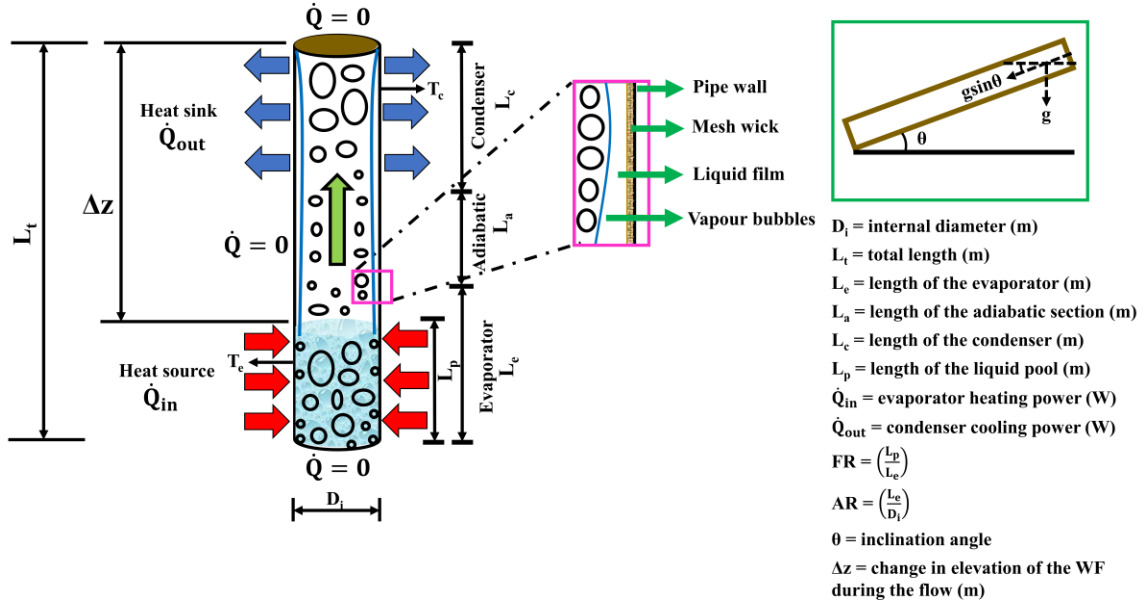


Figure 1.3 Schematic of a HP in operation.

Table 1.1 The primary and secondary variables influencing the heat transfer rate in a TS and a HP.

	Variable	Definition
Primary performance variable	\dot{Q}_{in} [W]	Input heating rate. This is typically an operating parameter for laboratory experiments on HP and TS. For industrial applications, this often needs to be determined.
	$\Delta T = T_e - T_c$	Temperature differential between the evaporator (T_e) and the condenser (T_c). This is evaluated from the known heat source and the sink condition usually known for a specific application or in lab experiments.
	Fill ratio (FR) = $\frac{L_p}{L_e}$	Ratio of the volume of the WF to the volume of the evaporator represented as $\frac{L_p}{L_e}$. This can be varied either by varying L_p for a fixed L_e and D_i or by varying L_p when L_e and D_i are varied in equal proportions. Figure 1.4a shows the schematic of the FR variation for a fixed L_e and D_i .
	Aspect ratio (AR) = $\frac{L_e}{D_i}$	Ratio of L_e and D_i (defined in Figure 1.3). This can be varied either by varying L_e keeping D_i fixed or by varying both L_e and D_i in unequal proportions keeping L_p . Figure 1.4b shows the schematic of the AR variation for a fixed D_i .
	Inclination angle (θ)*	Angle between the TS and the HP axis with either the horizontal or vertical plane.
Secondary performance variable	L_c	Condenser length
	L_a	Adiabatic length
	WF	Working fluid
	Wall material	Examples : Copper, stainless steel
	Coolant flow rate	The flow rate of the coolant at the condenser. This is typically an operating parameter for laboratory experiments.
		* In this thesis, θ is taken with respect to the horizontal plane, and it is considered positive in counter-clockwise direction.

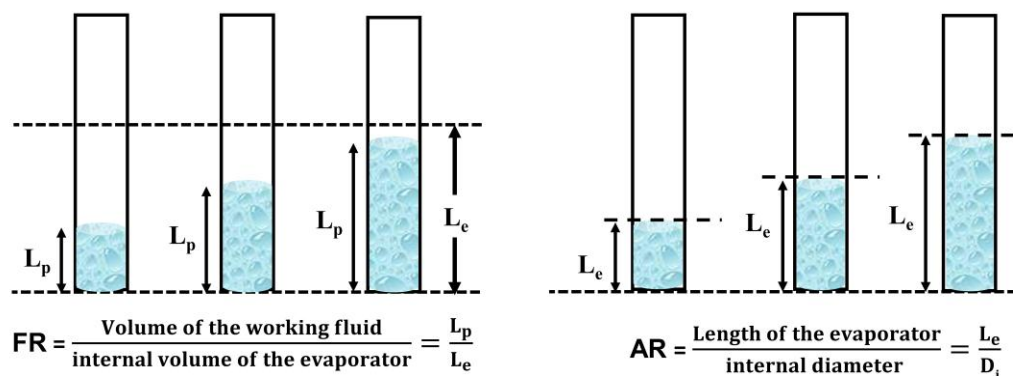


Figure 1.4 a) Schematic showing the variation in fill ratio (FR) for a fixed aspect ratio (AR) (i.e. at fixed L_e and D_i). b) Schematic showing the variation in AR at fixed FR (i.e. fixed L_p).

When the TS or HP is exposed to an external heat source (at the evaporator), the WF absorbs heat proportional to its latent heat of vaporization, causing a phase change of the WF from its liquid state to its vapour state. The buoyant force combined with the high vapour pressure at the evaporator causes the WF to rise against gravity and move towards the condenser (which is coupled with a heat sink), where the WF condenses and releases the latent heat to the heat sink. The condensate then returns back to the evaporator under the action of gravity, and/or by the capillary action of the wick in the case of a HP. The condensate liquid starts boiling again while it passes through the evaporator. In a TS, the condensate can only return by gravitational forces and so the evaporator must always be located below the condenser, whereas for a HP it can be in any orientation.

Although conventional TS and HP are circular in cross-section various other shapes such as rectangular (flat HP) and conical (rotating HP) are designed for specific applications. Different configurations of TS and HP are determined by the design constraints of the application and the desired rate of heat transfer. They include flat (Wang and Vafai, 2000, Xuan et al., 2004, Amatachaya and Srimuang, 2010), rotating (Gray, 1969, Song et al., 2004, Lian et al., 2016, Li and Liu, 2020), concentric annular (Faghri, 1989, Faghri and Thomas, 1989, Nouri-Boryjerdi and Layeghi, 2005) and loop HP (Kaya et al., 1999a, 1999b Hoang, 1999, Ku, 1999, Chen et al., 2005, Siedel et al., 2015).

TS and HP are used in a multitude of applications such as heating, ventilation and air-conditioning (HVAC) systems, ground source heat pumps, electronics cooling and

spacecraft thermal management. Figure 1.5a and 1.5b show a miniature flat HP inside a laptop and a miniature cylindrical HP inside the CPU core, respectively. A potentially important application of TS and HP has been towards the rapid cooling of thermoplastic, thermosetting and ceramic materials inside mold cavity systems (Zhang et al., 2002, Stulov, 2012, Singh et al., 2017). TS or HP inside mold cavity systems are usually known as thermal pins. A schematic of a HP inside a mold cavity system is shown in Figure 1.6. HP can provide a high rate of efficient and uniform cooling to specific areas of injected materials resulting in much shorter mold cycles. A reduction in mold cycle time will increase productivity rates, reduce cost, and may improve the quality of the molded materials. This is beneficial in increasing the economic and energy efficiency of the plastic injection molds (PIM) industry, much of which services the automotive manufacturing sector.

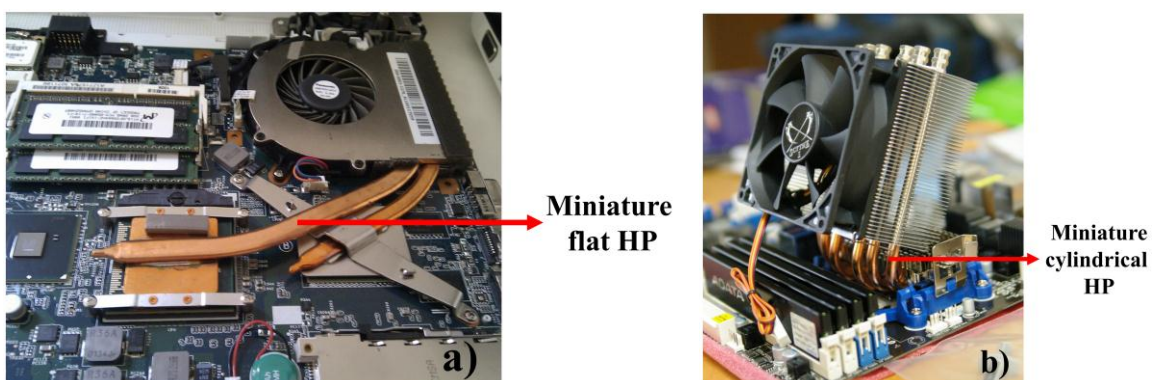


Figure 1.5 a) Miniature flat HP inside a Laptop b) Miniature cylindrical HP inside a CPU core.
Adapted from www.commonswiki.org/

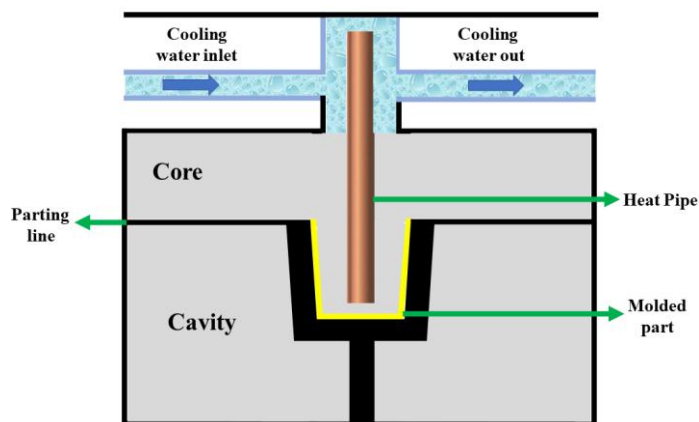


Figure 1.6 HP inside a mold cavity system. Adapted from www.norenthermal.com.

The thermal operating conditions in mold cooling applications are dictated by the temperature of the heating source (T_{source} ; typically, 120°C - 290°C depending upon the injected material) and the cooling sink (T_{sink}). The geometric operating conditions are limited mainly by the space available inside the molds and the system orientation.

The next section lays out the fundamental concepts of the fluid mechanics, thermodynamics and heat transfer governing the fluid flow and heat transfer within TS and HP.

1.2 Theoretical background

This section illustrates the principles of fluid mechanics, thermodynamics and heat transfer associated with the operation of TS and HP. The relevant equations for predicting the pressure drop (ΔP), temperature drop (ΔT), and thermal resistance (R) are presented to provide guidelines for selecting the appropriate geometrical dimensions of a TS or HP and the wick structures (in the case of a HP). It is noted that although some of the equations presented in this section are available in HP textbooks (Chi, 1976, Faghri, 1995, Reay and Kew, 2006), certain equations have been treated algebraically by the present author and presented in a form most frequently used in engineering. In this regard, modifications to the existing equations have been made wherever desirable.

1.2.1 The fluid mechanics of HP and TS

For a TS or a HP to operate continuously, the pressure differential driving the fluid flow (ΔP_{drive}) must always be greater than the total pressure drop inside a TS and a HP system. Mathematically, this can be expressed as

$$\Delta P_{\text{drive}} \geq \Delta P_v + \Delta P_l + \Delta P_{\text{hydro,v}} + \Delta P_{\text{hydro,l}} + \Delta P_{\text{others}} \quad (1.1)$$

where ΔP_v , ΔP_l are the frictional pressure drops, $\Delta P_{\text{hydro,v}}$, $\Delta P_{\text{hydro,l}}$ are the hydrostatic pressure drops of the vapour and the liquid phase of the WF, respectively. ΔP_{others} denotes the pressure drop from the other components through which a WF may pass, if present within the TS or a HP. Equation (1.1) is a generic form of the pressure balance expression

necessary for the WF to circulate continually. The subsequent sub-sections will discuss how these terms can be estimated *a priori*.

1.2.1.1 Estimations of the hydrostatic pressure drop, ΔP_{hydro}

$\Delta P_{\text{hydro,l}}$ and $\Delta P_{\text{hydro,v}}$ can be computed as (Reay and Kew, 2006)

$$\Delta P_{\text{hydro,l}} = -\rho_l(\Delta z)g\sin\theta \quad (1.2)$$

$$\Delta P_{\text{hydro,v}} = -\rho_v(\Delta z)g\sin\theta \quad (1.3)$$

where Δz is the difference between the initial and the final position of the WF during the flow, ρ_l and ρ_v are the density of the liquid phase and the vapour phase, respectively, g is the acceleration due to the gravity and θ is the angle of inclination from the horizontal plane (see Figure 1.3) and is considered positive in counter-clockwise direction. The wick does not influence the hydrostatic pressure drop (since there are no wick parameters in the expressions of $\Delta P_{\text{hydro,l}}$ and $\Delta P_{\text{hydro,v}}$) and, therefore, $\Delta P_{\text{hydro,l}}$ and $\Delta P_{\text{hydro,v}}$ are identical for both HP and TS. The next section presents the equations for estimating the liquid pressure drop ΔP_l .

1.2.1.2 Estimation of the liquid pressure drop, ΔP_l

ΔP_l within a TS is caused due to the frictional drag at the TS walls whereas ΔP_l within a HP is caused due to the frictional drag within the wick structures. This sub-section analyses ΔP_l within a TS followed by the analyses of ΔP_l within HP in the subsequent paragraphs.

Different liquid flow regimes exist inside the TS depending upon the film flow Reynolds number, Re_F (see equation 1.7 below). For $Re_F < 40$, the film flow is laminar, for $30 \leq Re_F < 1800$, the film flow is laminar-wavy (unsteady laminar flow) and for $Re_F > 1800$, the film flow is turbulent. Evidence from the previous experiments on TS show that the turbulent flow regime is almost never observed (Andros, 1980, Hirshburg, 1980, Fadhl, 2016) and, thus, the pressure drop due to turbulent liquid film flow will not be discussed.

ΔP_l in the hydrodynamically developing region can be estimated as (Shah, 1978)

$$\Delta P_{1,\text{ent}} = 4f_{\text{ent}}[L_{\text{ent}}^+] \left[\frac{1}{2} \rho_l u_l^2 \right] \quad (1.4)$$

where f_{ent} is the apparent Fanning friction factor and L_{ent}^+ is the dimensionless entrance length given as $L_{\text{ent}}^+ = \frac{L_{\text{ent}}}{D_h}$ (Shah, 1978). L_{ent} can be estimated as

$$L_{\text{ent}} \sim \delta_{C,F} \text{Re}_F \quad (1.5)$$

where $\delta_{C,F}$ is the thickness of the condensate film estimated as (Bergman et al., 2018)

$$\delta_{C,F} = \left[\frac{3}{4} \text{Re}_F \frac{\mu_l}{\rho_l} \frac{\mu_l}{(\rho_l - \rho_v)} \frac{1}{g \sin \theta} \right]^{\frac{1}{3}} \quad (1.6)$$

Re_F can be estimated as

$$\text{Re}_F = \frac{\rho_l u_l D_{h,l}}{\mu_l} = \frac{4 \rho_l u_l \delta_{C,F}}{\mu_l} = \frac{4 \dot{m}_c}{\pi D_i \mu_l} = \frac{4 \dot{Q}_{\text{out}}}{\pi D_i h'_{fg} \mu_l} = \frac{4 \dot{Q}'_{\text{out}} L_c}{h'_{fg} \mu_l} \quad (1.7)$$

where u_l is the mean velocity of the film flow, $u_l = \left[\frac{g \sin \theta (\rho_l - \rho_v) \delta_{C,F}^2}{3 \mu_l} \right]$, D_h is the hydraulic diameter of the duct (equivalent to D_i for circular cross-sectioned cylinder), μ_l is the dynamic viscosity of the liquid phase, \dot{m}_c is the condensate mass flow rate ($\dot{m}_c = \frac{\dot{Q}_{\text{out}}}{h_{fg}}$), \dot{Q}_{out} is the output cooling rate from the condenser ($\approx \dot{Q}_{\text{in}}$ at steady state condition), \dot{Q}'_{out} is the output heat flux, h'_{fg} is the modified latent heat of vaporization (where $h'_{fg} = h_{fg}(1 + 0.68 \frac{C_p \Delta T}{h_{fg}})$) and h_{fg} is the latent heat of vapourization. The value of f_{ent} in equation (1.4) can be estimated as (Shah, 1978)

$$f_{\text{ent}} = \frac{1}{\text{Re}_F} \left[\frac{3.44}{\sqrt{L_{\text{ent}}^+}} + \frac{\frac{1.25}{4L_{\text{ent}}^+} + 16 - \frac{3.44}{\sqrt{L_{\text{ent}}^+}}}{1 + 0.00021(L_{\text{ent}}^+)^{-2}} \right] \quad (1.8)$$

ΔP_1 for a fully developed laminar film flow ($\text{Re}_F < 40$) can be estimated as

$$\Delta P_{1,\text{lam}} = 4f_{\text{lam}}[L_{\text{lam}}^+] \left[\frac{1}{2} \rho_l u_l^2 \right] \quad (1.9)$$

where f_{lam} is the Fanning friction factor for the laminar regime film flow estimated as $f_{lam} = 24/Re_F$ and L_{lam}^+ is the dimensionless laminar length calculated as $L_{lam}^+ = \frac{L_{lam}}{D_h}$. If L_{ent} is significant, then the length over which the fully developed laminar flow is prevalent can be taken as $L_{lam} = (L_c + L_a + (L_e - L_p)) - L_{ent}$. If L_{ent} is negligible, then $L_{lam} \approx (L_c + L_a + (L_e - L_p))$.

ΔP_1 for a wavy laminar film can be estimated using

$$\Delta P_{1,wavy} = 4f_{wavy,lam} [L_{wavy,lam}^+] \left[\frac{1}{2} \rho_l u_{l,wavy,lam}^2 \right] \quad (1.10)$$

where $f_{wavy,lam}$ is the Fanning friction factor for the wavy laminar regime, computed using $\frac{|\tau_{wavy,lam}|}{\frac{1}{2} \rho_l u_{l,wavy,lam}^2}$, and $L_{wavy,lam}^+$ is the dimensionless wavy laminar length calculated as $L_{wavy,lam}^+ = \frac{L_{wavy,lam}}{4\delta_{wavy,lam}}$. The method to estimate $u_{l,wavy,lam}$, $\tau_{wavy,lam}$ and $\delta_{wavy,lam}$ for different surface wave profiles (sinusoidal, teardrop shape) will not be discussed here but can be referred to Pierson and Whitaker (1977) and Hirshburg (1980) where those methods are described in detail. Figure 1.7 shows a schematic of the flow of a falling liquid film illustrating the different characteristic lengths associated with the flow.

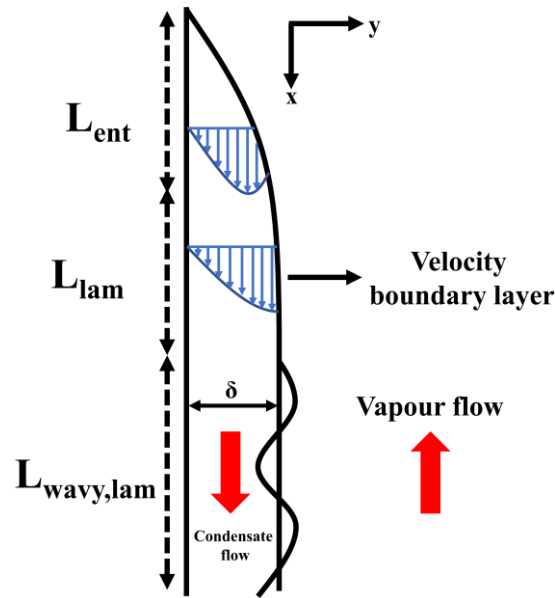


Figure 1.7 Schematic of the falling liquid film showing all the relevant parameters. L_{ent} , L_{lam} and $L_{wavy,lam}$ are not drawn to scale.

The flow of the liquid within the HP wick structure is laminar because the liquid velocity through a wick is very low (Chi, 1976, Reay and Kew, 2006). ΔP_1 for the liquid flow through a wick ($\Delta P_{1,w}$) can be estimated using

$$\Delta P_{1,w} = 4f_{\text{lam}} \left[\frac{L_{\text{eff}}}{D_{h,w}} \right] \left[\frac{1}{2} \rho_1 u_{1,w}^2 \right] \quad (1.11)$$

where $u_{1,w}$ is the liquid velocity through a wick and $D_{h,w}$ is the hydraulic diameter of a wick, respectively. Mathematical manipulation of equation (1.11) results in a pressure drop expression similar to Darcy's (1856) law for pressure drop obtained for a porous medium as

$$\Delta P_{1,w} = F_{1,w} L_{\text{eff}} \dot{Q}_{\text{out}} \quad (1.12)$$

where $F_{1,w}$ is the frictional coefficient for the liquid flow in a wick expressed as $F_{1,w} = \left[\frac{\mu_1}{KA_w h_{fg} \rho_1} \right]$, K is the wick permeability computed as $K = \frac{1}{2} \left[\frac{\varepsilon_w D_{h,w}^2}{f_{\text{lam}} \text{Re}_{\text{liq},w}} \right]$, A_w is the wick cross-sectional area, $A_w = \frac{\pi}{4} (D_i^2 - D_v^2)$, D_v is the vapour core diameter and ε_w is the wick porosity. As the mass flow varies within the evaporator and the condenser, an effective length L_{eff} , where $L_{\text{eff}} = \left(\frac{L_e + L_c}{2} \right) + L_a$ needs to be used instead of the simple geometric length. The variables ε_w , $D_{h,w}$ and $(f_{\text{lam}} \text{Re}_{\text{liq},w})$ required for evaluating K for various wick structures are illustrated in Table A.1 in Appendix A. The schematic of the various wick structures is also shown in Figure A.1 in Appendix A for completeness. The pressure drop estimations for the vapour flow in both TS and HP are described in the next subsection.

1.2.1.3 Estimation of the vapour pressure drop, ΔP_v

The vapour pressure drop results from the frictional drag, shear stress at the liquid vapour interface, and the dynamic pressure effects. However, in a TS the vapour may come into contact with the TS walls only at the start-up and during the occurrence of a dry patch in the event of liquid film breakdown (Fujita and Ueda, 1978 a, b). Therefore, under normal steady state operating conditions, ΔP_v in a TS due to the wall frictional drag is likely to

be zero. However, ΔP_v in a HP will be caused by the frictional drag in the wick, the shear stress at the liquid vapour interface and the dynamic pressure effects.

ΔP_v arising from the dynamic pressure ($\Delta P_{v,d}$) effects due to inertia in a TS and a HP is given by Reay and Kew (2006) as

$$\Delta P_{v,d} = \rho_v u_v^2 \quad (1.13)$$

where $\rho_v u_v^2$ represents the momentum flux in the axial direction and u_v is the vapour velocity (the missing coefficient 0.5 in equation (1.13) is not explained in Reay and Kew, 2006). Substituting $u_v = \left[\frac{\dot{Q}_{in}}{A_v \rho_v h_{fg}} \right]$ (where A_v is the cross-sectional area of the vapour core) and including a coefficient β (representing the vapour flow through different cross-sections for e.g., circular tubes, rectangular tubes, or flow through a circular annuli) in equation (1.13) results in

$$\Delta P_{v,d} = \beta \left[\frac{\dot{Q}_{in}^2}{\rho_v A_v^2 h_{fg}^2} \right] \quad (1.14)$$

Equations (1.13) and (1.14) are valid for both TS and HP, the only difference being the size of the vapour core cross-sectional area (A_v). Since A_v for a HP is smaller than that of a TS, for a given tube diameter, due to the presence of a wick, $\Delta P_{v,d}$ in a HP is expected to be higher than that in a TS. The values of β for different flow cross-sections are illustrated in Table A.2 in Appendix A.

$\Delta P_{\text{shear},l-v}$ arising from the shear stress at the liquid vapour interface can be estimated as

$$\Delta P_{\text{shear},l-v} = \left[4\tau_i \frac{L_{\text{eff}}}{D_i} \right] \quad (1.15)$$

where τ_i is the interfacial shear stress caused due to the liquid flow. τ_i can be estimated as (Brauer, 1971, Gross, 1992)

$$\tau_i = \left[\frac{f_i}{2} \right] \rho_v u_v^2 = \frac{1}{2} f_i \left[\frac{\dot{Q}_{in}^2}{\rho_v A_v^2 h_{fg}^2} \right] \quad (1.16)$$

where f_i is the Fanning friction factor for the liquid vapour interfacial shear estimated as (Gross, 1992)

$$f_i = \left[\frac{89.5}{\varphi^2} \right] + \left[\frac{0.051}{\varphi^{0.25}} \right] \quad (1.17)$$

φ is a non-dimensional constant estimated as

$$\varphi = c^* \left(\frac{Re_v}{Re_F^n} \right) \left(\frac{\rho_l}{\rho_v} \right)^{0.4} \left(\frac{\mu_v}{\mu_l} \right)^{0.67} \left(\frac{2\delta^*}{D_i} \right)^{0.5} \quad (1.18)$$

where c^* is a non-dimensional constant, n is the exponent of Re_F . $c^* = 4.76$ and $n = 0.6$ for $Re_F \geq 160$ and $c^* = 1.31$ and $n = 0.25$ for $Re_F < 160$. $\delta^* = 1.44\delta_v(Re_F)^{0.33}$ for $Re_F \leq 2064$ and $\delta^* = 0.303\delta_v(Re_F)^{0.583}$ for $Re_F > 2064$. δ_v is the characteristic scale of the condensate film thickness estimated as (Gross, 1992)

$$\delta_v = \sqrt[3]{\frac{\mu_l^2}{g \sin \theta \rho_l (\rho_l - \rho_v)}} \quad (1.19)$$

ΔP_v arising from the frictional effects in a HP ($\Delta P_{v,f}$) is given by

$$\Delta P_{v,f} = 4f_v \left[\frac{L_{eff}}{D_{h,v}} \right] \left[\frac{1}{2} \rho_v u_v^2 \right] \quad (1.20)$$

where f_v is the Fanning friction factor for the vapour flow and $D_{h,v}$ is the hydraulic diameter for the vapour flow ($D_{h,v} = 4 \left(\frac{\text{cross-sectional area}}{\text{wetted perimeter}} \right)$). A similar technique to that used while deriving (1.12) is applied to equation (1.20) resulting in

$$\Delta P_{v,f} = F_v L_{eff} \dot{Q}_{in} \quad (1.21)$$

where F_v is the frictional coefficient of the vapour flow expressed as $F_v = \left[\frac{2(f_v Re_v) \mu_v}{A_v h_{fg} \rho_v D_{h,v}^2} \right]$ and Re_v is the vapour flow Reynolds number computed as $Re_v = \left[\frac{\dot{Q}_{in} D_{h,v}}{\mu_v A_v h_{fg}} \right]$. The expressions for f_v for different vapour flow conditions is summarized in Table A.3 in Appendix A. The next paragraph describes the pressure driving potential, ΔP_{drive} required to cause the fluid flow inside TS and HP.

1.2.1.4 Estimation of the pressure driving potential, ΔP_{drive}

ΔP_{drive} comprises two components, one which is generated due to the vapour temperature differential between the evaporator and the condenser in a thermodynamic cycle (referred to as ΔP_{therm}) and the other generated due to the surface tension of the WF at the curved menisci of a wick referred as ΔP_{cap} (this term is also known as the capillary pressure). For a TS, ΔP_{therm} alone facilitates the pumping process inside the WF, whereas for a HP, both P_{therm} and ΔP_{cap} drive the fluid flow. The capillary pressure ΔP_{cap} is discussed next.

The maximum capillary pressure, $\Delta P_{\text{cap,max}}$ that can be produced within a wick is given by the Laplace and Young relation (1806) as

$$\Delta P_{\text{cap,max}} = \frac{2\sigma}{r_c} \quad (1.22)$$

where σ is the surface tension force coefficient and r_c is the effective pore radius of a wick. If σ is constant at the interface, then $\Delta P_{\text{cap,max}}$ depends only on r_c (r_c is equivalent to the radius of curvature of the WF meniscus at the wick). The development of capillary pressure at the liquid-vapour interface is shown schematically in Figure 1.8. The expressions for r_c for various types of wicks are summarized in Table A.4 in Appendix A. Thermodynamic concepts need to be invoked in order to estimate ΔP_{therm} which is done in the next section.

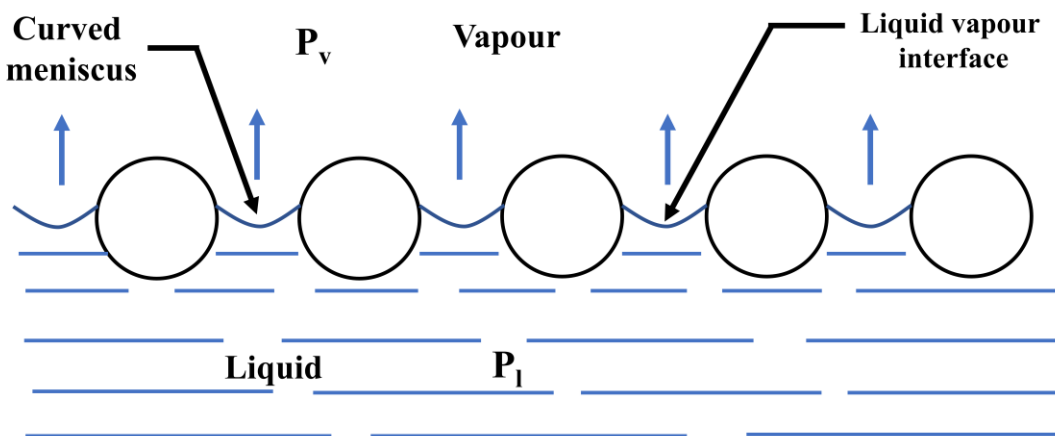


Figure 1.8 Development of the capillary pressure at the curve liquid-vapour interface.

1.2.2 The thermodynamics of TS and HP

A temperature differential ($\Delta T_{e,c}$) between the vapour in the evaporator and the condenser must exist so that a vapour pressure differential, $\Delta P_{e,c}$ (where $\Delta P_{e,c} = \Delta P_{\text{therm}}$) can exist in order to drive the WF from the evaporator toward the condenser. The relation between $\Delta P_{e,c}$ and $\Delta T_{e,c}$ can be obtained either from the Clapeyron equation (without the ideal gas approximation), equation 1.23, or from the Clapeyron-Clausius equation (using the ideal gas approximation), equation 1.24, (Cengel et al., 2019). The equations can be expressed as

$$\Delta P_{e,c} = \Delta T_{e,c} \left[\frac{h_{fg}(T = T_{v,e})}{T_{v,e} v_{lv}(T = T_{v,e})} \right] = \Delta T_{e,c} \left[\frac{h_{fg}(T = T_{v,c})}{T_{v,c} v_{lv}(T = T_{v,c})} \right] \quad (1.23)$$

$$\Delta P_{e,c} = \Delta T_{e,c} \left[C^* \frac{h_{fg}(T = T_{v,e})}{\bar{R} T_{v,e}^2} e^{-\frac{h_{fg}(T = T_{v,e})}{\bar{R} T_{v,e}}} \right] = \Delta T_{e,c} \left[C^* \frac{h_{fg}(T = T_{v,c})}{\bar{R} T_{v,c}^2} e^{-\frac{h_{fg}(T = T_{c,\text{sat}})}{\bar{R} T_{v,c}}} \right] \quad (1.24)$$

where C^* is a dimensional constant (N/m^2) whose value is different at different saturation states, \bar{R} is the specific gas constant, v_l , v_v are the specific volumes of the saturated liquid and the saturated vapour, respectively and $v_{lv} = v_v - v_l$. $T_{v,e}$ and $T_{v,c}$ denotes the temperatures of the vapour at the evaporator and the condenser sections, respectively. Since the source temperature (T_{source}) for which the TS or HP is designed is typically known, $T_{v,e}$ ($T_{v,e}$ is the temperature of the vapour at the evaporator) can be estimated if the boiling thermal resistance is known. Once $T_{v,e}$ is determined, $h_{fg}(T = T_{v,e})$ and $v_{fg}(T = T_{v,e})$ for equations (1.23) and (1.24) can be determined from the steam table. The operating temperature (T_{op}) of the TS and the HP can be estimated as

$$T_{\text{op}} = T_{v,e} - \frac{1}{2} \Delta T_{e,c} \quad (1.25)$$

where $\Delta T_{e,c} = T_{v,e} - T_{v,c}$ and $T_{\text{op}} = \frac{1}{2}(T_{v,e} + T_{v,c})$. Equations (1.23), (1.24) and (1.25) also help determine whether the values of $\Delta T_{e,c}$ obtained from these equations are physically achievable. Subtracting T_{op} from $\Delta T_{e,c}$ yields

$$\Delta T_{e,c} - T_{\text{op}} = \frac{1}{2}(T_{v,e} - 3T_{v,c}) \quad (1.26)$$

If $\Delta T_{e,c} - T_{op} \geq 0$ then $T_{v,e} \geq 3T_{v,c}$ i.e., when $T_{v,c} = 273.15[\text{K}]$ then $T_{v,e} > 819.45[\text{K}]$, which is physically unrealistic for distilled water as the WF, since its critical temperature is $647.1[\text{K}]$. Similar conclusions can be derived for other WF. This suggests that even if $\Delta P_{e,c} \geq \sum \Delta P_{drops}$ ($\sum \Delta P_{drops}$ denotes the sum of all the pressure drops) the heat transfer operation will not start until $\Delta T_{e,c} < T_{op}$. Similar conclusions were obtained by Richter and Gottschlich (1990).

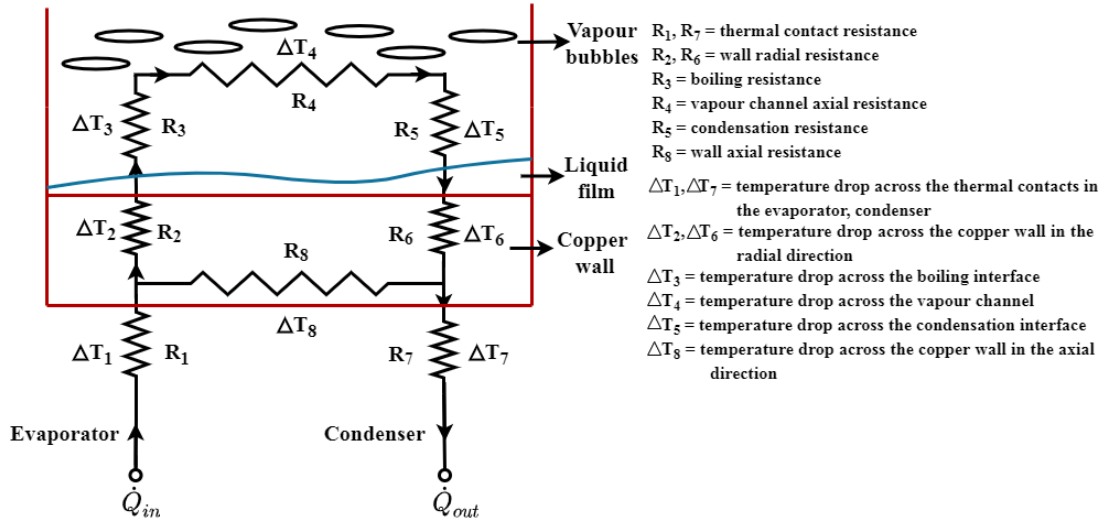
At present, there are no quantitative methods for determining the entropy changes and the entropy generated during the thermodynamic cycle. These are considered important as they give fundamental insights into how property changes during the various thermodynamic processes. The gap has been addressed in Chapter 3. The heat transfer theory of TS and HP is described in the next subsection.

1.2.3 The Heat transfer theory of TS and HP

If the sink temperature (T_{sink}) is chosen such that $\Delta T_{e,c} < T_{op}$, then it can be shown that the desired time (equivalent to the cycle time in mold cooling applications) to transfer a given quantity of heat is directly proportional to the thermal resistance. Thus, the thermal resistance plays the most important role in determining the thermal performance of TS and HP. The next two subsections describe the thermal resistance of a TS and a HP and shows how it can be estimated for each component.

1.2.3.1 The thermal resistance of a TS

A schematic of the thermal resistance network of a TS is shown in Figure 1.9 (adapted from Reay and Kew, 2006), where each thermal resistance, R_1 to R_8 , and the temperature drop across the components, ΔT_1 to ΔT_8 are delineated in the figure. Assuming that the evaporator and the condenser are in thermal equilibrium with their respective heat source or sink, the thermal contact resistances (R_1 and R_7) can be assumed to be negligible (Fadhl, 2016, Jouhara and Robinson, 2010). Therefore, the significant thermal resistances in the thermal network of a TS are R_2 , R_3 , R_4 , R_5 , R_6 and R_8 .



R_2, R_6 and R_8 can be calculated using Fourier's law of heat conduction as $R_2 = \frac{\ln\left(\frac{D_o}{D_i}\right)}{2\pi L_e k_{wall}}$, $R_6 = \frac{\ln\left(\frac{D_o}{D_i}\right)}{2\pi L_c k_{wall}}$ (Bergman et al., 2011), $R_8 = \frac{L_e + L_a + L_c}{A_{wall} k_{wall}}$ (Reay and Kew, 2006); a slightly different expression for R_8 is reported in Fadhl (2016) and Jafari et al., (2016), where $R_8 = \frac{0.5L_e + L_a + 0.5L_c}{A_{wall} k_{wall}}$, where D_o is the outer diameter of the TS, D_i , L_e , L_a and L_c are already defined in Figure 1.3, A_{wall} is the cross-sectional area of the TS given as $A_{wall} = \frac{\pi}{4} (D_o^2 - D_i^2)$ (Reay and Kew, 2006) and k_{wall} is the thermal conductivity of the TS wall material. Utilizing the kinetic theory of gas and the Clapeyron equation (Clausius-Clapeyron equation for an ideal gas approximation), R_3 (R_{boil}) and R_5 (R_{cond}) can be estimated as (see section 2.3.7.5 in Reay and Kew, 2006 for the derivation)

$$R_3 = \frac{(2\pi\bar{R}T_{v,e})^{0.5} v_{fg}(T = T_{v,e})T_{v,e}}{A_{e,i} h_{fg}^2(T = T_{v,e})} \quad (R_3 = \frac{(2\pi\bar{R}T_{v,e})^{0.5} \bar{R}T_{v,e}^2}{A_{e,i} h_{fg}^2(T = T_{v,e}) P_{v,e}}) \quad (1.27)$$

$$R_5 = \frac{(2\pi\bar{R}T_{v,c})^{0.5} v_{fg}(T = T_{v,c})T_{v,c}}{A_{c,i} h_{fg}^2(T = T_{v,c})} \quad (R_5 = \frac{(2\pi\bar{R}T_{v,c})^{0.5} \bar{R}T_{v,c}^2}{A_{c,i} h_{fg}^2(T = T_{v,c}) P_{v,c}}) \quad (1.28)$$

where $A_{e,i}$, $A_{c,i}$ are the internal evaporator and condenser surface area given as $A_{e,i} = \pi D_i L_e$, $A_{c,i} = \pi D_i L_c$, respectively. For, convenience, R_3 and R_5 will be denoted by R_{boil} and

R_{cond} from here on throughout the thesis. R_4 can be estimated as by equations (1.23) and (1.24) as

$$R_4 = \left[\frac{\Delta P_{e,c} T_{v,e} v_{fg}(T = T_{v,e})}{h_{fg}(T = T_{v,e}) \dot{Q}_{in}} \right] \left(R_4 = \left[\frac{\Delta P_{e,c} \bar{R} T_{v,e}^2}{h_{fg}(T = T_{v,e}) P_{v,e} \dot{Q}_{in}} \right] \right) \quad (1.29)$$

The overall thermal resistance of a TS ($R_{O,TS}$) can then be calculated as $R_{O,TS} = \left(\frac{1}{(R_2 + R_{\text{boil}} + R_4 + R_{\text{cond}} + R_6)} + \frac{1}{R_8} \right)^{-1}$. The thermal resistance equations for the different components of the TS are summarised in Table 1.2 for completeness. The next section describes the thermal resistance of a HP.

Table 1.2 Thermal resistance equations for different components of a TS.

Thermal resistance	TS
R_1	Negligible
R_2	$\frac{\ln\left(\frac{D_o}{D_i}\right)}{2\pi L_e k_{\text{wall}}}$
R_3 (R_{boil})	$\left[\frac{(2\pi \bar{R} T_{v,e})^{0.5} v_{fg}(T = T_{v,e}) T_{v,e}}{A_e h_{fg}^2(T = T_{v,e})} \right], \left[\frac{(2\pi \bar{R} T_{v,e})^{0.5} \bar{R} T_{v,e}^2}{A_e h_{fg}^2(T = T_{v,e}) P_{v,e}} \right]$
R_4	$\left[\frac{\Delta P_{e,c} T_{v,e} v_{fg}(T = T_{v,e})}{h_{fg}(T = T_{v,e}) \dot{Q}_{in}} \right], \left[\frac{\Delta P_{e,c} \bar{R} T_{v,e}^2}{h_{fg}(T = T_{v,e}) P_{v,e} \dot{Q}_{in}} \right]$
R_5 (R_{cond})	$\left[\frac{(2\pi \bar{R} T_{v,c})^{0.5} v_{fg}(T = T_{v,c}) T_{v,c}}{A_c h_{fg}^2(T = T_{v,c})} \right], \left[\frac{(2\pi \bar{R} T_{v,c})^{0.5} \bar{R} T_{v,c}^2}{A_c h_{fg}^2(T = T_{v,c}) P_{v,c}} \right]$
R_6	$\frac{\ln\left(\frac{D_o}{D_i}\right)}{2\pi L_c k_{\text{wall}}}$
R_7	Negligible
R_8	$\frac{L_e + L_a + L_c}{A_{\text{wall}} k_{\text{wall}}}, \frac{0.5 L_e + L_a + 0.5 L_c}{A_{\text{wall}} k_{\text{wall}}}$
$R_{O,TS}$	$\left(\frac{1}{(R_2 + R_{\text{boil}} + R_{\text{cond}} + R_6)} + \frac{1}{R_8} \right)^{-1}$

1.2.3.2 The thermal resistance of a HP

The only difference in the thermal resistance network of a HP from a TS is the incorporation of two additional thermal resistance components ($R_{2,w}$ and $R_{6,w}$) and the modification of R_8 , due to the presence of wick structure (Figure 1.10).

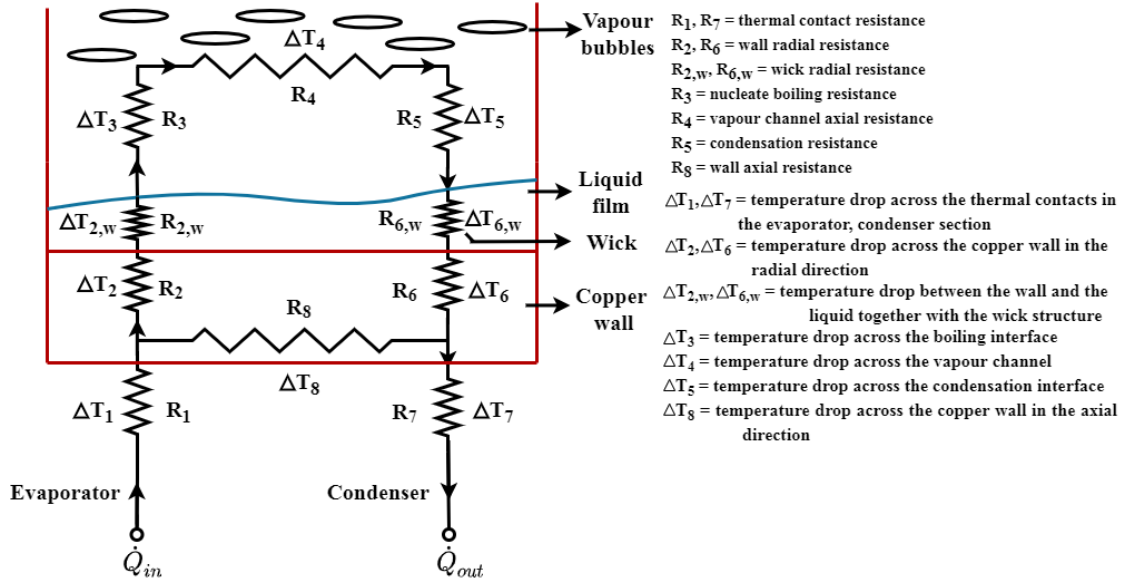


Figure 1.10 Thermal resistance network of a typical HP oriented in the horizontal direction. The horizontal orientation is only for illustration of the different thermal resistance components.

The modified R_8 , now termed as $R_{8,mod}$ is calculated as $R_{8,mod} = \frac{L_e + L_a + L_c}{(A_{wick}k_{eff,wick}) + (A_{wall}k_{wall})}$

or $R_{8,mod} = \frac{0.5L_e + L_a + 0.5L_c}{(A_{wick}k_{eff,wick}) + (A_{wall}k_{wall})}$, where A_{wick} is the cross-sectional area of the wick

given as $A_{wick} = \frac{\pi}{4}(D_i^2 - D_v^2)$, D_v is the vapour core diameter (where $D_v = D_i - 2d$, d is the

wick thickness) and $k_{eff,wick}$ is the effective thermal conductivity of the wick. $k_{eff,wick}$ for various wick structures is shown in Table A.5 in Appendix A. $R_{2,w}$ and $R_{6,w}$ can be

calculated using Fourier's law of heat conduction for a plane wall as $R_{2,w} = \frac{d}{k_{eff,wick}A_{e,i}}$

and $R_{6,w} = \frac{d}{k_{eff,wick}A_{c,i}}$ (Reay and Kew, 2006). A slightly different expression for $R_{2,w}$ and

$R_{6,w}$ reported in Chi (1976) utilizes the cylindrical wall geometry to calculate $R_{2,w}$ and

$R_{6,w}$ as $R_{2,w} = \frac{\ln(\frac{D_i}{D_v})}{2\pi L_e k_{eff,wick}}$ and $R_{6,w} = \frac{\ln(\frac{D_i}{D_v})}{2\pi L_c k_{eff,wick}}$. The overall thermal resistance of a HP

($R_{O,HP}$) can be calculated as $R_{O,HP} = \left(\frac{1}{(R_2 + R_{2,w} + R_3 + R_4 + R_5 + R_{6,w} + R_6)} + \frac{1}{R_8} \right)^{-1}$. The equations

for the thermal resistance of different components of the HP are summarized in Table 1.3 for completeness.

Table 1.3 Thermal resistance equations for different components of a HP.

Thermal resistance	HP
R_1	Negligible
R_2	$\frac{\ln\left(\frac{D_o}{D_i}\right)}{2\pi L_e k_{wall}}$
$R_{2,w}$	$\frac{d}{k_{eff,wick} A_e} + \frac{\ln\left(\frac{D_i}{D_v}\right)}{2\pi L_e k_{eff,wick}}$
$R_3 (R_{boil})$	$\left[\frac{(2\pi \bar{R} T_{v,e})^{0.5} v_{fg}(T = T_{v,e}) T_{v,e}}{A_e h_{fg}^2(T = T_{v,e})} \right], \left[\frac{(2\pi \bar{R} T_{v,e})^{0.5} \bar{R} T_{v,e}^2}{A_e h_{fg}^2(T = T_{v,e}) P_{v,e}} \right]$
R_4	$\left[\frac{\Delta P_{e,c} T_{v,e} v_{fg}(T = T_{v,e})}{h_{fg}(T = T_{v,e}) \dot{Q}_{in}} \right], \left[\frac{\Delta P_{e,c} \bar{R} T_{v,e}^2}{h_{fg}(T = T_{v,e}) P_{v,e} \dot{Q}_{in}} \right]$
$R_5 (R_{cond})$	$\left[\frac{(2\pi \bar{R} T_{v,c})^{0.5} v_{fg}(T = T_{v,c}) T_{v,c}}{A_c h_{fg}^2(T = T_{v,c})} \right], \left[\frac{(2\pi \bar{R} T_{v,c})^{0.5} \bar{R} T_{v,c}^2}{A_c h_{fg}^2(T = T_{v,c}) P_{v,c}} \right]$
$R_{6,w}$	$\frac{d}{k_{eff,wick} A_c} + \frac{\ln\left(\frac{D_i}{D_v}\right)}{2\pi L_c k_{eff,wick}}$
R_6	$\frac{\ln\left(\frac{D_o}{D_i}\right)}{2\pi L_c k_{wall}}$
R_7	Negligible
$R_{8,mod}$	$\frac{L_e + L_a + L_c}{(A_{wick} k_{eff,wick}) + (A_{wall} k_{wall})} + \frac{0.5L_e + L_a + 0.5L_c}{(A_{wick} k_{eff,wick}) + (A_{wall} k_{wall})}$
$R_{O,HP}$	$\left(\frac{1}{(R_2 + R_{2,w} + R_{boil} + R_{cond} + R_{6,w} + R_6)} + \frac{1}{R_g} \right)^{-1}$

1.3 Review of previous work on TS and HP

This section presents a brief review of the previous parametric studies on TS and HP. The aim here is to identify the shortcomings and the primary knowledge gaps associated with the thermal performance of TS and HP. This is not an exhaustive literature review (which will be presented in the next chapter) but, rather, a focused review on studies attempting to elucidate the effects of operating and geometric parameters.

A plethora of experimental studies have examined the thermal performance of TS with varying magnitudes of \dot{Q}_{in} , AR, FR and θ (Lee and Mittal, 1972, Shiraishi et al., 1982, Negishi and Sawada, 1983, Sauciu et al., 1995, Noie, 2005, Noie et al., 2009, Baojin et al., 2009, Jouhara and Robinson, 2010, Alizadehdakhel et al., 2010, Amatachaya and Srimuang, 2010, Abdullahi, 2015, Jafari et al., 2017a, b). The temperature distributions along the length of the TS have been reported for these operating conditions. However, none of the studies explain the trends in response to changes in the thermal and the geometric operating conditions. Moreover, the boiling (h_{boil}) and the condensation (h_{cond}) heat transfer coefficients have only been characterised in some studies (Noie, 2005,

Emami et al., 2008, Baojin et al., 2009, Amatachaya & Srimuang, 2010, Jouhara and Robinson, 2010, Jafari et al., 2017a, b, Kim et al., 2018), whilst others (Noie et al., 2009, Alizadehdakhel, 2010, Shabgard et al., 2014, Alammam et al., 2016, Gedik, 2016, Alammam et al., 2018) do not report the heat transfer coefficients at all. No definitive conclusions on the nature of the variation of h_{boil} and h_{cond} with \dot{Q}_{in} , AR, FR and θ can be derived. Part of this issue is the lack of consistency between the results obtained from the different studies and insufficient explanations being provided to explain the reported trends of h_{boil} and h_{cond} . No study has compared and synthesized these data sets to arrive at common conclusions, which restricts the prediction of the boiling thermal resistance (R_{boil}) and condensation thermal resistance (R_{cond}) for a given operating condition.

Different sets of boiling and condensation heat transfer correlations (Kruzhilin, 1947, Rohsenow, 1952, Labuntsov, 1972, Kusuda and Imura, 1973, Shiraishi et al., 1982, Kutateladze, 1990, Chowdhury et al., 1997) are used by different authors (Sauciuc et al., 1995, Noie, 2005, Baojin et al., 2009, Jafari et al., 2017a) to compare their h_{boil} and h_{cond} values. However, no reasons are given as to why a specific correlation was chosen over others. Jouhara and Robinson (2010) argued that there is no correlation or set of correlations that can predict the boiling heat transfer coefficient accurately in a TS and, thus, comparisons with all the available correlations must be made to select the correlation with the best prediction capability. This technique has flaws as the boiling correlation that is termed the best (Jouhara and Robinson, 2010, Jafari et al., 2017b) has been shown to either overpredict or underpredict the heat transfer coefficient or the thermal resistance by $\pm 30\%$. Although the condensation heat transfer coefficient has rarely been reported, those that are reported follow a similar procedure of comparison of the data with those obtained from the available correlations (Jouhara and Robinson, 2010, Jafari et al., 2017b). This restricts one from choosing a consistent correlation to predict h_{boil} and h_{cond} accurately for any TS under a given operating condition.

Only a limited number of experiments exist characterizing the effects of different operating parameters on conventional HP (Bowman, 1987, Devarakonda et al., 2005, Kempers et al., 2006, 2008, Sukchana and Jaiboonma, 2013, Brahim et al., 2014, Lips and Lefèvre, 2014). The primary reason for this is the widespread attention given to the

analysis of flat HP (Cao et al., 1997, Hwang et al., 2007, Do et al., 2008, Wang et al., 2011, Chen and Chou, 2015, Li et al., 2016) and micro HP (Babin et al., 1990, Kim et al., 2003, Do et al., 2008, Mahmood and Akhanda, 2008, Wang et al., 2010, Hung and Seng, 2011) because of their application in consumer electronics and semiconductor devices. However, in all electrical components, the round HP are molded to reform their shape into a flat tube. Nevertheless, Wang et al., (2011) and Chen and Chou (2015) showed that both the evaporator and condenser lengths have significant impacts on the heat transfer limit of a HP. The effects of \dot{Q}_{in} , FR and θ have been studied for nanofluids-based HP (Naphon et al., 2008, Hung et al., 2013, Ghanbarpour, 2017) which suggests that the operating parameters that influence the thermal performance of TS also affects the thermal performance of HP.

Almost all the previous studies on TS and HP have focussed on evaluating the thermal performance of these devices without any thermodynamic considerations. The WF undergoes a change of phase and repeatedly goes through a succession of thermodynamic processes and states. Since the WF carries thermal energy with it, it is essential to evaluate its state at different points in the thermodynamic cycle in order to gain a fundamental understanding of the changes in the thermodynamic properties. The previous thermodynamic studies (Richter and Gottschlich, 1990, Zuo and Faghri, 1998, Khalkhali et al., 1999) did not analyze the thermodynamic processes in a comprehensive manner and contained some key omissions. There are inconsistencies between the results presented in Richter and Gottschlich, (1990), Zuo and Faghri, (1998), Khalkhali et al., (1999). No quantitative evaluation of the entropy changes and entropy generated during the thermodynamic processes has been made. This prevents one from identifying the components responsible for entropy generation and how entropy generation during the various processes can be minimized.

The previous computational fluid dynamics (CFD) studies on TS (Alizadehdakhel et al., 2010, Kafeel and Turan, 2013, Fadhl et al., 2013, Alammar et al., 2016, Xu et al., 2016, Wang et al., 2018, Wang et al., 2019, Tarokh et al., 2021) and HP (Famouri, 2014, Mwaba et al., 2014) have provided either incorrect or incomplete details of the modelling approaches, which poses a significant challenge when attempting to reproduce and

validate those results. Furthermore, potential issues with mass and energy conservation have been noted while attempting to replicate the results from those studies (Alizadehdakhel et al., 2010, Fadhl et al., 2013, Kafeel and Turan, 2013, Kim et al., 2015, Xu et al., 2016, Wang et al., 2019). None of the previous studies report the pressure, velocity and temperature fields inside the TS. Taken together, this makes previous CFD results impossible to reproduce and, therefore, they cannot be used as a basis for further modelling development toward mold cooling applications.

This brief assessment of the parametric studies identifies the primary knowledge gaps in this field. They are

- i) A lack of explanation of the previous trends in the temperature distribution and the thermal performance metric for TS. This is due to two reasons. Firstly, no synthesis and evaluation of these data sets have been undertaken to arrive at consistent conclusions. Secondly, the data are not analysed with respect to the boiling and condensation behaviour of the WF in response to changes in \dot{Q}_{in} , AR, FR and θ . Thirdly, the range of values of the different operating parameters were not appropriately varied in the previous TS studies in order to obtain a complete understanding of their influence on the boiling and condensation thermal resistances.
- ii) Incomplete and inaccurate analysis of the thermodynamic cycle of a TS and a HP. This indicates that some of the thermodynamic state points determined previously on the temperature-specific entropy (T-s) diagram were inaccurate, and the analyses shown in order to estimate the entropy changes and the entropy generation were incomplete.
- iii) A lack of correct, consistent predictive correlations for the boiling and the condensation thermal resistances for a TS and a HP. This originates from the fact that the previous boiling and condensation equations, when compared to the experimental data, demonstrate large variability (more than $\pm 30\%$) between the actual and the predicted values of h_{boil} , h_{cond} , (or R_{boil} and R_{cond}).

In view of the deficiencies described above, it is clear that improved thermodynamic and heat transfer modelling and analyses of TS and HP need to be undertaken, along with a

more comprehensive experimental parametric investigation of a TS. The present work, which investigates the thermal characteristics of a TS, contributes to the fundamental understanding of its behaviour under different operating conditions.

1.4 Motivation and objectives of the present research

The work presented in this thesis was motivated by the need to reduce the cooling time of the plastic injected molds required by the automotive industry. The idea of the project was conceived by the industrial partner, Acrolab Ltd., a leading company in HP technologies.

Considering the nature of the proposed study, the work is divided into two parts. The objectives of the first part of this work address the knowledge gaps identified in i), ii) and iii) of section 1.3. These objectives are to:

- i) Conduct a critical synthesis and analysis of the prior experimental TS data to gain a preliminary understanding of how operating conditions influence the flow behaviour inside TS. The WF flow behaviour directly influences the boiling, condensation, and the overall thermal resistance of TS.
- ii) Develop a thermodynamic model for predicting the entropy changes and the entropy generated during the different thermodynamic processes within a TS and a HP. This will provide a fundamental understanding of the state of the WF as it passes through the various thermodynamic processes and aid in the design and performance optimization of TS and a HP.
- iii) Develop a theoretical boiling and condensation thermal resistance network model for TS and HP.

The research gap identified from i) forms the basis of the second part of this work which are to:

- i) Investigate the performance characteristics of a fixed diameter TS experimentally, by appropriately varying the values of \dot{Q}_{in} , FR and AR and interpret the heat transfer characteristics at the evaporator and the condenser.

Additionally, the experimental data is also used to

- ii) Validate the new boiling and the condensation thermal resistance models with the previous and the present experimental data for its use in academia and industrial applications.

The objectives described above were achieved in the laboratory and the computing facilities at the University of Western Ontario.

The practical outcomes of this work are directly applicable for

- i) Optimizing the design and thermal performance of TS and
- ii) Predicting the boiling and condensation thermal resistances of a TS and a HP under a given thermal and geometrical operating condition.

The next section outlines the scope of the present work and its limitations.

1.5 Scope of the present work

The scope of the present study includes a combination of theoretical and experimental investigation of a fixed diameter copper-water TS under different operating conditions. The critical analysis of the previous TS data, thermodynamic evaluation of TS and HP, and the development of the thermal resistance model are part of the theoretical development of this work. Experimentation, data analysis and interpretation of the TS heat transfer data form the experimental part of this work.

The next section describes the general layout of the thesis and briefly summarizes the key topics discussed in each chapter.

1.6 Thesis Organization

This thesis is written in “Monograph” format, which consists of eight chapters, a list of references and appendices.

The present chapter, Chapter 1, provides the reader with general background on TS and HP and describes the physical phenomena associated with heat transfer. The main operational variables influencing the thermal performance have been outlined. The key governing principles of fluid mechanics, thermodynamics and heat transfer are discussed, along with the equations that are relevant for predicting pressure drops. A brief review of the previous studies on TS and HP is presented next, which helps to identify the research gaps and define the overall objectives of this research. The scope of the research in order to address those objectives is then outlined.

Chapter 2 presents the results from the synthesis and evaluation of the previous experimental data on a fixed diameter TS. This has been done in order to i) gain a preliminary understanding of the effects of the operational conditions on the thermal resistance of TS ii) identify the gaps in the previous experimental operational conditions and iii) identify the knowledge gaps related to the prediction of the thermal resistance of TS and HP.

The next chapter, Chapter 3, presents a detailed thermodynamic evaluation of TS and HP. The entropy change and the entropy generation associated with each process are derived. Further, proposals are made so that the entropy generated during the TS and HP can be minimised.

Chapter 4 describes the new set of boiling and condensation thermal resistance equations developed for prediction purposes. Further, it is shown how these equations can qualitatively characterize the variation in thermal resistances with the operational parameters outlined in Chapter 1.

Chapter 5 discusses the experimental methodology, where the details of the various equipment used, the experimental setup, the data reduction procedure and the uncertainty associated with the data recorded from each piece of equipment are described.

Chapter 6 presents the results from the present experimental work. The effects of \dot{Q}_{in} and FR on the pool boiling, film boiling, and condensation thermal resistances are considered independently.

Chapter 7 presents the results of the validation of the boiling correlations. In this chapter, and the model constants are estimated, and it is demonstrated how the results address the knowledge gaps identified from the synthesis of the previous experimental data identified in Chapter 2.

Finally, Chapter 8 summarizes the key quantitative findings and the original contributions from this study. The specific areas that require further investigation to improve the understanding of the working phenomena inside TS and HP are suggested. This forms the recommendations for future work.

1.7 Summary

This section summarizes the items discussed in this chapter. Firstly, the heat transfer phenomena within TS and HP are described. The key variables influencing the thermal resistance of TS and HP are outlined and described. Secondly, the fundamental principles of fluid mechanics, thermodynamics and heat transfer governing the heat transfer in TS and HP are discussed. Thirdly, a brief qualitative review of the existing studies of TS and HP is undertaken to identify the primary knowledge gaps associated with the thermal performance of TS and HP. Fourthly, the primary objectives arising from the knowledge gaps are outlined, along with the scope of the present work. Fifthly, the thesis organization is outlined, together with the details of the work presented in each chapter.

The next chapter presents the results from the critical synthesis and evaluation of the previous TS data to gain a preliminary understanding of the performance of TS under varying \dot{Q}_{in} and FR.

Chapter 2

2 Synthesis and analysis of the previous thermosyphon data

This chapter presents a critical analysis of the previous experimental data delineating the effects of the input heating power \dot{Q}_{in} and the fill ratio (FR) on the boiling (R_{boil}) and condensation (R_{cond}) thermal resistances of thermosyphons (TS). This has been done to achieve two primary objectives which are i) to discover the important data trends and gain an understanding of how these operating conditions influence R_{boil} and R_{cond} , and ii) to identify the gaps in the previous experimental conditions and provide suggestions for appropriately varying these operational parameters. The work presented in this chapter satisfies the objective i) outlined in section 1.4 in Chapter 1 and establishes the basis for the experimental work reported in Chapters 5 and 6. The chapter is divided into three sections. The first two sections evaluate the effects of \dot{Q}_{in} and FR on R_{boil} and R_{cond} . The third section summarizes the work and provides recommendations related to ii).

A lot of prior studies (Shiraishi et al., 1982, Noie 2005, Baojin et al., 2009, Alizadehdakhel et al., 2010, Amatachaya and Srimuang, 2010, Fadhl, 2016, Jafari et al., 2017 a, b, Kim et al., 2018) have examined the performance of copper-distilled water thermosyphons (TS) experimentally. However, the key boiling and the condensation behaviour was either not reported or was reported with very little explanations. The conclusions drawn regarding the influence of the \dot{Q}_{in} and FR on the overall thermal resistance are specific to those studies. No parametric trends from the previous data have been established, which fails to answer the question “How does the thermal resistance vary with \dot{Q}_{in} and FR, and what mechanisms govern those behaviours”. No prior attempts have been made to synthesize the data from different studies and compare them. Therefore, a quantitative re-assessment of the previous experimental data on TS is carried out to understand how \dot{Q}_{in} and FR influence R_{boil} and R_{cond} .

The results of the assessment are as follows. First, the temperature distribution along the length of the TS is presented and discussed. Next, the boiling and condensation curves

are examined to characterize the behaviour in different boiling and condensation regimes. This is followed by an examination of the relationship between ΔT and R_{boil} , R_{cond} . Then, the effects of the operating parameters on ΔT are examined, followed by the effects of the same parameters on R_{boil} and R_{cond} . The next subsection investigates the effects of \dot{Q}_{in} followed by an investigation of the effects of FR.

2.1 Effects of \dot{Q}_{in} on the thermal performance of TS

2.1.1 Evaluation of the temperature distribution

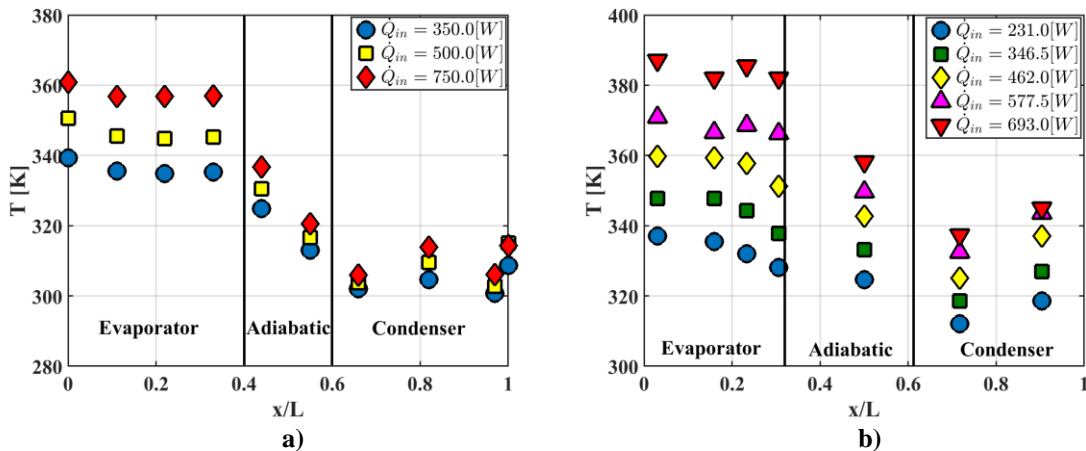
Figure 2.1 (a-i) shows the steady state temperature distribution along the length of the TS at varying \dot{Q}_{in} from previous studies. Those studies are summarized in Appendix B for completeness. The trends described here are based on the author's own observation and interpretation of the data.

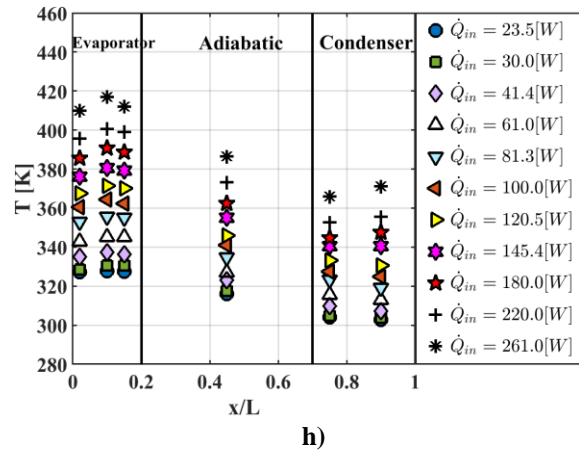
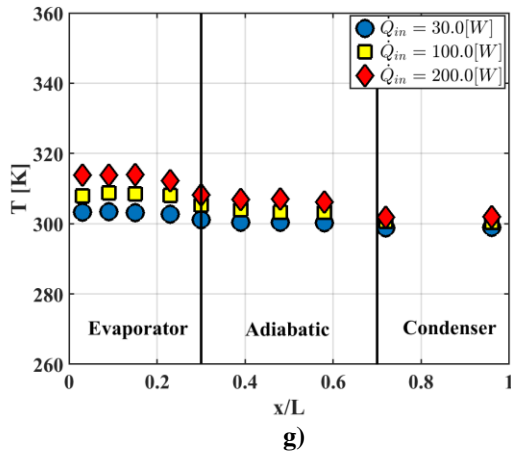
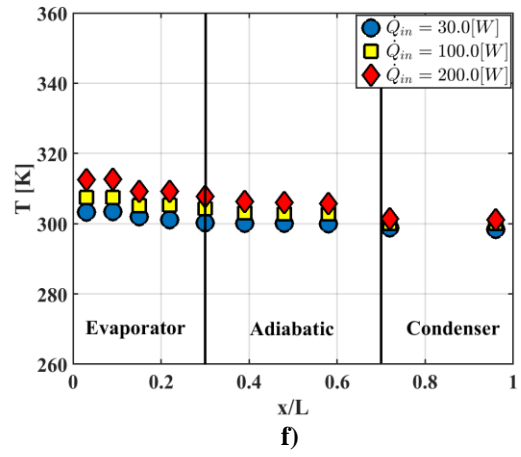
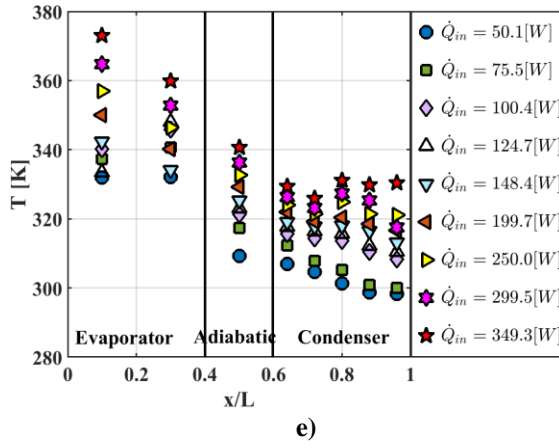
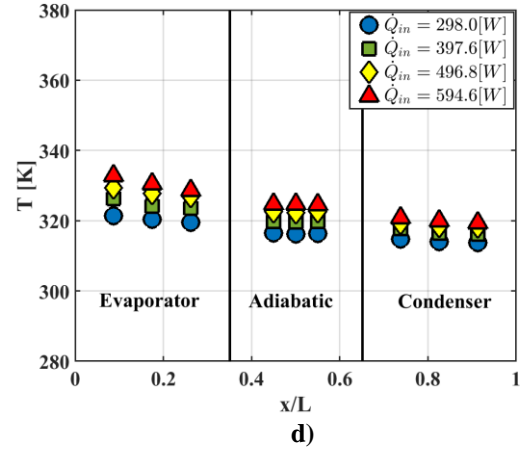
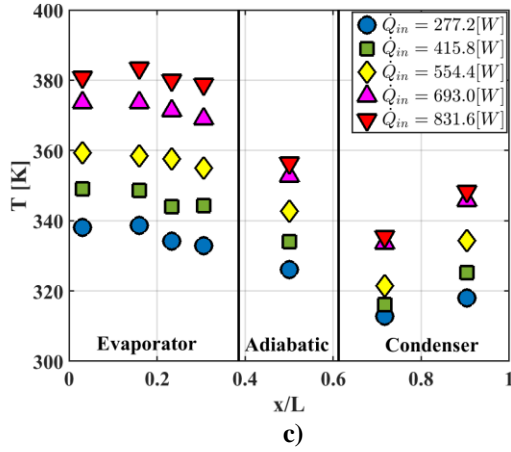
There are two consistent trends that can be observed. Firstly, the temperature magnitudes are higher in the evaporator, followed by a sharp decrease in the adiabatic section. The temperatures continue to decrease, reaching a minimum value at the start of the condenser, with a slightly higher temperature towards the end of the condenser. The averaged temperature of the adiabatic section (T_a) is typically assumed to be equal to T_v , where T_v is the vapour temperature (Baojin et al., 2009, Amatachaya and Srimuang, 2010, Jouhara and Robinson, 2010). Since the heat transfer is from the evaporator surface towards the core, the adiabatic temperatures are lower than the evaporator. Similarly, the condenser WF temperature must be lower than the evaporator to facilitate the WF circulation. This explains the lower temperatures at the condenser.

The lower surface temperature at the start of the condenser observed in Figure 2.1 (a, b, c, e, h, i) is due to the coolant inlet being almost always located near to the start of the condenser (it refers to the section right after the adiabatic section). This causes the thermocouples located in the vicinity of the coolant inlet to record an intermediate value between the coolant and the condensate temperature. The slightly higher temperature observed towards the end of the condenser is primarily due to two reasons. Firstly, the high temperature vapour flow meets the end cap of the condenser where condensation is

initiated. Secondly, the thickness of condensate layer increases in the direction of gravity. Hence, the condensation thermal resistance near the condenser top end is less than the start of the condenser indicating higher heat transfer to the coolant near the condenser top end. The effects of the above two phenomena may cancel out each other when the coolant inlet is located near the condenser top end (Jafari et al., 2017 a, b). A more uniform temperature along the condenser is then observed (see Figure 2.1(f, g)).

Secondly, with an increase in \dot{Q}_{in} , the evaporator, adiabatic, and condenser surface temperatures increase. However, the effects are more prominent at the evaporator than the adiabatic and the condenser section (Figure 2.1). The increase in the evaporator surface temperature is due to an increase in the heat flux (\dot{Q}'_{in}) ($\dot{Q}'_{in} = \frac{\dot{Q}_{in}}{A_{e,o}}$, $A_{e,o}$ is the evaporator outer surface area) with \dot{Q}_{in} at fixed $A_{e,o}$. Nukiyama's (1966) observation of saturated pool boiling on a plane surface demonstrates $\dot{Q}'_{in} \propto (\Delta T)^3$, where ΔT at the evaporator is equivalent to $\Delta T_{e,a}$ ($\Delta T_{e,a} = T_e - T_a$, and T_e is the average evaporator surface temperature). This implies that the adiabatic temperature must increase slowly at higher \dot{Q}_{in} to facilitate higher $\Delta T_{e,a}$. This causes the temperature data points in the adiabatic section to lie in close proximity to each other (Figure 2.1 (a-i)). For a perfectly insulated TS under steady state operation, $\dot{Q}_{out} \approx \dot{Q}_{in}$, where \dot{Q}_{out} is the rate at which the heat leaves the condenser. A higher \dot{Q}_{out} gives a higher $\Delta T_{a,c}$ ($\Delta T_{a,c} = T_a - T_c$, T_c is the condenser temperature; see the condensation curve in section 2.1.3), resulting in a similar trend in the condenser surface temperatures.





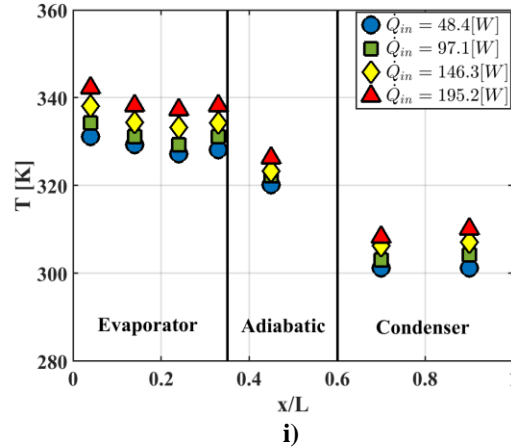


Figure 2.1 Temperature distributions along the length of a TS for varying \dot{Q}_{in} at fixed AR, FR and θ adapted from a) Alizadehdakhel, (2010) (AR = 22.86, FR = 0.5, $\theta = 90^\circ$) b) Amatachaya and Srimuang, (2010) (AR = 9.81, FR = 0.6, $\theta = 90^\circ$) c) Amatachaya and Srimuang, (2010) (AR = 11.78, FR = 0.6, $\theta = 90^\circ$) d) Baojin et al., (2009) (AR = 15.56, FR = 0.36, $\theta = 90^\circ$) e) Fadhl, (2016) (AR = 9.90, FR = 0.5, $\theta = 90^\circ$) f) Jafari et al., (2017b) (AR = 4.54, FR = 0.35, $\theta = 90^\circ$) g) Jafari et al., (2017b) (AR = 4.54, FR = 1.0, $\theta = 90^\circ$) h) Jouhara and Robinson, (2010) (AR = 6.67, FR = 1.59, $\theta = 90^\circ$) i) Noie et al., (2009) (AR = 9.81, FR = NA, $\theta = 90^\circ$).

2.1.2 Evaluation of the boiling thermal resistance, R_{boil}

There are two components of R_{boil} , depending upon the FR. When $FR < 1$, the thermal resistances due to both the pool ($R_{B,P}$, B for boiling and P for pool) and the falling film boiling ($R_{B,F}$, F for film) exist. When $FR \geq 1$, only $R_{B,P}$ exists. Assuming a uniform heat flux distribution in the evaporator, the heat flux into the fluid will be identical for pool ($\dot{Q}'_{in,f,P}$) and film ($\dot{Q}'_{in,f,F}$) boiling. Thus, $\dot{Q}'_{in,f} = \frac{\dot{Q}_{in}}{A_{e,i}} = \dot{Q}'_{in,f,P} = \frac{\dot{Q}_{in,P}}{A_{e,i,P}} = \dot{Q}'_{in,f,F} = \frac{\dot{Q}_{in,F}}{A_{e,i,F}}$, where, $\dot{Q}_{in,P}$ and $\dot{Q}_{in,F}$ are the input heating rate at the liquid pool and the film, and $A_{e,i} = \pi D_i L_e$, $A_{e,i,P} = \pi D_i L_p$ and $A_{e,i,F} = \pi D_i (L_e - L_p)$, respectively.

Traditionally, the boiling curve (Figure 2.2) by Nukiyama (1966) is used to identify the different pool boiling regimes. In Figure 2.2, the slope of OA (natural convection) is lower than the slope of AB (where nucleation and separation of the bubbles takes place). The slope of AB \approx the slope of BP. Point P represents a change in the boiling curve behaviour (where the interference between the bubbles has now started to inhibit the fluid motion in the microlayer next to the surface). Beyond this point, $\dot{Q}'_{in,f}$ increases slowly with ΔT , meaning that the slope of PC $<$ slope of AP. The slope of the $\dot{Q}'_{in,f}$ versus ΔT

curve is a measure of the boiling unit conductance (Andros, 1980) and, hence, this parameter has been utilized to compare the boiling behaviour in the subsequent sections.

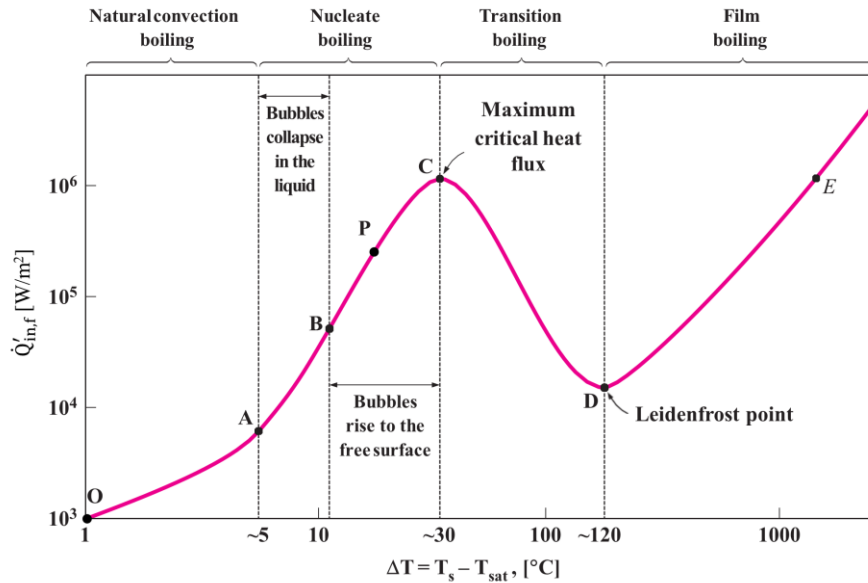


Figure 2.2 Typical boiling curve for water at saturation pressure $P_{\text{sat}} = 101.325$ kPa from a plane horizontal heated surface (adapted and modified from (Cengel and Ghajar, 2020). Original plot was by Nukiyama (1966).

2.1.2.1 Evaluation of the pool boiling resistance, $R_{B,P}$

For a plane heated surface, $\dot{Q}'_{in,f} \propto (\Delta T)^{\frac{5}{4}}$ or $(\Delta T)^{\frac{4}{3}}$ for natural convection boiling (see equations 9.30 and 9.31 in Bergman et al., 2018). In the nucleate pool boiling regime, $\dot{Q}'_{in,f} \propto (\Delta T)^3$ (Rohsenow, 1952, Yamagata et al., 1955). These arguments, along with the shape of the boiling curve, suggest that pool boiling behaviour can be represented by a power law relationship as

$$\dot{Q}'_{in,f} = C_1 (\Delta T_P)^{n_1} \quad (2.1)$$

where $\Delta T_P \approx \Delta T_{e,a}$, n_1 is a dimensionless exponent, $n_1 > 1$ (El-Genk and Saber, 1998, Bergman et al., 2018) and C_1 is a dimensional proportional constant (depends on the WF properties) whose unit depends on the values of n_1 . That equation (2.1) represents the nucleate pool boiling data in a TS is shown in Figure 2.3, where $\dot{Q}'_{in,f}$ is plotted against ΔT_P on a log-log plot.

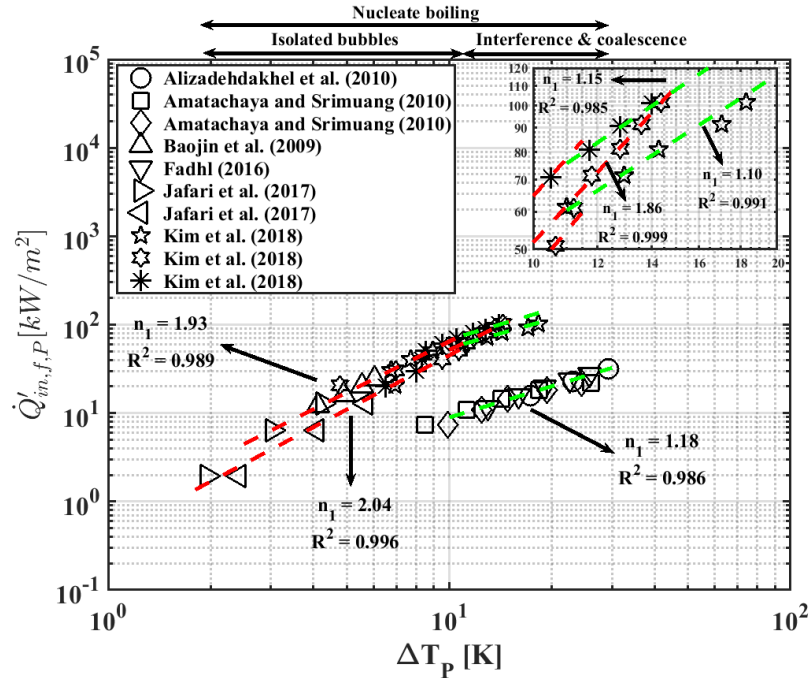


Figure 2.3 Characteristic boiling curve of the published data.

Two distinct slopes are identified within $2[\text{K}] \leq \Delta T_P \leq 30[\text{K}]$ determined from the best-fit curve to the data using the non-linear least square regression algorithm of MatLab with 95% confidence bounds. The slope of $1.86 \leq n_1 \leq 2.04$ within $2[\text{K}] \leq \Delta T_P \leq 15[\text{K}]$ represents bubble nucleation within the nucleate boiling regime (since $n_1 > 1.33$), whereas the slope $1.10 \leq n_1 \leq 1.18$ within $10[\text{K}] \leq \Delta T_P \leq 30[\text{K}]$ represents the effects of vapour slugs within the nucleate boiling regime. The higher slope within $2[\text{K}] \leq \Delta T_P \leq 15[\text{K}]$ suggests formation and separation of the isolated bubbles inducing considerable fluid mixing and, hence, heat transfer enhancement. This is followed by significant bubble interference and coalescence effects within $10[\text{K}] \leq \Delta T_P \leq 30[\text{K}]$ inhibiting the liquid motion causing a reduction in heat transfer.

Two conclusions can be derived from the above discussion. Firstly, the slope of the nucleate pool boiling curve for a TS is found to be lower than that for a plane surface. This may be due to the presence of bubble coalescence and interference effects at all times during bubble formation inside enclosed cavities. Kusuda and Imura (1973) reported $n_1 \approx 1.67$, whilst Semena and Kiselev (1978) reported $n_1 \sim 2$, which is consistent with the value obtained from the present analysis. Secondly, the bubble interference effects are more significant at a higher ΔT_P during pool nucleate boiling. As bubbles from

diametrically opposite surface may interact at higher ΔT_P , this phenomenon is highly likely. The slope of the $\dot{Q}'_{in,f}$ versus ΔT_P data in Ueda et al. (1989) decreases with D_i , confirming the presence of bubble interference effects within D_i .

The expression $\dot{Q}'_{in,f} = \left(\frac{1}{R_{B,P} A_{e,i} FR} \right) \Delta T_P$, combined with equation (2.1), yields

$$\left(\frac{1}{R_{B,P} A_{e,i} FR} \right) = C_1 (\Delta T_P)^{n_2} \quad (2.2)$$

where $R_{B,P}$ is computed as $R_{B,P} = \left(\frac{\Delta T_P}{\dot{Q}'_{in,FR}} \right)$ and $n_2 = (n_1 - 1)$. The term $\left(\frac{1}{R_{B,P} A_{e,i} FR} \right)$ represents the liquid pool thermal resistance normalized by $A_{e,i}$ and FR . As ΔT_P dictates the different boiling behaviour, and, thus, different heat transfer rates, $\left(\frac{1}{R_{B,P} A_{e,i} FR} \right)$ must be a function of ΔT_P . This is illustrated by equation (2.2) and shown in Figure 2.4 along with the magnitudes of n_2 representing different boiling regimes.

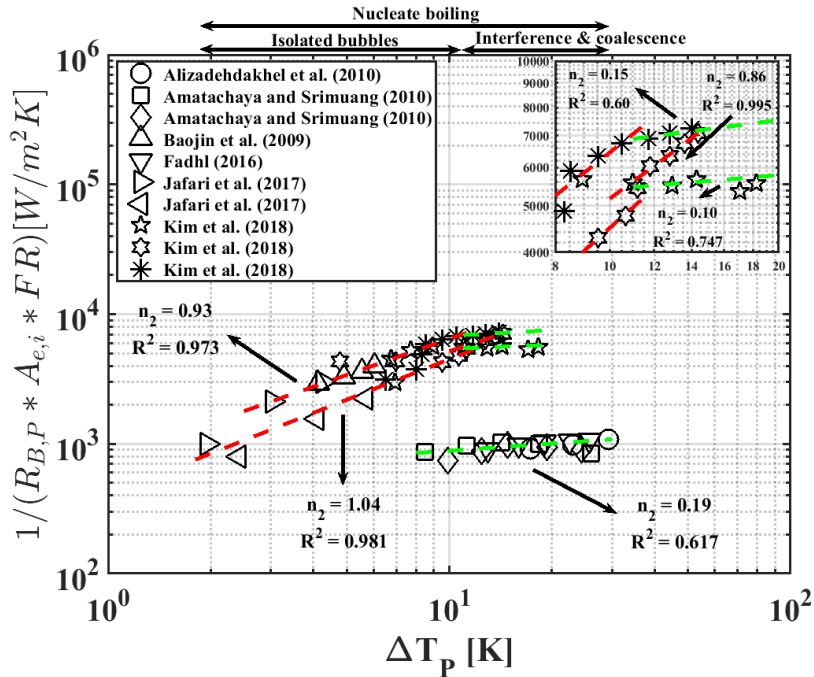


Figure 2.4 Variation of $1/(R_{B,P} A_{e,i} FR)$ with ΔT_P .

The values of n_2 obtained in Figure (2.4) demonstrate consistency with the values of n_1 estimated in figure (2.3) (see Table 2.1). However, the R^2 coefficients of the slopes are worse, due to the error propagation in the value of $R_{B,P}$ through values of ΔT_P and \dot{Q}'_{in} .

The R^2 coefficients of the best-fit straight lines in the “interference and coalescence” regime in Figure 2.4 are significantly worse. This is caused by an increase in $R_{B,P}$ beyond $\Delta T_P \approx 21[\text{K}]$ for Amatachaya and Srimuang (2010). Similar increase in $R_{B,P}$ are observed for Kim et al. (2018) within $10[\text{K}] \leq \Delta T_F \leq 13[\text{K}]$. The increase in $R_{B,P}$ is an indication that the heat transfer limits may have been reached within these studies. However, since, the power-law relationship in equation (2.2) indicates a decrease in $R_{B,P}$ at all ΔT_P (since $n_1 > 1$), the data from Amatachaya and Srimuang (2010) and Kim et al. (2018) causes a significant deterioration in the R^2 coefficient.

Combining equations (2.1) and (2.2), a relationship between $R_{B,P}$ and $\dot{Q}'_{in,f}$ is obtained as

$$\left(\frac{1}{R_{B,P} A_{e,i} FR} \right) = C_1^{\frac{1}{n_1}} (\dot{Q}'_{in,f})^{\frac{n_1-1}{n_1}} \quad (2.3)$$

A relationship between $R_{B,P}$ and \dot{Q}_{in} can be derived from equation (2.3) as

$$\left(\frac{1}{R_{B,P} (A_{e,i})^{\frac{1}{n_1}} FR} \right) = C_1^{\frac{1}{n_1}} (\dot{Q}_{in})^{\frac{n_1-1}{n_1}} \quad (2.4)$$

where $n_3 = \left(\frac{n_1-1}{n_1} \right)$. \dot{Q}_{in} and $\dot{Q}'_{in,f}$ exhibit identical power-law relationships with $R_{B,P}$ (see equations 2.3 and 2.4). Equation (2.3) can, thus, be utilized to represent the influence of \dot{Q}_{in} on $R_{B,P}$.

Figure 2.5 plots $\left(\frac{1}{R_{B,P} A_{e,i} FR} \right)$ versus $\dot{Q}'_{in,f}$ validating equation (2.3). As expected, the R^2 coefficient of the best-fit curve in the “interference and coalescence” regime is worse than the bubble initiation and mixing. However, the estimated slopes are consistent with those obtained in Figures 2.3 and 2.4 which suggests that the equations (2.1 - 2.4) are valid, consistent and correctly represents the behaviour of the data in the nucleate pool boiling regime examined here.

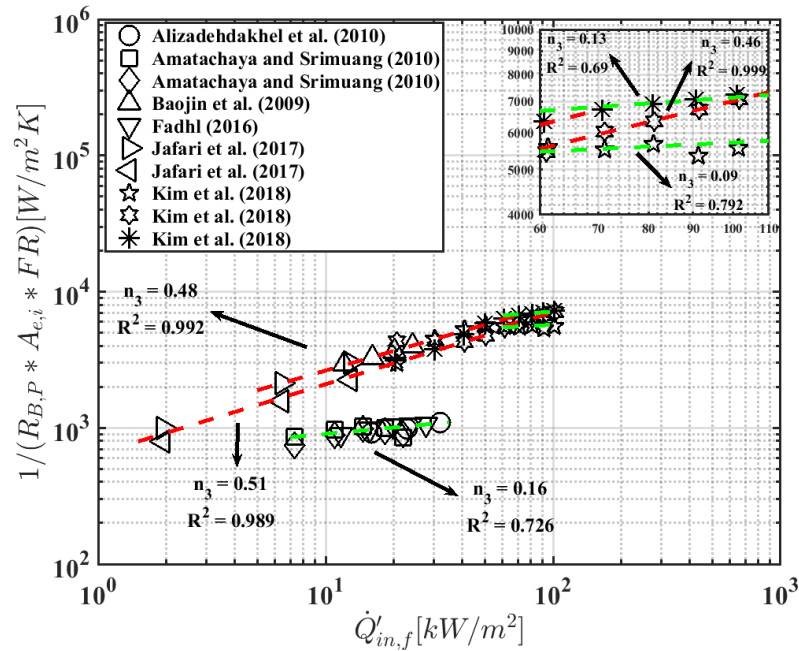


Figure 2.5 Variation of $(1/R_{B,P}A_{e,i}FR)$ with $\dot{Q}'_{in,f}$.

Table 2.1 Comparison of n_2 , n_3 obtained from equations (2.4) and (2.7) and figures 2.4 and 2.5.

	Exponent	n_1	n_2		n_3	
		n_1 from figure 2.3	$n_2 = (n_1 - 1)$	n_2 from figure 2.4	$n_3 = \left(\frac{n_1-1}{n_1}\right)$	n_3 from figure 2.5
Boiling regimes	Bubble initiation and mixing	1.86 - 2.04	0.86 - 1.04	0.86 - 1.04	0.46 - 0.51	0.46 - 0.51
	Interference and coalescence	1.10 - 1.18	0.10 - 0.18	0.10 - 0.19	0.09 - 0.15	0.09 - 0.16

Differentiating $R_{B,P}$ with respect to \dot{Q}_{in} from equation (2.4) yields

$$\frac{dR_{B,P}}{d\dot{Q}_{in}} \propto -\left(\frac{n_1-1}{n_1}\right) (\dot{Q}_{in})^{\left(\frac{1}{n_1}-2\right)} \quad (2.5)$$

Equation (2.5) indicates that the rate of change of $R_{B,P}$ with \dot{Q}_{in} is negative, meaning $R_{B,P}$ will always decrease with \dot{Q}_{in} and the rate at which $R_{B,P}$ decrease, decays with increase in \dot{Q}_{in} . Equation (2.5) may now explain the various rates of decrement in the overall thermal resistance ($R_{O,TS}$) with \dot{Q}_{in} in Shiraishi et al. (1982), Khandekar (2007), Jouhara and Robinson (2010), Abdullahi (2015), Fadhil (2016) and Jafari et al. (2017a). The variation in $R_{B,F}$ is examined next.

2.1.2.2 Evaluation of the film boiling resistance, $R_{B,F}$

The heat transfer regimes in film boiling are similar to pool boiling (Semena and Kiselev, 1978, Shiraisi et al., 1982, El-Genk and Saber, 1998). Hence, the same form of equations (2.1 - 2.4) are valid for the film boiling. However, the term $\left(\frac{1}{R_{B,P}A_{e,i}FR}\right)$ in equations (2.2) to (2.4) will be replaced by $\left(\frac{1}{R_{B,F}A_{e,i}(1-FR)}\right)$, where $R_{B,F}$ is now normalized by $A_{e,i}$ and $(1 - FR)$, respectively. Since, $\dot{Q}'_{in,f,P} = \dot{Q}'_{in,f,F}$ and $\Delta T_F \approx \Delta T_P$, Figures 2.3, 2.4 and 2.5 can be used to illustrate the film boiling behaviour.

Observations made by Rychkov and Pospelov (1959), Parizhskiy et al. (1972), Fletcher et al. (1974), Mesler (1976) and Mesler and Mailen (1977) suggest that film nucleate boiling require a lower temperature differential to achieve the same rate of heat transfer than pool nucleate boiling. Since, it is assumed that $\Delta T_F \approx \Delta T_P$, the magnitudes of ΔT_F and ΔT_P cannot be compared directly. Thus, the temperature differential within the film (ΔT_F) required to achieve the same $\dot{Q}_{in,P}$ are compared. $\dot{Q}_{in,P} = \dot{Q}_{in} \times FR$, whereas $\dot{Q}_{in,F} = \dot{Q}_{in} \times (1 - FR)$, respectively. Therefore, $R_{B,F} < R_{B,P}$ for $FR < 0.5$, $R_{B,F} > R_{B,P}$ for $FR > 0.5$ and $R_{B,P} = R_{B,F}$ at $FR = 0.5$. The ΔT_F required to transfer $\dot{Q}_{in,P}$ through the film for $FR < 0.5$ is shown in Table 2.2.

Table 2.2 Comparisons of ΔT_P and ΔT_F when $FR < 0.5$.

Reference	ΔT_P (Pool nucleate boiling)	ΔT_F (Film nucleate boiling)
Baojin et al. (2010) (FR = 0.36)	4.1	2.3
	4.9	2.8
	5.6	3.1
	6.0	3.4
Jafari et al. (2017b) (FR = 0.35)	1.9	1.1
	3.0	1.6
	4.3	2.3
Kim et al. (2018) (FR = 0.25)	6.9	2.3
	6.7	2.3
	7.7	2.6
	8.9	2.9
	11.0	3.7
	12.9	4.3
	14.3	4.8
	17.1	5.7
18.3	6.1	

The values shown in Table 2.2 suggest that heat transfer is enhanced during film nucleate boiling only when $FR < 0.5$. As $FR < 0.5$ provides a larger surface area for film flow, more evaporator surface area and nucleation sites are available for bubble inception.

Two different mechanisms can be attributed to the high heat transfer rate observed in the film boiling within $2[\text{K}] \leq \Delta T_P \leq 15[\text{K}]$. Cerza and Sernas (1985) showed that the heat transfer enhancement is due to additional energy transfer into the bubble through liquid evaporation at the bubble base before venting. Mesler and Mailen (1977) demonstrated that during the venting procedure (see Newitt et al., 1954 for a more detailed description) additional nucleated bubbles are generated from disturbances in the liquid film. These secondary nucleated bubbles amplify the heat transfer in a way similar to how isolated bubbles enhance heat transfer at the onset of nucleate pool boiling.

The heat transfer decrement within $10[\text{K}] \leq \Delta T_F \leq 30[\text{K}]$ can be explained by the film breakdown phenomena (Fujita and Ueda, 1978b). With an increase in ΔT_F , the formation rate of bubbles within the film increases. At high bubble densities, the bubbles burst, and intermittent dry patches may appear on the surface beneath the vapour bubbles (Patten and Turmeau, 1970). The liquid droplets formed by the bursting of the vapour bubbles are entrained by the upward-flowing vapour flow. Fujita and Ueda (1978b) showed that the droplet entrainment rate increases with the heat flux i.e. $\left(\frac{\Gamma_d}{L_F}\right) \propto \left(\frac{\Gamma}{L_F}\right) (\dot{Q}'_{in,f})^{2.5}$, where $\left(\frac{\Gamma_d}{L_F}\right)$ is the droplet entrainment rate per unit width per unit length of the heating length (where, $L_F = L_e - L_p$) and $\left(\frac{\Gamma}{L_F}\right)$ is the film flow rate per unit length of the heating length.

The liquid layer beneath the bubbles undergoes continuous evaporation. Both these effects cause the film flow rate to decrease considerably (Fujita and Ueda, 1978b) which may cause a large dry patch to form. This may induce a breakdown of the falling film (Fujita and Ueda, 1978b), where the minimum liquid flow rate to maintain a continuous film is not satisfied anymore. This phenomenon will cause $R_{B,F}$ to increase. This could be the reason why $\left(\frac{1}{R_{B,F} A_{e,i}(1-FR)}\right)$ plotted versus ΔT_F would show the slope n_2 for Alizadehdakhel et al. (2010) ($FR \approx 0.5$), Amatachaya and Srimuang (2010) ($FR \approx 0.6$), and Fadhl (2016) ($FR \approx 0.5$) to be lower than those of Baojin et al. (2009) ($FR \approx 0.36$),

Jafari et al. (2017b) ($FR \approx 0.35$), Kim et al. (2018) ($FR \approx 0.25$). The variation in R_{cond} with \dot{Q}_{in} is investigated next.

2.1.3 Evaluation of the condensation thermal resistance, R_{cond}

Similar to the boiling curve, a condensation curve exists (Figure 2.6) that shows the dropwise, transition and filmwise condensation regime. The shape of the condensation curve is similar to a boiling curve i.e. straight-line slopes are obtained on a log-log plot for dropwise ($\Delta T \sim 20[K]$) and filmwise condensation ($10[K] \leq \Delta T \leq 400[K]$).

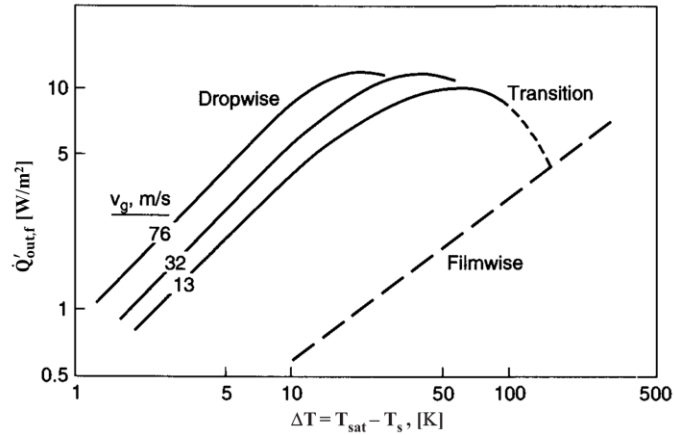


Figure 2.6 Typical condensation curve for steam at 1 atm pressure for a vertical circular copper plate (adapted and modified from Rohsenow et al., 1998). The term V_g in the figure represents the steam velocity at which dropwise condensation occurs. Original plot was by Takeyama and Shimizu (1974).

Based on the shape of the filmwise condensation curve and Nusselt's theory (1916) for laminar filmwise condensation, it is hypothesized that a power law relationship between $\dot{Q}'_{out,f}$ and $\Delta T_{C,F}$ exists (equation 2.6).

$$\dot{Q}'_{out,f} = C_2(\Delta T_{C,F})^{n_4} \quad (2.6)$$

Here, $\dot{Q}'_{out,f}$ is the output heat flux at the condenser defined as $\dot{Q}'_{out,f} = \frac{\dot{Q}_{out}}{A_{c,i}}$, \dot{Q}_{out} is the output heating rate, $\Delta T_{C,F}$ is the wall subcooling defined as $\Delta T_{C,F} \approx \Delta T_{a,c}$, $A_{c,i} = \pi D_i L_c$, where $A_{c,i}$ is the internal surface area of the condenser, n_4 is a dimensionless condensation heat transfer exponent and C_2 is a dimensional proportional constant (depends on the WF properties) whose unit depend on the magnitudes of n_4 . That such a relation holds between $\dot{Q}'_{out,f}$ and $\Delta T_{C,F}$ for filmwise condensation is shown in Figure 2.7.

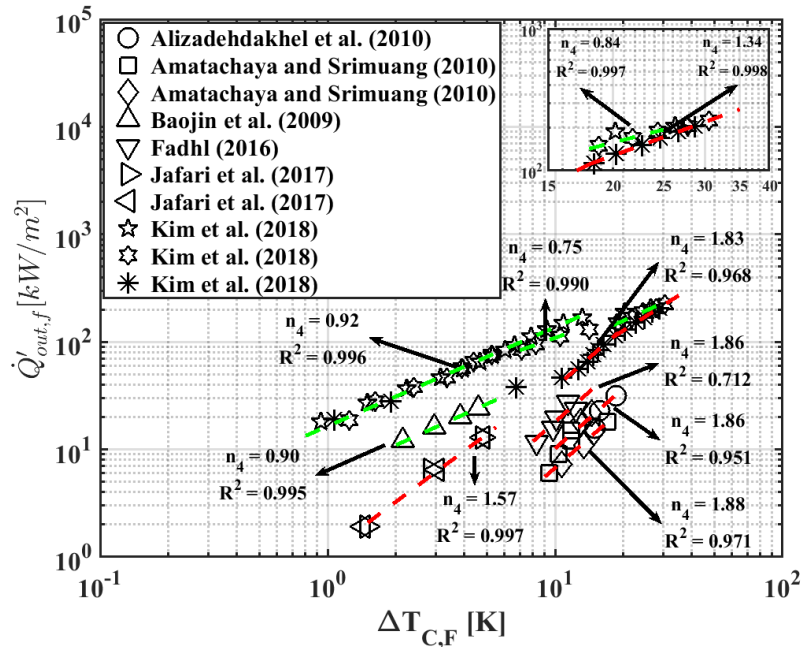


Figure 2.7 Characteristic condensation curve. The green coloured dashed lines represent the slope of the data when $n_4 < 1$, whereas the red coloured dashed lines represent the slope of the data when $n_4 > 1$.

Two distinct behaviour of the slopes are observed within $0.9[\text{K}] \leq \Delta T_{C,F} \leq 30 [\text{K}]$ represented by green ($n_4 < 1$) and red dashed lines ($n_4 > 1$). However, the slopes do not correlate to any specific ranges of $\Delta T_{C,F}$. The data from Jafari et al. (2017b), Alizadehdakhel (2010), Amatachaya and Srimuang (2010) and Fadhl (2016) demonstrate $n_4 > 1$, whilst the data from Baojin et al. (2009) and Kim et al. (2018) exhibit $n_4 < 1$. The implications are that $\dot{Q}'_{out,f}$ increases more rapidly with $\Delta T_{F,C}$ when $n_4 > 1$, whilst the opposite is true when $n_4 < 1$. Thus, the condensation thermal resistance ($R_{C,F}$; $R_{cond} = R_{C,F}$) is observed to be both increasing and decreasing with $\Delta T_{C,F}$. This is evident from Figure 2.8 where $\left(\frac{1}{R_{C,F A_{c,i}}}\right)$ is plotted against $\Delta T_{C,F}$ based on the relation

$$\left(\frac{1}{R_{C,F A_{c,i}}}\right) = (\Delta T_{C,F})^{n_4 - 1} \quad (2.7)$$

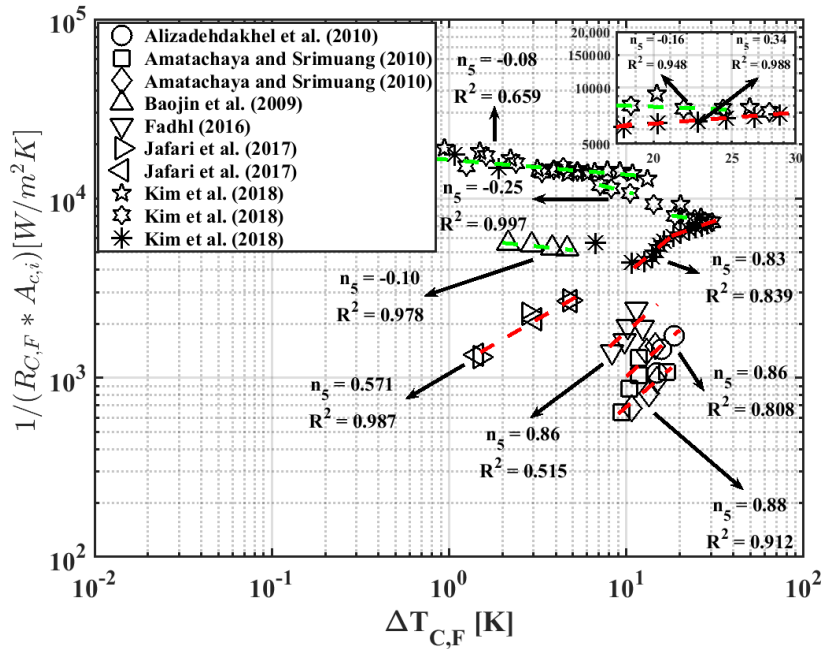


Figure 2.8 Variation of $1/(R_{C,F}A_{c,i})$ with $\Delta T_{C,F}$. The green coloured dashed lines represent the slope of the data when $R_{C,F}$ increases with $\Delta T_{C,F}$, whereas the red coloured dashed lines represent the slope when $R_{C,F}$ increases with $\Delta T_{C,F}$.

The values of n_5 , where $n_5 = (n_4 - 1)$ obtained for various sets of data in Figure 2.8 are consistent with Figure 2.7 (see Table 2.3). However, the R^2 coefficients are worse. This is hypothesized to be due to the error propagation in the values of $R_{C,F}$ through \dot{Q}'_{out} and $\Delta T_{C,F}$ values. Figure 2.8 reveals that the rate at which $R_{C,F}$ increases with $\Delta T_{C,F}$ ($-0.25 \leq n_5 \leq -0.10$) is lower than the rate at which $R_{C,F}$ decreases with $\Delta T_{C,F}$ ($0.34 \leq n_5 \leq 0.86$). Combining equations (2.6) and (2.7), a relationship between $R_{C,F}$ and $\dot{Q}'_{out,f}$ is obtained as

$$\left(\frac{1}{R_{C,F}A_{c,i}}\right) = C_2^{\frac{1}{n_4}} (\dot{Q}'_{out,f})^{\frac{n_4-1}{n_4}} \quad (2.8)$$

where $n_6 = \left(\frac{n_4-1}{n_4}\right)$. Note that \dot{Q}'_{in} exhibits the same influence on $R_{C,F}$ as $\dot{Q}'_{out,f}$ (assuming $\dot{Q}'_{in} \approx \dot{Q}'_{out}$) and, thus, equation (2.8) may be utilized to represent the effects of \dot{Q}'_{in} on $R_{C,F}$. A plot of equation (2.8) is shown in Figure 2.9. The values of n_6 obtained are consistent with Figure 2.7 (see Table 2.3).

Table 2.3 Comparison of n_5 , n_6 with that obtained from figures 2.7c, 2.7d and 2.7e, 2.7f.

	Exponent	n4	n5		n6	
		n4 from figure 2.7	$n_5 = (n_4 - 1)$	n5 from figure 2.8	$n_6 = \left(\frac{n_4 - 1}{n_4}\right)$	n6 from figure 2.9
References	Alizadehdakheel et al. (2010)	1.86	0.86	0.86	0.46	0.46
	Amatachaya and Srimuang (2010)	1.88	0.88	0.88	0.47	0.47
	Baojin et al. (2009)	0.90	-0.10	-0.10	-0.11	-0.11
	Fadhl (2016)	1.86	0.86	0.86	0.46	0.47
	Jafari et al. (2017b)	1.57	0.57	0.57	0.36	0.36
	Kim et al. (2018)	1.83, 1.34, 0.92, 0.84, 0.75	0.83, 0.34, -0.08, -0.16, -0.25	0.83, 0.34, -0.08, -0.16, -0.25	0.45, 0.25, -0.09, -0.19, -0.33	0.45, 0.26, -0.09, -0.19, -0.33

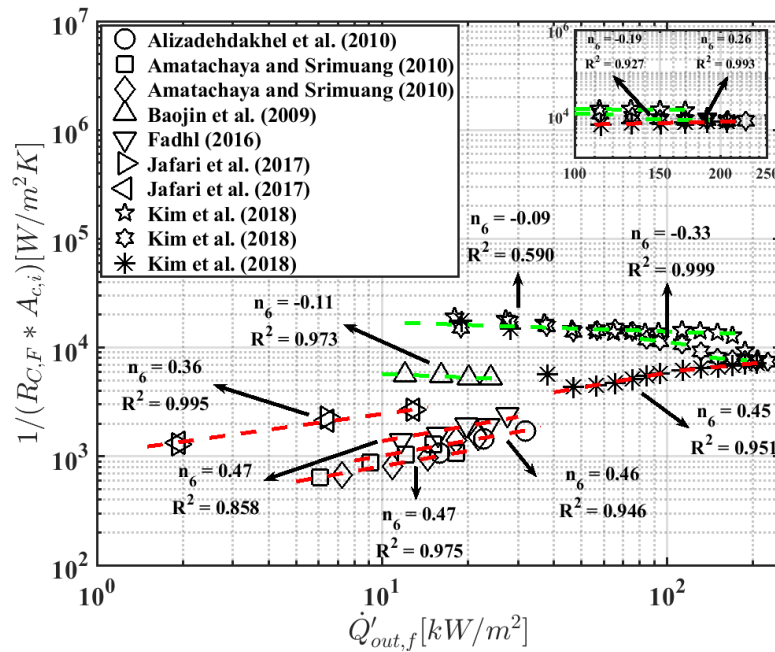


Figure 2.9 Variation of $1/(R_{C,F} A_{c,i})$ with $\dot{Q}'_{out,f}$. The green coloured dashed lines represent the slope of the data when $R_{C,F}$ increases with $\dot{Q}'_{out,f}$, whilst the red coloured dashed lines represent the slope when $R_{C,F}$ decreases with $\dot{Q}'_{out,f}$.

Similar to Figure 2.8, $R_{C,F}$ increases with $\dot{Q}'_{out,f}$ in Baojin et al. (2009) and Kim et al. (2018), whilst for other studies, $R_{C,F}$ decreases with $\dot{Q}'_{out,f}$. It is also noted that $R_{C,F}$ increases with $\dot{Q}'_{out,f}$ at a slower rate ($-0.33 \leq n_6 \leq -0.09$) than the rate at which $R_{C,F}$ decreases ($0.26 \leq n_6 \leq 0.46$). The next section examines the condensate flow states and the influence of the counter-current vapour flow to explain the behaviour of the observed trends.

2.1.4 Condensate flow states

The condensate flow states can be identified by estimating the film Reynolds number, Re_F , where $Re_F = \frac{4\dot{Q}_{out}}{\pi D_i h'_{fg} \mu_l}$ and a dimensionless parameter, P , where $P = \left[\frac{k_l L_c (\Delta T_{C,F})}{\mu_l h'_{fg}} \left(\frac{g}{v_l^2} \right)^{1/3} \right]$ (Bergman et al., 2018). $P \lesssim 15.8$ ($0 \leq Re_F \leq 30$) represents laminar flow, $15.8 \lesssim P \lesssim 2530$ ($30 \leq Re_F \leq 1800$) represents laminar-wavy flow and $P \gtrsim 2530$ ($Re_F \geq 1800$) represents turbulent flow regime, respectively. Here, μ_l and v_l are the dynamic and kinematic viscosities of the liquid phase, L_c is the condenser length, h_{fg} and h'_{fg} are the unaltered and modified latent heat of vapourization and h'_{fg} ($h'_{fg} = h_{fg} + 0.68c_{p,l}(\Delta T_{C,F})$), respectively. The estimates of Re_F and P from various studies are shown in Table 2.4.

Table 2.4 Estimates of Re_F and P for the different studies analyzed in the present work. The liquid properties are evaluated at the film temperature (T_f), whereas the h'_{fg} is evaluated at T_{sat} .

\dot{Q}_{out} [W]	D_i [m]	L_c [m]	$\Delta T_{a,c}$ [K]	Re_F	P
Alizadehdakhel et al. (2010)					
350.00	0.0175	0.40	14.9	15.53	63.17
500.00			15.8	24.06	76.77
700.00			18.5	36.03	101.58
Amatachaya and Srimuang (2010) (AR = 9.81)					
231.00	0.032	0.38	9.4	6.62	50.43
346.50			10.4	11.43	70.65
462.00			11.7	17.62	102.06
577.00			11.7	24.45	121.70
693.00			16.9	31.81	201.24
Amatachaya and Srimuang (2010) (AR = 11.78)					
277.20	0.032	0.38	10.7	8.05	58.63
415.80			13.4	13.55	89.18
554.40			14.9	20.58	124.56
693.00			12.9	30.32	143.24
831.60			14.5	37.95	171.80
Baojin et al. (2009)					
298.00	0.0225	0.35	2.2	11.16	9.14
397.60			2.9	15.76	13.82
496.80			3.8	20.51	19.24
594.63			4.6	25.35	24.58
Fadhl (2016)					
148.43	0.0202	0.20	8.3	6.87	24.3
199.74			9.8	9.78	31.49
250.04			10.1	12.98	36.01
299.52			12.3	16.20	47.02
349.27			11.4	20.50	49.77
Jafari et al. (2017b) (FR = 0.35)					
30	0.033	0.15	1.5	0.55	1.52
100			2.8	1.92	3.14
200			4.8	4.01	5.74

Jafari et al. (2017b) (FR = 1)					
30	0.033	0.15	1.4	0.55	1.48
100			3.1	1.94	3.46
200			4.8	4.07	5.95

Upon examining Table 2.4, it becomes evident that the condensate flow states represented by Re_F are inconsistent with those represented by P . In almost all the studies, the Re_F values represent a laminar flow, whereas the values of P suggest flows in the laminar-wavy regime. The plot of Nusselt number (Nu) versus Re_F shown in Figure 2.10 also does not determine the correct flow states (Note that the Nu versus Re_F relations for different condensate flow states are shown in Table 2.5 for completeness).

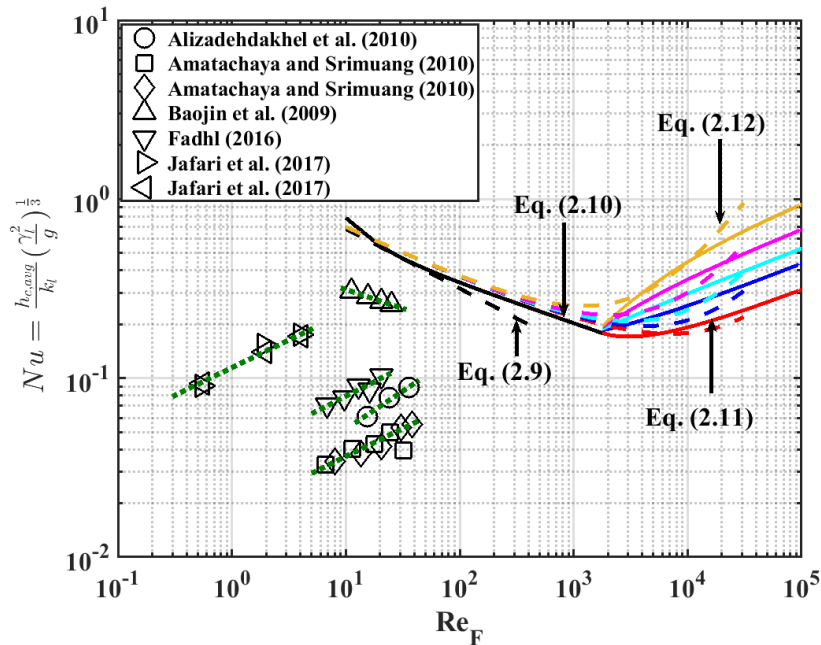


Figure 2.10 Plot of Nu versus Re_F . The solid and dashed coloured lines represent various values of the liquid Prandtl number. $Pr_1 = 1$ (red), $Pr_1 = 2$ (blue), $Pr_1 = 3$ (cyan), $Pr_1 = 4$ (magenta), $Pr_1 = 5$ (yellow). The green coloured dotted lines represent the slope of the data.

Table 2.5 Expressions of $Nu = f(Re_F)$ representing different condensate flow states.

Flow state	Nu
Wave-free laminar $0 < Re_F \leq 30$	$1.47Re_F^{-(1/3)}$ (Nusselt, 1916) (Eq. 2.9)
Laminar- wavy $30 \leq Re_F \leq 1800$	$\frac{Re_F}{1.08Re_F^{1.22} - 5.2}$ (Kutateladze, 1963) (Eq. 2.10)
Turbulent $30 \leq Re_F \leq 1800$	$\frac{Re_F}{8750 + 58Pr_1^{-0.5}(Re_F^{0.75} - 253)}$ (Labuntsov, 1957) (Eq. 2.11)
All regimes ($10 \leq Re_F \leq 31000$)	$1.33Re_F^{-(1/3)} + 9.56 \times 10^{-6}Re_F^{(0.89)}Pr_1^{0.94} + 8.22 \times 10^{-2}$ (Chun and Kim, 1991) (Eq. 2.12)

However, two consistent trends can be observed from Figure 2.10. Firstly, the Nu values are lower than that predicted by equation (2.9) (which represent quiescent-vapour conditions). This suggests the presence of the effects that decrease the heat transfer coefficient, which are i) shear stress at the liquid-vapour interface and ii) droplet entrainment. Secondly, Nu increases with Re_F within individual set of data for all studies except Baojin et al. (2009). This indicates the presence of i) enhanced molecular mixing within the condensate film due to disturbances at the liquid-vapour interface and ii) entrainment effects caused by a high-density ratio (ρ_l/ρ_v). Similar observations in Nu can also be made from the plots presented in Ueda et al. (1989) and Gross (1992) (see Figure 2.11). The effects of the counter-current flow are examined next in the next paragraph.

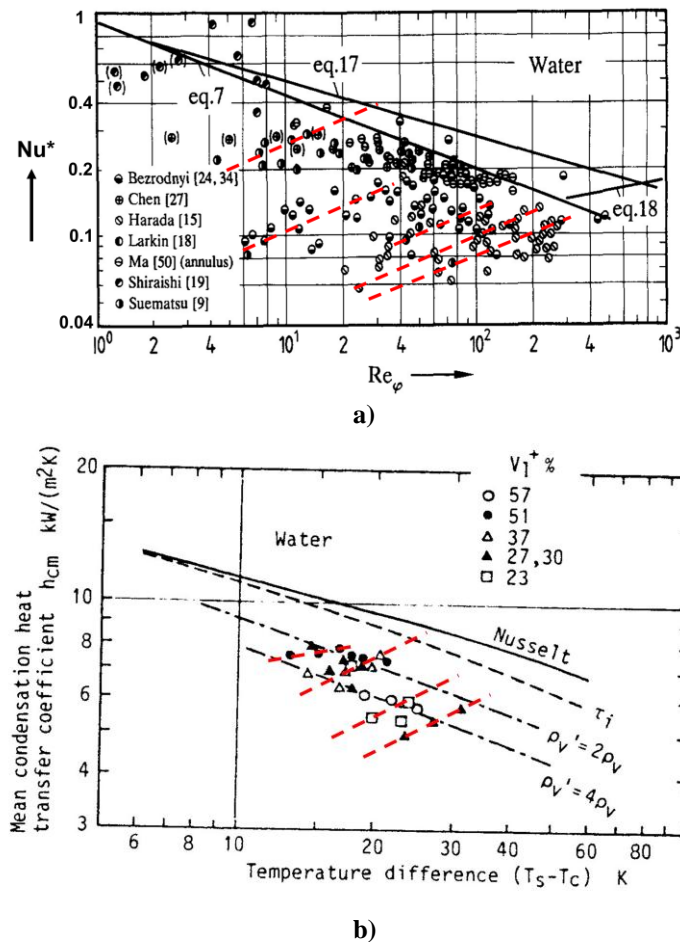


Figure 2.11 a) Plot of Nusselt number versus Re_F adapted from Gross et al. (1992) with permission.
b) Plot of $h_{c,avg}$ versus $\Delta T_{C,F}$ adapted from Ueda et al. (1989).

The countercurrent vapour velocity, u_v estimated as $u_v = \frac{4\dot{Q}_{in}}{\pi D_f^2 h_{fg} \rho_v}$ for different studies are shown in Table 2.6 along with the vapour Reynolds number, Re_v , where $Re_v = \frac{\mu_l}{\mu_v} Re_F$. It is

observed that u_v for Baojin et al. (2009) are at least 2 to 8 times higher than Jafari et al. (2017b). The high u_v values can cause droplet entrainment from the liquid film and deposit them onto the condensate increasing its thickness and reducing the condensation heat transfer. This explains why Nu show a decreasing trend with Re_F in Baojin et al. (2009).

Table 2.6 Re_v and u_v values estimated for the different studies.

References	\dot{Q}_{out} [W]	Re_v	u_v [m/s]
Alizadehdakhel et al. (2010)	350.00	1095.28	8.93
	500.00	1543.45	10.32
	700.00	2132.61	11.53
Amatachaya and Srimuang (2010) (AR = 9.81)	231.00	386.45	1.35
	346.50	565.74	1.40
	462.00	734.88	1.26
	577.00	901.71	1.21
Amatachaya and Srimuang (2010) (AR = 11.78)	693.00	1062.04	1.06
	277.20	462.31	1.53
	415.80	678.74	1.62
	554.40	883.81	1.51
Baojin et al. (2009)	693.00	1074.61	1.30
	831.60	1278.25	1.35
	298.00	722.95	5.20
	397.60	955.05	5.90
Fadhl (2016)	496.80	1184.49	6.51
	594.63	1409.36	7.06
	148.43	392.34	2.60
	199.74	522.68	3.03
	250.04	647.55	3.28
Jafari et al. (2017b) (FR = 0.35)	299.52	768.95	3.50
	349.27	884.98	3.31
	30.00	52.31	0.59
Jafari et al. (2017b) (FR = 1)	100.00	172.91	1.74
	200.00	342.97	3.12
	30.00	52.27	0.58
Jafari et al. (2017b) (FR = 1)	100.00	172.58	1.70
	200.00	342.13	3.00

The above argument, however, does not explain the increase in Nu with Re_F for Jafari et al. (2017b). Hashimoto and Kaminaga (2002) demonstrated that the effect of entrainment also depends on the liquid-vapour density ratio (ρ_l/ρ_v). At low $\dot{Q}'_{out,f}$, the film is thinner and, consequently, the amount of the entrained liquid is higher than at high $\dot{Q}'_{out,f}$. The scale of the condensate film thickness ($\delta_{c,F}$) and the density ratio (ρ_l/ρ_v) estimated from the data of Jafari et al. (2017b) (see Table 2.7), shows $\delta_{c,F}$ to be small and (ρ_l/ρ_v) to be very high compared to Baojin et al. (2009). This indicates that at low Re_F , there is a

higher possibility of entrained liquid droplets being deposited on the condensate film surface, increasing its thickness. As Re_F increases, the condensate film thickness due to condensation increases, but the lower entrainment rate causes the overall film thickness to be lower than that of the preceding Re_F , suggesting an increment in the heat transfer coefficient. This possibly explains the trends in the data of Jafari et al. (2017b).

Table 2.7 Comparison of the condensate film thickness and the density ratio between Baojin et al. (2009) and Jafari et al. (2017b).

References	$\dot{Q}'_{out,f}$ [kW/m ²]	$\delta_{C,F}$ (m)	$\left(\frac{\rho_l}{\rho_v}\right)$
Baojin et al. (2009)	12.05	7.00×10^{-5}	16493.96
	16.07	7.58×10^{-5}	13949.01
	20.08	8.07×10^{-5}	12278.49
	24.04	8.49×10^{-5}	11078.54
Jafari et al. (2017b) (FR = 0.35)	1.93	3.16×10^{-5}	40667.38
	6.43	4.65×10^{-5}	36094.95
	12.86	5.78×10^{-5}	32151.72
Jafari et al. (2017b) (FR = 1.00)	1.93	3.16×10^{-5}	40034.16
	6.43	4.63×10^{-5}	35118.25
	12.86	5.75×10^{-5}	30843.13

2.1.5 Interim summary

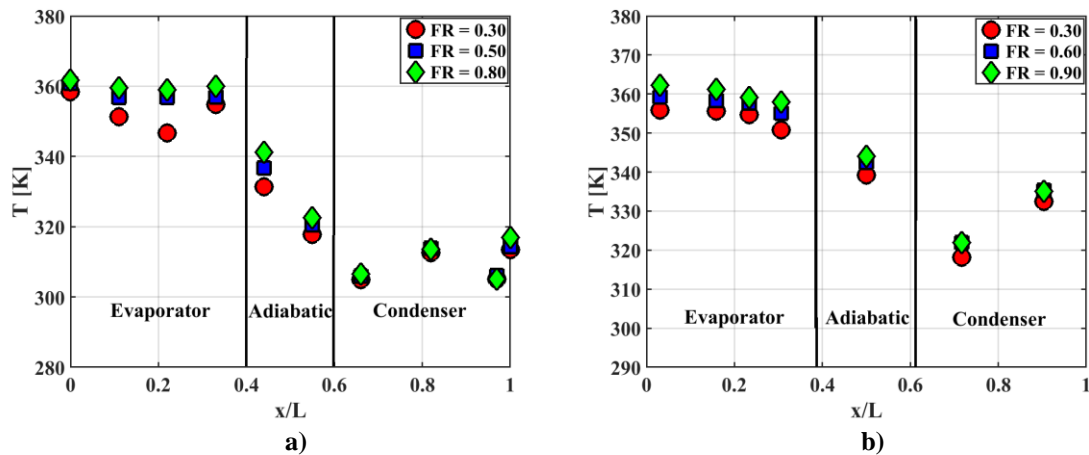
An interim summary highlighting the key aspects from the above analyses is presented. Firstly, it has been shown that R_{boil} and R_{cond} demonstrate a power-law relationship with $\dot{Q}'_{in,f}$ and $\dot{Q}'_{out,f}$. The boiling and condensation inside a TS pass through similar regimes to those illustrated in the boiling and condensation curves. Secondly, the heat transfer decrement at a higher ΔT_P in pool boiling is due to bubble interference and coalescence effects, whereas in film boiling, it is due to film breakdown phenomena. Thirdly, two different trends in the variation of $R_{C,F}$ (or Nu) with $\dot{Q}'_{out,f}$ is observed. The differences are due to the combined effects of the counter-current vapour flow and entrainment.

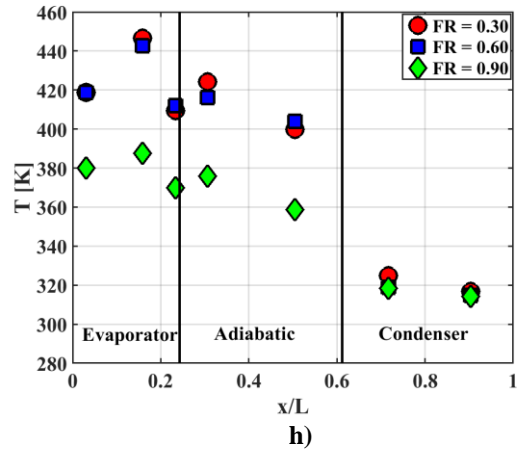
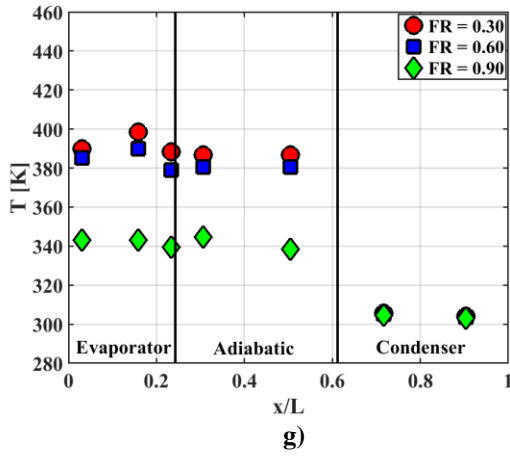
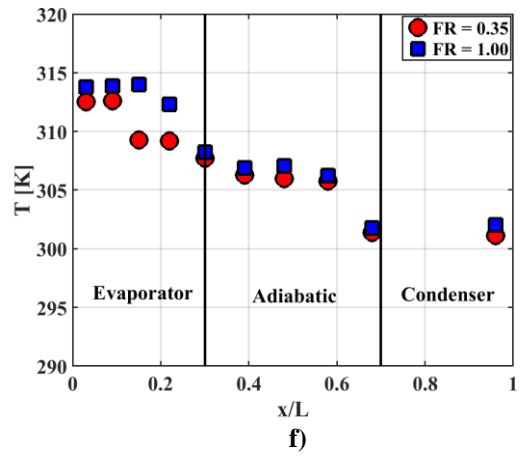
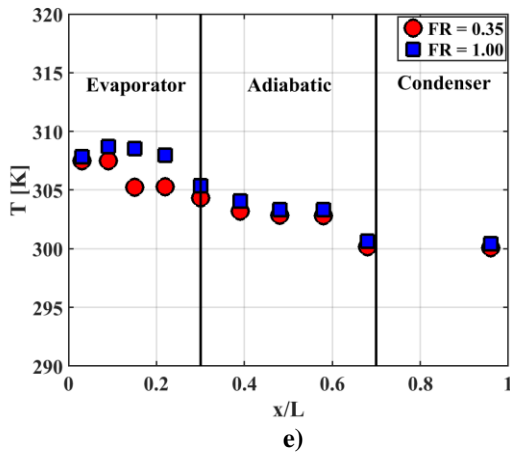
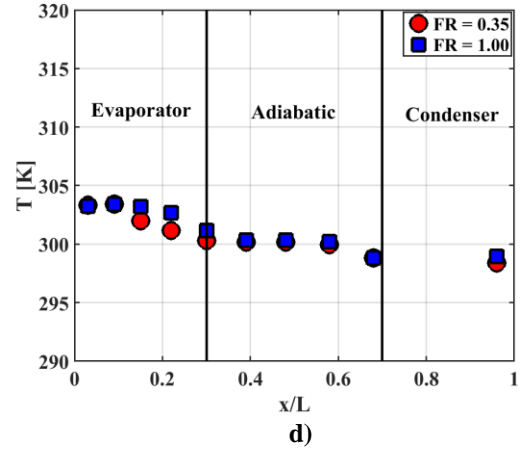
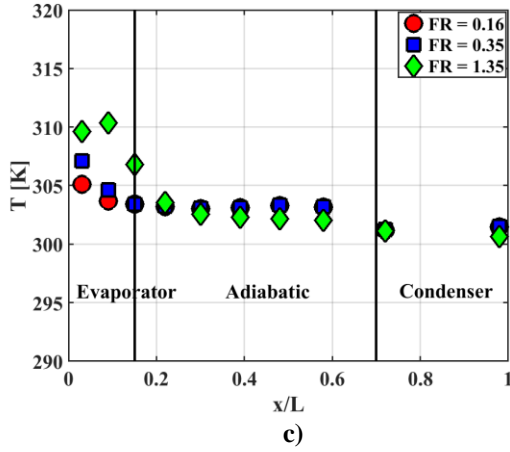
There is one caveat to the analysis made here. Given that the log-log plots are shown with some data consist of three points (for e.g. Alizadehdakhel et al., 2010, Jafari et al., 2017b), it is possible that the slopes may change slightly while adding or removing a data point. Hence, no specific comparison between the slopes between the studies are made. The goal of this analysis is not to estimate the precise values of the slopes but, rather, to illustrate the general trend in the variations of R_{boil} and R_{cond} with \dot{Q}'_{in} from previous data. The next section examines the effects of the FR on overall thermal performance.

2.2 Effects of the FR on the thermal performance of TS

2.2.1 Effects of FR on the temperature distribution

Figure 2.12 (a-j) shows the temperature distribution along the length of the TS for different FR at fixed \dot{Q}_{in} , AR and θ ($\theta = 90^\circ$). Three consistent trends are observed. Firstly, the variation in temperatures along the length of the TS is similar to that observed while \dot{Q}_{in} was varied. Hence, the reasons explaining the temperature variation can be referred to in section 2.1.1. Secondly, the effects of varying FR are more prominent in the evaporator than the adiabatic and the condenser section. This is the expected, as the liquid pool length (L_p) governs the number of nucleation sites and influences the boiling thermal resistance. Thirdly, the temperatures are consistently higher for higher FR in figures 2.12 (a-f). This is due to the fact that the heat input not utilized in evaporating the WF will be absorbed by the wall material and the WF as sensible heat, causing the evaporator section temperature to rise. The temperature distributions shown in figures 2.12 (e-h) (Noie, 2005), however, do not follow this trend. Since, Noie (2005) did not discuss the reasons either, it is hypothesized that the published data from Noie (2005) are inaccurate.





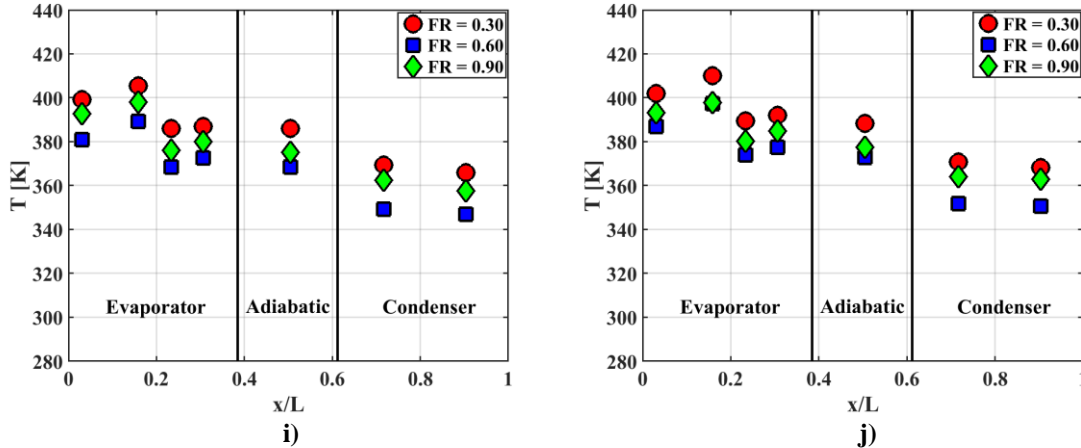


Figure 2.12 Temperature distribution along the length of the TS for at three different FRs at fixed \dot{Q}_{in} , AR and θ adapted from a) Alizadehdakhel et al. (2010) ($\dot{Q}_{in} = 700[\text{W}]$, AR = 22.86, $\theta = 90^\circ$) b) Amatachaya and Srimuang (2010) ($\dot{Q}_{in} = 554.4[\text{W}]$, AR = 11.78, $\theta = 90^\circ$) c) Jafari et al. (2017a) ($\dot{Q}_{in} = 100[\text{W}]$, AR = 2.27, $\theta = 90^\circ$) d) Jafari et al. (2017b) ($\dot{Q}_{in} = 30[\text{W}]$, AR = 4.54, $\theta = 90^\circ$) e) Jafari et al. (2017b) ($\dot{Q}_{in} = 100[\text{W}]$, AR = 4.54, $\theta = 90^\circ$) f) Jafari et al. (2017b) ($\dot{Q}_{in} = 200[\text{W}]$, AR = 4.54, $\theta = 90^\circ$) g) Noie (2005) ($\dot{Q}_{in} = 215[\text{W}]$, AR = 9.52, $\theta = 90^\circ$) h) Noie (2005) ($\dot{Q}_{in} = 830[\text{W}]$, AR = 9.52, $\theta = 90^\circ$) i) Noie (2005) ($\dot{Q}_{in} = 670[\text{W}]$, AR = 15.08, $\theta = 90^\circ$) j) Noie (2005) ($\dot{Q}_{in} = 830[\text{W}]$, AR = 15.08, $\theta = 90^\circ$).

2.2.2 Evaluation of the pool boiling thermal resistance ($R_{B,P}$)

Before evaluating the influence of FR on $R_{P,B}$, one must understand i) how FR influences ΔT_P and ii) the relationship between ΔT_P and $R_{P,B}$. The next subsequent paragraphs examine these aspects.

Figure 2.13 shows the plot of FR versus ΔT_P . The data from Noie (2005) have been omitted from this analysis for the reasons described above. It is evident from Figures 2.12 and 2.13 that there are no studies where FR has been varied more than three times. Hence, the discussion of the trends is based only on a small sample of data. Two distinct trends from Figure 2.13 can be observed. Firstly, ΔT_P increases with FR when AR < 10. Secondly, ΔT_P remains nearly constant with FR when AR > 10. Excluding the data from Jafari et al. (2017b) (AR = 4.54) (as it only comprises of two data-points), the data from Jafari et al. (2017a) show a power-law relationship between ΔT_P and FR. The slope of the data estimated by fitting a power-law equation of the form (equation 2.13) gives $n_7 = 0.91$.

$$\Delta T_P = C_3(\text{FR})^{n_7} \quad (2.13)$$

For Alizadehdakhel et al. (2010) and Amatachaya and Srimuang (2010), however, $n_7 \approx 0$.

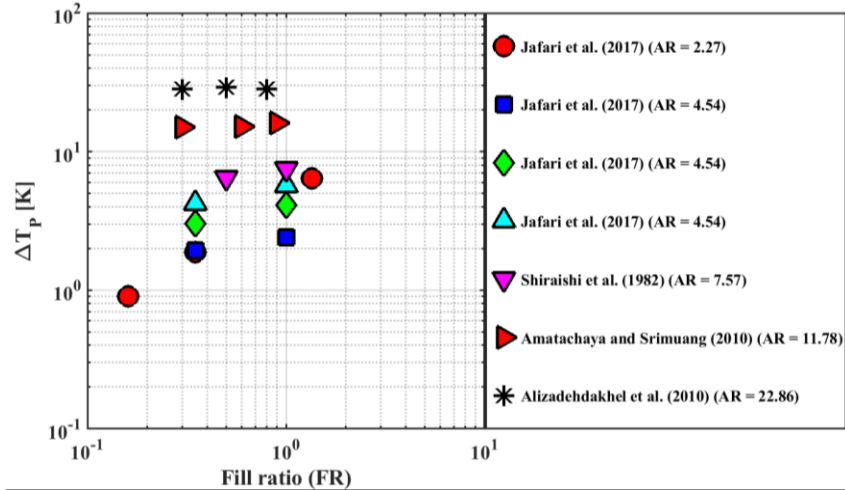


Figure 2.13 Variation in ΔT_P with FR.

The variation in the $R_{B,P}$ with ΔT_P and FR can be derived from equation (2.13) as

$$R_{B,P} = \frac{1}{C_3^{n_7}} (\Delta T_P)^{\frac{n_7-1}{n_7}} \quad (2.14)$$

$$R_{B,P} = \frac{C_3}{\dot{Q}_{in}} (FR)^{n_7-1} \quad (2.15)$$

Figures (2.14) and (2.15) show the plots of $R_{B,P}$ versus ΔT_P and $R_{B,P}$ versus FR. The slope of the data estimated from Jafari et al. (2017a) show consistent behaviour in figures (2.14) and (2.15) as $\left(\frac{n_7-1}{n_7}\right)$ and (n_7-1) are estimated to be -0.09 and -0.08 , respectively. Note that the last data point from Jafari et al. (2017a) (AR = 2.27) corresponds to FR = 1.35 and, thus, $R_{B,P}$ is slightly higher than if $\dot{Q}_{in,P} = \dot{Q}_{in} \times FR$ was considered.

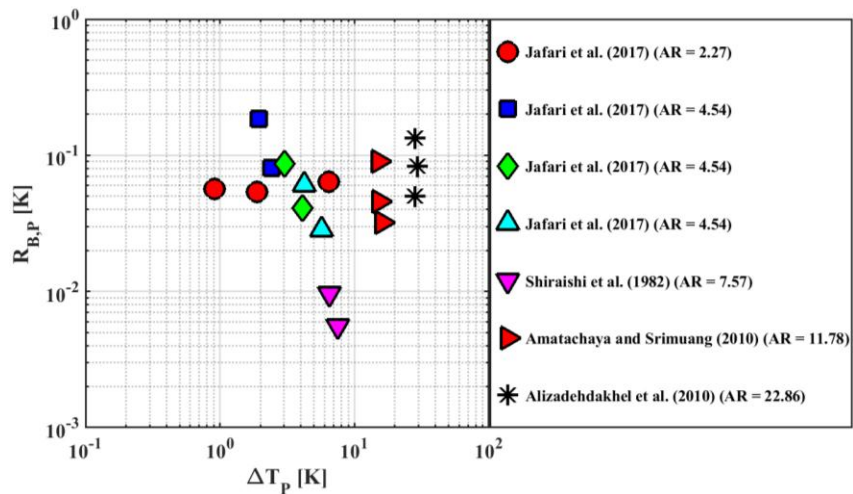


Figure 2.14 Variation in $R_{B,P}$ vs ΔT_P

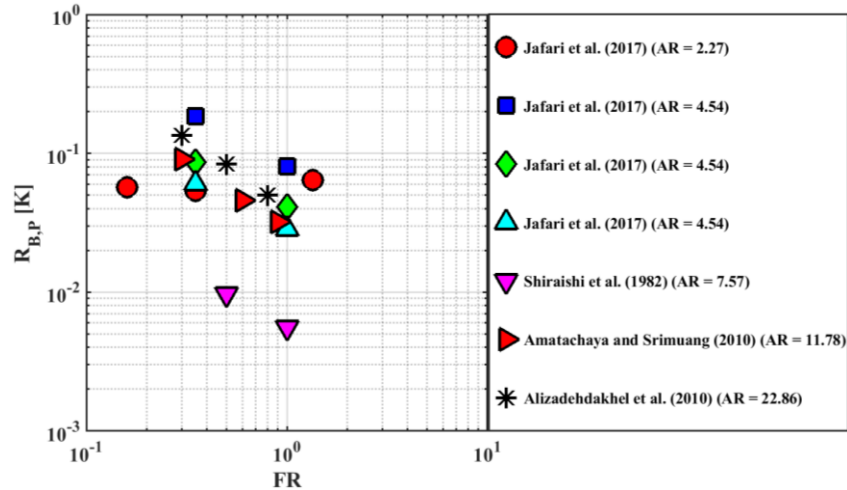


Figure 2.15 Variation in $R_{B,P}$ with FR

Some interesting features can be observed from the data of Alizadehdakhel et al. (2010) and Amatachaya and Srimuang (2010) in figures (2.14) and (2.15). Substituting $\Delta T_P \approx C_3$ from equation (2.13) into equation (2.14), gives $R_{B,P} \approx \frac{C_3}{\dot{Q}_{in}}$, suggesting that $R_{B,P}$ should stay constant. However, $R_{B,P}$ is shown to decrease in figure 2.14. Therefore, equation (2.14) holds true only when ΔT_P is not a constant. Substituting $n_7 \approx 0$ in equation (2.15) yields $R_{B,P} \approx \frac{C_3}{\dot{Q}_{in}} (FR)^{-1}$, which is consistent with the trends observed in Figure 2.15.

$R_{B,P}$ is computed as $R_{B,P} = \left(\frac{\Delta T_P}{\dot{Q}_{in} FR} \right)$ which shows that $R_{B,P} = f(\Delta T_P, FR)$. Typically, FR is seen to influence ΔT_P (see Jafari et al., (2017a, b) and the results in Chapter 6). However, for Alizadehdakhel et al. (2010) and Amatachaya and Srimuang (2010), since FR does not influence ΔT_P , $R_{B,P}$ decreases solely due to FR since $R_{B,P} \propto (FR)^{-1}$.

Several competing effects may explain this phenomenon. Logical reasoning suggests that as FR is increased, the number of nucleation sites along L_p will increase. Thus, there is a possibility that more number bubbles detach from the surface inducing considerable fluid motion, decreasing $R_{B,P}$. However, increased bubble formation may also cause significant bubble interference and coalescence, thereby increasing $R_{B,P}$. At $AR > 10$, the dominant flow pattern is bubbly and churn flow at the evaporator core (Terdtoon et al., 1998, 1999). This may cause $R_{B,P}$ to decrease. It is hypothesized that the first and the third effects dominate over the second effect subsequently decreasing $R_{B,P}$ as $R_{B,P} \propto (FR)^{-1}$. The variation in $R_{B,F}$ with FR is examined next.

2.2.3 Evaluation of the film boiling resistance ($R_{B,F}$)

Since $\Delta T_F = \Delta T_P$, the plot of FR versus ΔT_P is not discussed. The variation in $R_{B,F}$ with ΔT_P and FR can be written as

$$R_{B,F} = \frac{C_3^{\frac{1}{n_7}}}{\dot{Q}_{in}} \frac{\Delta T_P}{\left(C_3^{\frac{1}{n_7}} - \Delta T_P^{\frac{1}{n_7}} \right)} \quad (2.16)$$

$$R_{B,F} = \frac{C_3}{\dot{Q}_{in}} \frac{(FR)^{n_7}}{(1-FR)} \quad (2.17)$$

Figure 2.16 show the plot of $R_{B,F}$ versus ΔT_P . The data from Jafari et al. (2017 a, b) and Shiraishi et al. (1982) are excluded from the plot as there are only two data points for film boiling. Thus, the data from Alizadehdakhel et al. (2010) and Amatachaya and Srimuang (2010) are only shown. For $n_7 \approx 0$, equation (2.16) gives $R_{B,F} = \infty$, which is incorrect. Thus, equation (2.16) is valid only when ΔT_P is not a constant. Substituting $n_7 = 0$ in equation (2.17) gives $R_{B,F} = \frac{C_3}{\dot{Q}_{in}} \frac{1}{(1-FR)}$, suggesting that $R_{B,F}$ increases with FR. The data points in Figure 2.16 show this trend, however, this is more evident in Figure 2.17, where the plot of $R_{B,F}$ versus $(1 - FR)$ is shown.

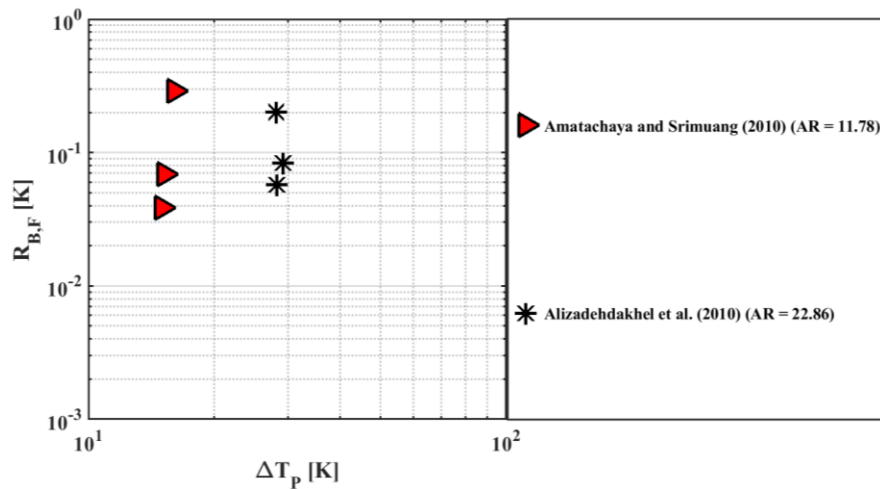


Figure 2.16 Variation in $R_{B,F}$ with ΔT_P

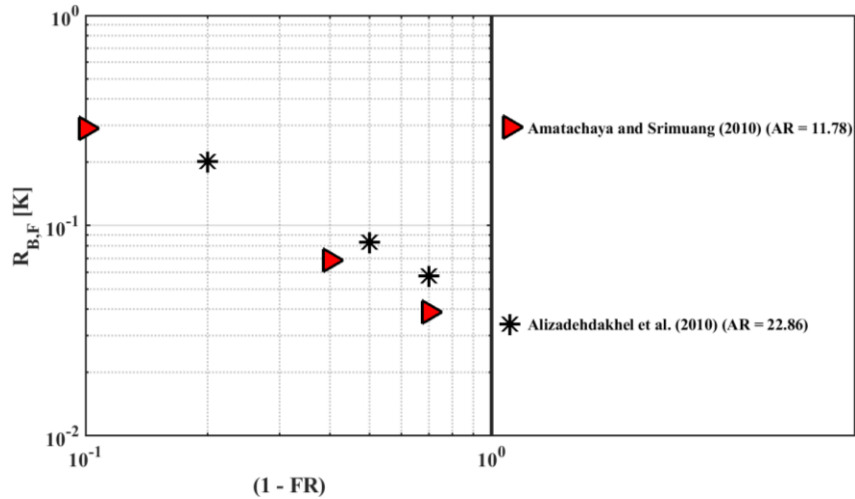


Figure 2.17 Variation in $R_{B,F}$ with $(1 - FR)$

Figure (2.17) confirms the $R_{B,F}$ versus FR relationship as the slope of the data estimated for Alizadehdakhel et al. (2010) and Amatachaya and Srimuang (2010) are -0.98 and -1.04 , respectively.

Based on the above discussion, it can be concluded that $R_{B,P}$ decreases, whilst $R_{B,F}$ increases with FR . The variation is such that that the overall boiling thermal resistance (R_B) stays nearly constant. The next sub-section examines the variation in $R_{C,F}$ with FR .

2.2.4 Evaluation of the condensation thermal resistance, $R_{C,F}$

This section examines i) the influence of FR on $\Delta T_{C,F}$ and ii) the relationship between $R_{C,F}$ and $\Delta T_{C,F}$.

Figure 2.18 shows the plot of FR versus $\Delta T_{C,F}$. The data from Noie (2005) have been excluded from the analysis, since $\Delta T_{C,F}$ as high as $91[K]$ have been reported which is physically incorrect. The data sets with only two data points for FR are also excluded. Thus, only the data from Joudi et al. (2000), Alizadehdakhel et al. (2010), Amatachaya and Srimuang (2010) and Jafari et al. (2017a) are analyzed. Although the data points are only three in number, a power-law equation of the form (equation 2.18) may be fitted to the data to estimate the slopes. The magnitude of the slope n_8 are shown in Table 2.8.

$$\Delta T_{C,F} = C_4 (FR)^{n_8} \quad (2.18)$$

where C_4 is a proportional constant (units $^{\circ}C$ or K) and n_8 is a dimensionless exponent.

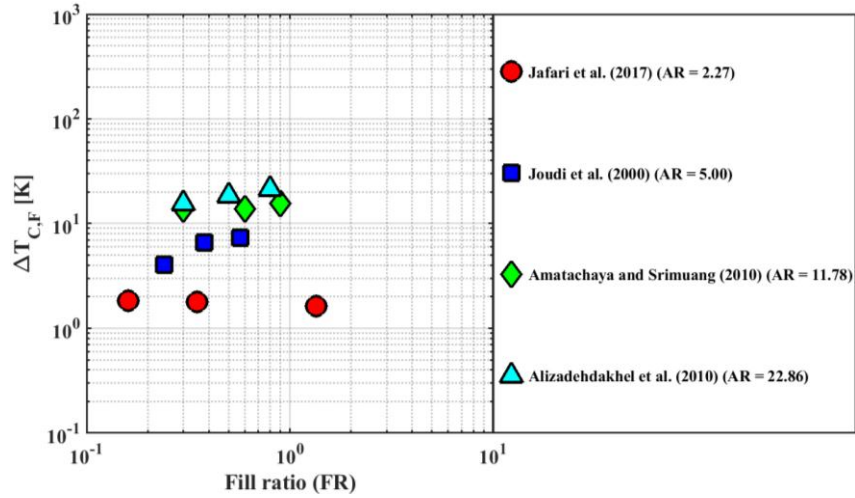


Figure 2.18 Variation in $\Delta T_{C,F}$ with FR.

Table 2.8 Estimates of n_s from figure 2.18.

Reference	n_s	R^2
Alizadehdakhel et al. (2010)	0.32	0.998
Amatachaya and Srimuang (2010)	0.10	0.627
Jafari et el. (2017a)	-0.06	0.959
Joudi et al. (2000)	0.61	0.884

Since, $R_{C,F} \propto (\Delta T_{C,F})$, the relation between $R_{C,F}$ and FR can be written as

$$R_{C,F} = \frac{C_4}{\dot{Q}_{in}} (FR)^{n_s} \quad (2.19)$$

The magnitudes of the slope estimated (not shown) from the plot of $R_{C,F}$ versus FR shown in Figure (2.19) demonstrate consistency with the values in Table 2.8 indicating that equation (2.19) is valid.

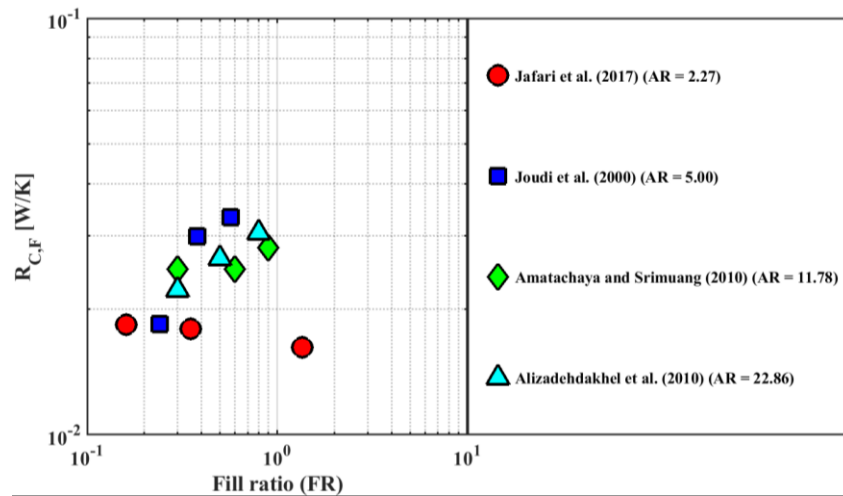


Figure 2.19 Variation in $R_{C,F}$ with FR.

The different magnitudes of the slope obtained in Table 2.8 for different studies are examined briefly through Figure 2.20, where the plots of Re_F versus FR, u_v versus FR and $\left(\frac{\rho_l}{\rho_v}\right)$ versus FR are shown.

Figure 2.20a reveals that Re_F is nearly independent of FR indicating the changes in h'_{fg} and μ_l are rather small. u_v is seen to nearly constant for $AR < 22.86$ suggesting that the changes in h'_{fg} and ρ_v with FR are inversely proportional. For Alizadehdakhel et al. (2010), h'_{fg} decreases by 0.75%, whilst ρ_v increases by 32.86% causing an overall reduction in the magnitudes of u_v . Thus, the effects of u_v on the heat transfer will be minimal. $\left(\frac{\rho_l}{\rho_v}\right)$ is nearly constant for $FR < 11.78$, whereas at higher AR, $\left(\frac{\rho_l}{\rho_v}\right)$ decreases. The decrement in $\left(\frac{\rho_l}{\rho_v}\right)$ indicates that both T_a and T_f increases. The increase in T_a can be explained by the reasons described in section 2.2.1. Since $\left(\frac{\rho_l}{\rho_v}\right)$ decreases, the entrainment effects are going to be minimal.

The above-mentioned observations do not explain the increase in $R_{C,F}$ for Joudi et al. (2000), Alizadehdakhel et al. (2010) and Amatachaya and Srimuang (2010). It is hypothesized that the increase in $R_{C,F}$ with FR is due to the more rapid accumulation of the condensate at the condenser section due to decrease in the travel length of the vapour flow. A comparison of the timescale of the vapour flow for these studies are compared in Table 2.9, which proves that with increase in FR, the time required for the vapour to reach the condenser section decrease causing the condensate to accumulate, increasing the condenser film thickness and the thermal resistance.

The rapid decrease in $R_{C,F}$ for the last data point in Jafari et al. (2017a) is hypothesized to be due to significant liquid carryover from the liquid pool into the condenser section as $FR = 1.35$. The transport rate of vapour is then reduced, which results in a thinner condensate film, thereby reducing $R_{C,F}$. Similar observations were reported by Andros (1980) for varying FR where the results from $FR = 0.92$ displayed higher heat transfer coefficient than at lower FR (0.15 - 0.61).

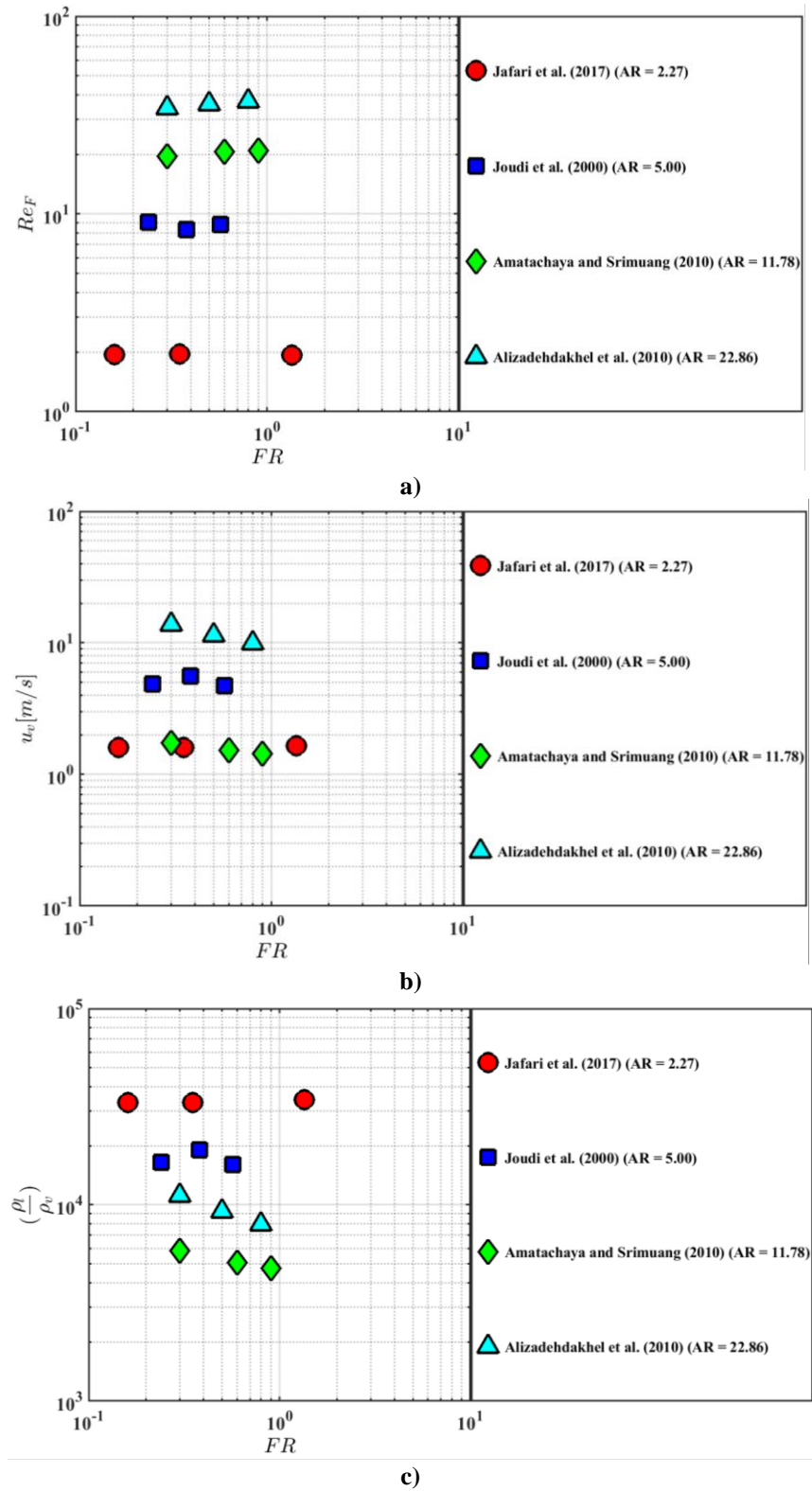


Figure 2.20 a) Variation in Re_F with FR b) Variation in $\left(\frac{\rho_l}{\rho_v}\right)$ with FR c) Variation in u_v with FR.

2.2.5 Interim summary

An interim summary highlighting the key data trends from the above analysis is presented. Firstly, it has been observed the evaporator surface temperature increases with FR regardless of \dot{Q}_{in} and AR values. This is due to the sensible heat absorption by the WF and the wall material. Secondly, the wall superheat (ΔT_P) has been observed to be nearly constant for $AR > 10$, whilst for $AR < 10$, $\Delta T_P \propto FR$. This is due to complex interactions between the generated bubbles which depends on the liquid pool length (L_p), the internal diameter (D_i) and AR. Thirdly, it has been shown that a power-law relationship exist between ΔT_P and FR, ΔT_P and the pool boiling resistance ($R_{B,P}$) and $R_{B,P}$ and FR. Fourthly, it has been shown that when ΔT_P is nearly constant, the film boiling thermal resistance ($R_{B,F}$) varies with FR as $R_{B,F} \propto (1-FR)^{-1}$. Fifthly, the condensation thermal resistance ($R_{C,F}$) is seen to decrease with FR, when there is a liquid carry over for $FR > 1$. For $FR < 1$, $R_{C,F}$ increases with FR due to a higher rate of accumulation of the condensate at the condenser.

2.3 Summary and recommendations

This chapter synthesized the available experimental data to present consistent conclusions about the relationship between the boiling and the condensation thermal resistances and \dot{Q}_{in} and FR. Simple mathematical equations proposed on the basis of the observed trends are shown to characterize the behavior of the data accurately. However, it is not known whether the magnitudes of the slopes obtained from the proposed equations are generic, as some of the slopes are estimated based on as few as three data points. Hence, more good quality, consistent data needs to be generated in order to validate the magnitudes of the power-law exponents and accurately estimate the correct form of the plots shown.

Based on the previously reported experimental modelling conditions, it is suggested that \dot{Q}_{in} be varied in such a way that different regimes of boiling and condensation film flow can be realized through a continuous set of data points passing through those regimes. It is evident from the analysis made in section 2.2 that FR has been varied maximum three times. Hence, FR should be varied in such a way that the effects of FR on the pool boiling and the film boiling thermal resistances could be understood in detail.

Chapter 3

3 Thermodynamic modelling of a thermosyphon and a heat pipe¹

Various thermodynamic processes occur inside thermosyphons (TS) and heat pipes (HP) during their operation. Those are i) sensible heating of the working fluid (WF) in the evaporator, ii) boiling phase change of the WF in the evaporator, iii) vapour flow from the evaporator to the condenser through the adiabatic section, iv) sensible cooling of the WF in the condenser, v) condensation phase change of the WF in the condenser, vi) liquid flow from the condenser to the evaporator through the adiabatic section.

Since the WF carries latent energy with it, it is essential to evaluate its state at different stages of the thermodynamic cycle to gain a fundamental understanding of the WF behaviour and how the changes in thermodynamic properties occur along these processes. The WF behaviour is best understood through a temperature-specific entropy (T-s) diagram or a specific enthalpy-specific entropy (h-s) diagram (from here on, the word “*specific*”, meaning on a per mass basis, will be assumed for entropy and enthalpy and omitted for brevity unless otherwise specified). The present work evaluates the state of the WF as it completes the thermodynamic cycle and provides insight into how changes in pressure, temperature, specific volume, enthalpy and entropy occur along the cycle.

The chapter is categorized into four sections. The first section reviews the thermodynamic cycle and the analysis from prior studies on HP in order to outline the strengths and weaknesses of those studies. The second section evaluates the entropy changes and entropy generated during the various thermodynamic processes. The third section describes methods to validate the thermodynamic model. The fourth section describes the other sources of entropy generation due to the finite temperature difference. The conclusions are presented in the fourth section.

¹ Excerpts from this chapter were presented at the Canadian Society of Mechanical Engineering conference, 2023. A version of this chapter is published in *Physics of Fluids*. doi.org/10.1063/5.017410.

Almost all of the previous studies on TS and HP have focused on evaluating the thermal performance of those devices without any thermodynamic considerations. Studies by Vasiliev and Konev (1982), Richter and Gottschlich (1990), Zuo and Faghri (1998) and Khalkhali et al., (1999) are the only relevant work that has been carried out on the thermodynamics of conventional HP. However, none of the studies analyzed the thermodynamic processes in a complete manner and they contained some key omissions. The next section assesses the previous thermodynamic studies and describes their deficiencies.

3.1 Previous thermodynamic studies and their deficiencies

Richter and Gottschlich (1990) proposed the T-s diagram shown in Figure 3.1, which delineates the various processes occurring inside a HP.

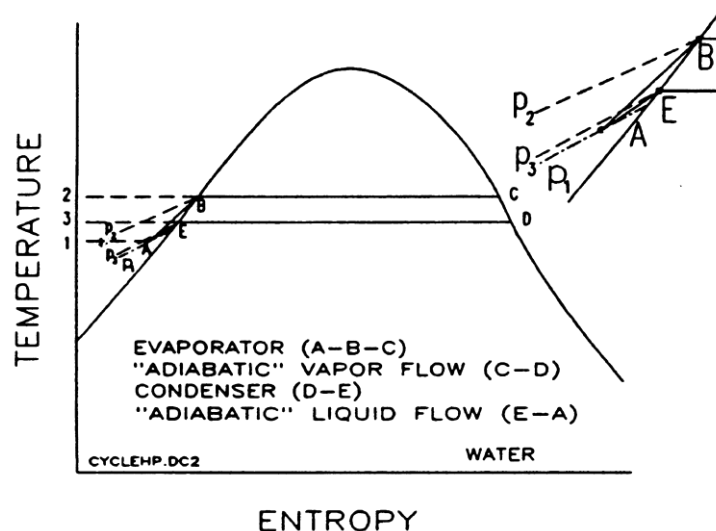


Figure 3.1 T-s diagram of a HP proposed by Richter and Gottschlich (1990) (adapted directly from the original reference with permission).

The obtained the temperature difference (ΔT) as a function of the operating temperature (T_{op}) and vapour the pressure differential (ΔP) (see section 1.2.2 in Chapter 1). Richter and Gottschlich (1990) postulated several reasons for the inconsistencies observed between the theoretical performance predictions and the actual HP performance. It was argued that a radial temperature gradient should exist in the adiabatic section in order to facilitate a pressure gradient so that the vapour does not block the flow of the liquid within the wicks. A radial temperature gradient can be achieved by some heat loss in the adiabatic section which will also provide necessary subcooling to the liquid return flow.

The authors also postulated that the process CD in Fig. 3.1 would be an isentropic process (the entropy increase due to friction would be balanced by the entropy decrease due to cooling, see Figure 3.2). These explanations are not correct for the following reasons. Firstly, the heat loss theory is not generalizable as it implies that a perfectly insulated HP would not work. Secondly, the exact entropy balance to make the process CD an isentropic process is questionable. Thirdly, the heat loss proposition in the adiabatic section violates the conditions for the maximum heat transfer through the HP as heat loss will result in less heat being transported to the condenser section.

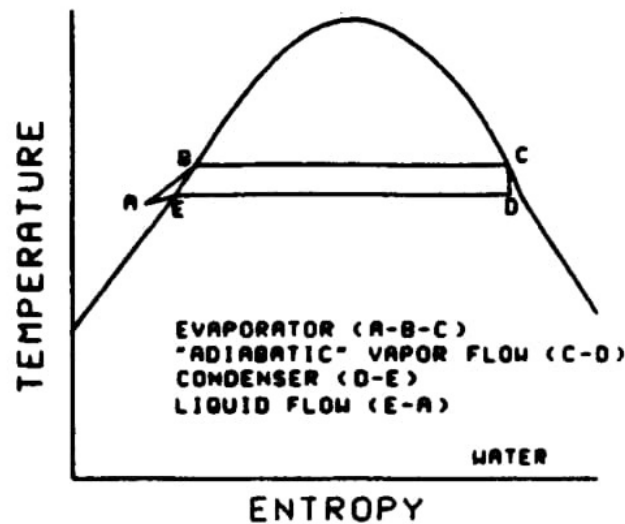


Figure 3.2 Actual thermodynamic cycle on a T-s diagram of a HP proposed by Richter and Gottschlich (1990) (adapted directly from the original reference with permission).

The T-s diagram shown in Figure 3.3 was proposed by Zuo and Faghri (1998). Curves oB and Cn represent boiling and condensation, respectively. Curve AB represents the heat addition to the WF, whereas curves BC and DA represent the vapour and the liquid flows through the adiabatic section.

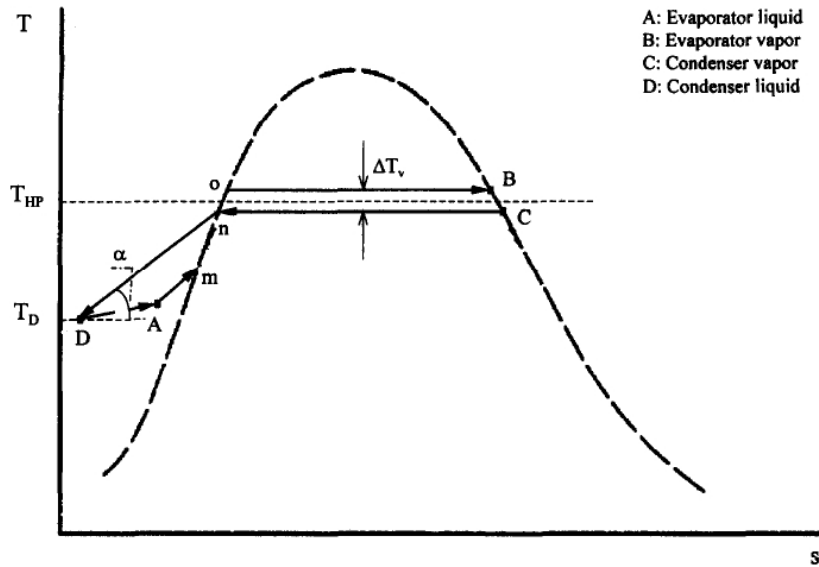


Figure 3.3 T-s diagram proposed by Zuo and Faghri (1998). T_{HP} is the HP operating temperature calculated as the average of T_B and T_C (adapted from the original reference with permission).

The authors analyzed each process briefly, utilizing the first law of thermodynamics. The equations were given as

$$\dot{Q}_{A-B} = \dot{m}(h_B - h_A) \text{ for process AB} \quad (3.1)$$

$$\dot{m}(h_C - h_B) = \dot{m}v_v(P_{v,C} - P_{v,B}) \text{ for process BC} \quad (3.2)$$

$$\dot{m}(h_D - h_C) = \dot{Q}_{C-D} \text{ for process CD} \quad (3.3)$$

$$\dot{m}(h_A - h_D) = \dot{m}v_l(P_{l,A} - P_{l,D}) \text{ for process DA} \quad (3.4)$$

where \dot{Q} is the heat transfer rate, h is the enthalpy, P is the pressure, \dot{m} is the mass flow rate, v is the specific volume of the WF, and subscripts l and v represent the liquid and the vapour phase, respectively. There are several inconsistencies between Figure 3.3 and the equations (3.2) and (3.4). Firstly, equation (3.4) implies that when $P_{l,A} < P_{l,D}$, h_A must be less than h_D . But this may not always be true. Evaluating the specific enthalpy changes between states A and D using the equation, $h = u + Pv$, gives

$$h_A - h_D \approx c_{avg}(T_{l,A} - T_{l,D}) + v_l(P_{l,A} - P_{l,D}) \quad (3.5)$$

where c_{avg} is the average specific heat of the liquid phase over the given temperature interval. Based on Figure 3.3, $c_{avg}(T_{1,A} - T_{1,D}) > 0$ and $v_l(P_{1,A} - P_{1,D}) < 0$. This gives rise to three different scenarios which are possible based on the relative magnitudes of $c_{avg}(T_{1,A} - T_{1,D})$ and $v_l(P_{1,A} - P_{1,D})$. Those are i) $h_A < h_D$ when $|c_{avg}(T_{1,A} - T_{1,D})| < |v_l(P_{1,A} - P_{1,D})|$ ii) $h_A \approx h_D$, when $|c_{avg}(T_{1,A} - T_{1,D})| \approx |v_l(P_{1,A} - P_{1,D})|$, and iii) $h_A > h_D$, when $|c_{avg}(T_{1,A} - T_{1,D})| > |v_l(P_{1,A} - P_{1,D})|$. The scenarios are demonstrated on a T-s diagram (Figure 3.4) of water.

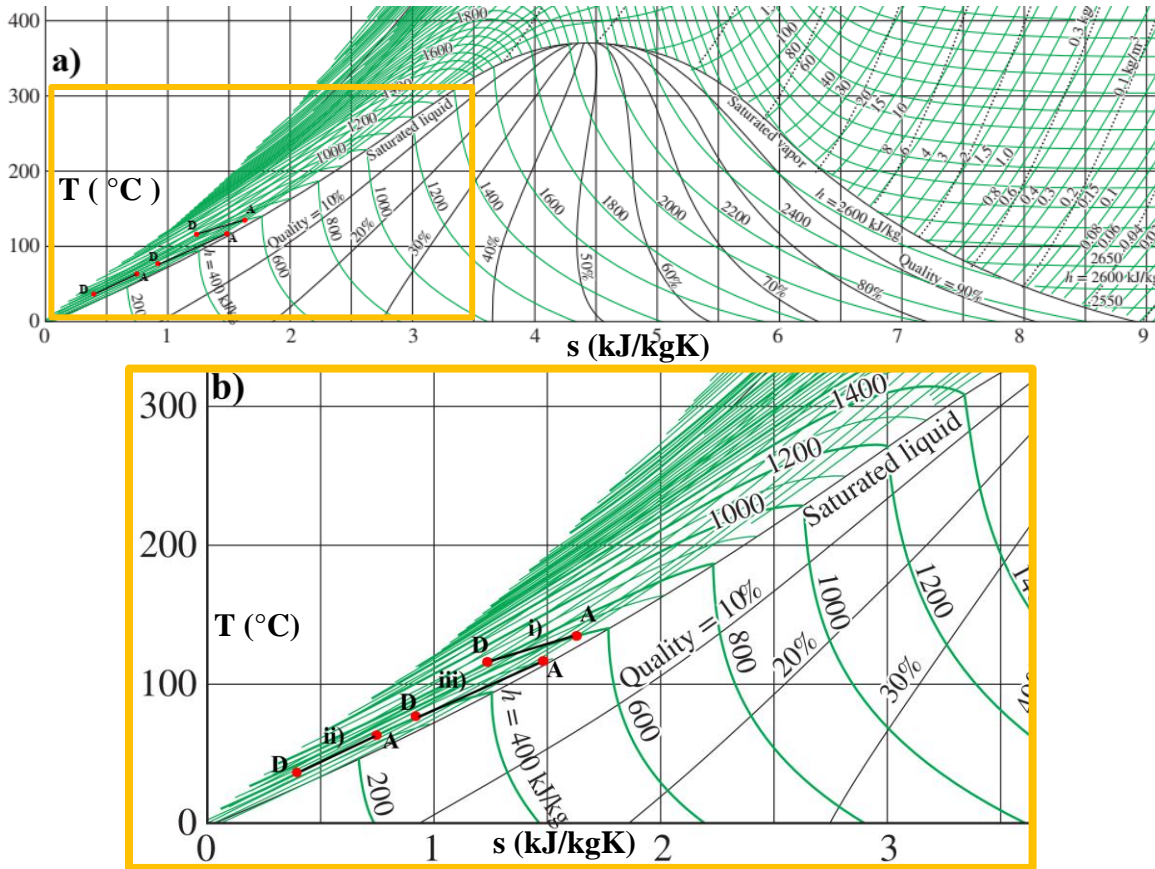


Figure 3.4 a) T-s diagram showing the process line DA. The x-axis represents the specific entropy [kJ/kgK] and the y-axis represents the temperature [°C]. The yellow box represents the region that has been magnified in b) for better illustration. b) The process lines DA for three different scenarios are indicated by the roman numbers.

It is now evident that equation (3.4) is not a general equation as it only correctly represents case i). Secondly, if the steady flow energy equation is applied to the flow processes in the adiabatic section, then the enthalpy should remain constant over the process (Nag, 2014, Cengel et al., 2019, White and Xue, 2021). The process lines BC and DA do not corroborate this and, therefore, equations (3.2) and (3.4) are not valid. Thirdly,

Zou and Faghri, (1999) assumed that the frictional pressure drop between states B and C in Figure 3.3 is equal to the pressure differential between states B and C driving the flow. This condition may not always be valid, such as in a TS when the hydrostatic gravitational potential is less than the liquid flow pressure drop. In a HP, when the magnitude of the capillary pressure is less than sum of the liquid flow pressure and the adverse gravitational pressure drops, this condition will not be valid (see equation 1.1).

The thermodynamic processes have also been plotted on a T-s diagram (Figure 3.5) by Khalkhali et al., (1999). States 1 and 2 indicate evaporator and condenser vapour, and states 3 and 4 indicate condenser and evaporator liquid. It was postulated that states 1 and 3 can be determined from the external heating and cooling conditions, whilst the WF pressures at states 2 and 4 can be determined from the WF mass flow rate and the HP dimensions. Utilizing $h_1 - h_2 = h_3 - h_4$, the states at point 2 and 4 can be determined. No further comments or analyses regarding the T-s diagram were provided by the authors.

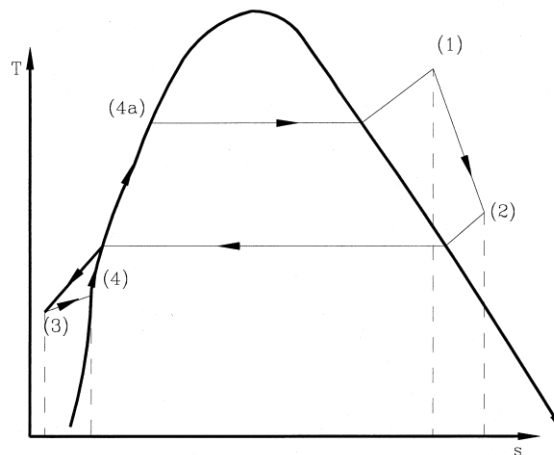


Figure 3.5 T-s diagram proposed by Khalkhali et al. (1999) (adapted from the original reference with permission).

Although the boiling and condensation process are identical in Figures 3.1 - 3.3 and 3.5, there are some key differences between the vapour and the liquid flow process lines on these diagrams. Firstly, the isentropic process line postulated by Richter and Gottschlich (1990) in Figure 3.2, has not been corroborated by other studies. Hence, it is not known whether the vapour flow through the adiabatic section requires heat loss. Secondly, the vapour flow process line (1→2) in the superheated region shown in Figure 3.5 has not been considered by the other studies. Whether the slope of the curve (1→2) is arbitrary or

whether it represents the vapour flow process correctly, therefore, cannot be determined. Thirdly, the curve representing the liquid return process in Figures 3.1 (and 3.2), 3.3 and 3.5 are different. Figure 3.1 (and 3.2) shows the liquid entropy to decrease going from a lower (P_3) pressure to a higher pressure (P_1), whereas Figures 3.3 and 3.5 show the liquid entropy to increase going from a higher pressure (P_D) to a lower pressure (P_A) (or $P_3 \rightarrow P_4$). Khalkhali et al., (1999) argued that the curve EA in Figure 3.1 (and 3.2) is inaccurate as the liquid entropy should increase, not decrease, due to the frictional losses at the wick. Fifthly, the sub-cooled liquid during sensible heating is shown to reach the saturated liquid state through a constant pressure process in Figure 3.1 (and 3.2), whereas it is shown to follow the saturated liquid curve in Figures 3.3 and 3.5 with an increase in pressure. Sixthly, in Figure 3.3 the liquid state arriving at the evaporator is shown to lie in the sub-cooled regime, whereas it lies on the saturated liquid line in Figure 3.5.

The differences and shortcomings of the above-mentioned T-s diagrams are now apparent. The liquid and vapour flow process lines between the different T-s diagrams are inconsistent. The analyses presented in the previous studies are incomplete since no quantitative evaluations of the entropy changes during the thermodynamic processes are made. Figures 3.1 - 3.3 and 3.5 represent the thermodynamic cycle of a HP, but it is not known whether the thermodynamic cycle would be identical for a TS.

Therefore, the primary objective of this chapter is to advance our understanding of thermodynamics of a TS and a HP so that more efficient designs of TS and HP can be developed and used. A thermodynamic model developed on the basis of the first and second laws of thermodynamics is utilized to theoretically analyze the entropy changes of the various thermodynamic processes and, thereby, determine the thermodynamic state of the WF. Based on the entropy change equations, different thermodynamic processes are represented through the process lines and process points on the T-s and h-s diagrams. Physical justifications validating the locations of the state points are provided. Analytical expressions predicting the changes in the temperature, pressure, specific volume, entropy and enthalpy during each thermodynamic process are derived. In addition, the equations for entropy generation are formulated which can be used for thermodynamic optimization based on entropy generation minimization (Bejan, 1995).

3.2 Evaluation of the entropy changes of the thermodynamic processes inside a TS and a HP

The first law of thermodynamics for a steady flow process within a control volume can be written as

$$\delta q - \delta w = dh + d(pe) + d(ke) \quad (3.6)$$

where δ , d represent the inexact and the exact differential symbol, respectively. δq is the differential amount of heat transfer into the system per unit mass, δw is the differential amount of work done by the system (i.e. the WF) on the surroundings per unit mass, dh , $d(ke)$ and $d(pe)$ are the differential changes in the specific enthalpy, kinetic energy and potential energy per unit mass, respectively. It is noted that for steady flow processes within a TS and a HP, the boundary work will be zero. For solid confining walls and wick, as in a TS and a HP, the viscous work is zero (White and Xue, 2021). The work required to push a fluid parcel into and out of the control volume is accounted for in the enthalpy term. As shaft work and electrical work are not present, δw in equation (3.6) is zero. The value of dh for the saturated liquid ($dh_{sat,l}$) and saturated vapour ($dh_{sat,v}$) will vary with temperature changes, ΔT (or changes in pressure, ΔP) during the process. The order of magnitude (O) of $dh_{sat,l}$ and $dh_{sat,v}$ computed for different ΔT ranges using the steam table are illustrated in Table 3.1.

Table 3.1 Order of magnitude of $dh_{sat,l}$ and $dh_{sat,v}$ at different ΔT ranges. O represents the order of magnitude computed as $N = a \times 10^b$ where $1 \leq a \leq 10$.

ΔT [°C]	O ($dh_{sat,l}$ [kJ/kg])	O ($dh_{sat,v}$ [kJ/kg])
1	0	0
5	1	1
10	1	1
25	2	1

In order for $d(pe)$ and $d(ke)$ to be of the $O \sim (10^0 \text{ kJ/kg})$, $\Delta z \rightarrow O \sim (10^2 \text{ m})$ and $\Delta u_{l,v} \rightarrow O \sim (10^1 \text{ m/s})$, whereas for $d(pe)$ and $d(ke)$ to be of the $O \sim (10^1 \text{ kJ/kg})$, $\Delta z \rightarrow O \sim (10^3 \text{ m})$ and $\Delta u_{l,v} \rightarrow O \sim (10^2 \text{ m/s})$, where Δz denotes the elevation change of the WF during the flow process, and $\Delta u_{l,v}$ denotes the change in velocity. Such high magnitudes of Δz and $\Delta u_{l,v}$ may not be observed in conventional TS and HP and, thus, $d(pe)$ and $d(ke)$ can be disregarded from the analysis.

The Gibbs equations for a thermodynamic system can be written as (Cengel et al., 2019)

$$Tds = du + Pdv \quad (3.7)$$

$$Tds = dh - v dP \quad (3.8)$$

where T , s , u , P , v and h denote the temperature, specific entropy, specific internal energy, pressure, specific volume, and specific enthalpy, respectively. The second law of thermodynamics, employing the increase of entropy principle for any flow process inside a TS and HP, can be written as

$$ds - \frac{\delta q}{T} = \delta s_{\text{gen}} \quad (3.9)$$

where δs_{gen} denotes the differential amount of specific entropy generated during the process. Substituting ds from equations (3.7) and (3.8) into equation (3.9) yields

$$\frac{du}{T} + \frac{Pdv}{T} - \frac{\delta q}{T} = \delta s_{\text{gen}} \quad (3.10)$$

$$\frac{dh}{T} - \frac{v dP}{T} - \frac{\delta q}{T} = \delta s_{\text{gen}} \quad (3.11)$$

Figure 3.6 shows a T-s diagram for different thermodynamic processes, illustrating the known state points with green-coloured circles and the unknown state points with purple-coloured circles. The unknown state points are placed in the correct region of the T-s diagram, but their exact position is arbitrary until further analysis is completed. The processes are summarized in Table 3.2 for completeness.

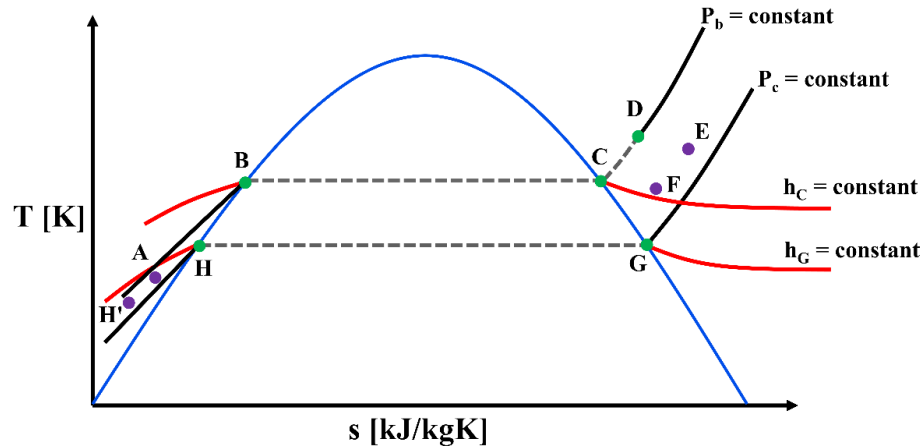


Figure 3.6 T-s diagram showing the known state points B, C, D, G and H (green coloured circles) and the process lines BC, CD and GH (dashed gray lines) inside a TS and a HP. The solid red and black curves represent the constant enthalpy and the pressure lines, respectively. The state points E, F and A are not known a priori and are represented by purple coloured circles.

Table 3.2 Descriptions of the thermodynamic processes inside a TS and a HP

Thermodynamic process	Description
AB	Sensible heating of the WF in the evaporator
BC	Boiling phase change in the evaporator
CD	Sensible superheating of the WF in the evaporator ($FR < 1$)
CF	Vapour flow from the evaporator to the condenser through the adiabatic section ($FR \geq 1$)
DE	Vapour flow from the evaporator to the condenser through the adiabatic section ($FR < 1$)
FG	Sensible cooling of the WF vapour in the condenser
GH	Condensation phase change in the condenser
HA	Liquid flow from the condenser to the evaporator through the adiabatic section (only for a TS)
HH'	Sensible cooling of the WF liquid in the condenser (for a HP)
H'A	Liquid flow from the condenser to the evaporator through the adiabatic section (for a HP)

It is noted that the pressures at state points B, C and D are equal to the boiling saturation pressure, P_b i.e. $P_B = P_C = P_D = P_b$. If E and F are found to lie on the constant pressure line P_c , then $P_E = P_F = P_G = P_c$ (P_c is the condensation saturation pressure). Consequently, $T_B, T_C = T_b$ and $T_G, T_H = T_c$.

Table 3.3 summarizes the expressions for the first law, the entropy changes and the entropy generation for process BC, CD and GH. The expressions for the rest of the thermodynamic processes are summarized later at the end of section 3.2 after the relevant analysis of those processes are completed. The evaluation of the entropy changes during processes CF, DE and HA are carried out in the next sub-sections.

Table 3.3 Expressions of the first law of thermodynamics, the entropy changes and s_{gen} for the BC, CD, and GH processes inside a TS and a HP.

Thermodynamic process	Expressions of first law of thermodynamics	Expressions of the entropy changes	s_{gen}	Comments
BC	$\delta q_{in,lat,BC} = dh_{BC}$	$s_C - s_B = \frac{h_{fg}(P = P_b)}{T_B}$	0	$s_C > s_B$ for all values of T_B
CD	$\delta q_{in,sen,CD} = dh_{CD}$	$s_D - s_C = c_{p,v,avg} \ln\left(\frac{T_D}{T_C}\right)$		$s_D > s_C$ when $T_D > T_C$
GH	$\delta q_{in,lat,GH} = dh_{GH}$	$s_H - s_G = -\frac{h_{fg}(P = P_c)}{T_G}$		$s_H > s_G$ for all values of T_G
Nomenclature:				
$\delta q_{in,lat}$ = differential amount of latent heat absorbed/released by the WF during the phase change process.				
$\delta q_{in,sen}$ = differential amount of sensible heat absorbed/released by the WF during the process.				
dh = differential specific enthalpy changes during the process.				
Note: $c_{p,v,avg}$ is assumed to be constant during CD indicating that the temperature change during CD is not large. If the temperature change is large and c_p varies non-linearly with temperature, then c_p can be expressed as $c_p = a + bT + cT^2 + dT^3$ where a, b, c and d are constants. For an ideal gas approximation, the expression of $s_D - s_C$ will be different which is discussed later in section 4.2.3.				

3.2.1 Entropy change during process CF inside a TS

The first law of thermodynamics (per unit mass) for any process (assuming $d(ke)$ and $d(pe) \cong 0$) can be written using equation (3.6) as

$$\delta q - dh = 0 \quad (3.12)$$

Equation (3.12) when applied to the vapour flow process CF ($FR \geq 1$) in a TS yields

$$dh \cong 0 \quad (\because Q \cong 0) \quad (3.13)$$

indicating $h_F \approx h_C$. Substituting dh from equation (3.13) into equation (3.8) yields an expression for the entropy change during CF in a TS as

$$s_{F,TS} - s_{C,TS} \approx -\int_{C,TS}^{F,TS} \left(\frac{v_v dP}{T}\right)_p \cong \frac{v_{v,avg,CF}}{T_{avg,CF}} (P_b - P_{F,TS}) \quad (3.14)$$

where it is assumed that variations in T and v are much less than changes in P between the state points C and F . The variation in T and v may be approximated as varying linearly over the pressure intervals and, thus, can be replaced by constant average values $T_{avg,CF}$ and $v_{v,avg,CF}$. $s_{C,TS}$ and $s_{F,TS}$ denote the specific entropies at state points C and F , respectively. The subscript “ p ” to the round bracket indicates the “*process*”. $P_{F,TS}$ is the pressure corresponding to state F . The location F at the end of the process is not known *a*

priori and, therefore, an estimate of its location is made with respect to the location of the vapour saturation state G, which can be determined directly from the steam tables provided that either T_b and T_c or P_b and P_c are known. The entropy changes between states C and G can be evaluated using equation (3.8) as

$$s_{G,\text{sat}} - s_{C,\text{sat}} = \int_{C,\text{sat}}^{G,\text{sat}} \left(\frac{dh}{T} \right)_{\text{sat}} - \int_{P_b}^{P_c} \left(\frac{v_v dP}{T} \right)_{\text{sat}} \cong \left[\left(\frac{h_{G,\text{sat}} - h_{C,\text{sat}}}{T_{\text{avg},\text{sat}}} \right) - \left(\frac{v_{v,\text{avg},\text{sat}}(P_c - P_b)}{T_{\text{avg},\text{sat}}} \right) \right] \quad (3.15)$$

where it is assumed that variations in T and v are much less than changes in h and P between state points C and G. The assumption does not lead to considerable errors (< 1%) in the entropy change calculations. $s_{C,\text{sat}}$, $s_{G,\text{sat}}$ are the saturated vapour specific entropies and $h_{C,\text{sat}}$, $h_{G,\text{sat}}$ are the saturated vapour specific enthalpies at points C and G, respectively. $T_{\text{avg},\text{sat}}$ is the average saturation temperature between C and G. The subscript “sat” on the round brackets denotes the “*saturation state*”. Subtracting equation (3.15) from equation (3.14), considering $s_{C,\text{TS}} = s_{C,\text{sat}}$ and $P_{C,\text{TS}} = P_b$, gives

$$s_{F,\text{TS}} - s_{G,\text{sat}} \cong \left(\frac{h_{C,\text{sat}} - h_{G,\text{sat}}}{T_{\text{avg},\text{sat}}} \right) - \left(\frac{v_{v,\text{avg},\text{sat}}(P_b - P_c)}{T_{\text{avg},\text{sat}}} \right) + \left(\frac{v_{v,\text{avg},\text{CF}}(P_b - P_{F,\text{TS}})}{T_{\text{avg},\text{CF}}} \right) \quad (3.16)$$

where $T_{\text{avg},\text{CF}}$ is the average temperature between the process C and F. $v_{v,\text{avg},\text{sat}}$ and $v_{v,\text{avg},\text{CF}}$ are the average specific volume values where $v_{v,\text{avg},\text{sat}} = \left(\frac{v_{v,\text{sat}}(\text{at } P=P_b) + v_{v,\text{sat}}(\text{at } P=P_c)}{2} \right)$, $v_{v,\text{avg},\text{CF}} = \left(\frac{v_{v,\text{sat}}(\text{at } P=P_b) + v_{v,\text{sat}}(\text{at } P=P_{F,\text{TS}})}{2} \right)$. Equation (3.16) defines the location of $s_{F,\text{TS}}$ with respect to $s_{G,\text{sat}}$. $(P_b - P_{F,\text{TS}})$ in equation (3.14) (and equation 3.16) is equal to the sum of the hydrostatic pressure drop ($\Delta P_{\text{hydro},v}$), the pressure drop ($\Delta P_{v,d}$) due to the dynamic pressure effects and the pressure drop ($\Delta P_{\text{shear},l-v}$) due to the shear stress at the liquid-vapour interface. Thus, $(P_b - P_{F,\text{TS}}) \approx [\Delta P_{\text{hydro},v} + \Delta P_{v,d} + \Delta P_{\text{shear},l-v}]$. The theoretical estimations of $\Delta P_{\text{hydro},v}$, $\Delta P_{v,d}$ and $\Delta P_{\text{shear},l-v}$ are provided in Chapter 1. $(P_b - P_c)$ is the overall pressure differential driving the flow and must be greater than or equal to the vapour pressure drop in order for the WF to circulate continuously. Therefore, $|(P_b - P_c)| \geq |(P_b - P_{F,\text{TS}})|$. Equations (3.14), (3.15) and (3.16) depict three important features, which are best demonstrated and explained with the help of a T-s diagram shown in Figure 3.7.

Firstly, if one navigates towards an arbitrary point F along the constant enthalpy line from point C, then it will be seen that that $P_{F,TS} < P_b$. Therefore, by equation (3.14) $s_{F,TS} > s_{C,TS}$, meaning that entropy will increase during the process CF. Secondly, since $s_{G,sat} > s_{C,sat}$ in equation (3.15), the absolute value of the $\int_{P_b}^{P_c} \left(\frac{v_v dP}{T} \right)_{sat}$ term must be greater than the absolute value of $\int_{C,sat}^{G,sat} \left(\frac{dh}{T} \right)_{sat}$. This can be explained by the fact that $\int_{C,sat}^{G,sat} \left(\frac{dh}{T} \right)_{sat}$ is negative, whilst $-\int_{P_b}^{P_c} \left(\frac{v_v dP}{T} \right)_{sat}$ is positive. This can be verified by doing a simple calculation on any arbitrary vapour saturation states based on the steam table for water. Thirdly, if $P_{F,TS} = P_c$ in equation (3.16), then equation (3.16) can be written as

$$s_{F,TS} - s_{G,sat} \cong \left(\frac{h_{C,sat} - h_{G,sat}}{T_{avg,sat}} \right) + (P_b - P_c) \left(\frac{v_{v,avg,CF}}{T_{avg,CF}} - \frac{v_{v,avg,sat}}{T_{avg,sat}} \right) \quad (3.17)$$

Equation (3.17) suggests that $s_{F,TS}$ will be greater than $s_{G,sat}$. This is based on the fact that $\left(\frac{v_{v,avg,CF}}{T_{avg,CF}} - \frac{v_{v,avg,sat}}{T_{avg,sat}} \right) > 0$ which can be proved either from the values from the steam table or by plotting the process points on the T-s diagram. Figure 3.7b also reveals that when $P_{F,TS} = P_c$, the maximum entropy $s_{F,TS}$ (denoted by $s_{F,max,TS}$) is obtained at the state point F. Fourthly, if $P_{F,TS} > P_c$ in equation (3.16), then $s_{F,TS}$ can either be greater than, equal to, or less than $s_{G,sat}$. In order to determine which scenario will prevail, the pressure corresponding to $h = h_C$ and $s = s_{G,sat}$ values need to be determined using the state postulate. Let that pressure be termed as P_{int} where the subscript “int” indicates “*intermediate*”. If $P_{F,TS} = P_{int}$, then $s_{F,TS} = s_{G,sat}$. If $P_{F,TS} > P_{int}$, then $s_{F,TS} < s_{G,sat}$. If $P_c < P_{F,TS} < P_{int}$, then $s_{F,TS} > s_{G,sat}$. All these scenarios have been illustrated on the T-s diagram in Figure 3.7b. It needs to be noted that whilst, P_c and P_{int} can be determined from the steam table and the state postulate, $P_{F,TS}$ can be determined analytically from the expression $(P_b - P_{F,TS}) \approx [\Delta P_{v,hydro} + \Delta P_{v,d} + \Delta P_{shear,l-v}]$. However, since $\Delta P_{v,hydro}$ and $\Delta P_{v,d}$ are of the $O \sim 10^{-3}$ [kPa] and $O \sim 10^{-2}$ [kPa], respectively, $(P_b - P_{F,TS}) \approx \left[4\tau_i \frac{L_{eff}}{D_i} \right]$ (see Chapter 1). It is postulated that $P_{F,TS}$ will likely be higher than P_c in order for the pressure drop to be less than the driving pressure differential. Fifthly, the magnitude of $T_{F,TS}$ can be estimated by extrapolating a straight line on the vertical T-axis from the intersection of $s_{F,TS}$ and the constant enthalpy line. Figure 3.7b shows that $T_{F,TS}$ will always be greater

than the saturation temperature corresponding to the pressure $P_{F,TS}$; thus, the vapour arriving at state F will be in a superheated state. For condensation to occur, this superheated vapour must first return back to the saturated vapour state at $P = P_c$, and it will do so by releasing sensible heat. If $P_{F,TS} = P_c$, then the sensible heat released can be computed using $c_{p,avg}(T_{G,sat} - T_{F,TS})$, where $c_{p,avg}$ is the average specific heat value over the given temperature interval. If $P_{F,TS} > P_c$, then the sensible heat released can be computed directly using the first law of thermodynamics as $(h_{G,sat} - h_{F,TS})$. Sixthly, if the vapour is assumed to be an ideal gas during the process CF, then expression (3.16) can be written as

$$s_{F,TS} - s_{G,sat} \cong \left(\frac{h_{C,sat} - h_{G,sat}}{T_{avg,sat}} \right) + \bar{R} \ln \left(\frac{P_c}{P_{F,TS}} \right) \quad (3.18)$$

where \bar{R} is the specific gas constant of the WF.

The value of s_{gen} for CF for a TS can be estimated using equation (3.11) as

$$s_{gen} \cong \frac{v_{v,avg,CF}(P_b - P_{F,TS})}{T_{avg,CF}} - \left[\frac{q_{in}}{T_b} - \frac{q_{in}}{T_{F,TS}} \right] \quad (3.19)$$

where $q_{in} = \left(\frac{Q_{in}}{m} \right) = \left(\frac{\dot{Q}_{in}}{\dot{m}} \right)$, Q_{in} , \dot{Q}_{in} are the input heat and the input heat rate, respectively. T_b , $T_{F,TS}$ are the boundary temperature of the adiabatic section towards the evaporator and the condenser side, respectively. The magnitude of the last term of equation (3.19) will be very small and, therefore, it can be neglected for practical purposes. In that case, $s_{gen} \cong s_{F,TS} - s_{C,TS}$. If the vapour is assumed to be an ideal gas, then equation (3.19) becomes

$$s_{gen} = \bar{R} \ln \left(\frac{P_b}{P_{F,TS}} \right) - \left[\frac{q_{in}}{T_b} - \frac{q_{in}}{T_{F,TS}} \right] \quad (3.20)$$

Equations (3.19) and (3.20) demonstrate that the entropy generated during CF in a TS can be minimized by reducing the vapor flow pressure drop in the system. The next subsection evaluates the entropy change during the process CF for a HP.

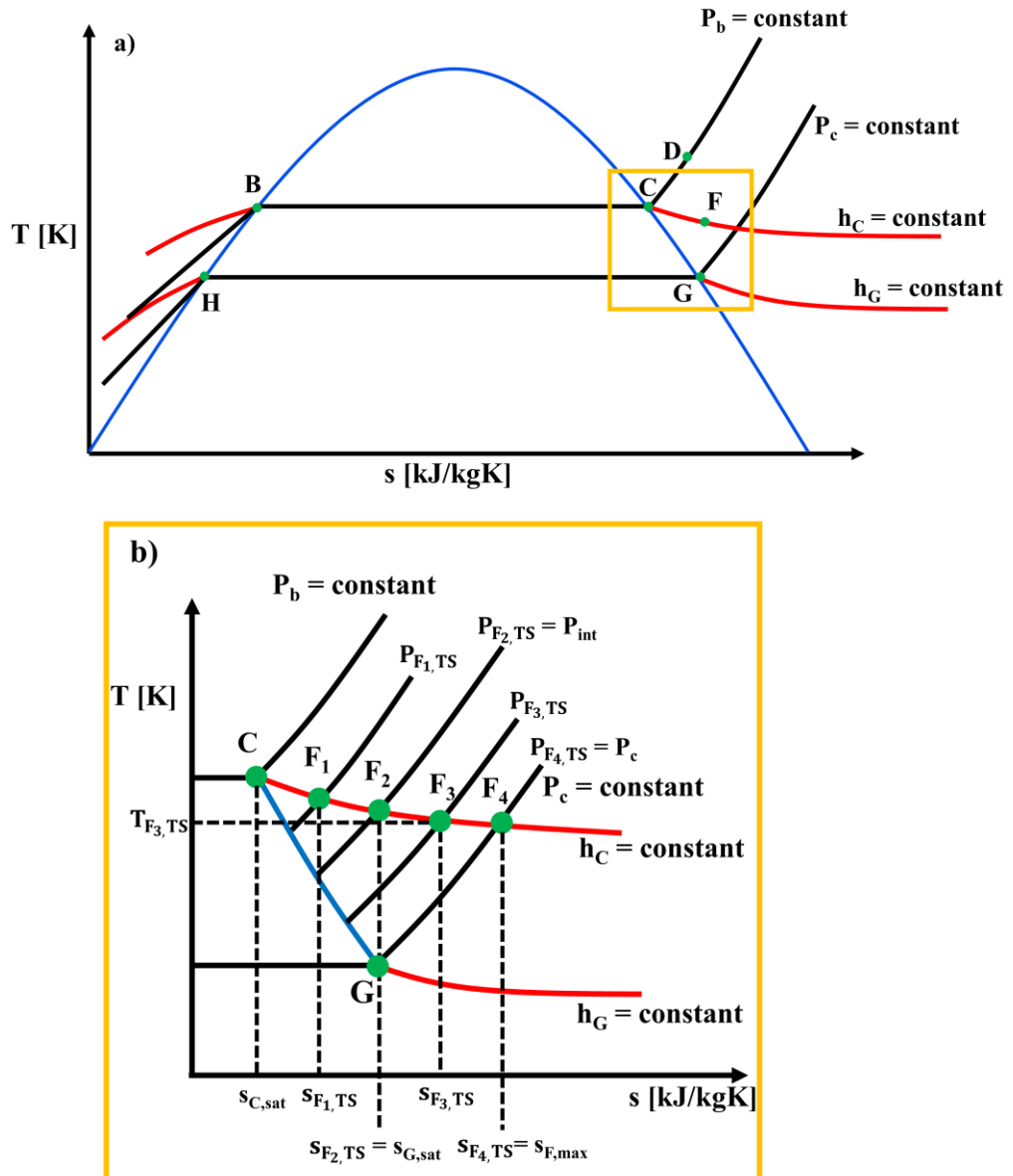


Figure 3.7 a) T-s diagram showing the relevant superheated regime where process CF occurs within a TS. The yellow box represents the region of interest that has been magnified in b) for better illustration. b) The magnified superheated regime showing different possible locations of the state point F along the constant enthalpy line, h_C . F1 represents the state point F, when $P_{F,TS} > P_{int}$; $s_{F_1,TS} < s_{G,sat}$. F2 is when $P_{F,TS} = P_{int}$; $s_{F_2,TS} = s_{G,sat}$. F3 is when $P_c < P_{F,TS} < P_{int}$; $s_{F_3,TS} > s_{G,sat}$. F4 is when $P_{F,TS} = P_c$; $s_{F_4,TS} = s_{F,TS,max} > s_{G,sat}$. $T_{F_3,TS}$ is the temperature corresponding to the state point F3,TS. The process line FG can be obtained by connecting the state points F and G.

3.2.2 Entropy change during process CF inside a HP

The primary difference between the flow process CF between a HP and a TS is the vapor pressure drop occurring along the flow through the adiabatic section. The vapor pressure drop in a TS is primarily due to the shear stress at the liquid vapor interface, whereas for

a HP, the vapor pressure drop is due to both the shear stress at the liquid vapor interface and the frictional drag within the wick.

Equation (3.12) for the flow process CF ($FR \geq 1$) in a HP will yield $dh \approx 0$. The equation for the entropy changes for CF in a HP can be written as

$$s_{F,HP} - s_{C,HP} \approx -\int_{C,HP}^{F',HP} \left(\frac{v_v dP}{T} \right)_p - \int_{F',HP}^{F,HP} \left(\frac{v_v dP}{T} \right)_p \cong \frac{v_{v,avg,CF'}}{T_{avg,CF'}} (P_b - P_{F',HP}) + \frac{v_{v,avg,CF}}{T_{avg,CF}} (P_{F',HP} - P_{F,HP}) \quad (3.21)$$

where F' may be considered as a hypothetical state point between C and F. $s_{C,HP}$, $s_{F,HP}$ are the specific entropies at point C and F, respectively. The first and the second terms on the RHS of equation (3.21) represent the entropy generated by the pressure drop caused by the interfacial shear at the liquid-vapour interface ($\Delta P_{shear,l-v}$) and that due to flow friction at the wick ($\Delta P_{v,f}$), respectively. F' represents the state point at the end of the pressure drop process due to the interfacial shear. One may argue that F' could represent the state point at the end of the flow friction process and F, the end of the interfacial pressure drop process, but, as will be seen, the conclusions will not be any different to those presented here. $P_{F',HP}$ is the pressure at state F' and $P_{F,HP}$ is the pressure at state F during the process. Thus, $(P_b - P_{F',HP}) \approx \Delta P_{shear,l-v} = \left[4\tau_i \frac{L_{eff}}{D_i} \right]$. Following the constant enthalpy line on a T-s diagram, it can be asserted that $P_{F',HP} < P_b$ and $P_{F,HP} < P_{F',HP}$, meaning that $s_{F,HP} > s_{C,HP}$ in equation (3.21). The location of point $s_{F,HP}$ with respect to point $s_{G,sat}$ can be determined using a similar strategy to that adopted while locating $s_{F,TS}$. Subtracting equation (3.15) from equation (3.21) gives

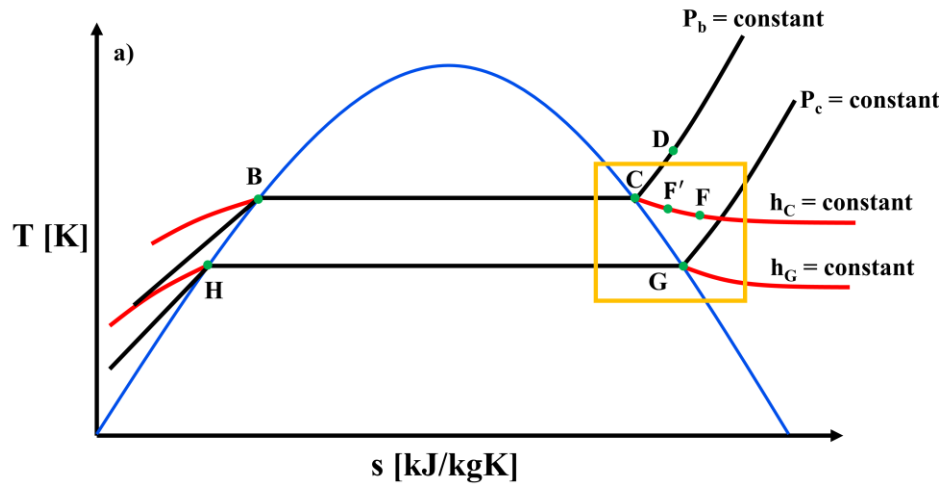
$$s_{F,HP} - s_{G,sat} \cong \left[\left(\frac{h_{C,sat} - h_{G,sat}}{T_{avg,sat}} \right) - \left(\frac{v_{v,avg,sat}(P_b - P_c)}{T_{avg,sat}} \right) \right] + \left(\frac{v_{v,avg,CF'}}{T_{avg,CF'}} (P_b - P_{F',HP}) \right) + \left(\frac{v_{v,avg,CF}}{T_{avg,CF}} (P_{F',HP} - P_{F,HP}) \right) \quad (3.22)$$

Equation (3.22) defines the location of $s_{F,HP}$ with respect to $s_{G,sat}$. It may be noted that $P_{F',HP}$ in equation (3.22) cannot be equal to P_c because if $P_{F',HP} = P_c$ then $s_{F',HP}$ (the specific entropy at state point F') will already be its maximum value (denoted by

$s_{F,HP,max}$). A further increase in specific entropy to accommodate the entropy generation term $\left(\frac{v_{v,avg,CF}}{T_{avg,CF}}(P_{F',HP} - P_{F,HP})\right)$ is not possible along the constant enthalpy line since that will cause the pressure within the HP to drop below P_c , which is not valid. This can be visualized from Figure 3.8a. Therefore, $P_{F',HP}$ must always be greater than P_c . Seven different scenarios are possible when $P_{F',HP} > P_c$. These are summarized in Table 3.4 and illustrated in Figure 3.8b.

Table 3.4 Illustration of different scenarios for $P_{F',HP}$ when $P_{F',HP} > P_c$.

Scenarios	Conditions for $P_{F',HP}$	Conditions for $\Delta P_{v,f}$	Conditions for $P_{F,HP}$	Conditions for $s_{F,HP}$	Comments
1	$P_{F',HP} > P_{int}$	$\Delta P_{v,f} < (P_{F',HP} - P_{int})$	$P_{F,HP} > P_{int}$	$s_{F,HP} < s_{G,sat}$	-
2	$P_{F',HP} > P_{int}$	$\Delta P_{v,f} = (P_{F',HP} - P_{int})$	$P_{F,HP} = P_{int}$	$s_{F,HP} = s_{G,sat}$	-
3	$P_{F',HP} > P_{int}$	$\Delta P_{v,f} = (P_{F',HP} - P_c)$	$P_{F,HP} = P_c$	$s_{F,HP} > s_{G,sat}$	$s_{F,HP} = s_{F,HP,max}$
4	$P_{F',HP} = P_{int}$	$\Delta P_{v,f} < (P_{F',HP} - P_c)$	$P_{F,HP} > P_c$	$s_{F,HP} > s_{G,sat}$	-
5	$P_{F',HP} = P_{int}$	$\Delta P_{v,f} = (P_{F',HP} - P_c)$	$P_{F,HP} = P_c$	$s_{F,HP} > s_{G,sat}$	$s_{F,HP} = s_{F,HP,max}$
6	$P_{F',HP} < P_{int}$	$\Delta P_{v,f} < (P_{F',HP} - P_c)$	$P_{F,HP} > P_c$	$s_{F,HP} > s_{G,sat}$	-
7	$P_{F',HP} < P_{int}$	$\Delta P_{v,f} = (P_{F',HP} - P_c)$	$P_{F,HP} = P_c$	$s_{F,HP} > s_{G,sat}$	$s_{F,HP} = s_{F,HP,max}$



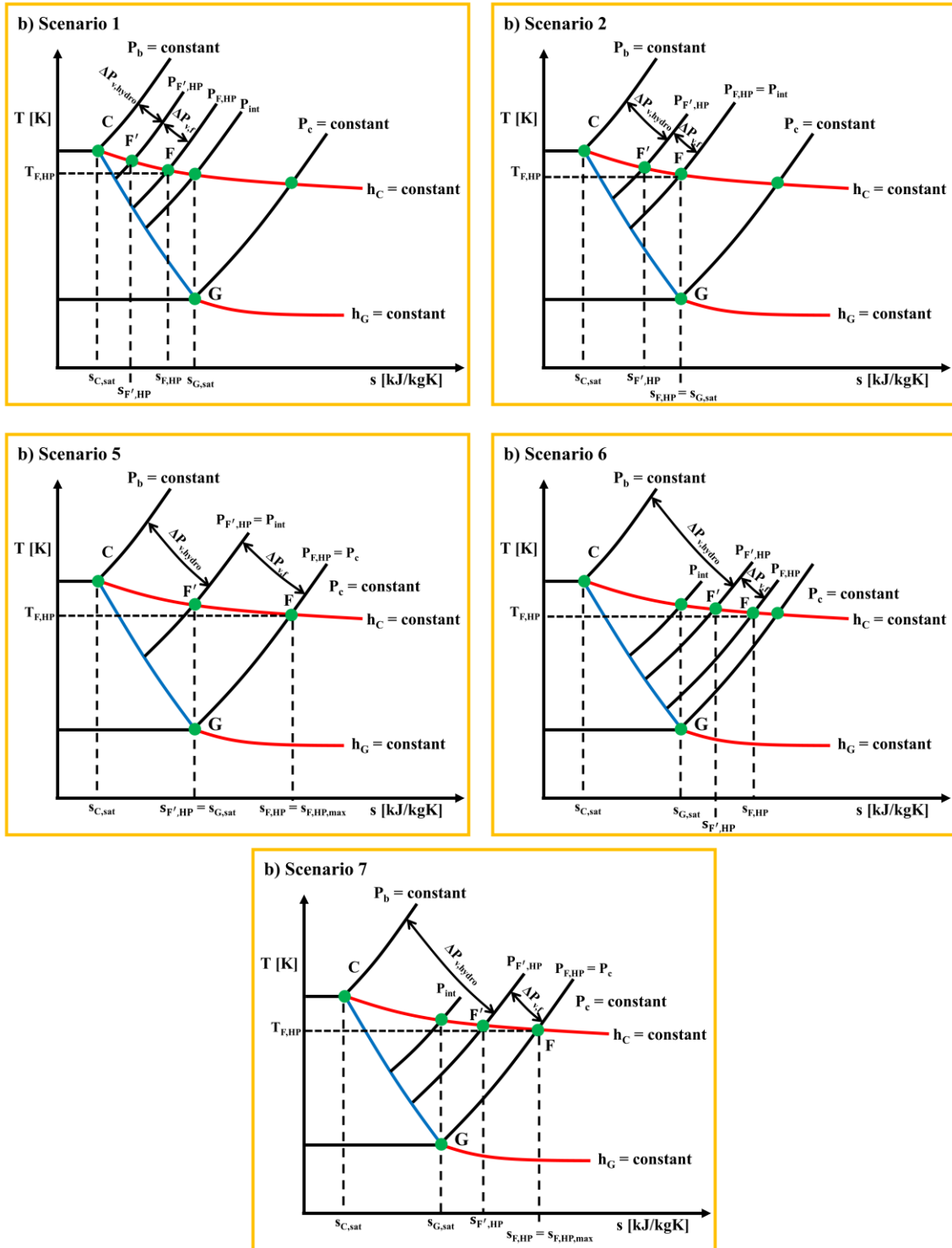


Figure 3.8 a) T-s diagram showing the relevant superheated regime where process CF occurs within a HP. The yellow box represents the region of interest that that has been magnified in b) for better illustration. b) The magnified area of the superheated regime shows seven possible scenarios when $P_{F',HP} > P_c$ illustrated in Table 4.3. The process line FG can be obtained by joining the state points F and G.

Which of these scenarios will prevail within a given HP will depend on the magnitudes of $P_{F',HP}$, P_{int} and $\Delta P_{v,f}$. P_{int} can be found from the state postulate, $\Delta P_{v,f}$ can be determined using equation (1.21) and $P_{F',HP}$ may be estimated using $(P_b - P_{F',HP}) \approx \Delta P_{shear,l-v} = \left[4\tau_1 \frac{L_a}{D_i}\right]$. If $P_{F,HP} = P_c$, then the sensible heat released can be computed using $c_{p,avg}(T_{G,sat} - T_{F,HP})$, where $c_{p,avg}$ is the average specific heat value over the temperature interval. If $P_{F,HP} > P_c$, then the sensible heat released can be computed directly using the first law of thermodynamics as $(h_{G,sat} - h_{F,HP})$. Once $s_{F,HP}$ is determined, the magnitude of $T_{F,HP}$ can be determined using a similar procedure to that described for a TS in section 3.2.1. If the vapour is assumed to be an ideal gas, then equation (3.22) can be re-written as

$$s_{F,HP} - s_{G,sat} \cong \left(\frac{h_{C,sat} - h_{G,sat}}{T_{avg,sat}} \right) + \bar{R} \ln \left(\frac{P_c}{P_{F,HP}} \right) \quad (3.23)$$

The value of s_{gen} for CF for a HP can be estimated using equation (3.11) as

$$s_{gen} \cong \left(\frac{v_{v,avg,CF'}}{T_{avg,CF'}} (P_b - P_{F',HP}) \right) + \left(\frac{v_{v,avg,CF}}{T_{avg,CF}} (P_{F',HP} - P_{F,HP}) \right) - \left[\frac{q_{in}}{T_b} - \frac{q_{in}}{T_{F,HP}} \right] \quad (3.24)$$

where $T_{F,HP}$ is the boundary temperature of the adiabatic section towards the condenser side. The ideal gas approximation would modify equation (3.24) as

$$s_{gen} = \bar{R} \ln \left(\frac{P_b}{P_{F',HP}} \right) + \bar{R} \left(\frac{P_{F',HP}}{P_{F,HP}} \right) - \left[\frac{q_{in}}{T_b} - \frac{q_{in}}{T_{F,HP}} \right] \quad (3.25)$$

Equations (3.24) and (3.25) demonstrate that the entropy generated during CF in a HP can be minimized by reducing either the interfacial pressure drop, or the vapor flow pressure drop through the wicks in the system. The next sub-section evaluates the entropy change during the process DE in a TS.

3.2.3 Entropy change during process DE in a TS

A similar form of equations for the entropy change and entropy generation can be obtained for the process DE (i.e. when $FR < 1$) inside a TS. Recall that $dh \approx 0$ for the flow process DE. It is hypothesized that the state point D can lie on the constant pressure line P_b or the constant specific volume line, v_b . In both cases, the pressure at state point D

will not be very different from each other. In the present analysis, the state point D is assumed to lie on the constant pressure line P_b . The temperature at state point D can be determined from $Q_{in,v}$ (Q_{in} to the vapour region) and the mass of the saturated vapour, m_v , exposed to superheating since, $Q_{in,v} = m_v c_{p,avg}(T_D - T_C)$, where $c_{p,avg,CD} = \left(\frac{c_{p(T=T_C)} + c_{p(T=T_D)}}{2}\right)$. Once T_D is determined, $s_{D,sh}$ ($s_{D,sh}$ is the entropy at state point D, the subscript “sh” denotes superheating, $s_{D,sh} = s_{D,TS}$) can be found either from the steam table (when $P_b > 10\text{kPa}$) or using equation (3.8), if an ideal gas approximation is used. If the temperature change is large i.e. $(T_D - T_C) > 40\text{K}$ (Cengel et al., 2019) and ideal gas approximation is being used, then equation (3.27) shown below can be used to determine $s_{D,sh}$ as

$$s_{D,sh} - s_{C,sat} = s_{D,sh}^o - s_{C,sat}^o \quad (3.27)$$

where $s_C^o = \int_0^{T_C} c_p(T) \left(\frac{dT}{T}\right)$ and $s_D^o = \int_0^{T_D} c_p(T) \left(\frac{dT}{T}\right)$. s_C^o and s_D^o can be found, for example, from Table A-23 in Cengel et al., (2019) at temperatures T_C and T_D . The location of the process point E is not known *a priori* and, hence, a similar strategy to that adopted previously while locating the process F, will be utilized here.

The entropy change during DE for a TS is given by

$$s_{E,TS} - s_{D,TS} \cong -\int_{D,TS}^{E,TS} \left(\frac{v_v dP}{T}\right)_p = \left(\frac{v_{v,avg,DE}(P_b - P_{E,TS})}{T_{avg,DE}}\right) \quad (3.28)$$

where $s_{D,TS}$, $s_{E,TS}$ denote the specific entropies at points D and E, respectively. Navigating towards point E along the constant enthalpy line from point D, it can be asserted that $P_{E,TS} < P_{D,TS}$, meaning $s_{E,TS} > s_{D,TS}$. This can be observed from Figure 3.9a. Let $(s_{D,TS} - s_{C,sat})$ from equation (3.27) be denoted by the variable s_{DC} . The value of $s_{DC} > 0$, since the entropy of the superheated vapour is greater than the entropy of the saturated vapour. Since both $s_{D,TS}$ and $s_{C,sat}$ are known, s_{DC} will also be known. Subtracting equation (3.15) from $(s_{D,TS} - s_{C,sat})$ will yield

$$s_{D,TS} - s_{G,sat} \cong s_{DC} - \left(\frac{h_{G,sat} - h_{C,sat}}{T_{avg,sat}}\right) + \left(\frac{v_{v,avg,sat}(P_c - P_b)}{T_{avg,sat}}\right) \quad (3.29)$$

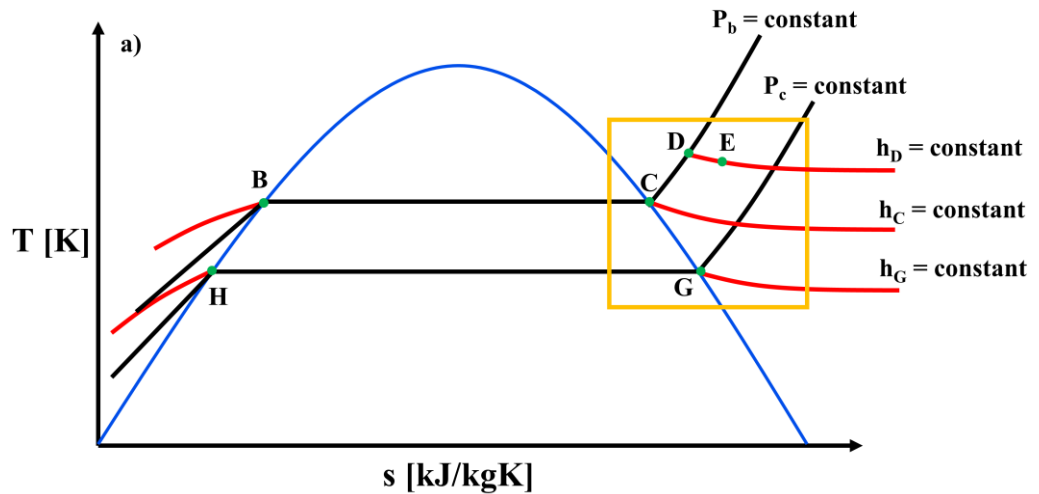
Adding equation (3.28) to equation (3.29) gives

$$s_{E,TS} - s_{G,sat} \cong s_{DC} + \left(\frac{h_{C,sat} - h_{G,sat}}{T_{avg,sat}} \right) - \left(\frac{v_{v,avg,sat}(P_b - P_c)}{T_{avg,sat}} \right) + \left(\frac{v_{v,avg,DE}(P_b - P_{E,TS})}{T_{avg,DE}} \right) \quad (3.30)$$

Equation (3.30) describes the location of $s_{E,TS}$ with respect to $s_{G,sat}$. If $P_{E,TS} = P_c$, then equation (3.30) can be written as

$$s_{E,TS} - s_{G,sat} \cong s_{DC} + \left(\frac{h_{C,sat} - h_{G,sat}}{T_{avg,sat}} \right) + (P_b - P_c) \left(\frac{v_{v,avg,DE}}{T_{avg,DE}} - \frac{v_{v,avg,sat}}{T_{avg,sat}} \right) \quad (3.31)$$

which indicates that $s_{E,TS} > s_{G,sat}$, since $\left(\frac{v_{v,avg,DE}}{T_{avg,DE}} - \frac{v_{v,avg,sat}}{T_{avg,sat}} \right) > 0$. This can be observed from Figure 3.9b when $E = E_4$. Figure 3.9b also reveals that when $P_{E,TS} = P_c$, $s_{E,TS}$ is at its maximum value (denoted by $s_{E,TS,max}$).



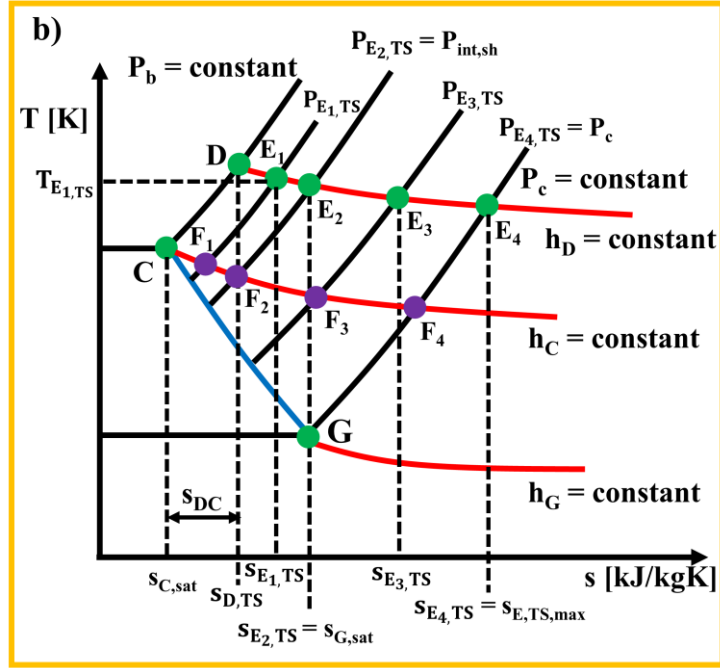


Figure 3.9 a) T-s diagram showing the relevant superheated regime where process DE occurs within the HP. The yellow box represents the regime that has been magnified in b) for better illustration. **b)** Possible locations of the state point E shown along the constant enthalpy line, h_D . E₁ represents the state point E, when $P_{E, TS} > P_{int, sh}$; $s_{E_1, TS} < s_{G, sat}$. E₂ is when $P_{E, TS} = P_{int, sh}$; $s_{E_2, TS} = s_{G, sat}$. E₃ is when $P_c < P_{E, TS} < P_{int, sh}$; $s_{E_3, TS} > s_{G, sat}$. E₄ is when $P_{E, TS} = P_c$; $s_{E_4, TS} = s_{E, TS, max} > s_{G, sat}$. $T_{E_1, TS}$ is the temperature corresponding to the state point E_{1, TS}. The state points F₁, F₂, F₃ and F₄ are shown by purple colour. The process line EG can be obtained by connecting the state points E and G.

Comparing equation (3.31) with equation (3.19) indicates that $s_{E, TS} > s_{F, TS}$ and $(s_{E, TS} - s_{F, TS}) = s_{DC}$. Geometric reasoning also validates this as the points C, D, E and F form a parallelogram at all pressures (see Figure 3.9b). Next, the pressure corresponding to $h = h_D$ and $s = s_{G, sat}$ needs to be determined from the state postulate. Let that pressure be termed $P_{int, sh}$. If $P_{E, TS} > P_{int, sh}$, then $s_{E, TS} < s_{G, sat}$. If $P_{E, TS} = P_{int, sh}$, then $s_{E, TS} = s_{G, sat}$ and if $P_c < P_{E, TS} < P_{int, sh}$, then $s_{E, TS} > s_{G, sat}$. All three different scenarios are illustrated in Figure 3.9b. $P_{E, TS}$ can be determined approximately using $(P_b - P_{E, TS}) \approx \Delta P_{shear, l-v} = \left[4\tau_1 \frac{L_a}{D_i} \right]$. It is postulated that $P_{E, TS}$ is likely to be greater than P_c , since that would yield $(P_b - P_{E, TS}) \leq (P_b - P_c)$, which would ensure that the WF is able to circulate continuously. Once, $s_{E, TS}$ is determined the magnitude of $T_{E, TS}$ can be determined by extrapolating a straight line on the vertical T-axis from the intersection of $s_{E, TS}$ and the constant enthalpy line, shown in Figure 3.9b. If the vapour at the superheated state is assumed to be an ideal gas, then equation (3.30) can be written as

$$s_{E,TS} - s_{G,sat} \cong s_{DC} + \left(\frac{h_{C,sat} - h_{G,sat}}{T_{avg,sat}} \right) + \bar{R} \ln \left(\frac{P_C}{P_{E,TS}} \right) \quad (3.32)$$

The value of s_{gen} for DE for a TS can, therefore, be estimated using equation (3.11) as

$$s_{gen} \cong \left(\frac{v_{v,avg,DE}}{T_{avg,DE}} (P_b - P_{E,TS}) \right) - \left[\frac{q_{in}}{T_D} - \frac{q_{in}}{T_{E,TS}} \right] \quad (3.33)$$

where T_D , $T_{E,TS}$ are the boundary temperature of the adiabatic section towards the evaporator and the condenser side, respectively. If an ideal gas approximation is used, then equation (3.33) is modified as

$$s_{gen} = \bar{R} \ln \left(\frac{P_b}{P_{E,TS}} \right) - \left[\frac{q_{in}}{T_D} - \frac{q_{in}}{T_{E,TS}} \right] \quad (3.34)$$

The next sub-section evaluates the entropy change during the process DE for a HP.

3.2.4 Entropy change during process DE in a HP

The enthalpy change is approximately zero ($dh \approx 0$) along the process line DE in a HP. The change in entropy during DE for a HP, therefore, can be written as

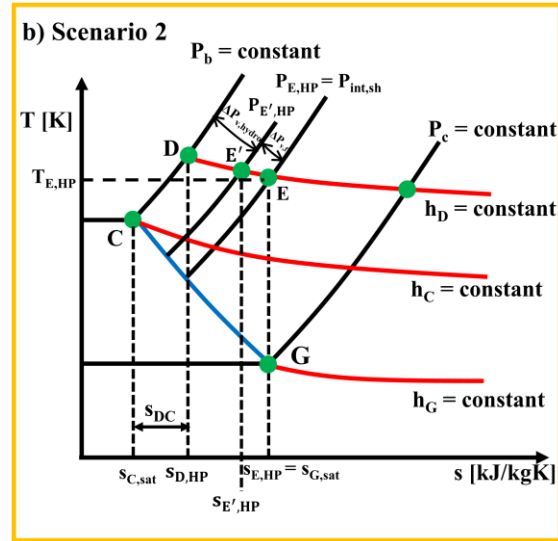
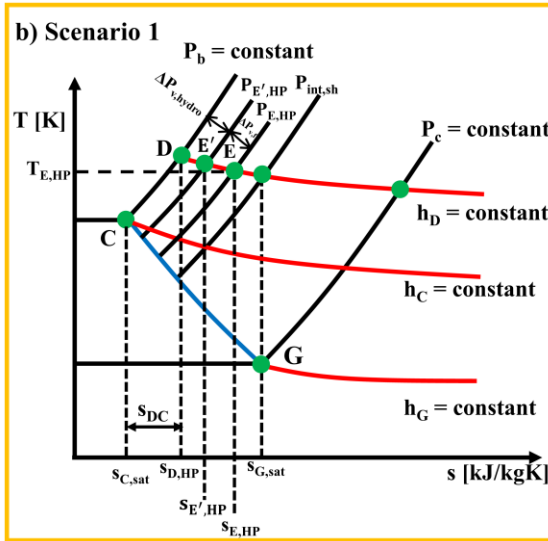
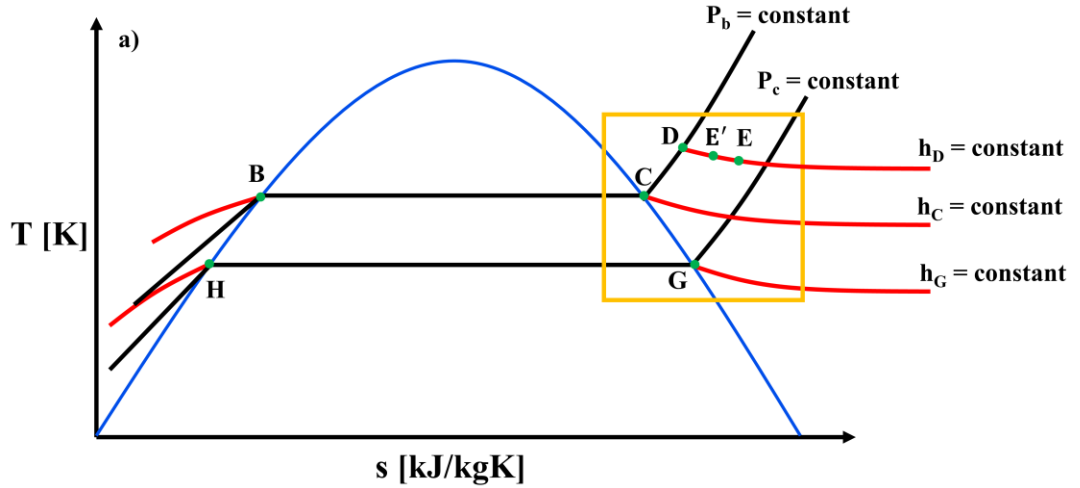
$$s_{E,HP} - s_{D,HP} \approx - \int_{D,HP}^{E,HP} \left(\frac{v_v dP}{T} \right)_p \approx - \int_{D,HP}^{E',HP} \left(\frac{v_v dP}{T} \right)_p - \int_{E',HP}^{E,HP} \left(\frac{v_v dP}{T} \right)_p \quad (3.35)$$

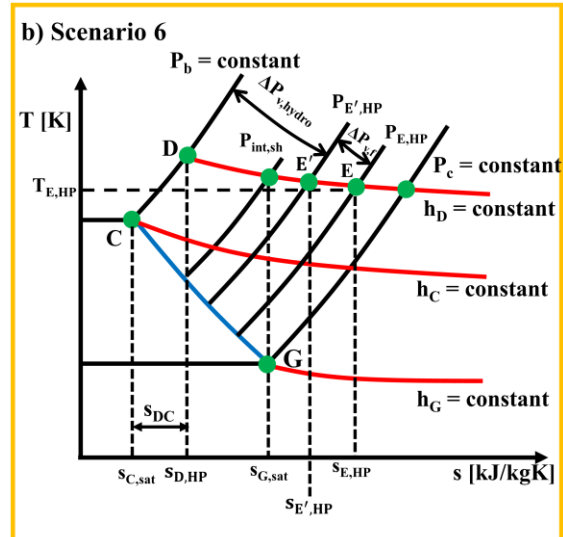
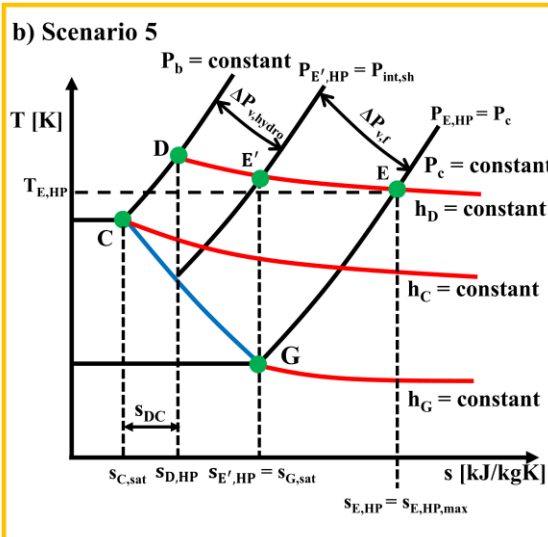
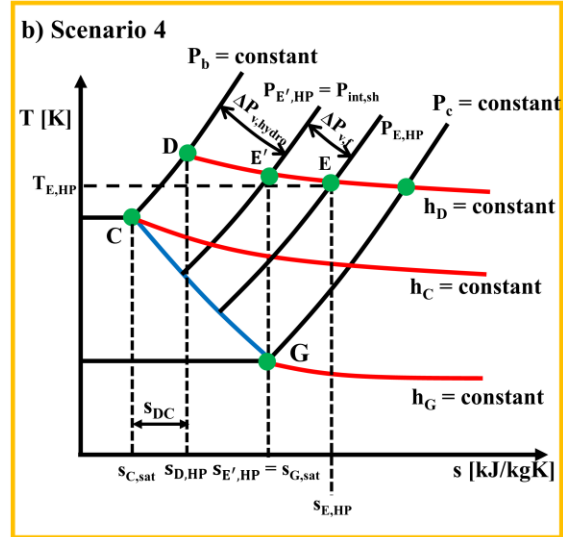
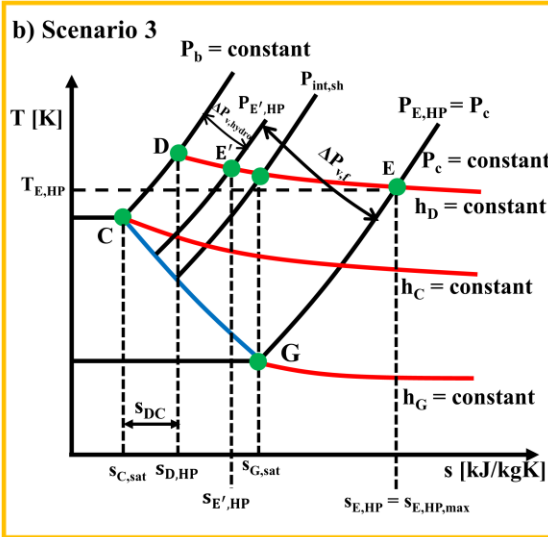
where $s_{D,HP}$, $s_{E,HP}$ denote the specific entropies at points D and E, respectively. The $\int_{D,HP}^{E',HP} \left(\frac{v_v dP}{T} \right)_p$ term denotes the entropy generated due to the pressure drop ($\Delta P_{shear,l-v}$) caused by τ_i and the $\int_{E',HP}^{E,HP} \left(\frac{v_v dP}{T} \right)_p$ term denotes the specific entropy generated due to flow friction at wick. E' is a hypothetical state point between points D and E (see Figure 3.10a). $P_{E',HP}$ is the pressure corresponding to state E' and $P_{E,HP}$ is the pressure corresponding to the state E reached at the end of the process. Adopting the same strategy to that used while deriving equation (3.30), equation (3.36) which locates $s_{E,HP}$ with respect to $s_{G,sat}$ can be written as

$$s_{E,HP} - s_{G,sat} \cong s_{DC} + \left(\frac{h_{C,sat} - h_{G,sat}}{T_{avg,sat}} \right) - \left(\frac{v_{v,avg,sat}(P_b - P_C)}{T_{avg,sat}} \right) + \left(\frac{v_{v,avg,DE'}}{T_{avg,DE'}} (P_b - P_{E',HP}) \right)$$

$$+ \left(\frac{v_{v,avg,DE}}{T_{avg,DE}} (P_{E',HP} - P_{E,HP}) \right) \quad (3.36)$$

$P_{E',HP}$ must be greater than P_c because of the reasons described in the paragraph following equation (3.23). Figure 3.10a illustrates the process DE schematically on a T - s diagram.





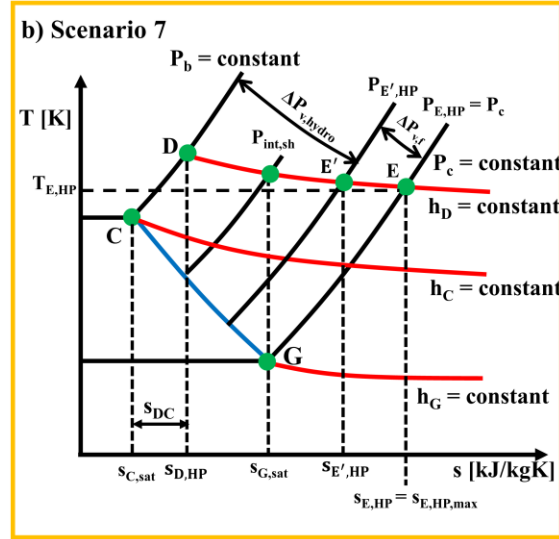


Figure 3.10 a) T-s diagram showing the relevant superheated regime where process DE occurs within a HP. The yellow box has been magnified for better illustration. b) The magnified area of the superheated regime shows seven possible scenarios when $P_{E',HP} > P_c$ as illustrated in Table 2.3. The process line EG can be obtained by joining the state points E and G.

When $P_{E',HP} > P_c$, seven different scenarios arise which are summarized in Table 3.5 and shown in Figure 3.10b. Which of these scenarios will prevail depends on the magnitude of $P_{E',HP}$, $P_{int,sh}$ and $\Delta P_{v,f}$. $P_{int,sh}$ can be found from the state postulate. $\Delta P_{v,f}$ can be determined using equation (1.21). $P_{E',HP}$ can be approximated from $(P_b - P_{E',HP}) \approx \Delta P_{shear,l-v} = \left[4\tau_i \frac{L_a}{D_i} \right]$. If $P_{E,HP} = P_c$, then the sensible heat released can be computed using $c_{p,avg}(T_{G,sat} - T_{E,HP})$, where $c_{p,avg}$ is the average specific heat value given by $c_{p,avg} = \left(\frac{c_p(at T = T_{G,sat}) + c_p(at T = T_{E,HP})}{2} \right)$. If $P_{E,HP} > P_c$, then the sensible heat released can be computed directly using the first law of thermodynamics as $(h_{F,sat} - h_{E,HP})$.

Table 3.5 Illustration of different scenarios when $P_{E',HP} > P_c$

Scenarios	Conditions for $P_{E',HP}$	Conditions for $\Delta P_{v,f}$	Conditions for $P_{E,HP}$	Conditions for SE_{HP}	Comments
1	$P_{E',HP} > P_{int,sh}$	$\Delta P_{v,f} < (P_{E',HP} - P_{int,sh})$	$P_{E,HP} > P_{int,sh}$	$SE_{HP} < SG_{sat}$	-
2	$P_{E',HP} > P_{int,sh}$	$\Delta P_{v,f} = (P_{E',HP} - P_{int,sh})$	$P_{E,HP} = P_{int,sh}$	$SE_{HP} = SG_{sat}$	-
3	$P_{E',HP} > P_{int,sh}$	$\Delta P_{v,f} = (P_{E',HP} - P_c)$	$P_{E,HP} = P_c$	$SE_{HP} > SG_{sat}$	$SE_{HP} = SE_{HP,max}$
4	$P_{E',HP} = P_{int,sh}$	$\Delta P_{v,f} < (P_{E',HP} - P_c)$	$P_{E,HP} > P_c$	$SE_{HP} > SG_{sat}$	-
5	$P_{E',HP} = P_{int,sh}$	$\Delta P_{v,f} = (P_{E',HP} - P_c)$	$P_{E,HP} = P_c$	$SE_{HP} > SG_{sat}$	$SE_{HP} = SE_{HP,max}$
6	$P_{E',HP} < P_{int,sh}$	$\Delta P_{v,f} < (P_{E',HP} - P_c)$	$P_{E,HP} > P_c$	$SE_{HP} > SG_{sat}$	-
7	$P_{E',HP} < P_{int,sh}$	$\Delta P_{v,f} = (P_{E',HP} - P_c)$	$P_{E,HP} = P_c$	$SE_{HP} > SG_{sat}$	$SE_{HP} = SE_{HP,max}$

Once $s_{E,HP}$ is determined, the magnitude of $T_{E,HP}$ can be determined by using a procedure similar to that described for a TS. This has been shown in Figure 3.10b. If an ideal gas approximation is used then equation (3.36) is modified as

$$s_{E,HP} - s_{G,sat} \cong s_{DC} + \left(\frac{h_{C,sat} - h_{G,sat}}{T_{avg,sat}} \right) + \bar{R} \ln \left(\frac{P_C}{P_{E,HP}} \right) \quad (3.37)$$

The value of s_{gen} for the process DE in a HP can be written using equation (3.11) as

$$s_{gen} \cong \left(\frac{v_{v,avg,DE'}}{T_{avg,DE'}} (P_b - P_{E',HP}) \right) + \left(\frac{v_{v,avg,DE}}{T_{avg,DE}} (P_{E',HP} - P_{E,HP}) \right) - \left[\frac{q_{in}}{T_D} - \frac{q_{in}}{T_{E,HP}} \right] \quad (3.38)$$

where $T_{E,HP}$ is the boundary temperature of the adiabatic section towards the condenser side. When an ideal gas approximation is used, equation (3.38) is modified as

$$s_{gen} = \bar{R} \ln \left(\frac{P_b}{P_{E',HP}} \right) + \bar{R} \ln \left(\frac{P_{E',HP}}{P_{E,HP}} \right) - \left[\frac{q_{in}}{T_D} - \frac{q_{in}}{T_{E,HP}} \right] \quad (3.39)$$

The entropy change and the entropy generation during the liquid flow through the adiabatic section (i.e. process HA) is evaluated in the next sub-section.

3.2.5 Entropy change during process HA

This section evaluates the process HA inside a TS and a HP. Equation (3.12) when applied to the flow process HA will yield (assuming $d(pe)$ and $d(ke) \cong 0$)

$$dh \cong 0 \quad (3.40)$$

The change in entropy along HA can, therefore, be written as

$$s_A - s_H \cong - \int_H^A \left(\frac{v_l dP}{T} \right)_p \quad (3.41)$$

or,
$$s_A - s_H \cong \left(\frac{v_{l,avg,HA}(P_H - P_A)}{T_{avg,HA}} \right) \cong \frac{v_{l,avg,HA}}{T_{avg,HA}} (\Delta P_{hydro,l} + \Delta P_i) \quad (3.42)$$

where s_A , s_H denote the specific entropies at points A, H, respectively. $T_{avg,HA}$ and $v_{l,avg,HA}$ are the average temperature and specific volume of the WF between state points H and A,

P_H and P_A are the pressures at state points H and A and $P_H = P_c$, respectively. Note that Δ in equation (3.42) refers to the pressure difference between the initial and the final states consistent with the convention followed in fluid mechanics textbooks (White and Xue, 2021). The pressure drop due to the shear stress at the liquid-vapour interface is small compared to the viscous forces acting on the liquid at the wall (Chen et al., 1984). Thus, $(P_H - P_A) \approx [\Delta P_{\text{hydro},l} + \Delta P_l]$, where $\Delta P_{\text{hydro},l} = -\rho_l(\Delta z)g\sin\theta$ ($\Delta z = z_{\text{initial}} - z_{\text{final}}$), and ΔP_l can be estimated using the relevant pressure drop equation (see section 1.2.1.2 in Chapter 1). The entropy changes between the vapour saturation states HB using equation (3.8) can be written as

$$s_{B,\text{sat}} - s_{H,\text{sat}} = \int_H^B \left(\frac{dh}{T}\right)_{\text{sat}} - \int_{P_c}^{P_b} \left(\frac{v_l dp}{T}\right)_{\text{sat}} \cong \left[\left(\frac{h_{B,\text{sat}} - h_{H,\text{sat}}}{T_{\text{avg},\text{sat}}}\right) - \left(\frac{v_{l,\text{avg},\text{sat}}(P_b - P_c)}{T_{\text{avg},\text{sat}}}\right) \right] \quad (3.43)$$

$s_{B,\text{sat}} > s_{H,\text{sat}}$ in equation (3.43), which can be shown using the steam table values. Subtracting equation (3.42) from equation (3.43) gives

$$s_{B,\text{sat}} - s_A \cong \left[\left(\frac{h_{B,\text{sat}} - h_{H,\text{sat}}}{T_{\text{avg},\text{sat}}}\right) - \left(\frac{v_{l,\text{avg},\text{sat}}(P_b - P_c)}{T_{\text{avg},\text{sat}}}\right) \right] - \frac{v_{l,\text{avg},\text{HA}}}{T_{\text{avg},\text{HA}}}(\Delta P_{\text{hydro},l} + \Delta P_l) \quad (3.44)$$

Equation (3.44) defines the location s_A with respect to $s_{B,\text{sat}}$. Since $\Delta P_{\text{hydro},l}$ and ΔP_l have opposite signs, two different flow conditions are possible i.e. $|\Delta P_{\text{hydro},l}| > |\Delta P_l|$ and $|\Delta P_{\text{hydro},l}| < |\Delta P_l|$ which are discussed in the next two-subsections.

1. Case when $|\Delta P_{\text{hydro},l}| > |\Delta P_l|$

The operating conditions at which $|\Delta P_{\text{hydro},l}| > |\Delta P_l|$ may be observed in a TS and a HP are shown in Appendix C. When $|\Delta P_{\text{hydro},l}| > |\Delta P_l|$, $P_A > P_H$ and $s_A < s_H$ in equation (3.42) and $s_A < s_{B,\text{sat}}$ in equation (3.43). That the above-mentioned scenarios are valid is illustrated in Figure 3.11, where the process HA is shown schematically on a T-s diagram. It is observed that when $P_A > P_H$, $T_A < T_H$, $s_A < s_H$. When $P_A \leq P_b$, $s_A < s_{B,\text{sat}}$. Note that the slope of the isobar on the T-s coordinates in the sub-cooled regime i.e. $\left(\frac{\partial T}{\partial s}\right)_{P,\text{HA}}$, is greater than the slope of the isenthalpic line i.e., $\left(\frac{\partial T}{\partial s}\right)_{P,\text{HA}}$. This has been considered while drawing the isobars and the isenthalpic lines on the T-s diagram in Figure 3.11.

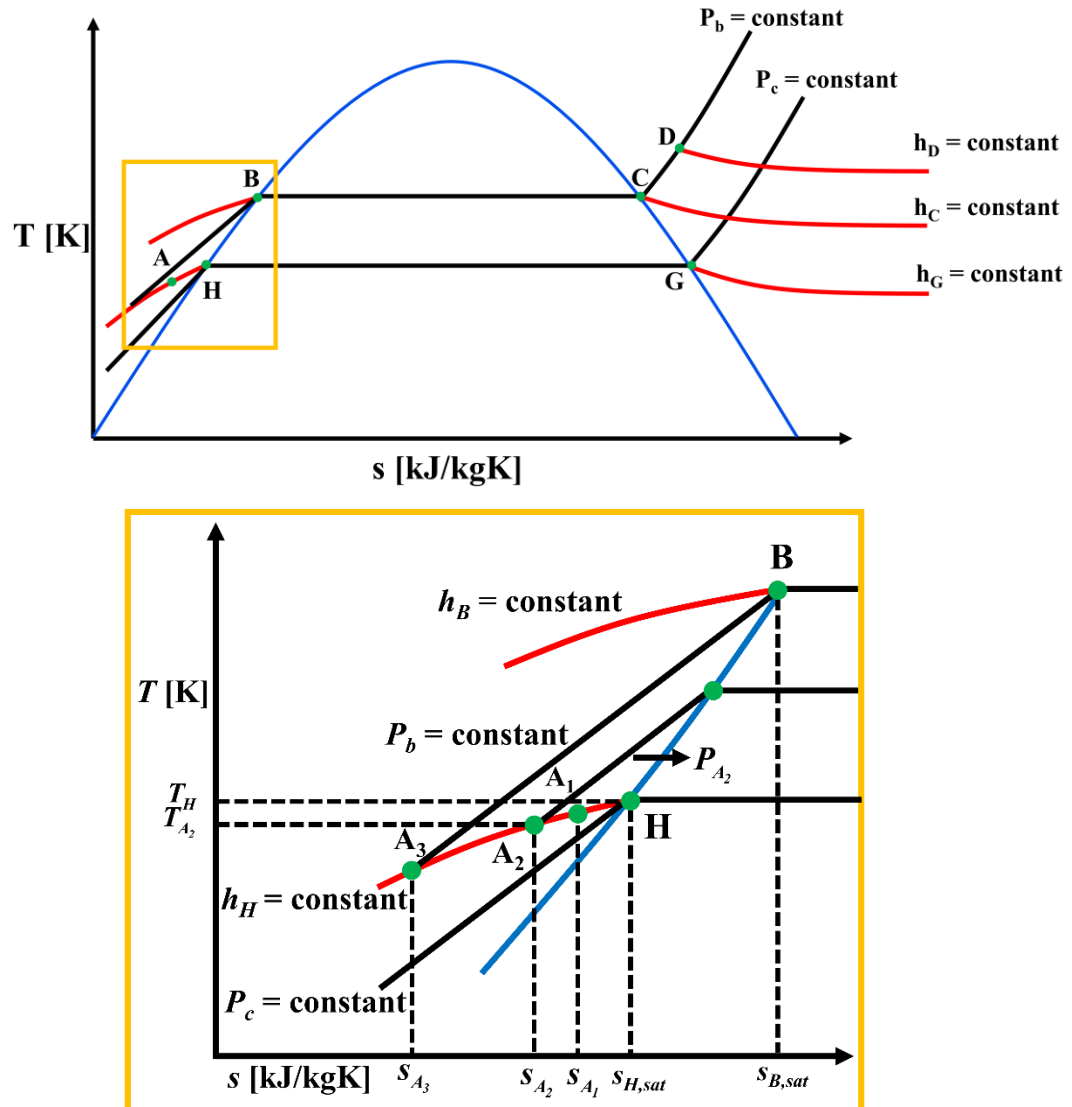


Figure 3.11 a) T-s diagram showing the relevant subcooled regime where process HA occurs within a TS. The yellow box represents the region of interest that has been magnified for better illustration. b) The magnified subcooled regime showing possible locations of the state point A along the constant enthalpy line, h_H . A_1 represents the state point A, when the effects of both $\Delta P_{1,\text{hydro}}$ and ΔP_1 are present. $P_{A_1} < P_b$; $s_{A_1} < s_{H,\text{sat}}$. A_2 is when $\Delta P_{1,f}$ is negligible. $P_{A_2} < P_b$; $s_{A_2} < s_{H,\text{sat}}$. A_3 is the limiting case, when $P_{A_3} = P_b$; $s_{A_3} > s_{H,\text{sat}}$. T_{A_2} is the temperature corresponding to the state point A_2 . The process line AB can be obtained by connecting the state points A and B.

Since the pressure differential driving the flow must be greater than the sum of the total pressure drops, it is hypothesized that $|(P_b - P_c)| \geq |(P_A - P_H)|$. Although P_A may be equal to P_b in theory, it must be less than P_b in practice due to the presence of the vapor pressure drops within a TS and a HP. If ΔP_1 is assumed to be small, then the term $\frac{v_{l,\text{avg,HA}}}{T_{\text{avg,HA}}}(\Delta P_1)$ in equation (3.42) will be negligible. This indicates that the distance between s_A and s_H will increase meaning that s_A will now lie further to the left of $s_{H,\text{sat}}$. This has

been demonstrated in Figure 3.11. Once s_A is determined, T_A can be estimated using a similar method to that demonstrated in section 3.21.

The value of s_{gen} for the process HA for a TS can be written using equation (3.11) as

$$s_{\text{gen}} \cong \left(\frac{v_{l,\text{avg,HA}}}{T_{\text{avg,HA}}} (\Delta P_l) \right) \quad (3.45)$$

The above analysis demonstrates that the entropy changes during a process (HA) can be negative inside a TS and a HP under certain conditions. Nonetheless, the entropy generated due to friction is positive (equation 3.45) which does not violate the entropy generation principle.

2. Case when $|\Delta P_{\text{hydro,l}}| < |\Delta P_{l,f}|$

This section analyzes the scenario when $|\Delta P_{\text{hydro,l}}| < |\Delta P_{l,f}|$ i.e., when there is a net pressure drop along the process. The operating conditions at which this may occur inside a TS and a HP are shown in Appendix C. Since there is a net pressure drop, the WF must undergo sensible cooling at the condenser before flowing through the adiabatic section in order to prevent vaporization. Similar arguments were presented by Zuo and Faghri (1999). Thus, the state point of the WF in the condenser should lie in the subcooled regime along the constant pressure line, P_c . Let this state point be designated as H'. Thus, $P_{H'} = P_c$. The entropy changes along the isobaric process HH' can be determined using equation (3.8) as

$$s_{H'} - s_H \cong c_{\text{avg,HH'}} \ln \left(\frac{T_{H'}}{T_H} \right) \quad (3.46)$$

where $s_{H'}$ denotes the entropy at point H' and $s_H = s_{H,\text{sat}}$. $T_{H'}$ and T_H are the temperatures at state points H' and H, respectively, and $T_H = T_{H,\text{sat}}$. $c_{\text{avg,HH'}}$ and $T_{\text{avg,HH'}}$ denote the average specific heat and the average temperature between the state points H and H', respectively. If one navigates towards any arbitrary state point H' along the constant pressure line P_c from H, it can be noted that $T_{H'} < T_H$. Therefore, $s_{H'} < s_H$ in equation (3.46).

H'A now represents the flow process through the adiabatic section. Equation (3.12) when applied to process H'A, assuming $d(pe)$ and $d(ke) \cong 0$, yields $dh \cong 0$. The change in entropy along H'A can, therefore, be written as

$$s_A - s_{H'} \cong \frac{v_{l,avg,H'A}}{T_{avg,H'A}} (P_{H'} - P_A) \quad (3.47)$$

where $T_{avg,H'A}$ and $v_{l,avg,H'A}$ are the average temperature and specific volume between the state points H' and A, respectively. Since it is assumed that the pressure drop is positive i.e. $P_A < P_{H'}$, $s_A > s_{H'}$ in equation (3.47). Figure 3.12 illustrates the process H'A on a T-s diagram.

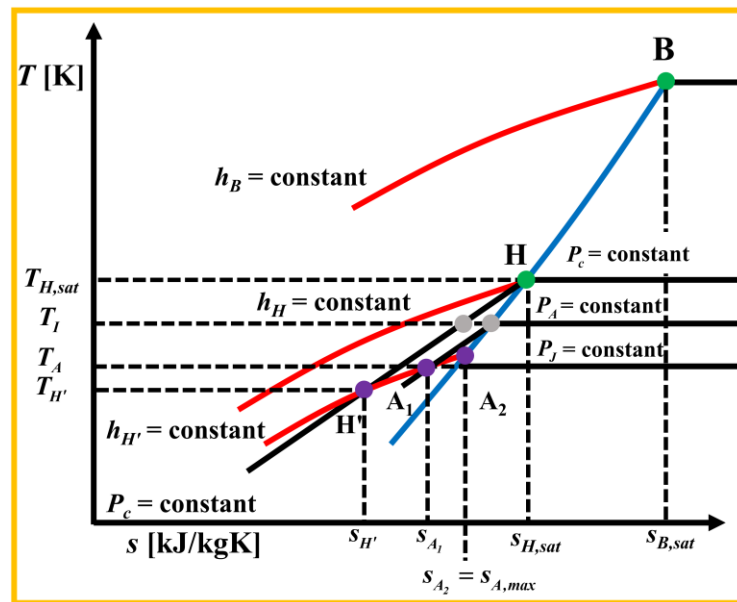


Figure 3.12 A magnified schematic of the subcooled regime showing the location of the state points H' and A along the constant pressure line, P_c and constant enthalpy line $h_{H'}$. A₁ represents a possible location of the state point A when $|\Delta P_{hydro,l}| < |\Delta P_l|$. A₂ represents the location of the state point A when $|\Delta P_{hydro,l}| > |\Delta P_l|$. A₃ represents the state point A for the limiting case when s_A is maximum i.e. $s_{A,max}$. $T_{H,sat}$, T_A and $T_{H'}$ are the temperature corresponding to state points H, A and H', respectively. $P_{H'} = P_c$. $T_{H'} < T_{H,sat}$; $s_{H'} < s_{H,sat}$. $P_A < P_{H'}$; $s_A > s_{H'}$. The gray colored circles represent the state points of the WF when $T_{H'} = T_l$. Note that the approximation $T_{H'} \approx T_A$ is not shown here as the schematic depicts a general representation of the process H'A.

The location of A (A₁ in Figure 3.12) is not known *a priori* and, therefore, an estimate of its location is made with respect to the location of the liquid saturation states, H and B. Adding equations (3.46) and (3.47) gives

$$s_A - s_H \cong c_{\text{avg,HH}'} \ln \left(\frac{T_{H'}}{T_H} \right) + \frac{v_{l,\text{avg,H}'A}}{T_{\text{avg,H}'A}} (P_{H'} - P_A) \quad (3.48)$$

Equation (3.48) defines the location of s_A with respect to s_H . The first term on the RHS of equation (3.48) is negative, whilst the second term is positive. However, s_A must be less than s_H because, if $s_A = s_H$, then the WF at the end of the flow through the adiabatic section will be a liquid-vapor saturated mixture. The maximum value of s_A is obtained (denoted by $s_{A,\text{max}}$) when point A lies on the saturated liquid line. Subtracting equation (3.48) from equation (3.43) gives

$$s_{B,\text{sat}} - s_A \cong \left[\left(\frac{h_{B,\text{sat}} - h_{H,\text{sat}}}{T_{\text{avg,sat}}} \right) - \left(\frac{v_{l,\text{avg,sat}}(P_b - P_c)}{T_{\text{avg,sat}}} \right) \right] - \left[c_{\text{avg,HH}'} \ln \left(\frac{T_{H'}}{T_H} \right) + \frac{v_{l,\text{avg,H}'A}}{T_{\text{avg,H}'A}} (P_{H'} - P_A) \right] \quad (3.49)$$

Equation (3.49) locates s_A with respect to $s_{B,\text{sat}}$. The first RHS term within the square bracket is positive, whilst the second RHS term is negative. This indicates that that $s_{B,\text{sat}} > s_A$. However, equations (3.46), (3.47), (3.48) and (3.49) cannot be solved without locating the state point H' first. An estimate of its location is presented next.

Assuming $dv \approx 0$ along H'A gives $c_{\text{avg,HH}'}(T_A - T_{H'}) \approx v_{l,\text{avg,H}'A}(P_{H'} - P_A)$ from the enthalpy change equation. An order of magnitude analysis reveals that for $O(T_A - T_{H'}) \sim 1[\text{K}]$, $O(P_{H'} - P_A) \sim 10^3 [\text{kPa}]$ which is physically unrealistic. Thus, $T_A \approx T_{H'}$. When the temperature of the inlet coolant ($T_{\text{in,coolant}}$) to the condenser section is known *a priori* (typically in laboratory experiments), the temperature at the state point H' can be assumed to be equal to $T_{\text{in,coolant}}$ i.e., $T_{H'} \approx T_A \approx T_{\text{in,coolant}}$. Since $P_{H'}$ and $T_{H'}$ are known, the state point H' can be determined from the state postulate. When $T_{\text{in,coolant}}$ and, thus, $T_{H'}$ is unknown then an approximation analysis must be undertaken. Since $P_{H'}$ is known ($P_{H'} = P_c$), P_A can be estimated from the pressure drop equation $(P_{H'} - P_A) \approx [\Delta P_{\text{hydro,l}} + \Delta P_1]$. Once, P_A is known, the saturation temperature corresponding to P_A can be estimated using the thermodynamic table or the Clapeyron equation. Let this temperature be T_I , where $T_I = T_{\text{sat}}(@ P = P_A)$, where T_{sat} denotes the saturation temperature. It is postulated that the magnitude of $T_{H'}$ should be such that $T_{H'} < T_I$. Because, if $T_{H'} \approx T_I$, the liquid can only sub cool to temperature T_I and the pressure drop from $P_{H'}$ to P_A along the constant

temperature line will make the WF a saturated liquid. The state point would be lying on the saturated liquid line where the constant pressure line P_A and the temperature line T_I intersect. Any heat added to the saturated liquid will cause boiling phase change to occur along P_A rather than P_b , which is the actual saturation pressure for boiling. When $T_{H'} \approx T_A < T_I$, the saturation pressure corresponding to the temperature T_A (designated as P_j) will be less than that of P_A . Therefore, specifying $T_{in,coolant} = T_{H'} < T_I$, gives a driving pressure differential $(P_b - P_j)$ greater than the maximum pressure drop in the system which is $(P_b - P_A)$. Thus, $T_{H'} = T_{in,coolant} < T_I$ is a suitable temperature condition to be specified for the inlet cooling fluid at the condenser. The changes in the different thermodynamic properties during processes HH' and $H'A$ are examined analytically in Appendix C.

The value of s_{gen} for the process $H'A$ is given by

$$s_{gen} \cong \frac{v_{l,avg,H'A}}{T_{avg,H'A}} (\Delta P_l) \quad (3.50)$$

Equation (3.50) demonstrates that the entropy generated during the liquid flow process can be minimized by minimizing the friction flow losses.

The above analyses show that the entropy changes during process HH' are negative, whilst the entropy changes during $H'A$ are positive. This is expected since there is sensible heat loss during HH' whereas, during $H'A$, the entropy is generated due to the frictional effects. As demonstrated in Appendix C, the occurrence of a particular scenario within a TS and HP depends upon the geometrical and the operating parameters and, thus, both flow conditions i.e., $|\Delta P_{hydro,l}| > |\Delta P_{l,f}|$ and $|\Delta P_{hydro,l}| < |\Delta P_{l,f}|$, are physically possible.

One caveat to the analysis made here is the assumption that $d(pe) \cong 0$. However, if the term $d(pe)$ is retained, then $dh = -d(pe)$, and the change in entropy along the adiabatic section will be given by

$$s_A - s_H \cong c_{avg,HH'} \ln \left(\frac{T_{H'}}{T_H} \right) + \frac{v_{l,avg,H'A}}{T_{avg,H'A}} (\Delta P_l) \quad (3.51)$$

The WF will undergo necessary subcooling first (H'H) followed by the process H'A. The T-s diagram will be identical to Figure 3.12. The next sub-section summarizes the equations for entropy change and the entropy generation for each thermodynamic process.

3.2.6 Summary of the equations

Table 3.6 summarizes the expressions for the first law of thermodynamics, the entropy changes and the entropy generation for processes AB, CF, DE, FG, EG, HA, HH' and H'A.

Table 3.6 Expressions of the first law of thermodynamics, the entropy changes and S_{gen} for AB, CF, DE, FG, EG, HA, HH', H'A processes inside a TS and a HP.

Thermodynamic process	Expressions of first law of thermodynamics	Expressions of the entropy changes	S_{gen}	Comments
AB	$\delta q_{in, sen, AB} = du_{AB}$	Equation (3.44) for both TS and a HP	0	$S_B > S_A$ at all T and P
CF	$dh_{CF} \cong 0$	Equation (3.14) for a TS	Equations (3.20) and (3.21) for a TS	$S_F > S_C$ at all T and P
		Equation (3.22) for a HP	Equations (3.25) and (3.26) for a HP	
DE	$dh_{DE} \cong 0$	Equation (3.28) for a TS	Equations (3.33) and (3.34) for a TS	$S_E > S_D$ at all T and P
		Equation (3.35) for a HP	Equations (3.38) and (3.39) for a HP	
FG	$\delta q_{out, sen, FG} = h_G - h_C$	Equations (3.16) for a TS	0	$S_F > S_G$ at all T and P
		Equation (3.23) for a HP		
EG	$\delta q_{out, sen, EG} = h_G - h_D$	Equation (3.30) for a TS	0	$S_E > S_G$ at all T and P
		Equation (3.36) for a HP		
HA	$dh_{HA} \cong 0$	Equation (3.42) for both TS and a HP	Equation (3.46) for both TS and a HP	$S_A < S_H$ at all T and P
HH'	$\delta q_{out, sen, HH'} = c(T_{H'} - T_H)$	Equation (3.46) for both TS and HP	0	$S_H > S_{H'}$ at all T and P
H'A	$dh_{H'A} \cong 0$	Equation (3.47) for both TS and HP	Equation (3.50)	$S_A > S_{H'}$ at all T and P
Nomenclature: $\delta q_{in, sen}$ = differential amount of sensible heat absorbed/released by the WF during the boiling/condensation process. du = differential specific internal energy change dh = differential specific enthalpy changes				

In order to determine whether the thermodynamic state points of the WF drawn on a T-s diagram are correct it is necessary that the same process points/lines be drawn on a h-s diagram to examine if those are consistent with the analyses made in sections 3.2.1 - 3.2.5. The h-s diagrams are shown in Appendix C for completeness..

3.3 Methods to validate the abovementioned analytical expressions

Since the process points and process-lines are drawn qualitatively on the T-s diagrams and h-s diagrams, the methods to validate those expressions and the diagrams are outlined. Both experimental and numerical results may be utilized to corroborate the analytical derivations.

3.3.1 Experimental method

Since the TS and HP are sealed under vacuum pressure, the saturation temperature at which boiling occurs (T_b) is fixed. Thus, T_b is a known variable provided that the sealed pressure is known. If the condensation thermal resistance is estimated *a priori* for a given operating condition (see Chapter 4), then T_c can be estimated. T_D can be determined from the superheating of vapour. Once, T_b , T_c and T_D are determined, $s_{B,sat}$, $s_{C,sat}$, s_D , $s_{G,sat}$ and $s_{H,sat}$ and $h_{B,sat}$, $h_{C,sat}$, h_D , $h_{G,sat}$ and $h_{H,sat}$ can be determined directly from the steam tables (Table A-4, Table A-5, Table A-6, Table A-23 from Cengel et al., 2019). The temperature measured at the end of the adiabatic section (or the start of the condenser section) can be used to estimate T_F (when $FR \geq 1$) and T_E ($FR < 1$). With the values of h_C and T_F known, s_F and P_F can be determined using the state postulate. Similarly, with $s_{G,sat}$ and $h_{C,sat}$ known, P_{int} can be determined. The value of s_F can then be compared to $s_{G,sat}$ and examine whether the RHS and left-hand side (LHS) of the equations (3.16) and (3.18) are consistent for a TS. The same approach could be adopted to compare s_E with $s_{G,sat}$ from equations (3.30) and (3.32). Similar strategy can be adopted to validate the equations for a HP. Which of the following scenarios from Table 3.4 and 3.5 are observed in a HP can then be determined.

The temperature measured at the start of the adiabatic section can be used to estimate T_A . Using the $h_{H,sat}$ and T_A values, P_A , s_A can be determined from the state postulate. The

values of s_A can then be compared to $s_{B,sat}$. Consequently, P_A can be compared to P_c and P_b . The RHS and the LHS terms of the equations (3.42), (3.44) and (3.49) can subsequently be validated.

3.3.2 Numerical method (using computation fluid dynamics (CFD))

Provided that the velocity, pressure and temperature fields available from the numerical simulations are within the accepted error limits, the pressures and temperatures at the specific state point locations (discussed in the previous section) along the centreline of the steady state flow field can be obtained. Utilizing this information, h and s can be determined from the steam tables. Thereby, comparisons of the s and P values between the different state points estimated by equations (3.16), (3.18), (3.30), (3.32), (3.42), (3.44) and (3.49) can be made to validate the RHS and the LHS terms of these equations.

Once the equations are validated, they can be used to determine the operating temperature of TS and HP at a given operating condition without performing experiments and numerical simulations.

The next section analyses the entropy generated from the other sources within a TS and the HP system. This helps identify the various components that are responsible for entropy generation and provides guidelines on how entropy can be minimized.

3.4 Other sources of entropy generation and its minimization

So far the entropy generated due to the frictional effects as the WF fluid flows through the adiabatic section is considered. However, there are other sources of entropy generation due to the irreversible processes within the evaporator, condenser and the adiabatic sections of a TS and a HP. Those process are listed in Table 3.7 and briefly discussed in the subsequent subsections. The primary objective of this section is to describe how the flow geometries and the operating conditions may be selected/varied in order to minimize the overall entropy generated within a TS and a HP system.

Table 3.7 Other sources of entropy generation inside a TS and a HP

Location of entropy generation	Causes of entropy generation
Entropy generation at the evaporator and the condenser wall	Heat transfer across the walls due to finite temperature difference between the TS and HP walls and the heat source and the sink
Entropy generation along the vapour flow	Heat transfer across the vapour flow due to finite temperature difference between the vapour in the evaporator and the condenser.
Entropy generation during boiling and condensation process	Fluid friction at the walls (TS) and the wick at the evaporator and the condenser (HP)
Entropy generation in forced convection	Finite temperature gradient and fluid friction

3.4.1 Entropy generation at the evaporator and the condenser wall

This section describes the entropy generated at the evaporator and the condenser walls due to heat transfer across a finite temperature difference across those walls. The entropy generated at the evaporator wall can be written using equation (3.9) as

$$s_{\text{gen,e,w}} = \left[\frac{q_{\text{out}}}{T_{\text{v,e}}} - \frac{q_{\text{in}}}{T_{\text{e}}} \right] \quad (3.52)$$

where $s_{\text{gen,e,w}}$ (subscript e, w denotes the evaporator and the wall, respectively) is the entropy generated at the evaporator wall, $T_{\text{v,e}}$ is the temperature of the vapour in the evaporator (comparing with the T-s diagram, $T_{\text{v,e}} = T_{\text{b}}$), T_{e} is the temperature of the outside surface of the evaporator and $q_{\text{out}} = \left(\frac{Q_{\text{out}}}{m} \right) = \left(\frac{\dot{Q}_{\text{out}}}{\dot{m}} \right)$. Assuming that there is no heat loss to the surroundings from the adiabatic section, $q_{\text{out}} \approx q_{\text{in}}$. If the thermal contact resistance between the heat source and the outside surface of the evaporator is assumed to be negligible, then $T_{\text{e}} \approx T_{\text{source}}$, where T_{source} is the temperature of the heat source. Hence, $\left(\frac{q_{\text{in}}}{T_{\text{e}}} \right)$ term in equation (3.52) $\approx \left(\frac{q_{\text{in}}}{T_{\text{source}}} \right)$. The $\left(\frac{q_{\text{in}}}{T_{\text{source}}} \right)$ term represents the entropy transfer from the heat source to the outside surface of the evaporator, whilst the $\left(\frac{q_{\text{out}}}{T_{\text{v,e}}} \right)$ term represents the entropy transfer from the inner surface of the evaporator to the WF. Equation (3.52) can, therefore, be written as

$$S_{\text{gen,e,w}} = q_{\text{in}} \left[\frac{T_{\text{source}} - T_{\text{v,e}}}{T_{\text{source}} T_{\text{v,e}}} \right] \quad (3.53)$$

T_{source} and q_{in} are usually specified for a specific industrial application for which a TS or a HP may be used. Hence, the only way $s_{\text{gen,e,w}}$ could be minimized is by increasing $T_{\text{v,e}}$ i.e. by reducing the temperature drop between the inner surface of the evaporator and the WF vapour. This could be achieved by decreasing the boiling thermal resistance (R_{boil}). R_{boil} , therefore, dictates the entropy generated at the evaporator wall.

Similarly, the entropy generated at the condenser wall can be written as

$$S_{\text{gen,c,w}} = \left[\frac{q_{\text{out}}}{T_{\text{cond}}} - \frac{q_{\text{in}}}{T_{\text{v,c}}} \right] \quad (3.54)$$

where $s_{\text{gen,c,w}}$ is the entropy generated at the condenser wall, $T_{\text{v,c}}$ is the temperature of the vapour in the condenser (comparing with the T-s diagram, $T_{\text{v,c}} = T_{\text{c}}$) and T_{cond} is the temperature of the outside surface of the condenser. If the contact resistance between the heat sink and the outside surface of the condenser is assumed to be negligible, then $T_{\text{cond}} \approx T_{\text{sink}}$, where T_{sink} is the temperature of the heat sink. Hence, $\left(\frac{q_{\text{out}}}{T_{\text{cond}}} \right) \approx \left(\frac{q_{\text{out}}}{T_{\text{sink}}} \right)$. The $\left(\frac{q_{\text{in}}}{T_{\text{v,c}}} \right)$ term represents the entropy transfer from the WF to the inside surface of condenser, whereas the $\left(\frac{q_{\text{out}}}{T_{\text{v,e}}} \right)$ term represents the entropy transfer from the outer surface of the condenser to the heat sink. Equation (3.54) can, therefore, be written as

$$S_{\text{gen,c,w}} = q_{\text{out}} \left[\frac{T_{\text{v,c}} - T_{\text{sink}}}{T_{\text{v,c}} T_{\text{sink}}} \right] \quad (3.55)$$

The value of q_{out} is fixed and so $s_{\text{gen,c,w}}$ can be minimized either i) by minimizing the $(T_{\text{v,c}} - T_{\text{sink}})$ term and ii) by increasing T_{sink} . $(T_{\text{v,c}} - T_{\text{sink}})$ can be minimized by minimizing the condensation thermal resistance (R_{cond}). Hence, provisions must be made to decrease R_{cond} and increase T_{sink} whenever possible, in order to minimize the entropy generation. T_{sink} can be increased by raising the temperature of the coolant flow flowing over the condenser section. The parameters that can be varied in order to minimize R_{cond} is shown in Chapter 4.

3.4.2 Entropy generation along the vapour flow

It is established in section 1.2.2 that a temperature differential between the vapour in the evaporator and the condenser is necessary to obtain the required pressure differential to drive the flow. This temperature differential along the vapour flow results in entropy generation which can be written as

$$S_{\text{gen,v}} = \left[\frac{q_{\text{out}}}{T_{\text{v,c}}} - \frac{q_{\text{in}}}{T_{\text{v,e}}} \right] \quad (3.56)$$

or,

$$S_{\text{gen,v}} = q_{\text{in}} \left[\frac{T_{\text{v,e}} - T_{\text{v,c}}}{T_{\text{v,e}} T_{\text{v,c}}} \right] \quad (3.57)$$

where $S_{\text{gen,v}}$ is the entropy generated along the vapour flow. The value of $S_{\text{gen,v}}$ can be minimized either i) by minimizing the $(T_{\text{v,e}} - T_{\text{v,c}})$ term and ii) by increasing $T_{\text{v,c}}$. $(T_{\text{v,e}} - T_{\text{v,c}})$ can be minimized by minimizing the vapour flow thermal resistance and $T_{\text{v,c}}$ can be increased by reducing the vapour flow thermal resistance.

Therefore, the total entropy generated ($S_{\text{gen,tot,w,v}}$) due to the temperature difference across the evaporator, condenser walls and across the WF vapour can be written (by adding equations 3.55, 3.56 and 3.57) as

$$S_{\text{gen,e,w}} + S_{\text{gen,c,w}} + S_{\text{gen,v}} = \left[\frac{q_{\text{out}}}{T_{\text{sink}}} - \frac{q_{\text{in}}}{T_{\text{source}}} \right] = q_{\text{in}} \left[\frac{T_{\text{source}} - T_{\text{sink}}}{T_{\text{source}} T_{\text{sink}}} \right] \quad (3.58)$$

Equation (3.58) is thermodynamically equivalent to the entropy generation within a system experiencing finite heat transfer q_{in} between two systems at different temperatures T_{source} and T_{sink} (Bejan, 1995). Equation (3.58) indicates that the overall entropy generated is proportional to $(T_{\text{source}} - T_{\text{sink}})$ and q_{in} and it can be minimized by either decreasing $(T_{\text{source}} - T_{\text{sink}})$ or q_{in} . If T_{source} and q_{in} are fixed, then $S_{\text{gen,tot,w,v}}$ can be minimized by increasing T_{sink} . This establishes a thermodynamic performance limit and that is the temperature differential between the heat source and the sink should be such that it is able to generate the minimum pressure differential required to overcome the total pressure losses within the TS and the HP system. Having a temperature differential higher than the minimum value will increase the overall entropy of the TS and the HP system and is, therefore, not recommended.

3.4.3 Entropy generation during boiling and the condensation process

It was assumed that no entropy was generated during the boiling and the condensation processes. However, fluid friction may play a significant role during inception and detachment of the vapour bubbles in the evaporator and during the formation of the liquid film in the condenser. This may generate some entropy. It can be quantified as

$$S_{\text{gen,boil}} = (S_C - S_B) - \frac{h_{\text{fg}}(P = P_b)}{T_B} = S_{\text{fg}}(P = P_b) - \frac{h_{\text{fg}}(P = P_b)}{T_B} \quad (3.59)$$

$$S_{\text{gen,cond}} = (S_H - S_G) + \frac{h_{\text{fg}}(P = P_c)}{T_F} = S_{\text{fg}}(P = P_c) + \frac{h_{\text{fg}}(P = P_c)}{T_F} \quad (3.60)$$

where $S_{\text{gen,boil}}$ and $S_{\text{gen,cond}}$ denote the entropies that may be generated during the boiling and condensation processes. It may be noted that both equation (3.59) and (3.60) are valid for a TS as well as a HP. Whether or not $S_{\text{gen,boil}}$ and $S_{\text{gen,cond}}$ are significant during the boiling and the condensation processes must be determined using experimental data.

3.4.4 Entropy generation due to the condensate flow in the condenser

As the condensate liquid flows along the condenser walls (in a TS) or through the wicks (in a HP), there will be entropy generated due to the viscous effects. The entropy generated at the condenser due to the liquid flow can be written using equation (3.11) as

$$\delta S_{\text{gen}} = \frac{dh}{T} - \frac{vdP}{T} - \frac{\delta q}{T} \quad (3.61)$$

Since $\delta q = dh$ at the condenser, equation (3.60) results in (after integrating)

$$S_{\text{gen}} = \frac{v_{1,H}(\Delta P_1)}{T_c} \quad (3.62)$$

where $v_{1,h}$ is the specific volume of the liquid at state H and $T_c = T_{H,\text{sat}}$. ΔP_1 for different flow regimes inside the TS and a HP can be estimated using the relevant equations presented in Chapter 1.

3.5 Conclusions

A model based on the first and second laws of thermodynamics is proposed that evaluates the thermodynamic processes occurring inside thermosyphons (TS) and heat pipes (HP). The model can be used to predict the thermodynamic state of the working fluid (WF) during any point in the thermodynamic cycle. The key conclusions obtained from this study are

- The WF always arrives at the condenser of a TS or HP in a superheated vapor state regardless of the fill ratio (FR). The entropy of the WF arriving at the condenser can be either less than, equal to or greater than the entropy of the saturated vapor. Three different scenarios are possible inside a TS whereas seven different scenarios are possible inside a HP. These scenarios are dictated by the nature of the pressure drop encountered by the WF flowing through the adiabatic section. The magnitudes of the pressure drops are function of the operational conditions.
- The WF always arrives at the evaporator of a TS or HP in a subcooled liquid state. Whether the WF in its liquid state undergoes additional subcooling depends on the magnitudes of the liquid frictional pressure drop (ΔP_l) and the hydrostatic pressure drop ($\Delta P_{\text{hydro},l}$). When $|\Delta P_l| > |\Delta P_{\text{hydro},l}|$, the WF must lose sensible heat in order to continue operation.
- The temperature of the heat sink may be raised in order to minimize entropy generation. This is feasible in industrial applications. The entropy generated due to the liquid flow in the condenser is entirely due to frictional effects.

There is one caveat to the analysis presented in this chapter and that is the qualitative estimation of the state points on the T-s diagrams and the h-s diagrams. Specifically, the magnitudes of h, s and T are not evaluated during the various thermodynamic processes. Nevertheless, section 3.3 discusses the methods by which the results of the present analysis can be validated using experimental and numerical results.

Chapter 4

4 Predicting the boiling and condensation thermal resistance of a thermosyphon and a heat pipe

This chapter presents new sets of equations capable of predicting the boiling and condensation thermal resistances of a thermosyphon (TS) and a heat pipe (HP) *a priori* under any given operating condition. The equations can not only be used to optimise the TS and HP performance variables but can also be used to predict their performance. The initial sets of equations are derived utilizing the Buckingham Pi-theorem (1914), and the final sets of equations are obtained by a phenomenological approach. The prediction capabilities of these equations are assessed qualitatively which show that they can quantify the changes in the thermal resistance with varying operating conditions. \dot{Q}_{in} (input heating power), aspect ratio (AR), fill ratio (FR) and θ (inclination angle from the horizontal).

The chapter is categorized into four main sections. The first section outlines the boiling and the condensation thermal resistance equations available in the HP text books (Chi, 1976, Reay and Kew, 2006) and evaluates those qualitatively with respect to the varying input heating power (\dot{Q}_{in}), fill ratio (FR), aspect ratio (AR) and the inclination angle (θ). The limitations of these equations are assessed, demonstrating why a new set of equations, presented in this chapter, is required. The second section outlines the different criteria to identify the pool and the film boiling regimes. The third section develops the new thermal resistance equations for pool and film boiling regimes. The effects of θ , on the liquid pool length are then examined. The fourth section develops the condensation thermal resistance equations for film condensation. The effects of the interfacial shear stress, heat capacity and the inclination angle on the film condensation resistances are analyzed. The fourth section evaluates the prediction capabilities of the newly developed boiling and condensation thermal resistance equations qualitatively in response to changes in \dot{Q}_{in} , AR, FR and θ . Finally, the key outcomes from this chapter are summarised in section five.

4.1 Evaluation of the previous expressions of boiling (R_{boil}) and the condensation (R_{cond}) thermal resistances

This section evaluates the boiling (R_{boil}) and the condensation thermal resistance (R_{cond}) equations from the HP textbooks and examines their applicability in characterizing the effects of varying \dot{Q}_{in} , FR, AR and θ . The evaluation of the previous correlations proposed in the TS literature is presented in Appendix D (see section D.1).

Table 4.1 outlines the boiling and the condensation thermal resistance expressions from Chi (1976) and Reay and Kew (2006). The next sub-paragraphs describes the deficiencies in these equations.

Table 4.1 Thermal resistance expressions for different components of a TS and a HP adapted from Reay and Kew (2006).

Thermal resistance	TS and HP	
	Without ideal gas approximation	Ideal gas approximation
$R_3 (R_{\text{boil}})$	$\left[\frac{(2\pi\bar{R}T_{v,e})^{0.5} v_{fg}(T = T_{v,e})T_{v,e}}{A_{e,i}h_{fg}^2(T = T_{v,e})} \right]$	$\left[\frac{(2\pi\bar{R}T_{v,e})^{0.5} \bar{R}T_{v,e}^2}{A_{e,i}h_{fg}^2(T = T_{v,e})P_{v,e}} \right]$
$R_5 (R_{\text{cond}})$	$\left[\frac{(2\pi\bar{R}T_{v,c})^{0.5} v_{lv}(T = T_{v,c})T_{v,c}}{A_{c,i}h_{fg}^2(T = T_{v,c})} \right]$	$\left[\frac{(2\pi\bar{R}T_{v,c})^{0.5} \bar{R}T_{v,c}^2}{A_{c,i}h_{fg}^2(T = T_{v,c})P_{v,c}} \right]$

The R_{boil} and R_{cond} expressions in Table 4.1 do not have \dot{Q}_{in} as a variable. A closer examination of these expressions reveal that all the variables are functions of the saturation temperature (T_{sat}). Since the TS and HP are typically sealed under sub-ambient pressure (which is a design parameter in TS/HP industry), the temperature at which the liquid boils ($T_{v,e} \sim T_{\text{sat}}$) is fixed. Thus, none of the variables in the R_{boil} expression will vary with \dot{Q}_{in} . Therefore, the R_{boil} expression can not predict the changes in the thermal resistance with \dot{Q}_{in} .

Although the condenser outside surface temperature can be predicted using the relevant Nusselt number equation (see equation 4-2 in Chi, 1976), the $T_{v,c}$ values in R_{cond} expression can only be estimated when R_{cond} is known. Thus, R_{cond} expression cannot be used to predict its variation due to change in \dot{Q}_{in} .

The R_{boil} expression does not contain L_p as a variable. Therefore, the variation in R_{boil} with FR (i.e. L_p), when L_e and D_i are fixed, cannot be determined. When L_e and D_i are

varied in equal proportions at fixed L_p , the R_{boil} and R_{cond} expressions reflect those effects through the $A_{e,i}$ and $A_{c,i}$ terms, where $A_{e,i} = \pi D_i L_e$ and $A_{c,i} = \pi D_i L_c$ denote the internal surface area of the evaporator and the condenser, respectively. The variations in L_e and D_i , however, also causes $\dot{Q}'_{\text{in},f}$ and $\dot{Q}'_{\text{out},f}$ to vary, as $\dot{Q}'_{\text{in},f} = \frac{\dot{Q}_{\text{in}}}{A_{e,i}}$ and $\dot{Q}'_{\text{out},f} = \frac{\dot{Q}_{\text{out}}}{A_{c,i}}$. However, since R_{boil} and R_{cond} expressions are inadequate to predict the changes in the thermal resistance with \dot{Q}_{in} or \dot{Q}_{out} , they cannot be used to predict the response due to changing heating conditions.

When AR is varied by varying L_e and L_p in equal proportions for a fixed D_i , the change in R_{boil} is reflected through the $A_{e,i}$ term. However, as discussed previously, the variation in R_{boil} with L_p cannot be determined. Similarly, when D_i is varied for fixed L_e and L_p , the changes in R_{boil} and R_{cond} are reflected through the $A_{e,i}$ and $A_{c,i}$ terms. However, the variation in D_i causes the working fluid (WF) flow behaviour of the WF to change inside the evaporator (Sauciuc et al., 1995, Khazaei et al., 2011), which are not characterized by these R_{boil} and R_{cond} expressions.

The expressions of R_{boil} and R_{cond} do not have θ as a variable. The liquid pool length, L_p and the condensate film thickness, $\delta_{c,f}$, which varies with θ , also do not appear as variables in the R_{boil} and R_{cond} expressions. Thus, the influence of θ on the variation of R_{boil} and R_{cond} cannot be determined.

In addition to the abovementioned deficiencies, there are several other drawbacks of the R_{boil} and R_{cond} expressions. Firstly, they do not characterize the different boiling and condensation regimes within a TS and a HP. Secondly, they do not represent the interaction between the relevant forces (e.g., inertial force, buoyancy force, viscous force, surface tension force, and gravitational force) acting on the WF during the flow. Without the terms representing the effects of these forces, an enormous amount of data from experiments or numerical simulations may need to be gathered for a specific set of TS and HP in order to be able to predict R_{boil} and R_{cond} accurately. This has been demonstrated in Chapter 2.

This present discussion may be summarized by noting that a more robust expression of R_{boil} and R_{cond} needs to be developed that can a) correctly represent the effects of the different interacting forces on the boiling and the condensation processes, b) characterise the trends of R_{boil} and R_{cond} with respect to varying \dot{Q}_{in} , FR, AR and θ , c) be used to estimate R_{boil} and R_{cond} for a TS and HP *a priori* for any combinations of \dot{Q}_{in} , FR, AR and θ and d) can be used to interpret and understand the previous and present experimental results.

The next section assesses the criteria reported by El-Genk and Saber (1998a, 1998b) to identify the different boiling regimes inside a TS.

4.2 Identification of different boiling regimes

The methods to identify the different boiling regimes within the liquid pool and the liquid film are assessed. This is necessary as it will enable one to correctly use the new R_{boil} equations appropriately for the different boiling regimes.

4.2.1 Pool boiling regime

The heat transfer modes within the liquid pool of the evaporator section may include natural convection, nucleate boiling, or a combination of these two processes depending upon the values of $\dot{Q}'_{\text{in},f}$ and L_p (El-Genk and Saber, 1998a). A schematic of different pool boiling modes within a TS is shown in Figure 4.1 for completeness. Several criteria to distinguish the different modes of pool boiling are available in the literature (see Andros, 1980, El-Genk and Saber, 1998a, Noie, 2005, Baojin et al., 2009). However, El-Genk and Saber (1998a) postulated a new criterion by which different pool boiling modes can be identified. The details of the criterion are discussed below.

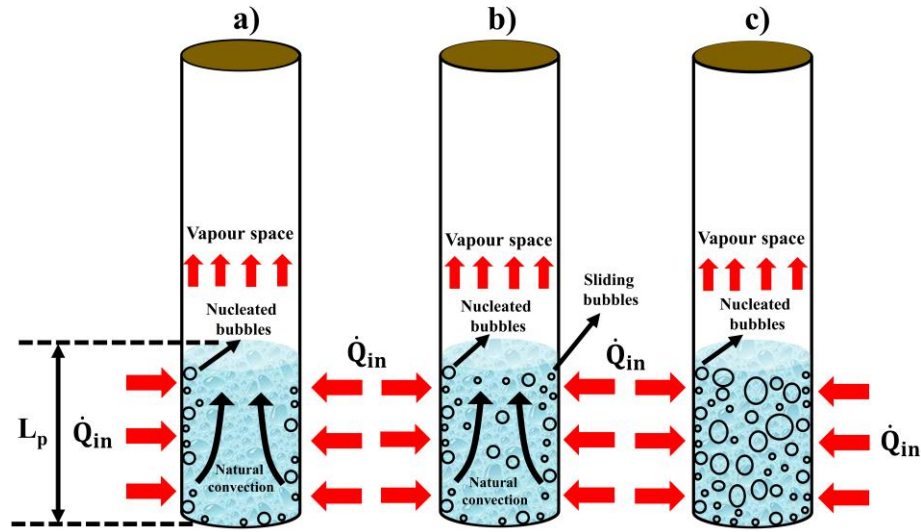


Figure 4.1 A schematic of a TS (HP) showing different pool boiling regimes adapted from El-Genk and Saber (1998a). a) Natural convection boiling (shown by black curve arrows) b) Mixed convection boiling c) Nucleate boiling.

A non-dimensional parameter (X_P) was proposed in El-Genk and Saber (1998a) given as

$$X_P = \varphi (Ra_l)^{0.35} (Pr_l)^{0.35} \left(\frac{P_{sat} D_b}{\sigma} \right)^{0.7} \left(\frac{\dot{Q}'_{in,f} D_b}{\rho_v h_{fg} \nu_l} \right)^{0.7} \quad (4.1)$$

Here, φ is the mixing coefficient, representing the combined effect of sliding and rising bubbles on nucleate boiling in small liquid pools. The subscripts l and v represent the liquid phase and the vapour phase, respectively. Ra denotes the Rayleigh number, Pr denotes the Prandtl number, P_{sat} denotes the saturation pressure, σ denotes the surface tension, ρ denotes the WF density, h_{fg} denotes the latent heat of vapourization, and ν denotes the kinematic viscosity of the WF. D_b represents the characteristic diameter of the vapour bubbles (discussed later in section 4.2.3). The thermophysical properties of the WF should be determined at T_{sat} . The mixing coefficient, φ , depends on the physical properties of the WF and is given by El-Genk and Saber (1998a) as

$$\varphi = \left(\frac{\rho_v}{\rho_l} \right)^{0.4} \left(\left(\frac{P_{sat} \nu_l}{\sigma} \right) \left(\frac{\rho_l^2}{\sigma g (\rho_l - \rho_v)} \right)^{0.25} \right)^{0.25} \quad (4.2)$$

For natural convection, $X < 10^6$; for mixed convection $10^6 \leq X \leq 2.1 \times 10^7$, and in the nucleate boiling regime, $X > 2.1 \times 10^7$. There are several drawbacks to this criterion.

Firstly, it is not known whether the exponents in equations (4.1) and (4.2) are derived from empirical fits to data or from theoretical derivations. Secondly, no studies have tested this relation. Therefore, the reliability of this criterion cannot be ensured. Thirdly, X has been shown to be a function of $\dot{Q}'_{in,f}$ in equation (4.1), but $\dot{Q}'_{in,f}$ depends on the boiling regime itself on the boiling curve. Thus, the applicability of X is debatable. The analysis in Chapter 2 reveal that it is neither $\dot{Q}'_{in,f}$ nor ΔT , but the slope estimated from $\frac{\log(\dot{Q}'_{in,f})}{\log(\Delta T)}$ determines the different pool boiling regimes.

Hence, additional tests using the experimental data from the present study have been performed to examine the validity of the criterion proposed by El-Genk and Saber (1998a). The results of the investigations are shown in Appendix D (section D.2).

4.2.2 Film boiling regime

The heat transfer mechanisms within the condensate film of the evaporator may include film evaporation (also known as laminar convection), nucleate boiling or a combination of these processes depending upon the $\dot{Q}'_{in,f}$ values and the WF properties (El-Genk and Saber, 1998b). A schematic of the different heat transfer regimes within a falling condensate film is shown in Figure 4.2 for completeness (adapted from El-Genk and Saber, 1998b).

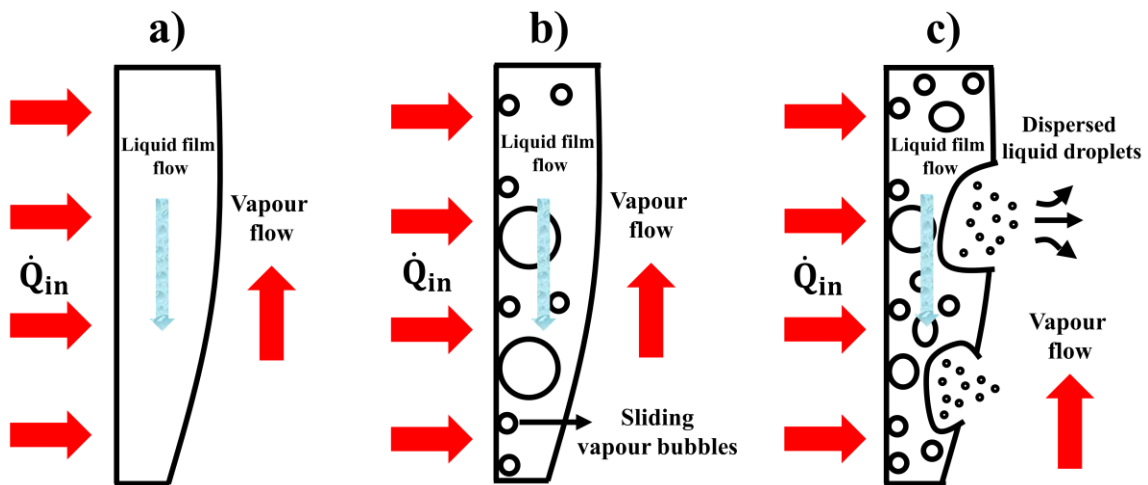


Figure 4.2 A schematic of a TS (HP) showing different film boiling regimes. a) Film evaporation b) Mixed convection boiling c) Nucleate boiling.

Several criteria to identify the different modes of film boiling can be found out in El-Genk and Saber (1998b). Similar to nucleate pool boiling, El-Genk and Saber (1998b) proposed a non-dimensional film parameter (η) to classify the different film boiling regimes. The parameter (η) is given as

$$\eta = \left(\frac{\text{Re}_{F,x}}{\text{Pr}_l} \right) \left(\frac{P_{\text{sat}} D_b}{\sigma} \right)^2 \left(\frac{\dot{Q}'_{\text{in},f} D_b}{\rho_v h_{fg} \nu_l} \right)^2 \quad (4.3)$$

where $\text{Re}_{F,x}$ denotes the local film Reynolds number at the evaporator, estimated as (El-Genk and Saber, 1998b)

$$\text{Re}_{F,x} = \frac{4\rho_l u_l \delta_{E,F}}{\mu_l} = \left(\frac{4\dot{Q}'_{\text{in},f}(L_e - x)}{\mu_l h_{fg}} \right) \quad (4.4)$$

where u_l is the average velocity of the film, μ_l denotes the dynamic viscosity of the liquid and $\delta_{E,F}$ is the thickness of the falling film at the evaporator. The variable x varies from $x = 0$ to $x = L_p$, where $x = 0$ denotes the location of the condensate film entering the evaporator, and $x = L_p$ denotes the location where the condensate film meets the liquid pool (see Figure 4.3). The liquid and the vapour phase properties in equations (4.3) and (4.4) should be evaluated at T_{sat} . For natural convection, $\eta \leq 10^9$; for mixed convection, $10^9 < \eta < 2.7 \times 10^{10}$, and for the nucleate boiling regime, $\eta \geq 2.7 \times 10^{10}$.

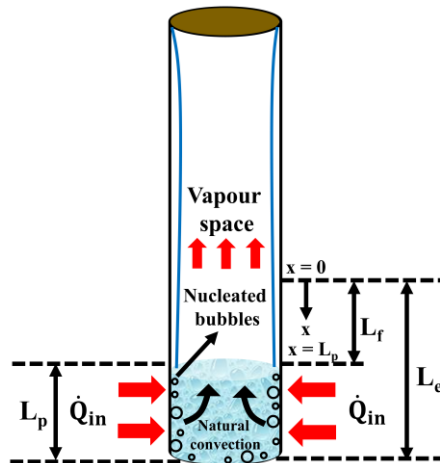


Figure 4.3 A schematic showing the condensate film flow at the evaporator. $x = 0$ and $x = L_p$ denote the location of the film at the evaporator entrance and the liquid pool.

The drawbacks to the above-mentioned criterion are similar to those discussed in section 4.2.1. Thus, additional evaluations using the present experimental data have been performed in Appendix D to examine the validity of equation (4.3).

The next two sections section develop new correlations for R_{boil} and R_{cond} in order to satisfy the objectives proposed in section 4.1. These correlations are expected to have a broader range of applications than those for TS and HP applications.

4.3 Development of new correlations for R_{boil}

This section develops new correlation equations for R_{boil} by employing the Buckingham's Pi theorem (Buckingham, 1914). The physical properties and variables on which the boiling thermal resistance could depend are i) the thermal driving potential, ΔT (where $\Delta T = |T_s - T_{\text{sat}}|$, T_s and T_{sat} refer to the evaporator inner surface and the saturation temperature, respectively), ii) the body force arising from the liquid-vapour density difference, $g(\rho_l - \rho_v)$, iii) the latent heat of vapourization, h_{fg} , iv) the surface tension at the liquid-vapour interface, σ , v) a characteristic length, L and vi) the thermophysical properties of the WF liquid or vapour (ρ , c_p , k , μ) (Bergman et al., 2018). Thus, $R_{\text{boil}} = f(\Delta T, g(\rho_l - \rho_v), h_{\text{fg}}, L, \sigma, \rho, c_p, k, \mu)$. Since there are ten variables and four primary dimensions, there are six non-dimensional π -terms which can be expressed as

$$\pi_1 = [L]^a [c_p]^b [\mu]^c [g(\rho_l - \rho_v)]^d R_{\text{boil}} \quad (4.5)$$

$$\pi_2 = [L]^a [c_p]^b [\mu]^c [g(\rho_l - \rho_v)]^d \Delta T \quad (4.6)$$

$$\pi_3 = [L]^a [c_p]^b [\mu]^c [g(\rho_l - \rho_v)]^d h_{\text{fg}} \quad (4.7)$$

$$\pi_4 = [L]^a [c_p]^b [\mu]^c [g(\rho_l - \rho_v)]^d \rho \quad (4.8)$$

$$\pi_5 = [L]^a [c_p]^b [\mu]^c [g(\rho_l - \rho_v)]^d k \quad (4.9)$$

$$\pi_6 = [L]^a [c_p]^b [\mu]^c [g(\rho_l - \rho_v)]^d \sigma \quad (4.10)$$

Dimensional analysis of equations (4.5) to (4.10) yields, π_1 , π_2 , π_3 , π_4 , π_5 and π_6 as

$$\pi_1 = L c_p \mu R_{\text{boil}} \quad (4.11)$$

$$\pi_2 = \frac{\mu^2 c_p \Delta T}{L^4 [g(\rho_1 - \rho_v)]^2} \quad (4.12)$$

$$\pi_3 = \frac{\mu^2 h_{fg}}{L^4 [g(\rho_1 - \rho_v)]^2} \quad (4.13)$$

$$\pi_4 = \frac{L^3 \rho g(\rho_1 - \rho_v)}{\mu^2} \quad (4.14)$$

$$\pi_5 = \frac{k}{\mu c_p} \quad (4.15)$$

$$\pi_6 = \frac{\sigma}{L^2 g(\rho_1 - \rho_v)} \quad (4.16)$$

π_5 and π_6 can be re-written as π'_5 and π'_6 , where $\pi'_5 = \frac{1}{\pi_5}$ and $\pi'_6 = \frac{1}{\pi_6}$, respectively. Thus,

$$\pi'_5 = \frac{\mu c_p}{k} \quad (4.17)$$

$$\pi'_6 = \frac{L^2 g(\rho_1 - \rho_v)}{\sigma} \quad (4.18)$$

Similarly, three other π terms can be derived as

$$\frac{\pi_2}{\pi_3} = \pi_7 = \frac{c_p \Delta T}{h_{fg}} \quad (4.19)$$

$$\pi_1 \pi_5 = \pi_8 = R_{\text{boil}} k L \quad (4.20)$$

$$\pi_3 \pi_4 = \left(\frac{h_{fg}}{L g} \right) \left(\frac{\rho}{\rho_1 - \rho_v} \right) \text{ as } \pi_9 = \frac{\rho_1 - \rho_v}{\rho} \quad (4.21)$$

The relevant π terms influencing R_{boil} and their definition are outlined in Table 4.2.

Table 4.2 Definition of the various π terms influencing R_{boil} .

π terms	Non-dimensional number
π_4	Archimedes number
π'_5	Prandtl number
π'_6	Bond number
π_7	Jakob number
π_8	Non-dimensional boiling resistance
π_9	Pressure dependency term (P_D)

A generic expression of dimensionless R_{boil} can, therefore, be formulated as a function of these π terms as

$$\pi_8 = f(\pi_4, \pi'_5, \pi'_6, \pi_7, \pi_9) \quad (4.22)$$

or,
$$[R_{\text{boil}}]L = f[Ar, Pr, Bo, Ja, P_D] \quad (4.23)$$

Equation (4.23) is valid for any boiling process. The next step is to apply this relationship to the different boiling modes and select the appropriate terms that may exert a significant influence on R_{boil} for a particular boiling heat transfer mode.

The power law form of the Nusselt number has been proven to be a suitable model for predicting various heat transfer mechanisms for external and internal flows (Churchill, 1977, Stephan and Abdelsalam, 1980, Bergman et al., 2018). Based on this argument, a possible form of equation (4.23) would be a power law representing the effects of the various dimensionless terms.

The next section applies this technique and derives the expressions of R_{boil} for the natural convection regime within the liquid pool.

4.3.1 Expression for R_{boil} for natural convection in the liquid pool

Natural convection is the dominant mode of heat transfer within the liquid pool when $\Delta T \leq 5[\text{K}]$ (Bergman et al., 2018). However, limited bubble nucleation at the bottom and along the heated wall may also contribute to the overall heat transfer in the pool (El-Genk and Saber, 1998a). Therefore, the boiling thermal resistance due to natural convection within the liquid pool, $R_{\text{NCB,P}}$ (the subscript “NCB” and “P” denotes natural convection boiling and pool, respectively) should include the terms representing the effects of the buoyancy force and the bubble nucleation. This includes the Archimedes number and the Bond number. The Archimedes number represents the effects of the buoyancy induced fluid motion on heat transfer. The Bond number measures the ratio the buoyancy force (which promotes bubble departure) and the surface tension force (which causes the bubble to adhere to the surface) (Bergman et al., 2018). This can be used to estimate the

characteristic diameter of a nucleated bubble, D_b as (Cole, 1967, Collier and Thome, 1999, El-Genk and Saber, 1998a)

$$D_b = C \sqrt{\frac{\sigma_1}{g(\rho_1 - \rho_v)}} \quad (4.24)$$

A variety of expressions with slightly different constants (C) for equation (4.24) have been proposed in different studies (see Cole, 1967 and Table 2 in Guichet et al., 2019). Determining the appropriate value of the constant in equation (4.24) is less important as it will be a part of the coefficient ($C_{NCB,P}$) (see equation 4.25) which can be determined from the experimental data. The Prandtl number should be included in the final form of $R_{NCB,P}$ to represent the effects of momentum diffusivity and thermal diffusivity for heat transfer to a boiling liquid (Rohsenow, 1952). The P_D term is included to represent the effects of pressure dependency on $R_{NCB,P}$ (Stephan and Abdelsalam, 1980). Taking all the non-dimensional terms into considerations, $R_{NCB,P}$ can, thus, be expressed as

$$R_{NCB,P}kL = C_{NCB,P}[Ar]^e[Pr]^f[Bo]^g[P_D]^h \quad (4.25)$$

where $C_{NCB,P}$ and e, f, g, h are constants defined as the coefficient and exponents of pool natural convection boiling, respectively. The constants need to be determined from experimental data as this form of equations has not been used in any previous studies. Note that, although the term representing a nucleated bubble (the Bond number) is included in equation (4.25), the Jakob number representing the relative effects of the latent energy absorption to the sensible heat transfer is not included. This is because the fluid motion is principally determined by the natural convection effects and not by the motion of the bubbles generated. The exclusion of Jakob number from equation (4.25) makes the $R_{NCB,P}$ term independent of the thermal driving potential term, i.e. ΔT . In order to include the effects of either ΔT or \dot{Q}_{in} , π_2 from equation (4.12) is utilized. A new dimensionless number proportional to the Archimedes number representing the effects of ΔT and retaining the effects of the characteristic length scale is proposed as $\left[\frac{c_p \Delta T}{Lg}\right]$, where $\pi_2 = \frac{\mu^2 c_p \Delta T}{L^4 [g(\rho_1 - \rho_v)]^2} = \left[\frac{c_p \Delta T}{Lg}\right] \left[\frac{\rho_v}{\rho_1 - \rho_1}\right] \left[\frac{1}{Ar}\right]$. This can be substituted for Ar in equation (4.25) to arrive at

$$R_{\text{NCB},pkL} = C_{\text{NCB},P} \left[\frac{c_p \Delta T}{Lg} \right]^e [\text{Pr}]^f [\text{Bo}]^g [P_D]^h \quad (4.26)$$

However, ΔT may not always be known *a priori* in laboratory experiments where the rate of heat transfer (\dot{Q}_{in}) is prescribed along the TS (or HP) through electrical resistance heat source. Replacing ΔT as $\Delta T = R_{\text{NCB},P} \dot{Q}_{\text{in},f,P}$ (where $\dot{Q}_{\text{in},f,P} = \dot{Q}_{\text{in}}(1-\text{FR})$) and c_p as $c_p = \left(\frac{k}{\mu}\right)\text{Pr}$, an alternate form of equation (4.26), is proposed as

$$(R_{\text{NCB},P})^{1-e} kL = C_{\text{NCB},P} \left[\frac{k \dot{Q}_{\text{in},f,P}}{\mu Lg} \right]^e [\text{Pr}]^{e+f} [\text{Bo}]^g [P_D]^h \quad (4.27)$$

There are two relevant characteristic lengths here, i.e. D_i and L_p . El-Genk and Saber (1998a) reported that bubble nucleation might be as important as natural convection with decreasing D_i and so D_i may be an appropriate characteristic length for the Bo term. The characteristic length in the second term of the right-hand side (RHS) of equation (4.27) will depend on L_p/D_i . For short liquid pool length within the TS and HP or large spacings between the opposite walls (i.e. small L_p/D_i ratio), the natural convection boundary layer development within the liquid pool height would be similar to that of an independent boundary layer developed over a heated, isolated plate in an infinite, quiescent medium (Bergman et al., 2018, Cengel and Ghajar, 2020). Thus, L_p may be the appropriate length scale when L_p/D_i ratio is small. For large L_p/D_i ratio, the natural convection boundary layers from opposite walls may interact and, therefore, D_i may be the appropriate length scale term. Expanding the terms of equation (4.27) for the two different L_p/D_i ratio cases gives

$$R_{\text{NCB},pkL_p} = [C'_{\text{NCB},P}]^i \left[\frac{\dot{Q}'_{\text{in},f,P}}{\mu_l g} \right]^j \left[\frac{D_i}{L_p} \right]^j \left[\frac{\mu_l C_{p,l}}{k_l} \right]^k \left[\frac{D_i^2 g (\rho_l - \rho_v)}{\sigma} \right]^l \left[\frac{\rho_l - \rho_v}{\rho_v} \right]^m \quad (4.28)$$

$$R_{\text{NCB},pkD_i} = [C'_{\text{NCB},P}]^i \left[\frac{\dot{Q}'_{\text{in},f,P}}{\mu_l g} \right]^j \left[\frac{L_p}{D_i} \right]^j \left[\frac{\mu_l C_{p,l}}{k_l} \right]^k \left[\frac{D_i^2 g (\rho_l - \rho_v)}{\sigma} \right]^l \left[\frac{\rho_l - \rho_v}{\rho_v} \right]^m \quad (4.29)$$

where $C'_{\text{NCB},P} = [(\pi)^e C_{\text{NCB},P}]$, $i = \frac{1}{(1-e)}$, $j = \frac{e}{(1-e)}$, $k = \frac{e+f}{(1-e)}$, $l = \frac{g}{(1-e)}$ and $m = \frac{h}{(1-e)}$ are constants defined as the coefficient and exponents of pool natural convection boiling, respectively. Equations (4.28) and (4.29) represent the small L_p/D_i ratio and the large L_p/D_i ratio cases. Note that in equations (4.28) and (4.29), the subscript “l” has been

added to denote that the liquid phase WF properties are being considered in these relations. The WF properties should be evaluated at the saturation temperature T_{sat} .

Which scenario among equations (4.28) and (4.29) is valid can be determined on the basis of the transversal curvature effect. This effect is significant when the natural convection boundary layer thickness ($\delta_{\text{NCB,P}}$) is of the same order of magnitude as the radius of the TS or a HP. Popiel et al. (2007) developed a slenderness criterion (see equation (4.30)) to determine whether the natural convection heat transfer from a vertical cylinder resembles that of a flat plate or a slender cylinder.

$$\text{Gr}_1^{0.25} \left(\frac{D_1}{L_p} \right) \leq 11.474 + \frac{48.92}{\text{Pr}_1^{0.5}} - \frac{0.006085}{\text{Pr}_1^2} \quad (4.30)$$

where Gr_1 represents the Grashof number for the liquid phase of the WF. Gr_1 can be estimated as

$$\text{Gr}_1 = \left(\frac{g\beta(\Delta T)L_p^3}{\nu_1^2} \right) \quad (4.31)$$

where β is the volumetric thermal expansion coefficient. Provided that Pr_1 is computed at known T_f (or T_{sat}), the RHS of equation (4.30) can be computed directly. The FR of a TS and HP is typically known, and, therefore, L_p is known. If the LHS < RHS term, then the cylinder is treated as a slender cylinder, whereas when the LHS term is greater, it is treated as a semi-infinite plate (Popiel et al., 2007). There is no evidence in the literature where the transverse curvature effects are shown to be significant for a TS and a HP and, therefore, equation (4.28) can be utilized for prediction.

It is also noted that the critical Grashof number (Gr_{crit}) for a vertical cylinder is $\text{Gr}_{\text{cr}} \approx 4 \times 10^9$ for $0.01 < \text{Pr}_1 < 100$ (Popiel et al., 2007, Popiel, 2008). Taking the limits of $\Delta T_{\text{e,a}}$ for natural convection boiling as 5[K] (for flat surfaces; Bergman et al., 2018), and roughly 3[K] for TS and HP (see Chapter 2), it is revealed that the laminar to turbulent transition of the natural convection boundary layer within the liquid pool occurs at high T_f and L_p values (see Table 4.3). Although such high L_p values are not typical for a conventional TS or a HP and, thus, may be valid for other non-conventional TS and HP.

Table 4.3 Estimation of L_p (m) at the critical Grashof number for two different superheat values.

Gr_{cr}	T_f [K]	$\beta \times 10^6$ [K ⁻¹]	v_l [m ² /s]	$\Delta T = 5$ [K]	$\Delta T = 3$ [K]
				L_p (m)	L_p (m)
4×10^9	290	174.0	1.081×10^{-6}	0.818	0.970
	300	276.1	8.576×10^{-6}	0.601	0.713
	310	361.9	6.998×10^{-6}	0.480	0.569
	350	624.2	3.748×10^{-6}	0.264	0.313
	373.15	750.1	2.912×10^{-6}	0.210	0.249
	400	896	2.315×10^{-6}	0.170	0.201
	420	1010	2.012×10^{-6}	0.148	0.176

The next section derives the equation for R_{boil} for nucleate boiling in the liquid pool.

4.3.2 Expression of R_{boil} for nucleate boiling in the liquid pool

The theory of surface boiling of subcooled liquids given by Rohsenow (1952) is utilized in deriving the thermal resistance due to nucleate pool boiling $R_{NB,P}$. The subscript “NB” represents nucleate boiling. $R_{NB,P}$ in the liquid pool may include the effects from the Prandtl number, the Jakob number and the Bond number. The inclusion of the Bond number is justified due to the bubble nucleation. Similarly, the inclusion of the Jakob number is based on the fact that the strength of the bubble motion (vapour flow rate) at the heated surface is determined by the ratio of the liquid superheat enthalpy at the heated surface temperature to the latent enthalpy of vapourization (Rohsenow, 1952, Cole, 1967). The Prandtl number needs to be included since it represents the effects of momentum diffusivity and thermal diffusivity on $R_{NB,P}$ (Bergman et al., 2018). $R_{NB,P}$ can, therefore, be expressed as

$$R_{NB,pkL} = C_{NB,P} [Pr]^n [Bo]^o [Ja]^p \quad (4.32)$$

where $C_{NB,P}$ and n , o , p are constants defined as the thermal resistance coefficient and exponents of nucleate pool boiling, respectively. The constants need to be determined from experimental data. A length scale that significantly influences the sliding bubbles along the heated wall and rising and departing bubbles in the pool will be the relevant length scale for the non-dimensional $R_{NB,P}$ term (either L_p or D_b). ΔT appears as a variable in the Jakob number term which may not always be known *a priori*. Thus, replacing ΔT as $\Delta T = R_{NB,P} \dot{Q}_{in,f,P}$ and $c_{p,l}$ as $c_{p,l} = \left(\frac{k_l}{\mu_l}\right) Pr_l$ in the Jakob number term and subsequently performing algebraic operations, equations (4.33) and (4.34) are obtained as

$$R_{NB,pk_l}D_b = [C'_{NB,P}]^q [Pr_l]^r [Bo_l]^s [Re_b]^t \quad (4.33)$$

$$R_{NB,pk_l}D_b = [C''_{NB,P}]^q [Pr_l]^r [Bo_l]^s [L_p/D_b]^t [Co^{-1}Re_b]^t \quad (4.34)$$

where Re_b is the bubble Reynolds number, and Co is the Confinement number ($Co = D_b/D_i$) (Bergman et al., 2018) and D_b is assumed as the relevant length scale influencing $R_{NB,P}$. Re_b is a measure of the local agitation of the fluid at the heating surface, and Co is a measure of the confinement effects on the nucleated bubble for a given channel diameter. $C'_{NB,P} = \left[\left(\frac{\pi}{6}\right)^k C_{NB,P}\right]$, $C''_{NB,P} = [(\pi)^k C_{NB,P}]$, $q = \frac{1}{(1-p)}$, $r = \frac{n+p}{(1-p)}$, $s = \frac{o}{(1-p)}$ and $t = \frac{p}{(1-p)}$, respectively. Equation (4.33) is obtained when Re_b is computed from $\dot{Q}_{in,f}$ as

$$Re_b = \frac{\rho_b u_b D_b}{\mu_l} = \frac{\dot{Q}_{in,f,P}}{\frac{\pi}{6} D_b h_{fg} \mu_l} \quad (4.35)$$

whilst equation (4.34) is obtained when Re_b is computed from $\dot{Q}'_{in,f}$ as

$$Re_b = \frac{\rho_b u_b D_b}{\mu_l} = \frac{\dot{Q}'_{in,f} D_b}{h_{fg} \mu_l} \quad (4.36)$$

where u_b is the mean velocity of the nucleated bubbles. While deriving equation (4.36), it is assumed that $(\dot{Q}_{in,f}/A_{e,i})_b = (\dot{Q}'_{in,f}/A_{e,i})$, where $(\dot{Q}_{in,f}/A_{e,i})_b$ is the heat transfer to the bubble per unit heating surface area while the bubble remains attached and $(\dot{Q}'_{in,f}/A_{e,i})$ is heat transfer to the fluid per unit heating area. $A_{e,i}$ denotes the internal surface area of the evaporator. The validity of this assumption was proved experimentally by Jakob (1941).

The occurrence of the Re_b term in equations (4.33) and (4.34) represents a vital flow feature. As the fluid motion within the liquid pool is forced by the bubble growth and separation from the heated surface, it is reasonable to represent this effect through Re_b , as in equations (4.33) and (4.34). Re_b can be estimated from known $\dot{Q}_{in,f}$ (or $\dot{Q}'_{in,f}$) and D_b values. The estimation of D_b is shown in section 4.3.1. Since equation (4.34) represents the effects of $\dot{Q}'_{in,f}$, the Co number and L_p , it is hypothesized that equation (4.34) will be superior for prediction than equation (4.33).

There are two relevant characteristic lengths for the Bo term in equation (4.34), i.e., D_i and L_p . For a small L_p/D_i ratio, the bubble interaction from the opposite walls may not be vigorous (because of large spacings between the heated walls), and in this case, L_p would be the appropriate length scale for the Bo term. For a large L_p/D_i ratio, the nucleated bubbles developing on opposite surfaces may mix more vigorously and hinder the overall heat transfer capability. This phenomenon has been reported by Sauciuc et al., (1995). Thus, D_i may be the appropriate length scale for the Bo term. The expansion of equation (4.34) for the two L_p/D_i ratio cases give

$$R_{NB,pk_l} D_b = [C''_{NB,P}]^q \left[\frac{\mu_l C_{p,l}}{k_l} \right]^r \left[\frac{L_p^2 g(\rho_l - \rho_v)}{\sigma} \right]^s \left[\frac{L_p}{D_b} \right]^t \left[\frac{D_i}{D_b} \right]^t \left[\frac{\dot{Q}'_{in,f} D_b}{h_{fg} \mu_l} \right]^t \quad (4.37)$$

$$R_{NB,pk_l} D_b = [C''_{NB,P}]^q \left[\frac{\mu_l C_{p,l}}{k_l} \right]^r \left[\frac{D_i^2 g(\rho_l - \rho_v)}{\sigma} \right]^s \left[\frac{L_p}{D_b} \right]^t \left[\frac{D_i}{D_b} \right]^t \left[\frac{\dot{Q}'_{in,f} D_b}{h_{fg} \mu_l} \right]^t \quad (4.38)$$

where equations (4.37) and (4.38) represent the small L_p/D_i ratio and the large L_p/D_i ratio cases, respectively. The third, fourth and the fifth RHS terms in equations (4.37) and (4.38), represent identical terms given by $\left[\frac{L_p}{D_b} \right] \left[\frac{D_i}{D_b} \right]$. Thus, either of the two equations can be used for prediction when $Co < 0.5$ and $Co \geq 0.5$. However, the length scale term on the LHS of the equations will differ for both cases. For large diameter TS and HP, the nucleated bubbles originating from the opposite surfaces may not interact during the flow and, therefore, either L_p or D_b can be the representative length scale for $R_{NB,P}$. When the effects of the confinement are significant, D_i may be used. All the terms on the RHS of equations (4.37) and (4.38) within the square brackets can be estimated *a priori* (except $[C''_{NB,P}]^q$) and, thus, both equations (4.37) and (4.38) can be used for prediction.

The next section derives the expression of R_{boil} for film evaporation.

4.3.3 Expression of R_{boil} for film evaporation

The film condensation resistance ($R_{B,F}$) can be computed from $R_{B,P}$ as $R_{B,F} = \left(\frac{FR}{1-FR} \right) R_{B,P}$. Therefore, when the estimates of $R_{B,P}$ are available, no separate correlation to predict

$R_{B,F}$ need to be used. However, if $R_{B,P}$ is not available, the following correlations may be used to estimate $R_{B,F}$.

In deriving the thermal resistance due to film evaporation, ($R_{E,F}$) (the subscripts “E” and “F” denote evaporation and film, respectively), Nusselt’s theory (1916) of laminar filmwise condensation is utilized. $R_{E,F}$ should, therefore, include the effects of the Archimedes number, the Prandtl number and the Jakob number. The inclusion of the Archimedes number can be justified by the fact that the characteristic thickness scale of the liquid film in the evaporator ($\delta_{E,F}$) may be determined from the relative magnitudes of the buoyancy force and the viscous force (El-Genk and Saber, 1998b) and the fact that the resistance to the heat transfer is caused by the thickness, $\delta_{E,F}$ of the falling film where

$$\delta_{E,F} \sim \sqrt[3]{\frac{\mu_l^2}{g\rho_l(\rho_l - \rho_v)}}.$$

However, natural convection within the film may induce additional fluid motion which can influence the rate of heat transfer through the falling film. The laminar-film condensation problem solved with the boundary-layer technique (Sparrow and Greg, 1959) demonstrate that the fluid acceleration terms have little effect on the heat transfer for WF having $Pr_l > 1$. The typical WF used in conventional TS and HP have Pr number have greater than 1 (distilled water, ammonia, R134a, distilled water-ethanol mixture) and, thus, the effects of natural convective motion and the boundary layer arising from it can be assumed to be negligible. However, for liquid metals as a WF, where $Pr_l < 1$, the convective acceleration terms will increase the thermal resistance (see Appendix 2 in Sparrow and Greg, 1959).

Since evaporation occurs at the liquid vapour interface and is the dominant mode of heat transfer, the rate of heat transfer into the film must be equal to the rate at which latent energy is absorbed by the film during evaporation, i.e. $\dot{m}h_{fg}$, where \dot{m} is the mass flow rate of the falling condensate film. This explains the inclusion of the Jakob number. The Prandtl number is included because of the reasons discussed while deriving $R_{NCB,P}$ and $R_{NB,P}$. $R_{E,F}$ can, therefore, be expressed as

$$R_{E,F}kL = C_{E,F}[Ar]^u[Pr]^v[Ja]^w \quad (4.39)$$

where $C_{E,F}$ and u , v , w are constants defined as the coefficient and exponents of film evaporation, respectively. They have to be determined from experimental data. Since the thermal resistance is governed by the thickness of the falling film, $\delta_{E,F}$ could be the relevant length scale for the non-dimensional $R_{E,F}$ term. Adopting similar algebraic manipulations to those used while deriving (4.33) and (4.34), equation (4.40) is obtained as

$$R_{E,F}k_i\delta_{E,F} = [C'_{E,F}]^x [Ar_i]^y [Pr_i]^z [D_i/\delta_{E,F}]^{a_1} [Re_F]^{a_1} \quad (4.40)$$

where Re_F is the film flow Reynolds number, $C'_{E,F} = \left[\left(\frac{\pi}{4}\right)^w C_{E,F}\right]$, $x = \frac{1}{(1-w)}$, $y = \frac{u}{(1-w)}$ and $z = \frac{v+w}{(1-w)}$ and $a_1 = \frac{w}{(1-w)}$, respectively. Re_F can be calculated as

$$Re_F = \frac{4\rho_l u_1 \delta_{E,F}}{\mu_l} = \frac{4\dot{Q}_{in,f,F}}{\pi D_i h'_{fg} \mu_l} = \frac{4\dot{Q}'_{in,f} L_f}{h'_{fg} \mu_l} \quad (4.41)$$

where u_1 is the average velocity of the falling film condensate and h'_{fg} is the modified latent heat of vapourization ($h'_{fg} = h_{fg} + 0.68c_{p,l}(\Delta T_{C,F})$).

There are two relevant characteristic lengths for the Ar term; the length of the condensate film exposed to the evaporator, i.e., $L_F = L_e - L_p$, and the thickness of the falling film $\delta_{E,F}$. As $\delta_{E,F}$ cannot be the characteristic length in the Ar term (the Ar term becomes unity in that case), L_F would be appropriate. This can be justified by the fact both that the buoyancy force and the viscous force on the falling condensate film act along the length L_F . Expanding equation (4.40) gives

$$R_{E,F}k_i\delta_{E,F} = [C'_{E,F}]^x \left[\frac{L_F^3 \rho_l g (\rho_l - \rho_v)}{\mu_l^2}\right]^y \left[\frac{\mu_l C_{p,l}}{k_l}\right]^z \left[\frac{D_i}{\delta_{E,F}}\right]^{a_1} \left[\frac{4\dot{Q}_{in}}{\pi D_i h_{fg} \mu_l}\right]^{a_1} \quad (4.42)$$

or,

$$R_{E,F}k_i\delta_{E,F} = [C'_{E,F}]^x \left[\frac{L_F^3 \rho_l g (\rho_l - \rho_v)}{\mu_l^2}\right]^y \left[\frac{\mu_l C_{p,l}}{k_l}\right]^z \left[\frac{D_i}{\delta_{E,F}}\right]^{a_1} \left[\frac{4\dot{Q}'_{in,f} L_f}{h_{fg} \mu_l}\right]^{a_1} \quad (4.43)$$

All the terms on the RHS of equations (4.42) and (4.43) within the square brackets can be estimated *a priori* (except the coefficient $[C'_{E,F}]^x$) and, thus, these equations can be used

for prediction. Note that the liquid properties should be evaluated at $T_{\text{film,C}}$, where $T_{\text{film,C}} = \left(\frac{T_{\text{sat}} + T_{\text{c,avg}}}{2} \right)$ and $T_{\text{c,avg}}$ is average condenser surface temperature.

The next section derives the expression of R_{boil} for the film nucleate boiling.

4.3.4 Expression of R_{boil} for the film nucleate boiling

The thermal resistance due to nucleate boiling in the falling film ($R_{\text{NB,F}}$) will comprise the Prandtl number, the Bond number and the Jakob number. The Jakob number is included because of the reasons discussed while deriving $R_{\text{E,F}}$. The Prandtl number and the Bond number are included based on the reasons described while deriving $R_{\text{NCB,P}}$ and $R_{\text{NB,P}}$. $R_{\text{NB,F}}$ can, therefore, be represented as

$$R_{\text{NB,FkL}} = [C_{\text{NB,F}}][\text{Pr}]^{b_1}[\text{Bo}]^{c_1}[\text{Ja}]^{d_1} \quad (4.44)$$

where $C_{\text{NB,F}}$ and b_1 , c_1 , d_1 are independent constants defined as the thermal resistance coefficient and the exponents of film nucleate boiling. The constants need to be estimated from experimental data. Since bubble nucleation is the primary mode of heat transfer at the wall, D_b would be the appropriate length scale term for the non-dimensional $R_{\text{NB,F}}$ term. Similar to nucleate boiling in the liquid pool, equation (4.44) can be represented in terms of Re_b as

$$R_{\text{NB,FkD}_b} = [C'_{\text{NB,F}}]^{e_1} [\text{Pr}]^{f_1} [\text{Bo}]^{g_1} [\text{Re}_b]^{h_1} \quad (4.45)$$

$$R_{\text{NB,FkD}_b} = [C''_{\text{NB,F}}]^{e_1} [\text{Pr}]^{f_1} [\text{Bo}]^{g_1} [L_F/D_b]^{h_1} [\text{Co}^{-1}\text{Re}_b]^{h_1} \quad (4.46)$$

where $[C'_{\text{NB,F}}] = \left[\left(\frac{\pi}{6} \right)^{d_1} C_{\text{NB,K}} \right]$, $C''_{\text{NB,F}} = [(\pi)^{d_1} C_{\text{NB,K}}]$, $e_1 = \frac{1}{(1-d_1)}$, $f_1 = \frac{(b_1+d_1)}{(1-d_1)}$, $g_1 = \frac{c_1}{(1-d_1)}$ and $h_1 = \frac{d_1}{(1-d_1)}$, respectively. Equation (4.45) is obtained when $\dot{Q}'_{\text{in,f,F}}$ is invoked in the expression for Re_b (see equation 4.35), whilst equation (4.46) is obtained when $\dot{Q}'_{\text{in,f}}$ is invoked (see equation 4.36). Since equation (4.46) represents the effects of $\dot{Q}'_{\text{in,f}}$, the Co number and L_F , it is hypothesized that it is more suitable to use than equation (4.45).

There are two relevant characteristic lengths for the Bond number; $L_F = L_e - L_p$ and $\delta_{E,F}$. Similar to nucleate boiling in the liquid pool, the characteristic length in the Bo term may depend on the $L_F/\delta_{E,F}$ ratio. For large $L_F/\delta_{E,F}$ (i.e. large L_F or small $\delta_{E,F}$), it is reasonable to assume $\delta_{E,F}$ as the appropriate length scale in the Bo term. This is justified by the fact that in the limiting case of a very large L_F (this may occur at very low FR), a continuous condensate film in the evaporator above the liquid pool may not be established. Hence, bubble nucleation will not occur along L_F (see Figure 4.4a for illustration) and, thus, L_F cannot be considered as a characteristic length. Taking $\delta_{E,F}$ as the relevant length scale term in the Bond number will yield an expression $\left(\frac{\delta_{E,F}}{D_b}\right)$. A variation of this parameter, $\left(\frac{\delta_{E,F}}{D_b}\right)^{1.5}$ has been defined previously as the viscosity number ($N_{\mu F}$) in El-Genk and Saber (1998b). In physical terms, the $\left(\frac{\delta_{E,F}}{D_b}\right)$ characterizes the relative effects of the surface tension force and the viscous force. This bears a strong resemblance to the Marangoni number. The Marangoni effect will cause a flow when there is a gradient of surface tension forces caused by a temperature gradient (Pearson, 1958). The effects of the Marangoni flow on the thermal performance of TS and HP have been demonstrated previously in Yang and Homsy (2006) and Savino and Paterna (2006). For small $L_F/\delta_{E,F}$, however, (i.e. at small L_F or large $\delta_{E,F}$), L_F may be considered as a suitable characteristic length. This is because the maximum possible diameter of the nucleated bubble (semicircular base edge) forming on the surface would be of the order of L_F , rather than $\delta_{E,F}$. This has been observed by high-speed photography in Fujita and Ueda (1978a, b), Mesler and Mailen (1977), Parken (1975), Cerza and Sernas (1985). A schematic of this phenomenon is shown in Figure 4.4b for completeness.

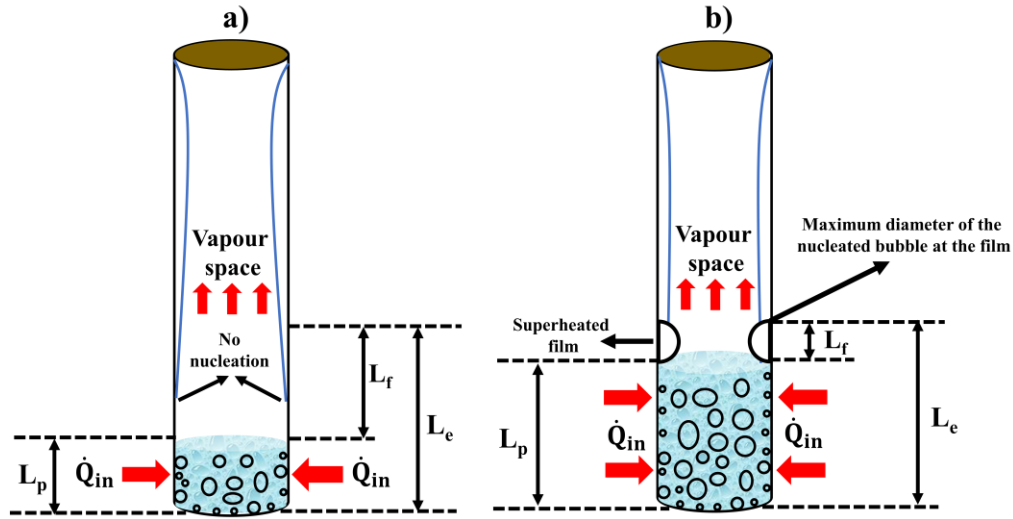


Figure 4.4 A schematic of the thin falling film boiling a) No nucleation at the falling film b) Maximum diameter of the nucleated bubble at the film.

The present analysis of $R_{NB,F}$ did not consider the effects of the liquid-vapour interfacial shear stress on the thickness of the condensate film since it is assumed that heat transfer by advection (forced motion of the liquid due to bubble generation and mixing) dominates the heat transfer through conduction. This is a reasonable assumption considering the fact that the Peclet number (Pe_F) of the film estimated as $Pe_F = Re_F Pr_l$ is $\gg 1$. However, the liquid vapour shear stress can entrain liquid particles from the film and transport them to the condenser end, which may cause the overall thermal resistance of the TS and HP to increase (Gross, 1992). Therefore, it may be essential to consider these effects through the Weber number (We), which represents the ratio of the inertial forces of the vapour (responsible for entraining the liquid droplets) and the surface tension force of the liquid resisting the entrainment. The Weber number can be estimated as

$$We = \left(\frac{\rho_v u_v^2 L}{\sigma_l} \right) \quad (4.47)$$

The characteristic length (it represents a dimension characterizing the liquid-vapour interface) in the We number is L_F for a TS, whereas for a HP it is related to the wick spacing (Reay and Kew, 2006). u_v can be estimated as

$$\mathbf{u}_v = \left(\frac{\dot{Q}_{in}}{A_{cr}\rho_v h_{fg}} \right) \quad (4.48)$$

Entrainment may occur when the We number is of the order 1 (Reay and Kew, 2006). In that case, it is reasonable to include the effects of the We number in equation (4.46). Thus, equation (4.46) in its expanded form (including We) for the two characteristics length scale scenarios give

$$R_{NB,FkD_b} = [C''_{NB,F}]^{e_1} \left[\frac{\mu_l C_{p,l}}{k_l} \right]^{f_1} \left[\frac{\delta_{eva,FG}^2 (\rho_l - \rho_v)}{\sigma} \right]^{g_1} \left[\frac{L_F}{D_b} \right]^{h_1} \left[\frac{D_i}{D_b} \right]^{h_1} \left[\frac{\dot{Q}'_{in,f} D_b}{h_{fg} \mu_l} \right]^{h_1} \left[\frac{\rho_v u_v^2 L_F}{\sigma_l} \right]^{i_1} \quad (4.49)$$

$$R_{NB,FkD_b} = [C''_{NB,F}]^{e_1} \left[\frac{\mu_l C_{p,l}}{k_l} \right]^{f_1} \left[\frac{L_F^2 g (\rho_l - \rho_v)}{\sigma} \right]^{g_1} \left[\frac{L_F}{D_b} \right]^{h_1} \left[\frac{D_i}{D_b} \right]^{h_1} \left[\frac{\dot{Q}'_{in,f} D_b}{h_{fg} \mu_l} \right]^{h_1} \left[\frac{\rho_v u_v^2 L_F}{\sigma_l} \right]^{i_1} \quad (4.50)$$

Except the first term, all the terms on the RHS of equations (4.49) and (4.50) can be estimated *a priori*, and thus, equations (4.49) and (4.50) can be used for prediction. The vapour properties should be evaluated at T_{sat} whereas the liquid properties should be evaluated at $T_{film,C}$.

The next section examines the effects of the inclination angle (θ) on the liquid pool length, L_p .

4.4 Effects of θ on the liquid pool length, L_p

While deriving the thermal resistance equations for R_{boil} , the inclination angle, θ (or any function of θ) did not appear in any of the expressions. Hence, the relevant equations from (4.25) to (4.50) are only suitable when TS and HP are oriented vertically, i.e. $\theta = 90^\circ$. However, when $0^\circ \leq \theta \leq 90^\circ$, the acceleration due to gravity along the length of the TS (or HP) and L_p will vary. This section examines this variation in more detail.

When the TS (HP) is inclined ($0^\circ \leq \theta \leq 90^\circ$), there is a buoyancy force component normal and parallel to the TS (HP) axis. The \vec{g} term appearing in the various non-dimensional terms representing the effects of the buoyancy parallel to the TS axis will be replaced by $g \sin \theta$. The influence of $g \cos \theta$ on the condensate film flow is discussed later in section 4.6. Next, the critical angles of inclinations are defined and discussed.

4.4.1 Critical angles of inclination (θ_{crit})

A critical angle of inclination (θ_{crit}) is the maximum angle of inclination (from the horizontal) below which R_{boil} can increase. For any given FR, there are two θ_{crit} defined as the first critical ($\theta_{1,\text{crit}}$) and the second critical angle ($\theta_{2,\text{crit}}$).

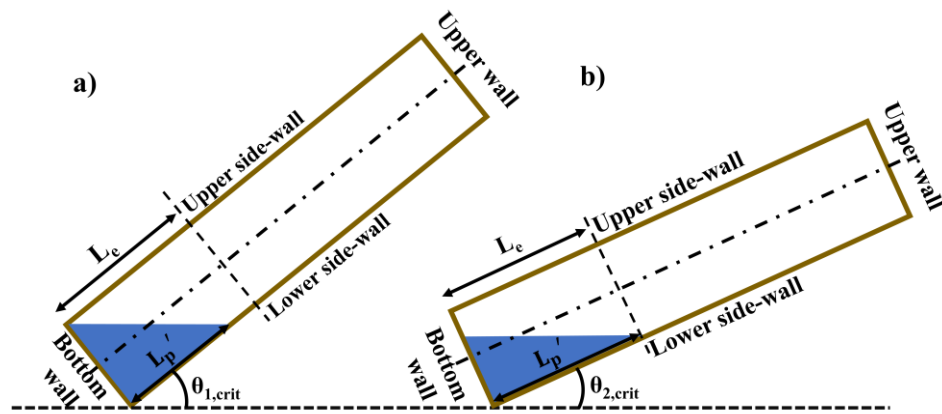
The first critical angle ($\theta_{1,\text{crit}}$) occurs when the liquid surface leaves the upper side wall of the evaporator completely and contacts the bottom wall (see Figure 4.5a and 4.5c). In this scenario, there will be no nucleation within the surface area left empty by the displaced liquid and, hence, there will no forced convection currents due to nucleation at the upper surface. The WF vapour phase will be in contact with the heater surface directly, giving rise to superheated vapour. It is hypothesized that the boiling thermal R_{boil} will increase in this configuration due to i) diffusion of heat within the vapour ii) natural convection currents within the vapour, and iii) the absence of bubble nucleation at the surface.

The second critical angle ($\theta_{2,\text{crit}}$) occurs when the liquid pool covers the entire evaporator length on the lower side wall of the evaporator (see Figure 4.5b and 4.5d) such that $L_p = L_e$. This is critical because tilting the cylinder slightly towards the horizontal plane will cause the WF to shift towards the adiabatic section (or the condenser section if the adiabatic section is absent) where no heating sources are present. Hence, a part of the WF will not contribute to any heat transfer. This may also cause the R_{boil} to increase. It is clear that when a TS or a HP is inclined, the length of the liquid pool in contact with the evaporator will change.

4.4.2 Estimates of (θ_{crit}) and modified liquid pool length (L_p')

Let the final length of the liquid pool in contact with the bottom wall be denoted by L_p' . This section examines the effects of θ on L_p' . First, the critical angles of inclination (θ_{crit}) for any given AR and FR are estimated. Second, the L_p' values for different θ ranging from 0° to 90° (including the θ_{crit}) are estimated. This analysis theoretically predicts the correct values of L_p' that can be substituted into the relevant R_{boil} equations, where L_p is used as a characteristic length.

Geometric reasoning suggests that for $0 < FR < 0.5$, $\theta_{1,crit} > \theta_{2,crit}$ (Figure 4.5a and 4.5b), whereas for $0.5 < FR < 1$, $\theta_{2,crit} > \theta_{1,crit}$ (Figure 4.5c and 4.5d). For $FR = 0.5$, $\theta_{1,crit} = \theta_{2,crit}$ (Figure 4.5e) and for $FR = 1$, $\theta_{2,crit} = 90^\circ$ and $\theta_{2,crit} > \theta_{1,crit}$ (Figure 4.5f). Utilizing the principles of trigonometry and algebra, $\theta_{1,crit}$ and $\theta_{2,crit}$ for FR ranging from 0.1 to 1 are determined. The values of $\theta_{1,crit}$ and $\theta_{2,crit}$ are summarised in Table 4.4. Examining the values of $\theta_{1,crit}$ and $\theta_{2,crit}$ from Table 4.4, it is noted that $\theta_{1,crit}$ and $\theta_{2,crit}$ are cotangent functions of both FR and AR , respectively. For $0.1 \leq FR \leq 1$, $\theta_{1,crit}$ can be expressed as $\cot^{-1}(2 \times FR \times AR)$. Similarly, $\theta_{2,crit}$ can be expressed as $\cot^{-1}\left(\frac{AR}{\sqrt{2 \times FR}}\right)$ for $0.1 \leq FR \leq 0.5$ and $\cot^{-1}(2 \times (1 - FR) \times AR)$ for $0.5 \leq FR \leq 1$. The TS and HP must operate above the critical angles of inclination for it to operate under a steady state condition. The values of L'_p estimated for different θ are summarised in Table 4.5. The expressions of L'_p for different ranges of FR are also presented which covers the entire range of scenarios that may be observed for a TS and a HP. Note that θ must be a known variable while using these equations.



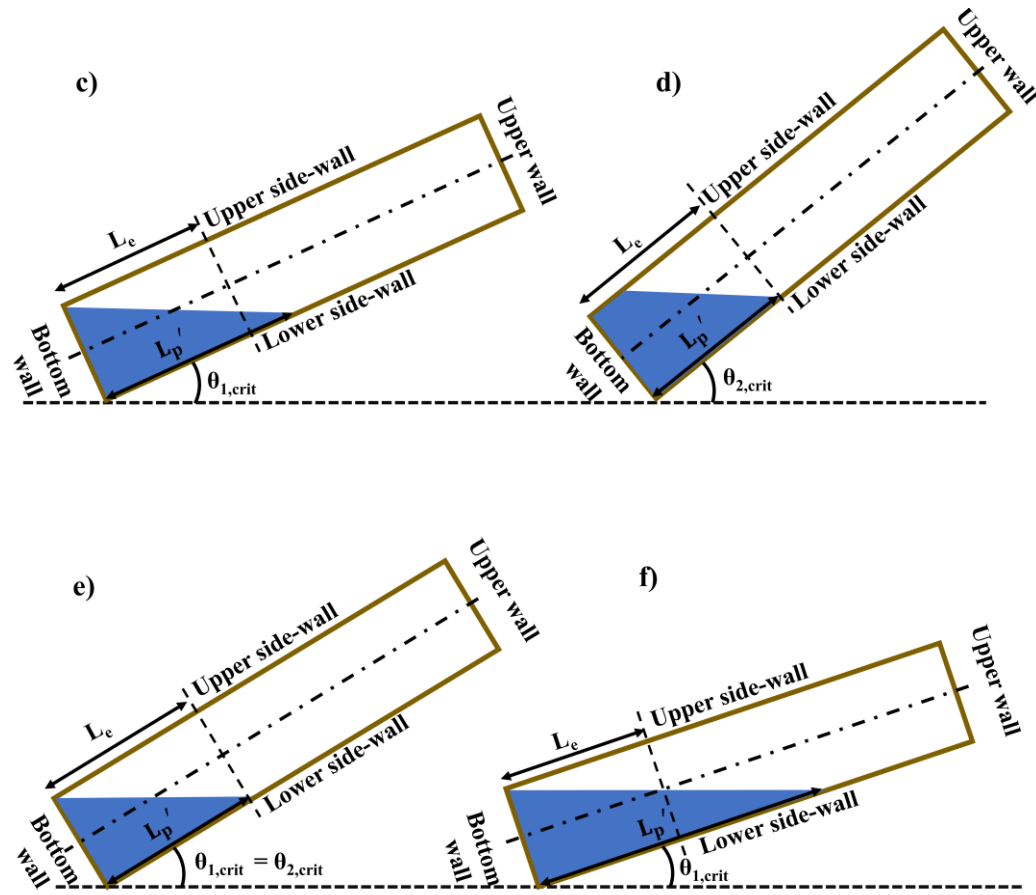


Figure 4.5 Schematic of the TS (or HP) showing a) $\theta_{1,crit}$ and b) $\theta_{2,crit}$ for $0 < FR < 0.5$ c) $\theta_{1,crit}$ and d) $\theta_{2,crit}$ for $0.5 < FR < 1$ e) $\theta_{1,crit} = \theta_{2,crit}$ for $FR = 0.5$ f) $\theta_{2,crit} = 90^\circ$, $\theta_{1,crit} < \theta_{2,crit}$ for $FR = 1$. For all the cases the rotation of the TS (HP) is in clockwise direction.

Table 4.4 Critical angles of inclination for various FR.

FR	$\theta_{1,crit}$	$\theta_{2,crit}$
0.1	$\cot^{-1} \left(\frac{0.2L_e}{D_i} \right)$	$\cot^{-1} \left(\frac{L_e}{0.45D_i} \right)$
0.2	$\cot^{-1} \left(\frac{0.4L_e}{D_i} \right)$	$\cot^{-1} \left(\frac{L_e}{0.63D_i} \right)$
0.3	$\cot^{-1} \left(\frac{0.6L_e}{D_i} \right)$	$\cot^{-1} \left(\frac{L_e}{0.77D_i} \right)$
0.4	$\cot^{-1} \left(\frac{0.8L_e}{D_i} \right)$	$\cot^{-1} \left(\frac{L_e}{0.89D_i} \right)$
0.5	$\cot^{-1} \left(\frac{L_e}{D_i} \right)$	$\cot^{-1} \left(\frac{L_e}{D_i} \right)$
0.6	$\cot^{-1} \left(\frac{1.2L_e}{D_i} \right)$	$\cot^{-1} \left(\frac{0.8L_e}{D_i} \right)$
0.7	$\cot^{-1} \left(\frac{1.4L_e}{D_i} \right)$	$\cot^{-1} \left(\frac{0.6L_e}{D_i} \right)$
0.8	$\cot^{-1} \left(\frac{1.6L_e}{D_i} \right)$	$\cot^{-1} \left(\frac{0.4L_e}{D_i} \right)$
0.9	$\cot^{-1} \left(\frac{1.8L_e}{D_i} \right)$	$\cot^{-1} \left(\frac{0.2L_e}{D_i} \right)$
1	$\cot^{-1} \left(\frac{2L_e}{D_i} \right)$	90°

Table 4.5 The modified liquid pool length, L'_p for different FR at various inclination angles. The angles have been represented in order of their magnitudes from higher to lower.

	θ	L'_p
$0 < FR < 0.5$	90°	$FR \times L_e$
	$\theta_{1,crit} < \theta < 90^\circ$	$FR \times L_e + \frac{D_i}{2 \tan \theta}$
	$\theta_{1,crit}$	$2FR \times L_e$
	$\theta_{2,crit} < \theta < \theta_{1,crit}$	$(2FR \times L_e + x_{L1})$, where x_{L1} is calculated from $\tan \theta = \left(\frac{D_i \left(\frac{2FR \times L_e}{2FR \times L_e + x_{L1}} \right)^{0.5}}{2FR \times L_e + x_{L1}} \right)$
	$\theta_{2,crit}$	L_e
	$0^\circ < \theta < \theta_{2,crit}$	$(L_e + x_{L2})$, where x_{L2} is calculated from $\tan \theta = \left(\frac{D_i \left(\frac{2FR \times L_e}{L_e + x_{L2}} \right)^{0.5}}{L_e + x_{L2}} \right)$
$FR = 0.5$	90°	$FR \times L_e$
	$\theta_{1,crit} < \theta < 90^\circ$	$FR \times L_e + \frac{D_i}{2 \tan \theta}$
	$\theta = \theta_{1,crit} = \theta_{2,crit}$	L_e
	$0^\circ < \theta < \theta_{2,crit}$	$L_e + x_{L3}$, where x_{L3} is calculated from $\tan \theta = \left(\frac{D_i \left(\frac{2FR \times L_e}{L_e + x_{L3}} \right)^{0.5}}{L_e + x_{L3}} \right)$
$0.5 < FR < 1$	90°	$FR \times L_e$
	$\theta_{2,crit} < \theta < 90^\circ$	$FR \times L_e + \frac{D_i}{2 \tan \theta}$
	$\theta_{2,crit}$	L_e
	$\theta_{1,crit} < \theta < \theta_{2,crit}$	$FR \times L_e + \frac{D_i}{2 \tan \theta}$
	$\theta_{1,crit}$	$2FR \times L_e$
	$0^\circ < \theta < \theta_{1,crit}$	$2FR \times L_e + x_{L4}$, where x_{L4} is calculated from $\tan \theta = \left(\frac{D_i \left(\frac{2FR \times L_e}{2FR \times L_e + x_{L4}} \right)^{0.5}}{2FR \times L_e + x_{L4}} \right)$
$FR = 1$	$\theta_{2,crit} = 90^\circ$	L_e
	$\theta_{1,crit} < \theta < \theta_{2,crit}$	$L_e + \frac{D_i}{2 \tan \theta}$
	$\theta_{1,crit}$	$2FR \times L_e$
	$0^\circ < \theta < \theta_{1,crit}$	$2FR \times L_e + x_{L5}$, where x_{L5} is calculated from $\tan \theta = \left(\frac{D_i \left(\frac{2FR \times L_e}{2FR \times L_e + x_{L5}} \right)^{0.5}}{2FR \times L_e + x_{L5}} \right)$

x_{L1} , x_{L2} , x_{L3} , x_{L4} and x_{L5} denote the distance travelled by the liquid at the bottom wall of the evaporator from its original position after it is inclined (see Figure 4.6).

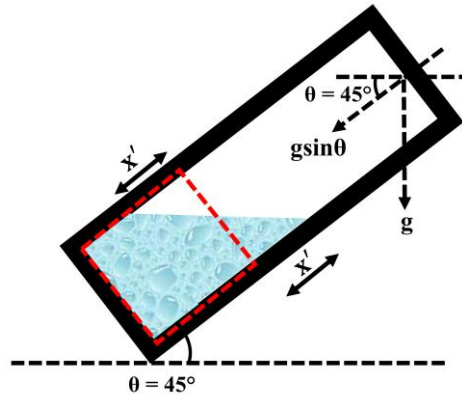


Figure 4.6 Magnified schematic image of the liquid pool within the evaporator for $\theta = 45^\circ$ showing x' . x' will be equal to x_{L1} , x_{L2} , x_{L3} , x_{L4} and x_{L5} at different θ .

The next section derives equations for the condensation thermal resistance (R_{cond}).

4.5 Development of new correlations for R_{cond}

Reflux condensation occurs inside TS and HP (Chen et al., 1984, 1987, Gross, 1992, Fiedler and Auracher, 2004). It is defined as the condensation process where vapour flows towards the condenser from the bottom through the core, whilst the condensate flows downwards concurrently under the action of gravity (Fiedler and Auracher, 2004).

The heat transfer at the surface of the condenser section may occur either through filmwise or dropwise condensation, or a combination of both these processes (Larkin, 1971, Andros, 1980, Baojin et al., 2009). A schematic of the filmwise and dropwise condensation process is shown in Figure 4.7 for completeness. Which of these processes occur depends on the condition (wettability) of the surface, i.e. the difference between the surface energy of the solid wall and the liquid condensate (Ma et al., 2000). The final expression for R_{cond} should, therefore, take into account the thermal resistances due to both filmwise and dropwise condensation depending on the surface free energy criterion. The correlations to predict the dropwise condensation resistance have been provided in Appendix D (see section D.4). The next section derives the thermal resistance of the condensate film ($R_{\text{C,F}}$).

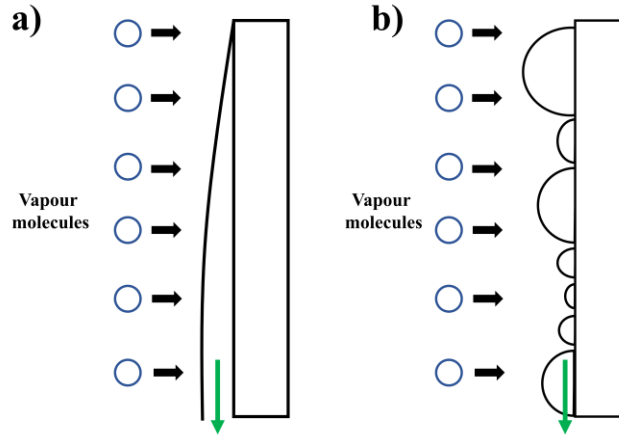


Figure 4.7 a) Filmwise condensation b) Dropwise condensation. The black arrow shows the direction of the heat transfer from the vapour molecules. The green arrow shows the direction of the flow of the film and the drop under the action of gravity.

4.5.1 Prediction equations for $R_{C,F}$

In film condensation, the primary resistance to the heat transfer ($R_{C,F}$) is caused by the thickness of the condensate film ($\delta_{C,F}$) (Chen et al., 1984, 1987, Gross, 1992) and, hence, $R_{C,F} \propto \delta_{C,F}$ (where $\delta_{C,F} \ll \frac{D_i}{2}$) (Seban and Hodgson, 1982, Spendel, 1982, Chen et al., 1984, 1987, Fiedler and Auracher, 2004). The scale of the condensate film thickness is

given as $\delta_v \sim \sqrt[3]{\frac{\mu_l^2}{g\rho_l(\rho_l - \rho_v)}}$ (Gross, 1992) (in the forgoing discussion, $\delta_v \sim \delta_{C,F}$ has been

assumed, unless otherwise specified). $\delta_{C,F}$ is affected both by the flow patterns of the condensate film (characterized by the global film Reynolds number Re_F , where $Re_F = \frac{4\rho_l u_l \delta_{C,F}}{\mu_l}$ ($= \frac{4\dot{Q}_{in}}{\pi D_i h'_{fg} \mu_l} = \frac{4\dot{Q}'_{out} L_c}{h'_{fg} \mu_l}$)) and the interfacial shear stress (τ_i) caused by the counter-current vapour flow (Colburn and Carpenter, 1951, Chen et al., 1984). The vapour flow is

characterized by the vapour flow Froude number (Fr_v), where $Fr_v = \frac{u_v^2}{gD_i}$, $u_v = \frac{4\dot{Q}_{in}}{\pi D_i^2 \rho_v h_{fg}} =$

$$\frac{4\dot{Q}'_{in} L_e}{D_i \rho_v h_{fg}} = \frac{4\dot{Q}'_{out} L_c}{D_i \rho_v h_{fg}}).$$

Three different flow patterns of the condensate film may be observed depending on Re_F . In the absence of the effects of τ_i , the flow is assumed to be laminar for $Re_F < 20$, laminar-wavy for $20 \leq Re_F \leq 1800$ and turbulent for $Re_F > 1800$ (McAdams, 1954, Chen et al., 1987, Gross, 1992, Bergman et al., 2018). However, at high τ_i , the condensate flow

becomes turbulent at $Re_F \sim 270$ for a co-current flow (Colburn and Carpenter, 1951), indicating that the effects of τ_i are prominent and, may, induce turbulence at a lower critical Re_F . The laminar-wavy flow pattern is found to decrease the average $\delta_{C,F}$ due to a reduction of $\delta_{C,F}$ between the wave crests (Figure 4.8) (Colburn and Carpenter, 1951, Gross, 1992). The presence of waves also increases the surface area, which enhances heat transfer (Chen et al., 1987, Collier and Thome, 1999). Hence, the overall $R_{C,F}$ decreases for $20 \leq Re_F \leq 1800$. Although $\delta_{C,F}$ increases in the turbulent flow regime, the momentum and energy exchange are vigorous which exceeds the effects of increasing $\delta_{C,F}$ (Gross, 1992). Thus, $R_{C,F}$ decreases for $Re_F > 1800$.

A finite τ_i decelerates the condensate film causing $\delta_{C,F}$ to increase and, consequently $R_{C,F}$. In summary, it can be concluded that the interfacial waviness and τ_i have an opposite influence on $\delta_{C,F}$ and, hence, on $R_{C,F}$. Therefore, the formulation of $R_{C,F}$ should include both the effects of surface waviness through Re_F and τ_i on it.



Figure 4.8 Schematic showing reduction of the average condensate film thickness due to the reduction of $\delta_{C,F}$ between the wave-crests. $\delta_{C,F,Red}$ is the reduced value of $\delta_{C,F}$.

Similar to the boiling thermal resistance, the condensation thermal resistance for a film flow ($R_{C,F}$) could be a function of a) the difference between the saturation and the average inner condenser surface temperature, ΔT , (where $\Delta T = |T_{sat} - T_s|$, T_s and T_{sat} refer to the surface and the saturation temperature, respective) b) $g(\rho_l - \rho_v)$, c) the latent heat, h_{fg} , d) the interfacial shear stress, τ_i , caused by the counter-current vapour flow e) a characteristic length, L and f) the thermophysical properties of the WF (ρ , c_p , k , μ). $R_{C,F}$

is considered to be independent of σ for filmwise condensation as the surface tension effects on the condensate flow are considered minimal, assuming that the falling condensate completely wets the condenser walls. Thus, $R_{C,F} = f(\Delta T, g(\rho_l - \rho_v), h_{fg}, L, \rho, c_p, k, \mu, \tau_i)$. Since there are 10 variables and 4 primary dimensions, a total of 6 non-dimensional π terms can be established. Dimensional analysis yields

$$\pi_1 = Lc_p\mu R_{cond} \quad (4.51)$$

$$\pi_2 = \frac{c_p\mu^2\Delta T}{L^4[g(\rho_l - \rho_v)]^2} \quad (4.52)$$

$$\pi_3 = \frac{\mu^2 h_{fg}}{L^4[g(\rho_l - \rho_v)]^2} \quad (4.53)$$

$$\pi_4 = \frac{L^3\rho[g\sin\theta(\rho_l - \rho_v)]}{\mu^2} \quad (4.54)$$

$$\pi_5 = \frac{k}{\mu c_p} \quad (4.55)$$

$$\pi_6 = \frac{\tau_i}{Lg[\rho_l - \rho_v]} \quad (4.56)$$

π_5 can be re-written as π'_5 where $\pi'_5 = \frac{1}{\pi_5}$. Similarly, $\frac{\pi_2}{\pi_3} = \pi_7 = \frac{c_p\Delta T}{h_{fg}}$, $\pi_1\pi_5 = \pi_8 = R_{C,F}kL$.

The relevant π terms influencing $R_{C,F}$ and their definition is outlined in Table 4.6.

Table 4.6 Definition of the various π terms influencing $R_{C,F}$.

π terms	Definition
π_4	Archimedes number
π'_5	Prandtl number
π_6	Non-dimensional interfacial shear stress
π_7	Jakob number
π_8	Non-dimensional condensation resistance

A generic expression of $R_{C,F}$ can, therefore, be formulated as a function of these π terms as

$$\pi_8 = f(\pi_4, \pi'_5, \pi'_6, \pi_7) \quad (4.57)$$

or,
$$R_{C,F}kL = f[Ar, Pr, Ja, \tau_i^*] \quad (4.58)$$

Similar to the derivation of R_{boil} , a power law approach (Churchill and Usagi, 1972) may be used for formulating the expressions of $R_{C,F}$ under the effects of τ_i .

4.5.1.1 Shear free condensation

At very low u_v , i.e., for $Fr_v \leq 1$, no appreciable τ_i at the liquid vapour interface exists (Takuma et al., 1983, Chen et al., 1984, Gross, 1992). $R_{C,F}$, in this case, can, therefore, be represented as

$$R_{C,F}kL = C_{C,F}[Ar]^{j_1}[Pr]^{k_1}[Ja]^{l_1} \quad (4.59)$$

where $R_{C,F}$ is the film condensation thermal resistance in the absence of shear effects, $C_{C,F}$ and j_1 , k_1 and l_1 are constants defined as the thermal resistance coefficient and exponents of shear-free filmwise condensation, respectively. The inclusion of the Archimedes number is based on the fact that the condensate film is now solely driven by gravity and retarded by wall shear stress due to viscosity. The Prandtl number represents the effects of momentum diffusivity and thermal diffusivity on $R_{C,F}$, whilst the Jakob number represents the transfer of the latent heat of vapourization released to the condenser surface.

There are two possible characteristic lengths here, L_c and $\delta_{C,F}$. Since $\delta_{C,F}$ cannot be the characteristic length for the Ar term (the Ar term will yield unity in that case), L_c is appropriate. The resistance to the heat transfer across the film is caused by $\delta_{C,F}$ and, thus, $\delta_{C,F}$ may be suitable as a characteristic length for the non-dimensional $R_{C,F}$ term. As the flow pattern of the condensate film is governed by Re_F in the absence of τ_i , it is appropriate to express equation (4.59) in terms of Re_F as

$$R_{C,F}k\delta_{C,F} = [C'_{C,F}]^{m_1}[Ar_1]^{n_1}[Pr_1]^{o_1} \left[\frac{D_i}{\delta_{C,F}} \right]^{p_1} [Re_F]^{p_1} \quad (4.60)$$

where $C'_{C,F} = \left[\left(\frac{\pi}{4} \right)^{l_1} C_{C,F} \right]$, $m_1 = \frac{1}{(1-l_1)}$, $n_1 = \frac{j_1}{(1-l_1)}$, $o_1 = \frac{k_1+l_1}{(1-l_1)}$, and $p_1 = \frac{l_1}{(1-l_1)}$, respectively.

It is expected that the related coefficient and exponents of equations (4.59) and (4.60) would be different for different ranges of Re_F describing the flow patterns of the condensate flow.

4.5.1.2 Sheared condensation

For $Fr_v \geq 5$, effects of τ_i on $R_{C,F}$ may be present (Spendel, 1982, Gross, 1992). $R_{C,F}$ in the presence of τ_i can, therefore, be represented as

$$R_{C,F,S}k_iL = C_{C,F,S}[Ar]^{a_2}[Pr]^{b_2}[Ja]^{c_2}[\tau_i^*]^{d_2} \quad (4.61)$$

where $R_{C,F,S}$ (the additional subscript ‘‘S’’ in $R_{C,F}$ represents shear) is the film condensation thermal resistance in the presence of τ_i , $C_{C,F,S}$ and a_2 , b_2 , c_2 and d_2 are constants defined as the thermal resistance coefficient and exponents of sheared filmwise condensation, respectively. The characteristic length in the non-dimensional $R_{C,F,S}$ and Ar terms is the same as discussed for equation (4.60). The (gL) term in the denominator of τ_i^* term (see equation 4.56) can be replaced by $\left(\frac{g\mu_l}{\rho_l}\right)^{2/3}$ (derived from the arithmetic manipulation of the interface Reynolds number (Re_I), where $Re_I = \left(\frac{\rho_l u_i L_i}{\mu_l}\right)$ and u_i is the interface velocity).

The criteria $Fr_v \geq 5$ and the ranges of Re_F are not suitable for categorizing the effects of τ_i on $R_{C,F,S}$ (see the discussion in sections 3.2, 3.3 and 5.3 in Gross, 1992). Therefore, a vapour flow Reynolds number Re_v , where $Re_v = \frac{\rho_v v_v D_i}{\mu_v} = \frac{4\dot{Q}_{in}}{\pi D_i h_{fg} \mu_v}$, may be suitable for categorizing the varying effects of τ_i at different vapour flow conditions. Spindel (1982) confirmed that for Re_v as low as 1250, the average $R_{C,F,S}$ decreases only by up to 4% in the presence of τ_i due to flow reversal. Conservatively, it can be assumed that for $Re_v < 1250$, the decrement in $R_{C,F,S}$ due to τ_i would be minimal ($< 4\%$). Equation (4.61) can now, be expressed in terms of Re_v as

$$R_{C,F,S}k_i\delta_{C,F} = [C'_{C,F,S}]^{e_2}[Ar_1]^{f_2}[Pr_1]^{g_2}\left[\frac{\mu_v}{\mu_l}\right]^{h_2}\left[\frac{D_i}{\delta_{C,F}}\right]^{h_2}[Re_v]^{h_2}[\tau_i^*]^{i_2} \quad (4.62)$$

where $C'_{C,F,S} = \left[\left(\frac{\pi}{4}\right)^{w_1} C_{C,F,S}\right]$, $e_2 = \frac{1}{1-c_2}$, $f_2 = \frac{a_2}{1-c_2}$, $g_2 = \frac{b_2+c_2}{1-c_2}$, $h_2 = \frac{c_2}{1-c_2}$ and $i_2 = \frac{d_2}{1-c_2}$, and the characteristic length in the Ar term is L_c . Equation (4.61) can also be represented in terms of Re_F as

$$R_{C,F,S}k_i\delta_{C,F} = [C'_{C,F,S}]^{e_2} [Ar_1]^{f_2} [Pr_1]^{g_2} \left[\frac{D_i}{\delta_{C,F}} \right]^{h_2} [Re_F]^{h_2} [\tau_i^*]^{i_2} \quad (4.63)$$

It is expected that the related coefficient and exponents of equations (4.62 - 4.63) estimated from the experimental data would be different for different regimes of the vapour flow. Which equation among (4.62) and (4.63) best represents the film thermal resistance data in the presence of τ_i in different vapour flow regimes cannot be determined theoretically and, therefore, need to be evaluated against the experimental data.

Two different formulations of τ_i^* are available in the literature. Chapter 1 shows the formulation of τ_i^* based on Brauer (1971). τ_i^* based on the Lockhart-Martinelli correlation (Dukler, 1960) is shown in Appendix D (section D.5). It is not known which correlation of τ_i^* is suitable for predicting $R_{C,F}$. A comparison of these formulations against the present experimental data reveal that τ_i^* estimated from Lockhart-Martinelli correlation is lower in comparison to τ_i^* values estimated using Brauer (1971). Such low values of τ_i^* are unreasonable considering that the effects of τ_i^* are significant in film condensation of water in vertical tube with countercurrent vapour flow (Thumm et al., 2001). Gross (1992) noted that for $\tau_i^* < 0.1$, no effects of τ_i^* on the heat transfer rate are observed. Thus, for $\tau_i^* < 0.1$, equation (4.60) should be used for predicting $R_{C,F}$ and *vice-versa*.

While deriving equations (4.59 - 4.63), certain aspects of $R_{C,F}$, were not taken into account. Those can be broadly classified into two effects, i.e., a) the effects of the sensible heat and the temperature distribution and b) the effects of θ . The effects of the sensible heat transfer on $R_{C,F}$ are discussed briefly in Appendix D (section D.6). The next section examines the effects of θ on $R_{C,F}$.

4.6 Effects of θ on $R_{C,F}$

When the TS is inclined, the film flow is two-dimensional. The effects of the inclination angle, θ on $R_{C,F}$ can, thus, be classified into two categories, a) the emergence of new flow regimes under the action of gravity at $0^\circ \leq \theta < 90^\circ$ and b) the circumferential variation of the condenser temperature.

When $0^\circ \leq \theta < 90^\circ$, two additional flow regimes will arise under the influence of gravity. Those are i) the flow of the condensate along the circumference of the tube due to the gravitational force component $g \sin \Phi \cos \theta$ (Φ is defined as the angular position of the condensate layer from the top of the cylinder) and ii) the axial flow of the condensate accumulated at the bottom of the tube due to the gravitational force component $g \sin \theta$. The flow regimes are shown schematically in Figure 4.9, where x , y and z denote the axial, normal and circumferential coordinates, respectively. Therefore, additional terms within $R_{C,F}$ equations may need to be included to represent these effects. These effects are analyzed in the next section. The effects of the circumferential flow are treated first, followed by the effects of the bottom condensate flow on $R_{C,F}$.

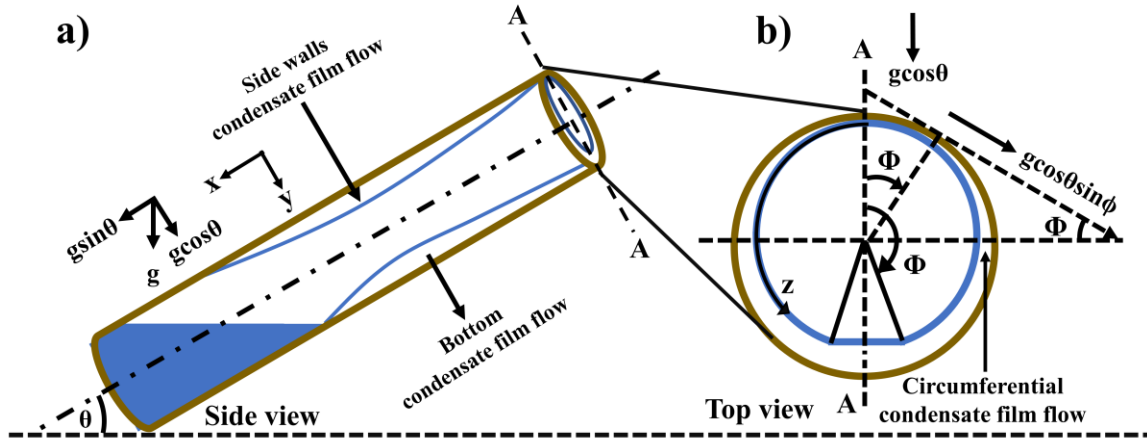


Figure 4.9 a) Schematic of the axial condensate film flow along the side walls. The decrement of the film thickness towards the evaporator section is typical. It may occur when the evaporator liquid pool is not sufficient, and the liquid film condensate starts to dry out. b) Schematic of the condensate film flow in the circumferential direction. x represents the direction along the tube in the downward direction, and the y direction is perpendicular to the fluid.

4.6.1 Effects of circumferential condensate film flow

The primary objective of this section is to obtain expressions of $\delta_{C,F}$ under the influence of the circumferential condensate flow. Hassan and Jakob (1958) and Fiedler and Auracher (2004) have derived a theoretical model for circumferential laminar condensate film flow on a finite inclined cylinder using Nusselt's (1916) assumptions of filmwise condensation. The model is rederived in Appendix D for completeness. The model gives the non-dimensional local film thickness, ψ as a function of X and Φ and is given as

$$\frac{\partial \Psi}{\partial X} + \sin \Phi \frac{\partial \Psi}{\partial \Phi} = \frac{4}{3} (1 - \Psi \cos \Phi) \quad (4.64)$$

where Φ is the peripheral angle of the condensate layer ($\Phi \rightarrow 0$ represents the top of the tube, whilst, $\Phi \rightarrow 180^\circ$ represents the bottom of the tube; see Figure 4.10a), X is defined as the dimensionless condenser length ($X = \left(\frac{2L_c}{D_i} \frac{1}{\tan \theta} \right)$), and ψ is defined as the dimensionless film thickness ($\psi = \frac{2\rho_l(\rho_l - \rho_v)gh_{fg}\delta_{C,F}^4 \cos \theta}{3k_l \Delta T D_i \mu_l}$). Equation (4.64) can be solved subject to the boundary conditions; at $X = 0$, $\Psi = 0$ (the condensate thickness at the topmost edge of the condenser being zero i.e. $\Psi = 0$ at $L_c = 0$), and at $\Phi = 0^\circ$ and 180° , $\frac{\partial \Psi}{\partial \Phi} = 0$ (due to the symmetry of the condensate film at $\Phi = 0^\circ$ and 180°). The numerical solution of ψ for various X and Φ values are presented in Hassan and Jakob (1958) and are listed in Appendix D (Table D.8) for completeness.

Two different sets of solutions are particularly relevant i.e. when $X > 3.2$ and the other when $X \leq 3.2$. Hassan and Jakob (1958) showed that the circumferentially and axially averaged heat transfer coefficient values of the condensate film corresponding to $X > 3.2$ are within 2% of those at $X \rightarrow \infty$ (see Figure 9 in Hassan and Jakob, 1958). Thus, for $X > 3.2$, the condensation can be assumed to be equivalent to that occurring in an infinitely long condenser, i.e., $\frac{L_c}{D_i} \approx \infty$. It is also evident that the differential equation for the film thickness in a horizontal cylinder is the same as that in an infinitely long inclined cylinder (since $\frac{\partial \psi}{\partial X} = 0$ at $X = \infty$ and $\frac{\partial \psi}{\partial X} = 0$ at $\theta = 0^\circ$). Thus, ψ can be treated as a constant and, if all the other variables in ψ remain fixed, then $\delta_{C,F}$ varies as $\delta_{C,F} \propto (\cos \theta)^{-\frac{1}{4}}$. Since $R_{C,F} \propto \delta_{C,F}$, $R_{C,F}$ may be considered to be directly proportional to $(\cos \theta)^{-\frac{1}{4}}$ for $X > 3.2$ for $90^\circ > \theta > 0^\circ$. This demonstrates that $R_{C,F}$ decreases with decreasing θ . This is consistent with the findings of Chaddock (1957) and Fiedler and Auracher (2004), who showed that the heat transfer rate is greater in the inclined position than in the vertical.

For cases where $X \leq 3.2$ and $90^\circ > \theta > 0^\circ$, the estimation of $\delta_{C,F}$ is complex since all the terms of equation (4.64) are now retained, and ψ is now a function of both X and Φ . As expected, the dimensionless film thickness ψ increases with both X and Φ (see Table D.8

in Appendix D). In order to estimate $\delta_{C,F}$, the first step is to determine the magnitude of X (denoted as X_f) and Φ (denoted as Φ_f) corresponding to the operating D_i , L_c and θ using $X = \left(\frac{2L_c}{D_i} \frac{1}{\tan\theta}\right)$. Φ_f can be estimated using the procedure outlined in Chato (1960) (described in the next section). Then, ψ need to be solved at X_f for various Φ values ranging from 0° to Φ_f , and subsequently at Φ_f for various X values ranging from 0 to X_f using equation (5.64). The solution would look as illustrated in Table 4.7. From ψ obtained at various X and Φ values, $\delta_{C,F}$ can be estimated as $\delta_{C,F} = \left[\frac{3\psi k_l \Delta T D_i \mu_l}{2\rho_l(\rho_l - \rho_v) g h_{fg} \cos\theta} \right]^{0.25}$. This would give $\delta_{C,F}$ as a function of both X and Φ , i.e. $\delta(X, \Phi)$ at a given θ (see Table 4.7). The circumferentially and axially averaged δ ($\delta_{\text{avg}, \Phi, X}$; the subscript C,F is dropped for convenience) can then be estimated as $\delta_{\text{avg}, \Phi, X} = \frac{1}{\Phi_f} \frac{1}{X_f} \iint_{0,0}^{\Phi_f, X_f} \delta(X, \Phi) d\Phi dX$. Since $R_{C,F}$ is proportional to $\delta_{\text{avg}, \Phi, X}$, therefore, $R_{C,F} \propto \frac{1}{\Phi_f} \frac{1}{X_f} \iint_{0,0}^{\Phi_f, X_f} \delta(X, \Phi) d\Phi dX$ for $X \leq 3.2$ for $90^\circ > \theta > 0^\circ$.

Table 4.7 Table illustrating the solution of the partial differential equation at X_f for $0^\circ \leq \Phi \leq \Phi_f^\circ$ and at Φ_f° for $0 \leq X \leq X_f$.

X_f						
Φ	0°	Φ_1°	Φ_2°	Φ_f°
ψ_Φ	ψ_{Φ_1}	ψ_{Φ_1}	ψ_{Φ_1}	ψ_{Φ_f}
δ_Φ	δ_{Φ_1}	δ_{Φ_2}	δ_{Φ_3}	δ_{Φ_f}
Φ_f°						
X	0	X_1	X_2	X_f
ψ_X	0	ψ_{X_1}	ψ_{X_1}	ψ_{X_f}
δ_X	0	δ_{X_2}	δ_{X_3}	δ_X

It is important that two new criteria now be established so that one can operate the TS/HP with different L_c at various θ as desired. For a fixed L_c and D_i , if θ is such that $0^\circ < \theta < \tan^{-1}\left(0.625 \frac{L_c}{D_i}\right)$, then condensation can be thought of as occurring on an infinitely long L_c . Whereas if $90^\circ > \theta \geq \tan^{-1}\left(0.625 \frac{L_c}{D_i}\right)$, then condensation can be assumed to be occurring over finite L_c . Similarly, for a fixed θ and D_i , if $L_c > (1.6D_i \tan\theta)$, then L_c is infinite, whereas if $L_c \leq (1.6D_i \tan\theta)$, then L_c is finite. Both criteria establish that the same TS/HP may act as an infinitely long inclined cylinder or a finite length inclined cylinder depending upon the values of θ and L_c .

At $\theta = 90^\circ$, there is no circumferential flow; hence, none of these additional terms will exist in the final expression of $R_{C,F}$. At $\theta = 0^\circ$, $X = \infty$ and $\delta_{C,F} \propto 1$ (using $\delta_{C,F} \propto (\cos\theta)^{-\frac{1}{4}}$). Therefore, at $\theta = 0^\circ$, no additional effects of the circumferential flow using the above approach are obtained on $R_{C,F}$. The effects of the circumferential flow at $\theta = 0^\circ$, therefore, must be predicted using a different method.

Chato (1960), using Nusselt's (1916) assumptions, showed that the condensation heat transfer coefficient for a horizontal tube (i.e. $\theta \approx 0^\circ$) is directly proportional to $\left[\int_0^\Phi \sin^{1/3} \Phi d\Phi \right]^{3/4}$ (this has been derived using the first approximation of the momentum and the energy equations for the condensate flow in Chato, 1960). Therefore, $R_{C,F} \propto \left[\int_0^\Phi \sin^{1/3} \Phi d\Phi \right]^{-3/4}$ for a horizontal tube. This relation can be extended to inclined tubes by considering Φ as a function of θ . The problem then essentially reduces to estimating Φ for different θ and subsequently computing $\left[\int_0^\Phi \sin^{1/3} \Phi d\Phi \right]^{-3/4}$. The procedure to estimate Φ for different θ are outlined in the next section.

4.6.2 Effects of the bottom condensate flow

If vapour shear is relatively low, the condensate forming on the side walls may collect at the bottom of the condenser section and starts flowing axially when $90^\circ < \theta \leq 0^\circ$. A schematic of this flow condition with all the geometric variables is shown in Figure 4.10. The variables are defined in Table 4.8.

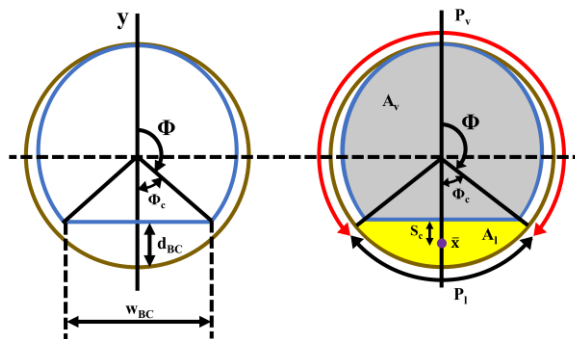


Figure 4.10 Geometry of the bottom condensate flow with all the geometrical variables annotated. The black and the red double arrow curve shows the wetted perimeter of the bottom condensate (P_l) and the vapour (P_v), respectively. The yellow (A_l) and the grey coloured (A_v) area shows the wetted cross-sectional area of the bottom condensate and the vapour, respectively. \bar{x} denotes the centroid of the circular segment formed by the bottom condensate flow.

Table 4.8 Definition of the geometrical parameters associated with the bottom condensate flow

Variable	Definition	Equation
Φ_C	Central half angle subtended by the bottom condensate	$\Phi_C = (180^\circ - \Phi)$
$\Phi_{C,M}$	Mean of the various central half angle along the condenser length	$\Phi_{C,M} = \frac{1}{N} \sum_{i=1}^N \Phi_C$
Φ_M	Mean peripheral angle of the condensate	$\Phi_M = (180^\circ - \Phi_{C,M})$
w_{BC}	Width of the bottom condensate	$w_{BC} = D_i \sin \Phi_C$
d_{BC}	Depth of the bottom condensate	$d_{BC} = \frac{D_i}{2} (1 - \cos \Phi_C)$
P_l	Wetted perimeter of the bottom condensate	$P_l = D_i \Phi_C$
P_v	Wetted perimeter of the vapour/side wall condensate	$P_v = D_i (\pi - \Phi_C + \sin \Phi_C)$
A_l	Wetted cross-sectional area of the bottom condensate	$A_l = \frac{D_i^2}{4} \left(\Phi_C - \frac{\sin(2\Phi_C)}{2} \right)$
A_v	Wetted cross-sectional area of the vapour	$A_v = \frac{D_i^2}{4} \left(\pi - \Phi_C + \frac{\sin(2\Phi_C)}{2} \right)$
Re_l	Reynolds number of the liquid flow	$Re_l = \frac{4\rho_l Q_l}{\mu_l P_l}$
Re_v	Reynolds number of the liquid flow	$Re_v = \frac{4\rho_v Q_v}{\mu_v P_v}$
$\frac{8A_l S_c}{D_i^3}$	Function appearing in equation (4.67)	$\frac{2}{3} \sin^3 \Phi_C - \cos \Phi_C \left(\Phi_C - \frac{\sin(2\Phi_C)}{2} \right)$
x^+	Dimensionless distance in the x-direction	$x^+ = \frac{x}{L_c}$

The depth of the bottom condensate axial flow (d_{BC}) is typically greater than the average condensate film thickness on the side wall (Chato, 1960). It has been shown, quantitatively, that the heat transfer through d_{BC} is negligible compared to the heat transferred through the side wall condensate film (see Figure 4.4 in Chato, 1960). Hence, the effect of d_{BC} is to reduce the effective heat transfer area (A_{eff} , where $A_{eff} = A_v$) in the condenser section. In other words, the bottom condensate axial flow increases $R_{C,F}$. The magnitude of d_{BC} decreases as θ increases (Chato, 1960), indicating a decrease in $R_{C,F}$. This improvement is counteracted by the effects of θ on the circumferential condensate flow, which demonstrates that as θ increases $R_{C,F}$ increases. If d_{BC} can be estimated, then A_{eff} area may also be determined. Both d_{BC} and A_{eff} are functions of Φ and, thus, in order to predict d_{BC} and A_{eff} , Φ needs to be estimated first. The next paragraph demonstrates the procedures to estimate Φ when $\theta = 0^\circ$ followed by the evaluation of Φ when $0^\circ < \theta < 90^\circ$.

The estimation of Φ at $\theta = 0^\circ$ is based on an *ad-hoc* procedure. It starts with an assumption of a constant mean central half angle, $\Phi_{C,M}$ (for e.g. 60°) and, subsequently, finding Φ_M , which is $180^\circ - 60^\circ = 120^\circ$. Using Φ_M value, Ω_l from equation (4.65) can be calculated as

$$\Omega_1 = 2 \left[\frac{g(\rho_l - \rho_v) k_f^3 D_1^3 (\Delta T)^3}{24 \mu_1 \rho_1^3 h_{fg}^3 \left(1 + 0.68 \frac{c_p \Delta T}{h_{fg}} \right)^3} \right]^{\frac{1}{4}} \left[\frac{4}{3} \int_0^\Phi \sin^{\frac{1}{3}} \Phi_M d\Phi_M \right]^{\frac{3}{4}} \quad (4.65)$$

where Ω_1 is the axial change in the liquid volumetric flow rate ($\Omega_1 = \frac{dQ_1}{dx}$). Thereafter, Q_1 can be calculated as $Q_1 = \Omega_1 L_c$, where Q_1 is the liquid volumetric flow rate. Using the Q_1 value, Φ_C at the outlet of the condenser can be estimated using the critical depth theory from the relation

$$\frac{(2\Phi_C - \sin 2\Phi_C)^3}{\sin \Phi_C} = 16 \left(\frac{\alpha}{\beta} \right) \frac{Q_1^2}{g \left(\frac{D_1}{2} \right)^5} \quad (4.66)$$

where α and β are constants. For laminar condensate flow i.e., $Re_1 < 3000$, $\sqrt{\frac{\alpha}{\beta}} \approx 1.414$, whereas for $Re_1 > 3000$, $\sqrt{\frac{\alpha}{\beta}} \approx 1.1$ (Chato, 1960). For $\frac{Q_1}{\sqrt{g \left(\frac{D_1}{2} \right)^5}} < 0.08$, Φ_C remains constant at 45° (Chato, 1960). The estimated accuracy of equation (4.66) as demonstrated in Chato (1960) is $\pm 3\%$ for Q_1 and $\pm 3^\circ$ for Φ_C . For fluids similar to Refrigerant-113, $\Phi_{CM} \approx 60^\circ$ up to $\frac{Q_1}{\sqrt{g \left(\frac{D_1}{2} \right)^5}} = 0.2$ (see Figure 7.1 in Chato, 1960). Thereby, Φ_M can be calculated as $(180^\circ - \Phi_{CM})$. Once Φ_M is known at the outlet of the condenser end, Φ_M along the condenser length needs to be estimated. This can be done by estimating Φ_C from the stepwise integration of equation (4.67) starting from the outlet end of the condenser, i.e., $x^+ = 1$ and proceeding along the condenser length.

$$d \left(\frac{8A_1 S_c}{D_1^3} \right) = \left\{ \frac{8A_1 \sin \theta}{D_1^3} + \frac{0.034 \Omega_1^2 \rho_1 (L_c - x)^2 w_{BC}}{A_v^2 \rho_v g D_1^3} - \frac{18 \mu_1 \Omega_1 x P_1^2}{A_1^2 \rho_1 g D_1^3} + \frac{8A_1 \rho_1 \Omega_1^2}{A_v^2 \rho_v g D_1^3} \left[\frac{0.00425 P_v (L_c - x)^2}{A_v} - 2(L_c - x) \right] - \frac{21.28 \Omega_1^2 x}{A_1 g D_1^3} \right\} dx \quad (4.67)$$

Integrating both sides of equation (4.67) over x^+ from position 1 to 2 (limits of x^+ may range from 1 to 0.8 for example), one obtains the following LHS and RHS terms as (see equations 4.68)

LHS term:

$$\frac{8A_1S_c}{D_1^3} \Big|_2 - \frac{8A_1S_c}{D_1^3} \Big|_1 \quad (4.68a)$$

RHS terms :

$$\text{Term I:} \quad \left[\frac{8L_c}{D_i} \right] \left[\frac{A_1}{D_1^2} \right] [\sin\theta] [x^+]^2 \quad (4.68b)$$

$$\text{Term II:} \quad -0.011 \left[\frac{\rho_l}{\rho_v} \right] \left[\frac{\Omega_1^2 L_c^2}{g D_1^5} \right] \left[\frac{L_c}{D_i} \right] \left[\frac{D_1^2}{A_v} \right]^2 [\sin\Phi_c] [(1-x^+)^3]_1^2 \quad (4.68c)$$

$$\text{Term III:} \quad -9 \left[\frac{\Omega_1^2 L_c^2}{g D_1^5} \right] \left[\frac{\mu_1}{\rho_l \Omega_1} \right] \left[\frac{D_1 P_1}{A_1} \right]^2 [x^{+2}]_1^2 \quad (4.68d)$$

$$\text{Term IV:} \quad 8 \left[\frac{\rho_l}{\rho_v} \right] \left[\frac{\Omega_1^2 L_c^2}{g D_1^5} \right] \left[\frac{A_1}{D_i^2} \right] \left[\frac{D_1^2}{A_v} \right]^2 \left[(1-x^+)^2 - 0.001417 [L_c] \left[\frac{P_v}{A_v} \right] (1-x^+)^3 \right]_1^2 \quad (4.68e)$$

$$\text{Term V:} \quad 10.64 \left[\frac{\Omega_1^2 L_c^2}{g D_1^5} \right] \left[\frac{D_1^2}{A_1} \right] [x^{+2}]_1^2 \quad (4.68f)$$

Note that term I on the RHS of the equation 4.68 is zero at $\theta = 0^\circ$. Φ_c at location 2 can be obtained from $\frac{8A_1S_c}{D_1^3} \Big|_2$ using the expression shown in the second last row of Table 4.8.

Following the same procedure, Φ at different locations (the limits of integration may vary from $x^+ = 0.8$ to 0.5 , $x^+ = 0.5$ to 0.2) along the condenser length can be obtained. If the mean value of Φ (Φ_M) over the entire length of the condenser is within 10° of the assumed Φ_M (this criterion has been put forward by Chato, 1960), then the agreement may be considered satisfactory. If not, then a new value of $\Phi_{C,M}$ should be assumed, and the above procedure repeated until an appropriate final value of Φ is obtained.

Since Φ at various θ ranging between $0^\circ < \theta < 90^\circ$ needs to be estimated, a function relating Φ and θ needs to be developed and plotted. This could be done following a similar procedure as described above. Assuming a value of $\Phi_{C,M}$, the corresponding Φ_M can be obtained. Ω_1 can then be calculated using equation (4.65). Experimental observations by Chato (1960) revealed that d_{BC} is mostly uniform along the length of the tube when $0^\circ < \theta < 90^\circ$ (see page 63 in Chato, 1960). Thus, the variations of the cross-sectional area A_1 can be neglected such that $d \left(\frac{8A_1S_c}{D_1^3} \right) \approx 0$ in equation (4.67). Using the value of Ω_1 , θ for the assumed Φ_M can be estimated from equation 4.68b by solving equations (4.68b – 4.68f), setting the integrating from the x^+ limits from $x^+ = 0.5$ and $x^+ = 1$ (Chato, 1960 showed that the results are not sensitive to the limits chosen and $x^+ = 0.5$

to 1 gives the best value). Using the same technique, θ corresponding to different assumed Φ_M can be estimated. Fitting the θ and Φ_M data sets will give a $\theta - \Phi_M$ curve (see Figure 4.11 which has been adapted from Chato, 1960), which can then be utilized to find Φ_M corresponding to the inclination angle θ at which the TS or the HP is operating. If the value of Φ_M is within 3° of the assumed Φ_M , then the agreement is satisfactory. If not, a new value of Φ_{CM} must be assumed, and the abovementioned procedure needs to be repeated to find the suitable Φ_M .

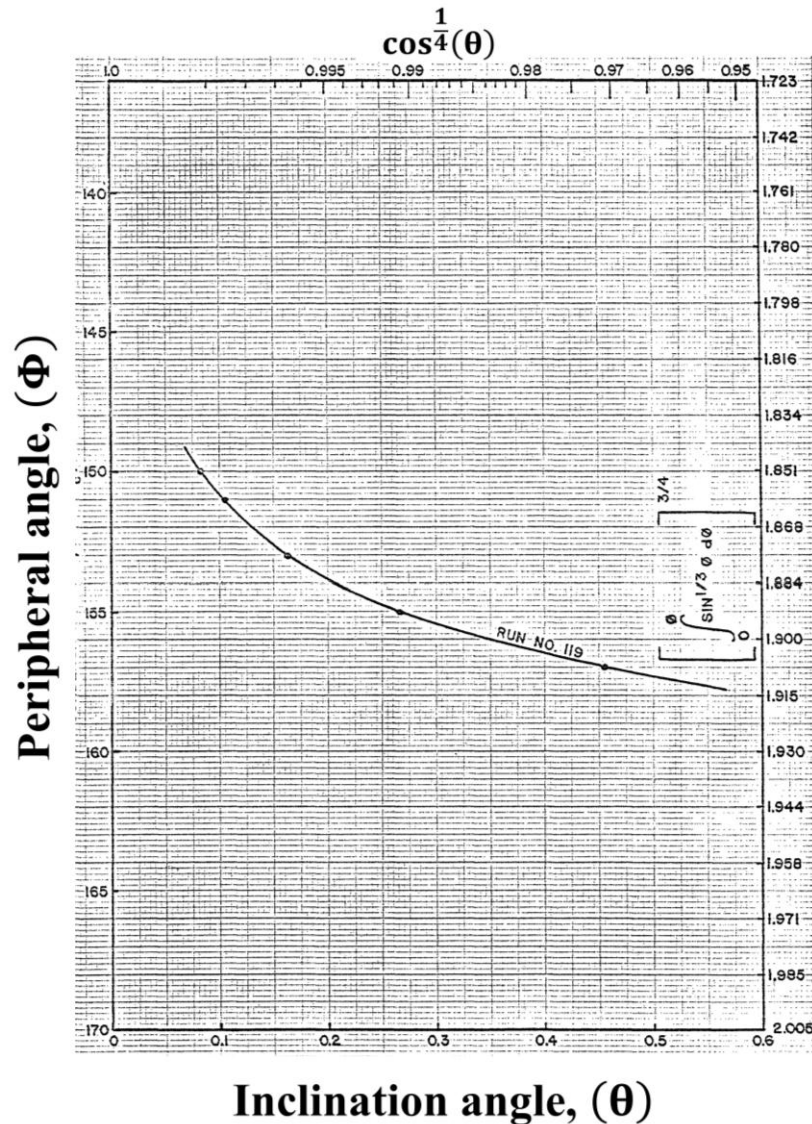


Figure 4.11 Plot of a typical Φ vs θ curve utilizing the method describe above (adapted from Chato, 1960).

With the final value of Φ_M , the effects of the circumferential and the bottom condensate flow on $R_{C,F}$ can be deduced. The next paragraph analyses the effects of the circumferential temperature variation of the wall, if present, on the overall $R_{C,F}$.

The heat transfer through the bottom condensate flow is negligible compared to the heat transferred through the walls of the condensate film flow $0^\circ \leq \theta < 90^\circ$ (Chato, 1960). Hence, the overall ΔT in this case is the sum of the individual temperature drops across the condensate film at the walls ($\Delta T_{C,F,W}$) and the condenser wall ($\Delta T_{C,W}$). Typically for TS and HP, $\Delta T_{C,W} \approx 0$ and, therefore, $\Delta T \approx \Delta T_{C,F,W}$. The non-dimensional film thickness ψ is a function of Φ (equation 4.64) and, therefore, varies circumferentially. Hence, there is a possibility that $\Delta T_{C,F,W}$ will also vary circumferentially. The problem now reduces to estimating and comparing the error between the case where $\frac{d(\Delta T_{C,F,W})}{d\Phi} \approx 0$ is considered and $\frac{d(\Delta T_{C,F,W})}{d\Phi} \neq 0$ is considered. The problem of circumferential temperature variation in a horizontal condenser has been investigated by Langen (1931), Bauermesiter (1941), Peck and Reddie (1951) and Bromley et al. (1952) who showed that $\frac{d(T_{C,F})}{d\Phi}$ is quite large at $\theta = 0^\circ$ and $\frac{d(T_{C,F,W})}{d\Phi} > \frac{d(T_{C,F,W})}{dL_c}$, where $\frac{d(T_{C,F,W})}{dL_c}$ is the longitudinal temperature gradient (Peck and Reddie, 1951). However, the conclusions drawn by Peck and Reddie (1951) and Bromley et al. (1952) from their experimental results show that the deviation in the overall heat transfer coefficient assuming a constant $\Delta T_{C,F,W}$ is negligible in comparison to the heat transfer coefficient obtained using the circumferentially averaged $\Delta T_{C,F,W}$ even when their experiments were carried out on a stainless steel and a Monel tube whose thermal conductivities are relatively lower ($k_{\text{Stainless steel}} = 15$ [W/mK], $k_{\text{Monel}} = 22$ [W/mK]) than that of a copper tube. Thus, , it is concluded that both longitudinal and circumferential condenser temperatures be measured so that an overall mean value of the condenser temperature can be obtained.

4.6.3 Summary of the effects of θ

Equations (4.59 - 4.68) representing the effects of the inclination angle can now be summarised as (Table 4.9)

Table 4.9 Prediction equations for $R_{C,F}$ based on different operating conditions of θ and Φ .

For $X > 3.2$ and $\theta = 0^\circ$	
$R_{C,F,k}\delta_{C,F}$ (without shear effects)	$[C'_{C,F}]^{m_1} [Ar_1]^{n_1} [Pr_1]^{o_1} \left[\frac{D_i}{\delta_{C,F}} \right]^{p_1} [Re_F]^{p_1} \left[\int_0^\Phi \sin^{1/3} \Phi d\Phi \right]^{-3/4}$
$R_{C,F,sk_i}\delta_{C,F}$ (with shear effects)	$[C'_{C,F,S}]^{e_2} [Ar]^{f_2} [Pr]^{g_2} \left[\frac{\mu_v}{\mu_l} \right]^{h_2} \left[\frac{D_i}{\delta_{C,F}} \right]^{h_2} [Re_v]^{h_2} [\tau_i^*]^{i_2} \left[\int_0^\Phi \sin^{1/3} \Phi d\Phi \right]^{-3/4}$
	$[C'_{C,F,S}]^{e_2} [Ar]^{f_2} [Pr]^{g_2} \left[\frac{D_i}{\delta_{C,F}} \right]^{h_2} [Re_F]^{h_2} [\tau_i^*]^{i_2} \left[\int_0^\Phi \sin^{1/3} \Phi d\Phi \right]^{-3/4}$
For $X > 3.2$ and $90^\circ > \theta > 0^\circ$	
$R_{C,F,k}\delta_{C,F}$ (without shear effects)	$[C'_{C,F}]^{m_1} [Ar_1]^{n_1} [Pr_1]^{o_1} \left[\frac{D_i}{\delta_{C,F}} \right]^{p_1} [Re_F]^{p_1} (\cos\theta)^{-\frac{1}{4}} \left[\int_0^\Phi \sin^{1/3} \Phi d\Phi \right]^{-3/4}$
$R_{C,F,sk_i}\delta_{C,F}$ (with shear effects)	$[C'_{C,F,S}]^{e_2} [Ar]^{f_2} [Pr]^{g_2} \left[\frac{\mu_v}{\mu_l} \right]^{h_2} \left[\frac{D_i}{\delta_{C,F}} \right]^{h_2} [Re_v]^{h_2} [\tau_i^*]^{i_2} (\cos\theta)^{-\frac{1}{4}} \left[\int_0^\Phi \sin^{1/3} \Phi d\Phi \right]^{-3/4}$
	$[C'_{C,F,S}]^{e_2} [Ar]^{f_2} [Pr]^{g_2} \left[\frac{D_i}{\delta_{C,F}} \right]^{h_2} [Re_F]^{h_2} [\tau_i^*]^{i_2} (\cos\theta)^{-\frac{1}{4}} \left[\int_0^\Phi \sin^{1/3} \Phi d\Phi \right]^{-3/4}$
For $X \leq 3.2$ and $90^\circ > \theta > 0^\circ$	
$R_{C,F,k}\delta_{C,F}$ (without shear effects)	$[C'_{C,F}]^{m_1} [Ar_1]^{n_1} [Pr_1]^{o_1} \left[\frac{D_i}{\delta_{C,F}} \right]^{p_1} [Re_F]^{p_1} \left[\frac{1}{\Phi X} \iint_{0,0}^{\Phi,X} \delta(X, \Phi) d\Phi dX \right] \left[\int_0^\Phi \sin^{1/3} \Phi d\Phi \right]$
$R_{C,F,sk_i}\delta_{C,F}$ (with shear effects)	$[C'_{C,F,S}]^{e_2} [Ar]^{f_2} [Pr]^{g_2} \left[\frac{\mu_v}{\mu_l} \right]^{h_2} \left[\frac{D_i}{\delta_{C,F}} \right]^{h_2} [Re_v]^{h_2} [\tau_i^*]^{i_2} \left[\frac{1}{\Phi X} \iint_{0,0}^{\Phi,X} \delta(X, \Phi) d\Phi dX \right] \left[\int_0^\Phi \sin^{1/3} \Phi d\Phi \right]^{-3/4}$
	$[C'_{C,F,S}]^{e_2} [Ar]^{f_2} [Pr]^{g_2} \left[\frac{D_i}{\delta_{C,F}} \right]^{h_2} [Re_F]^{h_2} [\tau_i^*]^{i_2} \left[\frac{1}{\Phi X} \iint_{0,0}^{\Phi,X} \delta(X, \Phi) d\Phi dX \right] \left[\int_0^\Phi \sin^{1/3} \Phi d\Phi \right]^{-3/4}$

The next section briefly evaluates the prediction capabilities of the newly developed equations for R_{boil} and R_{cond} .

4.7 Evaluation of the prediction capabilities of R_{boil} and R_{cond}

The new sets of R_{boil} and R_{cond} expressions are assessed qualitatively to determine their prediction capabilities with varying \dot{Q}_{in} , AR, FR and θ .

Examining the expressions of R_{boil} for different boiling regimes in the liquid pool and the film (equations 4.28 and 4.29, 4.37, 4.38, 4.42, 4.43, 4.49 and 4.50), it is observed that all the expressions contain either \dot{Q}_{in} or $(\dot{Q}'_{in,f})$ as a variable. The R_{boil} expressions can,

therefore, be used to predict the changes in the thermal resistance with \dot{Q}_{in} or $(\dot{Q}'_{in,f})$ directly.

Similarly, all the R_{boil} expressions contain L_p as a variable. Therefore, these expressions can be used to predict the changes in the thermal resistance with FR (i.e. L_p). Moreover, these expressions also contain D_i and $\dot{Q}'_{in,f}$ as variables which can predict the changes in the thermal resistance with FR when L_e and D_i are varied proportionally at fixed L_p .

Since the R_{boil} expressions contain $\dot{Q}'_{in,f}$ and L_p as a variable, the effects of the variation in AR caused by varying L_e at fixed FR can be predicted through these expressions. Similarly, the effects of varying AR through D_i can also be predicted.

It has been shown in section 4.4 that L_p varies with θ . Thus, the final liquid pool length L'_p can be substituted for L_p in the relevant R_{boil} expressions in order to predict the changes in the thermal resistance with θ .

The expressions of R_{cond} for filmwise condensation contain $\delta_{C,F}$, L_c and \dot{Q}_{in} or \dot{Q}'_{out} as variables. Therefore, the variation in either L_c or \dot{Q}'_{out} can be predicted using these equations. The expressions also include θ and Φ as variables (Table 4.9). Thus, the effects of the change in the inclination angle can be predicted using these equations

4.8 Summary

A new set of boiling and condensation thermal resistance equations are developed in this chapter utilizing the Buckingham Pi-theorem and a phenomenological approach. The new set of boiling and condensation equations includes all the primary performance variables known to influence the thermal resistances of TS and HP. Hence, they can be used to predict the thermal resistance of TS and HP under any given operating condition. The next part of the thesis describes the experimental investigation of TS. This is done in order to create a robust experimental database of TS performance that can be interpreted through the newly developed resistance models in this Chapter.

Chapter 5

5 Experimental Methodology

This chapter describes the experimental test rig and the apparatus, details of the thermosyphons (TS), the experimental procedure and the methods of data reduction. A brief discussion on the uncertainty and repeatability of the results is made here, with detailed analysis shown in Appendix E and F.

A total of eleven copper-distilled water TS were experimentally tested in the present investigation. The TS were manufactured and fabricated at Acrolab Ltd, Canada. The effects of the varying input power (\dot{Q}) (and, thus, heat flux, \dot{Q}'_{in} and $\dot{Q}'_{in,f}$, where \dot{Q}'_{in} is the heat flux to the evaporator and $\dot{Q}'_{in,f}$ is the heat flux to the fluid), the fill-ratio (FR) and the aspect-ratio (AR) on the boiling and the condensation behaviour were examined in this study. The experiments were carried out in an experimental test rig built at the University of Western Ontario (UWO). A brief description of the test rig is provided first followed by the description of the instruments associated with the experimental test rig.

5.1 Test-rig

The experimental test-rig used in the present study is designed and assembled at the Advanced Fluid Mechanics lab in the University of Western Ontario. A schematic and an actual diagram of the experimental test rig is shown in Figures 5.1 and 5.2. The heating and the cooling arrangement of the TS is shown through a CAD model in Figure 5.3. The TS was physically supported by clamping it to a vertically oriented retort stand (see Figure 5.3).

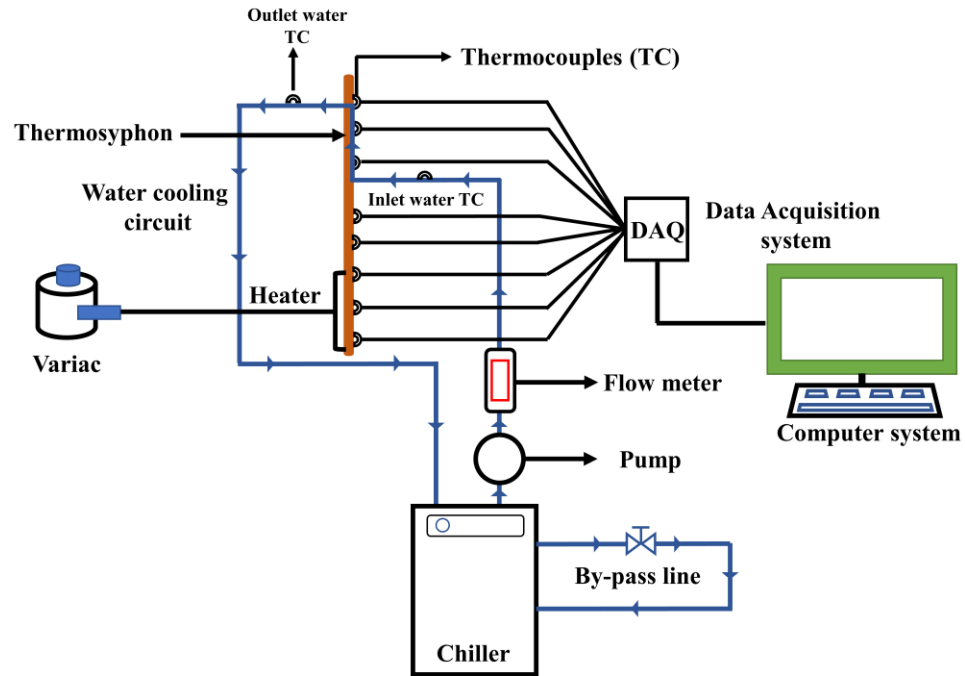


Figure 5.1 Schematic of the test-rig.

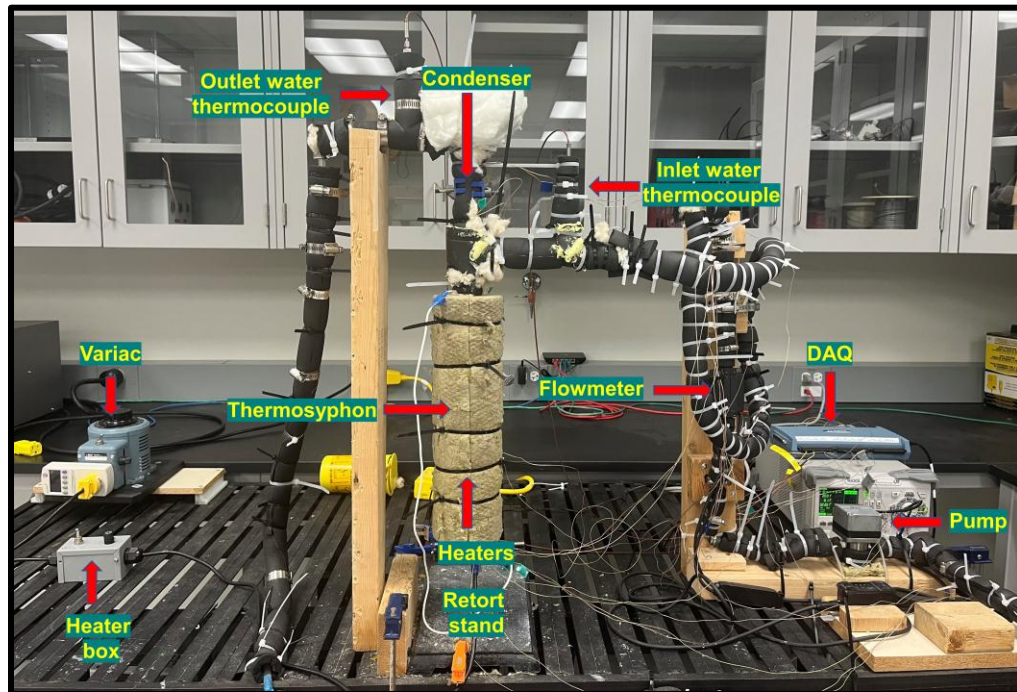


Figure 5.2 Experimental test-rig

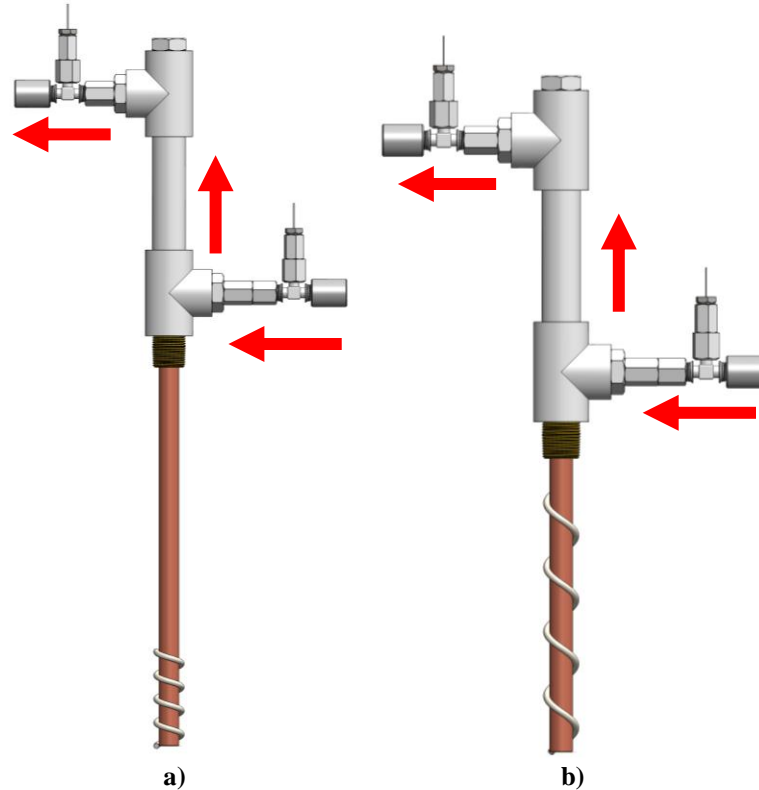


Figure 5.3 CAD model (created by Zichen Fan) showing the heating and the cooling arrangement of the TS inside the test-rig. The red arrows show the direction of the cooling water flowing through the condenser. The silver color coil represents the rope heater. The waterline TC are shown by vertical probes (represented by vertical lines) going into the water line.

As observed from Figure 5.3, the evaporator section of the TS was heated by an evenly wrapped rope heater. The input voltage to the rope heaters was varied through a Variac. The evaporator section was insulated using the mineral wool insulation to prevent heat loss to the surroundings (see Figure 5.2). The variation in the evaporator length was achieved by adjusting the length of the heater, which was spirally wrapped around the TS (see Figure 5.3). Figure 5.3(a) shows the smallest length of the evaporator section used in the experiments at 0.08m, whilst Figure 5.3(b) shows the longest length of the evaporator section at 0.18m.

The condenser section is cooled via cooling water pumped through the cooling jacket with an insulated outer surface (flexible rubber foam pipe insulation). The variations in the condenser length were achieved by varying the inserted length of the TS into the vertical cooling jacket (see Figure 5.3).

The cooling line and the surface TC were individually referenced to an ice bath and the water chiller. While measuring the evaporator temperatures, none of the surface TC were positioned directly above the heaters. Measurement and recording of the TC temperature output was accomplished using the DAQ system using the Instacal and TracerDAQ Pro softwares.

Five TC were installed on the evaporator. Two TC were installed along the liquid pool length (L_p) and one pair of TC was installed circumferentially opposite to each along the liquid film length (L_f) near to the liquid pool surface. Additionally, one TC was placed along L_f but near to the adiabatic section. Four TC were installed on the adiabatic section. Two TC were positioned circumferentially, at a distance of 0.1 inch from where the evaporator section ends. One TC was located 0.2 inch from the evaporator section end, and another TC was placed at 9 inch from the bottom end. The same convention was used for the adiabatic TC locations across various tested TS. Four TC were installed in the condenser. Since, the effects of the inclination angle (θ) were not examined, all the TC were installed axially along the condenser length (L_c). To minimize noise in TC readings caused by incoming water flow at the condenser, the TC near the water jacket inlet were installed circumferentially opposite, and a similar strategy was adopted for TC near the water jacket outlet. Two additional TC were installed in the water-jacket, one at the inlet and one at the outlet, to measure the temperature of the cooling water as it enters and exits the system.

5.2 Test- rig Instrumentation details

The instruments utilized in the test-setup are listed in Table 5.1 and are described below.

Table 5.1 Lists of all the instruments and its function.

Instruments	Function
Water recirculating chiller	To recirculate water at a preset temperature.
Magnetic drive gear pump	To recirculate water through the system.
Ultrasonic flow meter	Measure the flowrate of the water.
Data-acquisition system	Record the temperature measurements from the system.
Thermocouples	For accurate temperature measurements.
Rope heaters	Provide heat input to the system.
Variac	Vary the input voltage to the heaters
Power meter	Measure the input voltage and current
Cross line laser	To ensure the vertical orientation of the TS on both planes

5.2.1 Water-recirculating chiller

A water-recirculating chiller (ThermoChill I LR) with a maximum cooling capacity of 700W was utilized to recirculate the water at a fixed preset temperature. Since the minimum flowrate provided by the chiller was above that required for the experiments, an additional by-pass loop was installed in order to recirculate the water within the chiller system. This ensured that the water coming from the system outlet line is sufficiently and homogeneously mixed, reducing the time for the tests to reach a steady state. The water was then fed back into the system inlet line connected to the water-cooling jacket.

5.2.2 Magnetic drive gear pump

A magnetic drive gear pump from Fluid-O-Tech was used to recirculate the water from the chiller through the test-rig. Since the flow rate requirements for the experiments were low (between 0.10 [L/min] to 0.20 [L/min]), the magnetic drive gear pump was found to be the most suitable based on the pump characteristic curve.

5.2.3 Ultrasonic flow sensor

A clamp-on-ultrasonic flow sensor (range 0 - 20 L/min) was utilized to measure the flow rate of the cooling rate circulated from the water chiller. The sensor sends and receives ultrasonic wave signals between its two transducers along, and against, the flow direction and measures the time required for the flow-directed waves to reach the other side of the transducer (time-of-flight measurement). The time difference required for the ultrasonic flow waves to propagate between the two transducers is used to estimate the fluid velocity and the volumetric flow rate. The ultrasonic flow sensor was calibrated against the auxiliary bucket tests (described in Appendix E) and the uncertainties in the volume flow measurements are evaluated in Appendix E.

5.2.4 Data acquisition system

A 24-bit data-acquisition system (OMB-DAQ-2416) was utilized to record the thermocouple temperature measurements. The DAQ makes high-resolution differential voltage measurements and linearizes the data (using the latest NIST linearization coefficients) to give accurate temperature readings. The OMB-DAQ-2416's noise

filtering feature ensures that there is least amount of noise in the final temperature readings. Since low temperature noise was the main concern during the experiments, the DAQ was operated at the minimum data rate of 2.5Hz. This was to ensure that sufficient averaging of the data samples (number of samples to average = 30000/data rate) is performed by the DAQ, before the final measurements are recorded.

5.2.5 Thermocouples

Two different thermocouples (TC) were used for the surface and the waterline temperature measurements. The surface TC were K-type solid conductor wires (30AWG with Neoflon PFA insulation) with a temperature rating of -210°C to 260°C (OMEGA Part# TT-K-30-100). A K-type grounded Mgo style long probe TC (diameter 1/16", length 5") with 316 stainless steel sheath and PFA insulation was used as the waterline TC. The uncertainties in the temperature measurements of the surface and the waterline TC are evaluated in Appendix E.

5.2.6 Rope heaters

A constant Wattage cable type rope heaters (McMaster Carr # 3642K22) were used to provide heat at constant rate into the TS. The heaters had a maximum wattage capacity of 50W at 120V AC voltage giving the resistance of the heaters as 288Ω . Power was supplied to the heaters from the wall outlet and varied using a Variac.

5.2.7 Variac

A Variac (superior electric POWERSTAT with ratings of 120V, 10A) was utilized to vary the input voltage to the heaters in order to vary the heat input rate into the TS. The input voltage was adjusted manually through a dial which is graduated in volts ranging from 0V-140V.

5.2.8 Power meter

A highly accurate power meter (P4400 Kill A Watt) was used to measure the root-mean-square (RMS) voltage and the current. The power meter has a voltage range of (35-125

Vrms) and a current range of (0 - 15A), respectively. The uncertainties in the voltage and the current measurements are evaluated in Appendix E.

5.2.9 Laser levels

A Dewalt self-levelling laser line generator was used to produce simultaneous horizontal and vertical lines perpendicular to each other to form a crosshair pattern. The crosshair pattern was then utilized as a reference point to ensure the vertical orientation of the TS in both planes before each test runs.

The next section describes how the investigated parameters were varied and the TS design.

5.3 Details of the TS

A total of eleven copper TS were investigated in the present study which includes one standard TS (used for the repeatability test) and ten custom designed TS. The length of all the TS are 0.4064[m]. The internal pressure of all the TS is between -27 to -29in Hg at room temperature (Acrolab Ltd). The FR was varied (keeping AR fixed) by varying the length of the liquid pool (L_p) in the first five TS. In the next five TS, the AR was varied by varying the evaporator length, L_e and L_p proportionally which yielded different AR values at fixed FR. The details of the first five TS where FR is being varied are listed in Table 5.2, whereas Table 5.3 lists the details of the next five TS were AR is being varied at a fixed FR.

Table 5.2 Details of the TS for cases where FR is varied at a fixed AR. The TS are named in the same convention as it was tested during the experiments.

TS #	L_e (m)	D_i (m)	AR	L_p (m)	FR
1	0.127	0.014	8.88	0.044	0.35
2				0.057	0.45
3				0.070	0.55
4				0.083	0.65
5				0.095	0.75

Table 5.3 Details of the TS for cases where FR is varied at a fixed AR. The TS are named in the same convention as it was tested during the experiments.

TS #	L_e (m)	D_i (m)	FR	L_p (m)	AR
6	0.076	0.014	0.5	0.038	5.33
7	0.114			0.057	7.99
8	0.127			0.063	8.88
9	0.146			0.073	10.21
10	0.178			0.088	12.43

Before selecting the respective FR and AR for a TS, it was verified that the heat inputs to the evaporator section and the FR chosen are below the critical limits for the entrainment limit, burn-out limit and the dry-out limit. A brief description of these limits along with the verification results are provided in Appendix G for completeness.

A computer-aided design (CAD) model of the evaporator and the cooling end of a standard Acrolab manufactured TS is shown in Figure 5.4. As evident, the design of the Acrolab manufactured TS is slightly different from a typical TS design reported in the literature. The extractable end cap in Figure 5.4 is the evaporator end. It is flat but has a recessed threaded hole brazed into the tubing. The threaded hole is used for installation and extraction of TS in the mold cooling applications. The capillary end of the TS is the condenser end which contains a small capillary tube (see Figure 5.4). The capillary tube is used to charge the working fluid (WF) into the TS and create the desired vacuum pressure. The capillary tube also serves as a mechanism to vent any non-condensable gases (NCG) generated within the system. The capillary end cap is typically potted with solder, cement or epoxy to protect the capillary tube.

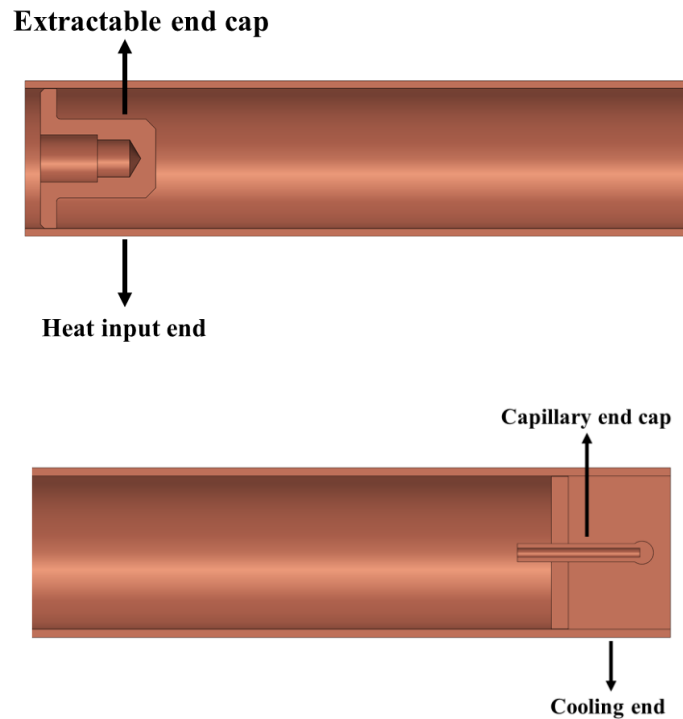


Figure 5.4 Extractable end (evaporator end) and the capillary end cap (condenser end) of the TS.

5.4 Experimental procedure

Each set of experiments was initiated by first starting the chiller and the pump to allow recirculation of the cooling water through the condenser section of the TS. Next, power was applied to the evaporator rope heaters. After a period of 15 minutes, the data was recorded at 0.17 [Hz] for a period of 90 minutes. This is the frequency corresponding to A/D data rate of 2.5 [Hz]. The initial transience within the system eventually reached a steady state condition observed on the strip chart recordings of the temperatures. The time required to achieve a steady state varied between 5 to 15 minutes. The voltage and current measurements, the cooling-water temperature, the cooling water flow rates were recorded at the start and at the end of each test runs. The cooling-water temperature and the cooling water flow rates were monitored throughout the experiment at specific time intervals to ensure that it did not vary during the runs.

Experimental data was taken in sequence from the smallest to the largest FR and AR. The power was increased sequentially from the lowest to highest voltage until geyser boiling was observed for some TS (having high FR).

5.5 Data reduction techniques

The power input (\dot{Q}_{in}) to the TS was computed as $\dot{Q}_{in} = VI$. The output cooling power (\dot{Q}_{out}) was computed as $\dot{Q}_{out} = \dot{m}c_p\Delta T$, where \dot{m} is the mass flow rate of the cooling water, c_p is the specific heat and ΔT is the temperature differential between the outlet and the inlet cooling water given as $(T_{w,out} - T_{w,in})$. $T_{w,in}$ and $T_{w,out}$ are the temperatures of the inlet and the outlet cooling water. \dot{m} is determined as $\rho_w \dot{V}$, where ρ_w is the density of the cooling water evaluated at T_{win} . c_p was also determined at T_{win} . The energy balance with the system was determined as $\frac{\dot{Q}_{out}}{\dot{Q}_{in}} \times 100$.

The average evaporator ($T_{e,avg}$), adiabatic ($T_{a,avg}$) and the condenser temperatures ($T_{c,avg}$) were computed by averaging the local temperatures from the TC measurements installed at appropriate locations (the subscript avg is dropped from here on for brevity). $T_e = \frac{T_1 + T_2 + \dots + T_{n_e}}{n_e}$, $T_a = \frac{T_1 + T_2 + \dots + T_{n_a}}{n_a}$, and $T_c = \frac{T_1 + T_2 + \dots + T_{n_c}}{n_c}$ where $n_e = 5$, $n_a = 4$ and $n_c =$

4, respectively. The pool boiling ($R_{B,P}$) and the film boiling ($R_{B,F}$) thermal resistances from the experimental measurements are computed as $R_{B,P} = \frac{(\Delta T_{e,a})}{\dot{Q}_{avg} \times FR}$ and $R_{B,F} = \frac{(\Delta T_{e,a})}{\dot{Q}_{avg} \times (1 - FR)}$, where $\Delta T_{e,a} = (T_e - T_a)$ and $\dot{Q}_{avg} = 0.5(\dot{Q}_{in} + \dot{Q}_{out})$, respectively. The condensation thermal resistance is computed as $R_{a,c} = \frac{(\Delta T_{a,c})}{\dot{Q}_{avg}}$. The Nusselt's number formulation used for characterizing the condenser performance has been shown later in the results and discussion chapter (Chapter 6).

5.6 Uncertainty in the measurements and repeatability of the experimental data

The uncertainties in the volume flow rate measurements, thermocouple temperature measurements, input heating power calculations, output cooling power calculations and the computed thermal resistances are shown in Appendix E. Since the degree of wall superheat ($\Delta T_{ea} = T_e - T_a$) is low at low heat fluxes (\dot{Q}'_{in}), the uncertainties associated with the pool boiling, film boiling and condensation resistance results are higher at low \dot{Q}'_{in} than at higher \dot{Q}'_{in} .

A standalone repeatability test was performed on the standard TS. This entailed taking measurements on the installed TS at same \dot{Q}_{in} , but on different days. Few test-runs were also performed where the TS was uninstalled and re-installed on the test-rig to examine the possibility of installation effects of the heaters and the thermocouple locations. In both the cases, the repeatability of the data was found to be within the uncertainty of the experimental measurements for different TS where \dot{Q}_{in} , FR and AR was varied. The details of the standard TS and the repeatability test conditions are given in Appendix F.

5.7 Parameters of investigation

The parameters of investigation in this study include the effects of input heating power \dot{Q}_{in} , the FR, and the AR on the steady state pool boiling, film boiling and the condensation thermal resistances for copper-distilled water TS. A summary of the parameter ranges covered in this work is given in Table 5.5.

The lower limit to \dot{Q}_{in} was constrained by the limitation of the power meter, which do not provide voltage readings below 40[V]. Nevertheless, voltages below 40[V] may not be suitable to induce nucleate boiling within the TS, justifying the choice of the lower limit. The upper limit to \dot{Q}_{in} was determined by the unsteady geyser boiling phenomena, observed for FR = 0.75 at 90[V] and 100[V], respectively. The lower limit of FR = 0.35, based on Imura et al. (1983), was chosen to avoid any unsteady dry out phenomena (see Appendix G). The upper limit of FR = 0.75 was chosen based on the observation that geyser boiling occurs at higher FR (see Appendix G). Since the fluid flow patterns and the heat transfer mechanisms are reported to be different for AR < 10 and AR \geq 10 (Terdtoon et al., 1998, Terdtoon et al., 1999), the range of AR was chosen to cover both these AR regimes.

Table 5.4 Summary of the parameters of investigation

Parameter	Values	Ranges of \dot{Q}_{in} (W)	Ranges of \dot{Q}'_{in} (kW/m ²)
FR	0.35	5.56 - 32.98	1.23 - 6.09
	0.45		
	0.55		
	0.65		
	0.75		
AR	5.33		2.05 - 10.14
	7.99		1.37 - 6.76
	8.88		1.23 - 6.09
	10.21		1.07 - 5.29
	12.43		0.88 - 4.35

5.8 Summary

The experimental methodology employed in this study is discussed in this chapter. The test-rig is described along with all the instruments associated with the rig. The heating and the cooling arrangements are discussed along with the methods of the data reduction to represent the experimental results. The entire range of the parameters varied as a part of the present investigation are outlined. The next chapter describes the heat transfer results characterizing the influence of the different operating parameters on the thermal behaviour of the TS.

Chapter 6

6 Experimental results and discussion

In this chapter, the steady state experimental results for the thermosyphons (TS) are presented and discussed. The chapter is divided into two major sections. Each section describes the results illustrating the effects of the input heating rate (\dot{Q}_{in}) and the fill ratio (FR), respectively on the pool boiling ($R_{B,P}$), film boiling ($R_{B,F}$) and the condensation thermal resistances ($R_{C,F}$). The subscripts B, P, F and C denote boiling, pool, film and condensation, respectively.

6.1 Effects of \dot{Q}_{in} on the thermal performance of TS

This section is divided into three parts, where each part describes the effects of \dot{Q}_{in} on $R_{B,P}$, $R_{B,F}$, and $R_{C,F}$ respectively. The steady state temperature distributions along the length of the TS at varying \dot{Q}_{in} are similar to the results for the standard TS shown in Appendix F and, thus, are not discussed here.

Both $R_{B,P}$ and $R_{B,F}$ exist when $FR < 1$. The resistances $R_{B,P}$ and $R_{B,F}$ are calculated as

$$R_{B,P} = \frac{\Delta T_{e,a}}{\dot{Q}_{in}FR} \quad (6.1)$$

$$R_{B,F} = \frac{\Delta T_{e,a}}{\dot{Q}_{in}(1-FR)} \quad (6.2)$$

where $FR = \frac{L_p}{L_e}$, $\Delta T_{e,a}$ is the wall superheat defined as $\Delta T_{e,a} = (T_e - T_a)$, and T_e , T_a are the average evaporator and the adiabatic surface temperatures, respectively. The next subsection evaluates the variation in $R_{B,P}$ with \dot{Q}_{in} , followed by investigation of $R_{B,F}$ and $R_{C,F}$ in the next subsequent sections.

6.1.1 Evaluation of the pool boiling resistance ($R_{B,P}$)

Different equations representing the pool boiling behaviour are discussed first in order to assess the trends from the plots of the boiling data.

6.1.1.1 Pool boiling equations

The equation characterizing the pool boiling behaviour can be represented as (Nukiyama, 1934, Rohsenow, 1952)

$$\dot{Q}'_{in,f,P} = C_1(\Delta T_P)^{n_1} \quad (6.3)$$

where $\dot{Q}'_{in,f,P}$ is the heat flux to the liquid pool (recall that $\dot{Q}'_{in,f,P} = \dot{Q}'_{in,f} = \frac{\dot{Q}_{in}}{A_{e,i}}$, where $A_{e,i} = \pi D_i L_e$ is the evaporator internal area), $\Delta T_P \approx \Delta T_{e,a}$ and C_1 ($C_1 > 0$) is the dimensional proportional constant (function of the WF properties) whose unit depends on the magnitudes of the exponent n_1 (in pool boiling, $n_1 > 1$; Bergman et al., 2018). The rate of change of $\dot{Q}'_{in,f,P}$ with respect to ΔT_P can, therefore, be written as

$$\frac{\partial(\dot{Q}'_{in,f,P})}{\partial(\Delta T_P)} = C_1 n_1 (\Delta T_P)^{n_1-1} \quad (6.4)$$

where $\frac{\partial(\dot{Q}'_{in,f,P})}{\partial(\Delta T_P)} > 0$, indicating that $\dot{Q}'_{in,f,P}$ will always increase with ΔT_P . This conclusion is important in applications where ΔT_P is an operating parameter and $\dot{Q}'_{in,f,P}$ is the dependent variable. From equation (6.3), the variation in ΔT_P with respect to $\dot{Q}'_{in,f,P}$ and \dot{Q}_{in} can be expressed as

$$\frac{\partial(\Delta T_P)}{\partial(\dot{Q}'_{in,f,P})} = \frac{1}{C_1^{n_1}} \frac{1}{n_1} (\dot{Q}'_{in,f,P})^{\frac{1}{n_1}-1} \quad (6.5)$$

$$\frac{\partial(\Delta T_P)}{\partial(\dot{Q}_{in})} = \frac{1}{(A_{e,i} C_1)^{\frac{1}{n_1}}} \frac{1}{n_1} (\dot{Q}_{in})^{\frac{1}{n_1}-1} \quad (6.6)$$

Equations (6.5) and (6.6) indicate that ΔT_P increases with $\dot{Q}'_{in,f,P}$, and \dot{Q}_{in} , however the rate at which ΔT_P increases, decays as $\dot{Q}'_{in,f,P}$ or \dot{Q}_{in} is increased. Utilizing equations (6.1) and (6.3), the relationship between $R_{B,P}$ and ΔT_P and the variation in $R_{B,P}$ with respect to ΔT_P can be expressed as

$$\left(\frac{1}{R_{B,P} A_{e,i} FR} \right) = C_1 (\Delta T_P)^{n_1-1} \quad (6.7)$$

$$\frac{\partial(R_{B,P})}{\partial(\Delta T_P)} = -\frac{(n_1-1)}{C_1 A_{e,i} FR} (\Delta T_P)^{-n_1} \quad (6.8)$$

Both equations (6.7) and (6.8) suggest that $R_{B,P}$ decreases with an increase in ΔT_P . Similarly, the relationship between $R_{B,P}$ and $\dot{Q}'_{in,f,P}$ (and \dot{Q}_{in}) and the rate of change of $R_{B,P}$ with respect to \dot{Q}_{in} can be expressed using equations (6.3) and (6.7) as

$$\left(\frac{1}{R_{B,P} A_{e,i} FR}\right) = C_1^{\frac{1}{n_1}} (\dot{Q}'_{in,f,P})^{\frac{n_1-1}{n_1}} \quad (6.9)$$

or,

$$\left(\frac{1}{R_{B,P} (A_{e,i})^{\frac{1}{n_1}} FR}\right) = C_1^{\frac{1}{n_1}} (\dot{Q}_{in})^{\frac{n_1-1}{n_1}} \quad (6.10)$$

$$\frac{\partial(R_{B,P})}{\partial(\dot{Q}_{in})} = -\left(\frac{1}{(C_1 A_{e,i})^{\frac{1}{n_1}} FR}\right) \left(\frac{n_1-1}{n_1}\right) (\dot{Q}_{in})^{\left(\frac{1}{n_1}-2\right)} \quad (6.11)$$

Since, $n_1 > 1$, $\left(\frac{1}{n_1} - 2\right) < 0$, indicating that $R_{B,P}$ will always decrease with increase in \dot{Q}_{in} , however, the rate at which $R_{B,P}$ decreases, decays with increasing \dot{Q}_{in} . Based on these equations, the plots of the boiling data are examined next.

6.1.1.2 Examination of the pool boiling behaviour

Figure 6.1 shows the plot of $\dot{Q}'_{in,f}$ versus ΔT_P , $\left(\frac{1}{R_{B,P} A_{e,i} FR}\right)$ versus ΔT_P and $\left(\frac{1}{R_{B,P} A_{e,i} FR}\right)$ versus $\dot{Q}'_{in,f,P}$ for various FR. The \dot{Q}_{in} values are varied from 6.68 [W] to 32.98 [W], respectively for all the FR except for FR = 0.75. For FR = 0.75, higher input heating rates ($\dot{Q}_{in} \approx 26.72$ [W], 32.98 [W]) were not considered, since unsteady temperature distributions along the TS length were observed. Therefore, data at a lower $\dot{Q}_{in} \approx 5.56$ [W] were obtained for FR = 0.75.

It is evident from Figure 6.1a that $\dot{Q}'_{in,f,P}$ and ΔT_P demonstrate a power law relationship (straight line slope is obtained on a log-log plot). This is also apparent in Figures 6.1b and 6.1c (6.1d) where the relationship between $\left(\frac{1}{R_{B,P} A_{e,i} FR}\right)$ and ΔT_P as well as $\left(\frac{1}{R_{B,P} A_{e,i} FR}\right)$

and $\dot{Q}'_{in,f,P}$ are shown. The straight-line slopes n_1 , (n_1-1) and $\left(\frac{n_1-1}{n_1}\right)$, although not shown in the Figures, are outlined in Table 6.1 for further evaluation.

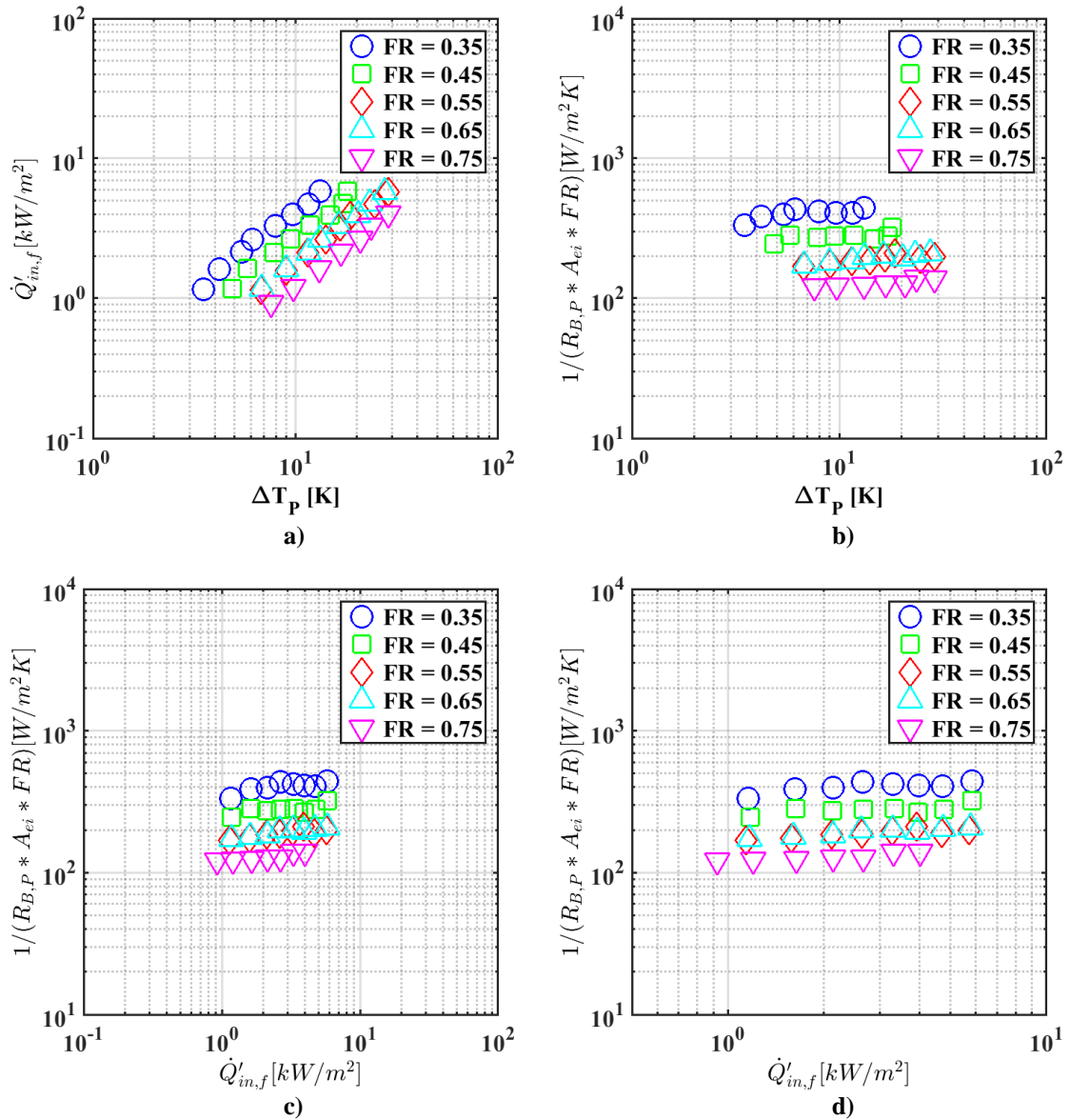


Figure 6.1 a) Boiling characteristic curve. b) Variation of $1/(R_{B,P}A_{e,i}FR)$ with ΔT_P . c) Variation of $1/(R_{B,P}A_{e,i}FR)$ with $\dot{Q}'_{in,f}$. d) Magnified figure of c).

Table 6.1 Estimates of the slope obtained by fitting a power law function of the form given by equations (6.1), (6.5) and (6.7).

FR	n_1	(n_1-1)	$\left(\frac{n_1-1}{n_1}\right)$	Boiling regimes
0.35	1.40	0.41	0.29	Bubble initiation, separation and mixing
	1.14	0.08	0.09	Bubble interference and coalescence effects
0.45	1.13	0.10	0.10	
0.55	1.10	0.11	0.10	
0.65	1.12	0.13	0.11	
0.75	1.13	0.12	0.10	

Two distinct slopes can be observed for the FR = 0.35 case (see Figure 6.1a). The data points within $3.5 \text{ [K]} \leq \Delta T_P \leq 6.1 \text{ [K]}$ exhibit a higher slope ($n_1 \sim 1.40$), whilst the data points within $7.9 \text{ [K]} \leq \Delta T_P \leq 13.2 \text{ [K]}$ demonstrate a slightly lower slope ($n_1 \sim 1.14$). The higher slope represents bubble separation inducing considerable fluid mixing effects resulting in enhanced heat transfer, whilst the lower slope indicates bubble coalescence and interference effects. The latter effect may have caused $R_{B,P}$ to increase at $\Delta T_P \sim 9.68, 11.56$, respectively (see Figures 6.1a and 6.1b, c) causing the slope values ($n_1 - 1$) and $\left(\frac{n_1-1}{n_1}\right)$ to be lower than the theoretical estimate (see second row corresponding to FR = 0.35 in Table 6.1). For $0.45 \leq \text{FR} \leq 0.75$, the data show a consistent slope of $n_1 \sim 1.10 - 1.13$ at all values of ΔT_P . The value is similar to the slope of the data for FR = 0.35 within $7.9 \text{ [K]} \leq \Delta T_P \leq 13.2 \text{ [K]}$. This indicates the presence of significant interference effects for $0.45 \leq \text{FR} \leq 0.75$ at all ΔT_P . The n_1 values obtained are consistent with the slope reported in the previous literature (for e.g., Kusuda and Imura, 1973, Semena and Kiselev, 1978) and the previous data synthesized in Chapter 2. The magnitudes of the slopes n_1 , $(n_1 - 1)$ and $\left(\frac{n_1-1}{n_1}\right)$ in Table 6.1 demonstrate consistent pool boiling behaviour across all sets of data in the present study.

The data points for FR = 0.55 and 0.65 (see Figure 6.1a) are nearly coincident at all values of $\dot{Q}'_{in,f}$ and ΔT_P . Similar observations were made by Andros (1980) for an annular steel TS (with a glass outer wall) for FR = 0.61 and 0.92 at $\dot{Q}'_{in,f} \geq 6 \text{ [kW/m}^2\text{]}$ with Freon-113 as the WF (see p. 90 in Andros, 1980). Andros (1980) observed that there is a net upward displacement of the liquid pool due to vapour bubbles resulting in a two-phase

mixture occupying the evaporator space above the liquid pool. Assuming Andros's (1980) observation applies here, it implies that the evaporator area covered by the liquid pool and the two-phase mixture is nearly equal for $FR = 0.55$ and 0.65 , respectively. Therefore, they show similar heat transfer behaviour.

As the primary objective is to examine the effects of \dot{Q}_{in} on $R_{B,P}$, a plot of $R_{B,P}$ versus \dot{Q}_{in} is shown in Figure 6.2. Equations (6.9) and (6.10) illustrate that the variation in $R_{B,P}$ with \dot{Q}_{in} is same as it is with $\dot{Q}'_{in,f}$, and the slope of the relationship is given by $-\left(\frac{n_1-1}{n_1}\right)$. The $\left(\frac{n_1-1}{n_1}\right)$ values shown in Table 6.1 suggest that $R_{B,P}$ decreases with increasing \dot{Q}_{in} but at a very slow rate of $\sim 0.09 - 0.11$. Only the data corresponding to $FR = 0.35$ have a slightly higher rate of decrement (~ 0.29) within $3.5 [K] \leq \Delta T_P \leq 6.1 [K]$. Figure 6.2 confirms these trends whereby a very slow variation in $R_{B,P}$ with \dot{Q}_{in} is observed. Thus, it is concluded that $R_{B,P}$ always decreases with increasing \dot{Q}_{in} , the rate of decrement being governed by the pool boiling behaviour.

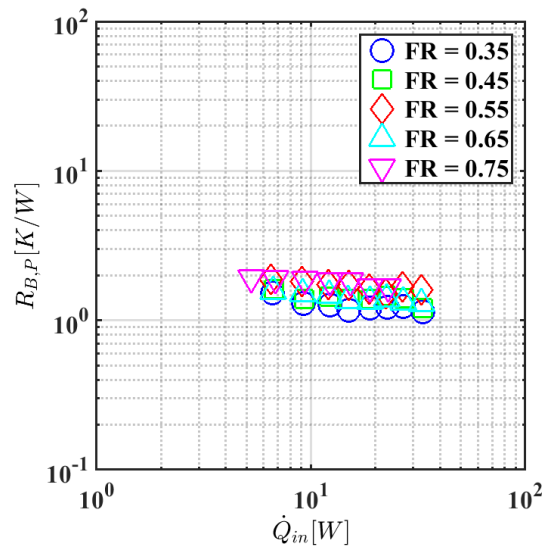


Figure 6.2 a) Variation in $R_{B,P}$ with \dot{Q}_{in} .

6.1.2 Evaluation of the film boiling resistance ($R_{B,F}$)

As the heat flux to the liquid film, $\dot{Q}'_{in,f,F} = \dot{Q}'_{in,f,P} = \dot{Q}'_{in,f}$ and the film wall-superheat, $\Delta T_F = \Delta T_P$, the film boiling behaviour can be represented by equations (6.1), (6.7) and (6.9)

and Figure 6.1 completely. However, the term $\left(\frac{1}{R_{B,F}A_{e,i}FR}\right)$ in equations (6.7) and (6.9) will be replaced by $\left(\frac{1}{R_{B,F}A_{e,i}(1-FR)}\right)$.

Before evaluating the variation in $R_{B,F}$ with $\dot{Q}'_{in,f}$, the different film flow regimes and the heat transfer mechanisms associated with those regimes are described in order to interpret the flow and the thermal behaviour from the present data. In this regard, the flow visualization results from Andros (1980) are discussed. It is hypothesized that the trends in the film boiling phenomena observed by Andros (1980) are also present in the data.

6.1.2.1 Film flow regimes

For low and moderate fill quantities, i.e., $0.03 \leq FR \leq 0.3$, four different flow regimes are observed with increasing \dot{Q}'_{in} (see Figure 5.4 in Andros, 1980). These are i) continuous evaporation of the liquid film ii) the stable rivulet regime iii) the unstable rivulet regime and iv) a regime characterized by bubble nucleation within the rivulets. Rivulets refer to the small stream of WF formed when the continuous condensate film breaks down at high $\dot{Q}'_{in,f}$ either due to surface tension gradients (Marangoni effect; Fujita and Ueda, 1978a, Hewitt and Hall-Taylor, 1970, Norman and McIntyre, 1960, Scriven and Sterling, 1960, Savino and Paterna, 2006) or due to bursting of vapour bubbles in the film (Fujita and Ueda, 1978b, Norman and McIntyre, 1960). A schematic of the formation of the rivulets from the liquid film is shown in Figure 6.3 for completeness.

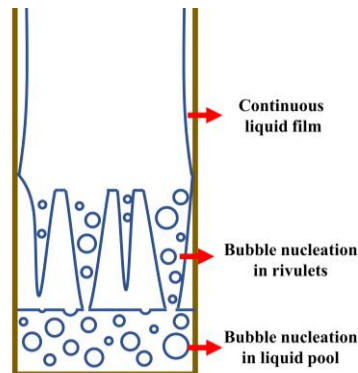


Figure 6.3 A schematic of the sectional front-view of a TS showing the formation of rivulets from the condensate film and nucleation within the rivulets (adapted from El-Genk and Saber, 1998b).

At large FR ($FR > 0.3$), the evaporator length available for the development of rivulets is considerably shorter. Thus, the formation of stable, unstable rivulets and nucleate boiling

within the rivulets is irregular (Andros, 1980). In many cases, two-phase mixture due to the expansion of liquid pool may occupy the entire evaporator section. The observations of Andros (1980) summarized in Table 6.2 show that the two-phase mixture occupies a greater evaporator volume after the expansion of the liquid pool at different $\dot{Q}'_{in,f}$. The different film flow regimes outlined for $FR > 0.3$ also reveal that for $FR \geq 0.46$, no rivulets are formed, and the film flow from the condenser is continuous at all times.

Table 6.2 Film boiling behaviour for $FR > 0.3$ at different $\dot{Q}'_{in,f}$. NA denotes not available.

Initial FR	$\dot{Q}'_{in,f}$ [kW/m ²]	FR after liquid pool expansion	Film boiling regimes
0.307	< 5	NA	1) Formation of stable rivulets. 2) Continuous film flow at the evaporator.
	8.00	0.42	1) Formation of unstable rivulets . 2) Local nucleation within the unstable rivulets
	16.5	0.53	1) Formation of unstable rivulets. 2) Vigorous nucleation within the unstable rivulets.
0.46	< 5	0.60	1) Formation of stable rivulets. 2) Continuous film flow at the evaporator.
	16.3	0.77	1) Existence of two-phase mixture. 2) No formation of the rivulets or bubble nucleation. 3) Continuous film flow at the evaporator.
0.614	11	1.00	1) Existence of the two-phase mixture at all times. 2) Continuous film flow at the evaporator.
0.921	NA	1.00	1) Existence of the two-phase mixture at all times. 2) Carryover of the two-phase mixture into the condenser region. 3) Continuous film flow at the evaporator.

6.1.2.2 Heat transfer regimes

The heat transfer mechanisms associated with the four different flow regimes are as follows. In continuous film regime, there is a) conduction across the liquid film and b) evaporation from the surface of the film. Increasing $\dot{Q}'_{in,f}$ increases the film mass flow rate (\dot{m}_f), and, thus, the film thickness. The film thermal resistance increases as a result. In the stable rivulet regime, the resistance increases due to two reasons. Firstly, the thickness of the film increases at the point of breakdown (Andros, 1980). Secondly, the edge of the film moves upward with increasing $\dot{Q}'_{in,f}$. Thus, additional thermal resistance due to the conduction in the solid wall at drier regions acts. In the unstable rivulet regime, the resistance decreases due to “wiping” action of the unstable rivulets (see p. 52 in Andros, 1980 for detailed description). During bubble nucleation within the rivulets, the resistance decreases due to the same reasons as in pool boiling.

6.1.2.3 Examination of the film boiling behaviour

The FR of the TS in the present study varies between 0.35 and 0.75. Based on the evidence presented in Table 6.2, rivulets may form at FR = 0.35 and 0.45, respectively. In order to investigate this, a plot of $R_{B,F}$ versus $\dot{Q}'_{in,f}$ is presented in Figure 6.4. The visual observations from Andros (1980) are utilized to explain the trends in the data.

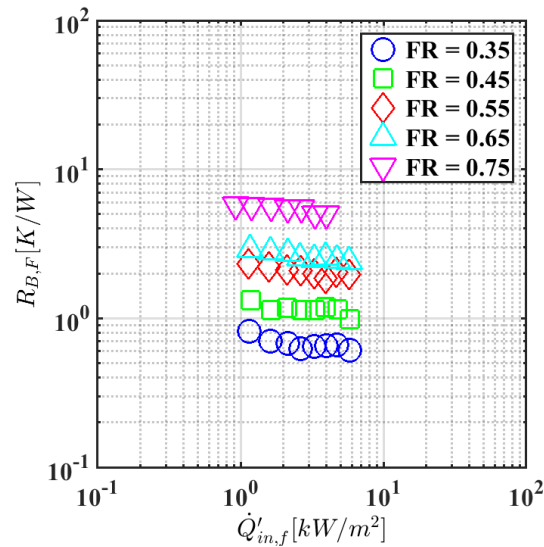


Figure 6.4 Variation in $R_{B,F}$ with $\dot{Q}'_{in,f}$.

Figure 6.4 reveals two distinct trends in the data. Firstly, for FR = 0.55, 0.65 and 0.75, $R_{B,F}$ shows a consistent decreasing trend with increasing $\dot{Q}'_{in,f}$ indicating that the continuous film flow above the liquid pool is more prevalent. Secondly, the high values of $R_{B,F}$ for FR = 0.55, 0.65 and 0.75 suggest that the heat transfer within the film is primarily through conduction and film surface evaporation. For FR = 0.35 and 0.45, however, between $2.5 \text{ [kW/m}^2] \leq \dot{Q}'_{in,f} \leq 5.0 \text{ [kW/m}^2]$, $R_{B,F}$ is seen to increase slightly followed by a decrement in its value. This indicates the formation of stable rivulets due to film breakdown. Similar observations were made by Andros (1980) at FR = 0.46 for $\dot{Q}'_{in,f} < 5.0 \text{ [kW/m}^2]$ (see p. 60 in Andros, 1980). The increase in $R_{B,F}$ is caused due to film thickening and the upward movement of the film edge post the breakdown mechanism. The decrement in $R_{B,F}$ for $\dot{Q}'_{in,f} > 5 \text{ [kW/m}^2]$ suggest that the rivulets have become unstable, and the heat transfer enhancement is caused due to the wavering motion of the rivulets causing rewetting of the evaporator surface (see p. 185 in Hirshburg, 1980).

Since film breakdown is hypothesized to occur for $FR = 0.35$ and 0.45 , respectively, the possibility for a dry patch occurrence is examined (see Appendix H). A dry patch may occur when there is a film breakdown, and the condensate mass flow rate is not sufficient to rewet the surface. The results from Appendix H reveal the occurrence and spreading of local dry patches at $FR = 0.35$ and 0.45 , respectively. Since $R_{B,F}$ has identical relationship with \dot{Q}_{in} and $\dot{Q}'_{in,F}$, no separate figure illustrating the variation in $R_{B,F}$ with \dot{Q}_{in} is shown.

6.1.3 Evaluation of the condensation thermal resistance ($R_{C,F}$)

6.1.3.1 Condensation equations

The shape of the characteristic condensation curve (for both filmwise and dropwise condensation) is similar to the boiling curve (Takeyama and Shimizu, 1974, Rohsenow, 1998). The equation representing the condensation behaviour can, thus, be expressed by

$$\dot{Q}'_{out,f} = C_2(\Delta T_{C,F})^{n_2} \quad (6.12)$$

where $\dot{Q}'_{out,f}$ is the output heat flux, $\Delta T_{C,F}$ is the wall subcooling, $\Delta T_{C,F} \approx \Delta T_{a,c} = (T_a - T_c)$. Here, T_c denotes the average condenser temperature, n_2 represents the slope of the condensation curve and C_2 is the dimensional proportional constant (depends on the WF properties) whose unit depends on the magnitude of n_2 . The other representative equations for condensation can be derived from equation (6.12) as (see Table 6.3 below)

Table 6.3 Representative condensation equations derived from equation (6.12)

Equation	Characteristics	Equation no
$\frac{\partial(\dot{Q}'_{out,f})}{\partial(\Delta T_{C,F})} = C_2 n_2 (\Delta T_{C,F})^{n_2-1}$	Rate of change of $\dot{Q}'_{out,f}$ with $\Delta T_{C,F}$	(6.13)
$\frac{\partial(\Delta T_{C,F})}{\partial(\dot{Q}'_{out,f})} = \frac{1}{C_2^{n_2}} \frac{1}{n_2} (\dot{Q}'_{out,f})^{\frac{1}{n_2}-1}$	Rate of change of $\Delta T_{C,F}$ with $\dot{Q}'_{out,f}$	(6.14)
$\frac{\partial(\Delta T_{C,F})}{\partial(\dot{Q}_{in})} = \frac{1}{(A_{c,i} C_2)^{\frac{1}{n_2}}} \frac{1}{n_2} (\dot{Q}_{in})^{\frac{1}{n_2}-1}$	Rate of change of $\Delta T_{C,F}$ with \dot{Q}_{in}	(6.15)
$\left(\frac{1}{R_{C,F} A_{c,i}}\right) = C_2 (\Delta T_{C,F})^{n_2-1}$	Relationship between $R_{C,F}$ and $\Delta T_{C,F}$	(6.16)
$\frac{\partial(R_{C,F})}{\partial(\Delta T_{C,F})} = -\frac{1}{C_2 A_{c,i}} (n_2 - 1) (\Delta T_{C,F})^{-n_2}$	Rate of change of $R_{C,F}$ with $\Delta T_{C,F}$	(6.17)
$\left(\frac{1}{R_{C,F} A_{c,i}}\right) = C_2^{n_2} (\dot{Q}'_{out,f})^{\frac{n_2-1}{n_2}}$	Relationship between $R_{C,F}$ and $\dot{Q}'_{out,f}$	(6.18)
$\left(\frac{1}{R_{C,F} (A_{c,i})^{\frac{1}{n_2}}}\right) = C_2^{n_2} (\dot{Q}_{in})^{\frac{n_2-1}{n_2}}$	Relationship between $R_{C,F}$ and \dot{Q}_{in}	(6.19)

$\frac{\partial(R_{C,F})}{\partial(\dot{Q}_{in})} = - \left(\frac{1}{(C_2 A_{c,i})^{n_1 FR}} \right) \left(\frac{n_2 - 1}{n_2} \right) (\dot{Q}_{in})^{\left(\frac{1}{n_2} - 2 \right)}$	Rate of change of $R_{C,F}$ with \dot{Q}_{in}	(6.20)
---	---	--------

6.1.3.2 Examination of the condensation behaviour

Unlike pool and film boiling, the exponent n_2 appearing in equations (6.12) to (6.20) does not exhibit a fixed value since both $n_2 > 1$ and $n_2 < 1$ have been observed in prior studies (see section 2.1.3 in Chapter 2). This is due to the fact that the heat transfer mechanism at the condenser is influenced by several factors. Those are i) the flow states of the falling film (Rohsenow, 1998, Bergman et al., 2018) ii) the interfacial shear stress at the liquid vapour interface (Chen et al., 1984, Gross, 1992) and iii) the entrainment effects (Hashimoto and Kaminaga, 2002).

Figure 6.5 shows the plot of $\dot{Q}'_{out,f}$ versus $\Delta T_{C,F}$, $\left(\frac{1}{R_{C,FA_{c,i}}} \right)$ versus $\Delta T_{C,F}$ and $\left(\frac{1}{R_{C,FA_{c,i}}} \right)$ versus $\dot{Q}'_{out,f}$. Figure 6.5a shows that $\dot{Q}'_{out,f}$ exhibits a power-law relationship with $\Delta T_{C,F}$. Additionally, Figures 6.5b and 6.5c also show power-law relationship between $\left(\frac{1}{R_{C,FA_{c,i}}} \right)$ and $\Delta T_{C,F}$, $\dot{Q}'_{out,f}$ suggesting that equations (6.12), (6.16) and (6.18) correctly represents the condensation behaviour. Visual examination of the data in Figure 6.5a show two distinct slopes for $0.35 \leq FR \leq 0.55$. The data within $1.26 \text{ [kW/m}^2] \leq \dot{Q}'_{out,f} \leq 2.89 \text{ [kW/m}^2]$ exhibit a much steeper slope, whilst the data within $3.61 \text{ [kW/m}^2] \leq \dot{Q}'_{out,f} \leq 6.38 \text{ [kW/m}^2]$ show a more gradual slope. No appreciable change in the slope for $FR = 0.65$ and 0.75 is observed. The behaviour of the slope is governed by the condensation regime and the change in the slope indicates a transition in the condensation flow regime.

The variation in $R_{C,F}$ with \dot{Q}_{in} is examined next in Figure 6.6. Equation (6.19) show that $R_{C,F}$ should decrease at the rate of $-\left(\frac{n_2 - 1}{n_2} \right)$. The slope of the data for $0.35 \leq FR \leq 0.55$ evaluated in Table 6.4 show that $R_{C,F}$ decreases rapidly $\left(\left(\frac{n_2 - 1}{n_2} \right) \sim 0.65 - 0.84 \right)$ within $6.50 \text{ [W]} \leq \dot{Q}_{in} \leq 15.20 \text{ [W]}$, whereas between $15.20 \text{ [W]} \leq \dot{Q}_{in} \leq 33.22 \text{ [W]}$, the rate of decrement is slower $\left(\left(\frac{n_2 - 1}{n_2} \right) \sim 0.35 - 0.50 \right)$. For $FR = 0.65$ and 0.75 , $R_{C,F}$ decreases at

a nearly constant rate of 0.65 indicating that there is no change in the condensation behaviour. Since $\left(\frac{n_2-1}{n_2}\right) > 0$, indicating $n_2 > 1$, implies that $\dot{Q}'_{out,f}$ increases more rapidly as $\Delta T_{C,F}$ is increased. From equations (6.17) and (6.20), it can also be concluded that $R_{C,F}$ always decreases with increasing $\Delta T_{C,F}$ and \dot{Q}'_{in} , however, the rate at which it decreases, decays with increasing $\Delta T_{C,F}$ and \dot{Q}'_{in} . The high slope values within $6.50 \text{ [W]} \leq \dot{Q}'_{in} \leq 15.20 \text{ [W]}$ for $0.35 \leq FR \leq 0.55$, suggest that heat transfer may be occurring through dropwise or mixed condensation instead of filmwise condensation. Both these condensation modes are, therefore, examined in the next sub-section.

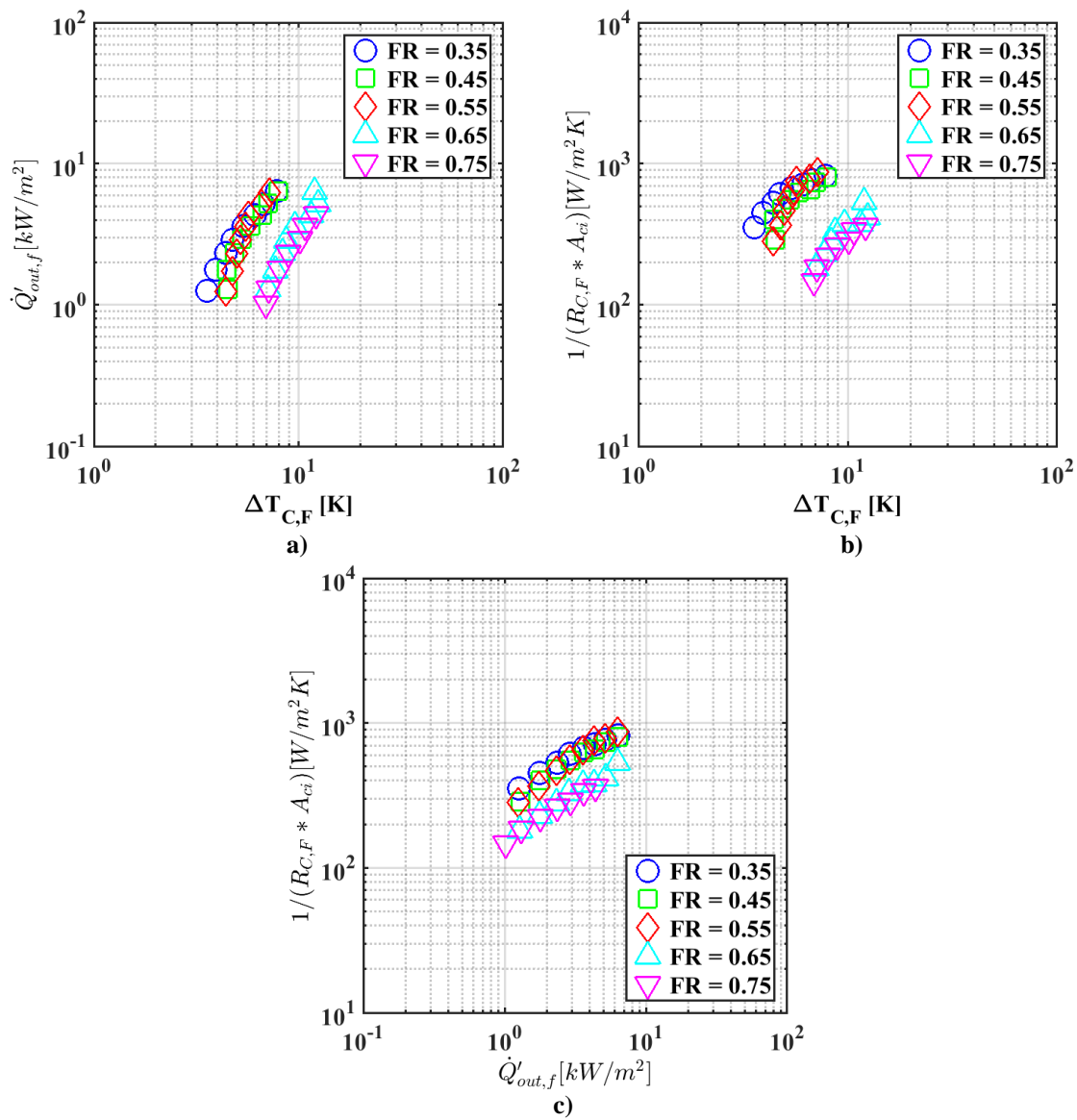


Figure 6.5 a) Condensation characteristic curve. b) Variation of $1/(R_{C,F}A_{c,i})$ with $\Delta T_{C,F}$. c) Variation of $1/(R_{C,F}A_{c,i})$ with $\dot{Q}'_{out,f}$.

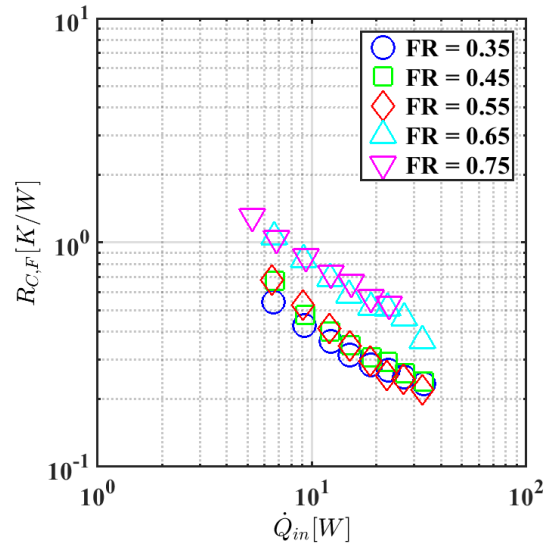


Figure 6.6 Variation in $R_{C,F}$ with \dot{Q}_{in} .

Table 6.4 The rate of change of $R_{C,F}$ with \dot{Q}_{in}

FR	$\left(\frac{n_2-1}{n_2}\right)$
0.35	0.65
	0.35
0.45	0.84
	0.46
0.55	0.80
	0.50
0.65	0.65
0.75	

6.1.3.3 Dropwise and mixed condensation regime

Andros (1980) observed both dropwise and mixed condensation in annular TS with water as a WF (see Fig. 5.2 in Andros, 1980). Dropwise condensation occurs when the condensed liquid does not wet the surface. As a result, drops form, grow, coalesce with adjacent droplets and finally, slide down the surface when the body force exceeds the surface tension force. Mixed condensation occurs when the liquid droplets begin to flatten on the condenser surface, giving patches of film condensation at a higher rate of coalescence (Andros, 1980). An approximate analysis undertaken in Appendix H reveal that mixed condensation is most likely occurring in the present experiments.

Further evidence supporting the occurrence of mixed condensation in the present experiments can be obtained from Citakoglu and Rose (1968) and Graham (1969), where $h_{c,F}$ (condensation heat transfer coefficient) is shown to increase with $\dot{Q}'_{out,f}$, albeit sharply at low $\dot{Q}'_{out,f}$, due to nucleation (see Figures 6.7 and 6.8). This trend is not typically observed for film condensation (Nusselt, 1916). At a higher $\dot{Q}'_{out,f}$, $h_{c,F}$ increase gradually as the number of nucleation sites reach a limit. The resemblance between the behaviour of $R_{C,F}$ in the present study (see Figure 6.5c) and Citakoglu and Rose (1968) as well as Graham (1969), infers that similar heat transfer mechanisms (drop initiation, growth, coalescence) may be occurring at the condenser.

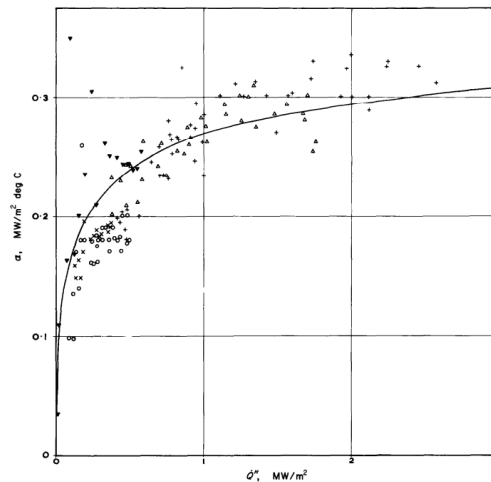


Figure 6.7 Variation in $h_{c,F}$ with $\dot{Q}'_{out,f}$ adapted from Citakoglu and Rose (1968) with permission.

Note that $\alpha \equiv h_{c,F}$ and $\dot{Q}'' \equiv \dot{Q}'_{out,f}$, respectively. The +, x and o symbols represent the data from Citakoglu and Rose (1968), whereas Δ and ∇ represent the data from Fevre and Rose (1965) and Tanner et al., (1965), respectively. The line (—) represent equation (30) in Fevre and Rose (1966).

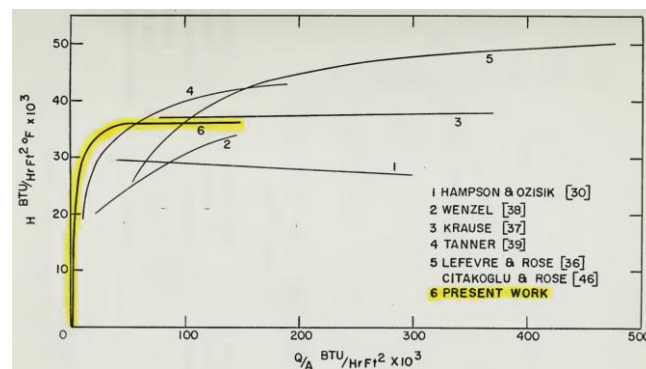


Figure 6.8 Variation in $h_{c,F}$ with $\dot{Q}'_{out,f}$ adapted from Graham and Griffith (1973) with permission. Note that $H \equiv h_c$ and $\frac{Q}{A} \equiv \dot{Q}'_{out,f}$, respectively. The “present work” highlighted in the plot with yellow outline refers to Graham’s (1969) own data.

The occurrence of film condensation is examined in the next section.

6.1.3.4 Filmwise condensation

Film condensation data is typically represented by plots of Re_F versus the average Nusselt number (Nu), where $Re_F = \frac{4\dot{Q}_{in}}{\pi D_i \mu_l h'_{fg}}$ and $Nu = \frac{h_{C,F}}{k_l} \left(\frac{Y_l}{g}\right)^{\frac{1}{3}}$, respectively (Bergman et al., 2018). $h_{C,F}$ is computed as $h_{C,F} = \frac{\dot{Q}'_{out,f}}{\Delta T_{C,F}}$, h'_{fg} and h_{fg} denote the modified and the unaltered latent heat of vapourization ($h'_{fg} = h_{fg} + 0.68c_{pl}(T_{sat} - T_s)$). c_{pl} , k_l , μ_l , ν_l are the specific heat, thermal conductivity, dynamic and kinematic viscosity of the WF in the liquid phase, respectively and $(T_{sat} - T_s) = \Delta T_{C,F} \approx \Delta T_{a,c}$. Various correlations between Re_F and Nu for different condensate flow states are available in the literature which are summarized in Table H.3 (Appendix H) for completeness.

It is noted that the Re_F values obtained in the present experiments are very low ($Re_F \sim 0.19 - 1.59$) compared to the typical Re_F reported in the literature ($Re_F \sim 1 - 38$; Andros, 1980, Alizadehdakhel et al., 2010, Amatachaya and Srimuang, 2010, Baojin et al., 2010, Jafari et al., 2017a, 2017b). This is due to two reasons. Firstly, owing to the low sealed pressure of the TS ($P_{sat} \sim 3115.1[\text{Pa}] - 9887.1[\text{Pa}]$), the maximum \dot{Q}_{in} that can be simulated before geyser boiling occurs is only $\sim 33.23[\text{W}]$ which is lower than typical \dot{Q}_{in} reported in the literature. Secondly, water has a high h_{fg} of the $O \rightarrow 10^6 [\text{J/kg}]$. Hence, Re_F which is $\propto \dot{Q}_{in}$ and $(h'_{fg})^{-1}$, will be very low. Since, the liquid inertial and the viscous forces are comparable in the present study, a continuous film flow may not be induced, suggesting drop condensation. Further evidence is provided in Kuznetsov et al., (2021), where drop condensation was observed for low heat fluxes ($0.7 [\text{kW/m}^2] \leq \dot{Q}'_{in,f,F} \leq 5.1 [\text{kW/m}^2]$) comparable to the present study. However, for such low system pressures and higher $\dot{Q}'_{in,f,F}$, liquid from the evaporator can be ejected towards the condenser due to violent boiling (Andros, 1980). This could lead to the formation of a continuous film over the condenser length, especially in regions that were previously operating in dropwise condensation mode (see p. 48 in Andros, 1980). As a result, mixed condensation is expected to occur. The next section examines the flow variables that influences $Re_{C,F}$.

6.1.3.5 Parametric effects

As previously mentioned, there are three primary variables that influence the condenser heat transfer rate. Those are i) the condensate flow states ii) the interfacial shear stress (τ_i) and iii) the entrainment effects. Thus, the effects of Re_F , τ_i and $\left(\frac{\rho_l}{\rho_v}\right)$ on Nu are examined in this section. In addition, iv) the liquid Prandtl number (Pr_l) (Thumm et al., 2001), and the v) vapour flow Froude number (Fr_v) (Spendel, 1982, Kusuda and Imura, 1983) which have also been reported to influence Nu which are examined in Appendix H. Since the effects of \dot{Q}_{in} is the primary subject of investigation, the influences of \dot{Q}_{in} on these parameters is evaluated first.

Figure 6.9a shows the plot of Re_F versus \dot{Q}_{in} . As \dot{Q}_{in} is increased, the film temperature (T_f) increases (see Figure 6.9b). Since, μ_l and h'_{fg} decreases with increase in T_f (see steam Table A.6 in Bergman et al., 2018), it can be deduced that μ_l and h'_{fg} are functions of \dot{Q}_{in} raised to some negative power. Thus, the slope of the Re_F versus \dot{Q}_{in} data will be greater than 1. This is verified in Figure 6.9a where the slope is determined to be ~ 1.11 .

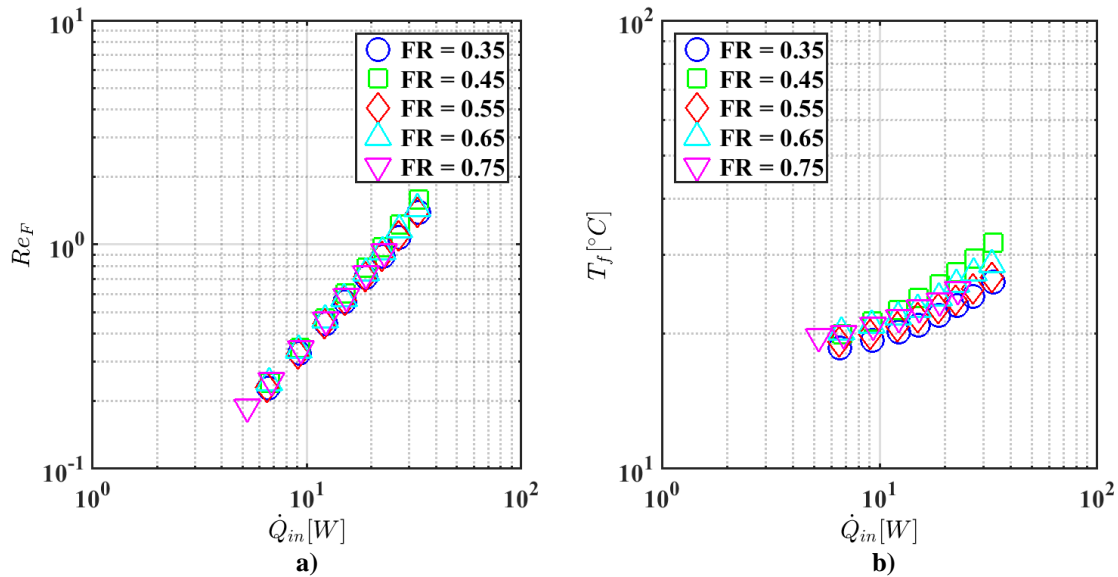


Figure 6.9 a) Variation in Re_F with \dot{Q}_{in} . b) Variation in T_f with \dot{Q}_{in} .

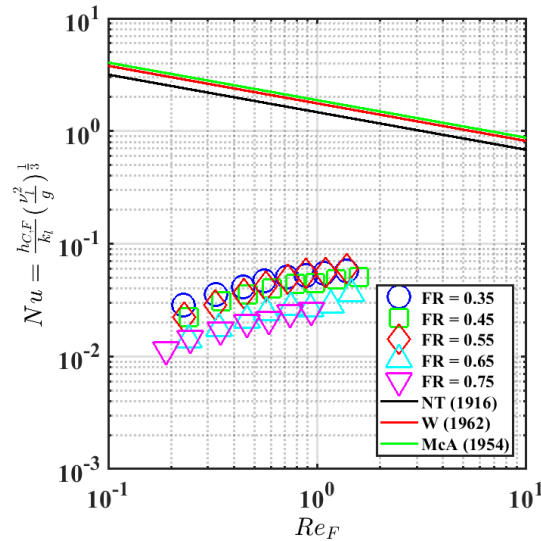
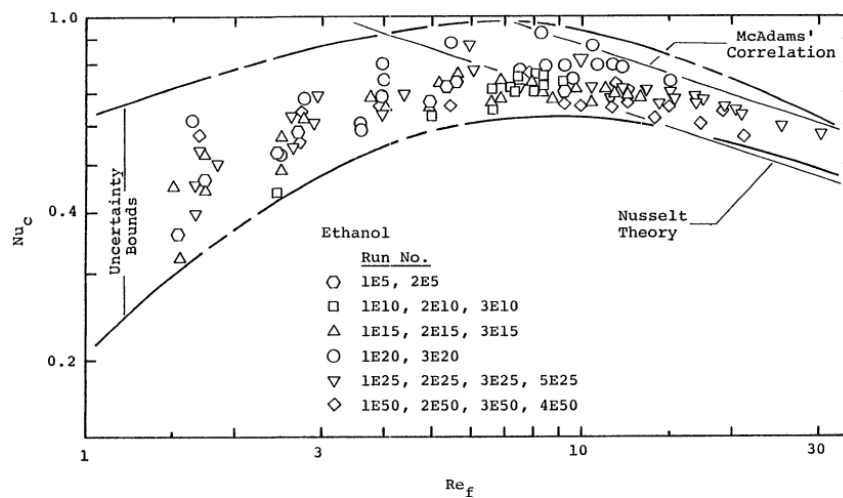


Figure 6.10 Variation in Nu with \dot{Q}_{in} . The blue, red and green solid lines represent the equation from Nusselt's theory (1916) (NT), Wilke's theory (W) (1962) and McAdams (1954) (McA). The Nu - Re_F equations from NT, W and McA are shown in Table H.3 in Appendix H.

The plot of Nu versus Re_F is shown in Figure 6.10 from which two important observations are made. Firstly, the Nu values show an increasing trend with Re_F until $Re_F \sim 0.8$ after which the Nu values tend to flatten out. Similar trends in the Freon -113 and the ethanol data of Andros (1980) were also observed at low Re_F (see Figure 6.11). Graham (1969) pointed out that the $h_{c,F}$ rises more sharply at lower $\dot{Q}'_{out,f}$ than at higher $\dot{Q}'_{out,f}$ due to the fact that with increase in \dot{Q}_{in} (and thus, Re_F), the number as well as the size of the drop nucleation sites increase rapidly indicating heat transfer enhancement. At higher \dot{Q}_{in} , the number of nucleation sites reaches a limit and, thus, are little influenced by \dot{Q}_{in} , indicating $h_{c,F}$ will be nearly constant (Graham, 1969). Also, at higher \dot{Q}_{in} , the counter current vapour velocities (u_v) obtained in the present study are high ($u_v \sim 1.8 - 3$ [m/s]). This may cause large shear stress to act on the drop surface, flattening the drops. The flat drops will occupy more surface area, leaving less area for active nucleation sites, decreasing heat transfer. Both of these reasons explain the nearly constant Nu values for $Re_F > 0.8$. It is also postulated that a further increase in Re_F may cause Nu values to decrease at the onset of pure film condensation. Secondly, all the data in the Re_F range $\sim 0.1 - 2$ fall well below the predictions from the Nusselt's theory (1916). Similar observations were also made by Andros (1980) with water as the WF. There are a number of reasons for this. Firstly, Nusselt's relation (1916), $Nu = 1.47(Re_F)^{-\frac{1}{3}}$ is valid for a

downward film flow and, therefore, may not hold true in the present scenario where dropwise and mixed condensation occurs. Secondly, the condensate droplets formed may not immediately move downward, as they need to attain a physical size where the gravitational effects exceed surface tension forces. Similar observations were reported in Fukano and Kadoguchi (1990). Thirdly, as the condensate mass flow rate (\dot{m}_c) is very small, significant axial heat conduction may occur at the evaporator. Andros (1980) observed that a portion of the bottom condenser surface was inactive as a result of axial conduction and the droplets adjacent to the inactive surface did not grow. Both these reasons suggest that the area over which active condensation is occurring is less than the total condenser surface area. Thus, the Nu values will be higher than those depicted in Figure 6.9b. Fourthly, the shear stress caused by the momentum transfer of condensing vapour have been shown to reduce the condensation heat transfer (Ueda et al., 1989). Fifthly, the presence of non-condensable gases within the system, even in minute concentrations (ppm), can drastically reduce the dropwise condensation heat transfer due to diffusion resistance (Citakoglu and Rose, 1968, Graham, 1969). While no condensable gases should typically be forming within the TS used in the present experiments (Acrolab Ltd.), its effects cannot be ruled out completely. The effects of τ_i on Nu is examined in the next section.



a)

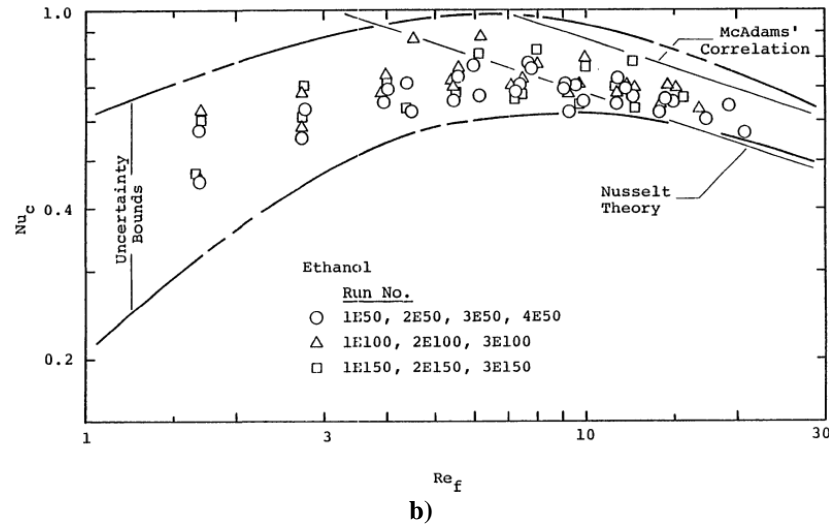


Figure 6.11 Variation in Nu with Re_f for ethanol WF at a) Small and intermediate FR and b) Intermediate and large FR. The figures are adapted from Andros (1980).

Figure 6.12a shows the plot of the non-dimensional interfacial shear stress (τ_i^*) versus \dot{Q}_{in} . τ_i^* is estimated as $\tau_i^* = \frac{\tau_i}{g(\rho_l - \rho_v)\delta_v}$, where δ_v is the characteristic scale of the

condensate film thickness estimated as $\delta_v = \sqrt[3]{\frac{\mu_l^2}{g \sin \theta \rho_l (\rho_l - \rho_v)}} \sim \left(\frac{\gamma_l^2}{g}\right)^{\frac{1}{3}}$ (Gross, 1992). The τ_i^*

values are seen to increase with \dot{Q}_{in} . This is expected since $\delta_v \propto (\gamma_l)^{\frac{2}{3}}$ and both γ_l and $(\rho_l - \rho_v)$ decrease with increasing T_f . The τ_i values are estimated by the expression $\tau_i =$

$\frac{1}{2} f_i \left[\frac{\dot{Q}_{in}^2}{\rho_v A_V^2 h_{fg}^2} \right]$, (where f_i is the Fanning friction coefficient; note that the complete

expression for f_i is given in Chapter 1) also increases with \dot{Q}_{in} raised to a power greater than 1. Thus, an overall increase in τ_i^* with \dot{Q}_{in} as observed in Figure 6.12a is justified.

Similar dependency of τ_i^* with \dot{Q}_{in} is reported in Rohsenow et al., (1956), Spindel (1982), Chen et al., (1987) and Gross (1992).

Figure 6.12b shows the plot of Nu versus τ_i^* . The variation in Nu is similar to the variation of Nu with Re_f , i.e., Nu increases with τ_i^* until $\tau_i^* \sim 0.02$, after which Nu values become nearly constant. While the effects of τ_i^* on “film” condensation are extensively studied (Rohsenow, 1956, Stainthorp and Batt, 1967, Hirshburg, 1980, Thumm et al., 2001), investigations of the effects of τ_i on drop condensation are limited (Tanner, 1964, Graham, 1969). Based on the available information, several competing effects of τ_i^* on drop condensation heat transfer can be identified. Firstly, an increase in τ_i^* can lead to the

early removal of large drops from the condenser surface, resulting in more active surface area for drop nucleation and, thus, heat transfer enhancement (Graham, 1969). Secondly, τ_i^* can remove the non-condensable gases from the vicinity of the condenser surface, thereby, improving heat transfer (Tanner, 1964, Graham, 1969). Thirdly, τ_i^* can cause large droplets to break into several small droplets, thereby, reducing heat transfer. Fourthly, an increase in τ_i^* decreases the average drop size (Tanner, 1964). Since, the conduction resistance is inversely proportional to the radius (r) of a drop, heat transfer will decrease. Fifthly, higher τ_i^* is observed to flatten the drops (promoting film flow), leading to a decrease in the heat transfer (O' Bara et al., 1967, Graham, 1969). Based on these effects, it is hypothesized that for $\tau_i^* \leq 0.02$, early removal of the large drops from the surface contributes towards heat transfer enhancement. However, for $\tau_i^* > 0.02$ (i.e., $w_v > 2.34$ [m/s]) the drops may start to flatten (O' Bara et al., 1967 observed flattening of drops for $w_v > 1.54$ [m/s]), leading to a decrease in the heat transfer coefficient.

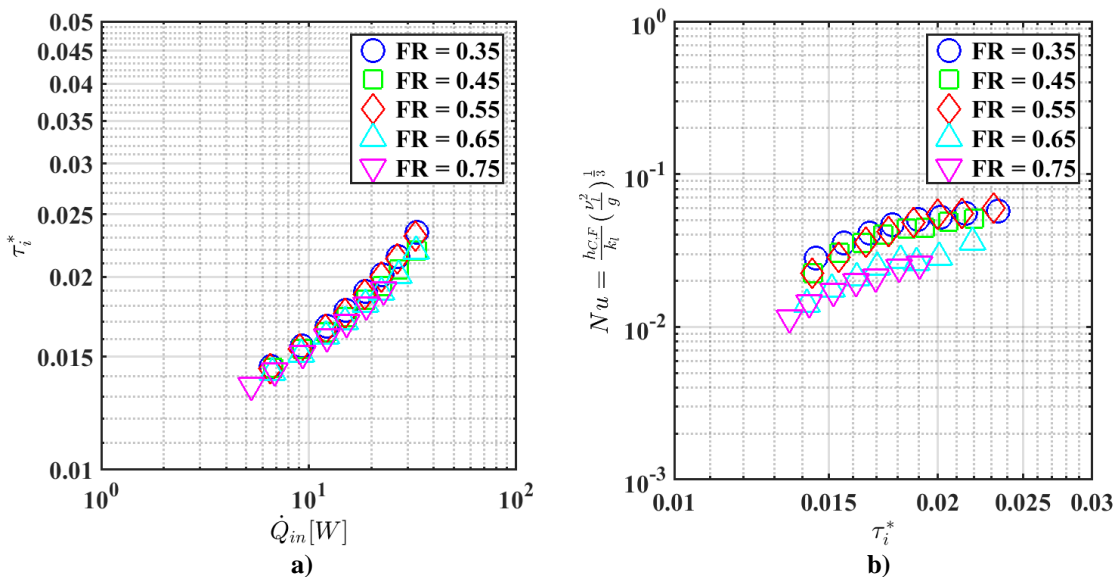
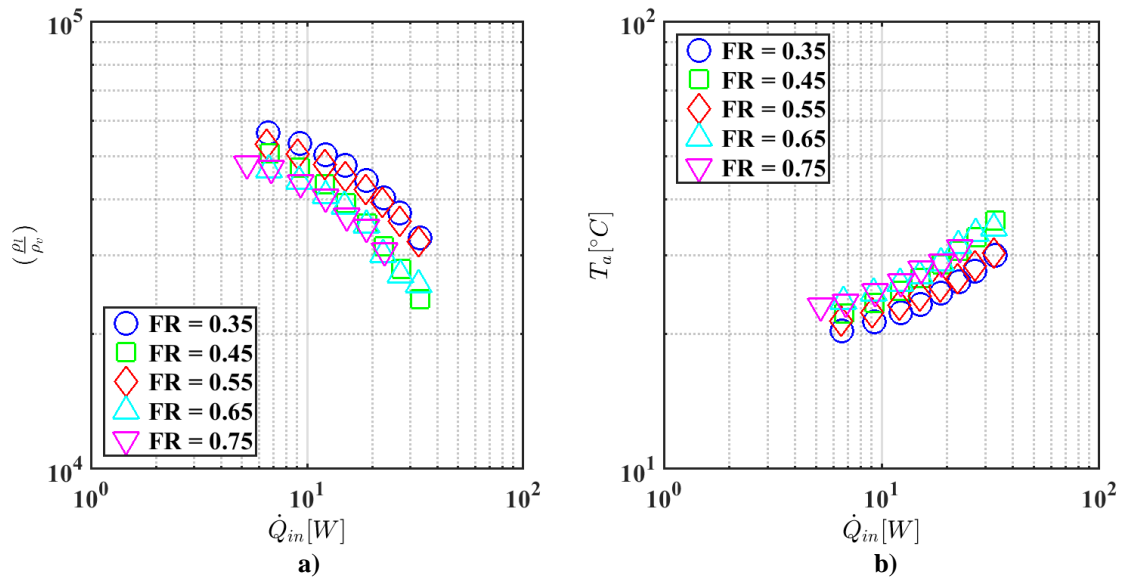


Figure 6.12 a) Variation in τ_i^* with \dot{Q}_{in} . b) Variation in Nu with τ_i^* .

The entrainment effects are characterised by the liquid, vapour density ratio $\left(\frac{\rho_l}{\rho_v}\right)$ (Hashimoto and Kaminaga, 2002). Figure 6.13a illustrates the relationship between the density ratio $\left(\frac{\rho_l}{\rho_v}\right)$ and \dot{Q}_{in} . The value of ρ_l decreases with T_f , whilst the value of ρ_v increases with T_a (i.e., with \dot{Q}_{in}) (see Figure 6.13b). This implies that $\left(\frac{\rho_l}{\rho_v}\right)$ decreases with \dot{Q}_{in} , as depicted in Figure 6.13a.

Figure 6.13c shows the plot of Nu versus $\left(\frac{\rho_l}{\rho_v}\right)$. Two distinct trends are observed. Firstly, the Nu values remain nearly constant with $\left(\frac{\rho_l}{\rho_v}\right)$ until reaching 4×10^4 , after which there is a steep decline in the Nu values. Hashimoto and Kaminaga (2002) have shown that as the density ratio increases, the amount of entrained liquid droplets from the film (or rivulets) increases. These liquid droplets transported by the vapour flow gets deposited on the condenser surface thereby decreasing the available “active” area for drop nucleation. Also, since the falling film thickness is thinner at lower \dot{Q}_{in} (i.e., higher $\left(\frac{\rho_l}{\rho_v}\right)$), it is logical to assume the effects of entrainment are larger on thinner films. The Nu values shown in Figure 6.13c, therefore, indicates that the density ratio has very little effects on Nu below $\left(\frac{\rho_l}{\rho_v}\right) \sim 4 \times 10^4$, but for $\left(\frac{\rho_l}{\rho_v}\right) \geq 4 \times 10^4$, a reduction in the heat transfer occurs due to possible entrainment effects.



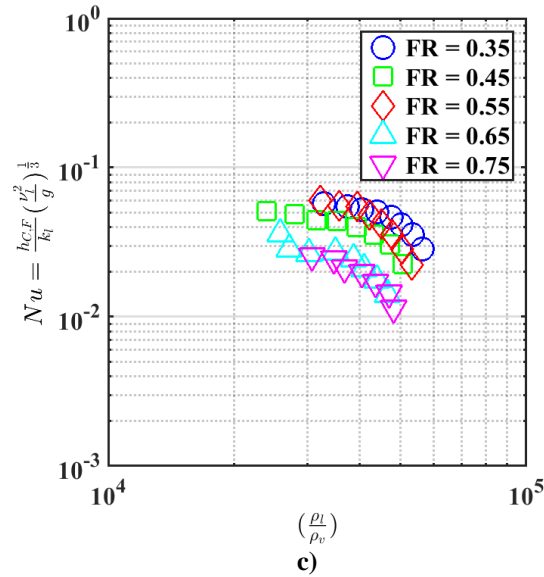


Figure 6.13 a) Variation in $\left(\frac{\rho_l}{\rho_v}\right)$ with \dot{Q}_{in} . b) Variation in T_a with \dot{Q}_{in} . c) Variation in Nu with $\left(\frac{\rho_l}{\rho_v}\right)$.

The next section examines the effects of the FR on boiling and condensation thermal resistances.

6.2 Effects of the FR on the thermal performance of TS

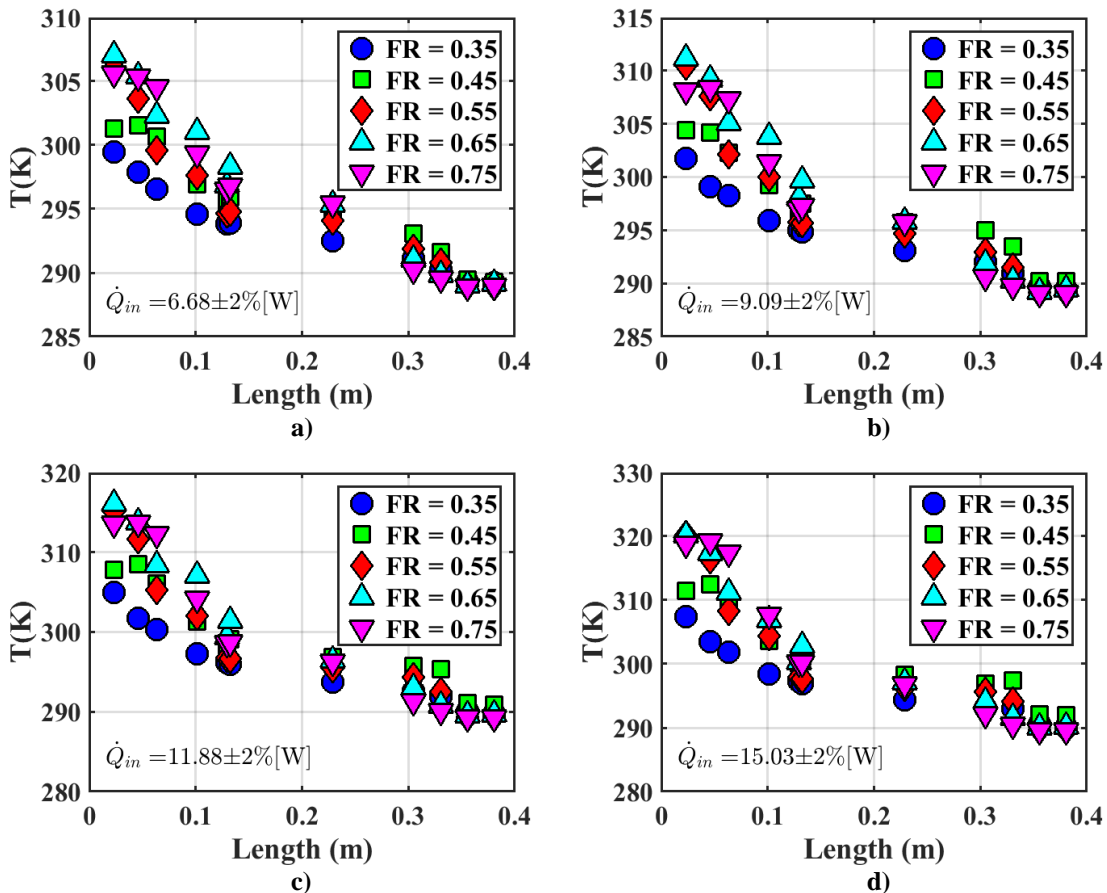
The effects of varying FR on the heat transfer characteristics of the TS are examined in this section. The effects of the FR on temperature distribution along the length of the TS is examined first followed by the effects of FR on $R_{B,P}$, $R_{B,F}$ and $R_{C,F}$.

6.2.1 Temperature distribution

Figure 6.14 (a-e) shows the temperature distribution along the length (L) of the TS for different FR at fixed \dot{Q}_{in} . Two consistent trends are observed from these Figures. Firstly, the temperature distribution demonstrate consistency across all FR. The effects of increasing FR are more prominent at the evaporator (i.e., $0[m] \leq L \leq 0.10[m]$) than at the condenser ($0.30[m] \leq L \leq 0.40[m]$). This is expected as the length of the liquid pool (L_p) influences the pool and the film boiling mechanisms more than the condensation mechanisms. Secondly, two opposite wall temperature characteristics are observed at the evaporator and the condenser. Whilst, the surface temperatures are higher for higher FR at the evaporator, they are lower at the condenser. This behaviour is consistent across all the examined \dot{Q}_{in} . Similar, observations were also made in Alizadehdakhel et al. (2010)

and Amatachaya and Srimuang (2010). If \dot{Q}_{in} is assumed to be such that $\dot{Q}_{in} = \dot{Q}_{pool,in} + \dot{Q}_{film,in} + \dot{Q}_{senisble,in}$, where $\dot{Q}_{pool,in}$ and $\dot{Q}_{film,in}$ are the heat input rates for phase change in the liquid pool and liquid film, respectively, then $\dot{Q}_{senisble,in}$ will be utilized to increase the temperature of the evaporator surface and the WF not undergoing phase change. Since the mass of liquid phase WF is higher at higher FR, the energy absorbed by the liquid pool will be larger. This may explain the higher surface temperatures at the evaporator.

The time scale required by the fluid parcel to reach the condenser is smaller at higher FR. Given that the liquid velocity is smaller than the vapour velocity, a greater accumulation of vapour droplets/film condensate is hypothesized to be occurring at the condenser at higher FR. An increased condenser thermal resistance and, therefore, a higher temperature drop is expected. This may explain the lower temperatures at the condenser at higher FR.



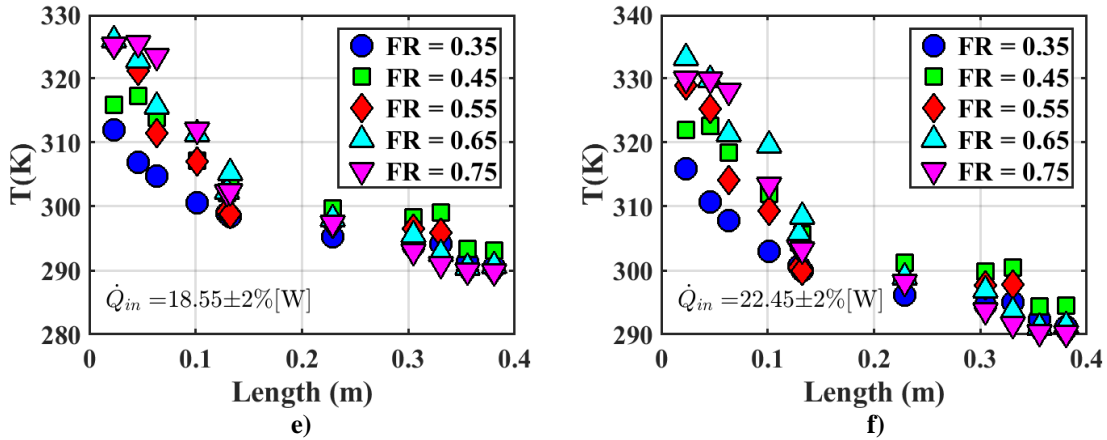


Figure 6.14 Temperature distribution along the length of the TS with varying FR for different \dot{Q}_{in} .

6.2.2 Evaluation of pool boiling resistance ($R_{B,P}$)

In this section, the variation in $R_{B,P}$ with FR is examined. Vapour bubble growth and dynamics depend, in a complex manner, on the wall superheat, ΔT_P (Andros, 1980, Bergman et al., 2018). Thus, ΔT_P governs the behaviour of $R_{B,P}$. The boiling equations described in section 6.1.1.1 cannot mathematically characterize the effects of FR on ΔT_P and $R_{B,P}$, since $\dot{Q}'_{in,f,P}$ is constant at various FR. Therefore, in order to understand how FR influences $R_{B,P}$, one must first understand i) How FR affects ΔT_P ? and ii) What is the relationship between ΔT_P and $R_{B,P}$? The next subsequent paragraphs aim to answer these questions.

Figure 6.15 shows the plot of FR versus ΔT_P for various fixed \dot{Q}_{in} . It is evident that with increasing FR, ΔT_P increases at all \dot{Q}_{in} , except for FR = 0.65, where a slight decrement or no change in ΔT_P is observed with respect to FR = 0.55. Similar trends (increasing ΔT_P with FR) were also reported by Andros (1980) and Hirshburg (1980). The slope estimated by fitting the data to a power-law equation of the form (excluding the data for FR = 0.65)

$$\Delta T_P = C_3(\text{FR})^{n_3} \quad (6.21)$$

reveal that ΔT_P has a power-law dependency with FR across all \dot{Q}_{in} values (see Table 6.5). In equation (6.21), C_3 has the same unit as ΔT_P .

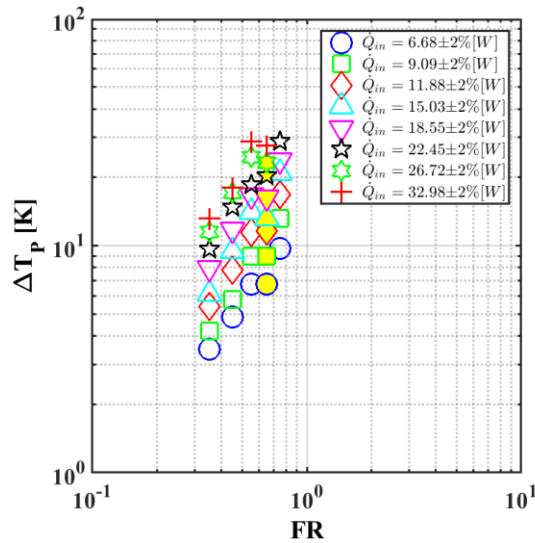


Figure 6.15 Variation in ΔT_P with FR. The data corresponding to FR = 0.65, have been highlighted in yellow for better visualizing the trend.

Table 6.5 Estimates of n_3 in Figure 6.15a.

\dot{Q}_{in} [W]	n_3
$6.68 \pm 2\%$	1.33
$9.09 \pm 2\%$	1.49
$11.88 \pm 2\%$	1.45
$15.03 \pm 2\%$	1.52
$18.55 \pm 2\%$	1.37
$22.45 \pm 2\%$	1.38

The ΔT_P values for FR = 0.55 and 0.65 are nearly equal at $\dot{Q}_{in} \leq 18.55$ [W], suggesting that the boiling mechanisms are similar. This is likely due to the resulting two-phase mixture (associated with the boiling liquid pool) occupying nearly the same evaporator volume, and heat transfer being dominated by the two-phase mixture. For $\dot{Q}_{in} > 18.55$ [W], however, ΔT_P decreases slightly for FR = 0.65 compared to FR = 0.55. The two-phase mixture for FR = 0.65 might be occupying a slightly higher volume than FR = 0.55, whereby the bubble generation and mixing effects are dominant over the interference and coalescence effects.

Since $n_3 > 1$ (Table 6.5), the wall superheat ΔT_P increases more rapidly as FR is increased, implying that a larger thermal driving potential is required to transport the same quantity of heat per unit time. The behaviour can be justified by the fact that at higher FR, more nucleated bubbles generated along L_p interact, thereby inhibiting the

liquid motion heat transfer at the evaporator. Utilizing equation (6.21), $R_{B,P}$ can be expressed as functions of ΔT_P and FR by

$$R_{B,P} = \frac{(C_3)^{\frac{1}{n_3}}}{\dot{Q}_{in}} (\Delta T_P)^{\frac{n_3-1}{n_3}} \quad (6.22)$$

$$R_{B,P} = \frac{C_3}{\dot{Q}_{in}} (FR)^{n_3-1} \quad (6.23)$$

Equations (6.22) and (6.23) also show that $R_{B,P}$ has power-law relationships with ΔT_P and FR, respectively. The variation in $R_{B,P}$ with ΔT_P and FR can, therefore, be written as

$$\frac{\partial(R_{B,P})}{\partial(\Delta T_P)} = \left(\frac{n_3-1}{n_3}\right) \frac{C_3^{\frac{1}{n_3}}}{\dot{Q}_{in}} (\Delta T_P)^{-\frac{1}{n_3}} \quad (6.24)$$

$$\frac{\partial(R_{B,P})}{\partial(FR)} = (n_3 - 1) \frac{C_3}{\dot{Q}_{in}} (FR)^{n_3-2} \quad (6.25)$$

Since, $\left(\frac{n_3-1}{n_3}\right)$ and $(n_3 - 1) > 0$, $R_{B,P}$ will increase with ΔT_P and FR. However, the rate at which $R_{B,P}$ increases, decays with increasing ΔT_P and FR. In order to validate equations (6.22) and (6.23), plots of $R_{B,P}$ versus ΔT_P and $R_{B,P}$ versus FR are shown in Figures 6.16. Excluding the data for FR = 0.65 and taking into account the uncertainty in the data, both plots show a nearly straight-line slope on the log-log plot confirming the validity of equations (6.20) and (6.21). The slopes estimated from Figure 6.16a and 6.16b outlined in Table 6.6 demonstrate consistency with the estimates shown in Table 6.5.

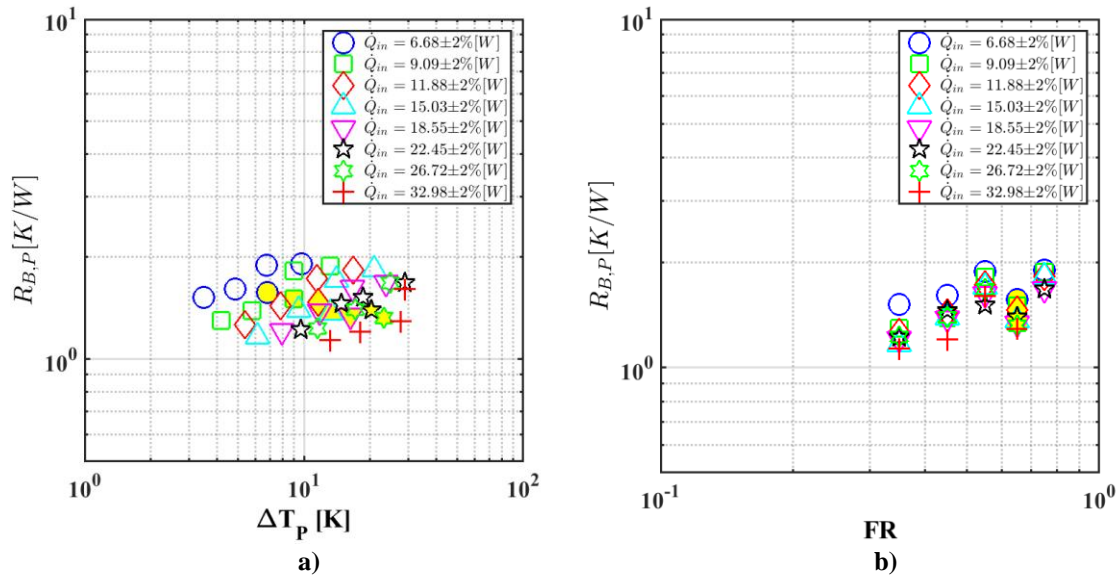


Figure 6.16 a) Variation in $R_{B,P}$ with ΔT_P c) Variation in $R_{B,P}$ with FR . The data corresponding to FR = 0.65, have been highlighted in yellow for better visualizing the trend without the data set.

Table 6.6 Estimates of the slopes in Figure 6.15b and 6.15c.

\dot{Q}_{in} [W]	$\left(\frac{n_3-1}{n_3}\right)$	$(n_3 - 1)$
$6.68 \pm 2\%$	0.24	0.31
$9.09 \pm 2\%$	0.35	0.51
$11.88 \pm 2\%$	0.33	0.49
$15.03 \pm 2\%$	0.37	0.54
$18.55 \pm 2\%$	0.30	0.38
$22.45 \pm 2\%$	0.28	0.38

The answers to the questions raised at the start of the section are as follows: i) ΔT_P increases with FR raised to a power greater than one (~ 1.44) ii) $R_{B,P}$ increases with ΔT_P raised to a power less than 0.3 (~ 0.29) and iii) $R_{B,P}$ increases with FR raised to power less than 0.5 (~ 0.42).

6.2.3 Evaluation of the film boiling resistance ($R_{B,F}$)

This section examines how FR influences $R_{B,F}$. Since the boiling curves for the film and for pool boiling are the same, those are not discussed here again. ΔT_P exhibits the same relationship (equation 6.21) with FR for film boiling as it does for pool boiling. Therefore, $R_{B,F}$ as a function of ΔT_P and FR can be written as

$$R_{B,F} = \frac{(C_3)^{\frac{1}{n_3}}}{\dot{Q}_{in}} \frac{\Delta T_P}{\left[C_3^{\frac{1}{n_3}} - \Delta T_P^{\frac{1}{n_3}} \right]} \quad (6.26)$$

$$R_{B,F} = \frac{C_3}{\dot{Q}_{in}} \frac{(FR)^{n_3}}{(1-FR)} = \frac{C_3}{\dot{Q}_{in}} \left(FR^{n_3} + FR^{(n_3+1)} + FR^{(n_3+2)} + FR^{(n_3+3)} + FR^{n_3} O(FR^4) \right) \quad (6.27)$$

Equation (6.26) suggests that $R_{B,F}$ increases with ΔT_P , since $\left[C_3^{\frac{1}{n_3}} - \Delta T_P^{\frac{1}{n_3}} \right] > 0$. Similarly, it can be argued that $R_{B,F}$ will increase with FR . Based on these observations, it is hypothesized that a power-law relationship exists between $R_{B,F}$ and ΔT_P and $R_{B,F}$ and ΔT_P FR given by

$$R_{B,F} = C_4 (\Delta T_P)^{n_4} \quad (6.28)$$

$$R_{B,F} = (C_3)^{n_4} C_4 (FR)^{n_3 n_4} \quad (6.29)$$

It should be noted that that the form of equation (6.28) may not be unique, as several other variations of equation (6.28) for example, $R_{B,F} = C_4(1 + \Delta T_P)^{n_4}$, $R_{B,F} = C_4(1 - \Delta T_P)^{-n_4}$, are possible depicting the same physical behaviour of $R_{B,F}$ with ΔT_P . These possibilities are not examined in the present discussion.

In order to confirm the validity of equations (6.28) and (6.29), plots of $R_{B,F}$ versus ΔT_P and $R_{B,F}$ versus FR are shown in Figure 6.17. The slope obtained by fitting equations (6.28) and (6.29) to the data points are illustrated in Table 6.7 along with the quality of the goodness of the fit. The obtained fit is very good suggesting that equations (6.28) and (6.29) can be used to quantify the influence of ΔT_P and FR on $R_{B,F}$. Comparing the exponents of ΔT_P and FR from equations (6.22) and (6.23) to (6.28) and (6.29), reveal that the effects of ΔT_P and FR are more pronounced on $R_{B,F}$ than $R_{B,P}$. This can also be proved by comparing equations (6.23) and (6.27) which give

$$R_{B,F} = \frac{FR}{(1-FR)} R_{B,P} \quad (6.30)$$

As FR increases, $R_{B,F}$ would increase more rapidly than $R_{B,P}$. The plots of $R_{B,P}$ and $R_{B,F}$ shown in Figures (6.2) and (6.4) validates this conclusion where the relative increments in $R_{B,F}$ are seen to be greater than $R_{B,P}$ with increasing FR.

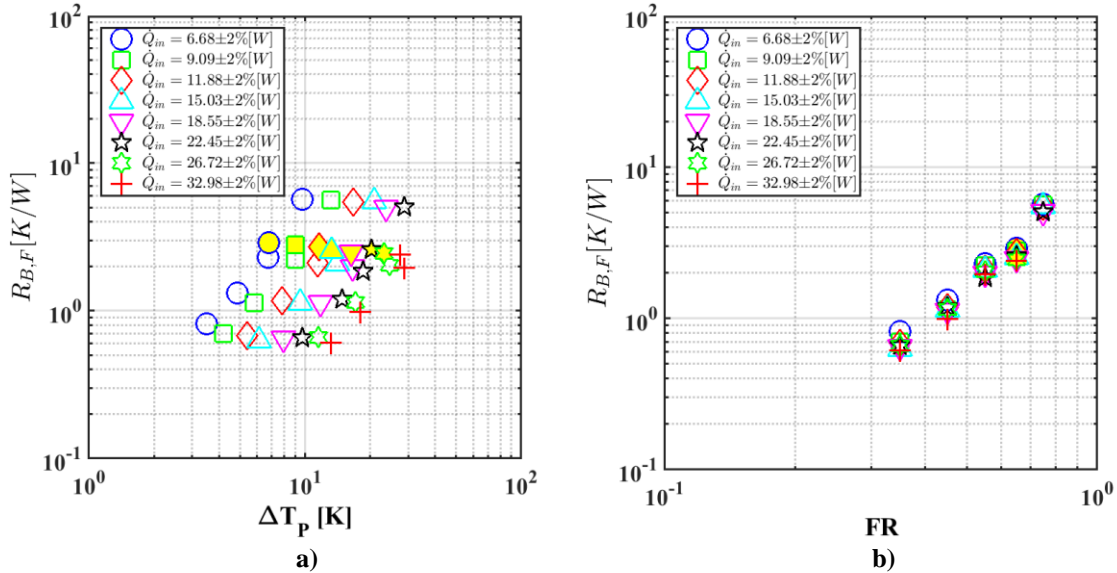


Figure 6.17 a) Variation in $R_{B,F}$ with ΔT_P c) Variation in $R_{B,F}$ with FR. The data corresponding to FR = 0.65, have been highlighted in yellow for better visualizing the trend without that data set.

Table 6.7 Estimates of n_4 and (n_3n_4) in Figure 6.17

\dot{Q}_{in} [W]	n_4	R^2	RMSE	(n_3n_4)	R^2	RMSE
$6.68 \pm 2\%$	2.19	0.993	0.232	2.81	0.998	0.122
$9.09 \pm 2\%$	2.14	0.990	0.274	2.99	0.999	0.107
$11.88 \pm 2\%$	2.19	0.990	0.266	2.98	0.999	0.093
$15.03 \pm 2\%$	2.15	0.991	0.261	3.05	0.999	0.073
$18.55 \pm 2\%$	2.27	0.989	0.254	2.90	0.998	0.082
$22.45 \pm 2\%$	2.15	0.997	0.147	2.95	0.996	0.156

The variation in $R_{B,F}$ with ΔT_P and FR can subsequently be derived using equations (6.26) and (6.27) as

$$\frac{\partial(R_{B,F})}{\partial(\Delta T_P)} = \frac{(C_3)^{\frac{1}{n_3}}}{\dot{Q}_{in}} \left[\frac{\frac{1}{C_3^{n_3} + (n-1)\Delta T_P^{n_3}}}{\left(\frac{1}{C_3^{n_3} - \Delta T_P^{n_3}} \right)^2} \right] \quad (6.31)$$

$$\frac{\partial(R_{B,F})}{\partial(FR)} = \frac{C_3}{\dot{Q}_{in}} \left[\frac{(FR)^{n_3-1}(n_3+FR-n_3FR)}{(1-FR)^2} \right] \quad (6.32)$$

Both equations (6.31) and (6.32) reveal that $R_{B,F}$ increases with ΔT_P and FR, however, the rate at which $R_{B,F}$ increases decays with increasing ΔT_P and FR. The next section examines the effects of FR on $R_{C,F}$.

6.2.4 Evaluation of the condensation film resistance ($R_{C,F}$)

The characteristic condensation curves have been discussed previously in section 6.1.3.2 and are, therefore, not presented here. Figure 6.18 shows the plot of $\Delta T_{C,F}$ versus FR. With the exception of FR = 0.55, the general trend in the data indicate increments in $\Delta T_{C,F}$ with FR.

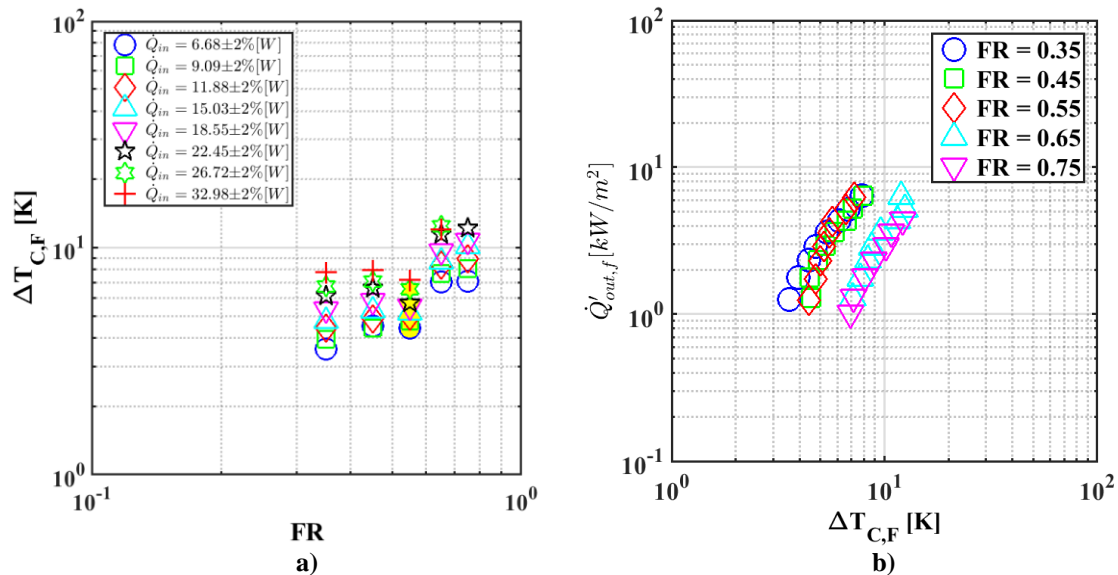


Figure 6.18 a) Variation in $\Delta T_{C,F}$ with FR. b) Condensation characteristic curve. The data corresponding to FR = 0.65, have been highlighted in yellow for better visualizing the trend without that data set.

However, the trend is not consistent. $\Delta T_{C,F}$ increases slightly from FR = 0.35 to 0.45 (with an average deviation $\sim 0.6[^\circ\text{C}]$), but between FR = 0.45 and 0.55, it shows an overall negligible variation ($\Delta T_{C,F} \sim 0.2[^\circ\text{C}]$). $\Delta T_{C,F}$ increases quite drastically from FR = 0.55 to 0.65 (with an average deviation $\sim 3.7[^\circ\text{C}]$), but thereafter show an overall variation of only $\Delta T_{C,F} \sim 0.4[^\circ\text{C}]$ between FR = 0.65 and 0.75, respectively. The closeness in the $\Delta T_{C,F}$ values between FR = 0.45, 0.55, and FR = 0.65, 0.75 suggests that the condensation mechanisms for these FR are similar. This hypothesis can be verified by examining the condensation curve in Figure 6.18b, where the data points at those respective FR are nearly coincident with each other. Also, FR = 0.35 and 0.45 exhibits a

combination of mixed and film condensation, whereas $FR = 0.65$ and 0.75 exhibits film condensation (see section 6.1.3). This is possibly the reason why $\Delta T_{C,F}$ is higher for $FR = 0.65, 0.75$ in comparison to $FR = 0.45, 0.55$. Excluding the data for $FR = 0.55$, a power law equation of the form similar to equation (6.21) may be fitted to Figure 6.18a. The equation can be written as

$$\Delta T_{C,F} = C_5(FR)^{n_5} \quad (6.33)$$

where C_5 is a dimensional constant having units of $\Delta T_{C,F}$. The slope estimated by fitting equation (6.33) to the data is outlined in Table 6.8. The n_5 magnitudes reveal that $\Delta T_{C,F}$ varies almost linearly with FR .

Table 6.8 Estimates of n_5 from Figure 6.18a.

\dot{Q}_{in} [W]	n_5
$6.68 \pm 2\%$	0.94
$9.09 \pm 2\%$	1.05
$11.88 \pm 2\%$	1.04
$15.03 \pm 2\%$	1.10
$18.55 \pm 2\%$	1.02
$22.45 \pm 2\%$	1.03

Since \dot{Q}_{in} is same across different FR , $R_{C,F} \propto \Delta T_{C,F}$. Hence, the $R_{C,F}$ versus $\Delta T_{C,F}$ plot shows a slope of one for all \dot{Q}_{in} values (see Figure 6.19a). Since $R_{C,F} \propto \Delta T_{C,F}$, $R_{C,F} \sim (FR)^{n_5}$. This is verified in Table 6.9 where an equation of the form (equation 6.34) is fitted against the $R_{C,F}$ versus FR data plotted in Figure 6.19b.

$$R_{C,F} = \frac{C_5}{\dot{Q}_{in}} (FR)^{n_5} \quad (6.34)$$

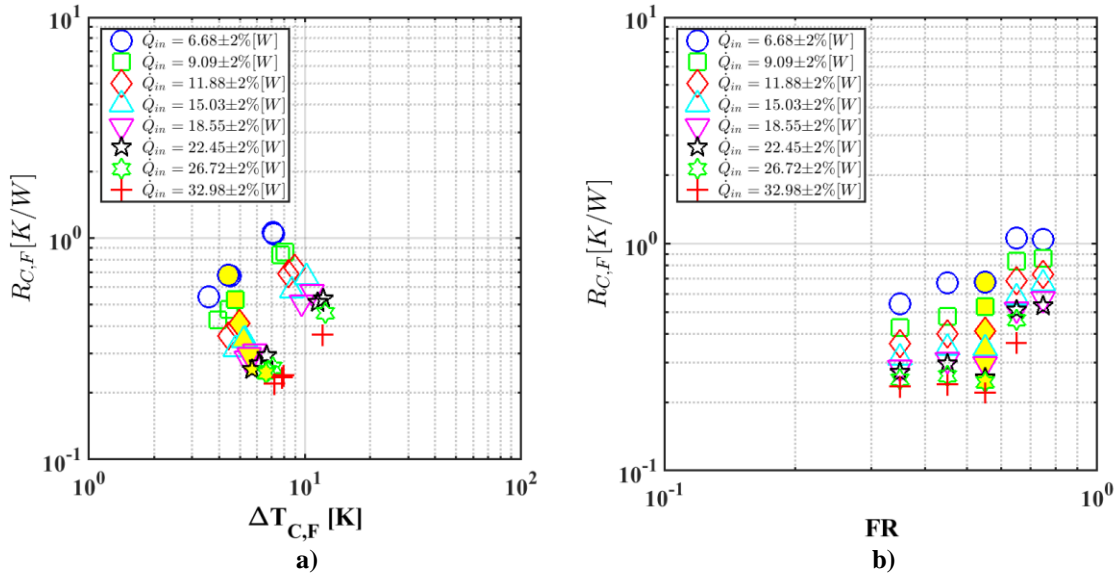


Figure 6.19 a) Variation in $R_{C,F}$ with $\Delta T_{C,F}$ b) Variation in $R_{C,F}$ with FR. The data corresponding to $FR = 0.65$, have been highlighted in yellow for better visualizing the trend without that data set.

Table 6.9 Estimates of n_5 from Figure 6.19b.

\dot{Q}_{in} [W]	n_5
$6.68 \pm 2\%$	0.91
$9.09 \pm 2\%$	1.04
$11.88 \pm 2\%$	1.03
$15.03 \pm 2\%$	1.09
$18.55 \pm 2\%$	1.02
$22.45 \pm 2\%$	1.01

The next section examines the effects of FR on Re_F , τ_i and $\left(\frac{\rho_l}{\rho_v}\right)$.

6.2.4.1 Parametric effects

The magnitudes of Re_F depend on μ_l and h'_{fg} , which are functions of T_f . Therefore, the influence of FR on T_f must be examined first. Figure 6.20a shows the plot of T_f versus FR. Two different trends are observed from Figure 6.20a. For $\dot{Q}_{in} \leq 9.09$ [W], the relative variation in T_f is seen to be smaller (~ 1.9 [°C]) than the relative variation within 9.09 [W] $\leq \dot{Q}_{in} \leq 32.98$ [W] (~ 5.0 [°C]). The T_f values do not show a consistent behaviour as they vary in zig zag pattern with FR at all \dot{Q}_{in} . This can be explained by expressing T_f as a function of T_c as

$$T_f = \frac{C_5}{2} (FR)^{n_5} + T_c \quad (6.35)$$

where a decrease in T_c (due to increase in $R_{C,F}$) with increasing FR will cause T_f to vary in a manner shown in Figure 6.20a.

In order to examine, whether the variation in T_f through FR causes Re_F to vary, a plot of Re_F versus FR is shown in Figure 6.20b. The Re_F values do not show a significant variation with increasing FR except for $\dot{Q}_{in} \geq 22.45$ [W], indicating that the variation in μ_1 and h'_{fg} with T_f is, rather small. Hence, it can be deduced that FR does not influence Re_F significantly. As Re_F is relatively independent of FR, the plot of Nu versus Re_F for different FR is not shown here.

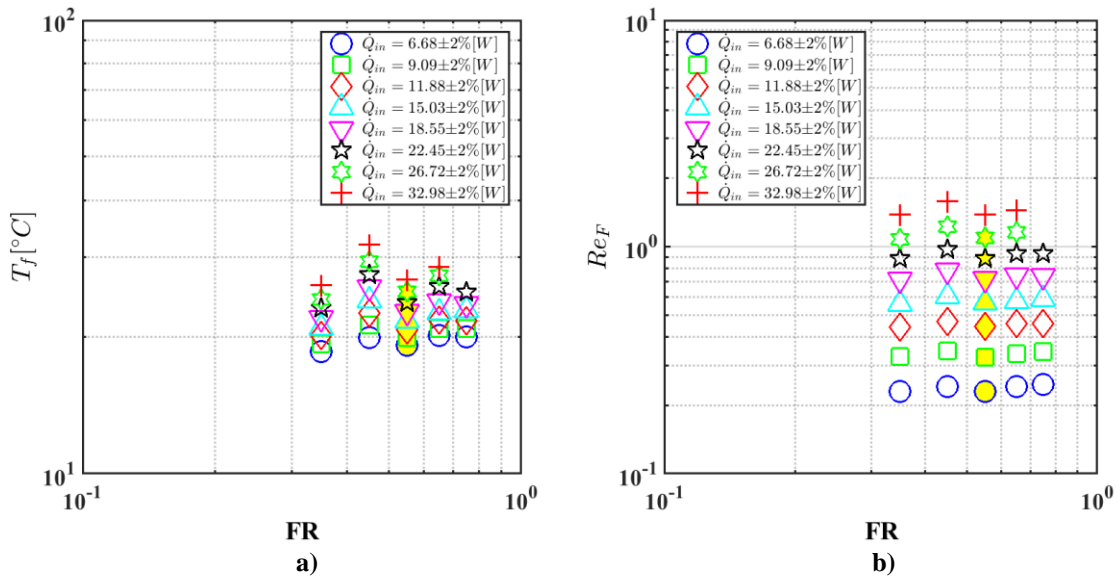


Figure 6.20 a) Variation in Re_F with FR b) Variation in T_f with FR. The data corresponding to FR = 0.65, have been highlighted in yellow for better visualizing the trend without that data set.

Figure 6.21 shows the plot of Nu versus FR. Since $R_{C,F}$ increases with FR (see Table 6.9), Nu should decrease in an identical manner with FR (excluding the data for FR = 0.55). This is validated in Figure 6.21 and Table 6.10 where the slopes of the data are evaluated.

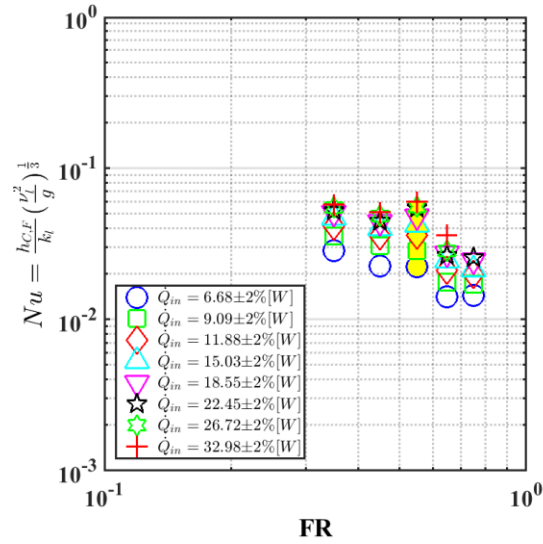


Figure 6.21 Variation in Nu with FR. The data corresponding to FR = 0.55, have been highlighted in yellow for better understanding.

Table 6.10 Estimates of n_5 from Figure 6.21.

\dot{Q}_{in} [W]	n_5
$6.68 \pm 2\%$	0.99
$9.09 \pm 2\%$	1.03
$11.88 \pm 2\%$	1.00
$15.03 \pm 2\%$	1.02
$18.55 \pm 2\%$	0.97
$22.45 \pm 2\%$	1.00

A plot of τ_i^* versus FR is shown in Figure 6.22. Similar to Re_F , τ_i^* demonstrates a weak dependency with FR for $\dot{Q}_{in} \geq 22.45$ [W]. The small variation in τ_i^* is caused primarily by the variation in the liquid phase properties through T_f . Based on this evidence, it is logical to assume that FR does not influence τ_i^* , significantly. Henceforth, the plot of Nu versus τ_i^* for different FR is not shown.

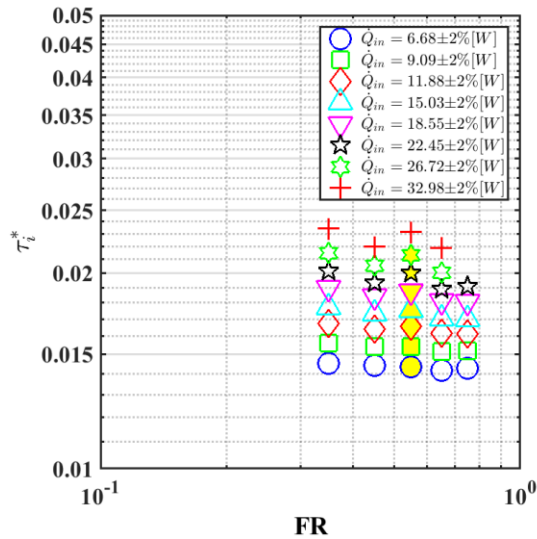
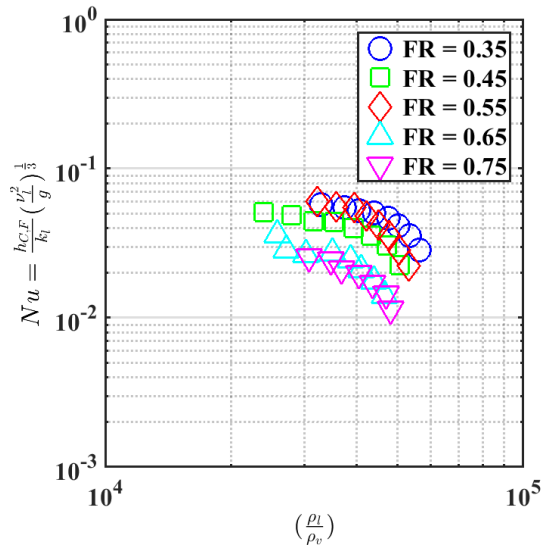
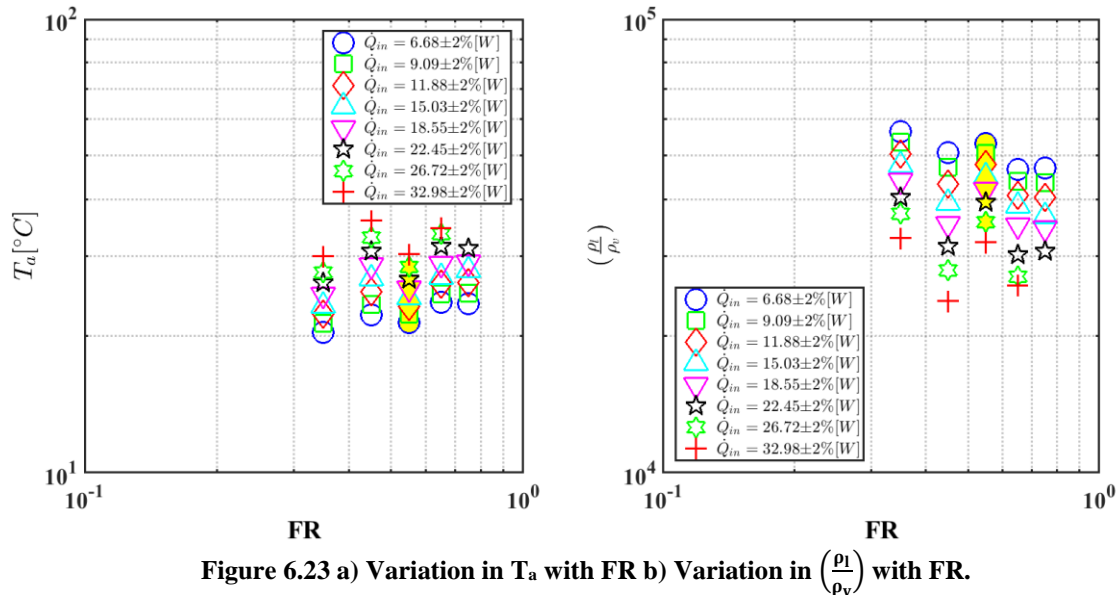


Figure 6.22 Variation in τ_i^* with FR. The data corresponding to FR = 0.55, have been highlighted in yellow for better understanding.

Both ρ_l and ρ_v are functions of FR through T_f (Figure 6.20a) and T_a (see Figure 6.23a). The equation for T_a can be written using equation (6.31) as

$$T_a = C_5(\text{FR})^{n_5} + T_c \quad (6.36)$$

ρ_l decreases with T_f , whilst ρ_v increases with T_a . Except for the data at FR = 0.55, $\left(\frac{\rho_l}{\rho_v}\right)$ should display a decreasing trend with FR. This is confirmed in Figure 6.23b, where $\left(\frac{\rho_l}{\rho_v}\right)$ is plotted against FR. A decrease in $\left(\frac{\rho_l}{\rho_v}\right)$ should demonstrate an increase in the Nu values. However, that is not the case in the Nu versus $\left(\frac{\rho_l}{\rho_v}\right)$ plot for different FR shown in Figure 6.24. This suggests that heat transfer reduction due to the deposition of the liquid droplets at higher FR at the condenser surface dominates over the heat transfer enhancement caused by the decrement in the entrainment effects.



6.3 Summary

In this chapter, the results illustrating the effects of the input heat rate, \dot{Q}_{in} and the fill-ratio, FR, on the pool ($R_{B,P}$), film ($R_{B,F}$), and condensation thermal resistance ($R_{C,F}$) have been analyzed. The key inferences from this analysis are as follows:

- The bubble coalescence and interference effects are significant during the liquid pool boiling at all \dot{Q}_{in} . This is due to the lower operating pressures of these TS which promote increased bubble formation and interaction. The smaller diameter of the TS also

enhances the likelihood of the bubbles interacting from diametrically opposite surfaces. These effects cause $R_{B,P}$ to be higher than the conventional nucleate pool boiling.

- For intermediate \dot{Q}_{in} , film breakdown followed by formation and spreading of dry patches occur at $FR = 0.35$ and 0.45 . $R_{B,F}$ increases at the point of dry patch spreading, whilst it decreases due to rewetting of the evaporator surface. For $FR = 0.55 - 0.75$, the trends in the data suggest a continuous film flow at all values of \dot{Q}_{in} . $R_{B,F}$ is higher in these cases, as the heat transfer is through conduction and surface evaporation.
- A combination of dropwise and mixed condensation is observed at lower \dot{Q}_{in} for $FR = 0.35, 0.45$ and 0.55 . This is due to the very low values of Re_F obtained at low \dot{Q}_{in} . At higher \dot{Q}_{in} , transition to film condensation occurs for all FR .
- Increase in \dot{Q}_{in} alters the condensate flow states, increases the interfacial shear stress and the entrainment effects. All these effects promote transition to film condensation and, thus, increase in $R_{B,F}$.
- The wall superheat is shown to demonstrate a power-law relationship with FR . Thus, $R_{B,P}$, $R_{B,F}$ and $R_{C,F}$ all demonstrate a power-law relationship with FR . The effects of FR are more pronounced on $R_{B,F}$ than $R_{B,P}$.
- The FR does not influence the condensate flow states (Re_F) and the effects of the interfacial shear stress. However, the entrainment effects are seen to decrease with increasing FR . This effect is less dominant over the effects of droplet deposition at the condenser surface occurring at higher FR .

Chapter 7

7 Validation of the pool boiling and film boiling thermal resistance model

This chapter validates the pool and the film boiling correlations developed in Chapter 4. Data from prior studies, along with the results from the present study, are utilized to determine the exponents and the coefficients of the thermal resistance equations. The chapter is divided into five sections. The first section describes the method for inclusion and exclusion of previous data. The second section outlines the regression method employed to correlate the data. The third section presents the results from the validation of the pool boiling equation, whilst the fourth section describes the results from the validation of the film boiling equation. The fifth section provides recommendations for the applicability of the equations in thermosyphon (TS) and heat pipe (HP) design. It is important to note that the validation of the condensation correlations is not covered in this chapter, as that is a part of the ongoing work.

7.1 Criteria for inclusion and exclusion of the previous studies

Since the present investigation is conducted on copper-distilled water TS with evaporator, condenser and adiabatic sections, the primary focus is on data available from studies on copper-distilled water TS with three heat transfer sections. The criteria adopted for the inclusion and exclusion of previous experimental data are outlined below

- i) Studies with well-documented experimental setups, providing detailed information on varying operational (heating input power (\dot{Q}_{in}), fill ratio (FR), aspect ratio (AR) and inclination angle (θ)), as well as geometric parameters (inner diameter (D_i), evaporator length (L_e), adiabatic length (L_e) and the condenser length (L_c)), were selected.
- ii) Since raw temperature data are not always available, studies reporting the temperature distribution along the length of the TS, either in graphical or tabular form,

were selected. Studies from which the extraction of the temperature data is difficult due to the data points represented in small-scale graphs were excluded.

iii) Only data providing evidence of fully established nucleate boiling and film boiling in previous studies were selected.

The studies satisfying the abovementioned criteria are outlined in Table 7.1, whilst Table 7.2 lists the studies that are excluded. It is clear from Table 7.2 that, despite the considerable number of literature on copper-distilled water TS, data from those studies cannot be evaluated for validation and prediction purposes.

Table 7.1 Details of the experimental conditions for the copper-water data sets used in the present analysis

Included studies	Operational parameters		
	\dot{Q}_{in} [W]	FR	AR
Alizadehdakheel et al. (2010)	350.00 - 700.00	0.30 - 0.80	22.86
Amatachaya and Srimuang (2010)	231.00 - 831.60	0.60	9.81 - 11.78
Baojin et al. (2009)	298.00 - 594.63	0.36	15.56
Fadhil (2015)	50.10 - 349.27	0.50	9.90
Jafari et al. (2017)	30.00 - 200.00	0.35 - 1.00	4.54
Joudi et al. (2000)	37.32 - 219.79	0.24 - 0.57	5.00
Mozumder et al. (2010)	2.00 - 10.00	0.55	10.00
Shiraishi et al. (1982)	43.54 - 1345.86	0.50 - 1.00	7.57

Table 7.2 List of studies excluded from the present analysis.

Excluded studies	Reasons for exclusion
Abdullahi (2015)	1) No adiabatic section. 2) Temperature data were presented as curves.
Alammar et al. (2018)	1) No adiabatic section. 2) Temperature data were presented as curves.
Emami et al. (2008)	1) No temperature data reported.
Kim et al. (2018)	1) No temperature data reported
Li et al. (1991)	1) No temperature data reported.
Negishi and Sawada (1983)	1) No adiabatic section. 2) No temperature data reported.
Nguyen-Chi et al. (1980)	1) No temperature data
Nguyen-Chi & Groll (1981)	1) No temperature data
Noie (2005)	1) For fixed AR, only data for two \dot{Q}_{in} was reported. 2) The temperature data at different FR demonstrates inconsistency.
Noie et al. (2007)	1) No temperature data.
Noie et al. (2009)	1) FR not reported.
Ong & E-Alalhi (1999)	1) No temperature data reported.
Payakaruk et al. (2000)	1) No temperature data reported.
Zuo and Gunnerson (1994)	1) No temperature data reported. 2) No FR and AR reported.

7.2 Regression method

A multi-parameter non-linear regression method is employed to correlate both past and present data with the boiling equations. The goal is to accurately estimate the exponents and the coefficients in the equations. Since there are numerous independent non-dimensional variables in the equations (for e.g. Prandtl number (Pr), Bubble Reynolds number (Re_b), Film Reynolds number (Re_F), Bond number (Bo), Jakob number (Ja), Archimedes number (Ar), Confinement number (Co) and the density ratio), a step-by-step procedure is adopted. In this procedure, each variable is added, and the resultant goodness of the power-law fit is determined. The procedure is continued until all coefficients and the exponents of the influencing parameters are determined, and the equations are able to represent the data accurately within the experimental uncertainty.

The non-linear least squares solver in MatLab, utilizing the Levenberg-Marquardt algorithm (Levenberg, 1944, Marquardt, 1963), is used to fit the equations to the data. The estimated coefficients and the exponents are defined based on those fitted values that gives the least summed square of the residuals between the predicted and the actual values. The goodness of the fit is evaluated through a series of statistical parameters, which include the coefficient of determination (R^2 coefficient), root-mean square error (RMSE), the number of data points within $\pm 15\%$ and $\pm 30\%$, and the number of true values lying within the 95% confidence intervals of the predicted values. The resultant fitted coefficients and exponents, which gives the i) highest R^2 coefficient ii) least RMSE ii) maximum number of data points within $\pm 15\%$ and $\pm 30\%$ and iv) the maximum number of data points within the confidence interval, are selected and presented.

A total of 70 data points from the previous study and 154 data points from the present study were utilized to fit the boiling equations. The data from the present study include all cases with varying \dot{Q}_{in} , FR and AR. In the first trial, all the 70 data points from the previous were utilized in the regression analysis. However, certain number of studies were excluded from the final analysis due to inconsistent behaviour in their boiling curve (refer Chapter 2) and considerable deviation of the results from the other authors.

The next section describes the results from fitting the pool boiling equation.

7.3 Pool boiling model validation

7.3.1 Present study

The characteristic nucleate pool boiling equation from Chapter 4 (equation 4.37 or 4.38), in its simplest form, can be expressed as

$$R_{NB,Pk_iL} = f\left(\text{Pr}_1, \text{Re}_b, \text{Co}, \frac{L_p}{D_b}\right) \quad (7.1)$$

where the subscripts NB and P denotes nucleate boiling and pool, respectively. $\text{Pr}_1 = \frac{\mu_l c_{p,l}}{k_l}$, $\text{Re}_b = \frac{\dot{Q}'_{in,f} D_b}{h_{fg} \mu_l}$ and $\text{Co} = \frac{D_b}{D_i}$. Here, D_b and D_i represent the bubble and internal diameter, $\dot{Q}'_{in,f}$ is the input heat flux to the fluid, μ_l , $c_{p,l}$, k_l are the dynamic viscosity, specific heat and thermal conductivity of the working fluid (WF) liquid phase.

Adopting the procedure outlined in Section 7.2, it was revealed that $\left[\frac{\rho_l - \rho_v}{\rho_v}\right]$ (derived as π_9 ; also known as the density ratio) exerts significant influence on $R_{NB,P}$. The vapour-flow Froude (Fr_v), defined as $\text{Fr}_v = \left[\frac{\dot{Q}'_{in,f,v}}{\rho_v h_{fg} \sqrt{g D_i}}\right]$, where $\dot{Q}'_{in,f,v} = \frac{\dot{Q}_{in}}{A_v}$ and A_v is the vapour cross-sectional area, has also been observed to affect the pool boiling heat transfer coefficient (Kusuda and Imura, 1973). Since, the FR and the AR are the primary performance variables, they need to be included in the final form of equation (7.1). Taking these factors into consideration, equation (7.1) can be re-written as

$$R_{NB,Pk_iL} = f\left(\text{Pr}_1, \text{Re}_b, \left[\frac{\rho_l - \rho_v}{\rho_v}\right], \text{Fr}_v, \text{Co}, \frac{L_p}{D_b}, \text{FR}, \text{AR}\right) \quad (7.2)$$

In equation (7.2), the terms that are functions of the WF properties (Pr_1 , Re_b , density ratio and Fr_v), are written first, followed by the length scale terms. One way to minimize uncertainty in the estimated coefficients and exponents is by reducing the number of non-dimensional variables. $R_{NB,P}$ expressed only as a function of the length scale terms is given by $R_{NB,P} = f\left(\frac{D_i}{D_b}, \frac{L_p}{D_b}, \frac{L_p}{L_e}, \frac{L_e}{D_i}\right)$. It is evident that there are only four relevant length scales D_b , L_p , L_e and D_i which can be combined appropriately as $\left[\frac{D_i}{D_b}\right]$ and $\left[\frac{L_p}{L_e}\right]$ terms,

representing Co and FR, respectively. Thus, the final form of equation (7.2) can be written as

$$R_{NB,pk_l L} = C(\text{Pr}_l)^a (\text{Re}_b)^b \left[\frac{\rho_l - \rho_v}{\rho_v} \right]^c (\text{Fr}_v)^d \left[\frac{D_i}{D_b} \right]^e \left[\frac{L_p}{L_e} \right]^f \quad (7.3)$$

Equation (7.3) will now be utilized to correlate the data from the present experiments. Note that any other pair of non-dimensional length scale variables, for example, $\left(\left[\frac{L_p}{D_b} \right], \left[\frac{L_e}{L_e} \right] \right)$ and $\left(\left[\frac{L_e}{D_i} \right], \left[\frac{L_p}{D_i} \right] \right)$, could have chosen. The pair $\left(\left[\frac{D_i}{D_b} \right], \left[\frac{L_p}{L_e} \right] \right)$ was chosen as it gave the best fit, evaluated through the different statistical parameters outlined in equation (7.1)

Figure 7.1 shows the plot of the predicted Y values against the true Y values along with the 45° parity line and the $\pm 15\%$ bounds, where $Y = \left[\frac{1}{R_{NB,pk_l L_p}} \right]$. This form of expression for Y was chosen over $Y = R_{NB,pk_l L_p}$ as it gave a better R^2 coefficient and a lower mean absolute deviation. The mean absolute deviation and the CoV of the predicted values are 8.9% and 10.4%, respectively. 87% of the points lie within the $\pm 15\%$ bounds, and 100% of the points lie within the $\pm 30\%$ bounds. The maximum error of the predicted value is 28.1%. The estimated coefficients and the exponents are outlined in Table 7.3, which are in the same order as the variables listed in equation (7.3). The maximum variation in the estimated exponents with different initial guesses was within $\pm 5\%$, providing confidence in using the exponents for further predictions.

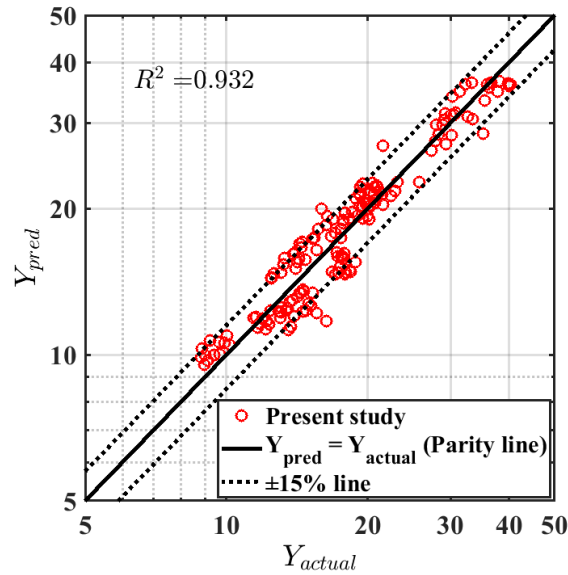


Figure 7.1 Plot of the predicted Y values versus the actual Y values.

Table 7.3 Estimated coefficients and exponents from the non-linear regression fitting

C	a	b	c	d	e	f	R ²	RMSE
8.50	-2.78	1.27	2.67	-1.23	-8.78	-1.40	0.932	1.99

Examining the coefficients, it is noted that C_0 exerts the maximum influence on $R_{NB,P}$. Therefore, in order to obtain the desired $R_{NB,P}$, one must vary D_i . It is emphasized that the magnitudes of the coefficients and the exponents shown in Table 7.3 may slightly change when any sets of data are added or omitted from the present analysis. However, the form of equation (7.3) will not change for different combinations of the coefficients and the exponents. The aim here is not to establish fixed values of the coefficients but, rather, to determine the correct form of the boiling equation and optimal magnitudes of the coefficients and exponents that can be used to predict the thermal resistance for the TS operating within the range covered within this study.

Figure 7.2 shows the 95% confidence intervals of the predicted Y values as error bars. The actual Y values are also plotted to show their location on the error bars. 96% of the actual Y values are within the 95% confidence intervals of the predicted values. Both these figures provide evidence that the fit is very good, considering the uncertainty in the experimental data. This indicates the nucleate pool boiling equation can successfully predict the thermal resistance of TS for varying \dot{Q}_{in} , FR, and AR.

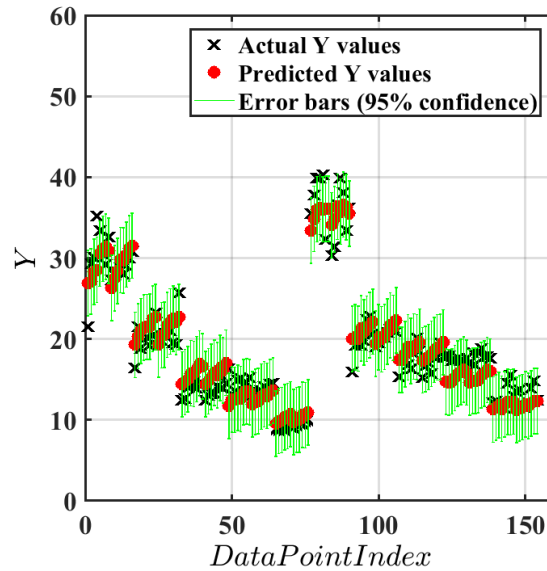


Figure 7.2 Plot showing 95% confidence intervals of the predicted data as error bars and the locations of the actual data on the error bars. The data point index ranges from the data corresponding to $FR = 0.35$ to $FR = 0.75$ and $AR = 5.33$ to $AR = 12.43$, respectively.

7.3.2 Previous studies

The length of the TS (L_t) and the internal diameter (D_i) varies between different studies. Hence, it is hypothesized that $\left(\frac{L_t}{D_i}\right)$ instead of $\left(\frac{L_e}{D_i}\right)$ is a more relevant non-dimensional scaling term influencing $R_{NB,P}$. Based on the arguments presented in the previous section on the dependency of $R_{NB,P}$ on the length scale terms, the final form of the equation for $R_{NB,P}$ can be written as

$$R_{NB,Pk_1L} = C(\text{Pr}_1)^a (\text{Re}_b)^b \left[\frac{\rho_l - \rho_v}{\rho_v}\right]^c (\text{Fr}_v)^d \left[\frac{D_i}{D_b}\right]^e \left[\frac{L_p}{D_b}\right]^f \left[\frac{L_t}{D_i}\right]^g \quad (7.4)$$

The hypothesis is tested by using $\left(\frac{L_e}{D_i}\right)$ in the final form of the equation which resulted in a poorer fit than $\left(\frac{L_t}{D_i}\right)$. Hence, equation (7.4) is used to correlate the previous data. Note that instead of $\left(\frac{L_t}{D_i}\right)$, other expressions including L_t for example, $\left(\frac{L_t}{L_p}\right)$ or $\left(\frac{L_t}{D_b}\right)$, could be used however, in all the cases, a similar fit as that of $\left(\frac{L_t}{D_i}\right)$ would be obtained. The term $\left(\frac{L_t}{D_i}\right)$ has been chosen based on the fact that a parameter representing the device AR must be included in the final form of the equation.

Figure 7.3 shows the plot of the predicted Y values versus the actual Y values, where $Y = \left[\frac{1}{R_{NB,P} k_1 D_b} \right]$. Note that D_b is used instead of L_p to non-dimensionalize the $R_{NB,P}$ term. This choice gave a better R^2 coefficient and a higher number of points within the $\pm 15\%$ and $\pm 30\%$ bounds. While D_b has a more pronounced effect on $R_{NB,P}$ in the previous studies, (L_p) has a more influence on the R_{NB} data in the present study. The reason for this behaviour is not examined here but it is hypothesized to be due to the difference in the number of nucleation sites per D_i and L_p . The mean absolute deviation and the CoV of the predicted values are 25.0% and 24.8%, respectively. 62% of the points lie within the $\pm 15\%$ bounds and 76.5% of the points lie within the $\pm 30\%$ bounds. The estimated coefficients and the exponents are outlined in Table 7.4 which are in the same order as the variables listed in equation (7.4).

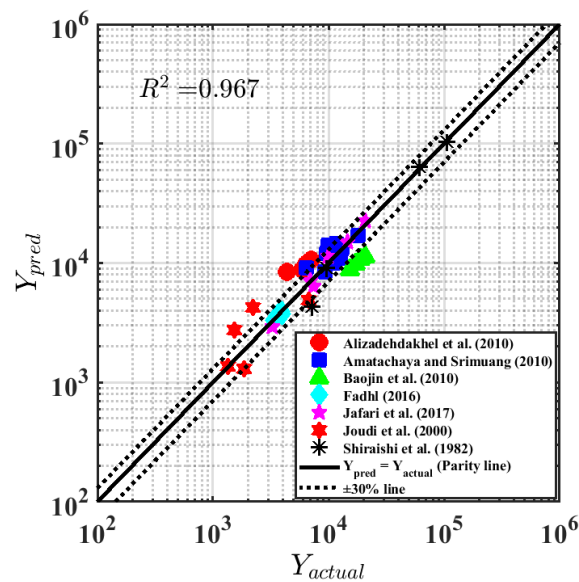


Figure 7.3 Comparison between the actual Y values and the predicted Y

Table 7.4 Estimated coefficients and exponents from the non-linear regression fitting

C	a	b	c	d	e	f	g	R^2	RMSE
9.55×10^{-7}	-3.98	0.33	2.07	0.45	2.75	0.73	-0.02	0.967	3.09×10^3

Figure 7.4 shows the plot of the 95% confidence intervals of the predicted Y values as error bars. The actual Y values are also shown on the plot to assess their location on the error bars. Nearly all predicted data, except for Baojin et al. (2009), lie close to the actual data. 93% of the actual Y values lie within the confidence intervals of the predicted Y

values, indicating a reasonably good fit. Three data points from Baojin et al. (2009) lie outside the confidence intervals.

Although the R^2 coefficient obtained from this analysis is slightly higher than that obtained from the analysis of the authors data, a lower percentage of points is observed to lie within the $\pm 15\%$ and the $\pm 30\%$ bounds. This could be due to a variety of reasons. Firstly, none of the previous studies report the overall energy balance achieved during the experiments. Some studies (Amatachaya and Srimuang, 2010) assume that there was no heat loss from the TS, which is inaccurate. Secondly, the overall uncertainties in the boiling thermal resistance is not always reported in the previous studies. Thirdly, in some studies, the experiments were not carried out for longer periods of time and, thus, sufficient number of steady state data were not gathered. Fourthly, few studies (Alizadehdakhel et al., 2010, Amatachaya and Srimuang, 2010) employed only a couple of thermocouples to measure the adiabatic surface temperature. Adiabatic surface temperatures may vary near the evaporator section and, thus, two TC are not sufficient to measure the spatial variation in temperature. Fifthly, a significant portion of the previous temperature data was gathered from the temperature distribution plots, and, thus, the uncertainty due to the extraction procedure is inherently included in the analyzed data. Nevertheless, Figure 7.4 provides evidence that the pool boiling correlation, with the related coefficients and exponents, can predict the data reasonably well.

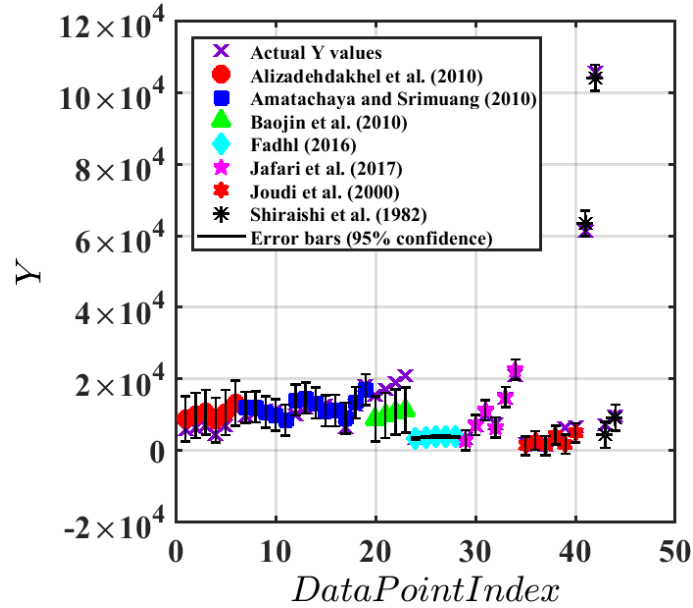


Figure 7.4 Plot showing 95% confidence intervals of the predicted data as error bars and the locations of the actual data on the error bars.

The next section validates the film boiling correlations.

7.4 Film boiling model validation

7.4.1 Present study

The film boiling thermal resistance, $R_{B,F}$, can be computed from $R_{B,P}$ as $R_{B,F} = \left(\frac{FR}{1-FR} \right) R_{B,P}$. However, this formulation can only be used when FR is known *a priori*, and the predicted values of $R_{B,P}$ are available. In cases, where the values of $R_{B,P}$ cannot be determined, film boiling equations must be used to predict $R_{B,F}$.

Chapter 6 provides evidence that the film boiling mode is dominated by conduction through the film and evaporation from the film surface. Therefore, the boiling equation for the film evaporation is utilized here. Based on the argument that minimum number of non-dimensional terms should be used while fitting the data, the final form of the film boiling equation (equation 4.42 or 4.43) can be written as

$$R_{E,F,pk_1L} = C(\text{Pr}_l)^a (\text{Re}_F)^b \left[\frac{\rho_l - \rho_v}{\rho_v} \right]^c (\text{Fr}_v)^d \left[\frac{L_f}{\delta_{E,F}} \right]^e \left[\frac{D_i}{\delta_{E,F}} \right]^f \left[\frac{L_p}{L_e} \right]^g \quad (7.5)$$

where the subscript E,F denotes evaporation and film, respectively. Figure 7.5 shows the plot of the predicted Y values against the actual Y values, where $Y = \left[\frac{1}{R_{NB,pk_1\delta_{E,F}}} \right]$. This form of expression for Y was chosen as it gave a better R^2 coefficient and a lower mean absolute deviation. The maximum percentage error of the predicted value was obtained to be 26.5%. 84% of the predicted values lie within the $\pm 15\%$ bounds and 100% of the predicted values lie within the $\pm 30\%$ bounds. The mean absolute deviation and the CoV of the predicted values were 9.0% and 10.5%, respectively. The estimated coefficients and the exponents are outlined in Table 7.5, where the order of the exponents is identical to the order of the variables in equation (7.5).

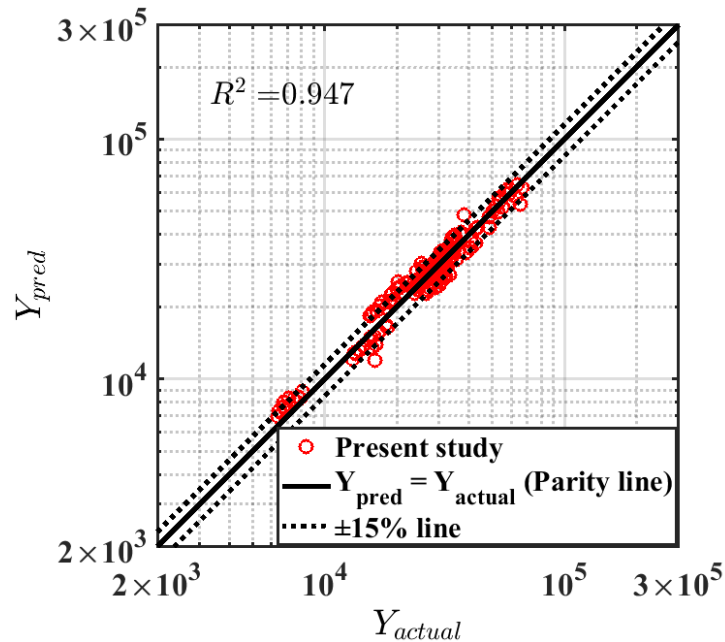


Figure 7.5 Plot of the predicted Y values versus the actual Y values.

Table 7.5 Estimated coefficients and exponents from the non-linear regression fitting

C	a	b	c	d	e	f	g	R^2	RMSE
0.17	-2.17	1.22	2.09	-1.16	-0.20	-0.48	-1.34	0.947	2.97×10^3

Figure 7.6 shows the 95% confidence intervals of the predicted Y values as error bars. It also illustrates how close the actual Y values are to the predicted Y values and the location of the actual Y values on the confidence intervals. 98% of the points lie within the confidence intervals, suggesting that equation (7.5) along with the estimated

coefficient and the exponents can accurately predict the $R_{B,F}$ values within the ranges investigated in this study.

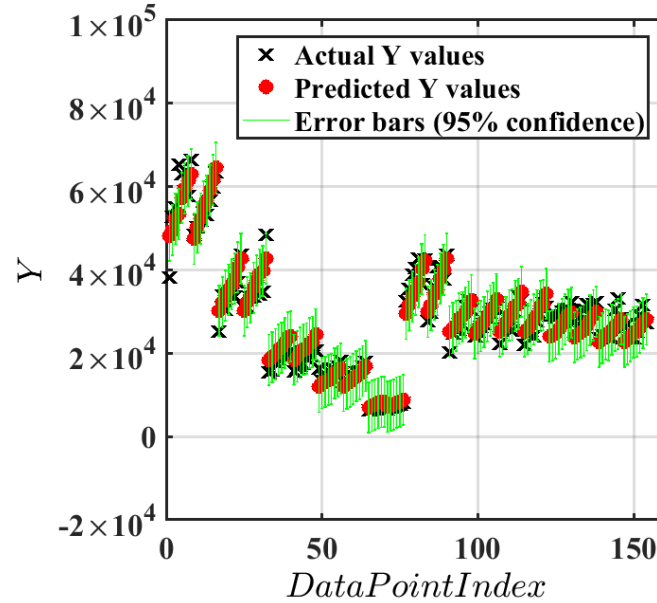


Figure 7.6 Plot showing 95% confidence intervals of the predicted data as error bars and the locations of the actual data on the error bars. The data point index ranges from the data corresponding to $FR = 0.35$ to $FR = 0.75$ and $AR = 5.33$ to $AR = 12.43$, respectively.

The next section assesses the film boiling equation in predicting the previous data.

7.4.2 Previous studies

The final form of the film boiling equation (4.50), based on the minimum number of non-dimensional variables, is obtained as

$$R_{NB,Fk}L = f\left(Pr_L, Re_F, \left[\frac{\rho_l - \rho_v}{\rho_v}\right], Fr_{v_f}, \left[\frac{L_f}{D_b}\right], \left[\frac{L_e}{D_i}\right], \left[\frac{L_t}{D_i}\right]\right) \quad (7.6)$$

Equation (7.6) when fitted to the previous data with $L = L_f$, demonstrated a slightly worse fit compared to the fit obtained against the equation for pool boiling (equation 7.4). The fit, not shown here, demonstrated high variability in the predicted data from Alizadehdakhel et al. (2010). This is hypothesized to be due to very high values of the vapour velocity, u_v obtained from Alizadehdakhel et al. (2010). u_v estimated as $u_v = \left[\frac{\dot{Q}_{in}}{A_{cr} h_{fg} \rho_v}\right]$, reached values as high as 13.75 [m/s], compared to other studies where u_v ranged between 0.3 ~ 6 [m/s]. In the fit, 44% of the data points were within $\pm 15\%$ bounds, whereas 56% of the data points were within $\pm 30\%$ bounds. The mean absolute

deviation and CoV was 32.8% and 37.2%, respectively. The R^2 coefficient was obtained as 0.838.

To better predict the data from Alizadehdakhel et al. (2010) and other studies, $R_{NB,F}$ was estimated from the predicted $R_{NB,P}$ values. Figure 7.7 shows a comparison of the predicted Y versus actual Y values where $Y = \left[\frac{1}{R_{NB,P} k_1 D_b} \right]$. The fit is improved as the 53.8% points lie within the $\pm 15\%$ bounds, whilst, 64.1% points lie within the $\pm 30\%$ bounds. The mean absolute deviation and the CoV were obtained as 27.4% and 28.5%, respectively. The R^2 coefficient was obtained as 0.803.

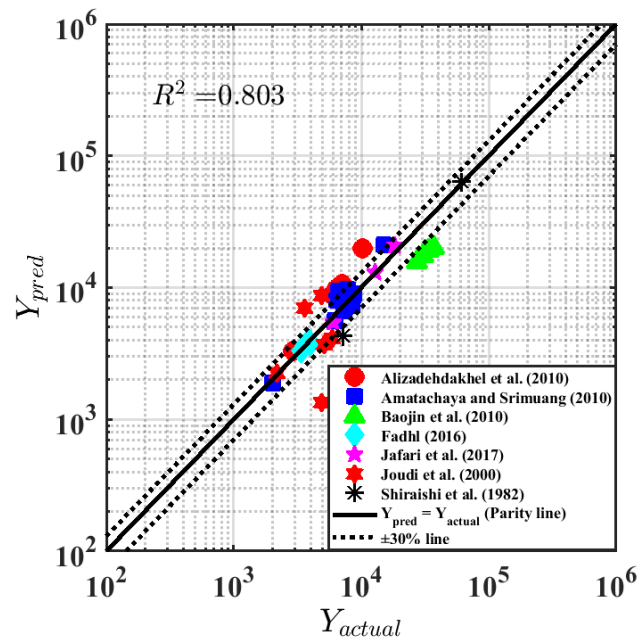


Figure 7.7 Plot of the predicted Y values versus the actual Y values.

Figure 7.8 shows the 95% confidence intervals of the predicted Y values as error bars along with the actual values. Except for the data from Baojin et al. (2009), all the data points lie within the confidence intervals, indicating that 89.74% of points fall within the interval. The error bars below 0 arise from the fact there are fewer data points for estimating RMSE error for those studies (Shiraishi et al., 1982) and the higher absolute RMSE error values for the outlier data points (Joudi et al., 2000).

The above discussion might suggest that the derived film nucleate boiling equation is not as robust as the pool boiling equation. However, that is not the case. Equation (7.6), when

plotted against the present data show that 82.5% of the points lie within the $\pm 15\%$ bounds, whereas 99.5% points lie within the $\pm 30\%$ bounds with an R^2 coefficient of 0.947. This suggest that the equation performs well against consistent data sets.

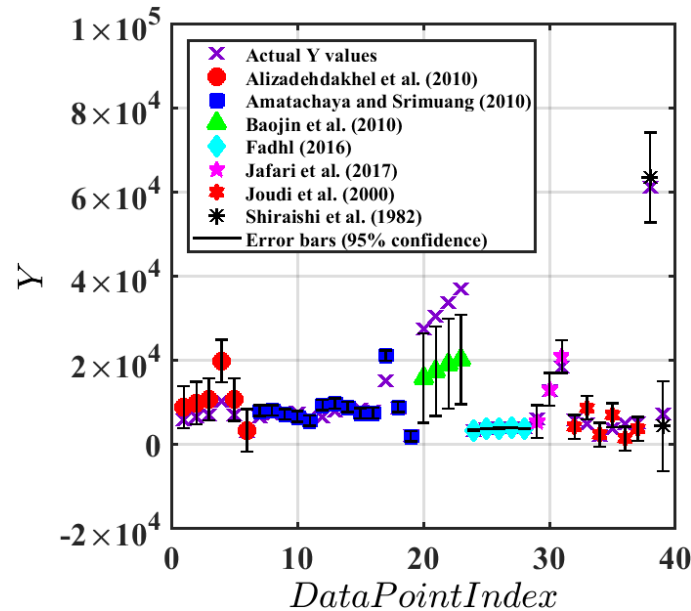


Figure 7.8 Plot showing 95% confidence intervals of the predicted data as error bars and the locations of the actual data on the error bars.

7.5 Summary and recommendations

This chapter evaluates the performance of the derived pool and film boiling thermal resistance equations against previous and present experimental data. The form of the equations is similar, representing the effects of the Reynolds number, the Prandtl number, the Froude number, and the density ratio. The other effects are accounted by the length scale ratios, which differ for nucleate pool, film evaporation and film nucleate boiling. The choice of the length scale ratios depends on the boiling mechanisms.

The performance of the equations against the present data is excellent as they predict the nucleate and film boiling thermal resistance within $\pm 15\%$. However, the prediction slightly worsens for the previous data. This could be attributed to the variation in the saturation pressure within the thermosyphons across different studies and uncertainties within the reported experimental data. In order to improve the confidence of the predicted coefficients and the exponents, more good quality consistent datasets need to be

compared against the equations. More experimental data are being gathered by the author from the ongoing experiments.

As an end user, one should predict either the pool boiling or the film boiling thermal resistance using these equations and then estimate the total boiling resistance (R_B) using the relation $R_B = FR \times R_{B,P}$ or $R_B = (1 - FR) \times R_{B,F}$. However, one must know *a priori*, the input heating rate (\dot{Q}_{in}), the liquid pool length (L_p), the evaporator length (L_e) and the vapour temperature (T_v) to estimate the thermal resistance from these equations. Typically, information on \dot{Q}_{in} and L_e is available from the intended thermosyphon application, and L_p is known from the manufacturer's specification. The performance of the thermosyphon can be evaluated once the vapour temperature is known, which can be estimated from the thermodynamic model proposed in Chapter 3.

The next chapter summarizes the key findings from this work and outlines the scope for the future work.

Chapter 8

8 Conclusions and recommendations for future work

The primary objective of this research was to develop a more rigorous understanding of the thermal performance of thermosyphons (TS) and heat pipes (HP) as a function of their design parameters and operating conditions. This was achieved through a combination of theoretical analyses and experimental modelling.

This chapter, based upon the findings, highlights the main conclusions from the present work. This chapter is divided into three parts. The first part describes the main findings from the theoretical analysis and the experimental testing of the TS. The second part outlines the novel contributions from this work, and the third section outlines the scope for future research.

8.1 Conclusions

8.1.1 Conclusions derived from the theoretical analyses

The key conclusions from the theoretical analyses of this work are summarized below

- The analyses of the previous data reveal that the boiling and the condensation behaviour inside copper (TS) pass through similar regimes to those illustrated in the typical boiling and the condensation curves. The slope of the boiling curves ($1.10 \leq n \leq 1.86$), however, are less than that obtained from the typical boiling curve ($n \approx 3$) for flat surfaces. This is due to significant bubble coalescence and interference effects inside cylindrical enclosures.
- The power-law equations derived based on the characteristic boiling and the condensation curves fully characterize the relationship between pool boiling thermal resistance ($R_{B,P}$), film boiling thermal resistance ($R_{B,F}$), condensation thermal resistance ($R_{C,F}$), and input heating rate (\dot{Q}_{in}). $R_{B,P}$ and $R_{B,F}$ consistently decrease with \dot{Q}_{in} ; however, the rate of decrease in $R_{B,P}$ and $R_{B,F}$ decays with increasing \dot{Q}_{in} . $R_{C,F}$ can either

increase or decrease with \dot{Q}_{in} depending on the condensate flow states and the effects of the countercurrent vapour flow.

- Based on the observed trends between $R_{B,P}$ and the fill ratio (FR), a power-law relationship between them is proposed, which correlates the data fairly well. $R_{B,P}$ decreases very slowly for the lowest AR = 2.27, whereas $R_{B,P}$ decreases with FR in an inversely proportional manner for the highest AR = 11.78 and 22.86. $R_{B,F} \propto (1 - FR)^{-1}$ for AR = 11.78 and 22.86. A power-law relationship between $R_{C,F}$ and FR is proposed which correlates the data very well. $R_{C,F}$ decreases with FR for FR > 1 due to the liquid carryover phenomena, whereas $R_{C,F}$ increases with FR for FR < 1, due to a higher rate of accumulation of the condensate at the condenser than the rate at which the liquid flows.
- The thermodynamic model developed for TS and a HP reveals that the working fluid (WF) enters the condenser in a superheated state, while it enters the evaporator in a sub-cooled state, irrespective of the operating conditions. The thermodynamic model also shows that \dot{Q}_{in} , FR, the aspect ratio (AR) and the device inclination angle (θ) influence the state of the WF at each stage of the thermodynamic cycle. The thermodynamic model can not only predict the changes in the thermodynamic properties but can also be used to estimate the operating temperature (T_{op}) of a TS and a HP, which is typically the adiabatic temperature (T_a).
- The non-dimensional thermal resistance equations developed for film and pool boiling have the same form of expressions. The expressions are functions of the Prandtl number (Pr), the bubble Reynolds number (Re_b) or the film Reynolds number (Re_F), the density ratio $\left(\frac{\rho_l - \rho_v}{\rho_v}\right)$, and the vapour flow Froude (Fr_v). The other parameters in the expressions are the relevant length scale ratios which represent the Archimedes number (Ar), the Bond number (Bo), FR and AR. For pool boiling, the relevant length scale ratios are $\left(\frac{D_i}{D_b}\right)$ and $\left(\frac{L_p}{L_e}\right)$, where D_i , D_b refers to internal and the departing bubble diameter and L_p , L_e denote the pool and the evaporator length. For film evaporation, the relevant length scale ratios are $\left(\frac{L_f}{\delta_{E,F}}\right)$, $\left(\frac{D_i}{\delta_{E,F}}\right)$ and $\left(\frac{L_p}{L_e}\right)$, whilst for film nucleate boiling, the relevant length

scale ratios are $\left(\frac{L_f}{D_b}\right)$, $\left(\frac{D_i}{D_b}\right)$ and $\left(\frac{L_e}{D_i}\right)$. L_f is the length of the liquid film and $\delta_{E,F}$ is characteristic film thickness at the evaporator.

- The effective liquid pool length (L'_p) for an inclined TS is a function of the FR, the evaporator length (L_e), and θ .
- The non-dimensional condensation thermal resistance equations for a vertical TS are functions of Pr, Re_F (or the vapour Reynolds number (Re_v)), the dimensionless shear stress (τ_i^*), and the length scale ratios given by $\left(\frac{L_c}{\delta_{C,F}}\right)$, $\left(\frac{D_i}{\delta_{C,F}}\right)$ and $\left(\frac{L_p}{L_e}\right)$. $\delta_{C,F}$ is the characteristic of the condensate film thickness.
- In an inclined position, both the circumferential condensate flow and the axial flow of the bottom condensate influence the condensation thermal resistances.

8.1.2 Conclusions derived from the experimental testing of TS

This section summarizes the key trends in $R_{B,P}$, $R_{B,F}$ and $R_{C,F}$ with varying \dot{Q}_{in} and FR from the TS investigated in this study. Some of the observed trends are interpreted using the visual observations of Andros (1980) and Hirshburg (1980).

- $R_{B,P}$ demonstrates a power-law relationship with \dot{Q}_{in} . $R_{B,P}$ decreases with \dot{Q}_{in} , and the decrement rate is governed by the pool boiling behaviour. For the TS examined in this study, significant bubble interference and coalescence effects are observed at all \dot{Q}_{in} , for all the FR except for FR = 0.35. Therefore, a slow decrease in $R_{B,P}$ with increasing \dot{Q}_{in} is observed.
- The pool boiling behaviour for FR = 0.55 and 0.65 is similar. This is hypothesized to be due to the expansion of the liquid pool resulting in a two-phase mixture. The heat flux ($\dot{Q}'_{in,f}$) versus the wall-superheat (ΔT_P) data for FR = 0.55 and 0.65 suggests that the resultant two-phase mixture occupies nearly the same evaporator volume.
- $R_{B,F}$ also demonstrates a power-law relationship with \dot{Q}_{in} . Film breakdown phenomenon accompanied by a dry-patch formation is observed at moderate \dot{Q}_{in} for

lower FR (FR = 0.35 and 0.45). At higher FR for all values of \dot{Q}_{in} , the boiling data suggests a continuous film flow above the liquid pool.

- $R_{C,F}$ demonstrates a power-law relationship with \dot{Q}_{in} . The TS examined in this study indicates that $R_{C,F}$ decreases with increasing \dot{Q}_{in} ; however, the rate decays with increasing \dot{Q}_{in} . The condensation data provide evidence of drop condensation at lower \dot{Q}_{in} for FR = 0.35 - 0.55, whereas at higher \dot{Q}_{in} , the condensation regime is mixed for all FR.
- Re_F increases with \dot{Q}_{in} raised to a power greater than one. The variation in Re_F with \dot{Q}_{in} is influenced by the variation of the dynamic viscosity (μ) and the modified latent heat of vapourization (h'_{fg}) with the film temperature (T_f).
- The Nusselt number (Nu) increases with $Re_F \sim 0.8$, after which Nu is observed to be nearly constant. However, the Nu values are below the predictions from the Nusselt theory (1916). This is hypothesized to be caused due to the inactive condenser surface area and small size of the condensate droplets.
- τ_i^* increases, whilst $\left(\frac{\rho_l}{\rho_v}\right)$ decreases with \dot{Q}_{in} . Both τ_i^* and $\left(\frac{\rho_l - \rho_v}{\rho_v}\right)$ influence Nu.
- $R_{B,P}$ demonstrates a power-law relationship with FR. The TS examined in this study shows that $R_{B,P}$ increase with FR raised to the power of ~ 0.42 . This indicates that the effects of bubble interference are more dominant than the effects caused by the increase in the bubble nucleation sites along L_p .
- Mathematically, $R_{B,F}$ demonstrates a Taylor-series expansion-type polynomial function with FR, given that $R_{B,P}$ demonstrates a power-law relationship with FR. However, $R_{B,F}$ can be expressed through a power-law relationship without loss in accuracy. $R_{B,F}$ increases more rapidly with FR than $R_{B,P}$ (~ 3 compared to 0.42 for $R_{B,P}$).
- $R_{C,F}$ increases linearly with FR. Re_F is nearly independent of FR at low FR (FR \leq 0.55), whilst at higher FR, Re_F shows a slow increasing trend. Similarly, τ_i^* is independent of FR at lower FR, whilst at higher FR, it shows a slow decreasing trend.

$\left(\frac{\rho_l}{\rho_v}\right)$ shows a decreasing trend with FR. However, this effect is dominated by the higher rate of droplet deposition at higher FR causing a net reduction in heat transfer.

- The boiling thermal resistance equations accurately predicts the boiling data from the previous study within $\pm 30\%$ with 95% confidence. The performance of those equations is even more superior in predicting the boiling data from the present study with varying \dot{Q}_{in} and FR, as the data are accurately predicted within 15% with 95% confidence intervals.

8.2 Novel contributions

The novel contributions from this study are outlined below

- A simple set of power-law expressions based on the boiling and the condensation curves has been derived to characterize the variation in the pool boiling ($R_{B,P}$), film boiling ($R_{B,F}$) and condensation thermal resistances ($R_{C,F}$) with \dot{Q}_{in} and FR. The model is powerful as it can identify and explain important data trends from any boiling and condensation data, irrespective of the geometrical and the operating parameters. The model can identify different pool, film and condensation regimes, and provide a preliminary understanding of the boiling and the condensation behaviour inside TS.
- A thermodynamic model has been developed, capable of predicting the thermodynamic state of the working fluid (WF) and its related properties at each stage of the thermodynamic cycle. The model can be utilized to locate the state points on a temperature-entropy (T-s) or a specific enthalpy-specific entropy (h-s) diagram, as well as estimate the operating temperature of a TS and a HP for a given set of geometrical and operating conditions.
- A new set of thermal resistance equations has been developed that can predict the pool, film boiling and film, drop condensation of a TS *a priori*, provided that the geometric and the operating conditions are known. The new equations are superior to the previously available correlations, as it accounts for the effects of different hydrodynamic forces, flow and thermal conditions influencing the performance of the TS.

- A robust experimental database of TS performance was created, for varying \dot{Q}_{in} , FR and AR. New data sets are being added to the database as a part of the ongoing work.
- Detailed analysis of the experimental data provided new insights into how \dot{Q}_{in} and FR influences the wall-superheat (ΔT_P), the wall-subcooling (ΔT_C), $R_{B,P}$, $R_{B,F}$ and $R_{C,F}$. These did not exist prior to this work as the available results, in most cases, are typically presented in terms of the overall thermal resistance (R_O) of the device.

8.3 Future work

This section outlines the scope of the future work in theoretical modelling, experimental characterization and computational fluid dynamics (CFD) modelling to better understand the performance of TS and heat pipes (HP) in mold cooling applications.

8.3.1 Analytical/theoretical modelling

- Develop a lumped capacitance model and integrate it into the proposed thermal resistance network model to characterize transient heat source conditions encountered in mold cooling applications.
- Develop a theoretical thermal resistance network model with the relevant parameters influencing the performance of flat and micro heat pipes. This model is relevant to electronics cooling.
- Optimize TS and HP designs based on minimization of entropy generation using the thermodynamic model developed in Chapter 4.
- Extend the applicability of the proposed thermal resistance formulations by testing them extensively against different WF and wall materials.
- Perform extensive validation of the proposed model utilizing more experimental data from TS experiments.

8.3.2 Experimental characterization

- Experimentally characterize the effects of changes in WF, wall material, condenser length (L_c) and the flowrate of the inlet coolant (\dot{m}_{coolant}) on $R_{B,P}$, $R_{B,F}$ and $R_{C,F}$.
- Visualize the flow patterns inside a glass TS under the influence of \dot{Q}_{in} , FR, AR and θ using high-speed imaging camera.

8.3.3 Computational fluid dynamics modelling (CFD) modelling

Development of an accurate computational fluid dynamics (CFD) modelling was part of the present study. Although this task was initially thought to be straightforward, numerous issues were uncovered with regards to a lack of mass and energy conservation in models as well as non-reproducible results published in the literature. Significant advances were made to address the energy and mass conservation; however, a slight decrease in the WF mass was still observed within the domain. The scope of future investigation on CFD modelling therefore includes the following points:

- Refine the previously developed CFD model to fully conserve mass within the domain.
- Validate the CFD model with experimental data and run a parametric study to visualize and understand its internal flow structures.
- Develop and validate a CFD model for HP by extending the TS model to include a porous region representing the wick material.
- Develop a conjugate heat transfer model for mold cooling applications involving HP. In this model, the mold will be modelled as a solid material, and the HP will be modelled as a region with variable thermophysical properties estimated based on the thermodynamic model developed in Chapter 4.

References

- Abdullahi, B., 2015. Development and optimization of heat pipe-based compound parabolic collector, PhD Thesis, *University of Birmingham*, United Kingdom (UK), pp. 1-318.
- Alammar, A.A., Al-Dadah, R.K. and Mahmoud, S.M., 2016. Numerical investigation of effect of fill ratio and inclination angle on a thermosiphon heat pipe thermal performance. *Applied Thermal Engineering*, 108, pp. 1055-1065.
- Alammar, A.A., Al-Dadah, R.K. and Mahmoud, S.M., 2018. Effect of inclination angle and fill ratio on geyser boiling phenomena in a two-phase closed thermosiphon—Experimental investigation. *Energy Conversion and Management*, 156, pp. 150-166.
- Alizadehdakhel, A., Rahimi, M. and Alsairafi, A.A., 2010. CFD modeling of flow and heat transfer in a thermosyphon. *International Communications in Heat and Mass Transfer*, 37(3), pp. 312-318.
- Amatachaya, P., & Srimuang, W., 2010. Comparative heat transfer characteristics of a flat two-phase closed thermosyphon (FTPCT) and a conventional two-phase closed thermosyphon (CTPCT). *International Communications in Heat and Mass Transfer*, 37(3), pp. 293-298.
- Andros, F.E., 1980. Heat transfer characteristics of the two-phase closed thermosyphon (wickless heat pipe) including direct flow observation. PhD Thesis. *Arizona State University*. United States of America (USA), pp. 1-368.
- Babin, B.R., Peterson, G.P. and Wu, D., 1990. Steady-state modeling and testing of a micro heat pipe. *ASME Journal of Heat Transfer*, 112, pp. 595-601.
- Baojin, Q., Li, Z., Hong, X. and Yan, S., 2009. Heat transfer characteristics of titanium/water two-phase closed thermosyphon. *Energy Conversion and Management*, 50(9), pp. 2174-2179.

Bauermeister, H.O., 1941. The condensation of organic vapors on a horizontal tube, PhD Thesis, *Illinois Institute of Technology*, United States of America (USA).

Bejan, A., (1995). Entropy generation minimization: the method of thermodynamic optimization of finite-size systems and finite-time processes. *CRC press*. United States of America (USA), pp. 1-400.

Bergman, T.L., Lavine, A.S., Incropera, F.P., & Dewitt, D.P., 2018. Fundamentals of Heat and Mass Transfer. 8th Edition, *John Wiley & Sons*, pp. 1-992.

Bowman, W.J., 1987. Simulated Heat-pipe vapor dynamics (friction). PhD Thesis. *Air Force Institute of Technology*, United States of America (USA), pp. 1-229.

Brahim, T., Dhaou, M.H. and Jemni, A., 2014. Theoretical and experimental investigation of plate screen mesh heat pipe solar collector. *Energy Conversion and Management*, 87, pp. 428-438.

Brauer. H., 1971. Grundlagen der Einphasen und Mehrphasenströmungen Sauerländer, Aarau, Frankfurt.

Bromley, L.A., Brodkey, R.S. and Fishman, N., 1952. Effect of Temperature Variation around a Horizontal Condenser Tube. *Industrial & Engineering Chemistry*, 44(12), pp. 2962-2966.

Buckingham, E., 1914. On physically similar systems; illustrations of the use of dimensional equations. *Physical Review*, 4(4), pp. 345-376.

Cao, Y., Gao, M., Beam, J.E. and Donovan, B., 1997. Experiments and analyses of flat miniature heat pipes. *Journal of Thermophysics and Heat Transfer*, 11(2), pp. 158-164.

Cengel, Y. A., Boles, M. A., & Kanoğlu, M., 2019. Thermodynamics: An Engineering Approach, 9th Edition. *New York: McGraw-Hill Education*. pp. 1-984.

Cengel, Y. and Ghajar, A., 2020. Heat and mass transfer: fundamentals and applications, 6th Edition, *McGraw-Hill Education*, pp. 1-1057.

- Cerza, M. and Sernas, V., 1985. A bubble growth model for nucleate boiling in thin, falling, superheated, laminar, water films. *International Journal of Heat and Mass Transfer*, 28(7), pp. 1307-1316.
- Chaddock, J., 1957. Film condensation of vapor in horizontal tubes. *Refrigerating Engineering*, 65, pp. 41-44.
- Chato, J.C., 1960. Laminar condensation inside horizontal and inclined tubes, PhD Thesis, *Massachusetts Institute of Technology*, United States of America (USA), pp. 1-204.
- Chen, J.S. and Chou, J.H., 2015. The length and bending angle effects on the cooling performance of flat plate heat pipes. *International Journal of Heat and Mass Transfer*, 90, pp. 848-856.
- Chen, S.J., Reed, J.G. and Tien, C.L., 1984. Reflux condensation in a two-phase closed thermosyphon. *International Journal of Heat and Mass Transfer*, 27(9), pp. 1587-1594.
- Chen, S.L., Gerner, F.M. and Tien, C.L., 1987. General film condensation correlations. *Experimental Heat Transfer*, 1(2), pp. 93-107.
- Chen, Y., Groll, M., Mertz, R., Maydanik, Y.F., & Vershinin, S.V., 2005. Steady-state and transient performance of a miniature loop heat pipe. *ASME, 3rd International Conference on Microchannels and Minichannels*, June 13-15, 2005, Toronto, Ontario, Canada, pp. 183-189.
- Chi, S.W., 1976. Heat pipe theory and practice: a sourcebook. *Hemisphere Publishing Corporation, McGraw-Hill Book Company*, pp. 1-242.
- Chowdhury, F.M., Kaminaga, F., Goto, K. and Matsumura, K., 1997. Boiling heat transfer in a small diameter tube below atmospheric pressure on a natural circulation condition. *Journal of Japan Association for Heat Pipe*, 16, pp. 14-16.

Chun, M.H. and Kim, K.T., 1991. A new natural convection heat transfer correlation for laminar and turbulent film condensation derived from a statistical analysis of existing models and data. *Nuclear Engineering and Technology*, 23(2), pp. 200-209.

Churchill, S.W. and Usagi, R., 1972. A general expression for the correlation of rates of transfer and other phenomena. *AIChE Journal*, 18(6), pp. 1121-1128.

Churchill, S.W., 1977. Comprehensive correlating equations for heat, mass and momentum transfer in fully developed flow in smooth tubes. *Industrial & Engineering Chemistry Fundamentals*, 16(1), pp. 109-116.

Citakoglu, E. and Rose, J.W., 1968. Some factors influencing the validity of heat-transfer measurements during dropwise condensation. *International Journal of Heat and Mass Transfer*, 11, pp. 523-537.

Colburn., A. P and Carpenter., E. F., 1951. The Effect of Vapor Velocity on Condensation inside Tubes, Proc. *General Discussion on Heat Transfer. IMechE/ASME*, pp. 20-26.

Cole, R., 1967. Bubble frequencies and departure volumes at sub atmospheric pressures. *AIChE Journal*, 13(4), pp. 779-783.

Collier, J.G. and Thome, J.R., 1999. Convective boiling and condensation. 3rd Edition, *Clarendon Press*, pp. 1-640.

Darcy, H., 1856. Les fontaines publiques de la ville de Dijon (Vol. 1). Victor Dalmont, éditeur. pp. 1-647.

Devarakonda, A., Xiong, D. and Beach, D.E., 2005, February. Intermediate temperature water heat pipe tests. *In AIP Conference Proceedings. American Institute of Physics*. February 13 -17, 2005, Albuquerque, New Mexico, United States of America (USA), 746(1), pp. 158-163.

Deverall, J.E., 1969. Mercury as a heat pipe fluid (No. LA-4300). *Los Alamos National Lab (LANL)*, Los Alamos, United States of America (USA), pp. 1-15.

Do, K.H., Kim, S.J. and Garimella, S.V., 2008. A mathematical model for analyzing the thermal characteristics of a flat micro heat pipe with a grooved wick. *International Journal of Heat and Mass Transfer*, 51(19-20), pp. 4637-4650.

Dukler, A.E., 1960. Fluid mechanics and heat transfer in vertical falling film systems. In *Chemical Engineering Program Symposium Series*. 56, pp. 1-10.

El-Genk, M.S. and Saber, H.H., 1998a. Heat transfer correlations for small, uniformly heated liquid pools. *International Journal of Heat and Mass transfer*, 41(2), pp. 261-274.

El-Genk, M.S. and Saber, H.H., 1998b. Heat transfer correlations for liquid film in the evaporator of enclosed, gravity-assisted thermosyphons. *ASME Journal of Heat and Mass Transfer*, 120(2), pp. 477 - 484.

Emami, M.R., Noie, S.H., and Khoshnoodi, M., 2008. Effect of aspect ratio and filling ratio on thermal performance of an inclined two-phase closed thermosyphon. *Iranian Journal of Science & Technology, Transaction B, Engineering*, 32 (B1), pp. 39-51.

Fadhl, B., 2016. Modelling of the thermal behaviour of a two-phase closed thermosyphon , PhD Thesis, *Brunel University*, United Kingdom (UK), pp. 1-204.

Fadhl, B., Wrobel, L.C. and Jouhara, H., 2013. Numerical modelling of the temperature distribution in a two-phase closed thermosyphon. *Applied Thermal Engineering*, 60(1-2), pp. 122-131.

Faghri, A., & Thomas, S., 1989. Performance characteristics of a concentric annular heat pipe: Part I - Experimental prediction and analysis of the capillary limit. *ASME Journal of Heat and Mass Transfer*, 111(4), pp. 844-850.

Faghri, A., 1989. Performance characteristics of a concentric annular heat pipe: Part 2- Vapor flow analysis. *ASME Journal of Heat and Mass Transfer*, 111(4), pp. 851-857.

Faghri, A., 1995. Heat pipe science and technology. *Taylor and Francis*, pp. 1-874.

Famouri, M., Carbajal, G. and Li, C., 2014. Transient analysis of heat transfer and fluid flow in a polymer-based micro flat heat pipe with hybrid wicks. *International Journal of Heat and Mass Transfer*, 70, pp. 545-555.

Fiedler, S. and Auracher, H., 2004. Experimental and theoretical investigation of reflux condensation in an inclined small diameter tube. *International Journal of Heat and Mass Transfer*, 47(19-20), pp. 4031-4043.

Fletcher, L.S., Sernas, V. and Galowin, L.S., 1974. Evaporation from thin water films on horizontal tubes. *Industrial & Engineering Chemistry Process Design and Development*, 13(3), pp. 265-269.

Fujita, T. and Ueda, T., 1978a. Heat transfer to falling liquid films and film breakdown - I: Subcooled liquid films. *International Journal of Heat and Mass Transfer*, 21(2), pp. 97-108.

Fujita, T. and Ueda, T., 1978b. Heat transfer to falling liquid films and film breakdown - II: Saturated liquid films with nucleate boiling. *International Journal of Heat and Mass Transfer*, 21(2), pp. 109-118.

Fukano, T. and Kadoguchi K., 1990, *Transactions of the Japan Society of Mechanical Engineering (JSME) Ser B*, 56:1475-1483.

Gedik, E., 2016. Experimental investigation of the thermal performance of a two-phase closed thermosyphon at different operating conditions. *Energy and Buildings*, 127, pp. 1096-1107.

Ghanbarpour, M., 2017. Investigation of thermal performance of cylindrical heat pipes operated with nanofluids, PhD Thesis, *KTH Royal Institute of Technology*, Sweden, pp. 1-108.

Gorbis, Z.R. and Savchenkov, G.A., 1976. Low temperature two-phase closed thermosyphon investigation. *2nd International Heat Pipe Conference*, 1976, Bologna, Italy, pp. 37-45.

Graham, C., 1969 The limiting transfer mechanisms of dropwise condensation. Ph.D. Thesis. *Department of Mechanical Engineering*. Massachusetts Institute of Technology (M.I.T), pp. 1-272.

Gray, V.H., 1969. The rotating heat pipe - A wickless, hollow shaft for transferring high heat fluxes. *American Society of Mechanical Engineers (ASME) and American Institute of Chemical Engineers (AIChE), Heat Transfer Conference*, August 3-6, 1969, Minneapolis, Minnesota.

Gross, U., 1992. Reflux condensation heat transfer inside a closed thermosyphon. *International Journal of Heat and Mass transfer*, 35(2), pp. 279-294.

Grover, G.M., Cotter, T.P., & Erickson, G.F., 1964. Structures of very high thermal conductance. *Journal of Applied Physics*, 35(6), pp. 1990-1991.

Hashimoto, H. and Kaminaga, F., 2002. Heat transfer characteristics in a condenser of closed two-phase thermosyphon: Effect of entrainment on heat transfer deterioration. *Heat Transfer-Asian Research: Co-sponsored by the Society of Chemical Engineers of Japan and the Heat Transfer Division of ASME*, 31(3), pp. 212-225.

Hassan, K.E. and Jakob, M., 1958. Laminar film condensation of pure saturated vapors on inclined circular cylinders. *Transactions of the American Society of Mechanical Engineers (ASME)*, 80(4), pp. 887-894.

Hewitt, G.F. and Hall-Taylor, N.S., 1970. Annular two-phase flow, *Oxford, England, Pergamon Press*, pp. 4-20.

Hirshburg, R.I., 1980. Laminar film flow phenomena-Theory and application to the two-phase closed thermosyphon. PhD Thesis, *Arizona State University*. United States of America (USA), pp. 1-346.

Hung, Y.H., Teng, T.P. and Lin, B.G., 2013. Evaluation of the thermal performance of a heat pipe using alumina nanofluids. *Experimental Thermal and Fluid Science*, 44, pp. 504-511.

- Hung, Y.M., Seng, Q., 2011. Effects of geometric design on thermal performance of star-groove micro-heat pipes. *International Journal of Heat and Mass Transfer*, 54(5-6), pp. 1198-1209.
- Hwang, G.S., Kaviany, M., Anderson, W.G. and Zuo, J., 2007. Modulated wick heat pipe. *International Journal of Heat and Mass Transfer*, 50(7-8), pp. 1420-1434.
- Jafari, D., Di Marco, P., Filippeschi, S. and Franco, A., 2017b. An experimental investigation on the evaporation and condensation heat transfer of two-phase closed thermosyphons. *Experimental Thermal and Fluid Science*, 88, pp. 111-123.
- Jafari, D., Filippeschi, S., Franco, A. and Di Marco, P., 2017a. Unsteady experimental and numerical analysis of a two-phase closed thermosyphon at different filling ratios. *Experimental Thermal and Fluid Science*, 81, pp. 164 - 174.
- Jafari, D., Franco, A., Filippeschi, S., & Di Marco, P., 2016. Two-phase closed thermosyphons: A review of studies and solar applications. *Renewable and Sustainable Energy Reviews*, 53, pp. 575-593.
- Jakob, M., 1941. Local Temperature Differences as Occurring in Evaporation, Condensation, and Catalytic Reaction. Temperature, Its Measurement and Control in Science and Industry, *Reinhold, New York*, p. 834.
- Joudi, K.A. and Witwit, A.M., 2000. Improvements of gravity assisted wickless heat pipes. *Energy Conversion and Management*, 41(18), pp. 2041-2061.
- Jouhara, H. & Robinson, A.J., 2010. Experimental investigation of small diameter two-phase closed thermosyphons charged with water, FC-84, FC-77 and FC-3283. *Applied Thermal Engineering*, 30(2-3), pp. 201-211.
- Kafeel, K. and Turan, A., 2013. Axi-symmetric simulation of a two-phase vertical thermosyphon using Eulerian two-fluid methodology. *Heat and Mass Transfer*, 49, pp. 1089-1099.

Kaya, T., Ku, J., Hoang, T.T., & Cheung, M.K., 1999a. Investigation of low power start-up characteristics of a loop heat pipe. *American Institute of Physics. AIP Conference Proceedings*, 31Jan-4th Feb 1999, Albuquerque, New Mexico, United States of America (USA), 458(1), pp. 799-804.

Kaya, T., Ku, J., Hoang, T. and Cheung, M.K., 1999b. Investigation of the temperature hysteresis phenomenon of a loop heat pipe. *33rd National Heat Transfer Conference*, August 15-17, 1999 Albuquerque, New Mexico, United States of America (USA), pp. 1-14.

Kempers, R., Ewing, D. and Ching, C.Y., 2006. Effect of number of mesh layers and fluid loading on the performance of screen mesh wick heat pipes. *Applied Thermal Engineering*, 26(5-6), pp. 589-595.

Kempers, R., Robinson, A.J., Ewing, D. and Ching, C.Y., 2008. Characterization of evaporator and condenser thermal resistances of a screen mesh wick heat pipe. *International Journal of Heat and Mass Transfer*, 51(25-26), pp. 6039-6046.

Khalkhali, H., Faghri, A., & Zuo, Z. J., 1999. Entropy generation in a heat pipe system. *Applied Thermal Engineering*, 19(10), pp. 1027-1043.

Khazaei, I., Hosseini, R., Kianifar, A. and Noie, S.H., 2011. Experimental consideration and correlation of heat transfer of a two-phase closed thermosyphon due to the inclination angle, filling ratio, and aspect ratio. *Journal of Enhanced Heat Transfer*, 18(1), pp. 31-40.

Kim, Y., Choi, J., Kim, S. and Zhang, Y., 2015. Effects of mass transfer time relaxation parameters on condensation in a thermosyphon. *Journal of Mechanical Science and Technology*, 29, pp. 5497-5505.

Kim, Y., Shin, D.H., Kim, J.S., You, S.M. and Lee, J., 2018. Boiling and condensation heat transfer of inclined two-phase closed thermosyphon with various filling ratios. *Applied Thermal Engineering*, 145, pp. 328-342.

Kruzhilin, G.N., 1947. Free-convection transfer of heat from a horizontal plate and boiling liquid. *Doklady AN SSSR (Reports of the USSR Academy of Sciences)*, 58(8), pp. 1657-1660.

Kusuda, H. and Imura, H., 1973. Boiling heat transfer in an open thermosyphon: Report 2, the influence of the physical property on a heat transfer coefficient and on a critical heat flux. *Bulletin of JSME*, 16(101), pp. 1734-1740.

Kutateladze, S.S., 1964. Fundamentals of heat transfer, 2nd Edition, New York, *Academic Press*, pp. 1-485.

Kuznetsov, G.V., Ponomarev, K.O., Feoktistov, D.V., Orlova, E.G., Lyulin, Y.V. and Ouerdane, H., 2021. Heat transfer in a two-phase closed thermosyphon working in Polar Regions. *Thermal Science and Engineering Progress*, 22, 100846, pp. 2-12.

Labuntsov, D.A., 1957. Heat transfer in film condensation of pure steam on vertical surfaces and horizontal tubes. *Teploenergetika*, 4(7), pp. 72-79.

Labuntsov, D.A., 1973. Heat transfer problems with nucleate boiling of liquids. *Thermal Engineering (USSR)*, 19 (9), pp. 21-28.

Langen, E., 1931. Der Einfluß des Luftgehaltes auf den Wärmeübergang bei kondensierendem Dampf. *Forschung auf dem Gebiet des Ingenieurwesens A*, 2(10), pp. 359-369.

Larkin, B.S., 1971. An experimental study of the two-phase thermosyphon tube. *Transactions of the Canadian Society of Mechanical Engineering (CSME)*, 14(B-6), pp. 1-8.

Le Fevre, E.J. and Rose, J.W., 1965. An experimental study of heat transfer by dropwise condensation. *International Journal of Heat and Mass Transfer*, 8(8), pp. 1117-1133.

Lee, Y. and Mital, U., 1972. A two-phase closed thermosyphon. *International Journal of Heat and Mass Transfer*, 15(9), pp. 1695-1707.

- Levenberg, K., 1944. A method for the solution of certain non-linear problems in least squares. *Quarterly of Applied Mathematics*, 2(2), pp. 164-168.
- Li, H., Akbarzadeh, A. and Johnson, P., 1991. The thermal characteristics of a closed two-phase thermosyphon at low temperature difference. *Heat Recovery Systems and CHP*, 11(6), pp. 533-540.
- Li, S.F., & Liu, Z.H., 2020. Parametric study of rotating heat pipe performance: A review. *Renewable and Sustainable Energy Reviews*, 117, pp. 109482-109503.
- Li, Y., Zhou, W., He, J., Yan, Y., Li, B. and Zeng, Z., 2016. Thermal performance of ultra-thin flattened heat pipes with composite wick structure. *Applied Thermal Engineering*, 102, pp. 487-499.
- Lian, W., Chang, W., & Xuan, Y., 2016. Numerical investigation on flow and thermal features of a rotating heat pipe. *Applied Thermal Engineering*, 101, pp. 92-100.
- Lips, S. and Lefèvre, F., 2014. A general analytical model for the design of conventional heat pipes. *International Journal of Heat and Mass Transfer*, 72, pp. 288-298.
- Ma, X., Rose, J.W., Xu, D., Lin, J. and Wang, B., 2000. Advances in dropwise condensation heat transfer: Chinese research. *Chemical Engineering Journal*, 78(2-3), pp. 87-93.
- Mahmood, S.L. and Akhanda, M.A.R., 2008. Experimental investigation of micro heat pipes of different cross-sections having same hydraulic diameter. *Journal of Thermal Science*, 17(3), pp. 247-252.
- Marquardt, D.W., 1963. An algorithm for least-squares estimation of nonlinear parameters. *Journal of the Society for Industrial and Applied Mathematics*, 11(2), pp. 431-441.
- McAdams, W.H., 1954. Heat transmission. 3rd Edition, *McGraw-Hill Book Company, Inc*, pp. 1-532.

- Mesler, R. and Mailen, G., 1977. Nucleate boiling in thin liquid films. *AIChE Journal*, 23(6), pp. 954-957.
- Mesler, R., 1976. A mechanism supported by extensive experimental evidence to explain high heat fluxes observed during nucleate boiling. *AIChE Journal*, 22(2), pp. 246-252.
- Mozumder, A.K., Akon, A.F., Chowdhury, M.S.H. and Banik, S.C., 2010. Performance of heat pipe for different working fluids and fill ratios. *Journal of Mechanical Engineering*, 41(2), pp. 96-102.
- Mwaba, M.G., Huang, X. and Gu, J., 2006. Influence of wick characteristics on heat pipe performance. *International Journal of Energy Research*, 30(7), pp. 489-499.
- Nag, P.K., 2013. Engineering thermodynamics, 5th Edition, India, *Tata McGraw-Hill Education*. pp. 1-914.
- Naphon, P., Assadamongkol, P. and Borirak, T., 2008. Experimental investigation of titanium nanofluids on the heat pipe thermal efficiency. *International Communications in Heat and Mass Transfer*, 35(10), pp. 1316-1319.
- Negishi, K. and Sawada, T., 1983. Heat transfer performance of an inclined two-phase closed thermosyphon. *International Journal of Heat and Mass Transfer*, 26(8), pp. 1207-1213.
- Newitt, D.M., 1954. Liquid entrainment 1. The mechanism of drop formation from gas vapour bubbles. *Transactions of the Institute of Chemical Engineers*, 32, pp. 244-261.
- Nguyen-Chi, H. and Groll, M., 1980, The influence of wall roughness on the maximum performance of closed two-phase thermosyphons. *15th Thermophysics Conference*, July 14-16, 1980, Snowmass, Colorado, pp. 1-8.
- Nguyen-Chi, H. and Groll, M., 1981. Entrainment or flooding limit in a closed two-phase thermosyphon. *Journal of Heat Recovery Systems*, 1(4), pp. 275-286.

- Noie, S.H., 2005. Heat transfer characteristics of a two-phase closed thermosyphon. *Applied Thermal Engineering*, 25(4), pp. 495-506.
- Noie, S.H., Heris, S.Z., Kahani, M. and Nowee, S.M., 2009. Heat transfer enhancement using Al₂O₃/water nanofluid in a two-phase closed thermosyphon. *International Journal of Heat and Fluid Flow*, 30(4), pp. 700-705.
- Noie, S.H., Sarmasti Emami, M.R. and Khoshnoodi, M., 2007. Effect of inclination angle and filling ratio on thermal performance of a two-phase closed thermosyphon under normal operating conditions. *Heat Transfer Engineering*, 28(4), pp. 365-371.
- Norman, W.S., and McIntyre, V., 1960. Heat transfer to a liquid film on a vertical surface. *Transactions of the Institute of Chemical Engineers.*, 27, pp. 301-307.
- Nouri-Borujerdi, A, & Layeghi, M., 2005. A review of concentric annular heat pipes. *Heat Transfer Engineering*, 26(6), pp. 45-58.
- Nukiyama, S., 1966. The maximum and minimum values of the heat Q transmitted from metal to boiling water under atmospheric pressure. *International Journal of Heat and Mass Transfer*, 9(12), pp. 1419-1433.
- Nusselt, W., 1916. Die Oberflächenkondensation des wasserdampfes", *Ver. deutsch. Ing.*, Bd 60, pp. 541-546.
- O'bara, JT, Killian, ES and Roblee Jr, LHS, 1967. Dropwise condensation of steam at atmospheric and above atmospheric pressures. *Chemical Engineering Science* , 22 (10), pp.1305-1314.
- Ong, K.S. and Haider-E-Alalhi, M., 1999. Experimental investigation on the hysteresis effect in vertical two-phase closed thermosyphons. *Applied Thermal Engineering*, 19(4), pp.399-408.
- Parizhskiy, O.V., Chepurnenko, V.P., Lagota, L.F. and Taranets, L.F., 1972. Study of boiling heat transfer with a falling film of refrigerant. *Heat Transfer-Soviet Research*, 4(4), pp. 43-47.

- Parken Jr, W.H., 1975. Heat transfer to thin water films on horizontal tubes., PhD Thesis, *Rutgers The State University of New Jersey*, United States of America (USA), pp. 1-292.
- Patten, T.D. and Turmeau, W.A., 1970. Some characteristics of nucleate boiling in thin liquid layers. *International Heat Transfer Conference*, August 31- September 5, 1970, Paris-Versailles, France, 4(23), pp. 1-11.
- Payakaruk, T., Terdtoon, P. and Ritthidech, S., 2000. Correlations to predict heat transfer characteristics of an inclined closed two-phase thermosyphon at normal operating conditions. *Applied Thermal Engineering*, 20(9), pp. 781-790.
- Pearson, J.R.A., 1958. On convection cells induced by surface tension. *Journal of Fluid Mechanics*, 4(5), pp. 489-500.
- Peck, R.E. and Reddie, W.A., 1951. Heat transfer coefficients for vapors condensing on horizontal tubes. *Industrial & Engineering Chemistry*, 43(12), pp. 2926-2931.
- Pierson, F.W. and Whitaker, S., 1977. Some theoretical and experimental observations of the wave structure of falling liquid films. *Industrial & Engineering Chemistry Fundamentals*, 16(4), pp. 401-408.
- Popiel, C.O., 2008. Free convection heat transfer from vertical slender cylinders: a review. *Heat Transfer Engineering*, 29(6), pp. 521-536.
- Popiel, C.O., Wojtkowiak, J. and Bober, K., 2007. Laminar free convective heat transfer from isothermal vertical slender cylinder. *Experimental Thermal and Fluid Science*, 32(2), pp. 607-613.
- Reay, D., & Kew, P., 2006. Heat pipes: theory, design and applications. *Butterworth-Heinemann*. pp. 1-397.
- Richter, R., & Gottschlich, J., 1990. Thermodynamic aspects of heat pipe operation. American Institute of Aeronautics and Astronautics (AIAA)/American Society of Mechanical Engineers (ASME), *5th Joint Thermodynamics and Heat Transfer Conference*, June 18-20, Seattle, Washington. pp. 1772-1781.

Rohsenow, W., Webber, J.H. and Ling, A.T., 1956. Effect of vapor velocity on laminar and turbulent-film condensation. *Transactions of the American Society of Mechanical Engineers (ASME), Journal of Fluids Engineering*, 78(8), pp. 1637-1642.

Rohsenow, W.M., 1952. A method of correlating heat-transfer data for surface boiling of liquids. *Transactions of the American Society of Mechanical Engineers (ASME), Journal of Fluids Engineering*, 74(6), pp. 969-975.

Rohsenow, W.M., Hartnett, J.P. and Cho, Y.I., 1998. Handbook of heat transfer, 3rd Edition. *New York: McGraw-Hill*, pp. 1-1501.

Rychkov, A.I. and VK, P., 1959. Heat Transfer During Film Evaporation of Caustic Soda Solutions. *Khim. Pro.*, CE-TRANS-3944, 5, p. 426.

Kutateladze, S.S., 1990 Heat Transfer and Hydrodynamic Resistance: Handbook (in Russian), *Energoatomizdat Publishing House*, Moscow, Chapter 12.7.

Sauciuc, I., Akbarzadeh, A. and Johnson, P., 1995. Characteristics of two-phase closed thermosiphons for medium temperature heat recovery applications. *Heat Recovery Systems and CHP*, 15(7), pp. 631-640.

Savino, R. and Paterna, D., 2006. Marangoni effect and heat pipe dry-out. *Physics of Fluids*, 18(11), pp. 1-4.

Scriven, L.E. and Sternling, C.V., 1960. The marangoni effects. *Nature*, 187(4733), pp. 186-188.

Seban, R.A. and Hodgson, J.A., 1982. Laminar film condensation in a tube with upward vapor flow. *International Journal of Heat and Mass Transfer*, 25(9), pp. 1291-1300.

Semena, M.G. and Kiselev, Y.F., 1978. Heat-exchange processes in the heat-supply zones of two-phase thermosiphons operating on freons 11, 113, and 142 and on water and ethanol. *Journal of Engineering Physics*, 35(2), pp. 895-899.

Shabgard, H., Xiao, B., Faghri, A., Gupta, R. and Weissman, W., 2014. Thermal characteristics of a closed thermosyphon under various filling conditions. *International Journal of Heat and Mass Transfer*, 70, pp. 91-102.

Shah, R.K., 1978. A correlation for laminar hydrodynamic entry length solutions for circular and noncircular ducts. *ASME Journal of Fluids Engineering*, 100(2), pp. 177-179.

Shiraishi, M., Kikuchi, K. and Yamanishi, T., 1982. Investigation of heat transfer characteristics of a two-phase closed thermosyphon. *In Advances in Heat Pipe Technology*. Pergamon, pp. 95-104.

Siedel, B., Sartre, V., & Lefèvre, F., 2015. Literature review: Steady-state modelling of loop heat pipes. *Applied Thermal Engineering*, 75, pp. 709-723.

Singh, M., Kondaraju, S., & Bahga, S.S., 2017. Enhancement of thermal performance of micro heat pipes using wettability gradients. *International Journal of Heat and Mass Transfer*, 104, pp. 400-408.

Song, F., Ewing, D., & Ching, C.Y., 2004. Experimental investigation on the heat transfer characteristics of axial rotating heat pipes. *International Journal of Heat and Mass Transfer*, 47(22), pp. 4721-4731.

Sparrow, E.M. and Gregg, J.L., 1959. A boundary-layer treatment of laminar-film condensation. *Journal of Heat Transfer*, 81(1), pp. 13-18.

Spendel, T., 1982. Laminar film condensation heat transfer in closed two-phase thermosyphons. *Proceedings of the IVth International Heat Pipe Conference*, 7-10 September 1981, London, UK, pp. 163-173.

Stainthorp, F. P., and Batt, R.S.W., The effect of co-current and counter-current air flow on the wave properties of falling liquid film. *Transactions of the Institute of Chemical Engineers*, 1967, 45, T372-T382.

- Stephan, K. and Abdelsalam, M., 1980. Heat-transfer correlations for natural convection boiling. *International Journal of Heat and Mass Transfer*, 23(1), pp. 73-87.
- Storch, T., Grab, T., Weickert, T., Gross, U., & Kasper, M., 2012. Wetting and film behavior of propane inside geothermal heat pipes. *16th International Heat Pipe Conference*, May 20-24, 2012, Lyon, France. pp. 1-3.
- Stulov, V.V., 2012. Cooling a slab continuous-casting mold. *Journal of Machinery Manufacture and Reliability*, 41(2), pp. 163-167.
- Sukchana, T. and Jaiboonma, C., 2013. Effect of filling ratios and adiabatic length on thermal efficiency of long heat pipe filled with R-134a. *Energy Procedia*, 34, pp. 298-306.
- Takaoka, M., Motai, T., Sakaya, M., Mochizuli, M., Mashiko, K., & Ito, M., 1985. Development of Long Heat Pipes and Heat-Pipe Applied Products. *Fujikura Technical Review*, (14).
- Takeyama, T. and Shimizu, S., 1974. On the transition of dropwise - film condensation. *Proceedings of the fifth International Heat Transfer Conference*. 3, pp. 274-278.
- Takuma, M., Maezawa, S. and Tsuchida, A., 1983, Studies on condensation heat transfer in two-phase closed thermosyphons. *Symposium on Mechanics for Space Flight*, March, pp. 247-255.
- Tanner, D.W., Potter, C.J., Pope, D. and West, D., 1965. Heat transfer in dropwise condensation-Part I: The effects of heat flux, steam velocity and non-condensable gas concentration. *International Journal of Heat and Mass Transfer*, 8(3), pp. 419-426.
- Tarokh, A., Bliss, C. and Hemmati, A., 2021. Performance enhancement of a two-phase closed thermosyphon with a vortex generator. *Applied Thermal Engineering*, 182, p. 116092.

Terdtoon, P., Chailungkar, M. and Shiraishi, M., 1998. Effects of aspect ratios on internal flow patterns of an inclined closed two-phase thermosyphon at normal operating condition. *Heat Transfer Engineering*, 19(4), pp. 75-85.

Terdtoon, P., Waowaew, N. and Tantakom, P., 1999. Internal flow patterns of an inclined, closed two-phase thermosyphon at critical state: case study I, effect of aspect ratio. *Experimental Heat Transfer*, 12(4), pp. 347-358.

Thumm, S., Philipp, C. and Gross, U., 2001. Film condensation of water in a vertical tube with countercurrent vapour flow. *International Journal of Heat and Mass Transfer*, 44(22), pp. 4245-4256.

Ueda, T., Miyashita, T. and Chu, P.H., 1989. Heat transport characteristics of a closed two-phase thermosyphon. *JSME International Journal*, Fluids engineering, heat transfer, power, combustion, thermophysical properties, 32(2), pp. 239-246.

Vasiliev, L. L., and Konev, S. V., 1982. Thermodynamic analysis of heat pipe operation. Advances in Heat Pipe Technology. *Proceedings of the IVth International Heat Pipe Conference*, 7–10 September 1981, London, UK, pp. 313-325.

Wang, G.S., Song, B. and Liu, Z.H., 2010. Operation characteristics of cylindrical miniature grooved heat pipe using aqueous CuO nanofluids. *Experimental Thermal and Fluid Science*, 34(8), pp. 1415-1421.

Wang, S., Chen, J., Hu, Y. and Zhang, W., 2011. Effect of evaporation section and condensation section length on thermal performance of flat plate heat pipe. *Applied Thermal Engineering*, 31(14-15), pp. 2367-2373.

Wang, X., Wang, Y., Chen, H. and Zhu, Y., 2018. A combined CFD/visualization investigation of heat transfer behaviors during geyser boiling in two-phase closed thermosyphon. *International Journal of Heat and Mass Transfer*, 121, pp. 703-714.

Wang, X., Zhu, Y. and Wang, Y., 2019. Development of pressure-based phase change model for CFD modelling of heat pipes. *International Journal of Heat and Mass Transfer*, 145, p.118763.

Wang, Y., & Vafai, K., 2000. An experimental investigation of the thermal performance of an asymmetrical flat plate heat pipe. *International Journal of Heat and Mass Transfer*, 43(15), pp. 2657-2668.

White, F.M., and Xue, H., 2021. Fluid Mechanics, 9th Edition. New York: *McGraw-Hill Education*. pp. 1-882.

Wilke, W., 1962. *Wärmeübergang an Rieselfilme, ForschHf. Vu. Dt. Ing.* 490, B28.

Xu, Z., Zhang, Y., Li, B. and Huang, J., 2016. Modeling the phase change process for a two-phase closed thermosyphon by considering transient mass transfer time relaxation parameter. *International Journal of Heat and Mass Transfer*, 101, pp. 614-619.

Xuan, Y., Hong, Y., & Li, Q., 2004. Investigation on transient behaviors of flat plate heat pipes. *Experimental Thermal and Fluid Science*, 28(2-3), pp. 249-255.

Yamagata, K., Hirano, F., Nishikawa, K. and Matsuoka, H., 1955. Nucleate boiling of water on the horizontal heating surface. *Memoirs of the Faculty of Engineering, Kyushu University*, 15(98), pp. 97-163.

Yang, L. and Homsy, G.M., 2006. Steady three-dimensional thermocapillary flows and dryout inside a V-shaped wedge. *Physics of Fluids*, 18(4), pp. 1-12.

Zhang, C., Mucciardi, F. and Gruzleski, J.E., 2002. Effects of heat pipe cooling on permanent mold castings of aluminum alloys. *International symposium on enabling technologies for light metals and composite materials and their end-products*; Montreal, Quebec, Canada, Aug 11-14, 2002. pp. 321-334.

Zuo, Z. J., & Faghri, A., 1998. A network thermodynamic analysis of the heat pipe. *International Journal of Heat and Mass Transfer*, 41(11), pp. 1473-1484.

Zuo, Z.J. and Gunnerson, F.S., 1994. Numerical modeling of the steady-state two-phase closed thermosyphon. *International Journal of Heat and Mass Transfer*, 37(17), pp. 2715-2722.

Appendix A: Appendix related to Chapter 1

A.1 Expressions of ε_w , $D_{h,w}$ and $(f_{lam}Re_{liq,w})$ for various wick structures

Table A.1 Expressions of ε_w , $D_{h,w}$ and $(f_{lam}Re_{liq,w})$ for various wick structures.

Wick structures	ε_w	$D_{h,w}$	$(f_{lam}Re_{liq,w})$	Flow regime	
Circular artery	1	$2R$	16	$Re_{liq,w} < 2000$	
	$R = \text{Radius of the liquid flow passage (pore radius)}$				
Rectangular channel	1	$\frac{2w\delta}{w+\delta}$	$24(1-1.3553\alpha^*+1.9467\alpha^{*2}-1.7012\alpha^{*3}+0.9564\alpha^{*4}-0.2537\alpha^{*5})$ (Shah and Bhatti, 1987)		
	$w = \text{groove width, } \delta = \text{groove depth, } \alpha^* = \text{passage aspect ratio, } \alpha^* = \frac{w}{\delta}$				
Open rectangular grooves	$\frac{w}{s}$	$\frac{4w\delta}{w+2\delta}$	$24(1-1.3553\alpha^*+1.9467\alpha^{*2}-1.7012\alpha^{*3}+0.9564\alpha^{*4}-0.2537\alpha^{*5})$ (Shah and Bhatti, 1987)		
	$w = \text{groove width, } s = \text{groove pitch, } \delta = \text{groove depth, } \alpha^* = \frac{w}{2\delta}$				
Circular annular wick	1	$2(R_1-R_2)$	$\frac{16(1-R^*)^2}{1+R^{*2}-2R_m^2}$ (Shah and Bhatti, 1987)		
	$R_1 = \text{radius of the outer circle, } R_2 = \text{radius of the inner circle, } R^* = R_2/R_1, R_m^* = \left(\frac{1-R^*}{2\ln(1/R^*)}\right)^{0.5}$				
Wrapped screen wick	$1 - \frac{1.05\pi Nd}{4}$	$\frac{d\varepsilon_w}{1-\varepsilon_w}$	61.0		$Re_{liq,w} < 10$
	$N = \text{mesh number, } d = \text{wire diameter}$				
Packed sphere, plain or sintered metal	Depends on packing mode ($\varepsilon_w = 0.48$ for cubic packing)	$\frac{2D\varepsilon_w}{3(1-\varepsilon_w)}$	33.3		
	$D = \text{average diameter of the sphere}$				

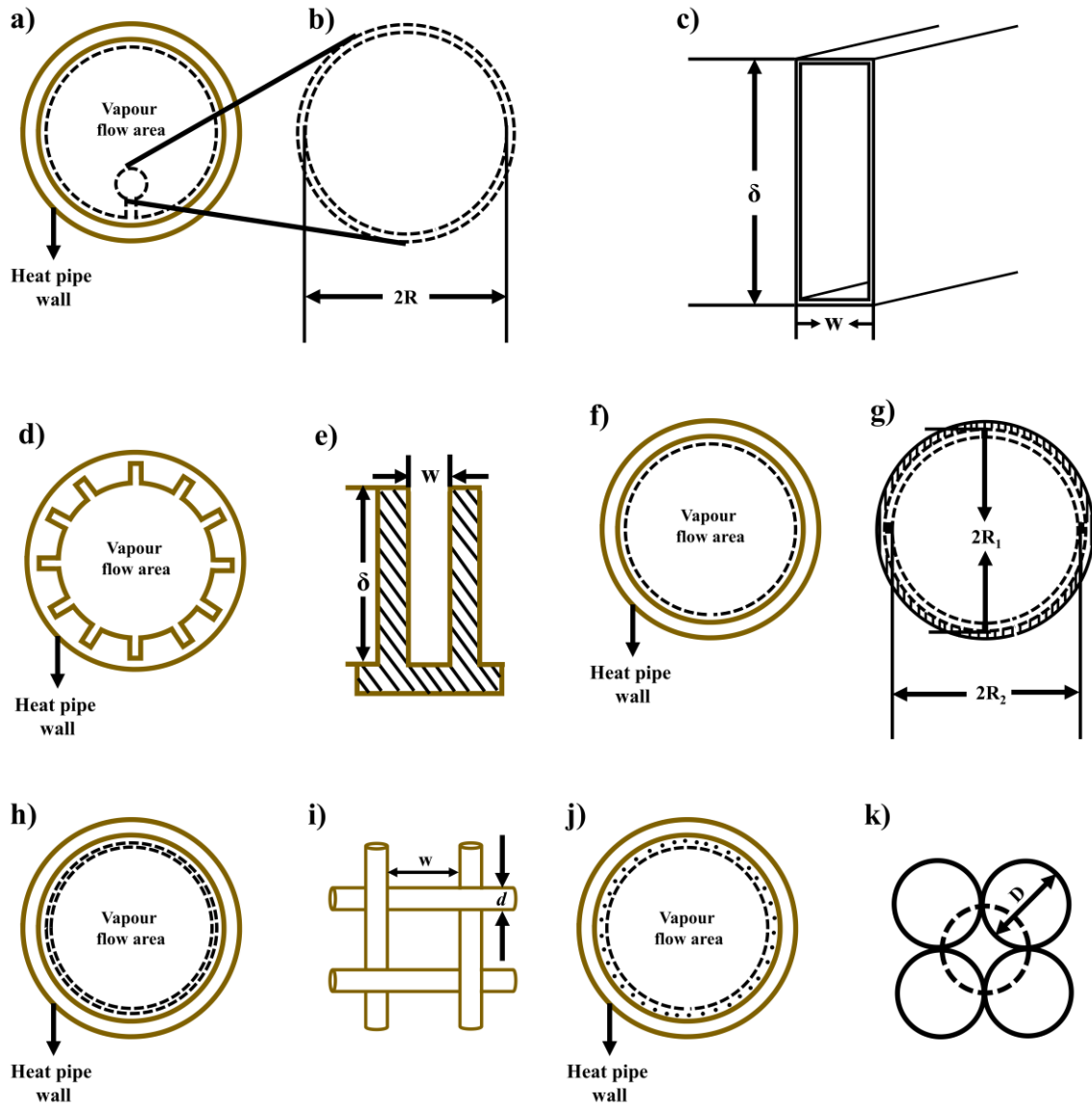


Figure A.1 Geometries of the different heat pipe (HP) wick structures. a) Top view of the circular artery HP. b) Cross-section of the circular artery. c) Cross-section of the rectangular channel d) Top view of the axial rectangular groove HP e) Cross-section of the rectangular grooves f) Top view of the circular annular wick HP g) Cross-section of the circular annular wick h) Top view of the wrapped screen HP i) Cross-section of the square wire mesh screen j) Top view of the sintered metal HP k) Cross-section of the packed spherical particles.

A.2 β for different flow cross-sections

Table A.2 β for various flow conditions (adapted from Chi, 1976).

Flow conditions	Flow state	β
$Re_v < 2300$, $M_v < 0.2$	Laminar and incompressible	1.25 for annular sections 1.33 for circular passages 1.44 for rectangular passages
$Re_v < 2300$, $M_v > 0.2$	Laminar and compressible	
$Re_v > 2300$, $M_v < 0.2$	Turbulent and incompressible	1.02
$Re_v > 2300$, $M_v > 0.2$	Turbulent and compressible	

A.3 Expressions for f_v for different vapour flow conditions

Table A.3 Expressions for f_v for different flow conditions (adapted from Chi, 1976).

Flow conditions	Flow state	f_v
$Re_v < 2300$, $M_v < 0.2$	Laminar and incompressible	$f_{v,LI}$ is determined from Table 1.2 for various wick structures
$Re_v < 2300$, $M_v > 0.2$	Laminar and compressible	$f_{v,LC} = f_{v,LI} \left[1 + \frac{(Y_v - 1)}{2} M_v^2 \right]^{-0.5}$. $f_{v,i}$ is determined from Table 1.2 for various wick structures
$Re_v > 2300$, $M_v < 0.2$	Turbulent and incompressible	$f_{v,TI} = \left[\frac{0.038}{Re_v^{0.25}} \right]$
$Re_v > 2300$, $M_v > 0.2$	Turbulent and compressible	$f_{v,TC} = f_{v,TI} \left[1 + \frac{(Y_v - 1)}{2} M_v^2 \right]^{-0.75}$; $f_{v,TC} = \left[\frac{0.038}{Re_v^{0.25}} \right]$
The subscript L, I in f_v represent laminar and incompressible flow states, respectively, whereas the subscript T,C represent turbulent and compressible flow states, respectively.		

A.4 Expressions for r_c for various types of wick structures

Table A.4 Expressions of r_c for various wick structures described in Table 1.2 (adapted from Chi, 1976).

Wick structures	r_c
Circular artery	r
Rectangular channel	$\frac{w\delta}{w+\delta}$
Open rectangular grooves	w ($\delta > w/2$)
Circular annular wick	$(R_1 - R_2)$ $R_1 =$ outer radii of the annuli $R_2 =$ inner radii of the annuli
Parallel wires	w $w =$ wire spacing
Wrapped screen wick	$\frac{w+d}{2} = \frac{1}{2N}$ $w =$ wire spacing, $d =$ wire diameter; $N =$ mesh number
Sintered metal with spherical shaped particles	0.21D $D =$ sphere diameter

A.5 $k_{\text{eff,wick}}$ for various wick structures

Table A.5 Expressions of the effective thermal conductivity, $k_{\text{eff,wick}}$ for various liquid saturated wick structures (adapted from Chi, 1976).

Wick structures	$k_{\text{eff,wick}}$	Usage
Wick structure and liquid in series	$\frac{1}{(1-\varepsilon)/k_w + \varepsilon/k_l}$	-
Wick structure and liquid in parallel	$(1-\varepsilon)k_w + \varepsilon k_l$	-
Wrapped screen	$\frac{k_l[(k_l+k_w)-(1-\varepsilon)(k_l-k_w)]}{[(k_l+k_w)+(1-\varepsilon)(k_l-k_w)]}$	Wrapped screen wicks
Packed spheres	$\frac{k_l[(2k_l+k_w)-2(1-\varepsilon)(k_l-k_w)]}{[(2k_l+k_w)+(1-\varepsilon)(k_l-k_w)]}$	Packed sphere wicks, porous-metal wicks
Sintered metal wick	$\frac{\pi}{8} \left(\frac{r_c}{r_s}\right)^2 k_w + \left[1 - \frac{\pi}{8} \left(\frac{r_c}{r_s}\right)^2\right] + \left[\frac{k_l k_w}{\varepsilon' k_w + k_l(1-\varepsilon')}\right], \varepsilon' = \frac{\varepsilon}{1 - \frac{\pi}{8} \left(\frac{r_c}{r_s}\right)^2}$	Sintered porous metal wicks with large contact radius
Rectangular grooves	$\frac{w_G k_l + w_{Gf} k_w}{w_G + w_{Gf}}$	Condenser section of the rectangular grooved wicks
	$\frac{(w_{Gf} k_l k_w \delta_G) + w_G k_l (0.185 w_f k_w + \delta_G k_l)}{(w_G + w_{Gf})(0.185 w_f k_w + \delta_G k_l)}$	Evaporator section of rectangular grooved wicks
<p>k_l = thermal conductivity of the liquid phase of the WF k_w = thermal conductivity of the wick material ε = wick porosity w_{Gf} = groove fin thickness w_G = groove thickness δ_G = groove depth</p>		

Appendix B: Appendix related to Chapter 2

Table B.1 compiles the previous studies that are used in synthesis and analysis in Chapter 2. Table B.2 compiles the heat transfer data from these studies.

Table B.1 Compiled data from the previous studies showing geometrical parameters, the fill ratio (FR) and the aspect ratio (AR).

References	Thermosyphon material	L _e (m)	L _a (m)	L _c (m)	D _i (m)	D _o (m)	WF	AR	FR	θ (degrees)
Alizadehdakheel et al. (2010)	Copper	0.40	0.20	0.40	0.0175	0.19	Distilled water	2.28	0.3, 0.5, 0.8	90°
Amatachaya & Srimuang (2010)		0.238, 0.314, 0.377	0.362, 0.286, 0.223	0.38	0.032	0.039		7.43, 9.81, 11.78	0.3, 0.6, 0.9	90°
Baojin et al. 2009		0.35	0.30	0.35	0.0225	0.025		15.55	0.36	90°
Fadhl (2016)		0.200	0.100	0.200	0.0202	0.022		9.90	0.5	90°
Jafari et al. (2017 a, b)		0.15	0.20	0.15	0.033	0.035		4.54	0.08, 0.16, 0.3, 0.50, 1	90°
		0.075	0.275	0.15				2.27	0.16, 0.35, 1.35	
Jouhara & Robinson (2010)		0.04	0.10	0.06	0.006	0.012		6.66	0.5, 1.59	90°
Joudi et al. (2000)		0.10	0.1, 0.3, 0.7	0.15	0.020	0.022		5	0.24, 0.38, 0.57	90°
Kim et al. (2018)		0.30	0.30	0.325	0.025	NA		12	0.25 - 1	5°-90°
Noie (2005)		0.238, 0.314, 0.377	0.362, 0.286, 0.223	0.38	0.025	0.032		7.45, 9.80, 11.8	0.3, 0.6, 0.9	90°
Noie et al. (2007)		0.41	0.18	0.41	0.0145	0.016		28.28	0.15, 0.22, 0.30	5°-90°
Noie et al. (2009)		0.35	0.25	0.40	0.0200	0.022		17.5	NA	90°
Shiraishi et al. (1982)		0.28	0.50	0.45	0.037	0.045		7.57	0.5, 1	90°

Table B.2 Compiled heat transfer data from the previous studies

References	Parameter variation	ΔT_{ea} [K]	ΔT_{ac} [K]	\dot{Q}_{in} [W]	T_a [K]
Alizadehdakhel et al. (2010)	Varying \dot{Q}_{in}	17.5	14.9	350.00	318.9
		22.9	15.9	500.00	323.6
		29.2	18.3	700.00	328.4
	Varying FR	28.2	15.6	700.00	324.6
		29.2	18.5	700.00	328.6
		28.2	21.4	700.00	331.9
Amatachaya and Srimuang (2010)	Varying \dot{Q}_{in}	8.5	9.4	231.00	324.7
		11.3	10.4	346.50	333.2
		14.2	11.7	462.00	342.8
		18.4	11.7	577.50	349.7
		26.0	16.9	693.00	358.2
	Varying \dot{Q}_{in}	9.90	10.7	277.20	326.1
		12.5	13.5	415.80	334.0
		14.8	14.9	554.40	342.8
		19.3	12.9	693.00	352.6
	Varying FR	24.4	14.5	831.60	356.4
		15.0	13.9	554.40	339.2
		15.2	13.9	554.40	342.4
	Baojin et al. (2009)	Varying \dot{Q}_{in}	16.1	15.6	554.40
4.1			2.2	298.00	316.4
4.9			2.9	397.60	319.8
5.6			3.8	496.80	322.5
Fadhil (2016)	Varying Q_{in}	6.0	4.6	594.60	324.7
		13.0	8.3	148.43	325.3
		16.0	9.8	199.74	329.2
		19.0	10.1	250.04	332.7
		22.5	12.3	299.52	336.3
		25.8	11.4	349.27	340.7

Jafari et al. (2017a)	Varying FR	0.91	1.84	100.00	303.16
		1.88	1.880	100.00	303.19
		6.41	1.62	100.00	302.52
Jafari et al. (2017b)	Varying Qin (FR=0.35)	1.94	1.48	30.00	300.09
		3.02	2.82	100.00	302.94
		4.25	4.76	200.00	306.00
	Varying Qin (FR=1)	2.41	1.43	30.00	300.31
		4.10	3.04	100.00	303.57
		5.70	4.80	200.00	306.72
Joudi et al. (2000)	Varying Qin (FR = 0.24)	4.44	8.04	58.05	307.75
		20.25	4.05	219.78	316.23
	Varying Qin (FR = 0.38)	6.32	5.51	37.32	304.98
		22.42	6.59	219.79	313.49
	Varying Qin (FR = 0.57)	1.96	1.04	37.32	306.11
		10.95	7.33	219.79	316.86
Shiraishi et al (1981)	Varying FR	6.50	1.30	1345.86	317.89
		7.52	2.88	1345.86	318.67
		1.80	0.31	43.54	318.72

Appendix C: Appendix related to Chapter 3

C.1 h-s diagram of various thermodynamic processes

The h-s diagrams delineating the processes BC, CD and GH are shown in Figure C.1. Figures C.2 and C.3 show the process lines CF, whereas Figures C.4 and C.5 show the process lines DE on a h-s diagram for a TS and a HP, respectively. Figures C.6 and C.7 show the process HA on a h-s diagram for a TS and a HP, respectively. No discussion regarding the process points and the process lines on these diagrams have been made here since those are the outcome of the analyses made in section 3.2.

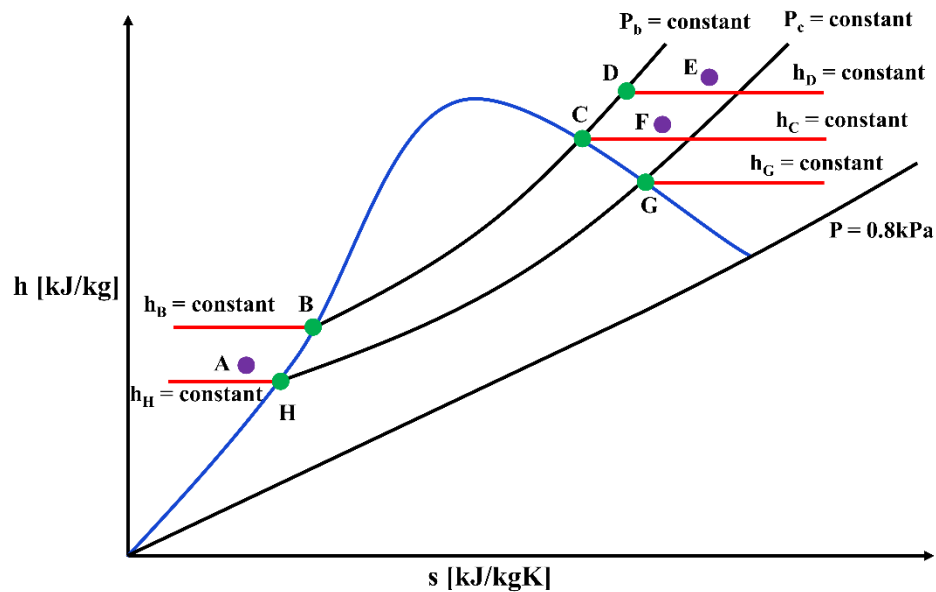


Figure C.1 h-s diagram showing the known state points B, C, D, G and H (green colored circles) and the process lines BC, CD and GH inside a TS and a HP. The solid red and black curves represent the constant enthalpy and the pressure lines, respectively. The unknown state points E, F and A are represented by the purple colored circles.

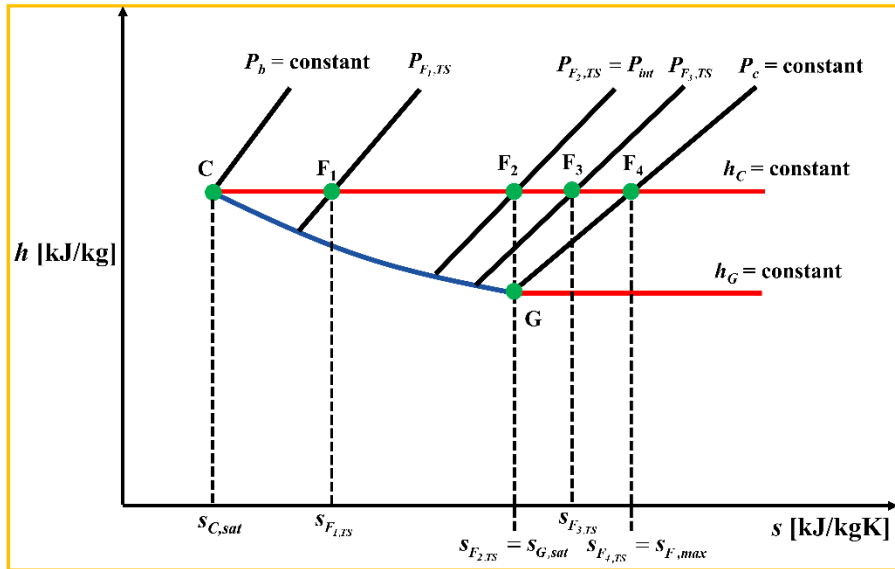
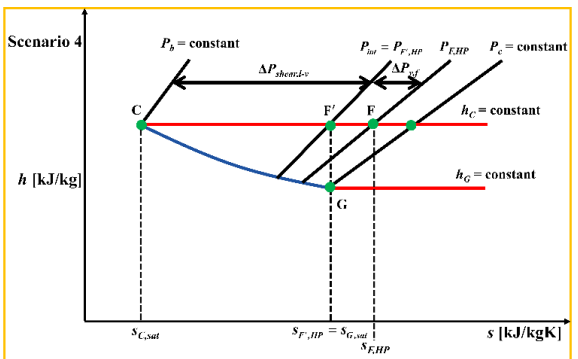
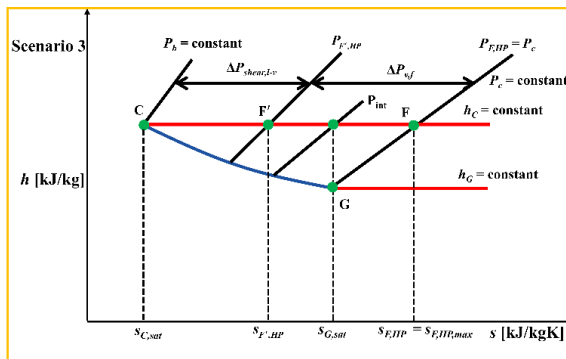
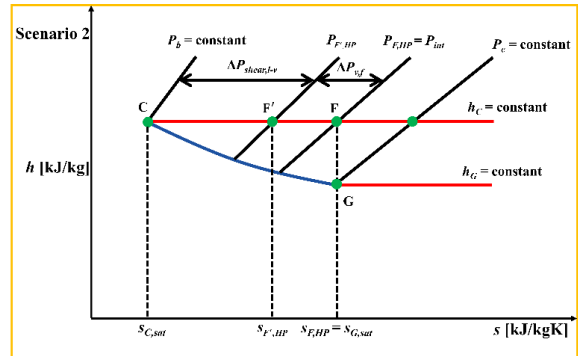
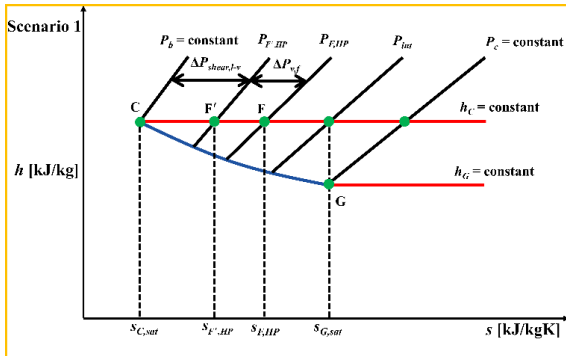


Figure C.2 A magnified schematic of the superheated regime showing possible locations of the state point F along the constant enthalpy line, h_c . F₁ represents the state point F, when $P_{F,TS} > P_{int}$; $s_{F1,TS} < s_{G,sat}$. F₂ is when $P_{F,TS} = P_{int}$; $s_{F2,TS} = s_{G,sat}$. F₃ is when $P_c < P_{F,TS} < P_{int}$; $s_{F3,TS} > s_{G,sat}$. F₄ is when $P_{F,TS} = P_c$; $s_{F4,TS} = s_{F,TS,max} > s_{G,sat}$. $T_{F3,TS}$ is the temperature corresponding to the state point F_{3,TS}. The process line FG can be obtained by connecting the state points F and G.



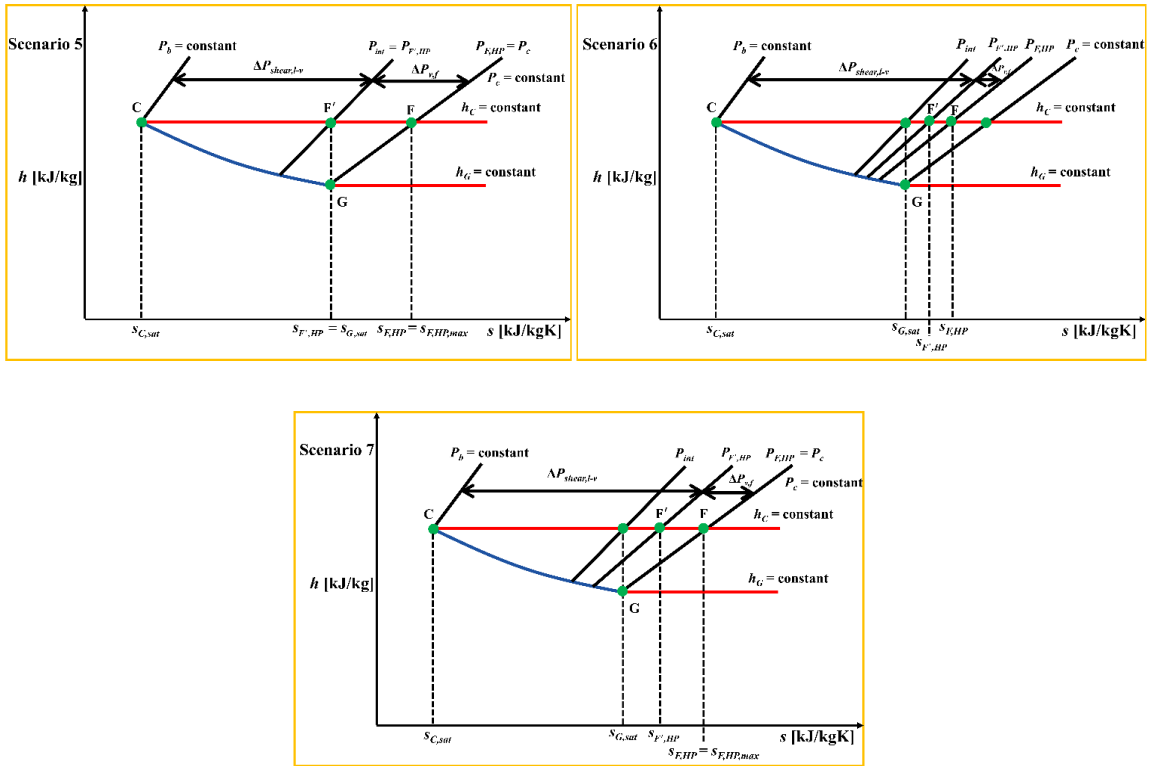


Figure C.3 A magnified schematic of the superheated regime illustrating of seven possible scenarios on a h-s diagram when $P_{F,HP} > P_c$ shown in Table 3.4. The process line FG can be obtained by joining the state points F and G.

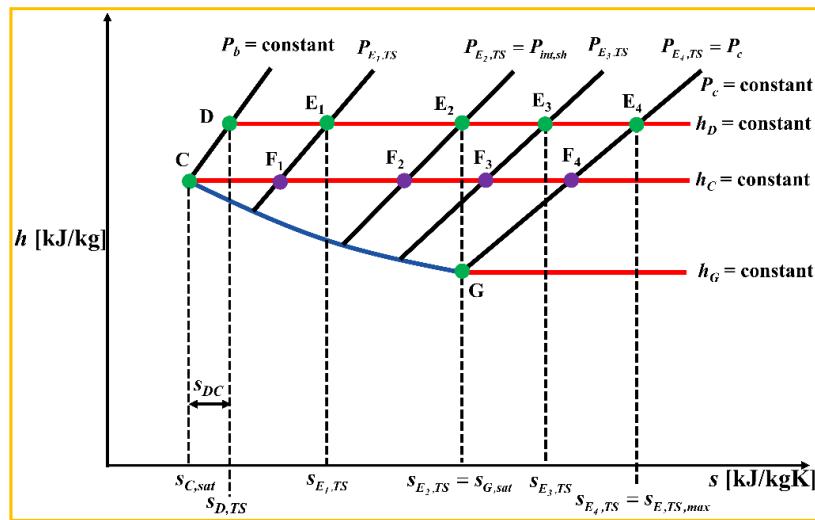


Figure C.4 A magnified schematic of the superheated regime showing possible locations of the state point E shown along the constant enthalpy line, h_D . E_1 represents the state point E, when $P_{E,TS} > P_{int,sh}$; $s_{E_1,TS} < s_{G,sat}$. E_2 is when $P_{E,TS} = P_{int,sh}$; $s_{E_2,TS} = s_{G,sat}$. E_3 is when $P_c < P_{E,TS} < P_{int,sh}$; $s_{E_3,TS} > s_{G,sat}$. E_4 is when $P_{E,TS} = P_c$; $s_{E_4,TS} = s_{E,TS,max} > s_{G,sat}$. $T_{E_1,TS}$ is the temperature corresponding to the state point $E_{1,TS}$. The state points F_1, F_2, F_3 and F_4 are shown by purple color. The process line EG can be obtained by connecting the state points E and G.

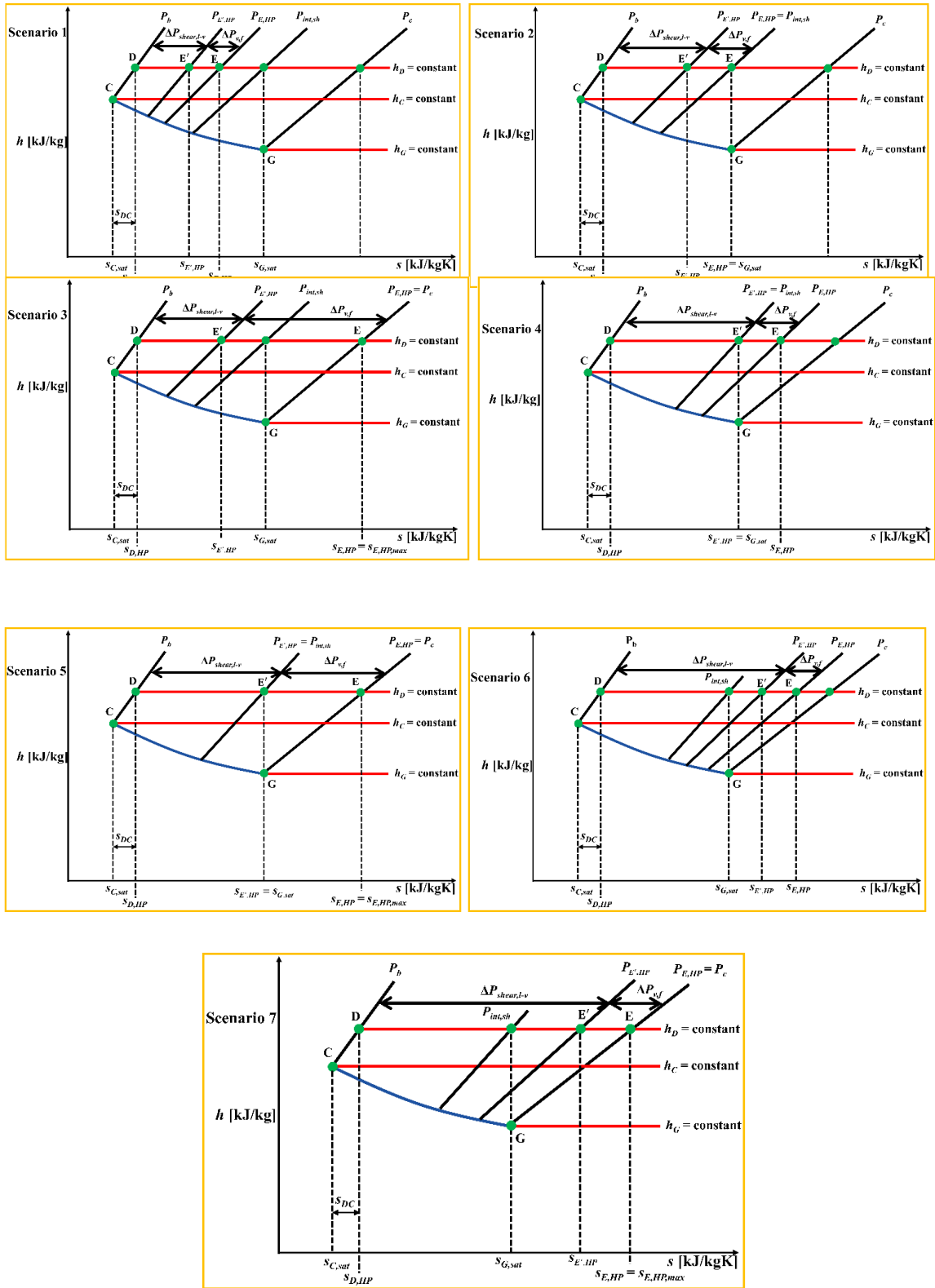


Figure C.5 A magnified schematic of the superheated regime illustrating seven possible scenarios on a h - s diagram when $P_{E',HP} > P_c$ as shown in Table 3.5. The process line EG can be obtained by joining state points E and G .

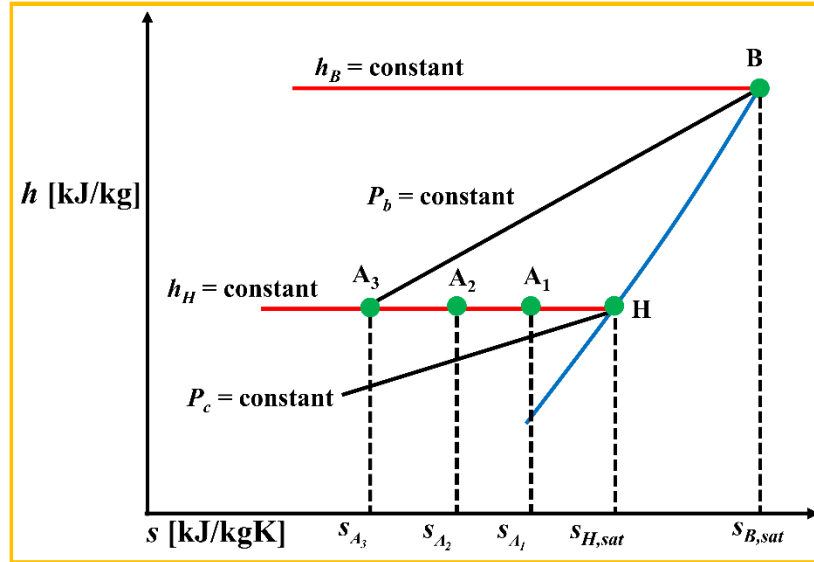


Figure 0.2 A magnified schematic of the subcooled regime showing possible locations of the state point A along the constant enthalpy line, h_H . A₁ represents the state point A, when $|\Delta P_{hydro,l}| > |\Delta P_l|$. $P_{A_1} < P_b$; $s_{A_1} < s_{H,sat}$. A₂ is when ΔP_l is negligible. $P_{A_2} < P_b$; $s_{A_2} < s_{H,sat}$. A₃ is the limiting case, when $P_{A_3} = P_b$; $s_{A_3} > s_{H,sat}$. T_{A_2} is the temperature corresponding to the state point A₂. The process line AB can be obtained by connecting the state points A and B.

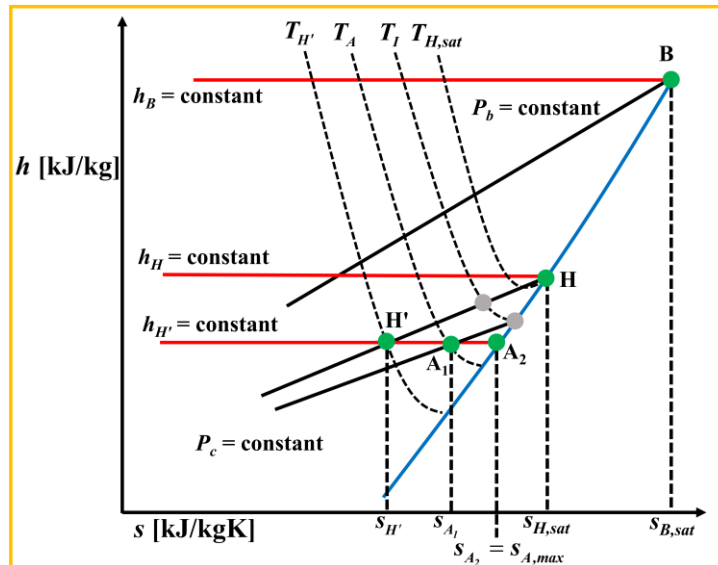


Figure C.7 A magnified schematic of the subcooled regime showing the location of the state points H' and A along the constant pressure line, P_c and constant enthalpy line $h_{H'}$. A₁ represents a possible location of the state point A when $|\Delta P_{hydro,l}| < |\Delta P_l|$. A₂ represents the location of the state point A when $|\Delta P_{hydro,l}| > |\Delta P_l|$. A₃ represents the state point A for the limiting case when s_A is maximum i.e. $s_{A,max}$. $T_{H,sat}$, $T_{A,HP}$ and $T_{H',HP}$ are the temperature corresponding to state points H, A and H', respectively. $P_{H'} = P_c$. $T_{H'} < T_{H,sat}$; $s_{H'} < s_{H,sat}$. $P_{A,HP} < P_{H',HP}$; $s_{A,HP} > s_{H',HP}$.

Appendix D: Appendix related to Chapter 4

D.1 Review of the prior heat transfer correlations from the literature

Guichet et al., (2019) pointed out that the nucleate pool boiling correlations (see Table D.1) by Rohsenow (1952), Imura et al. (1979), Stephan and Abdelsalam (1980) and El-Genk and Saber (1997) are suitable for predicting the boiling heat transfer coefficients for a thermosyphons (TS). There still exists, however, considerable uncertainty in the description of their predictive capabilities.

Table D.1 Previous nucleate-boiling heat transfer correlations. Stephan and Abdelsalam's (1980) correlation is not shown in the table since it was developed for natural convection. NB denotes nucleate boiling.

Authors	Heat transfer correlation
Rohsenow (1952)	$h_{e,NB,Ro} = \frac{(\dot{Q}'_{in,f})^{2/3}}{\frac{C_{sf} h_{fg}}{C_{pl}} \left(\frac{D_b}{h_{fg} \mu_l} \right)^{0.33} Pr_l^n}$ $C_{sf} = 0.0147; n = 1 \text{ (Vachon et al., 1968) [water/polished copper]}$ $C_{sf} = 0.015; n = 0.81 \text{ (Pioro, 1999) [water/copper]}$ $C_{sf} = 0.017; n = 0.76 \text{ (Pioro et al., 2004) [water/copper]}$
Imura et al. (1979)	$h_{e,NB,Im} = 0.32 \left(\frac{\rho_l^{0.65} k_l^{0.3} C_{pl}^{0.7} g^{0.2}}{\rho_v^{0.25} h_{fg}^{0.4} \mu_l^{0.1}} \right) \left(\frac{P_v}{P_a} \right)^{0.3} \left(\frac{\dot{Q}'_{in,f}}{\pi D_o L_e} \right)^{0.4}$
El-Genk and Saber (1997)	$\frac{h_{e,NB,El-Ga}}{h_{e,NB,Ku}} = 1 + 4.95 \left[\left(\frac{\rho_v}{\rho_l} \right)^{0.4} \left(\frac{P_v v_l}{\sigma} \left(\frac{\rho_l^2}{\sigma g (\rho_l - \rho_v)} \right)^{0.25} \right)^{0.25} \right]$ $h_{e,NB,Ku} = 6.95 \times 10^{-4} \left(\frac{k_l}{L_b} \right) Pr_l^{0.35} \left(\frac{\dot{Q}'_{in,f} D_b}{\rho_v h_{fg} v_l} \right)^{0.7} \left(\frac{P D_b}{\sigma} \right)^{0.7}$
<u>Nomenclature:</u>	
$\dot{Q}'_{in,f}$ = heat flux into the fluid v_l = kinematic viscosity of the liquid phase Pr_l = Prandtl number of the liquid phase $\left(\frac{\mu_l C_{pl}}{k_l} \right)$ P_v = vapor pressure (also known as the saturation pressure) D_b = bubble length scale (also known as pool boiling characteristic dimension) = $\sqrt{\frac{\sigma}{g(\rho_l - \rho_v)}}$ h_{fg} = latent heat of vapourization D_d = bubble departure diameter = $0.0204 D_b \beta_{con}$ β_{con} = contact angle (usually taken as 45°) P_a = atmospheric pressure C_{sf}^* = coefficient in Pioro (2004) correlation, but a function of a specific heating surface-fluid combination. m = power-exponent of Pr_l in Pioro (2004) correlation. C_{sf} = coefficient in Rohsenow (1952), but a function of a specific heating surface-fluid combination. n = power-exponent of Pr_l in Rohsenow (1952) correlation.	

The accuracy of the heat transfer correlation by Rohsenow (1952) decreases with decrease in the FR and, it is most suitable in the case where $FR = 1$ (Guichet et al., 2019). This may be due to the fact that Rohsenow's (1952) correlation does not include L_p as a

variable. The inclination angle (θ) is not included either and, therefore, Rohsenow's (1952) correlation cannot be used to predict the boiling thermal resistances at varying FR and θ . Moreover, the exponent of the heat flux is 0.66 derived from boiling from plane heated surfaces and, thus, is debatable.

Imura et al.'s (1979) correlation also do not include L_p , θ and D_i as variables. The exponent to the heat flux is 0.4 and, thus, inconsistent with Rohsenow's (1952). The predicted boiling heat transfer coefficient when plotted against experimental data of Shiraishi et al., (1982) showed uncertainty within $\pm 30\%$.

Stephen and Abdelasalam's (1980) correlations were specifically developed for natural convection boiling. As a result, these correlations are neither tested against different pool boiling regimes nor against any TS. Nevertheless, these equations have similar drawbacks as that of Rohsenow (1952).

El-Genk and Saber (1997) modified Kutateladze 's (1959) correlation by introducing a mixing coefficient. Besides the fact that these correlations have do not have L_p , θ and D_i as variables, El-Genk and Saber's (1997) correlations have not been used in any recent TS literature in the last two decades (2000-2020). The reliability of El-Genk and Saber (1997) correlation is, therefore, not guaranteed.

There is a biased selection of the previous boiling and the condensation correlations for a validating experimental and numerical data (see Sauciuc et al., 1995, Noie et al., 2005, Baojin et al., 2009, Jouhara and Robinson, 2010, Jafari et al., 2017a, b, Kim et al., 2018). The reasons describing the agreement or disagreement of the experimental data with the specific correlations chosen for validation are not discussed in any previous literature. That a specific set of experimental data can be predicted from a given correlation within acceptable accuracy is arbitrary and case specific.

D.2 Verification of the pool boiling and the film criteria by El-Genk and Saber (1998a, b)

The X_p and the η values estimated from the present data using equations (4.1) and (4.3) suggest that natural convection boiling is occurring within the pool and the film for TS, where FR is varied between 0.35-0.75. However, this conclusion is not correct, as ΔT_P across those TS for various \dot{Q}_{in} varies between 3.50 [°C] and 28.76 [°C]. The deduction that no bubble generation and mixing is occurring at such high ΔT_P is physically unrealistic. Thus, equations (4.1) and (4.3) do not accurately identify the different boiling regimes, at least for the TS tested in this study.

D.3 Prediction equations for $R_{C,D}$

Dropwise condensation within a TS/HP has been observed in Larkin (1971) and Andros (1980). The favourable conditions for dropwise condensation to occur within TS and HP include using a WF with strong, cohesive forces (e.g. water) and coating the condenser wall with a substance that inhibits wetting or by mixing promoters with the WF (for e.g. silicon oil, oleic acid).

The dropwise condensation resistance ($R_{C,D}$) of a single drop consists of three different thermal resistance components acting in series (Graham, 1969) shown in Figure D.1. These are the thermal resistance due to the drop curvature ($R_{C,D,Curve}$), the thermal resistance due to interfacial heat transfer ($R_{C,D,I}$), and the thermal resistance due to the drop conduction ($R_{C,D,Cond}$). Graham (1969), Graham and Griffith (1973) reported that at atmospheric pressure, $R_{C,D,Cond}$ is more dominant (accounts for 90% of the total resistance; Graham, 1969), whilst at lower pressure both $R_{C,D,I}$ and $R_{C,D,Cond}$ are dominant. $R_{C,D,Curve}$ will exist whenever dropwise condensation is taking place at all pressures.

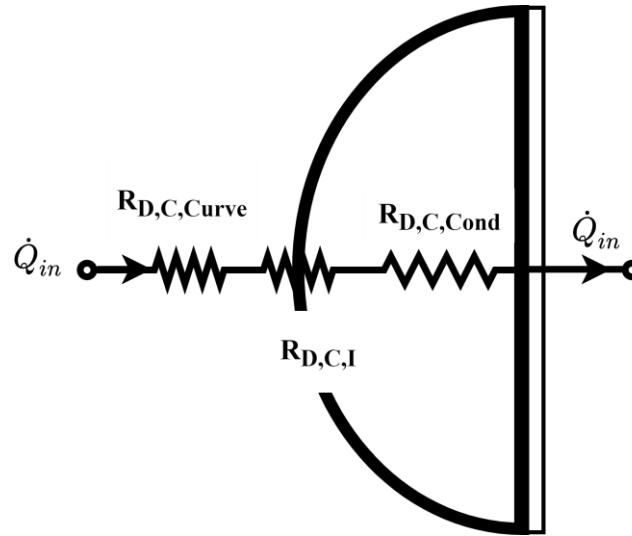


Figure D.1 Thermal resistance network model for dropwise condensation.

The next paragraph derives $R_{C,D,Curve}$ first followed by the derivation of $R_{C,D,I}$ and $R_{C,D,Cond}$. The derivations are based on the model of dropwise condensation proposed by Rose (1966, 1967) and Graham (1969). In the following derivations, the shape of the drop is assumed to be hemispherical (Graham and Griffith, 1973, Nijaguna, 1974, Rose, 1980, Tanasawa, 1991), although a spherical drop may also be assumed for analysis (Fevre and Rose, 1966). The primary resistance to heat transfer is caused by the drops and not through the bare surfaces between the drops. Since there are drops of different sizes on the condensing surface, the dropwise condensation resistance will be dependent on the distribution of the drop sizes and, therefore, may be non-uniform. Owing to that, the distribution of heat transfer rate may also be non-uniform. Therefore, a mean value of the heat transfer rate is considered for determining the mean thermal resistance. This is done by evaluating the heat transfer through a single drop and then summing it over all the drops based on the drop size distribution.

D.2.1 Prediction equation for $R_{D,Curve}$

The temperature drop due to curvature resistance ($\Delta T_{D,Curve}$) of a single hemispherical drop is given as (Fevre and Rose, 1966, Graham, 1969, Graham and Griffith, 1973, Tanasawa, 1991)

$$\Delta T_{D,Curve} = \left[\frac{2T_{sat}\sigma}{h_{fg}\rho_l} \right] \frac{1}{r} \quad (D.1)$$

When $\Delta T_{D, \text{Curve}}$ due to curvature is equal to the total temperature drop ($\Delta T_{D, \text{Tot}}$), the minimum size of the drop which can exist on the surface is (Graham, 1969)

$$r_{\min} = \left(\frac{2T_{\text{sat}}\sigma}{h_{\text{fg}}\rho_l} \right) \frac{1}{\Delta T_{D, \text{Tot}}} \quad (\text{D.2})$$

Substituting $\left(\frac{2T_{\text{sat}}\sigma}{h_{\text{fg}}\rho_l} \right)$ from equation (D.2) in equation (D.1) gives the final form of $\Delta T_{D, \text{Curve}}$ as a function of the total temperature drop ($\Delta T_{D, \text{Tot}}$) as

$$\Delta T_{D, \text{Curve}} = \left(\frac{r_{\min}}{r} \right) \Delta T_{D, \text{Tot}} \quad (\text{D.3})$$

Let the heat transferred through the curvature interface of a single drop be $\dot{Q}_{D, \text{Curve}}$. $\dot{Q}_{D, \text{Curve}}$ can, therefore, be expressed as a function of $\Delta T_{D, \text{Curve}}$ and $R_{D, \text{Curve}}$ as

$$\dot{Q}_{D, \text{Curve}} = \frac{\Delta T_{D, \text{Curve}}}{R_{D, \text{Curve}}} \quad (\text{D.4})$$

The mean heat transfer rate \dot{Q}_{in} , therefore, can be calculated from $\dot{Q}_{D, \text{Curve}}$ as

$$\dot{Q}_{\text{in}} = \int_{r_{\min}}^{r_{\max}} \dot{Q}_{D, \text{Curve}} A(r) dr \quad (\text{D.5})$$

where r_{\max} and r_{\min} are the effective maximum and minimum drop radius and $A(r)dr$ is the fractional area covered by drops having base radius in the range $r, r + dr$. The radius of the smallest viable drop r_{\min} is given as $r_{\min} = \left(\frac{2\sigma T_{\text{sat}}}{h_{\text{fg}}\rho_l} \right) \frac{1}{\Delta T_{D, \text{Tot}}}$ (Graham and Griffith, 1973, Rose 1980, Tanasawa 1991), whereas the radius of the largest drop is given as $r_{\max} = K_3 \sqrt{\frac{\sigma}{(\rho_l - \rho_v)g}}$ where $K_3 = 0.44$ for dropwise condensation of steam on vertical plates (derived from dimensional analysis). Rose (1980) and Tansawa (1991) showed that the average $r_{\max} \approx 1\text{mm}$. The theoretical expression for $A(r)$ is given by Rose and Glicksman (1973) as

$$A(r) = \frac{1}{r} \left\{ 0.871 \left(\frac{r}{r_{\max}} \right)^{1/2} - 1.39 \left(\frac{r}{r_{\max}} \right) + 1.296 \left(\frac{r}{r_{\max}} \right)^2 \right\} \quad (\text{D.6})$$

Substituting $\Delta T_{D, \text{Curve}}$ from equation (D.3) in equation (D.4), followed by the substitution of the final form of $\dot{Q}_{D, \text{Curve}}$ from equation (D.4) in equation (D.5), gives

$$\dot{Q}_{\text{in}} = R_{D, \text{Curve}}^{-1} \Delta T_{D, \text{Tot}} r_{\text{min}} \int_{r_{\text{min}}}^{r_{\text{max}}} \frac{1}{r} A(r) dr \quad (\text{D.7})$$

or,

$$\frac{R_{D, \text{Curve}}}{R_{D, \text{Tot}}} = r_{\text{min}} \int_{r_{\text{min}}}^{r_{\text{max}}} \frac{1}{r} A(r) dr \quad (\text{D.8})$$

where $R_{D, \text{Tot}} = \frac{\Delta T_{D, \text{Tot}}}{\dot{Q}_{\text{in}}}$.

Evaluating the integral in equation (D.8), therefore, yields

$$\frac{R_{D, \text{Curve}}}{R_{D, \text{Tot}}} = r_{\text{min}} \left[\left\{ -\frac{1.742}{r_{\text{max}}^{0.5}} (r_{\text{max}}^{-0.5} - r_{\text{min}}^{-0.5}) \right\} + \left\{ -\frac{1.39}{r_{\text{max}}} \ln \left(\frac{r_{\text{max}}}{r_{\text{min}}} \right) \right\} + \left\{ \frac{1.296}{r_{\text{max}}^2} (r_{\text{max}} - r_{\text{min}}) \right\} \right] \quad (\text{D.9})$$

D.2.2 Prediction equation for $R_{C, D, I}$

The temperature drop due to interfacial heat transfer ($\Delta T_{D, I}$) across a single hemispherical drop can be given as (Graham and Griffith, 1973)

$$\Delta T_{D, I} = \frac{\dot{Q}_{D, I}}{h_I A_D} \quad (\text{D.10})$$

where $\dot{Q}_{D, I}$ is the interfacial heat transfer rate through a single drop of radius r , A_D is the surface area of the hemispherical drop given as $2\pi r^2$ and h_I is the interfacial heat transfer coefficient. Two formulations for h_I exist in the literature. Nabavian and Bromley (1963) reported $h_I = \left[\frac{2\alpha}{2-\alpha} \right] \left[\frac{M}{2\pi R T_{\text{sat}}} \right] \frac{h_{fg}^2 \rho_v}{T_{\text{sat}}}$, where α is the accommodation coefficient for mass transfer ($= 1$ for clean water, Graham and Griffith, 1973) and M is the molecular weight of the WF. by Fevre and Rose (1966) postulated $h_I = \left(\frac{n-1}{n+1} \right) \frac{K_2 h_{fg}^2 \rho_v}{T_{\text{sat}}} \left(\frac{2\pi}{RT_{\text{sat}}} \right)^{1/2}$, $n = c_p/c_v$, and K_2 is a constant given by the ratio of the base area of the drop to its curved surface area, i.e. $\pi r^2 / 2\pi r^2 = 1/2$. The mean heat transfer rate \dot{Q}_{in} can, therefore, be calculated as

$$\dot{Q}_{\text{in}} = \int_{r_{\text{min}}}^{r_{\text{max}}} \dot{Q}_{D, I} A(r) dr \quad (\text{D.11})$$

Substituting $\dot{Q}_{D,I}$ from equation (D.10) in equation (D.11) and evaluating the integral in (D.11) gives

$$\frac{1}{R_{D,I}} = 2\pi h_I \left[\{0.3484(r_{\max}^{2.5} - r_{\min}^{2.5})\} + \{0.4633(r_{\max}^3 - r_{\min}^3)\} + \{0.324(r_{\max}^4 - r_{\min}^4)\} \right] \quad (D.12)$$

where $R_{C,D,I} = \frac{\Delta T_{D,I}}{\dot{Q}_{in}}$.

D.2.3 Prediction equation for $R_{C,D,Condu}$

The temperature difference due to heat conduction ($\Delta T_{D,Condu}$) through a single hemispherical drop is given by

$$\Delta T_{D,Condu} = \frac{K_1 \dot{Q}_{D,Condu} r}{k_I A_{B,D}} \quad (D.13)$$

where $\dot{Q}_{D,Condu}$ is the drop conduction heat transfer rate through a single drop, $A_{B,D}$ is the base area of the hemispherical drop calculated as πr^2 , and K_1 is a shape factor constant, accounting for the shape of the drop. $K_1 = 0.241$ (McCormick 1963, 1965), 0.25 (Fatica and Katz, 1949, Graham and Griffith, 1973), 0.66 (Fevre and Rose, 1966). The mean heat transfer rate \dot{Q}_{in} can, therefore, be calculated as

$$\dot{Q}_{in} = \int_{r_{\min}}^{r_{\max}} \dot{Q}_{D,Condu} A(r) dr \quad (D.14)$$

Substituting $\dot{Q}_{D,Condu}$ from equation (D.13) in equation (D.14) and evaluating the integral in equation (D.14) gives

$$\frac{1}{R_{C,D,Condu}} = \frac{\pi k_I}{K_1} \left[\left\{ \frac{0.581}{r_{\max}^{0.5}} (r_{\max}^{1.5} - r_{\min}^{1.5}) \right\} + \left\{ \frac{0.695}{r_{\max}} (r_{\max}^2 - r_{\min}^2) \right\} + \left\{ \frac{0.432}{r_{\max}^2} (r_{\max}^3 - r_{\min}^3) \right\} \right] \quad (D.15)$$

where $R_{C,D,Condu} = \frac{\Delta T_{D,Condu}}{\dot{Q}_{in}}$.

If dropwise condensation is the only dominant mode of heat transfer at the condenser, then $R_{D,C} = R_{C,D,Curve} + R_{C,DI} + R_{C,D,Condu}$.

D.3 Shear stress formulation based on Lockhart-Martinelli correlation

This shear stress formulation is valid for a turbulent vapour flow. This condition is similar to the criterion postulated in Chapter 4 i.e. the effects of τ_i are significant on $Re_{F,C}$ when $Re_v \geq 1250$. For a turbulent vapour flow, the dimensionless interfacial shear stress (τ_i^*) can be specified as (Chen et al., 1987)

$$\tau_i^* = - \left(\frac{0.023}{D_i^2 g^{2/3}} \frac{\mu_l^{1.33} \mu_v^{0.2}}{\rho_v \rho_l^{0.3333}} \right) Re_F^{1.8} \quad (D.16)$$

The negative sign implies that τ_i^* is acting opposite to gravity. A steady state mass balance was utilized to relate Re_v and Re_F while deriving equation (D.16).

When the TS or a HP experiences a flooding limit (discussed in section G.3 in Appendix G), reflux condensation will cease to exist. Thus equation (D.16) is only applicable when

$$Re_F \leq \tilde{D}_i^{3/2} \left(\frac{C_K}{Bo^{1/4}} \right)^2 \left(\frac{\rho_v}{\rho_l} \right)^{1/2} \quad (D.17)$$

where $\tilde{D}_i^{3/2}$ is defined as

$$\tilde{D}_i^{3/2} = D_i \left(\frac{g}{v_l^2} \right)^{1/3} \quad (D.18)$$

and C_K is defined as

$$C_K = \sqrt{3.2} \tanh \left(\frac{Bo^{1/4}}{2} \right) \quad (D.19)$$

The Bond number Bo is defined as

$$Bo = D_i \left(\frac{\rho_l g}{\sigma} \right)^{1/2} \quad (D.20)$$

D.4 Effects of the condensate sensible heat on $R_{C,F}$

The contribution of the sensible heat, if any, is to decrease, the condensate film thickness, $\delta_{C,F}$ and, therefore, $R_{C,F}$. Physical reasoning supporting this statement has been provided by Bromley (1952). Typically, the Jakob number for ordinary fluids and saturated water vapour is small i.e., $\left[\frac{c_{p,l}\Delta T}{h_{fg}} \right] < 1$. However, for saturated liquid metal vapours at high P_{sat} and large ΔT , even though $\left[\frac{c_{p,l}\Delta T}{h_{fg}} \right] \ll 1$, the effects of the sensible heat transport on the $R_{C,F}$ are quite considerable (Bromley, 1952). Chato's, (1960) analysis (see p.30 and Figure 3.3 Chato's, (1960)) show that small Pr number fluids tend to increase the thermal resistance, whilst large Pr number fluids decrease the overall thermal resistance slightly. The inclusion of sensible heat modifies the latent heat as h'_{fg} in the Jakob number, whereas the temperature distribution modifies the coefficient of $\left[\frac{c_{p,l}\Delta T}{h_{fg}} \right]$ in the new h'_{fg} expression (Rohsenow, 1956). Three different expressions of h'_{fg} are available in the literature given by Bromley (1952), Rohsenow (1956) and Chen (1961). Those are summarized in Table D.6 for completeness. However, Bromley's (1952) analysis to determine h'_{fg} has been considered inaccurate by Rohsenow (1956) as the effect of the crossflow within the condensate film was neglected. Hence, only the expressions of h'_{fg} given by Rohsenow (1956) and Chen (1961) are examined.

Table D.2 Modifications to h_{fg} considering the effects of sensible heat transfer and the temperature distribution across the condensate film. $c_2 = 1$ represent a linear temperature distribution, whilst $c_2 > 1$ represent a non-linear temperature distribution.

References	Temperature distribution $\frac{T(y)-T_{c,avg}}{T_v-T_{c,avg}} \propto y^{c_2}$	h'_{fg}
Bromley (1952)	$c_2 = 1$	$h_{fg} \left(\frac{\left(1 + 0.375 \left[\frac{c_{p,l}\Delta T}{h_{fg}} \right] \right)^{1/4}}{\left(1 + 0.23 \left[\frac{c_{p,l}\Delta T}{h_{fg}} \right] \right)^{3/16}} \right)$
	$c_2 > 1$	$h_{fg} \left(1 + 0.40 \left[\frac{c_{p,l}\Delta T}{h_{fg}} \right]^2 \right)$
Rohsenow (1956)	$c_2 = 1$	$h_{fg} \left(1 + 0.38 \left[\frac{c_{p,l}\Delta T}{h_{fg}} \right] \right)$
	$c_2 > 1$	$h_{fg} \left(1 + 0.68 \left[\frac{c_{p,l}\Delta T}{h_{fg}} \right] \right)$
Chen (1961)	$c_2 > 1$	$h_{fg} \left(\frac{1 + 0.68 \left[\frac{c_{p,l}\Delta T}{h_{fg}} \right] + 0.02 \left[\frac{c_{p,l}\Delta T}{h_{fg}} \right]^2 (Pr_1)^{-1}}{1 + 0.85 \left[\frac{c_{p,l}\Delta T}{h_{fg}} \right] (Pr_1)^{-1} - 0.15 \left[\frac{c_{p,l}\Delta T}{h_{fg}} \right]^2 (Pr_1)^{-1}} \right)^{1/4}$

It is quite evident that the effects of $0.38 \left[\frac{c_{p,l} \Delta T}{h_{fg}} \right]$ or $0.68 \left[\frac{c_{p,l} \Delta T}{h_{fg}} \right]$ on $R_{C,F}$ from Rohsenow's (1956) expression are significant only at high values of $\left[\frac{c_{p,l} \Delta T}{h_{fg}} \right]$. Table D.7 shows $0.38 \left[\frac{c_{p,l}}{h_{fg}} \right]$ and $0.68 \left[\frac{c_{p,l}}{h_{fg}} \right]$ magnitudes for saturated water at different T_{sat} values which indicate that in order for these terms to be significant (for e.g. $h'_{fg} = 1.2h_{fg}$), a large degree of supercooling is required ($\Delta T > 225[K]$ for $c_2 = 1$ and $\Delta T > 125[K]$ for $c_2 > 1$), a condition which may not be realized in practical TS and HP applications. Thus, $R_{C,F}$ equations can be used without any modifications to the Jakob number. For low Pr number fluids ($0.003 \ll Pr_l \ll 0.03$) such as liquid metals, Chen's (1961) expression may be utilized while estimating $R_{C,F}$. A more detailed discussion on condensation of metal vapours could be found in Chen's (1961), Rohsenow (1972) and Tanasawa (1991).

Table D.3 Magnitudes of $0.38c_{p,l}/h_{fg}$ and $0.68c_{p,l}/h_{fg}$ at different T_{sat} values.

T_{sat} [K]	$\frac{c_{p,l}}{h_{fg}}$ [1/K]	$0.38 \left[\frac{c_{p,l}}{h_{fg}} \right]$	$0.68 \left[\frac{c_{p,l}}{h_{fg}} \right]$
298.15	1.711×10^{-3}	0.65×10^{-3}	1.16×10^{-3}
300	1.714×10^{-3}	0.65×10^{-3}	1.16×10^{-3}
305	1.722×10^{-3}	0.65×10^{-3}	1.17×10^{-3}
310	1.730×10^{-3}	0.66×10^{-3}	1.18×10^{-3}
315	1.740×10^{-3}	0.66×10^{-3}	1.18×10^{-3}
320	1.749×10^{-3}	0.66×10^{-3}	1.19×10^{-3}
325	1.759×10^{-3}	0.67×10^{-3}	1.20×10^{-3}
330	1.768×10^{-3}	0.67×10^{-3}	1.20×10^{-3}
473.15	2.348×10^{-3}	0.89×10^{-3}	1.60×10^{-3}

D.5 Theoretical model for circumferential laminar condensate film flow

The Navier-Stokes (NS) equation for a thin film condensate steady flow can be written as

$$\rho_l \left[u \frac{\partial u}{\partial x} + v \frac{\partial u}{\partial y} \right] = - \frac{\partial P}{\partial x} + \mu \left(\frac{\partial^2 u}{\partial x^2} + \frac{\partial^2 u}{\partial y^2} \right) + \rho_l g \quad (D.21)$$

Equation (D.21) is subjected to the following assumptions

- i) The advection term $u \frac{\partial u}{\partial x} \approx 0$, owing to the low velocity of the fluid.
- ii) $v \approx 0$, assuming that there is no crossflow across the condensate.
- iii) $\frac{\partial^2 u}{\partial x^2} \ll \frac{\partial^2 u}{\partial y^2}$, invoking the boundary layer approximation.

- iv) The free stream pressure gradient due to quiescent vapour conditions yields $\frac{\partial P}{\partial x} = \rho_v g$
- v) Negligible shear stress exists at the liquid-vapour interface.

Utilizing these assumptions, equation (D.21) results in

$$\frac{\partial^2 u}{\partial y^2} = -\frac{g}{\mu_1}(\rho_1 - \rho_v) \quad (\text{D.22})$$

As the flow is two-dimensional (2D) the axial flow is defined by the “u” component of the velocity and the circumferential flow is defined by the “w” component of the velocity. The velocity distribution of the condensate film flowing around the circumference at any point is represented by the tangent to the circumference at that point.

Applying equation (D.22) for the circumferential flow yields

$$\frac{\partial^2 w}{\partial y^2} = -\frac{g \cos \theta \sin \phi}{\mu_1}(\rho_1 - \rho_v) \quad (\text{D.23})$$

Integrating equation (D.23) twice and applying the boundary conditions; at $w(y=0) = 0$ and $\left. \frac{\partial w}{\partial y} \right|_{y=\delta} = 0$ yields

$$w(y) = \frac{g}{\mu_1} \cos \theta \sin \phi (\rho_1 - \rho_v) \left[\delta y - \frac{y^2}{2} \right] \quad (\text{D.24})$$

Similarly, the u component of velocity can be obtained as

$$u(y) = \frac{g}{\mu_1} \sin \theta (\rho_1 - \rho_v) \left[\delta y - \frac{y^2}{2} \right] \quad (\text{D.25})$$

The mean velocities across the film thickness are obtained as

$$w_{\text{mean}} = \frac{1}{\delta} \int_0^\delta w dy = \frac{g}{\mu_1} \cos \theta \sin \phi (\rho_1 - \rho_v) \left[\frac{\delta^2}{3} \right] \quad (\text{D.26})$$

$$u_{\text{mean}} = \frac{1}{\delta} \int_0^\delta u dy = \frac{g}{\mu_1} \sin \theta (\rho_1 - \rho_v) \left[\frac{\delta^2}{3} \right] \quad (\text{D.27})$$

The mass flow rate is a function of the x and the z coordinates and, thus,

$$d\dot{M} = \frac{\partial \dot{M}_x}{\partial x} dx + \frac{\partial \dot{M}_z}{\partial z} dz \quad (D.28)$$

At the liquid-vapour interface , the rate of heat transfer into the film must be equal to the rate of the energy released due to condensation i.e.

$$d\dot{q} = h_{fg}d\dot{M} \quad (D.29)$$

or,
$$k\left(\frac{\Delta T}{\delta}\right) dx dz = h_{fg}\left[\frac{\partial \dot{M}_x}{\partial x} dx + \frac{\partial \dot{M}_z}{\partial z} dz\right] \quad (D.30)$$

The mass flow rate in the x and z directions can be written as

$$\dot{M}_x = \rho_1 u_{\text{mean}} \delta dz ; \dot{M}_z = \rho_1 w_{\text{mean}} \delta dx \quad (D.31)$$

Substituting w_{mean} and u_{mean} from equations (D.26) and (D.27) into (D.31) and subsequently performing $\frac{\partial \dot{M}_x}{\partial x}$ and $\frac{\partial \dot{M}_z}{\partial z}$ and re-substituting the expressions in equation (D.30) a final form of equation is obtained as

$$\frac{3k_1(\Delta T)\mu_1 R}{\delta^4 h_{fg} \rho_1 (\rho_1 - \rho_v) g \cos \theta} = \frac{3}{\delta} \sin \phi \frac{\partial \delta}{\partial \phi} + \cos \phi + \frac{3R}{\delta} \tan \theta \frac{\partial \delta}{\partial x} \quad (D.32)$$

where $z = R\phi$ and $dz = R d\phi$. Defining ψ as $\psi = \frac{2\rho_1(\rho_1 - \rho_v)gh_{fg}\delta_{F,C}^4 \cos \theta}{3k_1 \Delta T D_1 \mu_1}$ and taking the expression $\frac{\partial \psi}{\partial \phi} = \psi \left(\frac{4}{\delta}\right) \frac{\partial \delta}{\partial \phi}$ and substituting it in equation (D.32), equation (D.33) is obtained as

$$\frac{1}{\psi} = \frac{3}{4} \sin \phi \frac{1}{\psi} \frac{\partial \psi}{\partial \phi} + \cos \phi + \frac{3R}{\delta} \tan \theta \frac{\partial \delta}{\partial x} \quad (D.33)$$

Defining X as $X = \frac{x}{R \tan \theta}$ and utilizing the expression $\frac{\partial \psi}{\partial X} = \psi \left(\frac{4R}{\delta}\right) \tan \theta \frac{\partial \delta}{\partial x}$ and substituting it in equation (D.33), equation (D.24) is obtained as

$$\sin \phi \frac{\partial \psi}{\partial \phi} + \frac{\partial \psi}{\partial X} = \frac{4}{3} (1 - \psi \cos \phi) \quad (D.24)$$

Equation (D.24) gives the non-dimensional local film thickness, ψ as a function of X and Φ (see equation 4.64) in Chapter 4. Conclusions derived from equation (D.24) are discussed in Chapter 4.

D.6 Numerical solution of ψ with respect to X and ϕ

The numerical solution of equation (D.24) shown in Table D.8 was originally tabulated by Hassan and Jakob (1958). Details about the solution procedure is available in Hassan and Jakob (1958).

Table 0.6 Results of the numerical solution of equation (D.19)

Φ [°]	X										
	0	0.2	0.4	0.8	1.2	1.6	2.0	2.4	2.8	3.2	∞
0	0	0.234	0.413	0.656	0.798	0.882	0.931	0.959	0.976	0.987	1.000
15	0	0.235	0.417	0.664	0.809	0.894	0.945	0.972	0.989	0.999	1.014
30	0	0.238	0.425	0.684	0.838	0.929	0.982	1.014	1.031	1.042	1.057
45	0	0.243	0.439	0.719	0.889	0.991	1.050	1.085	1.106	1.118	1.134
60	0	0.249	0.459	0.771	0.967	1.086	1.157	1.198	1.223	1.237	1.257
75	0	0.256	0.484	0.842	1.081	1.227	1.316	1.368	1.398	1.416	1.442
90	0	0.264	0.515	0.940	1.242	1.437	1.555	1.625	1.667	1.691	1.725
105	0	0.273	0.551	1.067	1.470	1.746	1.919	2.023	2.086	2.122	2.171
120	0	0.282	0.591	1.229	1.796	2.221	2.503	2.677	2.781	2.842	2.922
135	0	0.291	0.632	1.425	2.256	2.973	3.499	3.843	4.053	4.179	4.341
150	0	0.298	0.669	1.642	2.881	4.205	5.376	6.250	6.829	7.186	7.635
160	0	0.302	0.688	1.778	3.364	5.455	7.629	9.580	11.104	12.123	13.397
170	0	0.304	0.701	1.877	3.795	6.760	10.977	16.256	21.711	26.624	34.600
180	0	0.305	0.706	1.917	3.989	7.531	13.586	23.938	41.918	73.539	∞

Appendix E: Appendix related to Chapter 5

Instrument calibration and uncertainty analysis of the experimental measurements

This Appendix describes the instrument calibration and reports the uncertainty estimates of the experimentally measured variables.

E.1 Instrument calibration

E.1.1 Calibration of the ultrasonic flow sensor

The clamp-on ultrasonic flow sensor (Keyence FD-XS20E) used in the present experiments was calibrated against the volume flow rate measurements obtained from the bucket (Pyrex 500ml graduated cylinder, each graduation corresponding to 10ml) and the stopwatch method.

The flow to the flow sensor was controlled by varying the speed of a magnetic drive gear pump (FG204XD0PT10000) connected to a DC power supply (RIGOL DP832). The time taken to fill the Pyrex cylinder was recorded using a Samsung Galaxy stopwatch (accurate to up to 100ms). Four different flow rates (\dot{V}_B) (each test repeated three times) from the bucket test were examined and compared against the flow rate (\dot{V}_S) displayed by the flow sensor (the flow sensor has a display resolution up to two decimal places). Those are shown in Table E.1 and plotted in Figure E.1 for completeness. As can be seen from Figure E.1, the flow sensor readings are within $\pm 5\%$ of the bucket test data and it improves with increasing flow rate. The maximum and the minimum error percentage (ε) between the flow sensor reading (\dot{V}_S) and the average of the bucket test data ($\dot{V}_{B,avg}$), where $\varepsilon = \frac{|\dot{V}_{B,avg} - \dot{V}_S|}{\dot{V}_{B,avg}} \times 100$, is 5.66% and 0.79%, respectively. Thereafter, a correction factor, termed as F_{corr} (where $F_{corr} = \frac{\dot{V}_{B,avg}}{\dot{V}_S}$) (defined as span in the flow sensor settings), was implemented to obtain the same flow rate as that obtained from the bucket test. A plot of F_{corr} versus \dot{V}_S is also shown in Figure E.2 along with the equation of the best-fit curve so that F_{corr} can be estimated at any intermediate flow rate readings.

Table E.1 Comparison of the volume flow rates obtained from the bucket test and the flow sensor.
 F_{corr} is used to adjust the flow rate reading from the flow sensor.

\dot{V}_B [mL/min]	$\dot{V}_{B,avg}$ (L/min)	\dot{V}_S (L/min)	(ϵ) (%)	F_{corr}
106.27	0.106	0.10	5.66	1.06
105.88				
105.72				
210.13	0.210	0.20	4.76	1.05
209.67				
210.28				
409.63	0.410	0.40	2.44	1.03
410.11				
409.21				
505.33	0.504	0.50	0.79	1.01
503.84				
503.60				

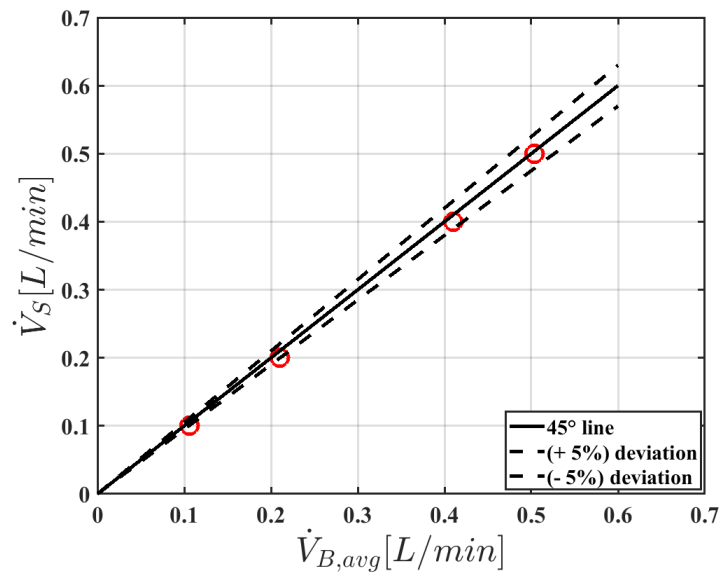


Figure E.1 Plot of \dot{V}_S versus $\dot{V}_{B,avg}$. The data close to 45° line indicate the closeness of \dot{V}_S to $\dot{V}_{B,avg}$.

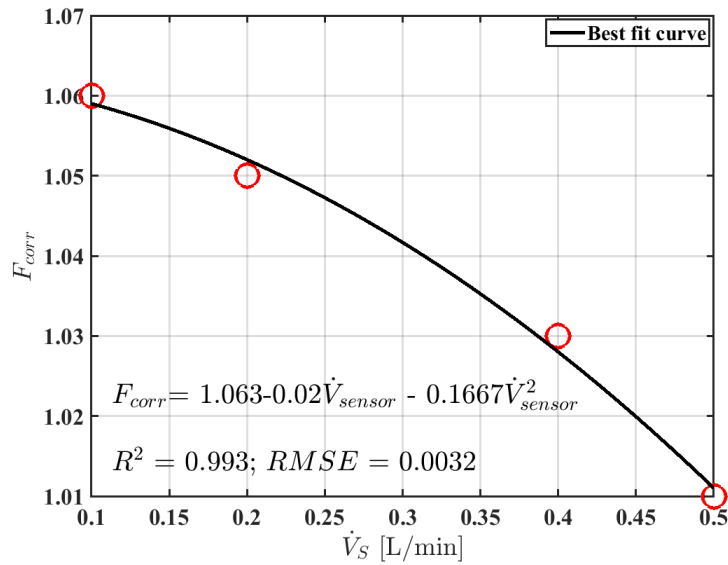


Figure E.2 Plot of F_{corr} versus \dot{V}_S . A polynomial equation of order 2 represents the best fit curve to the data.

The uncertainty associated with the volume flow rate measurements from the bucket test is discussed in section E.3.

E.1.2 Calibration of the K-Type surface and the waterline thermocouples

The thermocouples (Type-K Grounded Mgo Style for the water line temperature measurements and Type-K Solid Conductor for surface temperature measurements) used in the present experiments were referenced against a cold-water bath and a chiller operating at 15°C. This was done to estimate the inherent measurement accuracy of the thermocouples. The DAQ was operated at a A/D data rate of 2.5Hz, whereas the data from the DAQ were acquired at a rate of 0.17Hz. This ensured that much of the noise is filtered out of the data, and the effects of the inherent noise of the DAQ system is minimal. The analysis was carried out after the temperature measurements had reached a steady state condition.

The inherent measurement accuracy of the thermocouples is discussed in section E.4.

E.2 Consideration of precision and bias uncertainty

This section reports the precision and bias errors in all the measured variables that are used in computing the heat transfer results shown in Chapter 6. This was done to ensure that the uncertainty analysis meets the guidelines of the American Society of Mechanical Engineers (ASME) standards (Abernethy et al., 1985, Rood and Telionis, 1991).

The precision uncertainty (ω_P) also known as random error describes the imprecision in the individual measurements and depends on the sample size. It is estimated using the t-distribution method (see Chapter 6 in Wheeler and Ganji, 2009).

The bias uncertainty (ω_B) also known as systemic error describes the inaccuracy in the measuring equipment which is independent of the sample size and does not vary during repeated measurements under the same experimental conditions.

ω_P and ω_B can be estimated for both a measured variable, x and a derived result R where $R = f(x_1, x_2, \dots, x_m)$ and x_1, x_2, \dots, x_m are m independent measured variables. The expressions for ω_P and ω_B for a measured variable are shown first, followed by the expressions for ω_P and ω_B of a derived result.

The precision uncertainty, ω_P for a variable x ($\omega_{P,x}$) measured n times can be estimated using

$$\omega_{P,x} = \pm t_P S_x; S_x = \left(\frac{\sum_{i=1}^n (x_i - \bar{x})^2}{(n-1)} \right)^{0.5} \quad (\text{E.1})$$

where t_P is a function of the degrees of freedom (ν) for multiple measurement experiments (where $\nu = n - 1$; it is determined from Table 6.6 in Wheeler and Ganji, 2009; for $n > 30$; $t_P = 2$), S_x is the precision index (standard deviation of the sample) of the variable x , \bar{x} is the mean of the variable computed as

$$\bar{x} = \frac{1}{n} \sum_{i=1}^n x_i \quad (\text{E.2})$$

ω_P for \bar{x} ($\omega_{P,\bar{x}}$) can be estimated using

$$\omega_{P,\bar{x}} = \pm t_P \left(\frac{S_x}{\sqrt{n}} \right) \quad (\text{E.3})$$

The bias uncertainty, ω_B for a variable x ($\omega_{B,x}$) is typically reported in manufacturers' specification of the equipment but can also be determined from calibration tests.

ω_P for a derived result R ($\omega_{P,R}$) can be estimated using

$$\omega_{P,R} = \pm t_{P,C} S_R; S_R = \left\{ \sum_{i=1}^m \left(S_{x_i} \frac{\partial R}{\partial x_i} \right)^2 \right\}^{0.5}; v_R = \frac{(S_R^2)^2}{\sum_{i=1}^m \left(\frac{1}{v_i} \left[\left(S_{x_i} \frac{\partial R}{\partial x_i} \right)^2 \right]^2 \right)} \quad (\text{E.4})$$

where $t_{P,C}$ is a function of the combined degrees of freedom (v_R), S_R is the precision index of the derived result R, S_{x_i} is the standard deviation of the individual measured variables, and v_i is the degrees of freedom of the individual elemental error.

ω_B for a derived result R ($\omega_{B,R}$) can be estimated using

$$\omega_{B,R} = \left\{ \sum_{i=1}^m \left(\omega_{B,x_i} \frac{\partial R}{\partial x_i} \right)^2 \right\}^{0.5} \quad (\text{E.5})$$

where ω_{B,x_i} is the bias uncertainty in the measured variable.

The total uncertainty for a variable x ($\omega_{tot,x}$) and the result R ($\omega_{tot,R}$) can be estimated using the root of the sum of the squares (RSS) (Coleman and Steel, 1989, Taylor, 1982) as

$$\omega_{tot,x} = \left[\omega_{P,x}^2 + \omega_{B,x}^2 \right]^{0.5} @95\% \text{ confidence levels} \quad (\text{E.6})$$

$$\omega_{tot,R} = \left[\omega_{P,R}^2 + \omega_{B,R}^2 \right]^{0.5} @95\% \text{ confidence levels} \quad (\text{E.7})$$

E.3 Uncertainty estimates in the volume flow rate measurements

The overall uncertainty in the volume flow rate measurements obtained using the clamp-on ultrasonic flow sensor include the analog to digital (A/D) conversion error, hysteresis, and system noise. The flow sensor inherently reduces the effects of the system noise by averaging multiple signals over a time period to recognize the correct waveform. The measurement error arising due to the A/D conversion error and the hysteresis error is minimized by calibrating the flow sensor against the measurement data from the bucket test (see section E.1.1).

The volume flow rate (\dot{V}_B) from the bucket test is determined as $\dot{V}_B = \frac{V_B}{t}$, where V_B is the measured volume of water in the “bucket” (in this case a Pyrex cylinder [ml]) and t represents the measured time in [min]. V_B is determined as $V_B = \frac{M_B}{\rho_w}$, where M_B is the mass of water measured using a weighing scale (Shimadzu UX2200H) and ρ_w is the density of water determined at its corresponding temperature (T_w) using the thermodynamics property table. T_w was measured using a digital pocket thermometer (McMaster Carr SKU 4135K28). Substituting V_B in the expression of \dot{V}_B gives $\dot{V}_B = \frac{M_B}{\rho_w t}$. Table E.2 shows the measured values of M_B , t and the value of \dot{V}_B obtained from the bucket test for four different flow rates each measured three times.

Table E.2 Measured variables from the bucket test. V_E denotes the volume examined.

V_E [ml]	M_B [gm] (measured)	T_w [°C] (measured)	ρ_w [gm/ml] (computed)	V_M [ml] (computed)	t (min) (measured)	\dot{V}_B [mL/min]
100	531.96	22.2	0.998	533.03	5.017	106.27
	528.86	22.1		529.92	5.005	105.88
	527.89	22.2		528.95	5.003	105.72
200	524.07	22.1		525.12	2.499	210.13
	522.49	22.0		523.54	2.497	209.67
	525.69	22.0		526.74	2.505	210.28
400	1028.16	22.1		1030.22	2.515	409.63
	1025.28	22.1		1027.33	2.505	410.11
	1020.58	22.1		1022.63	2.499	409.21
500	1005.62	22.2		1007.64	1.994	505.33
	1004.66	22.2		1006.67	1.998	503.84
	1004.18	22.4		1006.19	1.998	503.60

The measured variables M_B , T_w and t contain both precision and bias uncertainties. Thus, ρ_w also contain bias uncertainties and precision uncertainties. ω_P for M_B , ρ_w and t is estimated using equation (E.1), whilst ω_B for the same variables is determined from the calibration tests. The total uncertainty (ω_{tot}) in M_B , ρ_w and t is estimated using equation (E.6).

The \dot{V}_B measurements contain both precision uncertainty (ω_{P,\dot{V}_B}) and the bias uncertainty (ω_{B,\dot{V}_B}). ω_{P,\dot{V}_B} can be estimated using equation (E.4) as

$$\omega_{P,\dot{V}_B} = \pm t_{p,C} S_{\dot{V}_B} \quad (E.8)$$

where $t_{p,C}$ is a function of the combined degrees of freedom ($v_{\dot{V}_B}$) determined from table

$$6.6 \text{ in Wheeler and Ganji (2009). } v_{\dot{V}_B} = \frac{(S_{\dot{V}_B}^2)^2}{\left[\frac{(S_{M_B} \frac{1}{\rho_w t})^4}{v_{M_B}} + \frac{(-S_{\rho_w} \frac{M_B}{t \rho_w^2})^4}{v_{\rho_w}} + \frac{(-S_t \frac{M_B}{\rho_w t^2})^4}{v_t} \right]} \text{ where } v_{M_B}, v_{\rho_w}$$

and v_t are the degrees of freedom of M_B , ρ_w and t which is equal to 2 (since total measurements are 3). $S_{\dot{V}_B} = \left[\left(S_{M_B} \frac{1}{\rho_w t} \right)^2 + \left(-S_{\rho_w} \frac{M_B}{t \rho_w^2} \right)^2 + \left(-S_t \frac{M_B}{\rho_w t^2} \right)^2 \right]^{0.5}$ where S_{M_B} , S_{ρ_w} and S_t are the precision index of the variables M_B , ρ_w and t and $S_{\rho_w} = 0$.

ω_{B,\dot{V}_B} can be estimated using equation (E.5) as

$$\omega_{B,\dot{V}_B} = \left[\left(\omega_{B,M_B} \frac{1}{\rho_w t} \right)^2 + \left(-\omega_{B,\rho_w} \frac{M_B}{t \rho_w^2} \right)^2 + \left(-\omega_{B,t} \frac{M_B}{\rho_w t^2} \right)^2 \right]^{0.5} \quad (E.9)$$

where ω_{B,M_B} , ω_{B,ρ_w} and $\omega_{B,t}$ are the bias uncertainty in M_B , ρ_w and t . It is to be noted that the average values of M_B and t have been used while calculating $S_{\dot{V}_B}$ and ω_{B,\dot{V}_B} . The total uncertainty in \dot{V}_B (ω_{tot,\dot{V}_B}) is estimated using equation (E.7) as

$$\omega_{tot,\dot{V}_B} = \left[(\omega_{P,\dot{V}_B})^2 + (\omega_{B,\dot{V}_B})^2 \right]^{0.5} \quad (E.10)$$

ω_P , ω_B and ω_{tot} estimated for M_B , ρ_w and t along with the sources of error are shown in Table E.3 along with the magnitudes of ω_{P,\dot{V}_B} , ω_{B,\dot{V}_B} and ω_{tot,\dot{V}_B} for completeness.

Table E.3 Precision and bias uncertainty in the measured values of M_B , ρ_w , t and $\dot{V}_{B,avg}$. The estimates are for 95% confidence levels. The units of ω_P change in each row and it is the units of the corresponding variable.

Variables		$(\omega_P) (\pm)$	Error sources	$(\omega_B) (\pm)$	Error sources	$\omega_{tot} (\pm)$
$T_w [^\circ\text{C}]$		0.2	Random	1.0	Manufacturing error	1.02
$\rho_w [\text{gm/mL}]$		2.27×10^{-5}	Random error propagation from temperature measurements	1.97×10^{-4}	Bias error from temperature measurements and data reduction error from property tables	1.99×10^{-4}
$t [\text{min}]$		0.019	Random	8.33×10^{-3}	Human error	0.020
		0.010				0.013
		0.020				0.022
		0.006				0.010
$M_B [\text{gm}]$		9.15	Random	0.045	Calibration error of the weighing scale	5.28
		6.88				3.98
		16.46				9.51
		3.16				1.82
$\dot{V}_{B,avg} [\text{ml/min}]$	105.96	1.67	Error propagation from M_B and t in $\dot{V}_{B,avg}$	0.176	Error propagation from M_B , ρ_w and t in $\dot{V}_{B,avg}$	1.68
	210.03	2.29		0.701		2.39
	409.65	5.68		1.365		5.84
	504.26	6.00		2.108		6.36

Table E.3 shows that ω_{tot, \dot{V}_B} increases with $\dot{V}_{B,avg}$, the maximum ω_{tot, \dot{V}_B} being ± 6.36 [ml/min] at $\dot{V}_B \sim 500$ [ml/min] and minimum ω_{tot, \dot{V}_B} being ± 1.68 [ml/min] at $\dot{V}_B \sim 100$ [ml/min], respectively. Thereby, a plot of $\omega_{\dot{V}_B}$ versus $\dot{V}_{B,avg}$ is shown in Figure E.3. Based on an *ad-hoc* assumption, a linear best fit (since that gave the least root mean square error (RMSE)) is plotted against the data to estimate the uncertainty at any intermediate measured flow rate. The equation to the best-fit straight line is provided in Figure E.3.

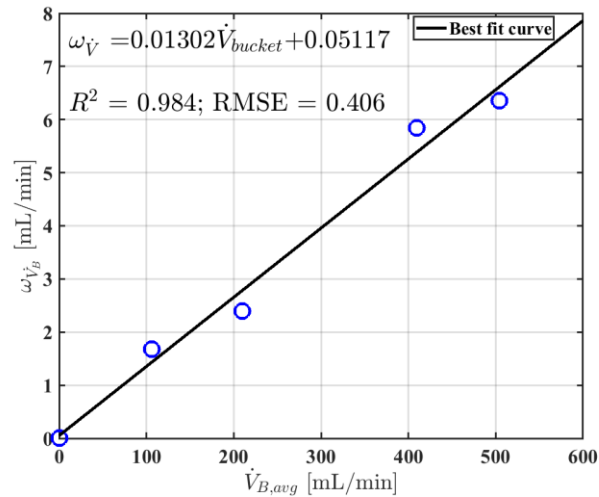


Figure E.3 Plot of $\omega_{\dot{V}_B}$ as a function of \dot{V}_B along with the linear best fit to the data.

E.4 Uncertainty estimates in the temperature measurements from thermocouples

The total uncertainty in the temperature measurements (ω_T) from the thermocouples (TC) include the inherent accuracy error of the TC ($\omega_{T,K-Type}$) and the measurement error (ω_{DAQ}) from the data acquisition system (OMB-DAQ-2416) to which the TC are connected. Since no individual information on the precision and bias uncertainty is available for the TC or the DAQ, it is assumed that $\omega_{T,K-Type}$ and ω_{DAQ} inherently combines both the precision and the bias uncertainties. ω_T can, therefore, be estimated as

$$\omega_T = \left[(\omega_{T,K-type})^2 + (\omega_{DAQ})^2 \right]^{0.5} \quad (E.11)$$

$\omega_{T,K-Type}$ includes the calibration uncertainty ($\omega_{T,K-Type,cali}$) and the error arising due to the manufacturing inaccuracies (ω_{man}). The maximum error tolerance for K-type thermocouple given by the American Society for Testing and Materials (ASTM) standard E 230 is either $\pm 2.2^\circ[C]$ or 0.75% of the measured value, whichever is greater.

ω_{DAQ} includes the cold-junction compensation (CJC) measurement error (ω_{CJC}), the polynomial linearization error (ω_{poly}), and the system noise (OMB-DAQ-2416 manual). The low frequency system noise was minimised by operating the DAQ at very low A/D data rate setting (i.e. 2.5 samples/sec). Based on the preliminary tests performed at various throughput rates (25[Hz], 10[Hz], 5[Hz] and 2.5[Hz]), it was observed that the

DAQ operating at 2.5Hz gives the least noise in the final data. At this frequency, the maximum data throughput rate for 16 differential thermocouple input connections is 0.16 [Hz].

The accuracy specifications for a typical K-Type thermocouple adapted from the OMB-DAQ-2416 manual are shown in Table E.4 for completeness. Those are plotted against the sensor temperature (T_s) range in figure E.4 along with a linear best fit curve, so that ω_{DAQ} for any intermediate temperature can be estimated.

Table E.4 K-type thermocouple accuracy specifications, including CJC measurement error (adapted from OMB-DAQ-2416 manual). $\omega_{\text{DAQ,max}}$ and $\omega_{\text{DAQ,typ}}$ are the maximum and the typical values of ω_{DAQ} .

A/D data rate	Sensor temperature range (T_s) ($^{\circ}\text{C}$)	Maximum accuracy error ($\omega_{\text{DAQ,max}}$) ($^{\circ}\text{C}$) (\pm)	Typical accuracy error ($\omega_{\text{DAQ,typ}}$) ($^{\circ}\text{C}$) (\pm)
2.5 S/s	-210	2.735	1.524
	0	0.948	0.457
	1372	2.396	1.941

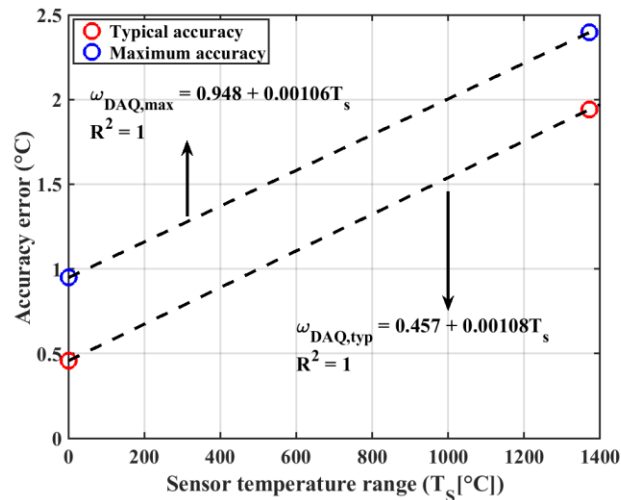


Figure E.4 Plot of $\omega_{\text{DAQ,max}}$ and $\omega_{\text{DAQ,typ}}$ as a function of sensor temperature.

The uncertainty (ω_T) in the waterline and the surface TC temperature measurements is determined from the auxiliary cold-water bath and the water chiller tests (at 15°C). Those are listed in Table E.5. ω_T and $\omega_{\bar{T}}$ denote the maximum uncertainty in the measured and the average temperature value and are assumed to include both the precision and the bias uncertainties of the TC and the DAQ.

Table E.5 Uncertainty estimates for the waterline and the surface thermocouples. $\omega_{\bar{T}}$ is the estimated uncertainty in the average value.

Thermocouple types	$\omega_T (\pm ^\circ\text{C})$ at 0°C	$\omega_{\bar{T}} (\pm ^\circ\text{C})$ at 0°C	$\omega_T (\pm ^\circ\text{C})$ at 15°C	$\omega_{\bar{T}} (\pm ^\circ\text{C})$ at 15°C
Waterline thermocouple	0.7	0.6	0.2	0.2
Surface thermocouple	0.6	0.4	0.3	0.2

E.5 Uncertainty estimates in the input heating power (\dot{Q}_{in}) calculations

The input heating power, \dot{Q}_{in} is calculated as $\dot{Q}_{in} = VI$, where V is the voltage, and I is the current drawn by the heaters. The voltage and the current measurements are made using an accurate power meter (P4400 Kill A Watt) whose maximum uncertainty is 1% and the typical uncertainty is 0.2% and 0.3% of the measured root-mean square (RMS) voltage and the current, respectively.

The precision uncertainty ($\omega_{P,\dot{Q}_{in}}$) in the measured \dot{Q}_{in} can be estimated using equation (E.4) as

$$\omega_{P,\dot{Q}_{in}} = \pm t_{P,C} S_{\dot{Q}_{in}} \quad (\text{E.11})$$

where $t_{P,C}$ is a function of the combined degrees of freedom, $S_{\dot{Q}_{in}}$ is the precision index of \dot{Q}_{in} , $S_{\dot{Q}_{in}} = \left[\left(S_V \frac{\partial \dot{Q}_{in}}{\partial V} \right)^2 + \left(S_I \frac{\partial \dot{Q}_{in}}{\partial I} \right)^2 \right]^{0.5}$ and S_V and S_I are the precision index for the voltage and the current measurements, respectively.

The bias uncertainty ($\omega_{B,\dot{Q}_{in}}$) in \dot{Q}_{in} measurements can be estimated using equation (E.5) as

$$\omega_{B,\dot{Q}_{in}} = \left[\left(\omega_{B,V} \frac{\partial \dot{Q}_{in}}{\partial V} \right)^2 + \left(\omega_{B,I} \frac{\partial \dot{Q}_{in}}{\partial I} \right)^2 \right]^{0.5} \quad (\text{E.12})$$

where $\omega_{B,V}$ and $\omega_{B,I}$ are the bias uncertainties in V and I .

The total uncertainty in \dot{Q}_{in} ($\omega_{\dot{Q}_{in}}$) is estimated using equation (E.7) as

$$\omega_{\dot{Q}_{in}} = \left[\left(\omega_{P,\dot{Q}_{in}} \right)^2 + \left(\omega_{B,\dot{Q}_{in}} \right)^2 \right]^{0.5} \quad (\text{E.13})$$

The precision and the bias uncertainties in the measured voltage and current measurements are shown in Table E.6 and E.7 for completeness. Table E.8 shows the overall uncertainty estimates in \dot{Q}_{in} computed using equation E.13.

Table E.6 Uncertainty estimates in the voltage measurements for the experiments where the fill ratio (FR) is varied from 0.35 to 0.75. The estimates are for 95% confidence levels. $\omega_{V,max}$ denote the maximum uncertainty levels.

Voltage (V)	$\omega_{P,V}$ (\pm V)	Error sources	$\omega_{B,V,max}$ (\pm V)	Error sources	$\omega_{V,max}$ (\pm V)
45.12	0.25	Uncertainties due to instability in the mains AC power and hysteresis of the test process.	0.45	Data-acquisition uncertainty in the recording device	0.51
52.56	0.57		0.53		0.78
60.06	0.49		0.60		0.77
67.47	0.40		0.67		0.78
75.05	0.46		0.75		0.88
82.63	0.34		0.83		0.90
90.20	0.42		0.90		0.99
100.07	0.60		1.00		1.16

Table E.7 Uncertainty estimates in the different current measurements for the experiments where the fill ratio (FR) is varied from 0.35 to 0.75. The estimates are for 95% confidence levels. $\omega_{I,max}$ denotes the maximum uncertainty levels.

Current (I)	$\omega_{P,I}$ (\pm A)	Error sources	$\omega_{B,I,max}$ (\pm A)	Error sources	$\omega_{I,max}$ (\pm A)
0.15	0	Uncertainties due to instability in the mains the AC power and hysteresis of the test process.	0.0015	Data-acquisition uncertainty in the recording device	0.0015
0.18	0		0.0018		0.0018
0.21	0		0.0021		0.0021
0.23	0		0.0023		0.0023
0.26	0		0.0026		0.0026
0.28	0.005		0.0028		0.0055
0.31	0		0.0031		0.0031
0.34	0.009		0.0034		0.0094

Table E.8 Uncertainty estimates in \dot{Q}_{in} at different heat input rate measurements for the experiments where FR is varied from 0.35 to 0.75. The estimates are for 95% confidence levels. $\omega_{\dot{Q}_{in,max}}$ denotes the maximum uncertainty levels.

\dot{Q}_{in} [W]	$\omega_{P,\dot{Q}_{in}}$ (\pm W)	$\omega_{B,\dot{Q}_{in}}$ (\pm W)	$\omega_{\dot{Q}_{in}}$ (\pm W)
6.77	0.038	0.096	0.10
9.46	0.102	0.133	0.17
12.61	0.103	0.178	0.21
15.52	0.091	0.219	0.24
19.51	0.119	0.276	0.30
23.22	0.351	0.328	0.40
27.96	0.126	0.395	0.41
34.21	0.749	0.484	0.89

E.6 Uncertainty estimates in the output cooling power (\dot{Q}_{out}) calculations

The output cooling power, \dot{Q}_{out} is calculated as $\dot{Q}_{out} = \dot{m}C_p\Delta T_w$, where \dot{m} [kg/s] and C_p [J/kgK] are the mass flow rate and the specific heat of the cooling water flow. ΔT_w [K] is the temperature difference between the outlet ($T_{w,out}$) and the inlet cooling water ($T_{w,in}$). \dot{m} is computed as $\dot{m} = \rho_w\dot{V}_B$, where ρ_w and \dot{V}_B are the density and the volume flow rate of the cooling water flow. Thus, $\dot{Q}_{out} = \rho_w\dot{V}_B C_p(T_{w,out} - T_{w,in})$. $T_{w,out}$ and $T_{w,in}$ contain both precision and bias uncertainties. Thus, ρ_w and C_p also contain precision and bias uncertainties. The precision, bias and the overall uncertainties in \dot{V}_B , ρ_w , C_p , $T_{w,out}$ and $T_{w,in}$ are shown in Table E.9 along with the sources of error for completeness.

\dot{Q}_{out} contain both precision ($\omega_{P,\dot{Q}_{out}}$) and bias uncertainties ($\omega_{B,\dot{Q}_{out}}$). $\omega_{P,\dot{Q}_{out}}$ can be estimated using equation (E.4) as

$$\omega_{P,\dot{Q}_{out}} = \pm t_{P,C} S_{\dot{Q}_{out}} \quad (E.14)$$

where $t_{P,C}$ is a function of the combined degrees of freedom, $S_{\dot{Q}_{out}}$ is the precision index

$$\text{of } \dot{Q}_{out} \text{ and } S_{\dot{Q}_{out}} = \left[\left(S_{\rho_w} \frac{\partial \dot{Q}_{out}}{\partial \rho_w} \right)^2 + \left(S_{\dot{V}_B} \frac{\partial \dot{Q}_{out}}{\partial \dot{V}_B} \right)^2 + \left(S_{C_p} \frac{\partial \dot{Q}_{out}}{\partial C_p} \right)^2 + \left(S_{\Delta T_w} \frac{\partial \dot{Q}_{out}}{\partial \Delta T} \right)^2 \right]^{0.5}$$

and $S_{\rho_w}, S_{C_p} = 0$. Since the flow rate is fixed at 0.18[L/min], $S_{\dot{V}_B} = 0$. $\frac{\partial \dot{Q}_{out}}{\partial \rho_w} = \dot{V}_B C_p \Delta T$,

$$\frac{\partial \dot{Q}_{out}}{\partial \dot{V}_B} = \rho_w C_p \Delta T, \quad \frac{\partial \dot{Q}_{out}}{\partial C_p} = \rho_w \dot{V}_B \Delta T, \quad \frac{\partial \dot{Q}_{out}}{\partial \Delta T} = -\rho_w \dot{V}_B C_p.$$

$\omega_{B,\dot{Q}_{out}}$ can be estimated using equation (E.5) as

$$\omega_{B,\dot{Q}_{out}} = \left[\left(\omega_{B,\rho_w} \frac{\partial \dot{Q}_{out}}{\partial \rho_w} \right)^2 + \left(\omega_{B,\dot{V}_B} \frac{\partial \dot{Q}_{out}}{\partial \dot{V}_B} \right)^2 + \left(\omega_{B,C_p} \frac{\partial \dot{Q}_{out}}{\partial C_p} \right)^2 + \left(\omega_{B,\Delta T} \frac{\partial \dot{Q}_{out}}{\partial \Delta T} \right)^2 \right]^{0.5} \quad (E.15)$$

The total uncertainty in \dot{Q}_{out} ($\omega_{\dot{Q}_{out}}$) can, therefore, be estimated using (E.7) as

$$\omega_{\dot{Q}_{out}} = \left[\left(\omega_{P,\dot{Q}_{out}} \right)^2 + \left(\omega_{B,\dot{Q}_{out}} \right)^2 \right]^{0.5} \quad (E.16)$$

The total uncertainty in the computed values of \dot{Q}_{out} are shown in Table E.10.

Table E.9 Precision and bias uncertainty estimates in ρ_w , $\dot{V}_{B,avg}$, C_p , $T_{w,out}$, $T_{w,in}$ and $T_{w,in}$. The estimates are for 95% confidence levels. The precision uncertainty for $T_{w,out}$ corresponds to the eight different \dot{Q}_{out} measurements.

Variables	$(\omega_P) (\pm)$	Error sources for precision uncertainty	$(\omega_B) (\pm)$	Error sources for bias uncertainty	$\omega_{tot} (\pm)$
ρ_w at 15 [°C] [kg/m ³]	0.006	Random error propagated from $T_{w,in}$ measurements.	0.032	Bias error from temperature and data reduction error from Popiel's (1998) relation	0.033 [kg/m ³]
$\dot{V}_{B,avg}$ at 0.18 [L/min]	2.31 [ml/min]	Curve fitting uncertainty	0.60 [ml/min]	Curve fitting uncertainty	3.98×10^{-8} [m ³ /s]
C_p [J/kgK]	0.23	Random error propagated from $T_{w,in}$ measurements.	1.73	Bias error from temperature and data reduction error from the property tables	1.74
$T_{w,out}$ [°C]	0.07	Randomness in the measurements	0.21	Calibration error, manufacturing inaccuracies, DAQ error	0.22
	0.06				0.22
	0.08				0.22
	0.11				0.24
	0.11				0.24
	0.05				0.22
	0.09				0.23
$T_{w,in}$ [°C]	0.11				0.25
					0.24

The bias error in the ΔT_w ($\omega_{B,\Delta T}$) in equation (E.15) is determined by taking the absolute difference between the ΔT_w obtained by assuming 90% energy balance within the system and the average of the measured ΔT_w values at different \dot{Q}_{out} [W]. The magnitudes of $\omega_{B,\Delta T}$ are shown in Table E.10 for completeness. As observed, $\omega_{B,\Delta T}$ is significantly low indicating that the waterline TCs have nearly identical bias uncertainties.

Table E.10 Precision, bias and overall uncertainty estimates in the computed values of \dot{Q}_{out} when AR is varied from 5.3 to 12.43. $\omega_{B,\Delta T}$ denotes the bias uncertainties in ΔT_w . The estimates are for 95% confidence levels.

\dot{Q}_{out} [W]	$\omega_{B,\Delta T_w}$ (°C)	$\omega_{P,\dot{Q}_{out}}$ (\pm W)	$\omega_{B,\dot{Q}_{out}}$ (\pm W)	$\omega_{\dot{Q}_{out}}$ (\pm W)
6.37	0.011	0.95	0.14	0.96
8.73	0.002	1.45	0.04	1.45
11.35	0.020	1.15	0.25	1.17
14.43	0.012	1.05	0.16	1.06
17.86	0.007	1.06	0.11	1.07
21.38	0.001	1.04	0.07	1.04
25.64	0.007	1.13	0.12	1.14
31.27	0.017	1.18	0.23	1.20

E.7 Uncertainty estimates in the computed thermal resistances.

E.7.1 Wall thermal resistances

The evaporator (R_2) and the condenser (R_6) wall thermal resistance due to radial heat

conduction, are computed as $R_2 = \frac{\ln\left(\frac{D_o}{D_i}\right)}{2\pi L_e k_{\text{wall}}}$, $R_6 = \frac{\ln\left(\frac{D_o}{D_i}\right)}{2\pi L_c k_{\text{wall}}}$ (Bergman et al., 2018).

Therefore, R_2 and R_6 contain only bias uncertainties propagated through the tolerances in D_i , D_o and L_c . The wall thermal resistance (R_8) due to axial heat conduction is calculated

as $R_8 = \frac{L_e + L_a + L_c}{A_{\text{wall}} k_{\text{wall}}}$ (Reay and Kew, 2007), where $A_{\text{wall}} = \frac{\pi}{4} (D_o^2 - D_i^2)$. Thus, R_8 only

includes bias uncertainty propagated through the tolerances L_e , L_a , L_c and A_{wall} . The uncertainties in R_2 , R_6 and R_8 can be estimated using equation (E.5) as

$$\omega_{R_2} = \left[\left(\omega_{B,D_i} \frac{\partial R_2}{\partial D_i} \right)^2 + \left(\omega_{B,D_o} \frac{\partial R_2}{\partial D_o} \right)^2 + \left(\omega_{B,L_e} \frac{\partial R_2}{\partial L_e} \right)^2 + \left(\omega_{B,k_{\text{wall}}} \frac{\partial R_2}{\partial k_{\text{wall}}} \right)^2 \right]^{0.5} \quad (\text{E.17})$$

$$\omega_{R_6} = \left[\left(\omega_{B,D_i} \frac{\partial R_6}{\partial D_i} \right)^2 + \left(\omega_{B,D_o} \frac{\partial R_6}{\partial D_o} \right)^2 + \left(\omega_{B,L_c} \frac{\partial R_6}{\partial L_c} \right)^2 + \left(\omega_{B,k_{\text{wall}}} \frac{\partial R_6}{\partial k_{\text{wall}}} \right)^2 \right]^{0.5} \quad (\text{E.18})$$

$$\omega_{R_8} = \left[\left(\omega_{B,D_i} \frac{\partial R_8}{\partial D_i} \right)^2 + \left(\omega_{B,D_o} \frac{\partial R_8}{\partial D_o} \right)^2 + \left(\omega_{B,L_e} \frac{\partial R_8}{\partial L_e} \right)^2 + \left(\omega_{B,L_a} \frac{\partial R_8}{\partial L_a} \right)^2 + \left(\omega_{B,L_c} \frac{\partial R_8}{\partial L_c} \right)^2 + \left(\omega_{B,k_{\text{wall}}} \frac{\partial R_8}{\partial k_{\text{wall}}} \right)^2 \right]^{0.5} \quad (\text{E.19})$$

where ω_{B,D_i} , ω_{B,D_o} , ω_{B,L_e} , ω_{B,L_a} , ω_{B,L_c} are the bias uncertainties in the D_i , D_o , L_e , L_a and the L_c , respectively. The bias uncertainty in k_{wall} ($\omega_{B,k_{\text{wall}}}$) for copper is assumed to be zero since a fixed value of k_{wall} of pure copper at 300K (i.e. 401 [W/mK]) is utilized in the calculations. Thus, the last terms in expressions (E.17), (E.18) and (E.19) are zero.

The expressions for $\frac{\partial R_2}{\partial D_i}$, $\frac{\partial R_2}{\partial D_o}$, $\frac{\partial R_2}{\partial L_e}$, $\frac{\partial R_6}{\partial D_i}$, $\frac{\partial R_6}{\partial D_o}$, $\frac{\partial R_6}{\partial L_c}$, $\frac{\partial R_8}{\partial D_i}$, $\frac{\partial R_8}{\partial D_o}$, $\frac{\partial R_8}{\partial L_e}$, $\frac{\partial R_8}{\partial L_a}$ and $\frac{\partial R_8}{\partial L_c}$ are straightforward and, thus, are not shown here. Table E.11 lists the estimated ω_{B,D_i} , ω_{B,D_o} , ω_{B,L_e} , ω_{B,L_a} , ω_{B,L_c} along with ω_{R_2} , ω_{R_6} and ω_{R_8} and the error sources.

Table E.11 Bias uncertainty estimates in the computed values of R_2 , R_6 and R_8 for $L_e = 0.127\text{m}$ and $D_o = 0.016\text{m}$ and $D_i = 0.014\text{m}$. Similar estimations can be done for other values of L_e and D_i . The estimates are for 95% confidence levels.

Variables	Error sources	$\omega_B (\pm)$
D_i (m)	Manufacturing tolerances	2.54×10^{-5}
D_o (m)		7.62×10^{-5}
L_e (m)	Human error	1.89×10^{-3}
L_a (m)		1.89×10^{-3}
L_c (m)		1.89×10^{-3}
R_2 (K/W)	Error propagation through D_i , D_o , L_e , L_a and L_c	1.60×10^{-3}
R_6 (K/W)		1.60×10^{-3}
R_8 (K/W)		1.42

E.7.2 Boiling resistances

The pool boiling ($R_{e,a,Lp}$; Note that $R_{B,P}$ has been used in the main text to denote the pool boiling resistance, thus $R_{B,P} = R_{e,a,Lp}$) and the film boiling ($R_{e,a,F}$) resistances from the experimental measurements are computed as $R_{e,a,Lp} = \frac{(\Delta T_{e,a})}{\dot{Q}_{avg} \times FR}$ and $R_{e,a,F} = \frac{(\Delta T_{e,a})}{\dot{Q}_{avg} \times (1 - FR)}$, where $\Delta T_{e,a} = (T_{e,avg} - T_{a,avg})$ and $\dot{Q}_{avg} = 0.5(\dot{Q}_{in} + \dot{Q}_{out})$, respectively. $T_{e,avg}$ and $T_{a,avg}$ are the average evaporator and the adiabatic temperatures computed as $T_{e,avg} = \frac{T_1 + T_2 + \dots + T_{n_e}}{n_e}$ and $T_{a,avg} = \frac{T_1 + T_2 + \dots + T_{n_a}}{n_a}$, where n_e and n_a are the total number of thermocouples utilized for measuring the evaporator and the adiabatic surface temperatures, respectively. $R_{e,a,P}$ and $R_{e,a,F}$, therefore, contain both precision and bias uncertainties.

The precision uncertainty ($\omega_{P,R_{e,a,P}}$) in $R_{e,a,P}$ can be estimated using equation (E.4) as

$$\omega_{P,R_{e,a,P}} = \pm t_{P,C} S_{R_{e,a,P}} \quad (\text{E.20})$$

where $t_{P,C}$ is a function of the combined degrees of freedom. $S_{R_{e,a,P}}$ can be estimated as

$$S_{R_{e,a,P}} = \left[\left(S_{\Delta T_{e,a}} \frac{\partial R_{e,a,P}}{\partial \Delta T_{e,a}} \right)^2 + \left(S_{\dot{Q}_{avg}} \frac{\partial R_{e,a,P}}{\partial \dot{Q}_{avg}} \right)^2 + \left(S_{FR} \frac{\partial R_{e,a,P}}{\partial FR} \right)^2 \right]^{0.5} \quad (\text{E.21})$$

where $S_{FR} = 0$, as the FR is fixed for a given thermosyphon under testing. Since, the $\Delta T_{e,a}$ measurements from the experiments are single-measurement experiments, accurate

determination of $S_{\Delta T_{e,a}}$ is not possible (Wheeler and Ganji, 2009). Thus, $S_{R_{e,a,P}}$ is estimated based only on the $\left(S_{\dot{Q}_{avg}} \frac{\partial R_{e,a,P}}{\partial \dot{Q}_{avg}}\right)$ term.

The bias uncertainty ($\omega_{B,R_{e,a,P}}$) in $R_{e,a,P}$ can be estimated using equation (E.5) as

$$\omega_{B,R_{e,a,P}} = \left[\left(\omega_{B,\Delta T_{e,a}} \frac{\partial R_{e,a,P}}{\partial \Delta T_{e,a}} \right)^2 + \left(\omega_{B,\dot{Q}_{avg}} \frac{\partial R_{e,a,P}}{\partial \dot{Q}_{avg}} \right)^2 + \left(\omega_{B,FR} \frac{\partial R_{e,a,P}}{\partial FR} \right)^2 \right]^{0.5} \quad (E.22)$$

The total uncertainty in $R_{e,a,P}$ ($\omega_{R_{e,a,P}}$) can, therefore, be estimated using (E.7) as

$$\omega_{R_{e,a,P}} = \left[\left(\omega_{P,R_{e,a,P}} \right)^2 + \left(\omega_{B,R_{e,a,P}} \right)^2 \right]^{0.5} \quad (E.23)$$

The estimations of terms $\omega_{B,\Delta T_{e,a}}$, $\omega_{B,\dot{Q}_{avg}}$ and $\omega_{B,FR}$ in equation (E.22) is discussed next.

The bias uncertainty in $\Delta T_{e,a}$ ($\omega_{B,\Delta T_{e,a}}$) can be estimated using equation (E.5) as

$$\omega_{B,\Delta T_{e,a}} = \left[\left(\omega_{B,T_{e,avg}} \frac{\partial \Delta T_{e,a}}{\partial T_{e,avg}} \right)^2 + \left(\omega_{B,T_{a,avg}} \frac{\partial \Delta T_{e,a}}{\partial T_{a,avg}} \right)^2 \right]^{0.5} \quad (E.24)$$

Assuming that the maximum average bias uncertainty of the surface TC is ± 0.62 [°C] (this is a conservative estimate at 0 [°C] considering that this value also contains the precision uncertainty), $\omega_{B,T_{e,avg}}$ and $\omega_{B,T_{a,avg}}$ can be estimated as $\omega_{B,T_{e,avg}} = \frac{1}{\sqrt{n_e}} \omega_{S,T} = \pm 0.27$ [°C] ($n_e = 5$) and $\omega_{B,T_{a,avg}} = \frac{1}{\sqrt{n_a}} \omega_{S,T} = \pm 0.31$ [°C] ($n_a = 4$), respectively, where the subscripts S, T denote “surface” and “thermocouple”, respectively. Thus, $\omega_{B,\Delta T_{e,a}} = \pm 0.41$ [°C].

The bias uncertainty in \dot{Q}_{avg} ($\omega_{B,\dot{Q}_{avg}}$), can be estimated as

$$\omega_{B,\dot{Q}_{avg}} = \left[\left(\omega_{B,\dot{Q}_{in}} \frac{\partial \dot{Q}_{avg}}{\partial \dot{Q}_{in}} \right)^2 + \left(\omega_{B,\dot{Q}_{out}} \frac{\partial \dot{Q}_{avg}}{\partial \dot{Q}_{out}} \right)^2 \right]^{0.5} \quad (E.25)$$

where $\frac{\partial \dot{Q}_{avg}}{\partial \dot{Q}_{in}} = \frac{1}{2} = \frac{\partial \dot{Q}_{avg}}{\partial \dot{Q}_{out}}$. Utilizing the values in Table E.8 and Table E.10, the values of $\omega_{B, \dot{Q}_{avg}}$ are computed and shown in Table E.12. The $S_{\dot{Q}_{avg}}$ values required to estimate $S_{R_{e,a,P}}$ are also shown in Table E.12 for completeness.

Table E.12 Bias uncertainty estimates in the measured values of \dot{Q}_{avg} . The estimates are for 95% confidence levels. $S_{\dot{Q}_{avg}}$ denotes the precision index in the \dot{Q}_{avg} measurements.

\dot{Q}_{avg} [W]	$\omega_{B, \dot{Q}_{in}}$ (\pm W)	$\omega_{B, \dot{Q}_{out}}$ (\pm W)	$\omega_{B, \dot{Q}_{avg}}$ (\pm W)	$S_{\dot{Q}_{avg}}$ (\pm W)
6.57	0.10	0.14	0.08	0.21
9.09	0.13	0.04	0.07	0.32
11.98	0.18	0.25	0.16	0.25
14.97	0.22	0.16	0.14	0.23
18.68	0.28	0.11	0.15	0.24
22.30	0.33	0.07	0.17	0.25
26.80	0.40	0.12	0.21	0.25
32.74	0.48	0.23	0.27	0.37

The bias uncertainty in FR ($\omega_{B,FR}$) can be estimated using equation (E.5) as

$$\omega_{B,FR} = \left[\left(\omega_{B,L_p} \frac{\partial FR}{\partial L_p} \right)^2 + \left(\omega_{B,L_e} \frac{\partial FR}{\partial L_e} \right)^2 \right]^{0.5} \quad (E.26)$$

where $\frac{\partial FR}{\partial L_p} = \left(\frac{1}{L_e} \right)$ and $\frac{\partial FR}{\partial L_e} = - \left(\frac{L_p}{L_e^2} \right)$. The $\omega_{B,FR}$ estimates are shown in Table E.13.

Table E.13 Uncertainty estimates in FR for $L_e = 0.127m$. The estimates are for 95% confidence levels.

FR	ω_{B,L_p} (\pm)	ω_{B,L_e} (\pm)	$\omega_{B,FR}$ (\pm)
0.35	6.03×10^{-4}	1.89×10^{-3}	0.007
0.45	5.90×10^{-4}		0.008
0.55	5.72×10^{-4}		0.009
0.65	5.50×10^{-4}		0.011
0.75	5.24×10^{-4}		0.012

Table E.14 shows the $\omega_{P,R_{e,a,P}}$, $\omega_{B,R_{e,a,P}}$ and $\omega_{R_{e,a,P}}$ estimates, respectively.

Table E.14 Precision, bias and overall uncertainty estimates in the computed values of $R_{e,a,P}$ for FR = 0.35 and 0.75. The estimates are for 95% confidence levels.

FR	\dot{Q}_{avg} [W]	$R_{e,a,P}$ (K/W)	$\omega_{P,R_{e,a,P}}$ (\pm K/W)	$\omega_{B,R_{e,a,P}}$ (\pm K/W)	$\omega_{R_{e,a,P}}$ (\pm K/W)
0.35	6.50	1.550	0.11	0.18	0.21
	9.21	1.303	0.10	0.13	0.16
	12.18	1.273	0.06	0.10	0.12
	15.02	1.170	0.04	0.08	0.09
	18.74	1.214	0.03	0.06	0.07
	22.52	1.236	0.03	0.05	0.06
	26.74	1.237	0.03	0.05	0.06
	33.01	1.154	0.03	0.04	0.05
0.75	6.77	1.910	0.13	0.09	0.16
	9.27	1.890	0.15	0.07	0.17
	12.12	1.841	0.09	0.06	0.11
	15.01	1.854	0.07	0.06	0.09
	18.62	1.702	0.05	0.04	0.06
	22.84	1.773	0.04	0.04	0.06

$\omega_{B,R_{e,a,P}}$ for all the other FR and all the AR cases can be similarly obtained utilizing equations (E.20) to (E.25).

The precision uncertainty ($\omega_{P,R_{e,a,F}}$) in $R_{e,a,F}$ can be estimated as

$$\omega_{P,R_{e,a,F}} = \pm t_{P,C} S_{R_{e,a,F}} \quad (E.27)$$

where $S_{R_{e,a,F}} = \left[\left(S_{\Delta T_{e,a}} \frac{\partial R_{e,a,F}}{\partial \Delta T_{e,a}} \right)^2 + \left(S_{\dot{Q}_{avg}} \frac{\partial R_{e,a,F}}{\partial \dot{Q}_{avg}} \right)^2 + \left(S_{FR} \frac{\partial R_{e,a,F}}{\partial FR} \right)^2 \right]^{0.5}$ and $t_{P,C}$ is the function of the combined degrees of freedom. The bias uncertainty ($\omega_{B,R_{e,a,F}}$) in $R_{e,a,F}$ can be estimated as

$$\omega_{B,R_{e,a,F}} = \left[\left(\omega_{B,\Delta T_{e,a}} \frac{\partial R_{e,a,F}}{\partial \Delta T_{e,a}} \right)^2 + \left(\omega_{B,\dot{Q}_{avg}} \frac{\partial R_{e,a,F}}{\partial \dot{Q}_{avg}} \right)^2 + \left(\omega_{B,FR} \frac{\partial R_{e,a,F}}{\partial FR} \right)^2 \right]^{0.5} \quad (E.28)$$

Thus, the total uncertainty in $R_{e,a,F}$ ($\omega_{R_{e,a,F}}$) can be estimated as

$$\omega_{R_{e,a,F}} = \left[\left(\omega_{P,R_{e,a,F}} \right)^2 + \left(\omega_{B,R_{e,a,F}} \right)^2 \right]^{0.5} \quad (E.29)$$

Table E.15 shows the estimated magnitudes of $\omega_{P,R_{e,a,F}}$, $\omega_{B,R_{e,a,F}}$ and $\omega_{R_{e,a,F}}$, respectively.

Table E.15 Precision, bias and overall uncertainty estimates in the computed values of $R_{e,a,F}$ for FR = 0.35 and 0.75. The estimates are for 95% confidence levels.

FR	\dot{Q}_{avg} [W]	$R_{e,a,F}$ (K/W)	$\omega_{P,R_{e,a,F}}$ (\pm K/W)	$\omega_{B,R_{e,a,F}}$ (\pm K/W)	$\omega_{R_{e,a,F}}$ (\pm K/W)
0.35	6.50	0.834	0.06	0.09	0.11
	9.21	0.702	0.06	0.07	0.09
	12.18	0.686	0.03	0.05	0.06
	15.02	0.630	0.02	0.04	0.04
	18.74	0.654	0.02	0.04	0.04
	22.52	0.666	0.02	0.03	0.04
	26.74	0.666	0.02	0.03	0.04
	33.01	0.620	0.02	0.02	0.03
0.75	6.77	5.732	0.40	0.27	0.48
	9.27	5.668	0.45	0.20	0.49
	12.12	5.525	0.26	0.15	0.30
	15.01	5.561	0.20	0.15	0.25
	18.62	5.105	0.15	0.11	0.19
	22.84	5.319	0.13	0.11	0.17

E.7.3 Condensation resistance

The condensation thermal resistance is computed as $R_{a,c} = \frac{(\Delta T_{a,c})}{\dot{Q}_{avg}}$. Thus, $R_{a,c}$ contains both bias and precision uncertainties. The precision uncertainty in $R_{a,c}$ can be estimated using equation (E.4) as

$$\omega_{P,R_{a,c}} = \pm t_{P,C} S_{R_{a,c}} \quad (E.30)$$

where $S_{R_{a,c}}$ is given by

$$S_{R_{a,c}} = \left[\left(S_{\Delta T_{a,c}} \frac{\partial R_{a,c}}{\partial \Delta T_{a,c}} \right)^2 + \left(S_{\dot{Q}_{avg}} \frac{\partial R_{a,c}}{\partial \dot{Q}_{avg}} \right)^2 \right]^{0.5} \quad (E.31)$$

The bias uncertainty in $R_{a,c}$ can be estimated using equation (E.5) as

$$\omega_{B,R_{a,c}} = \left[\left(\omega_{B,\Delta T_{a,c}} \frac{\partial R_{a,c}}{\partial \Delta T_{a,c}} \right)^2 + \left(\omega_{B,\dot{Q}_{avg}} \frac{\partial R_{a,c}}{\partial \dot{Q}_{avg}} \right)^2 \right]^{0.5} \quad (E.32)$$

The total uncertainty in $R_{a,c}$ can be estimated using equation (E.7) as

$$\omega_{R_{a,c}} = \left[(\omega_{P,R_{a,c}})^2 + (\omega_{B,R_{a,c}})^2 \right]^{0.5} \quad (E.33)$$

Since, $\omega_{B,T_{c,avg}} = \omega_{B,T_{a,avg}} = \pm 0.3[^\circ\text{C}]$, $\omega_{B,\Delta T_{a,c}} = \pm 0.4[^\circ\text{C}]$. Table E.16 shows the magnitudes of $R_{a,c}$ and the estimated values of $\omega_{P,R_{a,c}}$, $\omega_{B,R_{a,c}}$ and $\omega_{R_{a,c}}$.

Table E.16 Precision, bias and overall uncertainty estimates in the computed values of $R_{a,c}$ for FR = 0.35 and 0.75. The estimates are for 95% confidence levels.

FR	\dot{Q}_{avg} [W]	$R_{a,c}$ (K/W)	$\omega_{P,R_{a,c}}$ (\pm K/W)	$\omega_{B,R_{a,c}}$ (\pm K/W)	$\omega_{R_{a,c}}$ (\pm K/W)
0.35	6.50	0.548	0.04	0.07	0.08
	9.21	0.428	0.03	0.05	0.06
	12.18	0.363	0.02	0.04	0.04
	15.02	0.317	0.01	0.03	0.03
	18.74	0.286	0.01	0.02	0.02
	22.52	0.272	0.01	0.02	0.02
	26.74	0.253	0.01	0.02	0.02
33.01	0.236	0.01	0.01	0.01	
0.75	6.77	1.048	0.07	0.07	0.10
	9.27	0.864	0.07	0.05	0.09
	12.12	0.733	0.03	0.04	0.05
	15.01	0.672	0.02	0.03	0.04
	18.62	0.595	0.02	0.02	0.03
	22.84	0.452	0.01	0.02	0.02

E.7.4 Overall thermal resistance

The overall thermal resistance is computed as $R_{e,c} = \frac{(\Delta T_{e,c})}{\dot{Q}_{avg}}$. Thus, $R_{e,c}$ contains both precision and bias uncertainties which can be estimated by using equations (E.4) and (E.5), respectively. The total uncertainty can be estimated using equation (E.7). Table E.17 shows the precision, bias and the overall uncertainties in the computed values of $R_{e,c}$.

Table E.17 Precision, bias and overall uncertainty estimates in the computed values of $R_{e,c}$ for FR = 0.35 and 0.75. The estimates are for 95% confidence levels.

FR	\dot{Q}_{avg} [W]	$R_{e,c}$ (K/W)	$\omega_{P,R_{e,c}}$ (\pm K/W)	$\omega_{B,R_{e,c}}$ (\pm K/W)	$\omega_{R_{e,c}}$ (\pm K/W)
0.35	6.50	1.091	0.08	0.06	0.10
	9.21	0.884	0.07	0.05	0.07
	12.18	0.809	0.04	0.04	0.06
	15.02	0.727	0.03	0.03	0.04
	18.74	0.711	0.02	0.02	0.03
	22.52	0.705	0.02	0.02	0.03
	26.74	0.686	0.02	0.02	0.03
33.01	0.639	0.02	0.01	0.02	
0.75	6.77	2.481	0.18	0.07	0.19
	9.27	2.281	0.18	0.05	0.19
	12.12	2.114	0.10	0.04	0.11
	15.01	2.061	0.07	0.03	0.08
	18.62	1.871	0.05	0.03	0.06
	22.84	1.782	0.04	0.02	0.04

It is noted that $R_{e,c}$ is computed directly from \dot{Q}_{avg} and $\Delta T_{e,c}$ and not by combining the individual resistances. Similarly, the uncertainties in $R_{e,c}$ is estimated through the uncertainties in \dot{Q}_{avg} and $\Delta T_{e,c}$, respectively.

Appendix F: Appendix related to Chapter 5

F. Repeatability in the experimental measurements

Numerous test runs were carried out for each thermosyphon (TS) to establish the repeatability of the experimental data for varying \dot{Q}_{in} (heat input rate), the fill ratio (FR) and the aspect ratio (AR). However, an auxiliary repeatability test was performed on a separate TS before investigating the effects of the above-mentioned operational conditions. This chapter reports the repeatability results from the auxiliary test run repeated three times. The results are presented in terms of the steady state temperature distribution along the length of the TS, the boiling and the condensation curves, and the data representing the boiling (R_B) and the condensation resistances (R_C). The details of the experimental parameters chosen for this auxiliary test is described below.

The evaporator (L_e) and the condenser lengths (L_c) are equal to 5in (0.127m). The liquid pool length (L_p) is 3.05in (0.046m) yielding a fill-ratio (FR) = 0.61 and aspect ratio (AR) = 8.88. The volume flow rate (\dot{V}) and the temperature of the cooling water (T_{win}) was fixed at 0.18[L/min] and at 23[°C], respectively. The effects of the cooling water temperature were examined during the repeatability tests by having $T_{win} = 15$ [°C]. Although, the average evaporator, adiabatic and the condenser temperatures were found to be lower at 15[°C], no significant differences were observed in the magnitudes of the boiling and the cooling excess temperatures. Table F.1 outlines the locations of the surface TC with respect to the heating end for completeness.

Table F.1 TC locations on the standard TS

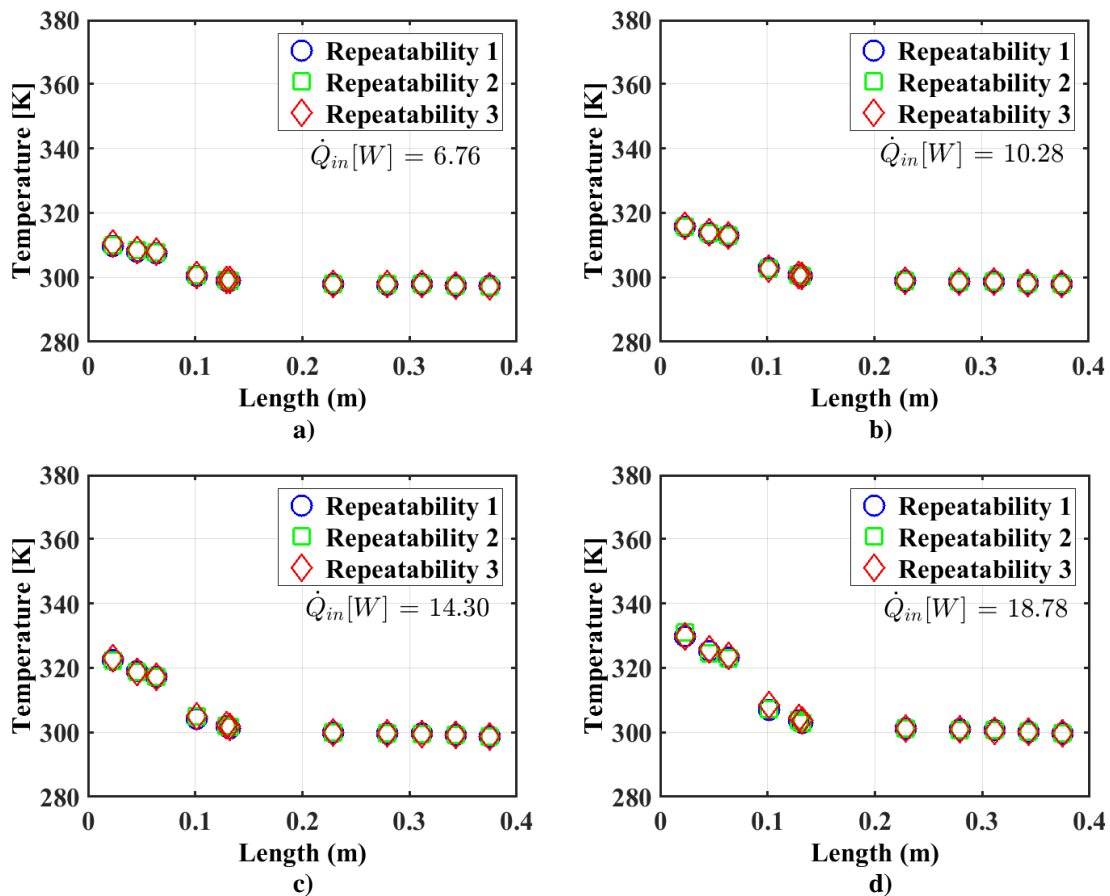
	Physical phenomena	TC locations
Evaporator	Pool boiling	1×0.9in, 1×1.8 in
	Film boiling	2×2.5 in, 1×4 in
Adiabatic section	Film flow at zero heat flux	2×5.1 in, 1×5.2 in, 1×9 in
Condenser section	Condensate flow	1 × 11 in, 1 × 12.25 in, 1 × 13.5 in, 1 × 14.75in

F.1 Temperature distribution along the length of the TS

Figures F.1(a-f) show the temperature profiles along the axial length of the TS for \dot{Q}_{in} varying from 6.76 [W] to 27.62 [W], equivalent to \dot{Q}'_{in} varying from 1.18 [kW/m²] to 4.85 [kW/m²]. The coefficient of variability (CoV) defined as the ratio of the sample

standard deviation to the mean ($\text{CoV} = \frac{\sqrt{\sum_{i=1}^n \frac{(x_i - \bar{x})^2}{(n-1)}}}{\sum_{i=1}^n \frac{x_i}{n}}$) is evaluated to assess the repeatability

of the data. The maximum CoV within the temperature measurements among all the axial locations is shown in Table F.2. The maximum variation within the temperature measurements normalized by the mean value is also shown in Table F.2. The visual examination of Figures F.1(a-f) and the CoV values indicate very low variability between the temperature measurements at all the TC locations demonstrating excellent repeatability.



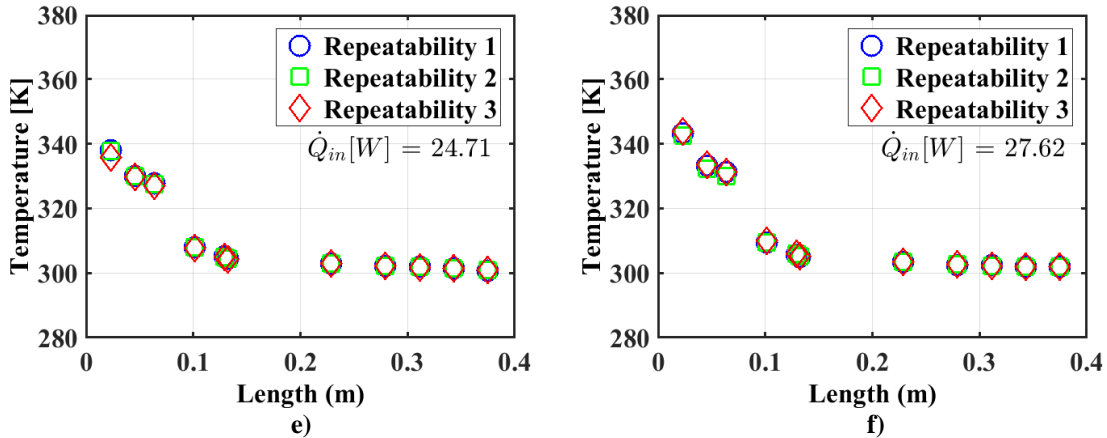


Figure F.1 Temperature distribution along the axial length of the TS plotted for three repeated trials for different \dot{Q}_{in} . The \dot{Q}_{in} range is shown in Table F.2.

Table F.2 Variation within the temperatures obtained from the repeatability tests. Wrt denotes with respect to.

\dot{Q}_{in} [W]	\dot{Q}'_{in} [kW/m ²]	Maximum CoV (%)	Maximum absolute variation wrt the mean (%)
6.76	1.18	0.11	0.13
10.28	1.80	0.04	0.05
14.30	2.51	0.13	0.15
18.78	3.29	0.24	0.27
24.71	4.34	0.38	0.43
27.62	4.85	0.21	0.24

F.2 Boiling and the condensation curve

Figure F.2 (a, b) shows the boiling ($\dot{Q}'_{in,f}$ vs ΔT_{ea}) and the condensation curve ($\dot{Q}'_{out,f}$ vs ΔT_{ac}) for the repeated trials demonstrating the variability in ΔT_{ea} and ΔT_{ac} . Tables F.3 and F.4 report the mean deviation in ΔT_{ea} and ΔT_{ac} computed as $\bar{d} = \sum_{i=1}^n \frac{|d_i|}{n}$, where \bar{d} is the mean deviation and d_i is the deviation of each measurement (x_i) from the mean (\bar{x}) given as $d_i = x_i - \bar{x}$ (Wheeler and Ganji, 2006). The mean deviation is normalized by the mean value \bar{x} and expressed as a percentage. The CoV within the ΔT_{ea} and ΔT_{ac} data is also shown in Tables F.3 and F.4 along with the averaged percentage difference between the recorded values. The $\frac{\bar{d}}{\Delta T_{ea}}$ and CoV for the last two \dot{Q}_{in} are seen to be higher than the previous \dot{Q}_{in} values. This is caused due to the occurrence of unsteady Geyser boiling phenomena (confirmed by a metallic sound; more details about Geyser boiling is in

Appendix G) during repeatability test run 2. The phenomenon is expected as the FR of the tested TS is high.

The temporal temperature distribution at the evaporator drops slightly below the steady state temperature achieved before the occurrence of Geyser. The average evaporator temperature thus, yields a slightly lower value during run 2. Nevertheless, $\frac{\bar{d}}{\Delta T_{ea}}$ and $\text{CoV}(\Delta T_{ea})$ values are lower than 2% and 5%, respectively confirming high repeatability among the measurements. The $\frac{\bar{d}}{\Delta T_{ac}}$ and $\text{CoV}(\Delta T_{ac})$ values are higher than the corresponding ΔT_{ea} values as the mean ΔT_{ac} values are lower. The $\frac{\bar{d}}{\Delta T_{ac}}$ and $\text{CoV}(\Delta T_{ac})$ values are below 5% and 7%, respectively demonstrating that the measurements of ΔT_{ac} are repeatable.

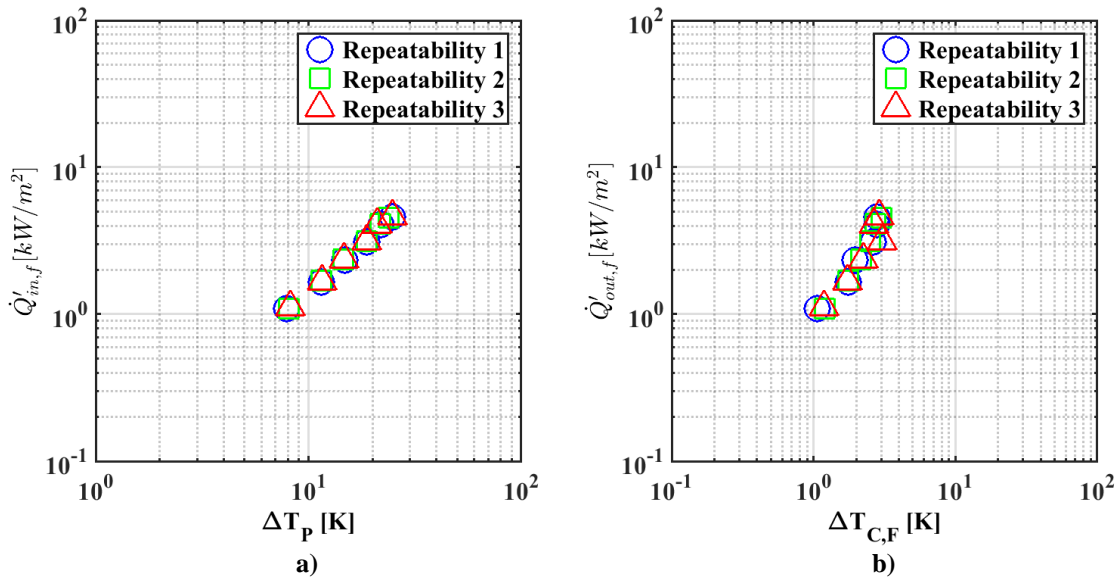


Figure F.2 Plot of the a) boiling curve and b) condensation curve for three repeated trials

Table F.3 Variation within ΔT_{ea} from the repeatability tests.

\dot{Q}_{in} [W]	\dot{Q}'_{in} [W/m ²]	$\frac{\bar{d}}{\Delta T_{ea}} \times 100$ (%)	$\text{CoV}(\Delta T_{ea})$
6.76	1.18	1.01	1.49
10.28	1.80	0.23	0.35
14.30	2.51	0.38	0.52
18.78	3.29	0.22	0.27
24.71	4.34	1.50	2.04
27.62	4.85	1.95	2.54

Table F.4 Variation within ΔT_{ac} from the repeatability tests.

\dot{Q}_{in} [W]	\dot{Q}'_{in} [W/m ²]	$\frac{d}{\Delta T_{ac}} \times 100$ (%)	CoV(ΔT_{ac})
6.76	1.18	2.95	3.89
10.28	1.80	0.17	0.22
14.30	2.51	2.74	2.87
18.78	3.29	4.89	6.58
24.71	4.34	1.49	2.23
27.62	4.85	2.46	3.65

F.3 Thermal resistance plots

Figure F.3a shows the boiling resistance (R_B) in the form of $\left(\frac{1}{R_{BA_{e,i}}}\right)$ plotted against $\dot{Q}'_{in,f}$ for the repeated trials. Similarly, the condensation resistance (R_C) was plotted as $\left(\frac{1}{R_{CA_{c,i}}}\right)$ against $\dot{Q}'_{out,f}$ in Figure F.3b. These plots demonstrate the variability in R_B and R_C within the repeated trials. Tables F.5 and F.6 shows the mean deviation in $\left(\frac{1}{R_{BA_{e,i}}}\right)$ and $\left(\frac{1}{R_{CA_{c,i}}}\right)$ normalized by the mean value along with the CoV values. The results demonstrate excellent repeatability among the computed $\left(\frac{1}{R_{BA_{e,i}}}\right)$ and $\left(\frac{1}{R_{CA_{c,i}}}\right)$ values from the measured .

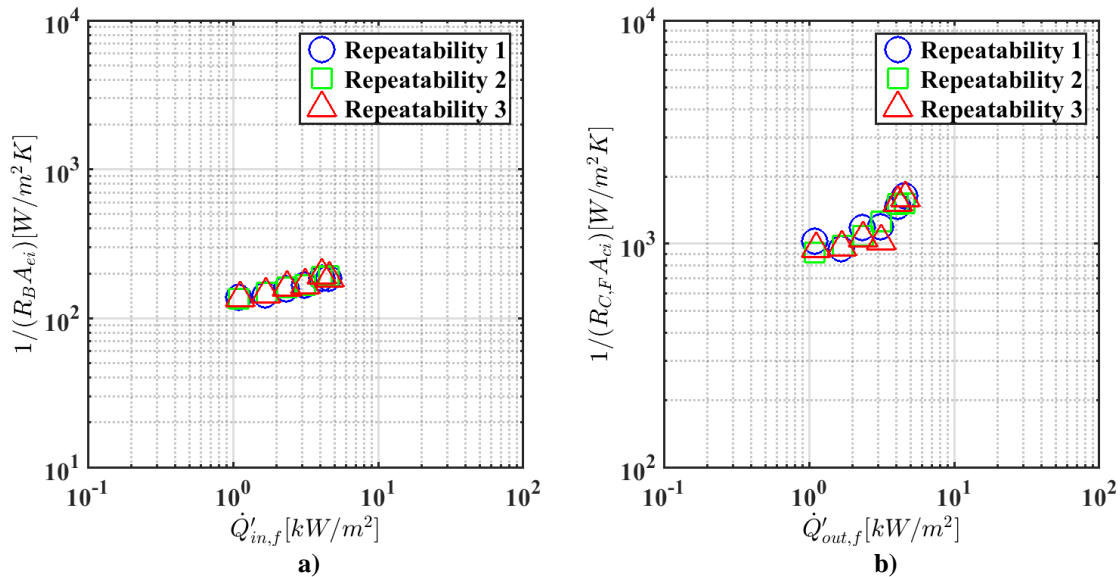


Figure F.3 a) Variation of $(1/R_{e,a}A_{e,i})$ with $\dot{Q}'_{in,f}$ b) Variation of $(1/R_{a,c}A_{c,i})$ with $\dot{Q}'_{out,f}$

Table F.5 Variations within $\left(\frac{1}{R_B A_{e,i}}\right)$ obtained from the repeatability tests.

\dot{Q}_{in} [W]	\dot{Q}'_{in} [W/m ²]	$\frac{\bar{d}}{\left(\frac{1}{R_B A_{e,i}}\right)} \times 100$ (%)	$CoV\left(\frac{1}{R_B A_{e,i}}\right)$
6.76	1.18	0.06	1.11
10.28	1.80	0.02	1.44
14.30	2.51	0.03	1.27
18.78	3.29	0.02	0.05
24.71	4.34	0.17	1.94
27.62	4.85	0.25	2.08

Table F.6 Variations within $\left(\frac{1}{R_C A_{c,i}}\right)$ obtained from the repeatability tests.

\dot{Q}_{in} [W]	\dot{Q}'_{in} [W/m ²]	$\frac{\bar{d}}{\left(\frac{1}{R_C A_{c,i}}\right)} \times 100$ (%)	$CoV\left(\frac{1}{R_C A_{c,i}}\right)$
6.76	1.18	2.29	3.36
10.28	1.80	0.89	1.25
14.30	2.51	2.17	3.10
18.78	3.29	4.64	6.38
24.71	4.34	1.49	2.16
27.62	4.85	2.81	3.86

Excluding the test runs where geyser phenomenon occurred (mostly at high FR), the results from the experimental investigation indicated excellent reproducibility of the steady-state data provided that the same experimental procedures were followed throughout.

Appendix G: Appendix related to Chapter 5

G Heat-transfer and the fill ratio limits

This chapter briefly describes the various heat transfer limits that may be encountered within a thermosyphon (TS) during its operation. Additionally, the minimum fill ratio requirement for a TS for is discussed. The heat transfer limitations in TS are primarily caused by dryout, burnout and the entrainment phenomena. Each of these phenomena may cause the TS to operate inefficiently despite satisfying the hydrodynamic and the thermodynamic limits.

G.1 Dry-out limit

The dryout limit may occur when the frictional losses of the liquid condensate flow and the interfacial liquid-vapour shear exceeds the gravitational force driving the condensate flow in a TS (Nguyen-Chi and Groll, 1981). It is reported to prevail for a very small FR and relatively small \dot{Q}'_{in} (Nguyen-Chi and Groll, 1981, Faghri, 1995), where $\dot{Q}'_{in} = \frac{\dot{Q}_{in}}{A_e}$.

Two slightly different phenomena may give rise to dryout limit. First, when \dot{Q}'_{in} is increased such that the amount of the WF in the evaporator is insufficient to transport the desired heat, then the evaporator starts to dry out (Nguyen-Chi and Groll, 1981). Second, when \dot{Q}'_{in} is raised to such a degree that the total condensate film has to be evaporated to transfer the heat before reaching the liquid pool in the evaporator. The condensate flow in this case reduces to zero with time and dryout occurs at the evaporator.

G.2 Burn-out limit

The burn-out phenomenon is analogous to film boiling phenomena in pool boiling. The vapour bubbles initiated at the onset of nucleate boiling start to form a vapour blanket at the wall preventing the direct contact of the WF liquid phase with the evaporator wall. Due to the poor thermal conductivity of the vapour, only a part of the heat input to the wall is transferred to the liquid and the rest is utilized in increasing the evaporator wall temperature. A significant pressure increase may accompany film boiling with the

possibility of TS wall rupture (Faghri, 1995). Burnout limit may occur at large FRs and high \dot{Q}'_{in} (Nguyen-Chi and Groll, 1981, Faghri, 1995).

G.3 Flooding/Entrainment limit

The flooding limit occurs when the relative velocity between the liquid and the vapour increases to such an extent that the interfacial shear stress retards the flow of the condensate liquid. This does not hinder the steady state operation of the TS (Nguyen-Chi et al, 1979). An additional increase in $\dot{Q}'_{in,ax}$ (where $\dot{Q}'_{in,ax} = \dot{Q}'_{in,flooding} \left(\frac{4L_e}{D_i} \right)$) will cause the interfacial shear stress to overcome the surface tension of the liquid condensate which may cause the liquid droplets to become entrained into the vapour flow and transported back to the condenser section. This phenomenon is known as entrainment and may give rise to unsteady state conditions. Both flooding and the entrainment limits are unfavorable since an increased concentration of the WF liquid phase in the condenser section raises the possibility of local dryout in the evaporator section. Flooding limit may occur at large FR, small \dot{Q}'_{in} but at high axial evaporator heat flux, $\dot{Q}'_{in,ax}$ (where $\dot{Q}'_{in,ax} = \dot{Q}'_{in,flooding} \left(\frac{4L_e}{D_i} \right)$) (Nguyen-Chi and Groll, 1981). It is clear that the (L_e/D_i) or in other words AR ratio influences the occurrence of the flooding limit.

G.4 Heat transfer limits

The maximum safe power density ($\dot{Q}'_{in,max}$) to operate the TS is 62000 [W/m²] (specified by Acrolab Ltd). Since the rope heaters in the present experiments supply a maximum wattage of 50W and the minimum L_e is 0.076m (at AR = 5.33), the maximum heat flux ($\dot{Q}'_{in,max}$) that can be achieved in the experiments is 14958.17 [W/m²]. The estimated values of $\dot{Q}'_{in,max}$ for dry-out, burn-out and the entrainment limits, using the correlations (Table G.1) from the literature, are tabulated in Table G.2 and Table G.3 for comparison. As evident from Tables G.2 and G.3, $\dot{Q}'_{in,max}$ in all experimental conditions are below the critical heat fluxes for the dryout, burnout and the entrainment limits.

Table G.1 Heat transfer correlations to estimate the critical heat flux for dryout, burnout and entrainment limits.

Authors	Heat transfer limits correlations
Cohen and Bayley, (1955) (Dryout limit)	$\left(\frac{\dot{Q}'_{cr,dryout}}{\rho_v h_{fg}}\right) \left[\frac{\sigma_1 g(\rho_1 - \rho_v)}{\rho_v^2}\right]^{-0.25} =$ $A_{cs} \left[\frac{g \rho_1^2}{3 \mu_1 L_e (\sigma g \rho_v^2 (\rho_1 - \rho_v))^{0.25}}\right] \left[\frac{V_t / \pi D_i}{L(4L_c/5) + L_a + (L_a + 3L_e/4)}\right]^3 \left[\frac{TFR - \rho_v / \rho_1}{1 - \rho_v / \rho_1}\right]^3$ <p>TFR = denotes the fill-ratio with respect to the total TS volume V_t = internal volume of the TS</p>
Strel'tsov (1975) (Dryout limit)	$\dot{Q}'_{cr,dryout} = \left[\frac{M}{0.8(L_e + L_c) + L_a}\right]^3 \left[\frac{h_{fg} g}{3 \mu_1 \pi^2 D_i^2 \rho_1}\right] \left[\frac{1}{\pi D_i L_e}\right]$
Rohsenow and Griffith (1955)	$\dot{Q}'_{cr,burnout} = 0.012 h_{fg} \rho_v \left[\frac{\rho_1 - \rho_v}{\rho_v}\right]^{0.6}$
Imura et al. (1983) (Burnout limit)	$\dot{Q}'_{cr,burnout} = 0.16 \left(1 - \exp\left[-\left(\frac{D_i}{L_e}\right) \left(\frac{\rho_1}{\rho_v}\right)^{0.13}\right]\right) h_{fg} [\sigma_1 g \rho_v^2 (\rho_1 - \rho_v)]^{0.25}$
Faghri et al. (1989) (Entrainment limit)	$\dot{Q}'_{cr,entrainment} = \left(\frac{\rho_1}{\rho_v}\right)^{0.14} \tanh^2(B_o)^{0.25} h_{fg} \frac{[\sigma_1 g \rho_v^2 (\rho_1 - \rho_v)]^{0.25}}{\left[1 + \left(\frac{\rho_v}{\rho_1}\right)^{0.25}\right]^2}$

Table G.2 The heat flux limits for dryout, burnout and entrainment phenomena for the TS where FR is varied.

Authors	TS#1	TS#2	TS#3	TS#4	TS#5
$\dot{Q}'_{cr,dryout}$ (W/m ²) (Cohen and Bayley, 1955)	2.22×10^6	4.72×10^6	8.63×10^6	1.42×10^7	2.19×10^7
$\dot{Q}'_{cr,dryout}$ (W/m ²) (Strel'tsov, 1975)	8.93×10^4	1.89×10^5	3.46×10^5	5.72×10^5	8.78×10^5
$\dot{Q}'_{cr,burnout}$ (W/m ²) (Rohsenow and Griffith, 1955)	4.09×10^5				
$\dot{Q}'_{cr,burnout}$ (W/m ²) (Imura et al., 1983)	1.11×10^5				
$\dot{Q}'_{cr,entrainment}$ (W/m ²) (Faghri et al., 1989)	1.73×10^5				

Table G.3 The heat flux limits for dryout, burnout and entrainment phenomena for the TS where AR is varied.

	TS#6	TS#7	TS#8	TS#9	TS#10
$\dot{Q}'_{cr,dryout}$ (W/m ²) (Cohen and Bayley, 1955)	1.20×10^6	4.39×10^6	6.49×10^6	1.15×10^7	2.99×10^7
$\dot{Q}'_{cr,dryout}$ (W/m ²) (Strel'tsov, 1975)	7.93×10^4	2.02×10^5	2.60×10^5	3.67×10^5	6.09×10^5
$\dot{Q}'_{cr,burnout}$ (W/m ²) (Rohsenow and Griffith, 1955)	4.09×10^5				
$\dot{Q}'_{cr,burnout}$ (W/m ²) (Imura et al., 1983)	1.61×10^5	1.20×10^5	1.11×10^5	9.91×10^4	8.41×10^4
$\dot{Q}'_{cr,entrainment}$ (W/m ²) (Faghri et al., 1989)	2.88×10^5	1.92×10^5	1.73×10^5	1.50×10^5	1.23×10^5

G.5 Minimum fill ratio requirement

Three different correlations (Table G.4) from the literature are used to determine the minimum fill ratio required to avoid the dryout and the burnout phenomena. The FR between those estimated from the correlations and those within the actual TS are compared in Tables G.5 and G.6, respectively. Tables G.5 and G.6 demonstrate that the FR within the TS are above the minimum fill criterion.

Table G.4 Correlations to determine the minimum fill ratio requirement. Note that Bartsch and Unk's (1987) formulation require $(T_{e,a} - T_{sat})$ and $(T_{e,a} - T_P)$ a priori and, hence not used to determine L_p .

Authors	Correlations
Strel'tsov (1975)	$M = \left[\frac{4}{5} (L_e + L_c) + L_a \right] \left[\frac{3\mu_l \pi^2 D_i^2 \rho_l \dot{Q}_{in}}{h_{fg} g} \right]^{\frac{1}{3}}$
Bartsch and Unk (1987)	$L_p = L_e - \left(\frac{1}{4k} \right) \left(\frac{\mu_l}{\rho_l^2 g h_{fg}} \right)^{\frac{1}{3}} \left(\frac{3}{\pi D_i} \right)^{\frac{4}{3}} \left[\frac{(\dot{Q}_{in})^{1.33}}{(T_{e,a} - T_{sat})} - \frac{(\dot{Q}_{in,P})^{1.33}}{(T_{e,a} - T_P)} \right]$
Imura et al., (1983)	$\frac{L_p}{L_e} = (0.2 - 0.33) + \frac{0.8L_c + L_a}{L_e} \frac{4}{D_i} \left(\frac{3\mu_l L_e \dot{Q}'_{cr,in}}{\rho_l^2 g h_{fg}} \right)^{\frac{1}{3}} + \frac{\rho_v}{\rho_l} \left[\frac{L_c + L_a}{L_e} - \frac{0.8L_c + L_a}{L_e} \frac{4}{D_i} \left(\frac{3\mu_l L_e \dot{Q}'_{cr,in}}{\rho_l^2 g h_{fg}} \right)^{\frac{1}{3}} \right]$ 0.2 and 0.33 should be taken for a TS with a smaller and larger diameter, respectively. No further quantification of the diameter is provided in Imura et al., (1983).

Table G.5 Comparison between the minimum fill ratio estimated from the correlations and that within TS 1-5.

Authors	$\dot{Q}'_{in,max}$ (W/m ²)	TS#1	TS#2	TS#3	TS#4	TS#5
Strel'tsov (1975) (Dryout limit)	Experiments 14958.17	7.95×10^{-4}				
M (kg) chosen		7.10×10^{-3}	9.10×10^{-3}	11.20×10^{-3}	13.20×10^{-3}	15.20×10^{-3}
Imura et al. (1983) (Burnout limit)	Experiments 14958.17	0.23				
	Acrolab 62000	0.25				
FR chosen		0.35	0.45	0.55	0.65	0.75

Table G.6 Comparison between the minimum fill ratio estimated from the correlations and that within TS 6-10.

	$\dot{Q}'_{in,max}$ (W/m ²)	TS#6	TS#7	TS#8	TS#9	TS#10
Strel'tsov (1975) (Dryout limit)	14958.17	8.41×10^{-4}	8.07×10^{-4}	7.96×10^{-4}	7.78×10^{-4}	7.50×10^{-4}
M (kg) chosen		6.10×10^{-3}	9.10×10^{-3}	10.20×10^{-3}	11.70×10^{-3}	14.20×10^{-3}
Imura et al. (1983) Burnout limit	Experiments 14958.17	0.26	0.24	0.23	0.23	0.22
	Acrolab 62000	0.29	0.26	0.25	0.24	0.23
FR chosen		0.50				

G.6 Geysler boiling

The Geysler boiling is the most commonly reported unsteady state phenomena in the literature and may be observed at high FR and \dot{Q}'_{in} (when the liquid is superheated; Negishi, 1983, Negishi and Sawada, 1984). During this phenomenon, the liquid slug travels as a packed liquid mass into the condenser. The vapour present in the condenser from the previous heat transfer cycle will be compressed and condensed instantly, resulting in a strike of the liquid slug at the top of the condenser. Hence, a smacking metallic sound could be heard which could be either due to the collapse of the vapour bubble or due to the smacking of the liquid slug against the condenser wall. This phenomenon is known as Geysler boiling. Following this, the liquid will transport back to the evaporator as a subcooled thin liquid film. The primary effect of this phenomena is the cyclic variations of the evaporator temperature (Casarosa and Latrofa, 1983). In the present experiments, Geysler boiling was observed once during the repeatability test. At FR = 0.65 and 0.75, Geysler boiling was observed (minimum 1 occurrence and maximum 5 occurrence). They yielded unsteady evaporator (sudden lowering), adiabatic and condenser (sudden increment) temperatures. These results are not considered while presenting the steady state results in Chapter 6.

Appendix H: Appendix related to Chapter 6

H Dry patch formation and rewetting

This section examines the formation of dry patch formation and rewetting and seeks to answer the following questions a) Whether or not a dry patch has formed ? b) Whether or not rewetting occurs ? and c) Whether or not spreading of the dry patch occurs and direction of its spreading ? In order to understand these mechanisms a schematic of the dry patch formation and thin film formation is shown in Figure H.1.

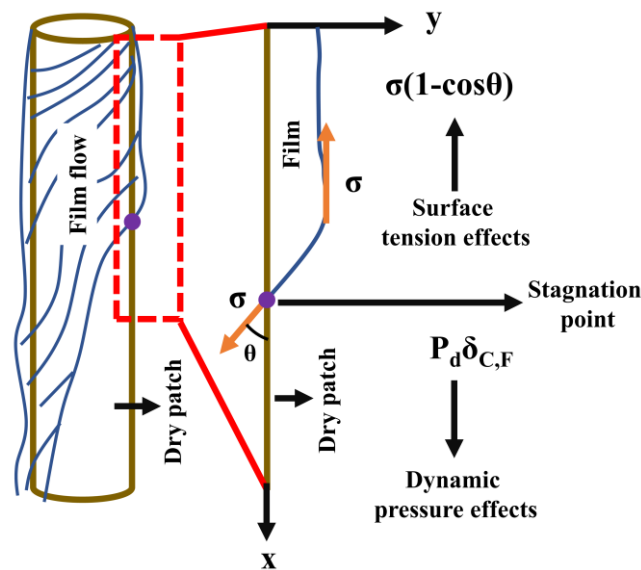


Figure H.1 Schematic showing dry patch formation and film breakdown. The purple colour point shows the stagnation point. σ is the surface tension and θ_c is the contact angle of the film at surface.

Dry patch formation

The thermodynamic analysis of the condensate flow reveal that the liquid film always arrives in a subcooled state at the evaporator (see Chapter 3). Thus, the dry patch formation for “subcooled liquid films” is of interest here. The breakdown of the heated subcooled falling film is primarily due to Marangoni effects.

The formation of a dry patch can be confirmed by evaluating a non-dimensional number (termed as the film distortion parameter) K , which is the ratio of the surface tension difference in the film ($\Delta\sigma$) to the dynamic pressure (P_d) multiplied by the film thickness of the uniform film ($\delta_{C,F}$) (Fujita and Ueda, 1978a). When K attains a nearly constant

value with increasing $\dot{Q}'_{in,f,F}$ (see Figure 7 and 8 in Fujita and Ueda, 1978a), a dry patch is formed. The expressions of K for a laminar film flow derived by Fujita and Ueda (1978a) is given as

$$K = 10.7 \left[\frac{\left(\frac{-\partial\sigma}{\partial T} \right) \dot{Q}'_{in}}{k_l \rho_l g \left(\frac{\nu_l^2}{g} \right)^{\frac{1}{3}}} \right] \frac{1}{Re_F^{\frac{4}{3}}} \quad (H.1)$$

where \dot{Q}'_{in} is the heat flux at the outer wall surface, σ is the surface tension, $\frac{\partial\sigma}{\partial T}$ is the surface tension gradient with temperature, T, Re_F is the film Reynolds number and k_l , ρ_l , ν_l are the thermal conductivity, liquid density and the kinematic viscosity of the liquid phase of the WF, respectively. All the liquid properties are calculated at the film temperature, T_f . When K attains a nearly constant value with increasing $\dot{Q}'_{in,f,F}$ (see Figure

7 and 8 in Fujita and Ueda, 1978a), a dry patch is formed. A plot of $K = \left[\frac{\left(\frac{-\partial\sigma}{\partial T} \right) \dot{Q}'_{in,w}}{k_l \rho_l g \left(\frac{\nu_l^2}{g} \right)^{\frac{1}{3}}} \right]$

versus Re_F within $2.5 \leq \dot{Q}'_{in,f,F} \leq 5$ for FR = 0.35 and 0.45 shown in Figure H.2 reveal that the intercept on the y axis of the plotted data is indeed constant ($K \sim 0.13$). This indicates that local dry patches have formed during film boiling.

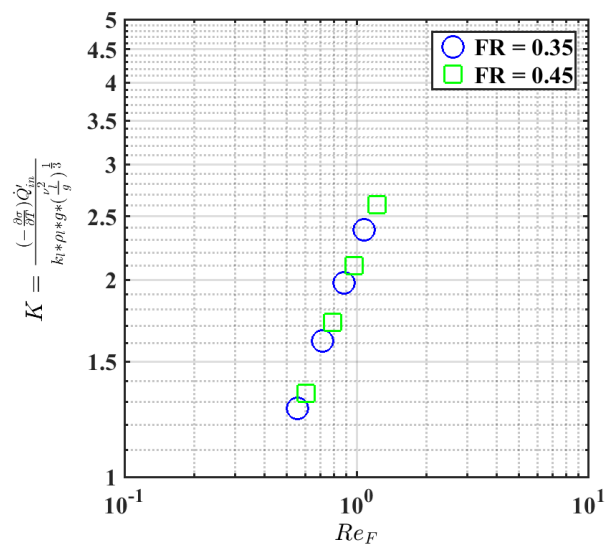


Figure H.2 Evidence of local dry patch formation

H.2 Dry patch stability and rewetting

If the dry patch remains the same size or it spreads, it is termed as a “stable” patch. If the dry patch is rewetted by the falling liquid film, then it is referred to as an “unstable” patch (Hirshburg, 1980). The stability of a dry patch can be quantified by an equation proposed by Hartley and Murgatroyd (1964), where the surface tension forces acting through a contact angle (θ_c) is balanced by the rewetting force due to the stagnation pressure of the falling film. Assuming the film flow is laminar (Nusselt flow), the equation for the maximum mass flow rate (\dot{m}_{dry}) per unit width of the surface (to wet the surface) is given by Hartley and Murgatroyd (1964) as

$$0.416\left(\frac{g}{\rho_1\mu_1}\right)^{1/3} \dot{m}_{dry}^{5/3} = \sigma(1-\cos\theta_c) \quad (\text{H.3})$$

where μ_1 is the dynamic viscosity of the WF liquid phase and θ_c is the contact angle at the surface. If the condensate mass flow rate per unit width (estimated as $\frac{\dot{Q}_{in}}{\pi D_i h_{fg}^*}$), $\dot{m}_c > \dot{m}_{dry}$, the dry patch will be rewetted. If, $\dot{m}_c < \dot{m}_{dry}$, the dry patch will spread in all directions along the surface.

H.3 Dry patch spreading and the influence of the vapour thrust

An indication of the dry patch spreading ($X_{dry-patch}$) is given by the ratio of the surface tension and the rewetting forces defined as

$$X_{dry-patch} = \frac{\sigma(1-\cos\theta_c)}{0.416\left(\frac{g}{\rho_1\mu_1}\right)^{1/3} \dot{m}_c^{5/3}} = \frac{\sigma(1-\cos\theta_c)}{0.416\left(\frac{g}{\rho_1\mu_1}\right)^{1/3} \left(\frac{\dot{Q}_{in}}{\pi D_i h_{fg}^*}\right)^{5/3}} \quad (\text{H.4})$$

With an increase in \dot{Q}_{in} , the WF liquid properties such as h_{fg} , ρ_l , μ_l and σ decrease, indicating that $X_{dry-patch}$ or in other words, the dry patch spreading will decrease. This suggests that the edge of the continuous film would move downwards instead of moving upward. This contradicts the direction of the flow of the film edge (see paragraph after Table 6.2) which is upwards at high $\dot{Q}'_{in,f,F}$ (Andros, 1980).

Zuber and Staub (1966) hypothesized that an additional force due to the vapour thrust of the evaporating film in the vicinity of the stagnation point acts on the film edge causing a net upward movement of the film edge. The force per unit area due to the vapour thrust is given by

$$F_{\text{vapour-thrust}} \sim \frac{\dot{Q}'_{\text{in}}}{\rho_v A_v h_{fg}^2} \sin \theta_c \quad (\text{H.5})$$

where A_v is the cross-sectional area of the vapour flow ($A_v = \frac{\pi}{4} D_i^2$). Thus, the movement of the film edge is governed by both the extent of the dry patch spreading and the increase in the vapour thrust.

Comparisons between \dot{m}_c and \dot{m}_{dry} and the estimates of $X_{\text{dry-patch}}$ and $F_{\text{vapour-thrust}}$ for $\text{FR} = 0.35$ and 0.45 at $2.5[\text{kW/m}^2] \leq \dot{Q}'_{\text{in,f,F}} \leq 5.0[\text{kW/m}^2]$ are shown in Table H.1. Since θ_c is not measured in the current experiments, \dot{m}_{dry} is estimated at $\theta_c = 30^\circ, 45^\circ$ and 60° . From Table 6.4, it is evident that $\dot{m}_c < \dot{m}_{\text{dry}}$ at all the θ_c values indicating the spreading of dry patches. Further evidence supporting this hypothesis is given by the magnitudes of $X_{\text{dry-patch}}$ and $F_{\text{vapour-thrust}}$ in Table H.1. Examining $X_{\text{dry-patch}}$ and $F_{\text{vapour-thrust}}$ values, it can be noticed that the ratio of dry patch spreading is slightly higher than the ratio of $F_{\text{vapour-thrust}}$ between two successive $\dot{Q}'_{\text{in,f,F}}$ values. This suggests that the dry patch spreading is more dominant than the upward thrust of the vapour flow at higher $\dot{Q}'_{\text{in,f,F}}$.

Table H.7 Analysis of the dry patch stability for the present experimental data. $X_{\text{dry-patch}}$ and $F_{\text{vapour-thrust}}$ are estimated at $\theta_c = 45^\circ$

FR = 0.35						
\dot{m}_{dry} (kg/ms)			\dot{m}_c (kg/ms)	Spreading or Rewetting	$X_{\text{dry-patch}}$	$F_{\text{vapour-thrust}}$
$\theta_c = 30^\circ$	$\theta_c = 45^\circ$	$\theta_c = 60^\circ$				
0.066	0.106	0.146	1.3×10^{-4}	Spreading	65×10^3	0.049
0.065	0.105	0.145	1.7×10^{-4}		44×10^3	0.071
0.065	0.104	0.144	2.0×10^{-4}		32×10^3	0.095
0.064	0.103	0.143	2.4×10^{-4}		24×10^3	0.125
FR = 0.45						
\dot{m}_{dry} (kg/ms)			\dot{m}_c (kg/ms)	Spreading or Rewetting	$X_{\text{dry-patch}}$	$F_{\text{vapour-thrust}}$
$\theta_c = 30^\circ$	$\theta_c = 45^\circ$	$\theta_c = 60^\circ$				
0.065	0.104	0.143	1.4×10^{-4}	Spreading	63×10^3	0.042
0.064	0.103	0.142	1.7×10^{-4}		42×10^3	0.059
0.064	0.102	0.140	2.1×10^{-4}		31×10^3	0.075
0.063	0.100	0.139	2.5×10^{-4}		22×10^3	0.097

H.4 Determination of dropwise and mixed condensation

Ma (1994) defined a surface free energy criterion, $\Delta\gamma$, where $\Delta\gamma = \gamma_l - \gamma_s$, γ_l and γ_s denote the surface free energies of liquid and solid surface, respectively. The surface free energy criterion for different condensation modes is outlined in Table H.2.

Table H.2 Condensation mode criteria adapted from Adamson (1990).

Surface free energy difference criteria (mJ/m ²)	Contact angle	Condensation modes
$\Delta\gamma \leq 0$	$\theta_c = 0^\circ$	Filmwise
$0 \leq \Delta\gamma \leq 33.33$	$0^\circ < \theta_c \leq 90^\circ$	Mixed condensation
$\Delta\gamma \geq 33.33$	$\theta_c \geq 90^\circ$	Dropwise

γ_s can be calculated from the measured contact angles between the liquid and the solid surface as (Owens and Wendt, 1967)

$$\gamma_s = \gamma_s^d + \gamma_s^p \quad (\text{H.6})$$

where γ_s^d and γ_s^p denote the dispersion and the polar component of the surface energy. γ_s^d and γ_s^p are given by

$$\gamma_s^d = \left(\frac{137.5 + 256.1 \cos \theta_c - 118.6 \cos^2 \theta_c}{44.92} \right)^2 \quad (\text{H.7})$$

$$\gamma_s^p = \left(\frac{139.9 + 181.4 \cos \theta_c - 41.5 \cos^2 \theta_c}{44.92} \right)^2 \quad (\text{H.8})$$

The surface energy of the liquid (γ_l) within $10^\circ\text{C} \leq T \leq 60^\circ\text{C}$ can be calculated as (Yan and Luo, 2005)

$$\gamma_l = 75.796 - 0.145T - 0.00024T^2 \quad (\text{H.9})$$

where γ_l is evaluated at the film temperature, T_f . The minimum γ_l value obtained for $0.35 \leq \text{FR} \leq 0.55$ within $6.50[\text{W}] \leq \dot{Q}_{\text{in}} \leq 15.20[\text{W}]$ is $72.17 \text{ [mJ/m}^2\text{]}$. For filmwise condensation to occur, i.e., $\Delta\gamma \leq 0$, $\theta_c \leq 19^\circ$. Similarly, for dropwise condensation to occur, i.e., $\Delta\gamma \geq 33.33$, $65^\circ \leq \theta_c \leq 180^\circ$. Thus, $19^\circ < \theta_c < 65^\circ$ can be categorized under the mixed condensation regime. The static contact angles of distilled non deaerate water drops on copper surfaces vary between 60° to 86° (Orlova et al., 2015), and this contact

angle decreases with a decrease in the volume flow rate of the drop formation. Given the very low mass flow rate of condensate (\dot{m}_c) in the present experiments, it is hypothesized that $19^\circ \leq \theta_c \leq 86^\circ$. Therefore, mixed condensation is most likely to occur.

H.5 Nusselt number-Reynolds number correlations

Table H.3 Nu versus Re_F correlations.

Film flow regime	References	Equations representing Nu- Re_F relationship
Laminar ($Re_F \leq 30$)	Nusselt (1916)	$Nu = 1.47(Re_F)^{-\frac{1}{3}}$
	McAdams (1954)	$Nu = 1.88(Re_F)^{-\frac{1}{3}}$
	Ueda and Tanaka (1974) Ueda and Nose (1974)	$Nu = 1.76(Re_F)^{-\frac{1}{3}}$
Laminar ($Re_F \leq 2460Pr_1^{-0.646}$)	Wilke (1962)	
Laminar-wavy ($30 \leq Re_F \leq 1800$)	Kutateladze (1963) Butterworth (1981)	$Nu = \frac{Re_F}{1.08Re_F^{1.22}-5.2}$
	Zazuli and Kutateladze (1963)	$Nu = 1.01(Re_F)^{-0.223}$
	Labuntsov Kutateladze and Gogonin (1979)	$Nu = 1.39(Re_F)^{-\frac{22}{75}}$
Laminar-wavy ($2460Pr_1^{-0.646} \leq Re_F < 1600$)	Wilke (1962)	$Nu = 0.0323(Re_F)^{0.2}Pr_1^{0.34}$
Turbulent $Re_F \geq 1800$	Kirkbride and Badger McAdams (1954)	$Nu = 0.0077(Re_F)^{0.4}$
	Chun and Seban (1971)	$Nu = \frac{2.297 \times 10^{-3}(Re_F)^{0.4}Pr_1^{0.65}}{1-(Re_{F,Tr})^{0.2}(Re_F)^{-0.6} + 2.269 \times 10^{-3}(Re_{F,Tr})^{1.22}(Re_F)^{-0.6}Pr_1^{0.65}}$ $Re_{F,Tr} = 5800Pr_1^{-1.065}$
		$Nu = \frac{2.297 \times 10^{-3}(Re_F)^{0.4}Pr_1^{0.65}}{1-(Re_{F,Tr})^{0.2}(Re_F)^{-0.6} + 2.269 \times 10^{-3}(Re_{F,Tr})^{1.22}(Re_F)^{-0.6}Pr_1^{0.65}}$ $Re_{F,Tr} = 2460Pr_1^{-1.065}$
Turbulent ($1600 \leq Re_F < 3200$)	Wilke (1962)	$Nu = 0.00102(Re_F)^{\frac{2}{3}}Pr_1^{0.344}$
Turbulent $Re_F \geq 3200$		$Nu = 0.00871(Re_F)^{\frac{2}{5}}Pr_1^{0.344}$
All film regimes $10 < Re_F < 3.1 \times 10^4$	Chun and Kim (1991)	$Nu = 1.33(Re_F)^{-\frac{1}{3}} + 9.56 \times 10^{-6}(Re_F)^{0.89}Pr_1^{0.94} + 8.22 \times 10^{-2}$

H.6 Effects of Prandtl number (Pr_1) on Nusselt number (Nu)

Figure H.3a shows the plot of the Prandtl number (Pr_1) versus \dot{Q}_{in} . Pr_1 is computed as $Pr_1 = \frac{\mu_l c_{p,l}}{k_l}$. As T_f increases, μ_l decreases, whilst k_l increases. Examining the steam table reveals that $c_{p,l}$ decreases until $\sim 40^\circ[C]$, whilst it increases after that range. The T_f magnitudes plotted in Figure 6.12 reveal that $T_f < 40^\circ[C]$ and, thus, $c_{p,l}$ will decrease with increase in \dot{Q}_{in} . Therefore, Pr_1 will decrease with \dot{Q}_{in} as seen in Figure 6.16a.

Figure H.3b shows the plot of Nu vs Pr_1 . The trend of Nu with Pr_1 is similar to that obtained for Nu vs $\left(\frac{\rho_l}{\rho_v}\right)$ i.e. Nu is nearly constant until $Pr_1 \sim 6.5$, after which there is steady decline in Nu values with Pr_1 . For heat transfer through a single droplet, the thermal diffusion plays a major role since conduction resistance accounts for almost 70-85% of total drop resistance (Graham., 1969). Since an increase in Pr_1 suggests a drop in the thermal diffusion term, the heat transfer is expected to be lower at higher Pr_1 than at lower Pr_1 . This has been shown in Figure H.3b. As Pr_1 decreases, the thermal diffusion should increase, indicating enhanced heat transfer. However, the trend in Nu values at lower Pr_1 suggest that the enhancement might be counterbalanced by the formation of the film (transition from dropwise to filmwise condensation) at higher \dot{Q}_{in} , where the heat transfer is hindered due to the thickness of the falling film.

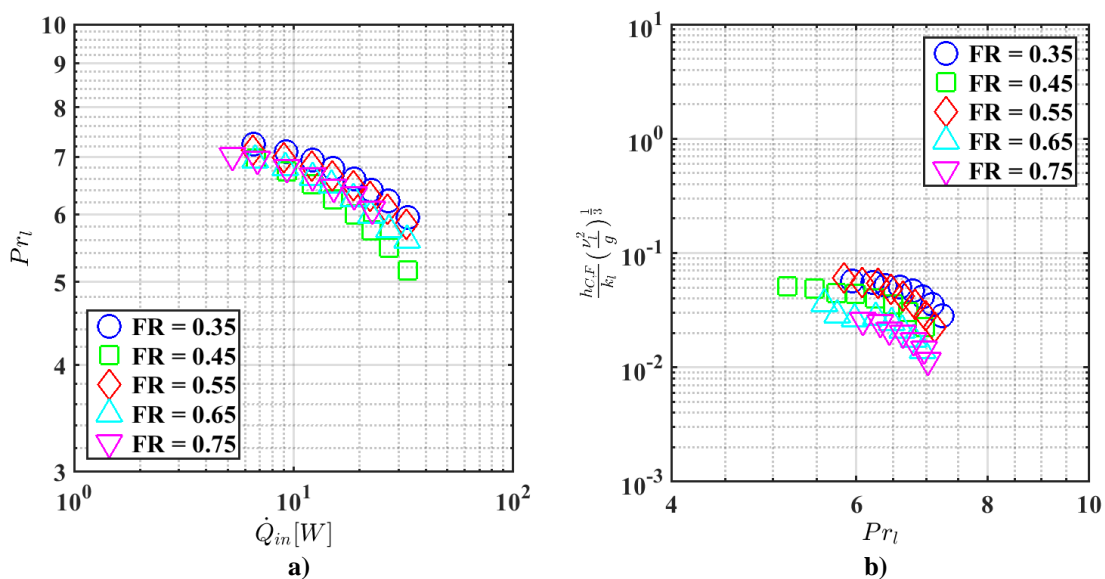


Figure H.3 a) Variation in Pr_1 with \dot{Q}_{in} . b) Variation in Nu with Pr_1 .

H.7 Effects of the vapour flow Froude number (Fr_v) on the Nusselt Number (Nu)

Figure H.4a shows the plot of the vapour flow Froude number (Fr_v) versus \dot{Q}_{in} . Fr_v is computed as $Fr_v = \frac{\dot{Q}_{in}^2}{A_{cr}^2 h_{fg}^2 \rho_v^2 g D_i}$ (Gross, 1992, Spindel, 1982). As \dot{Q}_{in} increases, h_{fg} decreases, whilst ρ_v increases and, therefore, these effects counteract each other. Also, since $Fr_v \propto \dot{Q}_{in}^2$, the overall variation in Fr_v with \dot{Q}_{in} depends on how h_{fg} and ρ_v varies with \dot{Q}_{in} . Figure H.4a also shows that there is a change in the slope of the data around $\dot{Q}_{in} \sim 16[W]$. The slope for $\dot{Q}_{in} \sim 16[W]$ and $\dot{Q}_{in} > 16[W]$ is estimated as 1.59 and 1.11, respectively, indicating that the increment in ρ_v is always higher than the decrement of h_{fg} with \dot{Q}_{in} . The effects are more significant at higher \dot{Q}_{in} and, thus, it can be hypothesized that the slope of Fr_v will decrease further with increasing \dot{Q}_{in} .

Figure H.4b shows the plot Nu vs Fr_v . The increase in Nu values with Fr_v suggests that the inertial effects of the vapour contribute to heat transfer enhancement. The reason for this behaviour can be explained by the effects of τ_i on the drop condensation heat transfer as the functional form of τ_i and Fr_v with respect to \dot{Q}_{in} are similar. An increase in the vapour flow inertia can, therefore, lead to i) early removal of the departing drops, ii) removal of the con-condensable gases and iii) flattening of the condensed droplets. The trend in the Nu values with Fr_v indicates that the first and the second terms are more dominant than the third term.

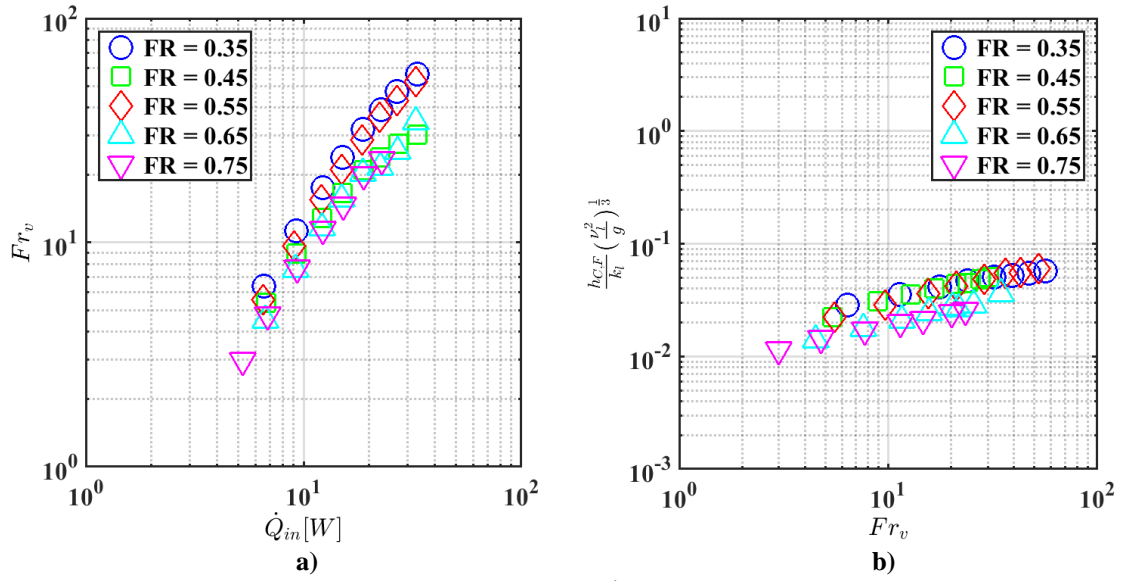


Figure H.4 a) Variation in Fr_v with \dot{Q}_{in} . b) Variation in Nu with Fr_v

**I.1 ELSEVIER LICENSE
TERMS AND CONDITIONS**

Mar 14, 2024

This Agreement between Mr. Dwaipayan Sarkar ("You") and Elsevier ("Elsevier") consists of your license details and the terms and conditions provided by Elsevier and Copyright Clearance Center.

License Number	5692171242779
License date	Dec 18, 2023
Licensed Content Publisher	Elsevier
Licensed Content Publication	International Journal of Heat and Mass Transfer
Licensed Content Title	Dropwise condensation—some factors influencing the validity of heat-transfer measurements
Licensed Content Author	E. Citakoglu, J.W. Rose
Licensed Content Date	Mar 1, 1968
Licensed Content Volume	11

Licensed Content Issue	3
Licensed Content Pages	15
Start Page	523
End Page	537
Type of Use	reuse in a thesis/dissertation
Portion	figures/tables/illustrations
Number of figures/tables/illustrations	1
Format	both print and electronic
Are you the author of this Elsevier article?	No
Will you be translating?	No
Title of new work	Modelling Thermosyphon performance for Mold cooling applications
Institution name	The University of Western Ontario, Canada
Expected presentation date	Jan 2024

Portions

Figure 11

Terms and Conditions

INTRODUCTION

1. The publisher for this copyrighted material is Elsevier. By clicking "accept" in connection with completing this licensing transaction, you agree that the following terms and conditions apply to this transaction (along with the Billing and Payment terms and conditions established by Copyright Clearance Center, Inc. ("CCC"), at the time that you opened your RightsLink account and that are available at any time at <https://myaccount.copyright.com>).

GENERAL TERMS

2. Elsevier hereby grants you permission to reproduce the aforementioned material subject to the terms and conditions indicated.

3. Acknowledgement: If any part of the material to be used (for example, figures) has appeared in our publication with credit or acknowledgement to another source, permission must also be sought from that source. If such permission is not obtained then that material may not be included in your publication/copies. Suitable acknowledgement to the source

I.2 ELSEVIER LICENSE TERMS AND CONDITIONS

Mar 14, 2024

This Agreement between Mr. Dwaipayan Sarkar ("You") and Elsevier ("Elsevier") consists of your license details and the terms and conditions provided by Elsevier and Copyright Clearance Center.

License Number	5692180824005
License date	Dec 18, 2023
Licensed Content Publisher	Elsevier
Licensed Content Publication	International Journal of Heat and Mass Transfer
Licensed Content Title	Drop size distributions and heat transfer in dropwise condensation
Licensed Content Author	Clark Graham, Peter Griffith
Licensed Content Date	Feb 1, 1973
Licensed Content Volume	16

Licensed Content Issue	2
Licensed Content Pages	10
Start Page	337
End Page	346
Type of Use	reuse in a thesis/dissertation
Portion	figures/tables/illustrations
Number of figures/tables/illustrations	1
Format	both print and electronic
Are you the author of this Elsevier article?	No
Will you be translating?	No
Title of new work	Modelling Thermosyphon performance for Mold cooling applications
Institution name	The University of Western Ontario, Canada
Expected presentation date	Jan 2024

Portions

Figure 3

Terms and Conditions

INTRODUCTION

1. The publisher for this copyrighted material is Elsevier. By clicking "accept" in connection with completing this licensing transaction, you agree that the following terms and conditions apply to this transaction (along with the Billing and Payment terms and conditions established by Copyright Clearance Center, Inc. ("CCC"), at the time that you opened your RightsLink account and that are available at any time at <https://myaccount.copyright.com>).

GENERAL TERMS

2. Elsevier hereby grants you permission to reproduce the aforementioned material subject to the terms and conditions indicated.

3. Acknowledgement: If any part of the material to be used (for example, figures) has appeared in our publication with credit or acknowledgement to another source, permission must also be sought from that source. If such permission is not obtained then that material may not be included in your publication/copies. Suitable acknowledgement to the source

I.3 JSME License

COPYRIGHT PERMISSION REQUEST

To
The Japan Society of Mechanical Engineers

【ATTENTION!】 JSME do not grant the permission of whole sentence as report (paper).

I am preparing material for

*Title: PhD Thesis

Author: Dwaipayan Sarkar

Book title or Journal title: Modelling thermal performance of thermosyphons for mold cooling applications

to be published by Publisher: Western University library thesis repository

I am requesting permission to use the material described below, in the original and subsequent editions and/or translations:

Author(s): Ueda, T., MIYASHITA, T. and Chu, P.H.

Title: _____

Book title: _____

Edition: _____ Page: _____

Publication date: _____

or

Journal title: Heat Transport characteristics of a closed two phase thermosyphon

Vol. 32, No. 2 Page or DOI: doi.org/10.1299/jsmeb1988.32.2_239

Publication date: 1989

Material to be used: Figure

Text title and Page: Mean heat transfer coefficient of the cooling section (Water) 241

Figure(s): Figure 5

Table(s): _____

Will appear in the publication* as text or labeled as:

Figure(s): Figure 2.11. Plot of $h_{c,avg}$ versus $\Delta T_{C,F}$ adapted from Ueda et al. (1989) with permission

Table(s): _____

I will credit the original source appears prominently with my book (Journal).

If you will kindly grant permission, please sign below and return one form.

Date: 22/12/2023

From

Name: Dwaipayan Sarkar

Affiliation: Western University, Canada

I grant the permission requested above.

Print name: Tatsunori Ogura

Publishing Department Manager
The Japan Society of Mechanical Engineers

Date: 15/01/2024

This is a License Agreement between Dwaipayan Sarkar ("User") and Copyright Clearance Center, Inc. ("CCC") on behalf of the Rightsholder identified in the order details below. The license consists of the order details, the Marketplace Permissions General Terms and Conditions below, and any Rightsholder Terms and Conditions which are included below.

All payments must be made in full to CCC in accordance with the Marketplace Permissions General Terms and Conditions below.

Order Date	14-Mar-2024	Type of Use	Republish in a thesis/dissertation
Order License ID	1461409-1	Publisher	AMERICAN INSTITUTE OF AERONAUTICS AND ASTRONAUTICS, INC.
ISSN	1533-6808	Portion	Image/photo/illustration

LICENSED CONTENT

Publication Title	Journal of thermophysics and heat transfer	Publication Type	e-Journal
Article Title	Thermodynamic aspects of heat pipe operation	Start Page	334
Author/Editor	American Institute of Aeronautics and Astronautics.	End Page	340
Date	01/01/1987	Issue	2
Language	English	Volume	8
Country	United States of America	URL	http://www.catchword.com/rpsv/catchword/aiaa/08878722/contp1.htm
Rightsholder	American Inst of Aeronautics & Astronautics (AIAA)		

REQUEST DETAILS

Portion Type	Image/photo/illustration	Distribution	Worldwide
Number of Images / Photos / Illustrations	1	Translation	Original language of publication
Format (select all that apply)	Print, Electronic	Copies for the Disabled?	No
Who Will Republish the Content?	Academic institution	Minor Editing Privileges?	No
Duration of Use	Life of current and all future editions	Incidental Promotional Use?	No
Lifetime Unit Quantity	Up to 499	Currency	CAD
Rights Requested	Main product		

NEW WORK DETAILS

Title	Modelling thermosyphon and heat pipe performance for mold cooling applications	Institution Name	University of Western Ontario
Instructor Name	Christopher DeGroot and Eric Savory	Expected Presentation Date	2024-03-14

ADDITIONAL DETAILS

Order Reference Number	N/A	The Requesting Person / Organization to Appear on the License	Dwaipayyan Sarkar
-------------------------------	-----	--	-------------------

REQUESTED CONTENT DETAILS

Title, Description or Numeric Reference of the Portion(s)	Figure 5	Title of the Article / Chapter the Portion Is From	Thermodynamic aspects of heat pipe operation
Editor of Portion(s)	Richter, Robert; Gottschlich, Joseph	Author of Portion(s)	Richter, Robert; Gottschlich, Joseph
Volume / Edition	8	Issue, if Republishing an Article From a Serial	2
Page or Page Range of Portion	334-340	Publication Date of Portion	1994-04-01

RIGHTSHOLDER TERMS AND CONDITIONS

Verification of copyright ownership is your responsibility. You should only submit requests for materials that are owned by AIAA. Please review the copyright statement for the source material before submitting a reprint permission request, to ensure that AIAA is the copyright owner: For AIAA meeting papers, journal papers, or books with independently authored chapters (e.g., many Progress Series volumes), look at the bottom of the first full-text page (not the cover page). There will be a footnote indicating who holds copyright. For other books, look at the copyright statement on the back of the title page. If the statement reads "Copyright by the American Institute of Aeronautics and Astronautics, Inc.," then AIAA is the copyright owner, and you may submit your request. If the statement reads otherwise, AIAA does not hold copyright, and cannot grant permission to reprint. You must seek permission from the copyright owner rather than AIAA. Preferred credit line for reprinted material: From [original title and authors]; reprinted by permission of the American Institute of Aeronautics and Astronautics, Inc. Note that the original source also should be cited in full in the reference list.

Marketplace Permissions General Terms and Conditions

The following terms and conditions ("General Terms"), together with any applicable Publisher Terms and Conditions, govern User's use of Works pursuant to the Licenses granted by Copyright Clearance Center, Inc. ("CCC") on behalf of the applicable Rightsholders of such Works through CCC's applicable Marketplace transactional licensing services (each, a "Service").

1) **Definitions.** For purposes of these General Terms, the following definitions apply:

"License" is the licensed use the User obtains via the Marketplace platform in a particular licensing transaction, as set forth in the Order Confirmation.

"Order Confirmation" is the confirmation CCC provides to the User at the conclusion of each Marketplace transaction. "Order Confirmation Terms" are additional terms set forth on specific Order Confirmations not set forth in the General Terms that can include terms applicable to a particular CCC transactional licensing service and/or any Rightsholder-specific terms.

"Rightsholder(s)" are the holders of copyright rights in the Works for which a User obtains licenses via the Marketplace platform, which are displayed on specific Order Confirmations.

I.5 ASME License

This is a License Agreement between Dwaipayan Sarkar ("User") and Copyright Clearance Center, Inc. ("CCC") on behalf of the Rightsholder identified in the order details below. The license consists of the order details, the Marketplace Permissions General Terms and Conditions below, and any Rightsholder Terms and Conditions which are included below.

All payments must be made in full to CCC in accordance with the Marketplace Permissions General Terms and Conditions below.

Order Date	14-Mar-2024	Type of Use	Republish in a thesis/dissertation
Order License ID	1461411-1	Publisher Portion	ASME INTERNATIONAL Image/photo/illustration
ISSN	1528-8943		

LICENSED CONTENT

Publication Title	Journal of heat transfer	Publication Type	e-Journal
Article Title	Heat Transfer Correlations for Liquid Film in the Evaporator of Enclosed, Gravity-Assisted Thermosyphons	Start Page	477
		End Page	484
		Issue	2
		Volume	120
Author/Editor	American Society of Mechanical Engineers.	URL	http://ojps.aip.org/ASMEjournals/HeatTransfer
Date	01/01/1959		
Language	English		
Country	United States of America		
Rightsholder	American Society of Mechanical Engineers ASME		

REQUEST DETAILS

Portion Type	Image/photo/illustration	Distribution	Canada
Number of Images / Photos / Illustrations	1	Translation	Original language of publication
Format (select all that apply)	Print, Electronic	Copies for the Disabled?	No
Who Will Republish the Content?	Academic institution	Minor Editing Privileges?	No
Duration of Use	Life of current edition	Incidental Promotional Use?	No
Lifetime Unit Quantity	Up to 499	Currency	CAD
Rights Requested	Main product		

NEW WORK DETAILS

Title	Modelling of thermosyphons for mold cooling applications	Institution Name	University of Western Ontario
--------------	--	-------------------------	-------------------------------

Instructor Name	Christopher DeGroot	Expected Presentation Date	2024-01-30
-----------------	---------------------	----------------------------	------------

ADDITIONAL DETAILS

Order Reference Number	N/A	The Requesting Person / Organization to Appear on the License	Dwaipayyan Sarkar
------------------------	-----	---	-------------------

REQUESTED CONTENT DETAILS

Title, Description or Numeric Reference of the Portion(s)	Figure 3	Title of the Article / Chapter the Portion Is From	Heat Transfer Correlations for Liquid Film in the Evaporator of Enclosed, Gravity-Assisted Thermosyphons
Editor of Portion(s)	El-Genk, M. S.; Saber, H. H.	Author of Portion(s)	El-Genk, M. S.; Saber, H. H.
Volume / Edition	120	Issue, if Republishing an Article From a Serial	2
Page or Page Range of Portion	477-484	Publication Date of Portion	1998-01-01

SPECIAL RIGHTSHOLDER TERMS AND CONDITIONS

Permission is granted for the specific use of the ASME Figure 3 ONLY as stated herein and does not permit further use of the materials without proper authorization. As is customary, we request that you ensure proper acknowledgment of the exact sources of this material, the authors, and ASME as original publisher.

Marketplace Permissions General Terms and Conditions

The following terms and conditions ("General Terms"), together with any applicable Publisher Terms and Conditions, govern User's use of Works pursuant to the Licenses granted by Copyright Clearance Center, Inc. ("CCC") on behalf of the applicable Rightsholders of such Works through CCC's applicable Marketplace transactional licensing services (each, a "Service").

1) **Definitions.** For purposes of these General Terms, the following definitions apply:

"License" is the licensed use the User obtains via the Marketplace platform in a particular licensing transaction, as set forth in the Order Confirmation.

"Order Confirmation" is the confirmation CCC provides to the User at the conclusion of each Marketplace transaction. "Order Confirmation Terms" are additional terms set forth on specific Order Confirmations not set forth in the General Terms that can include terms applicable to a particular CCC transactional licensing service and/or any Rightsholder-specific terms.

"Rightsholder(s)" are the holders of copyright rights in the Works for which a User obtains licenses via the Marketplace platform, which are displayed on specific Order Confirmations.

"Terms" means the terms and conditions set forth in these General Terms and any additional Order Confirmation Terms collectively.

"User" or "you" is the person or entity making the use granted under the relevant License. Where the person accepting the Terms on behalf of a User is a freelancer or other third party who the User authorized to accept the General Terms on the User's behalf, such person shall be deemed jointly a User for purposes of such Terms.

"Work(s)" are the copyright protected works described in relevant Order Confirmations.

I.6 ELSEVIER LICENSE TERMS AND CONDITIONS

Mar 14, 2024

This Agreement between Mr. Dwaipayan Sarkar ("You") and Elsevier ("Elsevier") consists of your license details and the terms and conditions provided by Elsevier and Copyright Clearance Center.

License Number	5692170157170
License date	Dec 18, 2023
Licensed Content Publisher	Elsevier
Licensed Content Publication	International Journal of Heat and Mass Transfer
Licensed Content Title	A network thermodynamic analysis of the heat pipe
Licensed Content Author	Z.J. Zuo,A. Faghri
Licensed Content Date	Jun 1, 1998
Licensed Content Volume	41

Licensed Content Issue	11
Licensed Content Pages	12
Start Page	1473
End Page	1484
Type of Use	reuse in a thesis/dissertation
Portion	figures/tables/illustrations
Number of figures/tables/illustrations	1
Format	both print and electronic
Are you the author of this Elsevier article?	No
Will you be translating?	No
Title of new work	Modelling Thermosyphon performance for Mold cooling applications
Institution name	The University of Western Ontario, Canada
Expected presentation date	Jan 2024

Portions

Figure 3

Terms and Conditions

INTRODUCTION

1. The publisher for this copyrighted material is Elsevier. By clicking "accept" in connection with completing this licensing transaction, you agree that the following terms and conditions apply to this transaction (along with the Billing and Payment terms and conditions established by Copyright Clearance Center, Inc. ("CCC"), at the time that you opened your RightsLink account and that are available at any time at <https://myaccount.copyright.com>).

GENERAL TERMS

2. Elsevier hereby grants you permission to reproduce the aforementioned material subject to the terms and conditions indicated.

3. Acknowledgement: If any part of the material to be used (for example, figures) has appeared in our publication with credit or acknowledgement to another source, permission must also be sought from that source. If such permission is not obtained then that material may not be included in your publication/copies. Suitable acknowledgement to the source

I.7 ELSEVIER LICENSE TERMS AND CONDITIONS

Mar 14, 2024

This Agreement between Mr. Dwaipayan Sarkar ("You") and Elsevier ("Elsevier") consists of your license details and the terms and conditions provided by Elsevier and Copyright Clearance Center.

License Number	5692170993331
License date	Dec 18, 2023
Licensed Content Publisher	Elsevier
Licensed Content Publication	Applied Thermal Engineering
Licensed Content Title	Entropy generation in a heat pipe system
Licensed Content Author	H. Khalkhali,A. Faghri,Z.J. Zuo
Licensed Content Date	Oct 1, 1999
Licensed Content Volume	19
Licensed Content Issue	10

Licensed Content Pages	17
Start Page	1027
End Page	1043
Type of Use	reuse in a thesis/dissertation
Portion	figures/tables/illustrations
Number of figures/tables/illustrations	1
Format	both print and electronic
Are you the author of this Elsevier article?	No
Will you be translating?	No
Title of new work	Modelling Thermosyphon performance for Mold cooling applications
Institution name	The University of Western Ontario, Canada
Expected presentation date	Jan 2024
Portions	Figure 4

Terms and Conditions

INTRODUCTION

1. The publisher for this copyrighted material is Elsevier. By clicking "accept" in connection with completing this licensing transaction, you agree that the following terms and conditions apply to this transaction (along with the Billing and Payment terms and conditions established by Copyright Clearance Center, Inc. ("CCC"), at the time that you opened your RightsLink account and that are available at any time at <https://myaccount.copyright.com>).

GENERAL TERMS

2. Elsevier hereby grants you permission to reproduce the aforementioned material subject to the terms and conditions indicated.

3. Acknowledgement: If any part of the material to be used (for example, figures) has appeared in our publication with credit or acknowledgement to another source, permission must also be sought from that source. If such permission is not obtained then that material may not be included in your publication/copies. Suitable acknowledgement to the source must be made, either as a footnote or in a reference list at the end of your publication, as follows:

I.8 AIP PUBLISHING LICENSE TERMS AND CONDITIONS

Mar 14, 2024

This Agreement between Mr. Dwaipayan Sarkar ("You") and AIP Publishing ("AIP Publishing") consists of your license details and the terms and conditions provided by AIP Publishing and Copyright Clearance Center.

License Number 5747651449561

License date Mar 14, 2024

Licensed Content
Publisher AIP Publishing

Licensed Content
Publication Physics of Fluids

Licensed Content Title Thermodynamic modeling of thermosyphons and heat pipes

Licensed Content Author Sarkar, D.; Savory, E.; DeGroot, C.

Licensed Content Date Dec 6, 2023

Licensed Content Volume 35

Licensed Content Issue	12
Type of Use	Thesis/Dissertation
Requestor type	Author (original article)
Format	Print and electronic
Portion	Excerpt (> 800 words)
Will you be translating?	No
Title of new work	Modelling Thermosyphon and heat pipe performance for Mold cooling applications
Institution name	The University of Western Ontario, Canada
Expected presentation date	Mar 2024
Portions	All the Figures and tables from the article. The equations are also used in my thesis.

Terms and Conditions

AIP Publishing -- Terms and Conditions: Permissions Uses

AIP Publishing hereby grants to you the non-exclusive right and license to use and/or distribute the Material according to the use specified in your order, on a one-time basis, for the specified term, with a maximum distribution equal to the number that you have ordered. Any links or other content accompanying the Material are not the subject of this license.

1. You agree to include the following copyright and permission notice with the reproduction of the Material: "Reprinted from [FULL CITATION], with the permission of AIP Publishing." For an article, the credit line and permission notice must be printed on the first page of the article or book chapter. For photographs, covers, or tables, the notice may appear with the Material, in a footnote, or in the reference list.
2. If you have licensed reuse of a figure, photograph, cover, or table, it is your responsibility to ensure that the material is original to AIP Publishing and does not contain the copyright of another entity, and that the copyright notice of the figure, photograph, cover, or table does not indicate that it was reprinted by AIP Publishing, with permission, from another source. Under no circumstances does AIP Publishing purport or intend to grant permission to reuse material to which it does not hold appropriate rights.
You may not alter or modify the Material in any manner. You may translate the Material into another language only if you have licensed translation rights. You may not use the Material for promotional purposes.
3. The foregoing license shall not take effect unless and until AIP Publishing or its agent, Copyright Clearance Center, receives the Payment in accordance with Copyright Clearance Center Billing and Payment Terms and Conditions, which are incorporated herein by reference.
4. AIP Publishing or Copyright Clearance Center may, within two business days of granting this license, revoke the license for any reason whatsoever, with a full refund payable to you. Should you violate the terms of this license at any time, AIP Publishing, or Copyright Clearance Center may revoke the license with no refund to you. Notice of such revocation will be made using the contact information provided by you. Failure to receive such notice will not nullify the revocation.

Curriculum Vitae

Name:	Dwaipayan Sarkar
Post-secondary Education and Degrees:	National Institute of Technology Durgapur, West Bengal, India 2011-2015 B.Tech.
	The University of Western Ontario London, Ontario, Canada 2016-2018 MEdSc.
	The University of Western Ontario London, Ontario, Canada 2018-2023 Ph.D.
Honours and Awards:	MITACS Accelerate 2018-2022
	NSERC Scholarship 2022-2023
Related Work Experience	Teaching Assistant The University of Western Ontario 2016-2022

Publications:

Sarkar, D., Upadhyay, N., Roy, S. and Rana, S.C., 2017. Immersed boundary simulation of flow through arterial junctions. *Sādhanā*, 42, pp. 533-541.

Sarkar, D. and Savory, E., 2021. Numerical modeling of freestream turbulence decay using different commercial computational fluid dynamics codes. *Journal of Fluids Engineering*, 143(4), p.041503.

Sarkar, D. and Savory, E., 2022. A prediction method for spatially decaying freestream turbulence. *Journal of Turbulence*, 23(3), pp.124-151.

Sarkar, D., Savory, E. and DeGroot, C., 2023. Thermodynamic modeling of thermosyphons and heat pipes. *Physics of Fluids*, 35(12).

Conference Presentations:

Sarkar, D., Graat, K., Savory, E., 2017. Effect of freestream turbulence on smooth flat plate heat transfer *CFD Society of Canada Conference*, University of Windsor, Windsor, June 18-20, pp. 1- 11.

Sarkar, D., Savory, E, 2018. A prediction tool for spatially decaying freestream turbulence, *Proceedings of the Canadian society for mechanical engineering International Congress*, May 27-30, 2018, Toronto, ON, Canada.

Sarkar, D., Savory, E. and DeGroot, C., 2019 CFD modelling of flow and heat transfer in a thermosyphon, *Proceedings of the Joint Canadian Society for Mechanical Engineering and CFD Society of Canada International Congress*, CSME-CFDSC Congress 2019, Western University, London, June 2-5, 2019.

Sarkar, D., Savory, E, 2019. Design of passive wind-tunnel grids using a prediction model for turbulence intensity, *Proceedings of the Joint Canadian Society for Mechanical Engineering and CFD Society of Canada International Congress*, CSME-CFDSC Congress 2019, Western University, London, June 2-5, 2019, pp. 1- 8.

Sarkar, D., Savory, E. and DeGroot, C., 2021 An investigation of thermal performance of heat pipes under different operating conditions, *Proceedings of the Canadian Society for Mechanical Engineering International Congress 2021*, Charlottetown, PEI, June 27-30, 2021 (Virtual).

Sarkar, D., Savory, E. and DeGroot, C., 2022 An investigation of thermal performance of heat pipes under different operating conditions, *Proceedings of the Canadian Society for Mechanical Engineering International Congress 2022*, University of Alberta, Edmonton, June 5-8, 2022.

Sarkar, D., Savory, E. and DeGroot, C., 2023, Thermodynamic evaluation of thermosyphons and heat pipes, *Proceedings of the Canadian Society for Mechanical Engineering International Congress 2023*, University of Sherbrooke, Sherbrooke, May 28-31, 2023, pp. 1-6.